The Topochemical Polymerisation of Radiation-Sensitive 10,12-Pentacosadiynoic Acid as Different Multicomponent Solid Forms

AMY VICTORIA HALL

The Topochemical Polymerisation of Radiation-Sensitive 10,12-Pentacosadiynoic Acid as Different Multicomponent Solid Forms

A thesis submitted in fulfilment of the requirements for the degree of

Doctor of Philosophy

In the Department of Chemistry at Durham University

By

Amy Victoria Hall

September 2020

Abstract

In this work, the relationship between the solid-state photoreactivity of 10,12-pentacosadiynoic acid (PCDA) and its X-ray structure has been established. The characterisation of PCDA was used to elucidate the structures of the different forms of a lithium salt of PCDA (Li-PCDA) as the single-crystal X-ray structures could not be obtained. Li-PCDA is currently used in radiochromic films due to its impressive colour change from colourless to blue upon irradiation. In addition to Li-PCDA, a lithium salt of 5,7-hexadecadiynoic acid was synthesised and displays greater photoreactivity than Li-PCDA upon UV irradiation. Additionally, a sodium salt of PCDA was crystallised and reveals the salt is outside of the topochemical postulate for reactivity and is, therefore, unreactive. Furthermore, a bismuth complex of PCDA was also synthesised, however, further work is required to fully understand the photoresponsive material.

To investigate how PCDA would behave as a cocrystal with organic coformers, model compounds of short-chain *n*-alkyl carboxylic acids cocrystallised with dipyridyl derivatives and were synthesised in solution and by grinding to give new materials. When PCDA was combined with the same dipyridyl coformers, the resulting cocrystals do not respond to UV irradiation. Additionally, when PCDA is combined with an aliphatic bifunctional compound, similar in structure to the bipyridyl coformers, a PCDA cocrystal salt is formed that is also unreactive to radiation. Further PCDA cocrystal salts are synthesised when combined with aliphatic monofunctional coformers that produce a range of colourful powders before and after UV exposure. The enhanced reactivity of the monofunctional cocrystal salts is reinforced by the X-ray structures which confirm that the structures adhere to the topochemical postulate, further emphasising the importance of the criteria to predict the photopolymerisation of diacetylene systems. These photosensitive materials contribute to the improvement of radiochromic materials, such as dosimetric films.

Declaration

The work described in this thesis was undertaken in the Department of Chemistry at Durham University (UK) between October 2017 and September 2020, under the supervision of Professor Jonathan W. Steed of Durham University and Dr Osama M. Musa of Ashland LLC. This work has not been previously submitted for a degree at this or any other university.

All X-ray structures were collected and processed by Dr Dmitry Yufit, apart from 2PCDA·bipip (Chapter 4) which was collected and processed by Dr Andrei Batsanov. Structures PCDA (Chapter 2), Na-PCDA (Chapter 2), and 2PCDA·4bipy (100K, Chapter 4) were collected on the I19 beamline of the Diamond Light Source synchrotron. All solid-state NMR data was collected by Dr David Apperley. All Raman spectroscopy data were collected by Dr Larry Senak at Ashland LLC. In Chapter 3, the single-crystals and powders were obtained in collaboration with Miss Yingfeng Zhang, an undergraduate student supervised by the author.

Statement of Copyright

Financial Support

This work was funded by Ashland LLC and the Engineering and Physical Sciences Research Council (EPSRC).

Publications

Scientific Papers:

1. "**The Crystal Engineering of Radiation-Sensitive Diacetylene Cocrystals and Salts**", A. V. Hall, D. S. Yufit, D. C. Apperley, L. Senak, O. M. Musa, D. K. Hood and J. W. Steed, *Chem. Sci.*, 2020, **11**, 8025-8035.
2. "**Properties and Applications of Stimuli-responsive Diacetylenes**", A. V. Hall, O. M. Musa, J. W. Steed, in preparation.

Book Chapters:

1. "**Hydration Behaviour of Polylactam Clathrate Hydrate Inhibitors and their Small-Molecule Model Compounds**", L. I. Chambers, A. V. Hall, O. M. Musa and J. W. Steed in *Handbook of Pyrrolidone and Caprolactam Based Materials: Synthesis, Properties and Industrial Applications*, Osama M. Musa, ed., Wiley: Chichester, 2020, ch 13, in press.
2. "**Cocrystals, Coamorphous Phases and Coordination Complexes of γ- and ε-Lactams**", A. V. Hall, L. I. Chambers, O. M. Musa, and J. W. Steed in *Handbook of Pyrrolidone and Caprolactam Based Materials: Synthesis, Properties and Industrial Applications*, Osama M. Musa, ed., Wiley: Chichester, 2020, ch 14, in press.

Patents:

1. US Provisional Patent Application No. 63/019,109 filed 1/5/20 "**Compositions Comprising Energy-Sensitive Adducts of Acetylenic Compounds**" O. M. Musa, D. K. Hood, A. V. Hall, and J. W. Steed.

Acknowledgements

Firstly, I would like to thank Nick Blagden for recommending I contact Jonathan Steed for a postgraduate position. Jon believed in me enough to accept me into his group and has supported me without hesitation for the last three years. I could not have asked for a more knowledgeable and kinder supervisor. I am also grateful for Osama Musa and the Advanced Materials team at Ashland for providing the opportunity to work on such an interesting and versatile project. In the department, I would like to thank Dmitry Yufit and David Apperley for their patience and analysing what may have seemed like an endless stream of samples. And of course, my PhD would not have been as enjoyable without the Steed group members for entertaining my random quips and poor quality jokes for the duration of my PhD (Jess Andrews, James Smith, Lottie Ayres, and Luke Chambers, I'm looking at you). I would especially like to thank my first summer student, Yingfeng (Linda) Zhang, for her hard work in the lab over the summer of 2018, which yielded excellent results that helped to shape the future of my PhD research.

Outside of the chemistry department, I would like to thank my parents, Stuart Hall and Lyndsay Marriott for trusting me to choose my own path in life. I would also like to say thank you to my brothers, Ashley Hall and Joseph Andrews, for helping me from afar. I would like to express my gratitude to Lee Guy for his constant reassurance of my progress when I could not remind myself, and for never once doubting my capabilities. You have done more for me than you know. Additionally, I would like to thank Les and Diane Guy for their continual support on my PhD journey and accepting me into their family. I am also grateful for my best friend, Elizabeth Gent, for always being there for me (and especially for gifting me biscuits during a global pandemic!).

This thesis is dedicated to my wonderful grandparents, Graham and Jacqueline Marriott, Verdun Hall, and Dee Evans.

Table of Contents

Abbreviations

2Bipy – 2,2'-Bipyridyl

4Bipy – 4,4'-Bipyridyl

AFM – Atomic Force Microscopy

AFM-FM – Atomic Force and Fluorescence Microscopy

API – Active Pharmaceutical Ingredient

APPCDA – *p*-Phenylenediamine PCDA

ASAP – Atmospheric Solids Analysis Probe

Azp – 4,4'-Azopyridine

Bipip – 4,4'-Bipieridine

BP – Benzophenone

BpdA – 4,4'-Biphenyldicarboxylic acid

Bpe – *trans*-1,2-bis(4-pyridyl)ethylene

ButA – Butanoic acid

Butam – *n*-Butylamine

CDP – Cyclic dipeptides

CNC – Cellulose nanocrystals

CNT – Carbon nanotube

COVID-19 – Coronavirus disease 2019

CSD – Cambridge Structural Database

DA-mPhC – bis(N-phenylcarbamate) diacetylene

DCDA – 10,12-Docosandiynoic acid

Dietam – Diethylamine

DMPC – 1,2-Dimyristoyl-*sn*-glycero-3-phosphocholine

DMPG – 1,2-Dimyristoyl-*sn*-glycero-3-phospho-(1′-*rac*-glycerol)

DNA – Deoxyribonucleic acid

DSC – Differential Scanning Calorimetry

EicoA – Eicosanoic acid

Etdiam – Ethylenediamine

EthA – Ethanoic acid

FDA – Food and Drug Administration

FTIR – Fourier Transform Infrared Spectroscopy

HDDA – 5,7-Hexadecadiynoic acid

HEEPCDA – 2-(2-Aminoethoxyl)ethanol PCDA

HexA – Hexanoic acid

HOMO – Highest Occupied Molecular Orbital

IUPAC – International Union of Pure and Applied Chemistry

LAG – Liquid Assisted Grinding

Li-HDDA – Lithium 5,7-hexadecadiynoate

Li-PCDA – Lithium 10,12-pentacosadiynoate

LUMO – Lowest Unoccupied Molecular Orbital

MA – Melamine

MALDI – Matrix-assisted Laser Desorption/Ionization

mBzA – 3-Aminobenzoic acid

MeOH – Methanol

MethA – Methanoic acid

miRNA – Micro ribonucleic acid

Morph – Morpholine

MPP - 2-Methyl-4′-(methylthio)-2-

morpholinopropiophenone

Na-PCDA – Sodium 10,12-pentacosadiynoate

NMR – Nuclear Magnetic Resonance

NPA – 6-Amino-2-naphthoic acid

NSOM – Near-Field Scanning Optical Microscopy

NTA – 2,2’2”-Nitrilotriacetate

PAM – Pralidoxime

pBzS – 4-Aminobenzenesulfonic acid

Pca – Pyrazine carboxamide

PCDA – 10,12-Pentacosadiynoic acid

PdA – 2,5-Pyridinedicarboxylic acid

PDA – Polydiacetylene

PentA – Pentanoic acid

PEO – Poly(ethylene oxide)

PF – Perfluorotetradecanoic acid

Piper – Piperidine

PU – Polyurethane

PVA – Polyvinyl alcohol

PVB – Polyvinyl butyral

PVDC – Polyvinylidene difluoride

PVP – Polyvinylpyrolidone

PXRD – Powder X-ray Diffraction

Pyz – Pyrazine

RNA – Ribonucleic acid

SC-XRD – Single Crystal X-ray Diffraction

SDS – Sodium Dodecyl Sulfate

SEM – Scanning Electron Microscopy

ssNMR – ^{13}C CP-MAS Solid State Nuclear Magnetic Resonance Spectroscopy

TCDA – 10,12-Tricosadiynoic acid

TePDA – Tetrahedral polydiacetylene

TGA – Thermogravimetric Analysis

TNT – Trinitrotoluene

UV – Ultraviolet

1. Introduction

1.1. Multicomponent Solid Forms

There are numerous ways in which molecules can be arranged in the solid state. For example, in crystalline and amorphous materials, which involve long-range and only local order, respectively. Crystalline multicomponent solid forms in stoichiometric ratios involve the formation of a cocrystal (two or more different neutral molecules in a crystal lattice joined by noncovalent interactions) or a salt (consists of two or more oppositely charged molecules in a crystal lattice).[1, 2] If one or more neutral molecules are crystallised with a solvent, they are named 'solvates', though if the solvent is water, the term 'hydrate' is used. However, crossovers exist between cocrystals and salts, for instance, cocrystal solvates, salt cocrystals, salt solvates, and cocrystal salt solvates.[3] This suggests that cocrystals and salts exist in the same continuum.[4, 5] Multicomponent forms that do not have a defined stoichiometry involve inclusion compounds, clathrates, and solid solutions.[6] For non-crystalline solids, amorphous and glass states exist, though if two or more low molecular weight coformers are combined and have a single glass-transition temperature, then coamorphous materials are formed. The relationships between these various solid forms are illustrated in Figure 1.1.

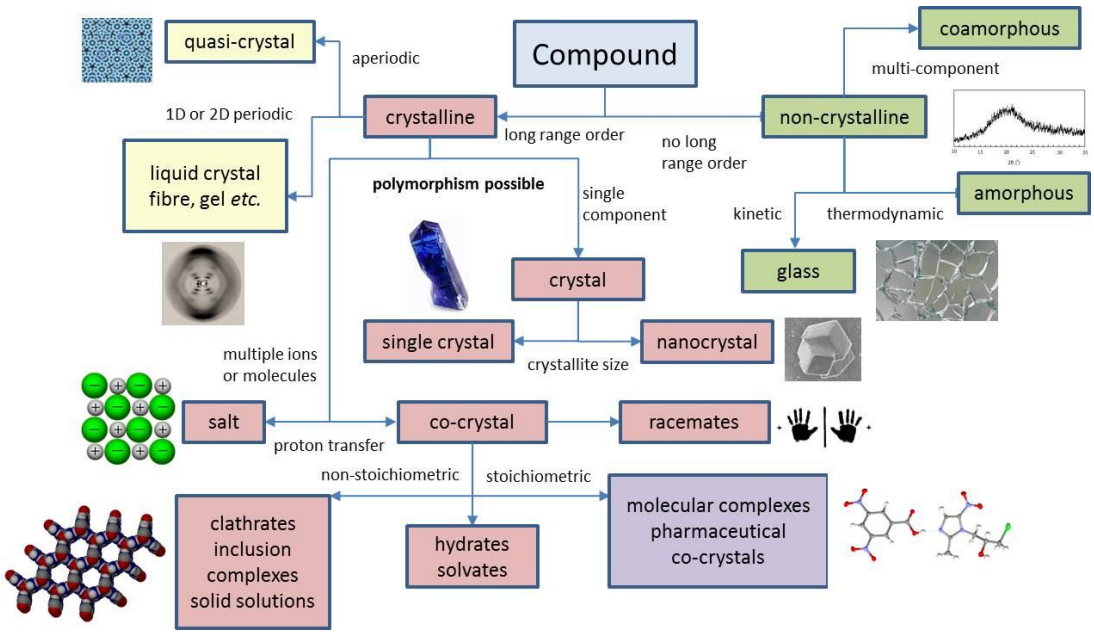

Figure 1.1. A summary of the relationship between different solid forms, reproduced with permission from reference 7.

Cocrystals and salts in particular are of significant interest to the pharmaceutical industry due to their potential to improve drug solubility, stability, and processing characteristics, compared to the pure active pharmaceutical ingredient (API) itself.[8] The Food and Drug Administration (FDA) classifies cocrystals as crystalline materials composed of two or more different molecules, typically APIs and approved, non-toxic cocrystal former (coformer), in the same crystal lattice.[9] The definition of a cocrystal extends further to include the coformers must be solids at room temperature, which actively excludes solvates and hydrates (pseudopolymorphs) and solid-state host-guest compounds.[1] However, this narrowing definition would mean that some materials (i.e. low melting solids) may be regarded as cocrystals in some laboratories and not others.[2, 10, 11] Additionally, the important difference between a cocrystal and a salt is the proton transfer from an acid to a base, however, depending on the temperature salts and cocrystals can interconvert.[4, 7, 12, 13] Also, all types of multicomponent solid forms can exhibit polymorphism, which is defined by McCrone as "a solid crystalline phase of a given compound resulting from the possibility of at least two different arrangements of the molecules of that compound in the solid state".[14] Out of all the different multicomponent solid forms, cocrystals are perhaps the most studied in terms of their polymorphic behaviour.[15-19] A 2007 study found that from 254 polymorph screens, 90 % gave rise to multiple solid forms, while more than 50 % of these forms exhibited polymorphism,[20] thus reinforcing the importance of polymorph screens for multicomponent forms.

1.2. Crystallisation Mechanisms

1.2.1. Crystal Nucleation and Growth

The formation of crystals in solution occurs by two principle steps, crystal nucleation and crystal growth. Nucleation involves the aggregation of molecules into an ordered cluster under non-equilibrium conditions. When the cluster reaches a critical size, supersaturation is achieved, and the nuclei will no longer re-dissolve and can form a stable nucleus.[21] The more supersaturated the solution, the smaller the size of the stable nucleus to result in more nuclei.[21, 22] Crystal nucleation can either be primary or secondary. Primary nucleation involves homogenous (spontaneous nucleation, though rare due to the large energy barrier) and heterogeneous (nucleation is induced by

external stimuli e.g. a foreign additive such as glass, hair, or dust).[23] Secondary nucleation is induced by the presence of crystalline material acting as a seed in the solution. Primary nucleation can be described by classical nucleation theory.[21] This theory states that all nuclei are formed by the combination of individual molecules until the critical nucleus radius is achieved, however, nucleation has to overcome an energy barrier in the supersaturated phase.[24] Although, numerous evidence has proved that nucleation behaves differently, the classical nucleation theory ignores the possibility that multiple sub-critical clusters may combine to form a nucleus.[25] In response to this, the non-classical (i.e. two-step) nucleation theory was hypothesised and provides a more comprehensive overview where the molecules aggregate as disordered and dense liquid clusters opposed to the defined clusters involved in classical nucleation theory.[23, 26] The two models of crystal nucleation are outlined in Figure 1.2.

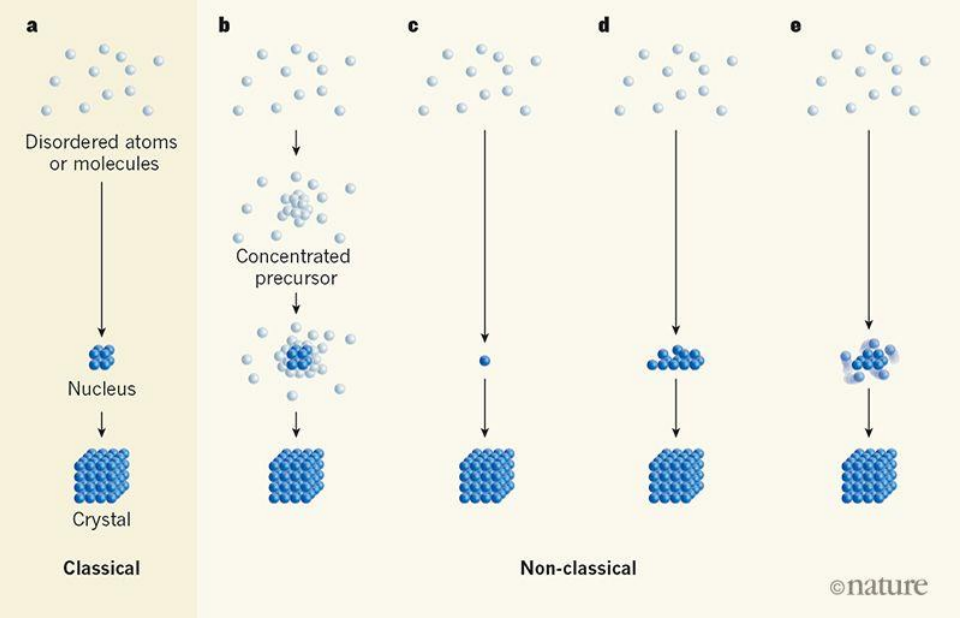

Figure 1.2. The classical and non-classical nucleation theories. a) Atoms or molecules in the classical nucleation theory organise into nuclei at a specific shape and size with defined edges. b) Non-classical nucleation theory describes the formation of disordered clusters that are more concentrated than the starting phase. c) Only one or a few atoms can act as a nucleus. d) Nuclei can adapt the lattice shape of the emerging crystal. e) Non-classical nucleation theory also describes the possibility that nuclei have diffuse edges and adopt non-equilibrium shapes. Figure reproduced with permission from reference 24.

Once a stable nucleus has formed from a supersaturated solution, crystal growth occurs to form a macroscopic material with well-defined faces. The crystal growth process is influenced by conditions such as temperature, pressure, degree of supersaturation, and presence of impurities.[22] To understand the kinetics and mechanisms involved in the process, different theories of crystal growth have been developed that include surface energy, adsorption at the growth surface, and rate of diffusion to explain how a crystal develops.[22] The surface energy theory (Gibbs-Curie-Wulff growth law) is based on thermodynamic equilibrium principles and suggests that the morphology of the resulting macroscopic crystal can be controlled by the most energetically unstable crystal faces forming the fastest and being replaced by the more stable, lower surface energy crystal faces to grow the crystal.[27, 28] However, this theory is limited as factors such as supersaturation are not considered.[27] Adsorption theories such as the terrace-ledge-kink theory are based on two-dimensional models that focus on the reversible placement of a growth unit (a cube in this instance) on a growing crystal at either flat surfaces (terrace), kinks, or step (ledge) sites.[29] A terrace involves contact at only one side of the growth unit and is likely to dissociate, while ledge sites provide two attachment surfaces of the growth unit, and kink sites provide three attachment surfaces and are, therefore, a favoured site.[30] Lastly, diffusion theories of crystal growth focus on the continual deposition of a solute from solution onto the growing crystal face caused by the concentration gradient.[31] Supersaturation is the driving force while diffusion is the limiting factor.

1.2.2. Crystallisation Methods

In crystallisation experiments from solution, the desired compound(s) goes through a series of stages to form a macroscopic crystal, Figure 1.3. Firstly, an undersaturated solution is created by dissolving the compound in a suitable solvent, either by excess solvent or at elevated temperature (A). Once the solvent begins to evaporate or cool, the system becomes supersaturated and exists in a metastable zone (B-D). The metastable zone can be divided into the dead zone (B) which marks primary heterogeneous crystallisation in unseeded crystallisations, while zone C represents the growth region only, and zone D marks crystal proliferation.[32] Increasing supersaturation gives rise to spontaneous primary nucleation (E) and is often referred to as the liable zone. In practice, many crystallisation techniques are possible, though the most popular methods are slow evaporation, slow cooling, vapour diffusion, and

the layering technique. The slow evaporation of an undersaturated solution (containing approximately 10 mg of the desired compound) occurs when the crystallisation container is exposed to the ambient conditions in the laboratory, though with the opening covered by a loose-fitting or pierced lid.[33] The covering of the container allows the solvent vapour to dissipate and keeps the crystallisation free from impurities such as dust and hair which will affect how the crystals nucleate and grow. In contrast, slow cooling requires a saturated solution to be exposed to heat until all of the material has dissolved and is then placed in a hot environment (e.g. temperature-controlled oven, water, oil bath) and allowed to cool to room temperature over a long period.[34] The vapour diffusion technique involves an inner container with approximately 4 mg of the desired compound dissolved in a solvent, with the outer container containing an antisolvent which is more volatile than the solvent used to dissolve the compound in the inner container.[35] Examples of recommended solvents for the vapour diffusion technique are present in Table 1.1. Lastly, the layering (liquid diffusion) technique requires the desired compound to be dissolved in a dense solvent to give a concentrated solution. A miscible antisolvent that is less dense than the lower layer is layered on top with the use of a pipette.[35] For insoluble compounds, a buffer layer can be used between the solution and antisolvent to lower the solubility of the system and result in crystallisation.[35] This technique is especially effective when a thin glass container such as an NMR tube is used due to the small surface area of the solution.[35]

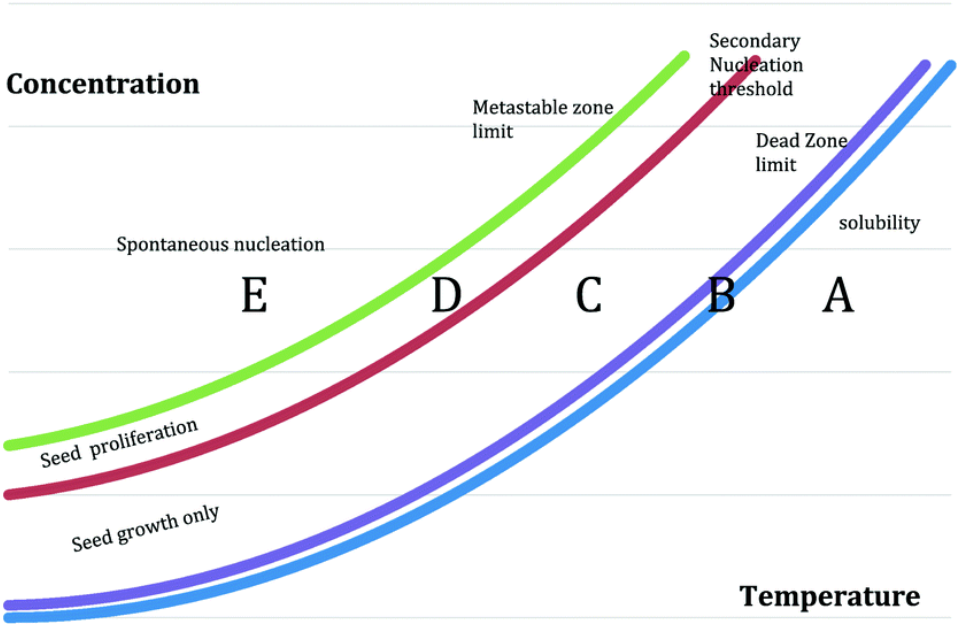

Figure 1.3. A generalised solution crystallisation diagram depicting the temperature and concentration-dependent regions as a solution is cooled from zones A-E. A is the undersaturated solution, while B, C, and D represent the metastable region. E is the region of spontaneous nucleation. The figure is reproduced with permission from reference 32.

Solvent	Antisolvent
Acetonitrile	Tetrahydrofuran
Acetone	Chloroform
Ethanol	Cyclohexane
Methanol	Hexane or tetrahydrofuran
Tetrahydrofuran	Cyclohexane
Water	Dioxane

Table 1.1. Recommended solvents and antisolvents for the vapour diffusion crystallisation technique for small molecules.[35]

1.3. Crystal Engineering

1.3.1. Characteristics of Intermolecular Interactions

Crystal engineering is defined as the understanding of intermolecular interactions (in the context of crystal packing) and its utilisation in the design and synthesis of new solids with the desired composition, structure, and physical properties.[36, 37] In the

1960s and 1970s, Schmidt and coworkers used crystal engineering principles to describe the photodimerisation of crystalline cinnamic acids in the solid state, which largely intertwines with the field of supramolecular chemistry through the incorporation of noncovalent interactions.[38-41] Desired interactions can be synthesised by combining specific functional groups to give rise to a precise set of structural units that act as molecular building blocks, termed supramolecular synthons.[42] Supramolecular synthons, therefore, provide key interactions that are mostly governed by their distance from one molecule to another and the directionality of the interaction.[43] The combination of supramolecular synthons contribute to the formation of a supermolecule. Examples of common homo- (interactions of the same functional groups) and heterosynthons (interactions between different functional groups) are shown in Figure 1.4. Supramolecular synthons can be divided into four different classifications: discrete (infinite intermolecular pattern) (D), chains (C), rings (R), or intramolecular hydrogen bonds (S).[44] These motifs can be further described by a useful, universal nomenclature (based on graph set analysis) to explain the number of hydrogen bond donors and acceptors.[44-46] For example, the carboxylic acid homosynthon can be described as a $R_2^2(8)$ hydrogen-bonded dimers, which corresponds to an eight-membered ring motif with two hydrogen bond donor atoms and two hydrogen-bond acceptor atoms.

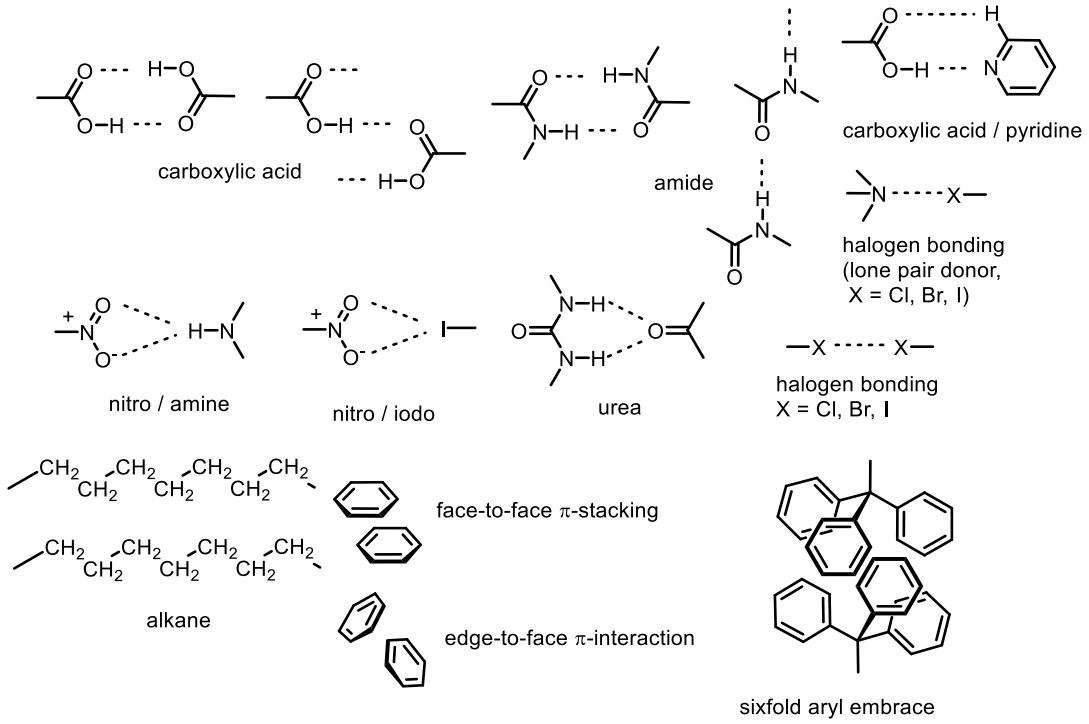

Figure 1.4. Common supramolecular synthons that may be used to predict and engineer crystal structures, reproduced with permission from reference 47.

The key noncovalent intermolecular interactions involved in crystal engineering are predominantly long-range forces such as hydrogen bonding, halogen bonding, and π-π interactions, though short-range forces such as van der Waals forces are not to be forgotten.[1, 47] Firstly, the hydrogen bond is defined by the International Union of Pure and Applied Chemistry (IUPAC) as "an attractive interaction between a hydrogen atom from a molecule or a molecular fragment, X-H, in which X is more electronegative than H, and an atom or a group of atoms in the same or a different molecule, in which there is evidence of bond formation".[48] The hydrogen bond can be divided into either strong, medium, or weak interactions, and their behaviour can be described as strongly covalent, moderately electrostatic, and mostly electrostatic/dispersion interactions, respectively.[49, 50] Hydrogen bond lengths from the hydrogen bond donor to hydrogen bond acceptor are typically classified as 2.2-2.5 Å for strong interactions, 2.5-3.2 Å for moderate interactions, and >3.2 Å for weak interactions.[49, 51] In addition to hydrogen bonding, halogen bonding interactions also influence crystal engineering. The halogen bond is defined IUPAC as "a net attractive interaction between an electrophilic region associated with a halogen atom in a molecular entity, and a nucleophilic region in another, or the same, molecular

entity".[52, 53] However, Desiraju and coworkers believe that the IUPAC definition only satisfies the symmetrical (type I) halogen bond, as bent (type II) bonds also exist.[54] Halogen bond interactions involve halogen···halogen and halogen···heteroatom interactions.[55] The hydrogen-bonded and halogen bonded supramolecular synthons are structurally similar and are therefore relatively predictable in crystal engineering.[54, 56] Aside from hydrogen and halogen bonds, π-stacking interactions are important in crystal engineering, especially due to their ability to stabilise cocrystal systems that contain an aromatic coformer.[57] π-π Interactions involve face-to-face stacking of aromatic units (C···C) and edge-to-face stacking (weak CH···π interactions).[58, 59] For both types of π-stacking interactions, the distance between ring centroids must be within 3.3-3.8 Å.[60] Additionally, short-range forces, such as van der Waals interactions, contribute to the overall stability of a crystal structure, predominantly by the close packing of alkyl chains.[47]

1.3.2. The Role of Mechanochemistry in Cocrystal Formation

The role of mechanochemistry in crystal engineering is not to be understated. Since the beginning of the 21st Century, mechanochemistry has become an important method for solid state synthesis and has proven to be a viable and clean alternative to solution chemistry where vast amounts of solvent and equipment are required.[61, 62] Additionally, mechanochemistry has shown to be effective in the synthesis of new solid forms (amorphous and crystalline, single and multicomponent forms, and as a route to polymorphs) especially cocrystals.[63] New solid forms can be obtained by either the grinding of dry powders, or with a drop of solvent to facilitate liquid assisted grinding (LAG).[64] Mechanochemistry (specifically the breaking or formation of chemical bonds) can be achieved through the simple grinding of powders by a pestle and mortar, or through mechanical methods such as the use of a ball mill (e.g. shaker/mixer mills or planetary mills).[65] Manual and mechanical grinding to form a new material are reliant upon the molecular movement and migration in crystalline solids, which suggests the solid state is a mobile environment.[66]

One of the first examples of pharmaceutical cocrystals synthesised by mechanical methods was in 1993 and involved the neat grinding of sulfadimidine and a variety of carboxylic acids (including aspirin).[67] The resulting cocrystals were also the same when synthesised by solution-based methods. Another important example of mechanochemical synthesis to obtain cocrystals is the polymorphic 2:1 aspirin and

4,4'-bipyridyl cocrystal – Form I (Form II is synthesised by the rapid cooling of solvent).[68] The cocrystal was synthesised by the dry grinding of components and the formation of a cocrystal was confirmed by Powder X-ray Diffraction (PXRD) analysis.[68] This cocrystal was originally synthesised by Zaworotko and coworkers but as a hexane solvate.[69] Therefore, the dry grinding of coformers to give a non-solvated cocrystal is of particular interest when synthesising pharmaceutical solids,[70] though the applications of mechanochemistry stretch beyond the use of small organic molecules.[71, 72]

1.4. Diacetylene Topochemistry

Diacetylenes are a well-studied class of photoactive compound, with 10,12-pentacosadiynoic acid (PCDA, Figure 1.5) as a common example.[73] Irradiation of PCDA with ultraviolet, X-ray, or γ-radiation results in photopolymerisation to give a polydiacetylene with an alternating ene-yne backbone.[74, 75] This monomer-to-polymer conversion is accompanied by a visible colour change from colourless to blue, with additional perturbations further changing the colour of the polydiacetylene from blue, to purple, to red, to yellow, and sometimes green depending on the polymer conformation and ordering, and hence extent of delocalisation of the conjugated backbone.[76-78] Diacetylenes undergo topochemical photopolymerisation not only as crystalline solids but also in semi-ordered media such as liquid crystals,[79-81] thin films,[82-85] vesicles,[86-88] and gels.[89-91] The chromic properties of the resulting polydiacetylenes are typically exploited in dosimeters, biosensors, and chemosensors.[92-94]

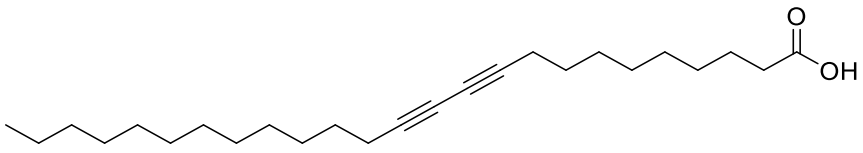

Figure 1.5. The structure of monomeric PCDA.

The first report of topochemical reactivity in the solid state was in 1964 by Schmidt and coworkers who investigated the [2+2] cycloaddition of *trans*-cinnamic acid polymorphs.[38, 95-97] From extensive crystallographic and photochemical studies, Schmidt formulated the topochemical postulate which states that the carbon-carbon

double bonds must be separated by a maximum distance of 4.2 Å for polymerisation to be successful.[98] Five years after the topochemical postulate was described for alkene systems, Wegner reported the first example of diacetylene polymerisation in the solid state,[39, 99] with Enkelmann proposing strict criteria for diacetylene reactivity in 1984 (Scheme 1.1).[100] Enkelmann's conditions suggest that adjacent diacetylene monomers react at a distance less than or equal to the van der Waals contact distance (*d*) of 3.8 Å, with a translational period repeat spacing (*r*) of 4.9 Å or less, along with the monomers at an orientation angle (θ) to the crystal axis at 45 °.[100] These parameters for diacetylene polymerisation aid in understanding the importance of molecular organisation in the topochemical reaction.[101, 102] There are two possible mechanisms responsible for the topochemical polymerisation of a diacetylene, known as the 'turnstile' and 'swinging gate' mechanisms, outlined in Figure 1.6. In the turnstile mechanism, when the monomers are exposed to radiation or heat, they pivot approximately 1 Å around the centroid of the diacetylene at 30 ° to bring carbon atoms C1 and C4' together to create a new bond.[103] This mechanism is most favoured for disubstituted diacetylenes,[103-106] while the swinging gate mechanism is typical for terminal diacetylenes.[107] In the swinging gate mechanism, the monomers pivot at C4' (with the R-group remaining stationary) allowing the C1 to move approximately 3 Å to join the rest of the polymer.[103, 104]

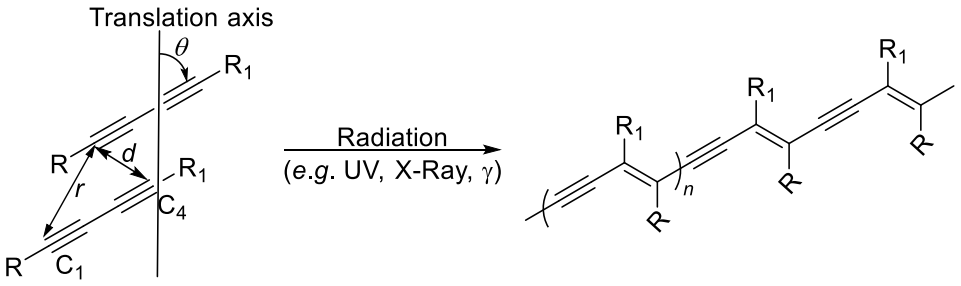

Scheme 1.1. Parameters required for the topochemical polymerisation of diacetylene monomers to result in a polydiacetylene. The C1-C4' distance (*d*) of the monomers must be ≤3.8 Å, and within the translational repeat distance (*r*) of ≤4.9 Å, with a tilt angle (θ) of 45 °.

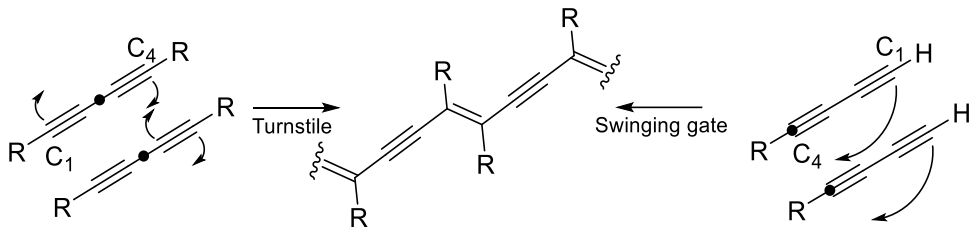

Figure 1.6. A simplified illustration of the two possible mechanisms of diacetylene polymerisation.

Diacetylene crystal structures are abundant in the literature, with some of the earlier structures arising from work by Enkelmann, that includes two bis(N-phenylcarbamate) diacetylene (DA-*m*PhC) structures that only differ by an methylene spacer length (*m*) of one methylene group in DA-1PhC (Figure 1.7) and four methylene groups in DA-4PhC.[108] Both structures photopolymerise, as the inter-alkyne distances are 3.65 and 3.53 Å,[109] respectively, and are within the topochemical postulate of 3.8 Å.[108] Monomer crystals of bis(N-phenylcarbamate) with five (DA-5PhC) and six (DA-6PhC) methylene spacer groups have also been structurally characterised, with inter-alkyne distances of 5.20 Å and 3.57 Å, respectively.[109] The large carbon-carbon distance of DA-5PhC is out of the range for topochemical reactivity, and as a result, the compound does not polymerise.[109] The topochemical parameters of DA-5PhC indicate that methylene spacer length has an impact on how the diacetylenes react in the solid state. It has been reported that the physical properties of similar compounds can be dictated by whether there is an odd or an even number of methylene groups in the spacer.[109, 110] The angle between the diacetylene and stacking axis in DA-5PhC is also vastly different from the topochemical criteria for diacetylene reactivity, at an angle of 69.3 °.[109]

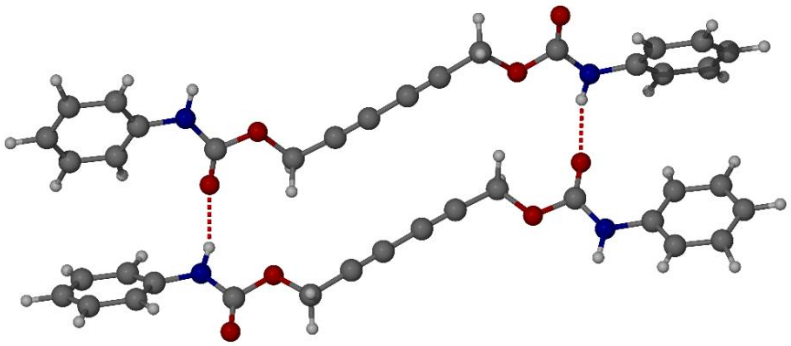

Figure 1.7. The X-ray structure of DA-1PhC in the crystallographic (010) plane.

A different diacetylene crystal structure of 4-(hexadeca-1,3-diyn-1-yl)benzoic acid that has no methylene spacer between the diacetylene moiety and the benzoic acid head group, proves to be outside of Enkelmann's parameters for topochemical reactivity, however, still photopolymerises (Figure 1.8).[111] The C1-C4' contact distance on adjacent diacetylene moieties is reported to be 4.41 Å,[111] although a C2-C3' contact distance of 4.03 Å was identified. These observations show that exceptions to the postulate are possible.[100, 111, 112] Polydiacetylene crystal structures have also been reported in the literature, including a polymer structure of poly(1,2-bis(phenylaminomethyl)-but-1-en-3-ynyl) (Figure 1.9), with complete monomer-to-polymer conversion obtained by thermal annealing at temperatures below the monomer melting point (no monomer crystal structure is available).[113]

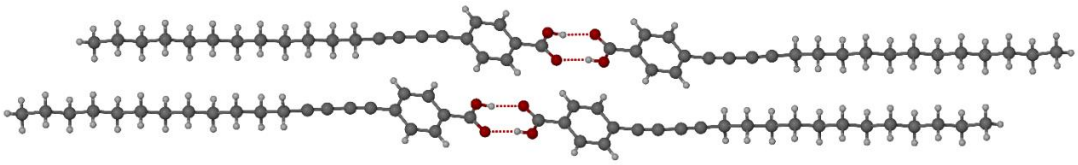

Figure 1.8. The X-ray structure of 4-(hexadeca-1,3-diyn-1-yl)benzoic acid in the crystallographic (100) plane, with adjacent reactive groups outside of the range for topochemical reactivity, though still photopolymerises in response to radiation.

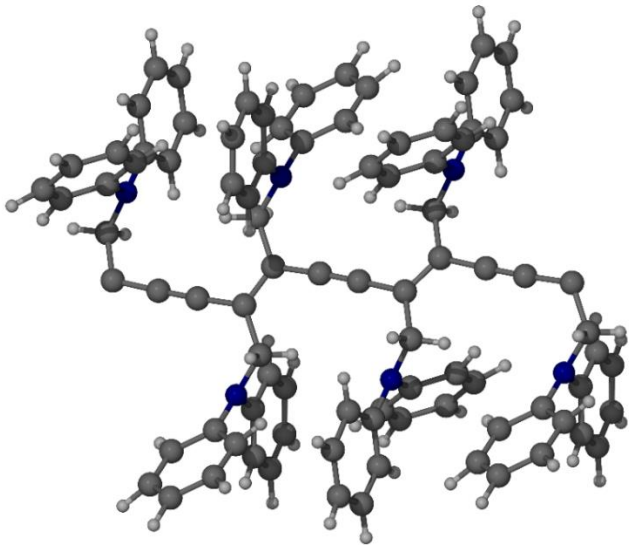

Figure 1.9. The structure of the polydiacetylene poly(1,2-bis(phenylaminomethyl)-but-1-en-3-ynyl).

The solid state structure and hence crystal engineering also plays a large role in diacetylene reactivity.[114] Salt formation and cocrystallisation of pharmaceutical drugs

can significantly change their properties,[1] this concept can also be applied to how diacetylenes respond to external stimuli. For instance, diacetylene ammonium salts such as 1-naphthylmethylammonium octa-2,4-diynoate contain a network of NH···O hydrogen bonds (Figure 1.10).[115] However, this salt does not meet the criteria for topochemical polymerisation as the closest inter-alkyne distance is 4.97 Å, the translational distance is 7.72 Å and the tilt angle is only 31 °.[115] However, a derivative of this material, 1-naphthylmethylammonium nona-2,4-diynoate, readily undergoes polymerisation in the solid-state in response to UV and γ-radiation.[115] The topochemical parameters for this salt are ideal for polymerisation as the inter-dialkyne distance is 3.66 Å, the translational distance is 4.88 Å, and the tilt angle is 47 °.[115]

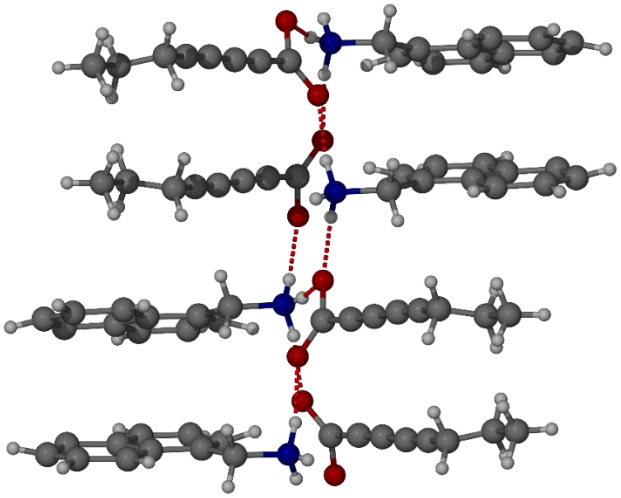

Figure 1.10. The X-ray structure of 1-naphthylmethylammonium octa-2,4-diynoate.

The solid-state polymerisation of 4,4'-butadiynedibenzylammonium dihexa-2,4-dienoate has also been described.[116, 117] However, the diacetylene portion of the salt does not polymerise, rather it is the diene moieties that are separated by 5.33 Å, with a monomer repeat distance of 4.88 Å and a tilt angle of 60 ° that react. These parameters are within the diene reactivity criteria (Figure 1.11).[116, 118] The X-ray structure of the 4,4'-butadiynedibenzylammonium dihexa-2,4-dienoate polymer shows polymerisation of the diene units as expected, with a shortened repeat distance when compared to the monomer, at a distance of 4.82 Å (Figure 1.12).[116]

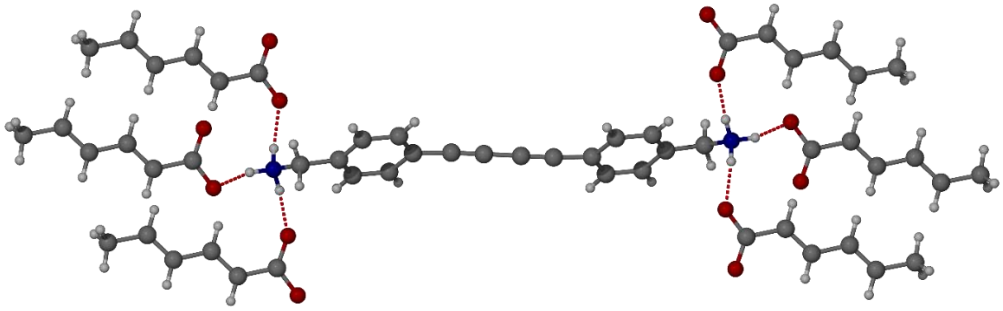

Figure 1.11. The X-ray structure of 4,4'-butadiynedibenzylammonium dihexa-2,4-dienoate.

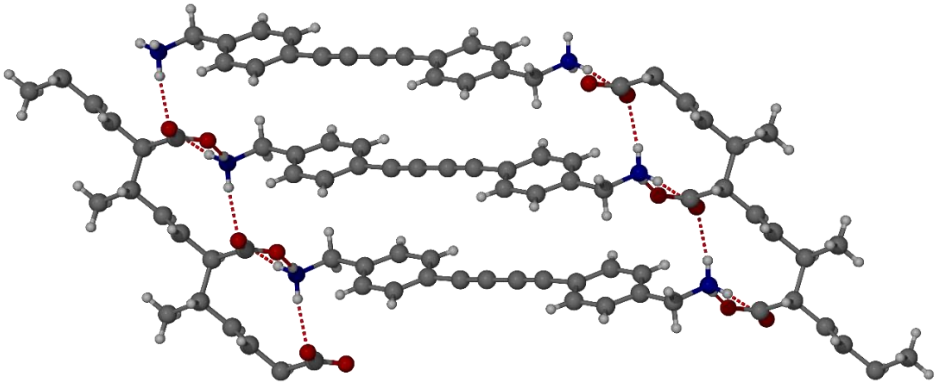

Figure 1.12. The X-ray structure of poly(4,4'-butadiynedibenzylammonium dihexa-2,4-dienoate).

In terms of diacetylene cocrystals, acetylene gas itself has been cocrystallised with a wide-range of small molecule coformers by condensing acetylene into quartz capillaries that already contain the coformer.[119] Diacetylenes have also been cocrystallised in more complex systems. For instance, a host-guest cocrystal approach has been used to design a hydrogen bonded network of a ureylene dicarboxylic acid host with 1,6-bis(4-pyridylcarboxylato)hexa-2,4-diyne guests (Figure 1.13).[120] The host molecules can control the intermolecular spacing of the substituted diacetylene guest through the utilisation of the strong pyridine-carboxylic acid OH···N and amino-carboxylic acid NH···O hydrogen bond synthons.[42] In this cocrystal system, the carbon-carbon triple bonds of the diacetylenes are separated by a distance of 3.94 Å with an orientation angle of 56.3 °, which is outside the values for topochemical polymerisation, however, the translational period repeat spacing is within the polymerisation range, at 4.71 Å.[120] Though this system is not topochemically reactive, the host molecule can be fine-tuned to design a system that allows the diacetylenes to

be within the distance for reactivity. Another host-guest cocrystal system involves a 1,5-bis(4'-pyridyl)ureylene host with a deca-4,6-diyne-1,10-dicarboxylic acid guest in a hydrogen-bonded network (Figure 1.14).[120] In this system, the adjacent diacetylenes stack with a reactive inter-alkyne distance of 4.06 Å and an orientation angle relative to the translation axis of 61.0 °. These values are outside of the range for polymerisation, though the translation repeat distance is within the criteria at 4.63 Å. Even though polymerisation does not occur, a host-guest strategy for cocrystallisation is a creative way to control and manipulate the reactivity of a diacetylene systems.[120, 121]

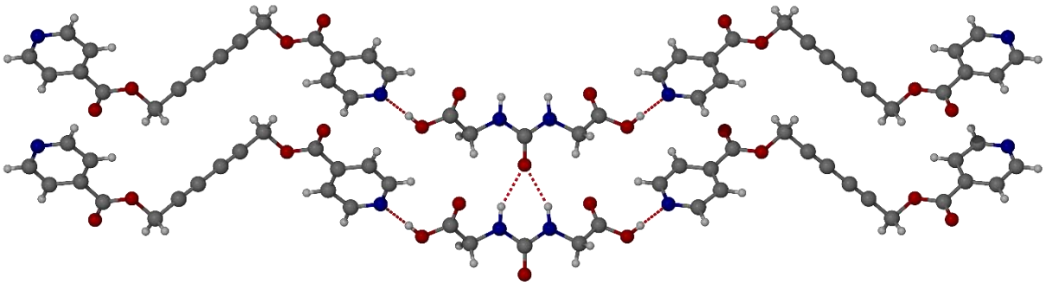

Figure 1.13. The X-ray structure of a ureylene dicarboxylic acid molecule interacting with 1,6-bis(4-pyridylcarboxylato)hexa-2,4-diyne by OH···N hydrogen bonds, with intermolecular NH···O hydrogen bonds forming urea tapes from the ureylene dicarboxylic acid portion of the cocrystal.

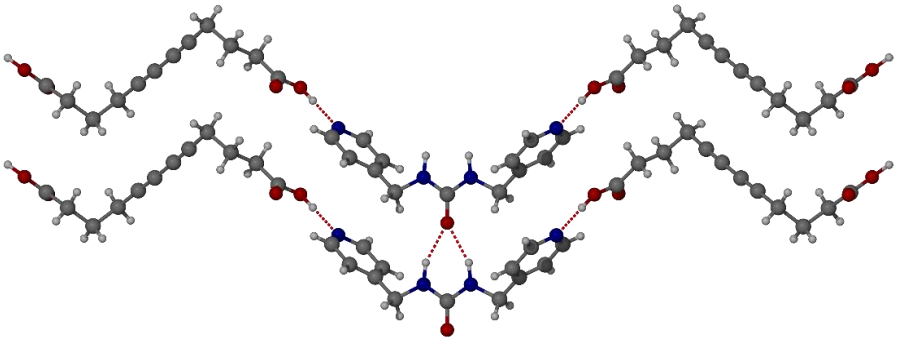

Figure 1.14. The X-ray structure of 1,5-bis(4'-pyridyl)ureylene and deca-4,6-diyne-1,10-dicarboxylic acid, joined by OH···N hydrogen bonds, with intermolecular NH···O hydrogen bonds forming urea tapes between 1,5-bis(4'-pyridyl)ureylene molecules.

Other examples of diacetylenes cocrystallised in a host-guest matrix involve the ability of N,N'-bis(pyridine-4-ylmethyl)oxalamide to control the reactivity of the terminal diacetylene penta-2,4-diynyl 3,5-dihydroxybenzoate (Figure 1.15A).[107] The resulting structure is a triple helix of alternating diacetylene and oxalamide molecules, with the diacetylene motif in the centre of the helix.[107] The acetylenic C1-C4' intermolecular distance is 3.64 Å and conforms to the topochemical postulate for reactivity.[107] As a result, after heating at 150 °C for 24 hours, the diacetylene cocrystal polymerises to give a cocrystal polydiacetylene structure, with the translational repeat distance shortening from 5.09 Å to 4.93 Å in the polymer (Figure 1.15B).[107]

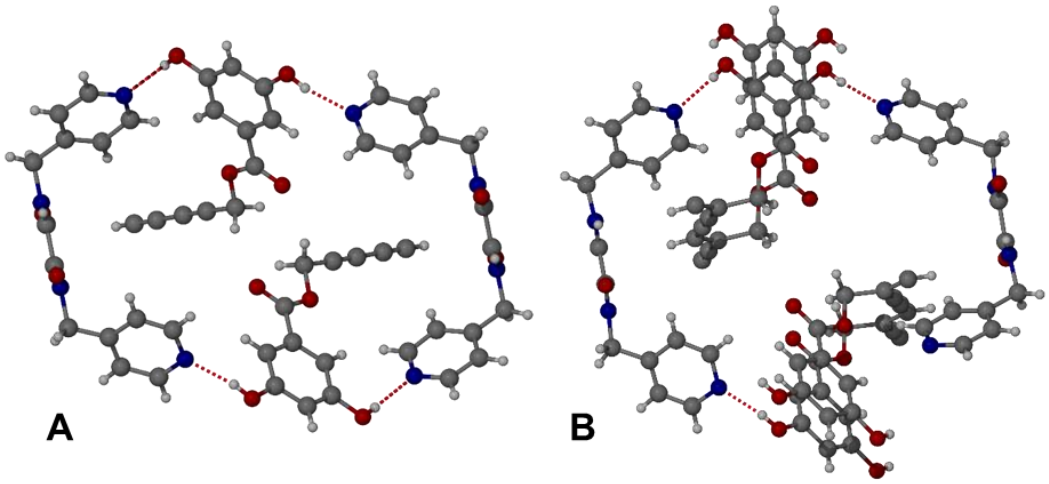

Figure 1.15. A) The X-ray structure of the terminal diacetylene penta-2,4-diynyl 3,5-dihydroxybenzoate cocrystallised with a oxalamide host, N,N'-bis(pyridine-4-ylmethyl)oxalamide. B) The polymerised cocrystal of penta-2,4-diynyl 3,5-dihydroxybenzoate and N,N'-bis(pyridine-4-ylmethyl)oxalamide, showing the ene-yne bonds of adjacent reactive groups.

In addition to host-guest systems, bispyridyl diacetylenes have been cocrystallised with oxalamide derivatives with different length spacer chains. Eight such cocrystal structures were reported in a single publication by Curtis and coworkers.[122] The two bispyridyl diacetylenes are 1,4-bis(3-pyridyl)buta-1,3-diyne[123] and 1,4-bis(4-pyridyl)buta-1,3-diyne[124] and before cocrystallisation, their closest C1-C4' intermolecular distances are 4.48 Å and 4.52 Å, which are outside the ranges for topochemical reactivity.[122] When the diacetylene hosts are combined with varying oxalamide guests such as N,N'-oxalyldiglycine, oxalamide-N,N'-bis(3-propionic acid), oxalamide-N,N'-bis(5-pentanoic acid), and oxalamide-N,N'-bis(6-hexanoic

acid), only the cocrystal of 1,4-bis(4-pyridyl)buta-1,3-diyne and N,N'-oxalyldiglycine can polymerise (Figure 1.16).[122] In this instance, the inter-alkyne distance is 3.62 Å, with a repeat distance of 4.93 Å and an orientation angle of 47.7 °.[122] No other combination of the bispyridyl diacetylene and oxalamide cocrystal underwent polymerisation.[122]

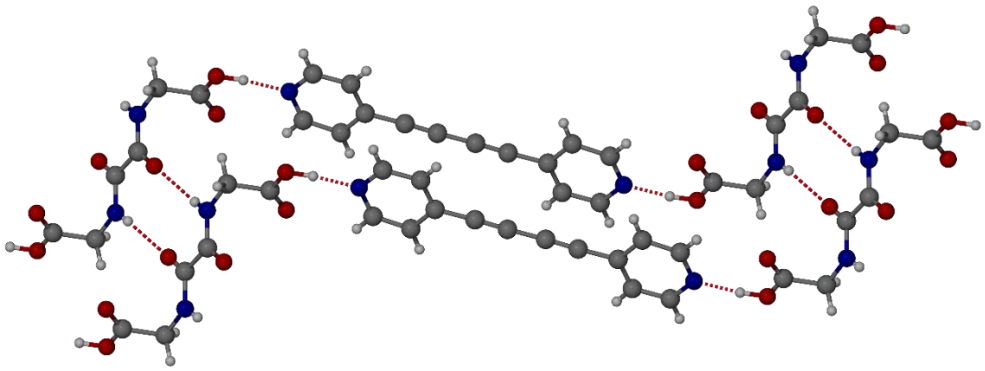

Figure 1.16. The X-ray crystal structure of 1,4-bis(4-pyridyl)buta-1,3-diyne and N,N'-oxalyldiglycine.

The importance of topochemistry has been shown by Goroff and coworkers through 1,4-di-iodobuta-1,3-diyne cocrystals with bis(3-pyridylmethyl)oxalamide (Figure 1.17).[56] A hydrogen bond network is formed between neighbouring oxalamide molecules, consisting of O···NH hydrogen bonds and N···I halogen bonds between the pyridyl nitrogen of the oxalamide, and the iodine atom of the diiodoalkyne at a distance of 2.83 Å. Both hydrogen bonds and halogen bonds contribute to the control of the alignment of the diacetylene moiety. However, the intramolecular C1-C4' distance is greater than the desired value, at 3.90 Å, along with a greater value for the repeat distance of the diacetylene units, at 5.11 Å, and a tilt axis of 51 °. All of these values contribute to the fact that the diacetylene monomer units do not topochemically react when exposed to radiation.[56] A para derivative of bipyridyl oxalamide was also synthesised, bis(4-pyridylmethyl)oxalamide, and cocrystallised with diiodobutadiyne, though still, the parameters for topochemical polymerisation remain outside of the necessary range.[56]

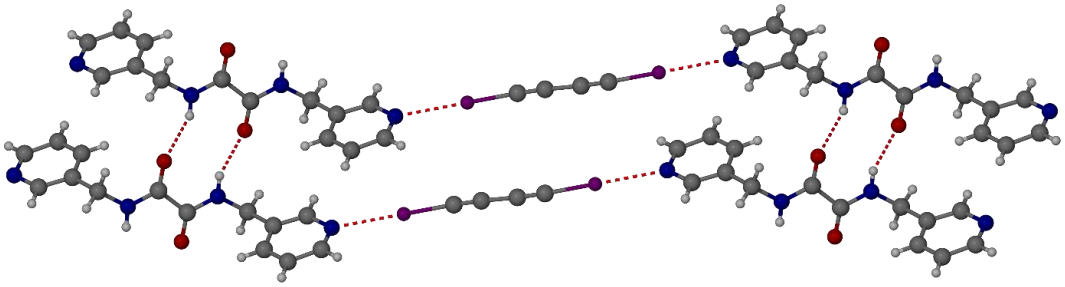

Figure 1.17. The halogen-bonded cocrystal of 1,4-di-iodobuta-1,3-diyne and bis(3-pyridylmethyl)oxalamide.

Other diiodobutadiyne cocrystals involve N,N'-bis(4-cyano)oxalamides with different length spacer groups in a further attempt to customise the topochemical reactivity. For example, N,N'-bis(4-cyanopropyl)oxalamide and 1,4-di-iodobuta-1,3-diyne forms a cocrystal that becomes dark and decomposes at room temperature without any evidence of polymerisation (Figure 1.18).[125] However, bis(4-cyanobutyl)oxalamide does polymerise,[126] even though the C1-C4' distance is slightly greater than the distances suggested by the topochemical postulate, at 3.88 Å (Figure 1.19).[125] In the monomeric cocrystal structure, the iodine atoms of 1,4-di-iodobuta-1,3-diyne are either halogen bonded to nitrile nitrogen atoms or oxygen atoms belonging to the oxalamide group.[125] Hydrogen bonds also form between molecules of bis(4-cyanobutyl)oxalamide, via the NH···O supramolecular synthon.[125] Cocrystals of bis(4-cyanopentyl)oxalamide and 1,4-di-iodobuta-1,3-diyne also polymerise, though the X-ray coordinates could not be determined for both the monomeric and polymeric structures.[125] In conclusion, the effect of different length alkyl spacer groups can drastically change the topochemical parameters for diacetylene cocrystal polymerisation. In this instance, the main difference between the cocrystals that do and do not polymerise are the number of hydrogen bonding interactions, which contribute to the control of the diacetylene units.

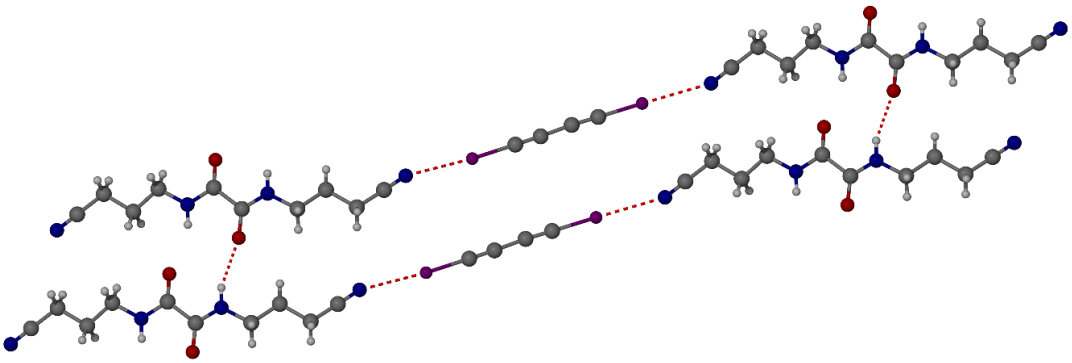

Figure 1.18. The X-ray structure of N,N'-bis(4-cyanopropyl)oxalamide and 1,4-di-iodobuta-1,3-diyne which does not undergo topochemical polymerisation.

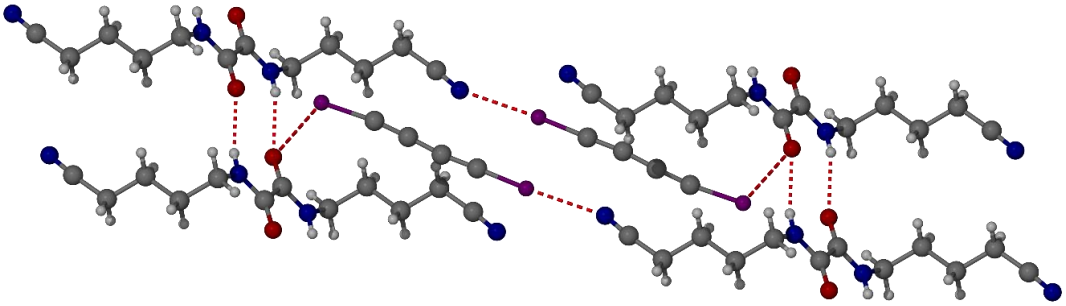

Figure 1.19. The X-ray structure of N,N'-bis(4-cyanobutyl)oxalamide and 1,4-di-iodobuta-1,3-diyne, which is able to topochemically polymerise.

Additional cocrystal systems involve the use of light-stable host molecules and light-sensitive guest molecules that crystallise as two different isomers that dimerise upon UV irradiation. An example is the cocrystallisation of 1,1,6,6-tetraphenyl-2,4-hexadiyne-1,6-diol and bis(isoquinolin-3(2H)-one, which crystallises in a monoclinic *C*2/*c* polymorph 1 (Figure 1.20A) and in an orthorhombic *Pbcn* polymorph 2 (Figure 1.20B).[127] Though the diacetylene hosts in the cocrystals are separated by too great a distance to polymerise, the isoquinolone guest is able to dimerise upon exposure to irradiation, as the carbon double bonds are separated by 3.71 Å (Schmitt's postulate suggests <4.2 Å).[39, 127] Polymorph 1 yields two identical isoquinolone isomers, while polymorph 2 also yields the same isomer as polymorph 1, and an additional isomer, which is related by an inversion centre.[127]

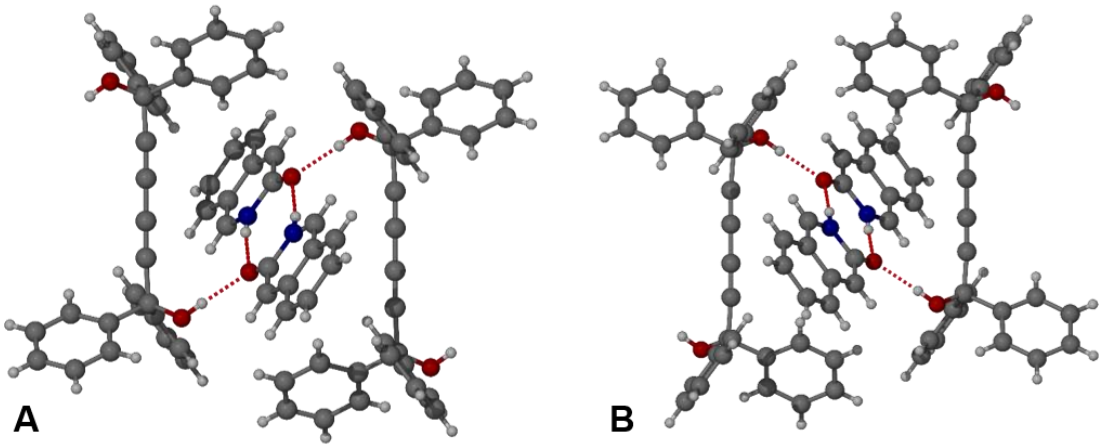

Figure 1.20. The X-ray structures of A) polymorph 1 B) polymorph 2 of 1,1,6,6-tetraphenyl-2,4-hexadiyne-1,6-diol and bis(isoquinolin-3(2H)-one. Both structures displayed perpendicular to the *b*-axis.

Another PCDA cocrystal system involves the successful cocrystallisation with melamine (MA).[128] The cocrystals were synthesised in a two-step process involving the co-assembly of PCDA and MA in water by a non-covalently connected micelle method (NCCM), and the annealing of the co-assembly at the melting point of PCDA (approx. 65 °C) for six hours but lower than the melting point of the cocrystals (87 °C) (Figure 1.21).[128] The hydrogen bond in the cocrystal is between the carboxylic acid O-H group of PCDA and an amine nitrogen atom of MA. Aromatic stacking is also present between neighbouring layers of MA.[128] It is hypothesised that the numerous noncovalent interactions within the polymerised cocrystal stabilise it and allow for the reversible thermochromism that is displayed when heated from 25 – 90 °C.[128]

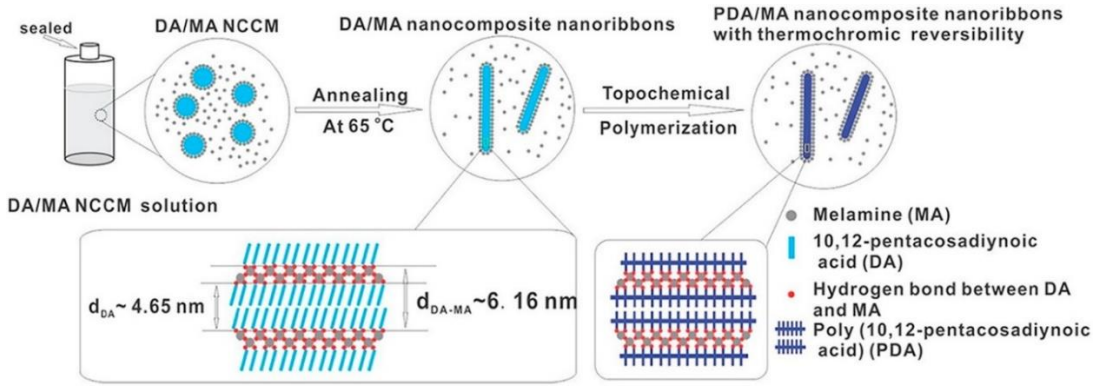

Figure 1.21. The preparation process for PCDA-MA cocrystals. Reproduced with permission from reference 128.

Aside from multicomponent forms of diacetylenes, simple diacetylenes have also been used as models to show anisotropic thermal expansion in single-crystal studies. In this case, a structure of a simple eight-carbon diyn-diol, (*S*,*S*)-octa-3,5-diyn-2,7-diol (Figure 1.22), has shown that with decreasing temperature from 330 K to 225 K, the *a*-axis contracts while the *b*- and *c*-axes expand, which is reversible in this temperature range.[129] The changes in cell axes with decreasing temperature gives examples of both uniaxial positive and biaxial negative linear thermal expansion and is due to the diacetylene molecules altering their tilt angles in opposing directions.[129] This rearrangement of molecules allows the diacetylene to maintain its anti-clockwise helical hydrogen bonding chain network whilst providing efficient packing of the structure and, therefore, the maximisation of interaction energies.[129] Interestingly, an enantiotropic polymorph of the same diyn-diol structure does not exhibit anisotropic linear thermal expansion as the hydrogen-bonded diacetylene chains exist in a clockwise helix, opposite to the polymorph mentioned above.[130] The difference in helicity of the hydrogen-bonded chains is a result of a 10 ° stacking angle change,[130] though no work has been undertaken on the topochemical reactivity of either of the polymorphs. A similar diyn-diol to (*S*,*S*)-octa-3,5-diyn-2,7-diol has been used as a host molecule for inclusion compounds with solvent molecules as a guest (Figure 1.23).[131]

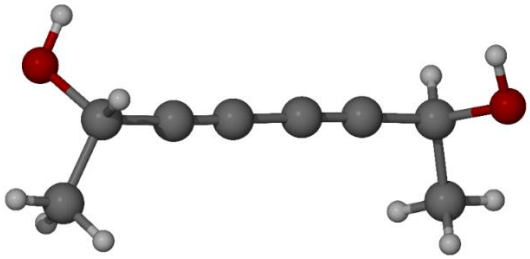

Figure 1.22. The structure of (*S*,*S*)-octa-3,5-diyn-2,7-diol.

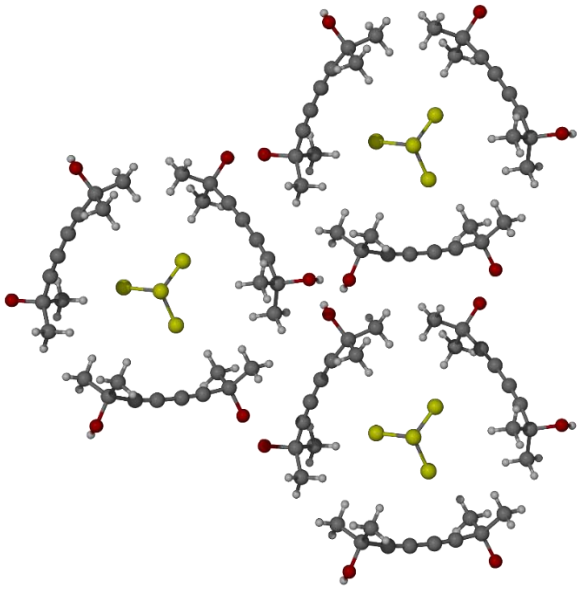

Figure 1.23. 2,7-Dimethyl-octa-3,5-diyne-2,7-diol showing solvent channels occupied by CCl_4.

1.5. Optical and Electronic Properties of Diacetylenes

The monomer-to-polymer transition of diacetylenes is accompanied by a colour change from colourless to blue, due to the formation of a conjugated ene-yne chromophore. The blue colour arises from π-π* transitions in the ordered, conjugated chain with the efficiency of the reorganisation controlling the degree of polymerisation of the diacetylene monomers.[132] The colour of the photoproduct can be further influenced by factors such as extended heating, pH change, mechanical stress, ligand-receptor interactions, and treatment with organic solvents. Additional stimuli upon the polydiacetylene applies strain to the structure, causing it to distort and give a blue (absorption maxima ~640 nm) to red (absorption maxima ~500 nm) chromic shift, which corresponds to different chain conformations and ordering.[133] The different chain conformations are caused by segmental rearrangement within the polydiacetylene assembly to alleviate strain through rotations around the C-C bonds.[134] These C-C rotations break the planarity of the backbone, which disrupt the delocalisation of the π electrons of the conjugated chain, and therefore, reduces the π orbital overlap so that the HOMO-LUMO energy gap is widened to allow the polydiacetylene to absorb light at a higher energy.[135-138] Calculations suggest that rotation of only five degrees is required to change the π orbital overlap and shift the

colour of the polydiacetylene from blue to red, which correlates to a planar structure adopting a non-planar conformation with rotated and/or distorted side chains.[139-142] Figure 1.24 shows the chromic properties of the blue-to-red chromic shift in response to a difference in the conjugation of the polydiacetylene chain.[133]

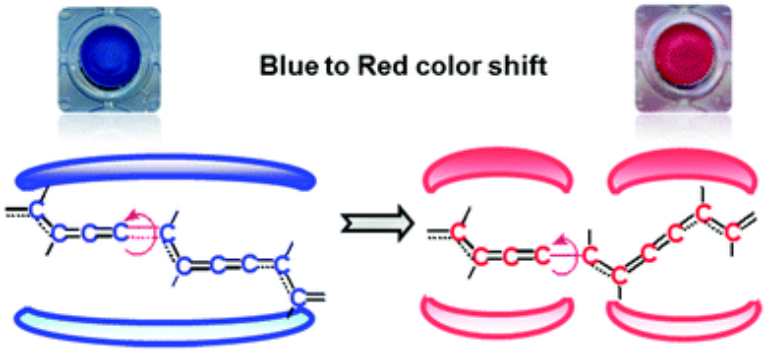

Figure 1.24. The chromic properties of polydiacetylenes caused by the rotations around the C-C bonds. Figure adapted with permission from reference 133.

Understanding the mechanism of the chromic changes of polydiacetylenes is imperative to control polydiacetylene-based colourimetric sensors. The control and interfacial properties of the order-disorder transition of PCDA vesicles when irradiated has been explored, through the adsorption behaviour of probe material ((4-(4-diethylaminostyry)-1-methylpyridinium iodide) on the vesicle surface.[143] Surface-specific second harmonic generation and zeta potential measurements show that the order-disorder transition largely involves the gradual distortion of the carboxyl terminated chains driven by backbone perturbation (Figure 1.25).[143] Additionally, as UV irradiation time increases, the adsorption and chain-chain interactions between the probe molecule and the surface of the vesicles become weaker, resulting in a decrease in adsorption density of the probe molecules as UV irradiation increases.[143] This finding suggests that as the duration of UV irradiation increases, structural changes occur that reduce conjugation and the planarity of the polydiacetylene through distorted side chains.

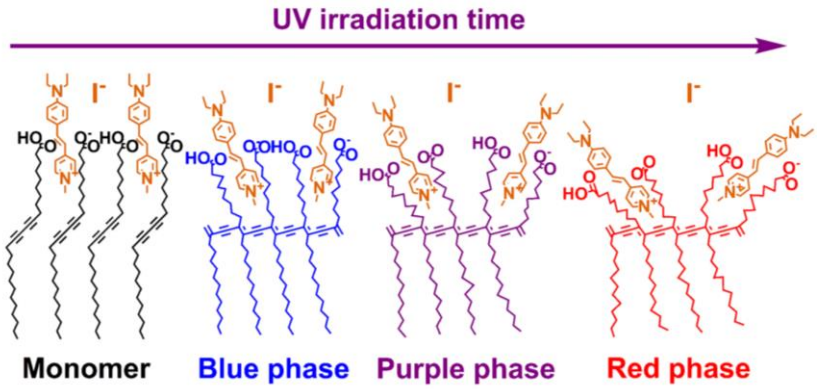

Figure 1.25. A model illustrating the movement of the carboxyl terminated chains from monomer to polymer forms, in the presence of probe materials on the PCDA vesicle surface. Figure reproduced with permission from reference 143.

1.6. The Effect of External Stimuli on Diacetylenes

1.6.1. The Effect of Extended Heating

Since the first report of the colour-changing properties of polydiacetylenes in response to heat in 1976,[144] thermochromism has become an important property for many functional materials, with thermochromic liquid crystals and leuco dyes as some of the more popular examples.[145, 146] Thermochromism in diacetylenes, especially PCDA, has been extensively studied and potential sensing applications include electrothermochromic displays,[147] counterfeiting detection,[148] printable[149] and microfluidic[150] thermal sensors, and smart textiles.[151] PCDA itself exhibits irreversible thermochromism, though if monomeric or polymeric PCDA is modified in any way, this can dramatically influence the colour exhibited and the reversibility of its colour changes. Vesicles containing only polymeric PCDA were heated to above 55 °C, an absorption band at approx. 540 nm (red) grows while the band at approx. 620 nm (blue) simultaneously decreases.[152] When the PCDA vesicles were heated to around 65 °C, only the red species is observed (Figure 1.26).[152, 153] The thermochromic transition temperatures of polymeric PCDA are very close to the melting temperature of monomeric PCDA, which is also around 65 °C.[152]

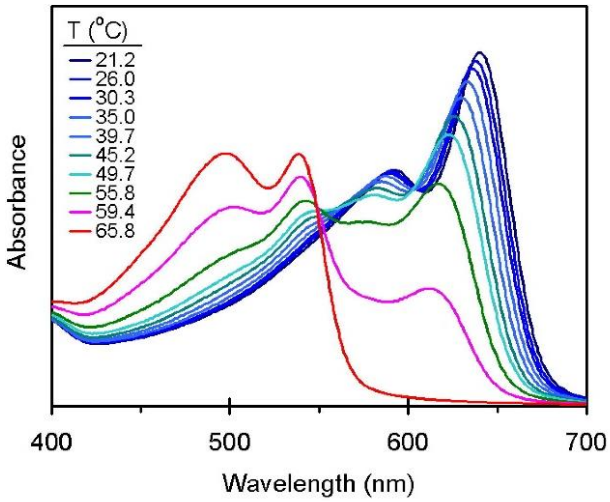

Figure 1.26. The UV-Vis absorbance spectra of PCDA heated from 21.2 – 65.8 °C. Figure adapted with permission from reference 152.

An example of the thermochromic properties of PCDA changing when in a modified environment is illustrated in a study involving the nanocomposites of PCDA intercalated with low molecular weight (10,000 g/mol) polyvinylpyrrolidone (PVP).[154] This nanocomposite system provides a reversible blue-to-purple colour change up to temperatures of 90 °C, with the colour transition occurring at around 85 °C.[154] The PCDA colour transition temperature is high compared to polydiacetylenes with shorter alkyl chains to PCDA, which illustrates greater interactions within the PCDA nanocomposite system.[152, 154, 155] Similar findings were found in films of PCDA and PVP that were heated to temperatures of 30, 50, 65 and 85 °C.[156] Differential scanning calorimetry (DSC) themograms of the heated films suggest that the films heated to 30 °C and 50 °C melt at 52 and 54 °C, respectively and do not display reversible thermochromism as PCDA is unable to reach its melting point (~ 65 °C) and diffuse into the surrounding PVP chains. However, the film heated to 65 °C has a high melting point of 75 °C and exhibits reversible thermochromism due to the intercalation of PCDA and PVP by hydrogen bonding in a "bricks and mortar" fashion (Figure 1.27). Surprisingly, the film heated to 85 °C melts at only 47 °C which suggests poor crystalline packing and an insight into its lack of its photoreactivity, as the 85 °C heated film was unresponsive to 254 nm of UV exposure, unlike the other films which polymerised without resistance.[156]

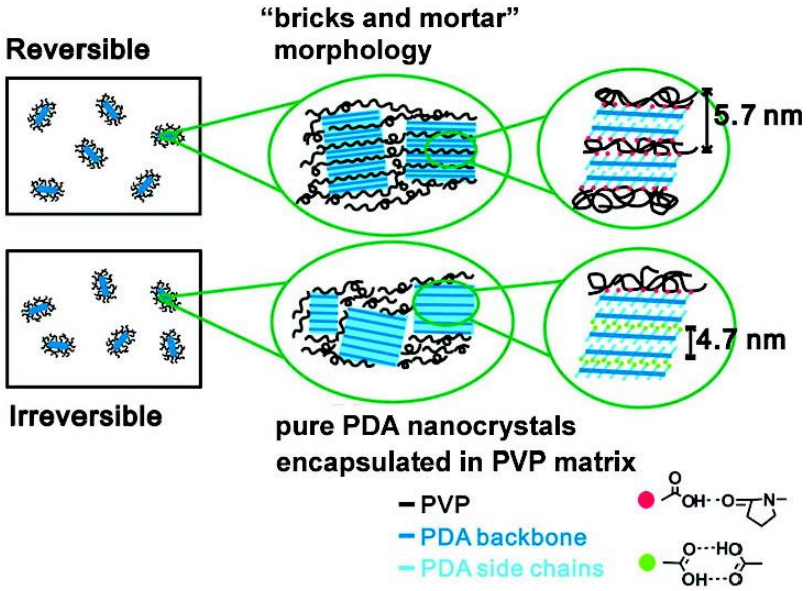

Figure 1.27. An illustration of the "bricks and mortar" analogy to explain the differences between reversible and irreversible thermochromism shown by films of PCDA and PVP. Polydiacetylene is abbreviated to 'PDA'. Reprinted with permission from reference 156. Copyright 2020 American Chemical Society.

Changes in the environment of PCDA also alters its thermochromic behaviour. The colour-change properties of films consisting of layers of PCDA monomer crystals intercalated with metals ions, in response to heating and cooling studies have been explored.[157] When the films were heated to 60 °C, thermal motion of the alkyl portion of PCDA is observed, regardless of the type of guest used.[157] However, when further heat (150 °C and 200 °C) is applied to the PCDA films containing divalent nickel and zinc respectively, a range of colours are observed, from an irreversible blue-to-yellow thermochromism with films of PCDA-Ni(II) (Figure 1.28c), and a reversible blue-to-purple-to-red thermochromism exhibited by PCDA-Zn(II) (Figure 1.28d).[157]

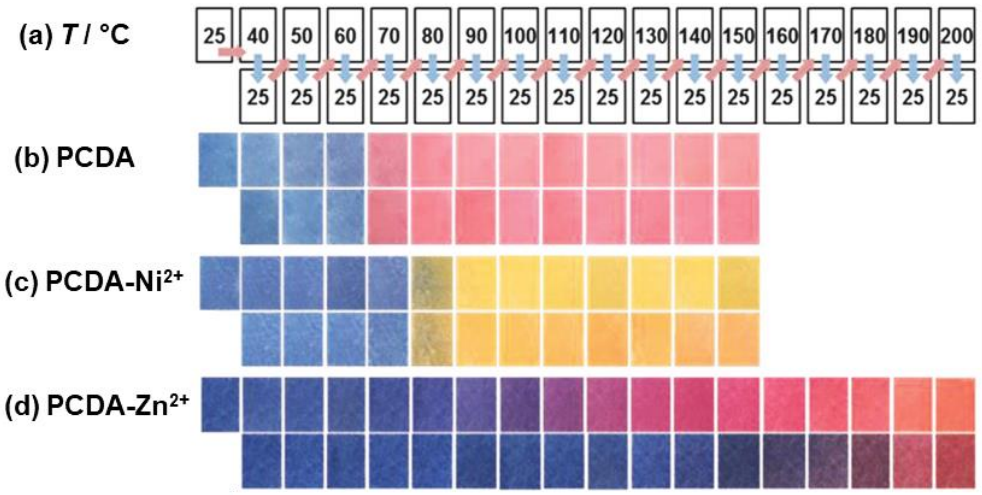

Figure 1.28. The temperature control (a) of the temperature-induced colour changes of films containing PCDA (a colour transition temperature (T_{trs}) of 65.4 °C) (b) and PCDA-Ni(II) from 25 °C – 150 °C (T_{trs} 77.9°C) (c), and PCDA-Zn(II) from 25 °C – 200 °C (T_{trs} 113.7 °C) (d). Figure adapted with permission from reference 157.

In situ powder X-ray diffraction measurements were undertaken to assess the differences in crystallinity of the metal ion films before and after heat treatment. The PXRD patterns of PCDA-Ni(II) changed considerably when heated above 100 °C and the original pattern could not be obtained on cooling, suggesting a strong link between visual irreversible thermochromism and the internal structure of the film.[157] In contrast, PCDA-Zn(II) visually exhibits reversible thermochromism, and the in situ PXRD pattern displays no differences before and after heating, suggesting that the internal structure has not become strained to a high degree and subsequently allows for the electronic properties of the polydiacetylene backbone to be regained.[157] In summary, the PXRD experiments reveal that the PCDA films with intercalated metal ions within the layers change in three stages. Firstly, in both PCDA-Ni(II) and PCDA-Zn(II), there is evidence of the thermal motion of the alkyl chains when the films are heated to 60 °C. Secondly, only the PCDA-Zn(II) film displays torsion of the polydiacetylene backbone to show a colour change above 100 °C. Finally, both PCDA-Ni(II) and PCDA-Zn(II) films become deformed with conformational changes, resulting in a lower crystallinity when heated to above 140 °C.[157] The differences in the behaviour of the two films can be attributed to the different metal ions present between the organic layers changing the behaviour of PCDA through the rigidity of the ions in the layered structure.[157] Additional work on PCDA films

involves the effect of PCDA derivatives on their thermochromic properties.[135] By incorporating aromatic head groups to PCDA such as the 3-aminobenzoic acid derivative (PCDA-mBzA) and 6-amino-2-naphthoic acid compound (PCDA-NPA), the polydiacetylenes exhibit reversible thermochromism rather than the typical observed irreversible process.[135] The increasing size of the PCDA derivatives also affects how the monomers pack in the solid state, and as a result, their colour and the response time of the film to heat.[135] The morphology of the polydiacetylenes also changes with the different head groups. When PCDA is structured as a vesicle, it obtains a spherical morphology, while PCDA-mBzA exhibits large rod-like shape assemblies (suggesting high molecular order), in contrast to PCDA-NPA which exists in large irregularly shaped particles.[135] These findings suggest that an increase in the head group size changes the packing parameter of the surfactant molecules, which dictates the morphology of polydiacetylene assemblies.[135, 158] The addition of aromatic groups to PCDA enhances the inter- and intramolecular interactions between polymerised layers to allow reversible thermochromism up to temperatures of 220 °C for PCDA-mBzA and 180 °C for PCDA-NPA. The polydiacetylene films ranged in colour from blue, to purple, to red, until the films became yellow and exhibited irreversible thermochromism at higher temperatures (230 °C for PCDA-mBzA and 190 °C for PCDA-NPA).[135] It was also found that dried films containing the different polydiacetylenes gave an enhanced colourimetric response compared to the same polydiacetylenes suspended in aqueous solution.[135]

1.6.2. The Importance of Hydrogen Bonds in Reversible Thermochromism

The process of reversible thermochromism is largely dependent on non-covalent interactions, such as hydrogen bonding, van der Waals forces, and π-π stacking.[111, 159-162] However, hydrogen bond interactions are the strongest and most important type of non-covalent interaction for thermochromic reversibility, as they allow the material to exhibit reversible thermochromism in a wider temperature range.[163-165] Monomeric PCDA displays irreversible thermochromism at temperatures above 65 °C due to the increased thermal motion and consequent weakening of the hydrogen bond as temperature increases. Modification of the PCDA carboxylic acid head group can result in reversibility due to enhanced hydrogen-bonding interactions by incorporating amine groups or changing the position of the carboxylic acid group on an aromatic ring to allow for intermolecular hydrogen bonding.[111, 135, 162, 166] A

study involving vesicles containing polymeric PCDA derivatives prove that hydrogen bonding is important for thermochromic reversibility and exhibits blue-red and red-blue colour transitions.[166] The PCDA derivative that exhibited the strongest reversibility to 100 °C heat for three minutes in this study was a diacetylene with a terminal mBzA group. The link between hydrogen bonding and reversible thermochromism exists due to strong head group interactions reducing the strain on the conjugated backbone when exposed to heat, which ultimately prevents the permanent distortion of the chain when the polydiacetylene is cooled.[167] Figure 1.29 illustrates the π-π stacking and carboxylic acid and amide hydrogen bonding in PCDA-mBzA that allow the polydiacetylene to adopt its original blue colouration before heat treatment.[163] Although PCDA-mBzA shows thermochromic reversibility when compared to PCDA, the mBzA derivative of another diacetylene, 10,12-tricosadiynoic acid (TCDA) displayed enhanced reversibility when compared to PCDA-mBzA.[163]

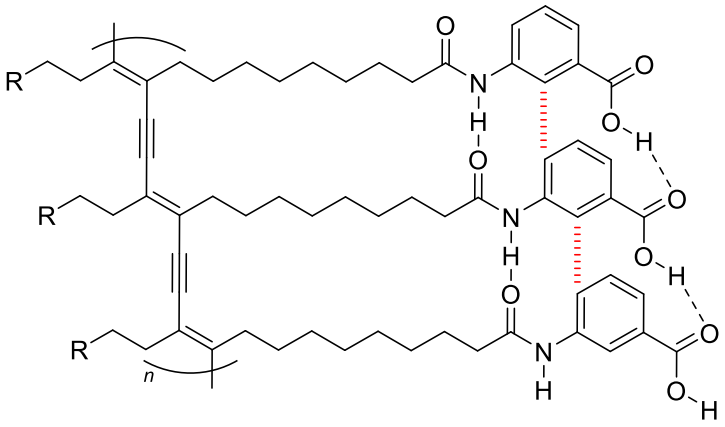

Figure 1.29. The intermolecular forces of PCDA-mBzA. Black dashed lines indicate hydrogen bonding, while red hashed lines indicate π-π stacking. R = $C_{12}H_{26}$.

Another study focusing on the thermochromic reversibility of PCDA-mBzA also investigated the importance of hydrogen bonds in the PCDA-mBzA films upon heating by the adsorption and desorption of cadmium(II) ions.[168] The adsorption of Cd(II) onto the film surface breaks the outer carboxylic O-H···O hydrogen bonds while keeping the amide N-H···O hydrogen bonds intact.[168] The removal of the carboxylic hydrogen bonds is due to the formation of a carboxylate salt of PCDA-mBzA which results in the film displaying irreversible thermochromism.[168] The desorption of Cd(II) allows the PCDA-mBzA film to partially regain its thermochromic reversibility through the recovery of the carboxyl hydrogen bonds,

which is displayed by a visible blue-to-red transition upon heating and a red-to-blue transition on cooling.[168] Therefore, the use of metal ions in polydiacetylene films is a useful way to adjust the thermochromic properties for the required application.

A well-known class of molecules known for their hydrogen bond forming capabilities are ureas, and when incorporated into a PCDA analogue, 10,12-docosadiynoic acid (DCDA) can provide excellent reversible thermochromic properties up to temperatures of 200 °C when appended with hydrophilic polyethyleneglycidyl moieties (Figure 1.30).[149] The reason for the impressive thermoreversibility is due to the bisurea tape formation that forms hydrogen-bonded networks throughout the polydiacetylene.[149] The substituted DCDA monomer can be transferred to paper substrates as ink and will photopolymerise from clear to blue when irradiated. Moreover, the system exhibits a range of colours from blue, purple, red and yellow upon heating to different temperatures.[149] A system with PCDA and a combined acetylurea group displays thermochromic reversibility up to temperatures of 150 °C.[169] The melting temperature of the polydiacetylene plays a large role in the thermochromic reversibility. In reversible thermochromic systems, if the sample is heated to greater than its melting temperature, then it is likely that the transition from reversible to irreversible thermochromism will occur.[169, 170]

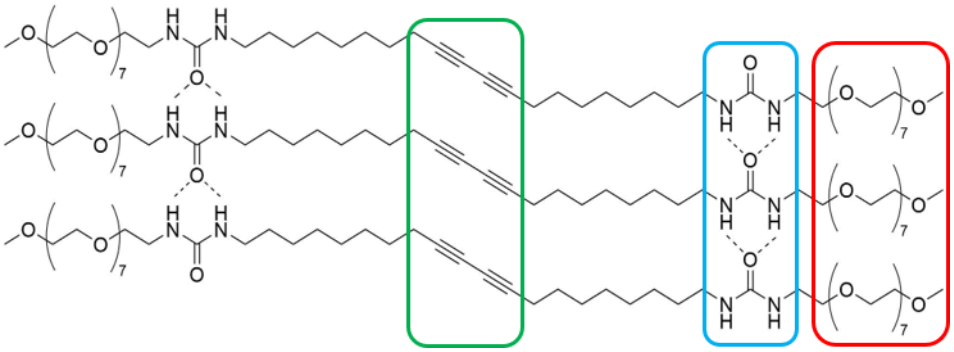

Figure 1.30. The hydrogen-bonded networks of a DCDA urea polyethyleneglycidyl derivative. The green box shows the region responsible for polymerisation, while the urea tapes in the blue box enhance self-assembly, and the region in the red box increases the water compatibility of the molecule.

Thermochromism has also been observed in conductive fibres comprised of aligned carbon nanotubes dip-coated with a PCDA derivative and an attached alternating glycine-alanine peptide segment with a terminal tyrosine group (GAGAGAGY,

Figure 1.31).[171] However, unlike most thermochromic studies with PCDA, the apparent thermochromism was not observed by direct heat, but through the application of electrical current to the fibres.[171] Milliseconds after the application of the electric current, a blue-to-red colour change was observed and then a red-to-purple transition. The response time of the fibre is correlated with the applied current.[171] Upon cooling for only 20 seconds, the fibres returned to their original blue colour, and even after 1000 cycles of current, scanning electron microscopy revealed that the fibres remained unchanged.[171] The impressive reversible thermochromism of the fibres are due to the multiple hydrogen bonds that are able to form from the peptide portion of the polydiacetylene between adjacent molecules.[171]

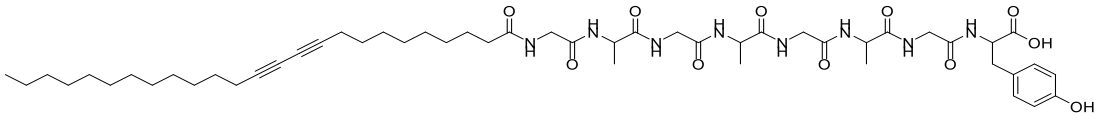

Figure 1.31. The molecular structure of monomeric PCDA modified with a peptide sequence.

Thermochromism has also been recognised in cyclic dipeptides (CDP) containing a PCDA derivative in which the PCDA is covalently bonded to (3*S*)-3-(hydroxymethyl)-piperazine-2,5-dione via an ester linkage.[172] The CDPs have a *cis*-amide functionality consisting of two hydrogen bonding acceptors and donors which allows for strong intermolecular bonding with adjacent CDPs.[172] Additionally, the chiral centre of the head group allows helical packing to self-assemble into bilayers which transform into either single-wall or multiwall structures (Figure 1.32).[172] These hydrogen-bonded supramolecular assemblies exhibit blue-to-red reversible thermochromism even after ten consecutive heat cycles from 25 – 90 °C, thereby adding to the list of thermally responsive functional materials that contain PCDA.[172]

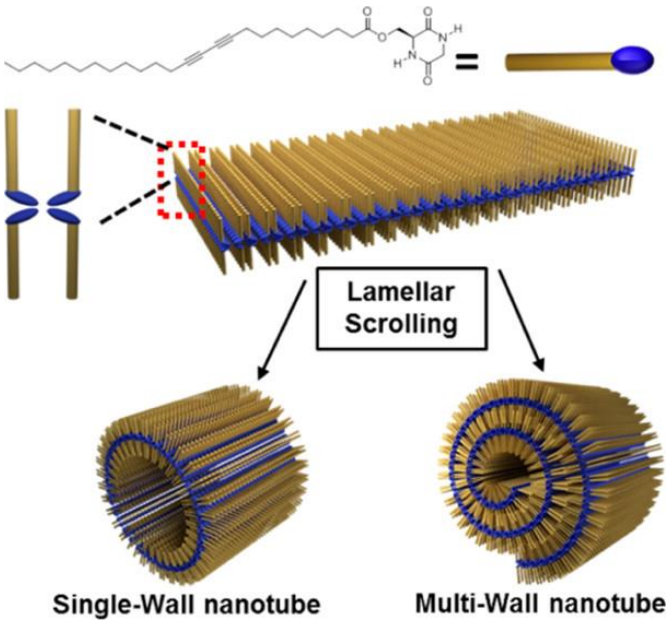

Figure 1.32. The self-assembly of cyclic dipeptide nanotubes of PCDA into bilayers leading to tubular structures of either single wall structures or multi-wall nanotubes. Reprinted with permission from reference 172. Copyright 2020 American Chemical Society.

1.6.3. The Effect of pH

The stability of PCDA films in response to pH changes can be modified, depending on the temperature at which the film was polymerised. Research into multi-layered Langmuir-Schaefer films of polymerised PCDA has been prepared at the air/water interface by exposure to 254 nm of UV radiation at 25 °C and 50 °C.[173] The polymerised films were treated with different pH levels ranging from pH 2-11, to investigate the chromic stability (blue-to-red transition) of the films in response to a change in pH.[173] The results show that the PCDA films polymerised at 50 °C display considerable chromatic stability against pH changes when compared to the 25 °C film equivalent, which was shown to be more sensitive to external stimuli due to its shorter intermolecular packing distance.[173] In contrast to polymerised PCDA films, polymerised PCDA vesicles also change colour with increasing pH.[173] At pH 4-8.8, the carboxylic acid protons of PCDA are deprotonated, which causes the breakage of the hydrogen bonds at the vesicle surface and allows a partial rearrangement of the polydiacetylene segments.[173] This partial rearrangement is accompanied by growth in the absorbance spectra at 650 nm to observe a blue colour.[173] At pH 8.9-10, the absorption spectra display a sharp increase at 500 nm, to exhibit a blue to red colour

transition. The red phase is due to a segmental rearrangement in the entire polymerised PCDA vesicles, opposed to only partial rearrangement at pH 4-8.8.[152] Additional work on the effect of pH on PCDA vesicles involves synthesising PCDA with a 1,4-bis(octyloxy)-2,3-diaminobenzene headgroup.[87] When the vesicle was irradiated, the colour changed from blue to red, and exhibited an irreversible red-yellow transition when exposed to a pH of 1. No colourimetric change occurred when the PCDA derivative was further exposed to a pH range of 2-13.[87]

An interesting application of the colourimetric response of PCDA to pH changes is the detection of *Escherichia coli* bacteria through electrospun fibres containing polymerised PCDA and a supporting polymer, either poly(ethylene oxide) (PEO) or polyurethane (PU).[174, 175] PCDA and polymer fibre composites that are blue in colour were immersed in *E. coli* culture and instantly changed from blue to red, indicating that the proteins secreted by the bacteria initiated the colour change.[176] There is also a positive correlation between a clearer colour change of the fibres and the increasing pH and concentration of bacteria, due to the concentration of the hydroxide ion at pH 11-13, which disrupts the hydrogen bonding of the polydiacetylene head groups. This colourimetric sensing system has the capabilities to be applied to medical textiles such as wound dressings and bandages to detect the presence of *E. coli*.[174] Also, a polydiacetylene-pH sensing system has been developed for the detection of the virulence-factor enzyme urease.[177] Ureolytic activity is catalysed by urease and is used in the diagnosis of a *Helicobacter sp.* infection,[178] and so a pH-sensitive colourimetric system has been designed for urease sensing, through the use of polymeric PCDA vesicles in different solutions.[177] As the pH increased, the PCDA vesicles gradually changed from blue, to purple, to red, with each colour indicating a specific pH value (blue = pH < 7, purple = pH of 7.5-8, red = pH of > 8.5). The colour transitions corresponding to the level of deprotonation of the polydiacetylene vesicles in basic solutions, which is also enhanced formation of ammonia in the urease-catalysed hydrolysis of urea, which increases the pH of the system.[177] The concentration of alkali ions can also be determined by polymerised PCDA when it is combined with nanoporous rice husk silica to form a pH indicator with a sensitivity that can detect alkali ions at concentrations less than 122 μm and can distinguish pH ranges from pH 9.9 to pH 11.4.[179] When this nanocomposite material is coated onto paper for mobile purposes, it forms the basis of a convenient colourimetric detector that changes colour

in the presence of OH^- ions from blue-to-red (Figure 1.33).[179] The paper detector is quick and simple to use, making the pH sensor useful for a primary water testing kit for relevant applications, with future work on amending the paper detectors so they are capable of detecting specific heavy metals.[179]

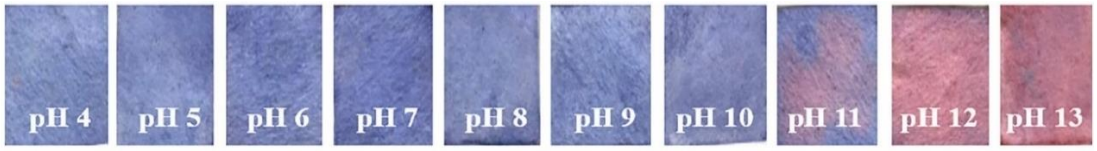

Figure 1.33. The colour change of the paper pH-sensor as the alkali concentration increases. Figure adapted with permission from reference 179.

1.6.4. The Effect of Organic Solvents

Many different approaches have been used to demonstrate that PCDA is capable of recognising various organic solvents, with some systems able to specifically identify individual solvents.[180, 181] Solvatochromic materials have been developed that can distinguish between different organic solvents, mainly through the use of polymer films.[182, 183] Sensors have been designed to consist of hydrogen-bonded alternating layers of polystyrene, a mixture of poly(4-vinylpyridine), and PCDA which are transparent until exposed to UV radiation, and subsequently become blue.[183] Upon the addition of tetrahydrofuran, dichloromethane, chloroform, ethyl acetate, or toluene, the film elicits a blue-to-red transition along with the generation of fluorescence, while acetone, ethanol, isopropanol, and hexane do not affect the PCDA/copolymer film.[183] These results suggest that the solvents have a weak affinity for the polystyrene layer of the film which results in the inability to penetrate the PCDA layer and therefore, the failure to interact and change colour or generate fluorescence (Figure 1.34).[183] The ability of the PCDA/copolymer films to change colour to specific solvents makes for a simple but effective solvatochromic and fluorescence sensor.

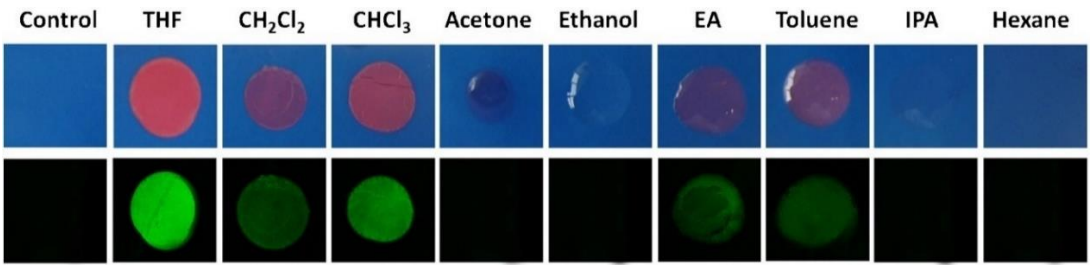

Figure 1.34. Images of different solvents on the PCDA/copolymer films (top) and their fluorescent microscopy images (bottom). Figure adapted with permission from reference 183.

Interaction of linear alcohols (methanol, ethanol, 1-propanol, 1-butanol, 1-pentanol) with polymerised PCDA vesicles shows a typical blue-to-red colour transition after exposure, though the longer the alkyl length of the alcohol, the greater the colourimetric response.[184] This is due to the swelling of the alcohols into the inner layers of the vesicles which weakens the hydrogen bond interactions and results in the rearrangement of the PCDA side chains and conjugated backbone to absorb different wavelengths of light.[184] The polarity of the alcohol also plays an important part in the penetration ability to the inner layers of the polydiacetylene vesicles, as less polar alcohol promotes the penetration into the hydrophobic layer of the vesicle, thus, induces a colour transition easier than solvents of higher polarity.[184] The degree of penetration of the solvent is also influenced by the position of the –OH group within the alcohol molecule; a higher concentration of 2-propanol is required to induce a colour transition, compared to 1-propanol, and branched alcohols result in a steric effect that hinders the penetration of the polydiacetylene vesicle.[184] However, when PCDA is modified with an ethylenediamine head group, the polydiacetylene can distinguish between 1-propanol and 2-propanol, or 1-propanol and ethanol, which provides an important structure-specific insight into the chemical sensing properties of polydiacetylene-based materials.[184] The presence of ethanol to PCDA vesicles results in swelling and increases in size with increasing ethanol concentrations.[185] The swelling of the vesicle results in the hydrogen bonds between the PCDA head groups breaking and weakens the dispersion interactions between the polydiacetylene side chains.[152] Low concentrations of ethanol do not result in a typical blue-to-red colour change, however, when the ethanol concentration is 60 % v/v or above, the colour transition occurs. This result suggests that a high degree of ethanol penetration is required to overcome the interactions of the PCDA head groups and side chains to yield segmental rearrangement of the chains.[152] A similar result was also found with acetone.[186]

An investigation of the behaviour of polymerised PCDA and PCDA derivatives in vesicles in water vs. heavy water produces interesting results.[187] PCDA derivatives include 2-(2-aminoethoxyl)ethanol (HEEPCDA) and *p*-phenylenediamine (APPCDA)

which are attached to the carboxylic acid group of PCDA (Figure 1.35).[187] For PCDA, there is no difference to the thermochromic properties in D_2O or H_2O as the colour of the vesicles remain red and does not revert to the initial blue colouration on cooling, opposed to HEEPCDA that shows reversible thermochromism with D_2O but not in H_2O in the temperature range of 25-70 °C.[187] The preference of HEEPCDA for D_2O in the colour reversibility may be due to stronger hydrogen bond interactions present with D_2O than in H_2O.[187] For the case of vesicles of APPCDA, the vesicles are thermochromically reversible in H_2O but not in D_2O from 25-90 °C, which is the opposite behaviour to that observed for HEEPCDA. For APPCDA, the greater number of non-covalent interactions contributes to the reversibility of APPCDA to heating and cooling cycles.[187] Therefore, it is important what solvent is used in PCDA systems as a small change in the molecular composition of solvent can have vast changes in the observed chromic properties of the system.

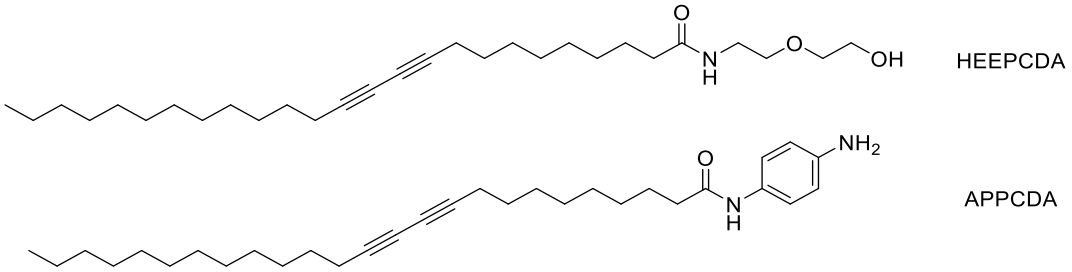

Figure 1.35. Structures of monomeric PCDA derivatives, HEEPCDA and APPCDA.

1.6.5. The Effect of Metal Ions

Materials containing PCDA and PCDA derivatives have been successful at the detection of different metal ions including alkali metals (lithium,[188] sodium,[189, 190] and caesium[191, 192]), transition metals (chromium(III),[193] manganese(II),[194] nickel(II),[195] copper(II),[195] zinc(II),[195-204] silver(I),[194, 205] cadmium(II),[168, 194, 206] iridium(III),[207] gold(III),[208] and mercury(II),[193, 194, 209]) and post-transition metals and metalloids (aluminium(III),[193] arsenic(III),[193, 209] tin(IV),[193] and lead(II)[193, 205, 210-212]), and the lanthanide element terbium(III).[213, 214] Many PCDA systems incorporating metal ions exhibit reversible thermochromism due to the enhanced electrostatic interactions between the cations and the carboxylate head group of PCDA, allowing the structural recovery of the conjugated backbone after the heat stimulus is removed.[197] Nanocomposites comprising of the intercalation of zinc oxide nanoparticles into PCDA assemblies have been studied by powder X-ray diffraction to investigate the

effect of metal ions on the interlamellar *d*-spacing of PCDA.[197] The interlamellar *d*-spacing of polymerised PCDA itself in the blue phase is 4.50 nm compared to 4.45 nm in the red phase (achieved by annealing the nanocomposites to 200 °C), however, when ZnO is incorporated into the PCDA assemblies, the blue phase *d*-spacing increases to 5.22 nm and the red phase of the nanocomposite has an interlamellar *d*-spacing of 5.54 nm.[197] Therefore suggesting that when the PCDA-ZnO nanocomposites are heated, the PCDA polymer side chains rearrange to incorporate the strain on the system.[197] Additional work on PCDA-Zn(II) nanocomposites includes the behaviour of monocarboxylic polydiacetylenes with different alkyl chain lengths, with the polydiacetylenes nanocomposites combined with zinc(II) ions and zinc oxide.[198, 215, 216] Shortening the length of the alkyl chain and the alkyl segment between the reactive alkyne moiety and the carboxyl head group in these nanocomposites drastically changes and their colour transition properties when heated, even though all polydiacetylene nanocomposites in this study exhibit reversible thermochromism.[198] When only the terminal alkyl chain is shortened by two methylene units, the colour-transition temperature of blue-to-purple is reduced by approximately 20 °C due to the weakening of dispersion interactions in the polydiacetylene nanocomposite layers.[152, 198] However, when the alkyl segment adjacent to the carboxyl head group is reduced, the colour-changing temperature trend is unpredictable in the Zn(II)/ZnO nanocomposites.[198]

Iridium complexes situated on the surface of PCDA vesicles can provide long fluorescence lifetime properties and when combined with a polydiacetylene, can also exhibit responsive blue-red properties.[207] Polymerised PCDA itself is fluorescent, though only in the red form, while the blue polymer form is non-emissive.[208, 217] The PCDA vesicles modulate the emission properties of the iridium complex through the blue-to-red colour transition, which enhances the fluorescence lifetime of the polydiacetylene system and allows a simpler way to spectrally differentiate the blue and red phases of the PCDA vesicles.[207] The fluorescence properties of PCDA can also be changed by heat. A structurally modified polymerised PCDA derivative, PCDA-EDEA that was blue in colouration and was placed in a microfluidic temperature sensor and was heated until the polydiacetylene became red and emitted fluorescence (Figure 1.36).[150] It was observed that the fluorescence of the red phase became more intense with increasing temperature (40-60 °C) until the polydiacetylene

is exposed to excessive heat (70-78 °C), where the fluorescence is then quenched and cannot be reversed.[150, 153] The sensing properties of PCDA vesicles have also been explored with the lanthanides, specifically though the use of PCDA-functionalised thiacalix[4]arene vesicles.[218] Calixarenes are three-dimensional host molecules that can be easily modified to act as supramolecular receptors for molecular recognition and sensing applications. In this case, the calixarene-PCDA vesicles display a colourimetric response to metal ions in the lanthanide series of elements (with a 10 mol % content of calixarene), with an enhanced blue-to-red colour change influenced by lanthanum(III) ions in particular. The transition is not observed when the two components are individually exposed to lanthanide ions.[218] The structure of the functional thiacalix[4]arene-PCDA vesicles are shown in Figure 1.37, with the PCDA-1 combination displaying an increased colourimetric response to lanthanum(III) when compared to PCDA-2.[218] The colour transition of the vesicles when in contact with lanthanide ions is due to the distortion of the calixarene cavity which ultimately disturbs the polydiacetylene backbone, alongside metal-induced aggregation and sedimentation of the vesicles.[218] An additional lanthanide ion that has been used in combination with PCDA is terbium(III) with bilayers of PCDA intercalated with terbium(III) ions positioned at the carboxyl head group of PCDA.[214] The nanosheets of PCDA-Tb(III) exhibited reversible thermochromism and reversible fluorescence up to temperatures of 90 °C.[214]

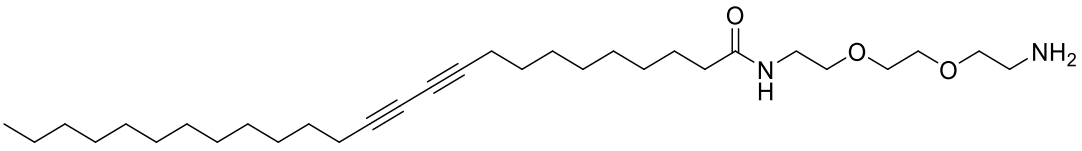

Figure 1.36. Structure of the PCDA diacetylene derivative, PCDA-EDEA.

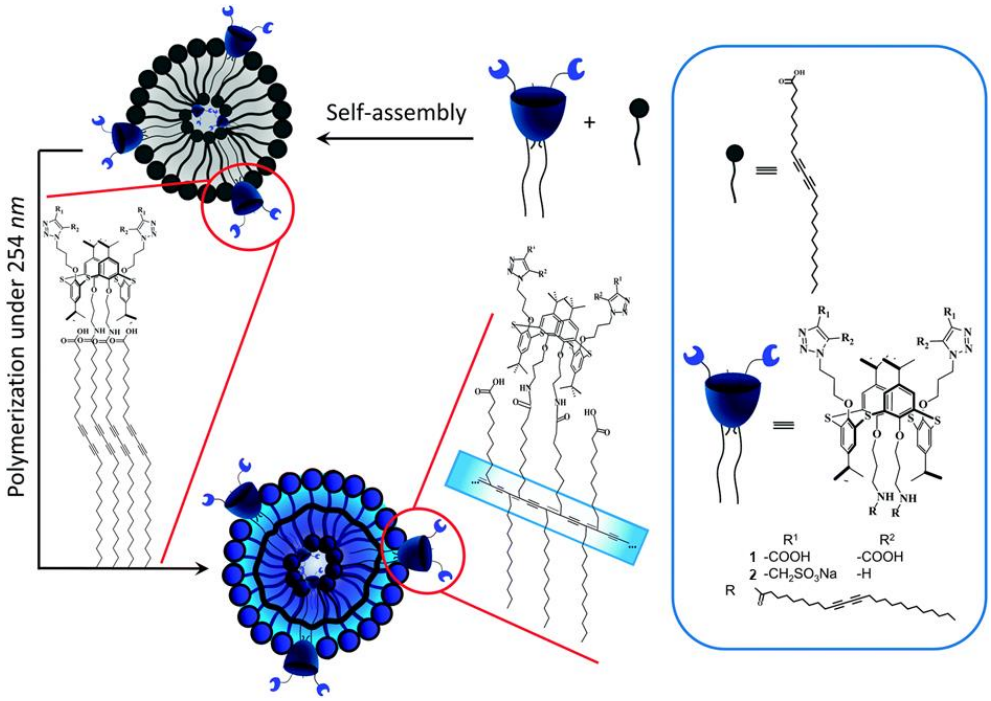

Figure 1.37. A schematic representation of functional thiacalix[4]arene-PCDA vesicles. Figure reproduced with permission from reference 218.

1.6.6. The Effect of Mechanical Stress

The first observation of mechanochromism in PCDA films at the nanometre scale was reported by Carpick and coworkers by atomic force microscopy (AFM) and near-field scanning optical microscopy (NSOM) accompanied by interfacial force microscopy.[219] It was observed that structural changes in PCDA films result in a blue-to-red colour change of the PCDA polymers caused by the shear forces between the cantilever/scanning tip of the AFM and NSOM experiments.[219] The blue-to-red transition will only occur if the AFM scan direction is perpendicular to the backbone direction, as the colour will not change if the film is scanned in a direction parallel to the polydiacetylene backbone.[220] The chromic transition exists even without the excitation laser present and without any heating of the contact zone.[219] It was found that the strongly anisotropic red polymer propagates along the backbone direction of the polydiacetylene by the red domains nucleating at film defects.[219] Once the red phase is established, additional tip-induced mechanochromism does not affect the red phase of polymerised PCDA.[219]

Films of PCDA and perfluorotetradecanoic acid (PF) in a 1:2 ratio respectively, were characterised by dual atomic force and fluorescence microscopy (AFM-FM) and were

irradiated by lasers with wavelengths of 532 nm and 254 nm.[82] Upon irradiation, all the PCDA was polymerised, with around 80 % of the polymer existing in the red phase (which is fluorescent), with the remaining ~20 % in the blue polymer phase.[82] The presence of PCDA polymer can also be determined by AFM height differences when compared to the underlying bare glass substrate the polymer is placed on, with a height difference of approximately 5 nm.[221] The addition of PF to PCDA films compresses the films to give a 1 $Å^2$ reduction in film area, as PF induces mechanical stress which results in the formation of the irreversible red polymer phase of PCDA upon irradiation.[222] Figure 1.38A and Figure 1.38B show AFM images of a polymerised PCDA derivative at the blue-to-red interface adjacent to a silicon dioxide defect in the film, with the heights of the blue and red phases to the substrate are approximately 22 and 9 Å, respectively.[220] Figure 1.38C shows a schematic representation of the two coloured polydiacetylene forms, with the planar "blue" form to the right of the image, becoming twisted and distorting the conjugation of the backbone, to result in the "red" form.[220]

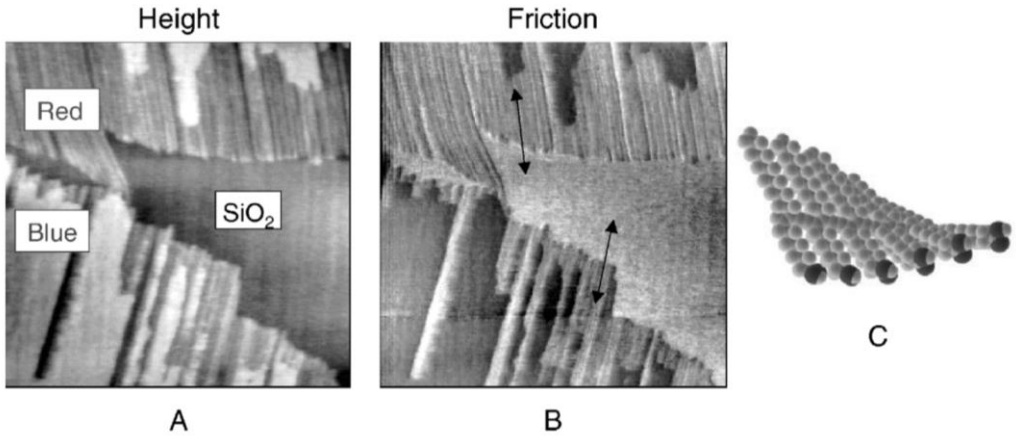

Figure 1.38. The AFM images of a region of polymerised N-(-2-ethanol)-10,12-pentacosadinamide film that was transformed under shear forces on a silicon dioxide substrate, with the fast scan direction along the *x*-axis. A) The blue phase = brightest, red phase = darkest. B) The blue phase = darkest, red phase = brightest, with the arrows indicating the backbone direction. C) A schematic of the blue-to-red transition of the polymer. Figure reproduced with permission from reference 220.

Conductive carbon nanotubes (CNT) coated in polymerised PCDA readily exhibit a blue-to-red colour change when exposed to an electric current. Unlike other PCDA systems, the PCDA-CNT composites are reversible with the colour change retained

when exposed to current cycles lower than 30 mA, with the CNTs reversing to the original blue state after only two seconds from the removal of the current.[223] The colour transition is reversible at 30 mA as the polydiacetylene backbone only temporarily deforms through the polarisation of the carbonyl group in the PCDA side chains, which decreases the conjugation of the backbone while the CNTs are exposed to the applied current.[223, 224] At higher current values, it is expected that the polydiacetylene will permanently deform, resulting in irreversible chromism of the PCDA-CNTs.[223] It was discovered that when the PCDA-CNTs are exposed to mechanical stress, the colour of the CNTs is dependent on the applied tensile stress to the CNT. A CNT fibre was exposed to a tensile strain of 0.55 GPa and remained blue, while at tensile stress values below 0.48 GPa, the PCDA-CNT fibres immediately became red.[223] However, if the applied tensile stress reached the range of 0.48-0.51 GPa and the mechanical stress was removed, the colour transition reversed from red-to-blue.[223] Electrochromic and mechanochromic PCDA-CNTs make for impressive functional materials with sensing properties that can be applied to many fields.

Powders of polymerised PCDA intercalated with guest organic amines reveal a mechano-responsive colour change that is clearly visible to the naked eye, with the responsiveness of the powders tuned by the type of alkyl amine or diamine used (with varying alkyl lengths from 4-16 carbon atoms long).[225] PXRD of the composites revealed that PCDA was no longer dimerised by O-H···O hydrogen bonds at the carbonyl head groups, and instead exist as ammonium salts.[225] The responsivity of the PCDA-powders to heat and mechanical stress were similar, as both stimuli resulted in an irreversible blue-to-red colour change, however, the colour change after rubbing the powder was found to be caused by shear stress, rather than by the frictional heat caused by rubbing.[225] As the effects of mechanical stress and heating were similar on the powders, the effect of rubbing the powders must have the same internal mechanism of accumulated torsion on the polydiacetylene backbone, which dictates the observed colourimetric changes. These stimuli-responsive powders have the potential to be applied to a variety of sensing and diagnostic materials.[225]

1.7. Applications of Diacetylenes

1.7.1. Dosimetry Technology

Dosimeters are typically two-dimensional films that work on the premise that when irradiated, the colour of the film changes from clear to blue, with the intensity of blue colour proportional to the amount of irradiation the film has received. This correlates with the degree of polymerisation of the diacetylenes present in the film. One of the most commonly used diacetylene based radiochromic sensors for therapeutic purposes are Gafchromic films, which are comprised of a lithium salt of PCDA.[188] The most used radiochromic film, Gafchromic EBT®, comprises of an active layer which is surrounded by a polyester cover (Figure 1.39) and is intended for recording radiation doses between 1 cGy and 40 Gy (with 1 cGy equivalent to 1 rad).[226] Alternative models of Gafchromic films can detect different dosage ranges than the EBT model due to changes in their chemical composition and thicknesses of the active layer in the films, with the different models detecting doses from 0.2 cGy-1000 Gy.[227] Previous discontinued radiochromic films models such as MD-55 contained PCDA as the diacetylene in the active layer, however, the MD-55 film was only useful at doses greater than 5 Gy.[228, 229] Additionally, PCDA has also been incorporated into films using polyvinyl alcohol (PVA)[92] and polyvinyl butyral (PVB)[230] as the polymer layer, compared to polyester in the Gafchromic films. The PCDA-PVA film exhibits a colour change from clear to dark blue at a dose range of 100 Gy-6000 Gy,[92] while the PVB film displays a dose range of 5-4000 Gy, though the range is dependent on the PCDA content within the films.[230] An important application of radiochromic films is their use on blood bags to indicate if the blood has been irradiated with gamma radiation before the blood is transferred between patients.[231] Once the film has been irradiated, the film will change colour from transparent red with the word “NOT” across the film, to opaque, which makes it clear to the handler which blood is safe to use (Figure 1.40).[232] This irradiation process prevents the spread of transfusion-associated graft-versus-host disease which is rare but can be fatal if an immunocompromised patient is exposed to the disease.[231] An alternative to 2D radiochromic films is the utilisation of 3D PCDA gel dosimeters which display a linear irradiation response in the dose range of 2-100 Gy.[233] The gel dosimeters are prepared through the dispersion of self-assembled nanovesicles of PCDA into a gel matrix, Figure 1.41. When compared to existing 3D dosimeters,[234, 235] the PCDA gel system provides excellent tissue equivalence, has high

spatial resolution and dose accuracy, and does not exhibit any dose rate, energy or temperature-dependent effects.[233]

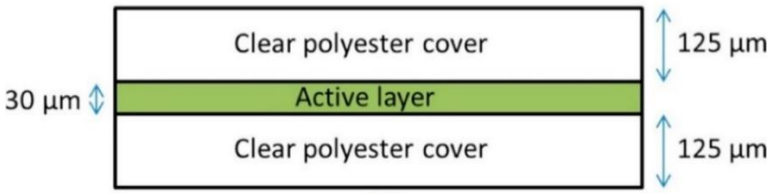

Figure 1.39. The composition of Gafchromic EBT3 film. Figure adapted with permission from reference 226.

Figure 1.40. Radiochromic film labels used for irradiation detection on blood bags. Figure reproduced from reference 232.

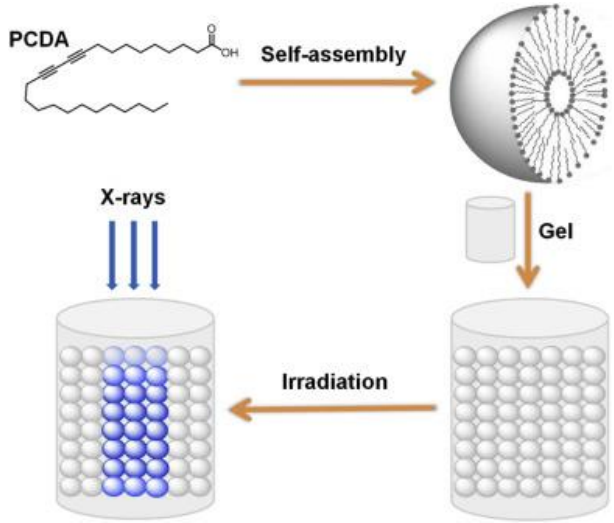

Figure 1.41. The preparation and application of PCDA vesicles to create a gel dosimeter. Reproduced with permission from reference 233.

1.7.2. Biosensors

Polydiacetylenes have the potential to produce a colourimetric response to a wide range of biomolecules such as proteins/enzymes,[177, 236-239] viruses,[240-242] bacteria,[174, 243-245] sugars,[246-248] and active ingredients.[249] A recent review on polydiacetylene-based sensors categorises the sensor application by the type of

chromism that is used e.g. thermochromism, solvatochromism, or electrochromism.[250] Polydiacetylene biosensors have real-world applications within the field of food safety, with PCDA vesicles able to detect the presence of *Salmonella* bacteria,[251] along with the detection of eight commonly used sanitisers and surfactants used in the food industry.[252] Recent work on treating bacterial infections includes the detection of pore-forming toxins by PCDA.[243] A polymerised PCDA nanoparticle-functionalised microgel has been designed to manage topical bacterial infections, with the specific nanoparticle morphology prepared by a 3D bioprinting process.[243] The 3D nanoparticle gel diffuses and neutralises the pore-forming toxins released from bacteria and has shown in mouse models that the microgel promotes tissue recovery after bacterial infection, and, therefore, has the potential to be developed into a larger-scale treatment in the future.[243] PCDA has also been extensively studied for its chromic properties when combined with biomolecules, for example, nucleic acids have been detected by modifying the head group of PCDA with an antibiotic, neomycin, which inhibits bacterial protein synthesis through binding to the 30S subunit of the bacterial ribosome.[253-255] Therefore, the neomycin head group of PCDA will act as a binding site for RNA resulting in a conformational change of the polymerised PCDA-neomycin complex and hence a blue-to-purple colourimetric change.[249] The detection of the veterinary fluoroquinolone antibiotic, enrofloxacin, has also been achieved through the synthesis of a nanoblend consisting of polymerised PCDA, triblock copolymer (poly(ethylene oxide)-poly(propylene oxide)-poly(ethylene oxide)), and sodium dodecyl sulfate (SDS).[256] The detection of enrofloxacin residues are important for human health, especially in terms of food safety and antimicrobial resistance. The colourimetric response of enrofloxacin to the nanoblend depends on the SDS concentration suggesting that the surfactant is as important as PCDA in the detection of enrofloxacin residues.[256] Alongside antibiotics, PCDA has also been used in enzyme-free systems to amplify the presence of miRNA in human serum at ultralow concentrations, as miRNA expression is dysregulated in human cancer and therefore, can serve as a potential biomarker for cancer diagnosis.[257, 258] The presence of DNA has also been detected through the utilisation of a *p-tert*-butyl thaicalix[4]arene with PCDA moieties on either side of the macrocyclic cavity.[259] When the PCDA residues are polymerised by UV exposure and the calixarene is in contact with calf thymus DNA, the macrocycle intercalates to form a lipoplex and displays a typical blue-to-red colour change from concentrations as low

as 20 μmol/L.[259] Polymerised PCDA has been incorporated into a microtube waveguide system whereby single-stranded miRNA is attracted to the surface of the PCDA microtube which facilitates an amplification reaction within the surface of the PCDA microtube, ultimately able to distinguish between cancer patients and healthy humans.[257] The detection of specific proteins is also possible when combining enzymes such as glutathione *S*-transferase,[236] phospholipase D,[93] and alkaline phosphatase[260] to PCDA head groups which elicits a colourimetric response. Interestingly, polymerised PCDA vesicles have also been combined with phospholipids (1,2-dimyristoyl-*sn*-glycero-3-phosphocholine (DMPC), 1,2-dimyristoyl-*sn*-glycero-3-phospho-(1′-*rac*-glycerol) (DMPG), and stearamide) to tune the surface potentials of vesicles designed for gene therapy (Figure 1.42A).[237] When model gene vectors Lipofectamine 2000, Entranster TM-H4000, and polyethylenimine are added to the phospholipid/polydiacetylene vesicles, a colour change is observed in less than five minutes from blue-to-red (Figure 1.42B).[237] From the UV-Vis data, the affinity constant was calculated to determine the sensitivity of each type of phospholipid/polydiacetylene vesicle combination used and revealed that the vesicles consisting of DMPC/PDA show the highest sensitivity towards gene vectors.[237] This polydiacetylene biosensing system demonstrates a rapid visualisation technique of gene vectors that has the potential for screening of carrier molecules for drug delivery.[237]

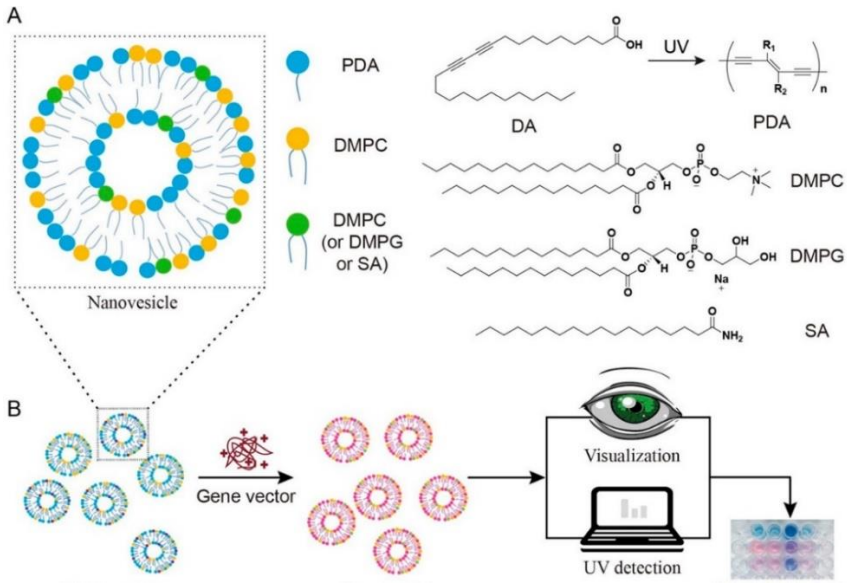

Figure 1.42. A) An illustration of the incorporation of different phospholipids into the polydiacetylene (PDA) nanovesicles. B) The rapid colour change of the phospholipid/polydiacetylene vesicles when in contact with gene vectors and the quantification of the colour change by UV-Vis analysis. Reprinted with permission from reference 237. Copyright 2020 American Chemical Society.

Research has been conducted for the colourimetric detection of the influenza A virus (pH1N1), through the modification of PCDA materials.[238] For instance, a recent study involves designing paper chips that contain a polymerised PCDA-imide derivative that detects the pH1N1 influenza strain with high sensitivity by an obvious blue-to-red colour change, ultimately for quick and easy point-of-care testing of the influenza A virus.[240] The PCDA derivative was mixed with PCDA and DMPC and a polyvinylidene difluoride (PVDC) membrane, with PCDA secured to the PVDC membrane through UV irradiation for one minute.[240] A colourimetric change occurs on the chip due to the binding events of the pH1N1 virus by the interaction of the influenza A virus nucleoprotein and nucleoprotein antibodies on the surface of the chip, and to intensify the colour change, the chip can be incubated or physically touched to enhance the thermochromic properties of the polydiacetylene system.[240] Though the sensitivities of the polydiacetylene-paper chip are too low for clinical applications, a smartphone application has been designed to visually detect a high concentration of viruses based on the colourimetric response of the paper chip results.[240]

1.7.3. Chemosensors

The detection of specific chemicals that pose a risk to human health and environmental welfare is of high importance, and multiple polydiacetylene systems have been developed to combat the issues. A World Health Organization 1990 review of the impact of pesticides on human health, estimated that over 3 million cases of severe acute poisoning were due to pesticides, and of these around 220,000 were the cause of death, indicating the need for a practical pesticide detection system.[261] A recent study uses a commonly used organophosphate insecticide, malathion, that can be detected by PCDA with pralidoxime (PAM) functionalised terminal group, enabling PCDA to bind to organophosphates and which would inhibit the pesticides' mechanism of action through the binding of acetylcholinesterases present in the synaptic cleft.[262] When polymerised PCDA/PAM binds to malathion, a blue-to-purple-to-red colour change is observed within seconds of binding and can be observed by the naked eye and quantified by electronic absorption studies.[262] Polymerised PCDA also can detect the presence of trinitrotoluene (TNT) when coupled with a TNT recognition motif comprised of a trimer peptide of tryptophan-histidine-tryptophan (Trp-His-Trp).[263] The binding of TNT to the peptide region results in a conformational change which alters the conjugated backbone of PCDA, resulting in a blue-to-red colour change.[263]

Polydiacetylene-based sensors are also helpful in the food industry, with the development of low-cost films that can detect the early release of gases due to food spoilage and are suitable for food packaging labels.[264] The ammonia-sensitive films consist of PCDA as the sensing material, cellulose nanocrystals (CNC) as the stabilising agent, and chitosan to provide a matrix. The components help to fabricate strong but flexible free-standing films that display a blue-to-red colour change when in the presence of ammonia over a wide temperature range of −20 to 24 °C.[264]

An impressive dual-stimuli responsive dendritic diacetylene has been designed with an aromatic head group and a PCDA tail that forms a tetraphenylmethane core capable of forming pores in the tight packing structure (Figure 1.43).[265] Once polymerised, the tetrahedral structure (TePDA) exhibits cross-linking to give the typical ene-yne carbon backbone and displays reversible blue-red-blue thermochromism at temperatures up to 134 °C.[265] The main application of TePDA is the detection of volatile organic compounds in the vapour phase. Paper strips were coated with TePDA and exposed to the vapours of dichloromethane, tetrahydrofuran, chloroform, benzene, toluene,

xylene in different concentrations (0.05 %-1.0 %) for one hour. Chloroform provided the greatest colourimetric response with a colour change from blue to light brown, while PCDA alone shows an indistinct colour transition at the maximum concentration of chloroform.[265] This intrinsically porous self-assembled material has the potential to be used in multi-disciplinary fields that require a system that is sensitive to more than one stimulus at a time.

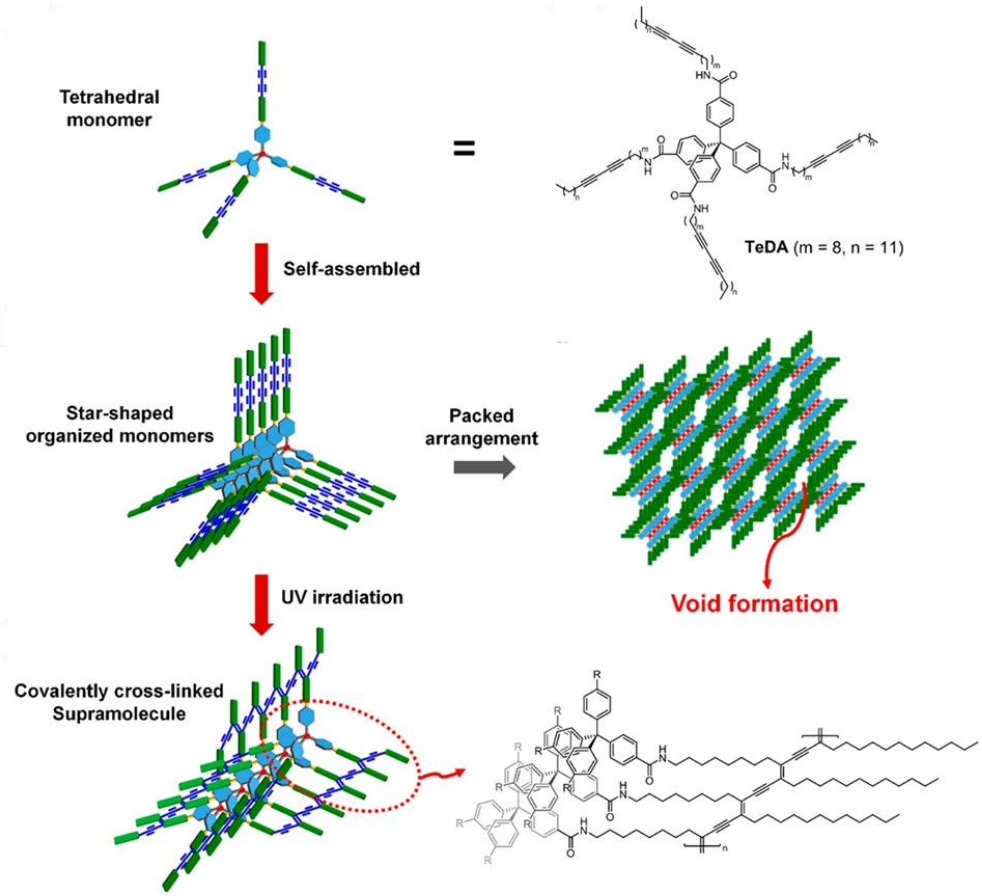

Figure 1.43. The formation of the self-assembled tetrahedral diacetylene in monomeric and polymeric forms. Reprinted with permission from reference 265. Copyright 2020 American Chemical Society.

The combination of PCDA and polymers have also been shown to enhance the sensing properties of the diacetylene. For instance, monomeric PCDA has been embedded in poly-ε-caprolactone polymer matrix through electrospinning and irradiated by UV exposure, which allows the polymer matrix to detect the presence of organic solvent additives in gasoline, through a visible blue-to-red colour change.[266] Another polymer matrix system involves electrodes coated with polymerised PCDA which are embedded in a porous polymer matrix containing PVP by a spin coating technique.[267]

The PCDA/PVP electrode acts as a vapour-sensing system, or an "artificial nose" for detecting different organic solvents, with each vapour determining a different capacitance transformation, which is fully reversible when the vapour is no longer in contact with the electrode.[267] Figure 1.44 summarises the capacitance responses of polydiacetylene/PVP thin films containing TCDA and PCDA to different solvents, with the responses colour coded to the degree of capacitance change.[267] These results illustrate the vapour selectivity for two different diacetylenes as the capacitance changes depending on the exposure of different vapours, with PCDA showing higher capacitance values in more solvents than TCDA.[267] A different study that involves electrical conductivity rather than the storage of electrical charge has focused on the effect of PCDA sulfonic acid derivatives as dopants to increase the thermal stability and maintain the electrical conductivity of polyaniline.[268] The PCDA derivatives were synthesised by derivatising the carboxylic acid group with either a 2-aminoethanesulfonic acid group or a 4-aminobenzenesulfonic acid (pBzS) group.[268] Upon polymerisation of the diacetylene dopants with polyaniline, the thermal stability was observed in the range 250-600 °C, with the sheet resistance of polymerised dopants maintained, when compared to polyaniline with dodecylbenzenesulfonic acid, which has the same functional group as PCDA-pBzS, though without the photoreactive diacetylene functionality.[268]

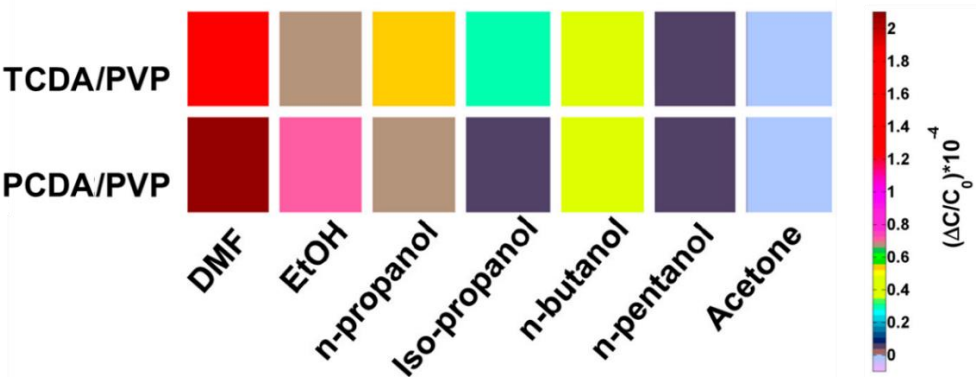

Figure 1.44. The capacitance responses of thin PVP composite films containing TCDA and PCDA to different gases, with the colour coded to the degree of capacitance change scale on the right. Figure adapted with permission from reference 267. Copyright 2020 American Chemical Society.

1.8. Project Aims and Overview

This work aims to further understand the relationship between the solid state photoreactivity of 10,12-pentacosadiynoic acid and its crystal structure, as there is no single-crystal X-ray structure of PCDA currently in the literature. Further to the full characterisation of PCDA, the diacetylene will be combined with various organic and inorganic compounds to investigate PCDA as different multicomponent solid state forms by the implementation of topochemical and crystal engineering principles.[103, 122, 269, 270] These principles will be used to systematically design different cocrystals and salts of PCDA to explicitly tailor the reactive moieties of PCDA which will optimise the resulting photosensitivity when the material is exposed to UV and X-ray radiation. The multicomponent forms will be synthesised in solution and by the application of mechanical grinding. The new PCDA cocrystals and salts will attempt to rival the active ingredient in marketed GAFchromic films which incorporates the lithium salt of PCDA.[188] As a result, this work will contribute to the improvement of radiochromic materials for dosimetric purposes.

1.9. References

1. J. W. Steed, *Chem. Commun.*, 2018, **54**, 13175-13182.
2. C. B. Aakeröy and D. J. Salmon, *CrystEngComm*, 2005, **7**, 439-448.
3. E. Grothe, H. Meekes, E. Vlieg, J. H. ter Horst and R. de Gelder, *Cryst. Growth Des.*, 2016, **16**, 3237-3243.
4. S. L. Childs, G. P. Stahly and A. Park, *Mol. Pharmaceutics*, 2007, **4**, 323-338.
5. N. Blagden, S. J. Colesb and D. J. Berry, *CrystEngComm*, 2014, **16**, 5753-5761.
6. N. A. Mir, R. Dubey and G. R. Desiraju, *Acc. Chem. Res.*, 2019, **52**, 2210-2220.
7. J. W. Steed, *Trends Pharmacol. Sci.*, 2013, **34**, 185-193.
8. G. Bolla and A. Nangia, *Chem. Commun.*, 2016, **52**, 8342-8360.
9. *Regulatory Classification of Pharmaceutical Co-Crystals Guidance for Industry*, U.S. Department of Health and Human Services, Food and Drug Administration Center for Drug Evaluation and Research (CDER), Maryland, 2018.
10. N. Schultheiss and A. Newman, *Cryst. Growth Des.*, 2009, **9**, 2950-2967.
11. L. J. Barbour, D. Das, T. Jacobs, G. O. Lloyd and V. J. Smith, in *Supramolecular Chemistry: From Molecules to Nanomaterials*, eds. J. W. Steed and P. A. Gale, Wiley, 2012, vol. 6.
12. M. Viertelhaus, R. Hilfiker, F. Blatter and M. Neuburger, *Cryst. Growth Des.*, 2009, **9**, 2220-2228.
13. S. Mohamed, D. A. Tocher and S. L. Price, *Int. J. Pharm.*, 2011, **418**, 187-198.

14. W. McCrone, in *Physics and Chemistry of the Organic Solid State*, eds. D. Fox, M. M. Labes and A. Weissberger, Wiley Interscience, New York, 1965, vol. 2, pp. 725-767.
15. A. Lemmerer, D. A. Adsmond, C. Esterhuysen and J. Bernstein, *Cryst. Growth Des.*, 2013, **13**, 3935-3952.
16. T. R. Shattock, K. K. Arora, P. Vishweshwar and M. J. Zaworotko, *Cryst. Growth Des.*, 2008, **8**, 4533-4545.
17. A. V. Trask, W. D. S. Motherwell and W. Jones, *Cryst. Growth Des.*, 2005, **5**, 1013-1021.
18. A. V. Trask, J. van de Streek, W. D. S. Motherwell and W. Jones, *Cryst. Growth Des.*, 2005, **5**, 2233-2241.
19. S. Aitipamula, P. S. Chow and R. B. H. Tan, *CrystEngComm*, 2014, **16**, 3451-3465.
20. G. P. Stahly, *Cryst. Growth Des.*, 2007, **7**, 1007-1026.
21. P. G. Vekilov, *Cryst. Growth Des.*, 2010, **10**, 5007-5019.
22. J. J. De Yoreo and P. G. Vekilov, *Biomineralization*, 2003, **54**, 57-93.
23. R. J. Davey, S. L. M. Schroeder and J. H. ter Horst, *Angew. Chem., Int. Ed.*, 2013, **52**, 2166-2179.
24. P. G. Vekilov, *Nature*, 2019, **570**, 450-452.
25. D. Erdemir, A. Y. Lee and A. S. Myerson, *Acc. Chem. Res.*, 2009, **42**, 621-629.
26. T. Yamazaki, Y. Kimura, P. G. Vekilov, E. Furukawa, M. Shirai, H. Matsumoto, A. E. S. Van Driessche and K. Tsukamoto, *Proc. Natl. Acad. Sci. U. S. A.*, 2017, **114**, 2154-2159.
27. J. Y. Weng, Y. P. Huang, D. L. Hao and Y. H. Ji, *Chin. J. Chem. Eng.*, 2020, **28**, 935-948.
28. R. J. Li, X. T. Zhang, H. L. Dong, Q. K. Li, Z. G. Shuai and W. P. Hu, *Adv. Mater.*, 2016, **28**, 1697-1702.
29. J. J. De Yoreo, L. A. Zepeda-Ruiz, R. W. Friddle, S. R. Qiu, L. E. Wasylenki, A. A. Chernov, G. H. Gilmer and P. M. Dove, *Cryst. Growth Des.*, 2009, **9**, 5135-5144.
30. P. G. Vekilov, *Prog. Cryst. Growth Charact. Mater.*, 2002, **45**, 175-193.
31. G. Sgualdino, G. Vaccari, G. Mantovani and D. Aquilano, *Prog. Cryst. Growth Charact. Mater.*, 1996, **32**, 225-245.
32. T. L. Threlfall and S. J. Coles, *CrystEngComm*, 2016, **18**, 369-378.
33. E. A. Losev and E. V. Boldyreva, *CrystEngComm*, 2018, **20**, 2299-2305.
34. R. H. Lin, M. W. Woo, C. Selomulya, J. P. Lu and X. D. Chen, *Ind. Eng. Chem. Res.*, 2013, **52**, 13449-13458.
35. B. Spingler, S. Schnidrig, T. Todorova and F. Wild, *CrystEngComm*, 2012, **14**, 751-757.
36. G. R. Desiraju, *Crystal engineering : the design of organic solids*, Elsevier, Amsterdam; New York, 1989.
37. C. B. Aakeroy, *Acta Crystallogr., Sect. B: Struct. Sci.*, 1997, **53**, 569-586.
38. M. D. Cohen and G. M. J. Schmidt, *J. Chem. Soc.*, 1964, 1996-2000.
39. G. M. J. Schmidt, *Pure Appl. Chem.*, 1971, **27**, 647-678.
40. B. Moulton and M. J. Zaworotko, *Chemical Reviews*, 2001, **101**, 1629-1658.
41. L. R. Macgillivray, G. S. Papaefstathiou, T. Friscic, T. D. Hamilton, D. K. Bucar, Q. Chu, D. B. Varshney and I. G. Georgiev, *Acc. Chem. Res.*, 2008, **41**, 280-291.
42. G. R. Desiraju, *Angew. Chem., Int. Ed. Engl.*, 1995, **34**, 2311-2327.

43. G. R. Desiraju, *J. Am. Chem. Soc.*, 2013, **135**, 9952-9967.
44. M. C. Etter, *Acc. Chem. Res.*, 1990, **23**, 120-126.
45. M. C. Etter, J. C. Macdonald and J. Bernstein, *Acta Crystallogr., Sect. B: Struct. Sci., Cryst. Eng. Mater.*, 1990, **46**, 256-262.
46. J. Bernstein, R. E. Davis, L. Shimoni and N. L. Chang, *Angew. Chem., Int. Ed.*, 1995, **34**, 1555-1573.
47. D. J. Berry and J. W. Steed, *Adv. Drug Deliv. Rev.*, 2017, **117**, 3-24.
48. E. Arunan, G. R. Desiraju, R. A. Klein, J. Sadlej, S. Scheiner, I. Alkorta, D. C. Clary, R. H. Crabtree, J. J. Dannenberg, P. Hobza, H. G. Kjaergaard, A. C. Legon, B. Mennucci and D. J. Nesbitt, *Pure Appl. Chem.*, 2011, **83**, 1637-1641.
49. G. A. Jeffrey, *An Introduction to Hydrogen Bonding*, Oxford University Press, Oxford, 1997.
50. G. R. Desiraju, *Acc. Chem. Res.*, 2002, **35**, 565-573.
51. T. Steiner, *Angew. Chem., Int. Ed.*, 2002, **41**, 48-76.
52. G. R. Desiraju, P. S. Ho, L. Kloo, A. C. Legon, R. Marquardt, P. Metrangolo, P. Politzer, G. Resnati and K. Rissanen, *Pure Appl. Chem.*, 2013, **85**, 1711-1713.
53. P. Muller, *Pure Appl. Chem.*, 1994, **66**, 1077-1184.
54. A. Mukherjee, S. Tothadi and G. R. Desiraju, *Acc. Chem. Res.*, 2014, **47**, 2514-2524.
55. G. Cavallo, P. Metrangolo, R. Milani, T. Pilati, A. Priimagi, G. Resnati and G. Terraneo, *Chem. Rev.*, 2016, **116**, 2478-2601.
56. N. S. Goroff, S. M. Curtis, J. A. Webb, F. W. Fowler and J. W. Lauher, *Org. Lett.*, 2005, **7**, 1891-1893.
57. S. P. Yelgaonkar, D. Kiani, J. Baltrusaitis and L. R. MacGillivray, *Chem. Commun.*, 2020, **56**, 6708-6710.
58. S. E. Wheeler, *J. Am. Chem. Soc.*, 2011, **133**, 10262-10274.
59. K. Biradha, C. Seward and M. J. Zaworotko, *Angew. Chem., Int. Ed.*, 1999, **38**, 492-495.
60. C. Janiak, *J. Chem. Soc., Dalton Trans.*, 2000, 3885-3896.
61. T. Friscic, C. Mottillo and H. M. Titi, *Angew. Chem., Int. Ed.*, 2020, **59**, 1018-1029.
62. J. L. Do and T. Friscic, *ACS Cent. Sci.*, 2017, **3**, 13-19.
63. S. L. James, C. J. Adams, C. Bolm, D. Braga, P. Collier, T. Friscic, F. Grepioni, K. D. M. Harris, G. Hyett, W. Jones, A. Krebs, J. Mack, L. Maini, A. G. Orpen, I. P. Parkin, W. C. Shearouse, J. W. Steed and D. C. Waddell, *Chem. Soc. Rev.*, 2012, **41**, 413-447.
64. D. Braga, L. Maini and F. Grepioni, *Chem. Soc. Rev.*, 2013, **42**, 7638-7648.
65. D. Hasa and W. Jones, *Adv. Drug Deliv. Rev.*, 2017, **117**, 147-161.
66. T. Friscic, I. Halasz, P. J. Beldon, A. M. Belenguer, F. Adams, S. A. J. Kimber, V. Honkimaki and R. E. Dinnebier, *Nat. Chem.*, 2013, **5**, 66-73.
67. M. R. Caira, L. R. Nassimbeni and A. F. Wildervanck, *J. Chem. Soc., Perkin Trans. 2*, 1995, 2213-2216.
68. S. M. Oburn, O. A. Ray and L. R. MacGillivray, *Cryst. Growth Des.*, 2018, **18**, 2495-2501.
69. R. D. B. Walsh, M. W. Bradner, S. Fleischman, L. A. Morales, B. Moulton, N. Rodriguez-Hornedo and M. J. Zaworotko, *Chem. Commun.*, 2003, 186-187.
70. F. Fischer, A. Heidrich, S. Greiser, S. Benemann, K. Rademann and F. Emmerling, *Cryst. Growth Des.*, 2016, **16**, 1701-1707.

71. E. Boldyreva, *Chemical Society Reviews*, 2013, **42**, 7719-7738.
72. G. Kaupp, *CrystEngComm*, 2009, **11**, 388-403.
73. N. Han, H. J. Woo, S. E. Kim, S. Jung, M. J. Shin, M. Kim and J. S. Shin, *J. Appl. Polym. Sci.*, 2017, **134**, 1-8.
74. P. C. M. Grim, S. De Feyter, A. Gesquiere, P. Vanoppen, M. Rucker, S. Valiyaveettil, G. Moessner, K. Mullen and F. C. De Schryver, *Angew. Chem., Int. Ed.*, 1997, **36**, 2601-2603.
75. C. Kantha, H. Kim, Y. Kim, J. M. Heo, J. F. Joung, S. Park and J. M. Kim, *Dyes Pigm.*, 2018, **154**, 199-204.
76. T. Kim, D. Moon, J. H. Park, H. Yang, S. Cho, T. H. Park and D. J. Ahn, *Nanoscale*, 2019, **11**, 7582-7587.
77. N. Mergu, H. Kim, G. Heo and Y. A. Son, *Dyes Pigm.*, 2019, **164**, 355-362.
78. T. Barisien, J. L. Fave, S. Hameau, L. Legrand, M. Schott, J. Malinge, G. Clavier, P. Audebert and C. Allain, *ACS Appl. Mater. Interfaces*, 2013, **5**, 10836-10841.
79. P. T. Hammond and M. F. Rubner, *Macromolecules*, 1997, **30**, 5773-5782.
80. T. Shimogaki, S. Dei, K. Ohta and A. Matsumoto, *J. Mater. Chem.*, 2011, **21**, 10730-10737.
81. D. Y. Kim, S. A. Lee, D. Jung, J. Koo, J. S. Kim, Y. T. Yu, C. R. Lee and K. U. Jeong, *Soft Matter*, 2017, **13**, 5759-5766.
82. H. Y. Araghi and M. F. Paige, *Surf. Interface Anal.*, 2017, **49**, 1108-1114.
83. S. Spagnoli, E. Briand, I. Vickridge, J. L. Fave and M. Schott, *Langmuir*, 2017, **33**, 1419-1426.
84. O. Yarimaga, B. Yoon, D. Y. Ham, J. Lee, M. Hara, Y. K. Choi and J. M. Kim, *J. Mater. Chem.*, 2011, **21**, 18605-18612.
85. S. Lee, D. Lee, C. S. Hong, J. E. Yang, J. S. Kang, Y. E. Sung and S. R. Paik, *Langmuir*, 2019, **35**, 11923-11931.
86. M. Kim, Y. J. Shin, S. W. Hwang, M. J. Shin and J. S. Shin, *J. Appl. Polym. Sci.*, 2018, **135**, 1-5.
87. K. Yoo, S. Kim, N. Han, G. E. Kim, M. J. Shin, J. S. Shin and M. Kim, *Dyes Pigm.*, 2018, **149**, 242-245.
88. Y. Singh and N. Jayaraman, *Macromol. Chem. Phys.*, 2017, **218**, 1-11.
89. Y. Meng, J. Jiang and M. H. Liu, *Nanoscale*, 2017, **9**, 7199-7206.
90. P. Sun, Y. C. Fu, J. Hu, L. Li, X. Wang, W. Huang and B. Jiang, *Nucl. Sci. Tech.*, 2015, **26**, 050301.
91. H. H. Fan, H. J. Jiang, X. F. Zhu, M. S. Zhu, L. Zhang and M. H. Liu, *Eur. Polym. J.*, 2019, **118**, 146-152.
92. M. Kozicki, E. Sasiadek, S. Kadlubowski, M. Dudek, P. Maras, A. Nosal and M. Gazicki-Lipman, *J. Photochem. Photobiol., A*, 2018, **351**, 179-196.
93. Z. J. Zhang, J. Li, F. Wang, T. W. Wei, Y. H. Chen, J. Qiang, T. Xiao and X. Q. Chen, *Sens. Actuators, B*, 2019, **282**, 636-643.
94. J. E. Yang, S. Lee, G. Bhak, M. Lee, D. H. Jeong, S. Jung and S. R. Paik, *Sens. Actuators, B*, 2016, **227**, 313-319.
95. M. D. Cohen, G. M. J. Schmidt and F. I. Sonntag, *J. Chem. Soc.*, 1964, 2000-2013.
96. G. M. J. Schmidt, *J. Chem. Soc.*, 1964, 2014-2021.
97. J. Bregman, G. M. J. Schmidt, K. Osaki and F. I. Sonntag, *J. Chem. Soc.*, 1964, 2021-2030.
98. F. L. Hirshfeld and G. M. J. Schmidt, *J. Polym. Sci. A*, 1964, **2**, 2181-2190.
99. G. Wegner, *Z. Naturforsch., B: J. Chem. Sci.*, 1969, **24**, 824-832.

100. V. Enkelmann, *Adv. Polym. Sci.*, 1984, **63**, 91-136.
101. R. H. Baughman, *J. Appl. Phys.*, 1972, **43**, 4362-4370.
102. R. H. Baughman and K. C. Yee, *J. Polym. Sci., Part D: Macromol. Rev.*, 1978, **13**, 219-239.
103. J. W. Lauher, F. W. Fowler and N. S. Goroff, *Acc. Chem. Res.*, 2008, **41**, 1215-1229.
104. Z. Li, F. W. Fowler and J. W. Lauher, *J. Am. Chem. Soc.*, 2009, **131**, 634-643.
105. D. Day and J. B. Lando, *Macromolecules*, 1980, **13**, 1478-1483.
106. H. Nakanishi, H. Matsuda, M. Kato, C. R. Theocharis and W. Jones, *J. Chem. Soc., Perkin Trans. 2*, 1986, 1965-1967.
107. X. Ouyang, F. W. Fowler and J. W. Lauher, *J. Am. Chem. Soc.*, 2003, **125**, 12400-12401.
108. V. Enkelmann, *J. Chem. Res., Synop.*, 1981, 344-345.
109. H. Tachibana, R. Kumai, N. Hosaka and Y. Tokura, *Chem. Mater.*, 2001, **13**, 155-158.
110. A. E. Smith, *J. Chem. Phys.*, 1953, **21**, 2229-2231.
111. C. Tanioku, K. Matsukawa and A. Matsumoto, *ACS Appl. Mater. Interfaces*, 2013, **5**, 940-948.
112. G. Kaupp, *CrystEngComm*, 2003, **5**, 117-133.
113. V. Enkelmann and G. Schleier, *Acta Crystallogr., Sect. B: Struct. Sci.*, 1980, **36**, 1954-1956.
114. K. Biradha and R. Santra, *Chem. Soc. Rev.*, 2013, **42**, 950-967.
115. A. Matsumoto, T. Kunisue, A. Tanaka, N. Tohnai, K. Sada and M. Miyata, *Chem. Lett.*, 2004, **33**, 96-97.
116. T. Odani, S. Okada, C. Kabuto, T. Kimura, H. Matsuda, A. Matsumoto and H. Nakanishi, *Chem. Lett.*, 2004, **33**, 1312-1313.
117. T. Odani, S. Okada, C. Kabuto, T. Kimura, S. Shimada, H. Matsuda, H. Oikawa, A. Matsumoto and H. Nakanishi, *Cryst. Growth Des.*, 2009, **9**, 3481-3487.
118. A. Matsumoto, K. Sada, K. Tashiro, M. Miyata, T. Tsubouchi, T. Tanaka, T. Odani, S. Nagahama, K. Inoue, S. Saragai and S. Nakamoto, *Angew. Chem., Int. Ed.*, 2002, **41**, 2502-2505.
119. M. T. Kirchner, D. Blaser and R. Boese, *Chem.-Eur. J.*, 2010, **16**, 2131-2146.
120. J. J. Kane, R. F. Liao, J. W. Lauher and F. W. Fowler, *J. Am. Chem. Soc.*, 1995, **117**, 12003-12004.
121. F. W. Fowler and J. W. Lauher, *J. Phys. Org. Chem.*, 2000, **13**, 850-857.
122. S. M. Curtis, N. Le, F. W. Fowler and J. W. Lauher, *Cryst. Growth Des.*, 2005, **5**, 2313-2321.
123. J. G. Rodriguez, R. MartinVillamil, F. H. Cano and I. Fonseca, *J. Chem. Soc., Perkin Trans. 1*, 1997, 709-714.
124. J. R. Allan, M. J. Barrow, P. C. Beaumont, L. A. Macindoe, G. H. W. Milburn and A. R. Werninck, *Inorg. Chim. Acta*, 1988, **148**, 85-90.
125. L. Luo, C. Wilhelm, A. W. Sun, C. P. Grey, J. W. Lauher and N. S. Goroff, *J. Am. Chem. Soc.*, 2008, **130**, 7702-7709.
126. A. W. Sun, J. W. Lauher and N. S. Goroff, *Science*, 2006, **312**, 1030-1034.
127. D. K. Cao, T. V. Sreevidya, M. Botoshansky, G. Golden, J. B. Benedict and M. Kaftory, *CrystEngComm*, 2011, **13**, 3181-3188.
128. J. Guo, K. Y. Fu, Z. B. Zhang, L. Y. Yang, Y. C. Huang, C. I. Huang, L. Zhu and D. Y. Chen, *Polymer*, 2016, **105**, 440-448.
129. D. Das, T. Jacobs and L. J. Barbour, *Nat. Mater.*, 2010, **9**, 36-39.

130. D. Das, T. Jacobs, A. Pietraszko and L. J. Barbour, *Chem. Commun.*, 2011, **47**, 6009-6011.
131. G. O. Lloyd, J. Alen, M. W. Bredenkamp, E. J. C. de Vries, C. Esterhuysen and L. J. Barbour, *Angew. Chem., Int. Ed.*, 2006, **45**, 5354-5358.
132. A. Mueller and D. F. O'Brien, *Chem. Rev.*, 2002, **102**, 727-757.
133. R. Jelinek and M. Ritenberg, *RSC Adv.*, 2013, **3**, 21192-21201.
134. R. W. Carpick, D. Y. Sasaki, M. S. Marcus, M. A. Eriksson and A. R. Burns, *J. Phys.: Condens. Matter*, 2004, **16**, 679-697.
135. C. Khanantong, N. Charoenthai, F. Kielar, N. Traiphol and R. Traiphol, *Colloids Surf., A*, 2019, **561**, 226-235.
136. J. Pang, L. Yang, B. F. McCaughey, H. Peng, H. S. Ashbaugh, C. J. Brinker and Y. Lu, *J. Phys. Chem. B*, 2006, **110**, 7221-7225.
137. C. Khanantong, N. Charoenthai, S. Wacharasindhu, M. Sukwattanasinitt, N. Traiphol and R. Traiphol, *J. Ind. Eng. Chem.*, 2018, **58**, 258-265.
138. J. J. Schaefer, C. B. Fox and J. M. Harris, *J. Raman Spectrosc.*, 2012, **43**, 351-359.
139. S. P. Scoville and W. M. Shirley, *J. Appl. Polym. Sci.*, 2011, **120**, 2809-2820.
140. H. Eckhardt, D. S. Boudreaux and R. R. Chance, *J. Chem. Phys.*, 1986, **85**, 4116-4119.
141. M. Schott, *J. Phys. Chem. B*, 2006, **110**, 15864-15868.
142. Y. Lifshitz, Y. Golan, O. Konovalov and A. Berman, *Langmuir*, 2009, **25**, 4469-4477.
143. S. L. Chen, X. F. Zhu, F. Y. Yang, X. C. Pan, W. Gan and Q. H. Yuan, *Chin. J. Chem. Phys.*, 2018, **31**, 269-276.
144. G. J. Exarhos, W. M. Risen and R. H. Baughman, *J. Am. Chem. Soc.*, 1976, **98**, 481-487.
145. C. R. Smith, D. R. Sabatino and T. J. Praisner, *Exp. Fluids*, 2001, **30**, 190-201.
146. K. Basnec, L. S. Perse, B. Sumiga, M. Huskic, A. Meden, A. Hladnik, B. Boh Podgornik and M. K. Gunde, *Sci. Rep.*, 2018, **8**, 1-10.
147. H. Shin, B. Yoon, I. S. Park and J. M. Kim, *Nanotechnology*, 2014, **25**, 1-8.
148. B. Yoon, J. Lee, I. S. Park, S. Jeon and J. M. Kim, *J. Mater. Chem. C*, 2013, **1**, 2388-2403.
149. B. Yoon, H. Shin, E. M. Kang, D. W. Cho, K. Shin, H. Chung, C. W. Lee and J. M. Kim, *ACS Appl. Mater. Interfaces*, 2013, **5**, 4527-4535.
150. S. Ryu, I. Yoo, S. Song, B. Yoon and J. M. Kim, *J. Am. Chem. Soc.*, 2009, **131**, 3800-3801.
151. R. V. Hansen, L. Zhong, K. A. Khor, L. X. Zheng and J. L. Yang, *Carbon*, 2016, **106**, 110-117.
152. N. Charoenthai, T. Pattanatornchai, S. Wacharasindhu, M. Sukwattanasinitt and R. Traiphol, *J. Colloid Interf. Sci.*, 2011, **360**, 565-573.
153. J. F. Joung, J. Baek, Y. Kim, S. Lee, M. H. Kim, J. Yoon and S. Park, *Phys. Chem. Chem. Phys.*, 2016, **18**, 23096-23104.
154. A. Kamphan, C. Khanantong, N. Traiphol and R. Traiphol, *J. Ind. Eng. Chem.*, 2017, **46**, 130-138.
155. A. Kamphan, N. Traiphol and R. Traiphol, *Colloids Surf., A*, 2016, **497**, 370-377.
156. Y. Gu, W. Q. Cao, L. Zhu, D. Y. Chen and M. Jiang, *Macromolecules*, 2008, **41**, 2299-2303.
157. M. Takeuchi, K. Gnanasekaran, H. Friedrich, H. Imai, N. Sommerdijk and Y. Oaki, *Adv. Funct. Mater.*, 2018, **28**, 1-11.

158. R. Nagarajan, *Langmuir*, 2002, **18**, 31-38.
159. J. P. Huo, Z. D. Hu, G. Z. He, X. X. Hong, Z. H. Yang, S. H. Luo, X. F. Ye, Y. L. Li, Y. B. Zhang, M. Zhang, H. Chen, T. Fan, Y. Y. Zhang, B. Y. Xiong, Z. Y. Wang, Z. B. Zhu and D. C. Chen, *Appl. Surf. Sci.*, 2017, **423**, 951-956.
160. L. Zhang, Y. Z. Yuan, X. H. Tian and J. Y. Sun, *Chin. Chem. Lett.*, 2015, **26**, 1133-1136.
161. R. Niu, X. L. Meng, D. D. Yang, Y. Chang and F. Zha, *Arabian J. Sci. Eng.*, 2015, **40**, 2867-2872.
162. S. Wacharasindhu, S. Montha, J. Boonyiseng, A. Potisatityuenyong, C. Phollookin, G. Tumcharern and M. Sukwattanasinitt, *Macromolecules*, 2010, **43**, 716-724.
163. S. H. Park, J. Roh and D. J. Ahn, *Macromol. Res.*, 2017, **25**, 960-962.
164. D. Bloor, *Chem. Phys. Lett.*, 1998, **295**, 63-69.
165. D. Bloor, *Macromol. Chem. Phys.*, 2001, **202**, 1410-1423.
166. J. M. Kim, J. S. Lee, H. Choi, D. Sohn and D. J. Ahn, *Macromolecules*, 2005, **38**, 9366-9376.
167. D. J. Ahn, S. Lee and J. M. Kim, *Adv. Funct. Mater.*, 2009, **19**, 1483-1496.
168. G. S. Lee, T. Y. Kim and D. J. Ahn, *J. Ind. Eng. Chem.*, 2018, **67**, 312-315.
169. O. Mapazi, P. K. Matabola, R. M. Moutloali and C. J. Ngila, *Sens. Actuators, B*, 2017, **252**, 671-679.
170. X. W. Yu, Y. H. Luo, W. X. Wu, Q. Yan, G. Zou and Q. J. Zhang, *Eur. Polym. J.*, 2008, **44**, 3015-3021.
171. X. Lu, Z. D. Zhang, X. M. Sun, P. N. Chen, J. Zhang, H. Guo, Z. Z. Shao and H. S. Peng, *Chem. Sci.*, 2016, **7**, 5113-5117.
172. M. J. Seo, J. Song, C. Kantha, M. I. Khazi, U. Kundapur, J. M. Heo and J. M. Kim, *Langmuir*, 2018, **34**, 8365-8373.
173. G. S. Lee, S. J. Hyun and D. J. Ahn, *Macromol. Res.*, 2018, **26**, 566-570.
174. J. P. Yapor, A. Alharby, C. Gentry-Weeks, M. M. Reynolds, A. Alam and Y. V. Li, *ACS Omega*, 2017, **2**, 7334-7342.
175. F. Hassan, C. Gentry-Weeks, M. Reynolds and Y. V. Li, *J. Appl. Polym. Sci.*, 2019, **136**, 1-14.
176. L. Silbert, I. Ben Shlush, E. Israel, A. Porgador, S. Kolusheva and R. Jelinek, *Appl. Environ. Microbiol.*, 2006, **72**, 7339-7344.
177. F. Jannah and J. M. Kim, *Dyes Pigm.*, 2019, **169**, 15-21.
178. J. P. Celli, B. S. Turner, N. H. Afdhal, S. Keates, I. Ghiran, C. P. Kelly, R. H. Ewoldt, G. H. McKinley, P. So, S. Erramilli and R. Bansil, *Proc. Natl. Acad. Sci. U. S. A.*, 2009, **106**, 14321-14326.
179. S. Song, H. B. Cho, H. W. Lee and H. T. Kim, *Mater. Sci. Eng., C*, 2019, **99**, 900-904.
180. D. H. Park, B. Kim and J. M. Kim, *Bull. Korean Chem. Soc.*, 2016, **37**, 793-794.
181. X. N. Wang, X. L. Sun, P. A. Hu, J. Zhang, L. F. Wang, W. Feng, S. B. Lei, B. Yang and W. W. Cao, *Adv. Funct. Mater.*, 2013, **23**, 6044-6050.
182. J. Lee, H. T. Chang, H. An, S. Ahn, J. Shim and J. M. Kim, *Nat. Commun.*, 2013, **4**, 1-9.
183. L. M. Guo and Y. Wang, *Sens. Actuators, B*, 2018, **277**, 172-178.
184. T. Pattanatornchai, N. Charoenthai, S. Wacharasindhu, M. Sukwattanasinitt and R. Traiphol, *J. Colloid Interface Sci.*, 2013, **391**, 45-53.
185. M. J. Shin and J. S. Shin, *J. Appl. Polym. Sci.*, 2019, **136**, 1-7.
186. R. Kassis, M. Bassil and A. Al Choueiry, *Mater. Res. Express*, 2019, **6**, 1-7.

187. M. J. Shin and J. D. Kim, *Langmuir*, 2016, **32**, 882-888.
188. S. Balakrishnan, S. Lee and J. M. Kim, *J. Mater. Chem.*, 2010, **20**, 2302-2304.
189. J. B. Pang, L. Yang, B. F. McCaughey, H. S. Peng, H. S. Ashbaugh, C. J. Brinker and Y. F. Lu, *J. Phys. Chem. B*, 2006, **110**, 7221-7225.
190. L. Yu and S. L. Hsu, *Macromolecules*, 2012, **45**, 420-429.
191. Y. J. Gwon, C. Kim and T. S. Lee, *Sens. Actuator, B*, 2019, **281**, 343-349.
192. J. Lee, M. Pyo, S. H. Lee, J. Kim, M. Ra, W. Y. Kim, B. J. Park, C. W. Lee and J. M. Kim, *Nat. Commun.*, 2014, **5**, 1-10.
193. Y. Y. Xu, S. Y. Fu, F. Y. Liu, H. Y. Yu and J. G. Gao, *Soft Matter*, 2018, **14**, 8044-8050.
194. D. A. Jose and B. Konig, *Org. Biomol. Chem.*, 2010, **8**, 655-662.
195. S. Wu, L. B. Pan, Y. J. Huang, N. Yang and Q. J. Zhang, *Soft Matter*, 2018, **14**, 6929-6937.
196. S. Seetha, R. Saymung, R. Traiphol and N. Traiphol, *J. Ind. Eng. Chem.*, 2019, **72**, 423-431.
197. N. Traiphol, A. Chanakul, A. Kamphan and R. Traiphol, *Thin Solid Films*, 2017, **622**, 122-129.
198. N. Phonchai, C. Khanantong, F. Kielar, R. Traiphol and N. Traiphol, *ACS Appl. Nano Mater.*, 2019, **2**, 4489-4498.
199. R. Potai, K. Faisadcha, R. Traiphol and N. Traiphol, *Colloids Surf., A*, 2018, **555**, 27-36.
200. A. Chanakul, R. Traiphol and N. Traiphol, *J. Ind. Eng. Chem.*, 2017, **45**, 215-222.
201. A. Chanakul, R. Traiphol and N. Traiphol, *Colloids Surf., A*, 2016, **489**, 9-18.
202. M. Okaniwa, Y. Oaki, S. Kaneko, K. Ishida, H. Maki and H. Imai, *Chem. Mat.*, 2015, **27**, 2627-2632.
203. T. Pattanatornchai, J. Rueangsuwan, N. Phonchai, N. Traiphol and R. Traiphol, *Colloids Surf., A*, 2020, **594**, 1-10.
204. N. Phonchai, C. Khanantong, F. Kielar, R. Traiphol and N. Traiphol, *Colloids Surf., A*, 2020, **589**, 1-10.
205. J. Guo, L. Y. Yang, L. Zhu and D. Y. Chen, *Polymer*, 2013, **54**, 743-749.
206. A. Fujimori, M. Ishitsuka, H. Nakahara, E. Ito, M. Hara, K. Kanai, Y. Ouchi and K. Seki, *J. Phys. Chem. B*, 2004, **108**, 13153-13162.
207. A. Sansee, A. Kamphan, R. Traiphol and F. Kielar, *Colloids Surf., A*, 2016, **497**, 362-369.
208. A. Tobias, W. Rooke and T. W. Hanks, *Colloid Polym. Sci.*, 2019, **297**, 85-93.
209. A. Motalebizadeh, H. Bagheri, S. Asiaei, N. Fekrat and A. Afkhami, *RSC Adv.*, 2018, **8**, 27091-27100.
210. D. E. Wang, Y. L. Wang, C. Tian, L. L. Zhang, X. Han, Q. Tu, M. S. Yuan, S. Chen and J. Y. Wang, *J. Mater. Chem. A*, 2015, **3**, 21690-21698.
211. Y. Li, L. H. Wang, X. Yin, B. Ding, G. Sun, T. Ke, J. Y. Chen and J. Y. Yu, *J. Mater. Chem. A*, 2014, **2**, 18304-18312.
212. S. Y. Zhang, B. L. Shi and G. Yang, *Macromol. Res.*, 2020, **28**, 51-56.
213. Q. Wang, G. Wang, X. Y. Huang and D. Y. Chen, *Chin. J. Chem. Phys.*, 2020, **33**, 357-364.
214. Y. S. Yao, K. Y. Fu, X. Y. Huang and D. Y. Chen, *Chin. J. Chem.*, 2017, **35**, 1678-1686.
215. A. Chanakul, N. Traiphol and R. Traiphol, *J. Colloid Interface Sci.*, 2013, **389**, 106-114.

216. N. Traiphol, N. Rungruangviriya, R. Potai and R. Traiphol, *J. Colloid Interface Sci.*, 2011, **356**, 481-489.
217. R. H. Baughman and R. R. Chance, *J. Polym. Sci., Part B: Polym. Phys.*, 1976, **14**, 2037-2045.
218. V. Burilov, A. Valiyakhmetova, D. Mironova, E. Sultanova, V. Evtugyn, Y. Osin, S. Katsyuba, T. Burganov, S. Solovieva and I. Antipin, *New J. Chem.*, 2018, **42**, 2942-2951.
219. R. W. Carpick, D. Y. Sasaki and A. R. Burns, *Langmuir*, 2000, **16**, 1270-1278.
220. A. R. Burns, R. W. Carpick, D. Y. Sasaki, J. A. Shelnutt and R. Haddad, *Tribol. Lett.*, 2001, **10**, 89-96.
221. H. Y. Araghi and M. F. Paige, *Langmuir*, 2011, **27**, 10657-10665.
222. H. Y. Araghi and M. F. Paige, *Can. J. Chem.-Rev. Can. Chim.*, 2013, **91**, 1130-1138.
223. H. S. Peng, X. M. Sun, F. J. Cai, X. L. Chen, Y. C. Zhu, G. P. Liao, D. Y. Chen, Q. W. Li, Y. F. Lu, Y. T. Zhu and Q. X. Jia, *Nat. Nanotechnol.*, 2009, **4**, 738-741.
224. Q. Cheng and R. C. Stevens, *Langmuir*, 1998, **14**, 1974-1976.
225. Y. Ishijima, H. Imai and Y. Oaki, *Chem*, 2017, **3**, 509-521.
226. C. Y. P. Ng, S. L. Chun and K. N. Yu, *Radiat. Phys. Chem.*, 2016, **125**, 176-179.
227. S. Devic, N. Tomic and D. Lewis, *Eur. J. Med. Phys.*, 2016, **32**, 541-556.
228. A. Rink, D. F. Lewis, S. Varma, I. A. Vitkin and D. A. Jaffray, *J. Med. Phys.*, 2008, **35**, 4545-4555.
229. N. V. Klassen, L. van der Zwan and J. Cygler, *Med. Phys.*, 1997, **24**, 1924-1934.
230. A. A. Abdel-Fattah and Y. S. Soliman, *Radiat. Phys. Chem.*, 2017, **141**, 66-72.
231. G. Moroff and N. L. C. Luban, *Transf. Med. Rev.*, 1997, **11**, 15-26.
232. A. LLP, RAD-SURE™ blood irradiation indicators, http://www.ashland.com/industries/medical/blood-safety/rad-sure-bood-irradiation-indicators, (accessed 14/01/2018).
233. P. Sun, Y. C. Fu, J. Hu, N. Hao, W. Huang and B. Jiang, *Radiat. Meas.*, 2016, **85**, 116-125.
234. C. Baldock, Y. De Deene, S. Doran, G. Ibbott, A. Jirasek, M. Lepage, K. B. McAuley, M. Oldham and L. J. Schreiner, *Phys. Med. Biol.*, 2010, **55**, 1-63.
235. A. T. Nasr, T. Olding, L. J. Schreiner and K. B. McAuley, *Phys. Med. Biol.*, 2013, **58**, 787-805.
236. Y. K. Jung and H. G. Park, *Sens. Actuators, B*, 2019, **278**, 190-195.
237. J. W. Wang, F. Zheng, H. Chen, Y. Ding and X. H. Xia, *ACS Sens.*, 2019, **4**, 977-983.
238. J. P. Jeong, E. Cho, D. Yun, T. Kim, I. S. Lee and S. Jung, *Polymers*, 2017, **9**, 1-9.
239. M. P. Leal, M. Assali, I. Fernandez and N. Khiar, *Chem. - Eur. J.*, 2011, **17**, 1828-1836.
240. S. U. Son, S. B. Seo, S. Jane, J. Choi, J. W. Lim, D. K. Lee, H. Kim, S. Seo, T. Kang, J. Jung and E. K. Lim, *Sens. Actuators, B*, 2019, **291**, 257-265.
241. J. L. Deng, Z. H. Sheng, K. Zhou, M. X. Duan, C. Y. Yu and L. Jiang, *Bioconjugate Chem.*, 2009, **20**, 533-537.
242. A. Reichert, J. O. Nagy, W. Spevak and D. Charych, *J. Am. Chem. Soc.*, 1995, **117**, 829-830.

243. J. Tao, X. Xu, S. Wang, T. Y. Kang, C. Z. Guo, X. Liu, H. Cheng, Y. Liu, X. Jiang, J. Mao and M. L. Gou, *ACS Macro Lett.*, 2019, **8**, 563-568.
244. T. V. de Oliveira, N. D. F. Soares, N. J. de Andrade, D. J. Silva, E. A. A. Medeiros and A. T. Badaro, *Food Chem.*, 2015, **172**, 428-432.
245. T. V. de Oliveira, N. D. F. Soares, D. J. Silva, N. J. de Andrade, E. A. A. Medeiros and A. T. Badaro, *Sens. Actuators, B*, 2013, **188**, 385-392.
246. M. Kim, Y. J. Shin, S. W. Hwang, M. J. Shin and J. S. Shin, *J. Appl. Polym. Sci.*, 2018, **135**, 1-5.
247. C. Wang, J. H. Park, S. W. Tan, C. Z. Cui, J. Y. Jin and D. J. Ahn, *J. Nanomater.*, 2017, 1-7.
248. D. E. Wang, J. H. Yan, J. J. Jiang, X. Liu, C. Tian, J. Xu, M. S. Yuan, X. Han and J. Y. Wang, *Nanoscale*, 2018, **10**, 4570-4578.
249. A. Kamphan, C. J. Gong, K. Maiti, S. Sur, R. Traiphol and D. P. Arya, *RSC Adv.*, 2017, **7**, 41435-41443.
250. X. M. Qian and B. Stadler, *Chem. Mat.*, 2019, **31**, 1196-1222.
251. T. V. de Oliveira, N. D. F. Soares, J. S. D. Coimbra, N. J. de Andrade, L. G. Moura, E. A. A. Medeiros and H. S. de Medeiros, *Sens. Actuators, B*, 2015, **221**, 653-658.
252. Y. Y. Zhang, J. Northcutt, T. Hanks, I. Miller, B. Pennington, R. Jelinek, I. Han and P. Dawson, *Food Chem.*, 2017, **221**, 515-520.
253. A. P. Carter, W. M. Clemons, D. E. Brodersen, R. J. Morgan-Warren, B. T. Wimberly and V. Ramakrishnan, *Nature*, 2000, **407**, 340-348.
254. H. J. Xi, E. Davis, N. Ranjan, L. Xue, D. Hyde-Volpe and D. P. Arya, *Biochemistry*, 2011, **50**, 9088-9113.
255. M. J. Shin and J. S. Shin, *J. Appl. Polym. Sci.*, 2020, **137**, 1-7.
256. J. D. Rezende, A. F. C. Pacheco, O. F. Magalhaes, Y. L. Coelho, M. Vidigal, L. H. M. da Silva and A. C. D. Pires, *Food Chem.*, 2019, **280**, 1-7.
257. C. L. He, M. Q. Wang, X. B. Sun, Y. Zhu, X. Zhou, S. Y. Xiao, Q. J. Zhang, F. N. Liu, Y. Yu, H. J. Liang and G. Zou, *Biosens. Bioelectron.*, 2019, **129**, 50-57.
258. Y. Peng and C. M. Croce, *Signal Transduction Targeted Ther.*, 2016, **1**, 1-9.
259. A. M. Valiyakhmetova, E. D. Sultanova, V. A. Burilov, S. E. Solovieva and I. S. Antipin, *Russ. Chem. Bull.*, 2019, **68**, 1067-1074.
260. D. E. Wang, X. H. Gao, G. B. Li, T. Xue, H. Yang and H. Y. Xu, *Sens. Actuators, B*, 2019, **289**, 85-92.
261. W. H. Organization, *Public health impact of pesticides used in agriculture*, Geneva, Switzerland, 1990.
262. Y. F. Zhang, L. Bromberg, Z. Lin, P. Brown, T. Van Voorhis and T. A. Hatton, *J. Colloid Interface Sci.*, 2018, **528**, 27-35.
263. J. Jaworski, K. Yokoyama, C. Zueger, W. J. Chung, S. W. Lee and A. Majumdar, *Langmuir*, 2011, **27**, 3180-3187.
264. L. H. Nguyen, S. Naficy, R. McConchie, F. Dehghani and R. Chandrawati, *J. Mater. Chem. C*, 2019, **7**, 1919-1926.
265. W. Jeong, M. I. Khazi, D. G. Lee and J. M. Kim, *Macromolecules*, 2018, **51**, 10312-10322.
266. S. Ali, F. Ahmed and A. Khatri, *Mehran Univ. Res. J. Eng. Technol.*, 2016, **35**, 287-292.
267. V. K. Rao, N. L. Teradal and R. Jelinek, *ACS Appl. Mater. Interfaces*, 2019, **11**, 4470-4479.

268. Y. K. Choi, H. J. Kim, S. R. Kim, Y. M. Cho and D. J. Ahn, *Macromolecules*, 2017, **50**, 3164-3170.
269. S. Bhattacharya, J. Stojakovic, B. K. Saha and L. R. MacGillivray, *Org. Lett.*, 2013, **15**, 744-747.
270. L. R. MacGillivray, *J. Org. Chem.*, 2008, **73**, 3311-3317.

2. Lithium and Sodium Salts of 10,12-Pentacosadiynoic Acid

2.1. Introduction

Long aliphatic unsaturated chains of carboxylic acids can be photoreactive when exposed to certain stimuli. For example, when PCDA is in optimal conditions for reactivity and exposed to radiation or heat, 1,4-addition polymerisation occurs to give a coloured polydiacetylene.[1] For this reason, PCDA has been incorporated into radiochromic films in the past for dosimetry purposes, however, more recently, sensitive films such as GAFchromic™ have been developed that are based on the lithium salt of PCDA (Li-PCDA). Therefore, the continued research and discovery of metal salts with tunable reactivity is very important to improve dosimetry technologies for different therapeutic uses. In this chapter, we highlight the characterisation of PCDA and its lithium and sodium salts, and the lithium salt of a PCDA analogue 5,7-hexadecadiynoic acid (Li-HDDA) and compare their photoreactivity.

To understand the solid-state packing of long-chain aliphatic carboxylates, an extensive literature survey of related structures was undertaken. There are a range of reports of X-ray structural characterisation of saturated *n*-alkyl carboxylic acids and these systems exhibit significant polymorphic tendency.[2-5] The *n*-alkyl carboxylic acids from one to twenty carbon atoms in length have all been structurally characterised either by single-crystal X-ray diffraction (SC-XRD) or PXRD methods.[6-16] Although, the *n*-alkyl acids are increasingly difficult to crystallise as the chain length increases, partly due to the flexibility of the chain. This is evident by the lack of structural information for heneicosanoic acid, for example, in the Cambridge Structural Database (CSD),[17] only the unit cell parameters are available for docosanoic acid, tetracosanoic acid, and hexacosanoic acid.[18, 19] Of the structures with CSD entries, all *n*-alkyl carboxylic acids dimerise in a $R_2^2(8)$ hydrogen-bonded motif.[20] The X-ray structures of saturated short and long-chain carboxylic acid as ligands to metal cations are also abundant in the literature,[21-24] though the complexes with *n*-alkyl carboxylates consisting of >10 carbon atoms in length are less common.[25] In order to undertake a systematic analysis, a CSD search with criteria involving an 'any metal' centre joined to at least two *n*-alkyl carboxyl ligands by 'any bond type' to at least one of the carboxylate oxygen atoms of each ligand, ranging from one to 22 carbon atoms in length was performed (Figure 2.1). This search resulted in 1449 entries, though not all are fully determined X-ray structures, as some entries only represent unit cell

parameters. The distribution of results separated into their respective alkyl carbon chain length are summarised in Figure 2.2. The metal centres are varied though largely consist of transition metals, with copper as the most common metal in these set of results at 344 hits (24 % of the total hits). Of these 344 hits, only 45 hits (13 %) consist of Cu(I), while the remaining 299 hits (87 %) involve Cu(II), consistent with the tendency of copper(I) to be stabilised by soft ligand donor atoms.[26, 27]

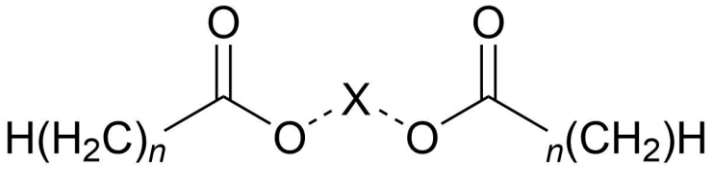

Figure 2.1. The search criteria for metal *n*-alkyl carboxylates in the CSD, bound to the metal ion (X) by at least two 'any bond types' denoted by a dashed line. The CH_2 chain ranges from zero to 22 carbon atoms in length.

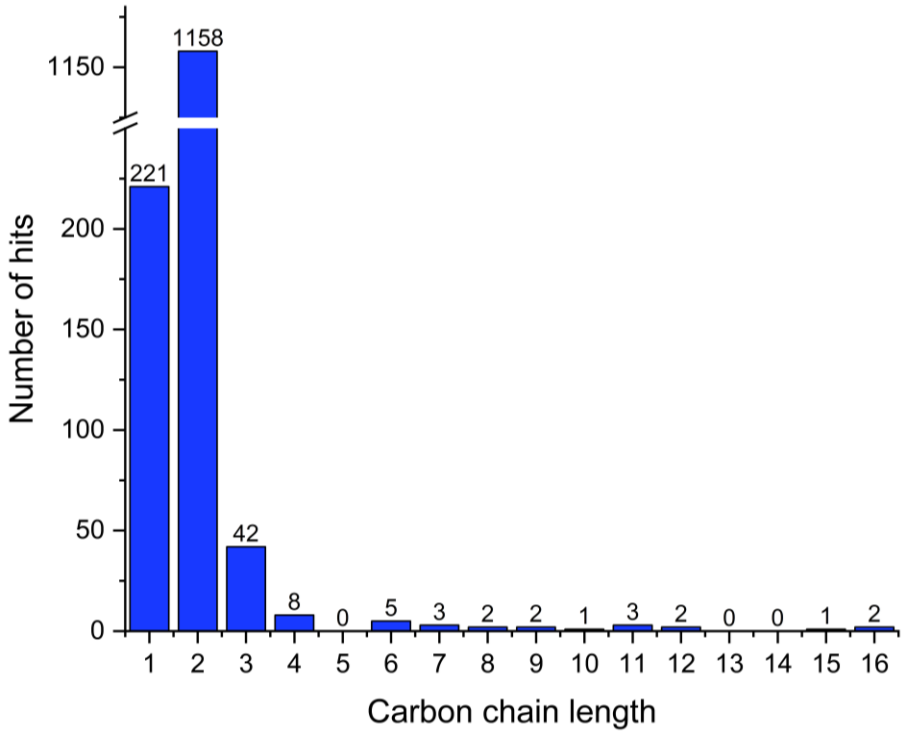

Figure 2.2. The number of results that matched the search criteria, and the carboxylic acid carbon chain length in each structure. Though carboxylate chains with 17 to 22 carbon atoms were searched for, they did not return any hits and therefore were not included in the figure.

An example of a typical Cu(II) complex is the X-ray structure of diammonia-bis(decanoato)copper(II) monohydrate (Figure 2.3). The Cu(II) ion is in a square planar geometry and is joined to two ammine nitrogen atoms at Cu-N distances of 1.95 and 2.06 Å.[28] Additionally, the central metal atom is also bound to two oxygen atoms of the carboxylate ligand, at Cu-O distances of 1.98 and 1.99 Å. The carbonyl oxygen atoms of the carboxylates also interact with the Cu(II) atom at long distances of 2.59 and 2.76 Å that arise from a Jahn Teller distortion. The decanoate chains adopt *anti*-conformations with C-C-C-C torsion angles ranging from 140-179 °.[28] Hydrogen bonding also occurs in the structure. The hydrogen atoms from the water molecule join to the carboxyl oxygen atom of the decanoate ligand at a moderate O···O distance of 2.83 Å, and to the nitrogen atoms at a slightly longer O···N distances of 3.02 and 3.08 Å.[28]

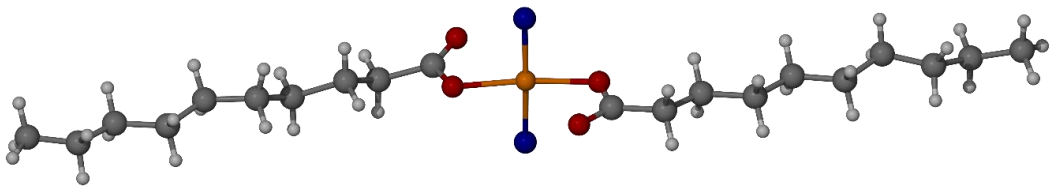

Figure 2.3. The X-ray structure of diammonia-bis(decanoato)copper(II) monohydrate (water molecule omitted). The positions of the three hydrogen atoms for each ammine ligand were not determined.[28]

The only CSD entry for a metal carboxylate with ligands of eleven carbon atoms in length is a structure derived from synchrotron PXRD analysis, consisting of a tetrahedral Zn(II) centre joined to two bridging and two bidentate undecanoate ligands, with two chains that are crystallographically independent (Figure 2.4).[25] The Zn-O distances range between 1.93 and 2.04 Å. The packing structure displays a lamellar stacking of polymeric sheets of the metal carboxylate that run parallel to (001).[25] The alkyl chains of the carboxylate ligands are in an all-*trans* conformation. This structure crystallises in the orthorhombic $Pna2_1$ space group. Two other polymorphs of this structure are known from unit cell data in the monoclinic space groups $P2_1/c$ and Cc and are likely to differ in packing of the carboxylate alkyl chains.[25]

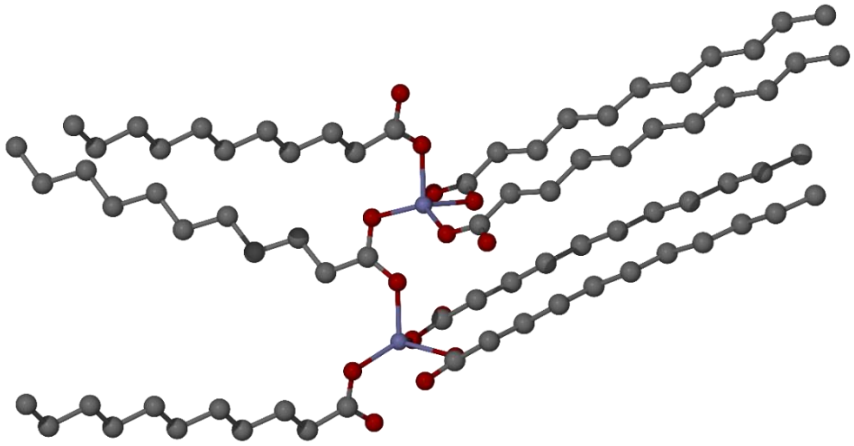

Figure 2.4. The X-ray structure of catena-(bis(μ_2-undecanoato-O,O')-zinc(II)). The hydrogen atoms were not located in the structure determination.[25]

A metal structure containing dodecanoate chains is a cobalt(II) dodecanoate complex which was serendipitously crystallised from a 1:3:1 mixture of a cobalt(II)-bis(trimethylsiyl)amide, dodecanoic acid, and hexadecylamine in methoxybenzene, respectively, and was heated to 60 °C to form a gel. After cooling, pink crystals formed consisting of diammine-bis(dodecanoato-O)-cobalt(II) that crystallised in *C*2/*c* (Figure 2.5).[29] The Co-O distances are 1.98 Å and the Co-N distances are 2.04 Å. The aliphatic chains of the decanoate ligands are in an all-*trans* conformation. Each amine N-H forms intermolecular hydrogen bonds to neighbouring carbonyl oxygen atoms and the oxygen atoms involved in Co(II) coordination, at N···O distances ranging between 2.93 and 3.04 Å.

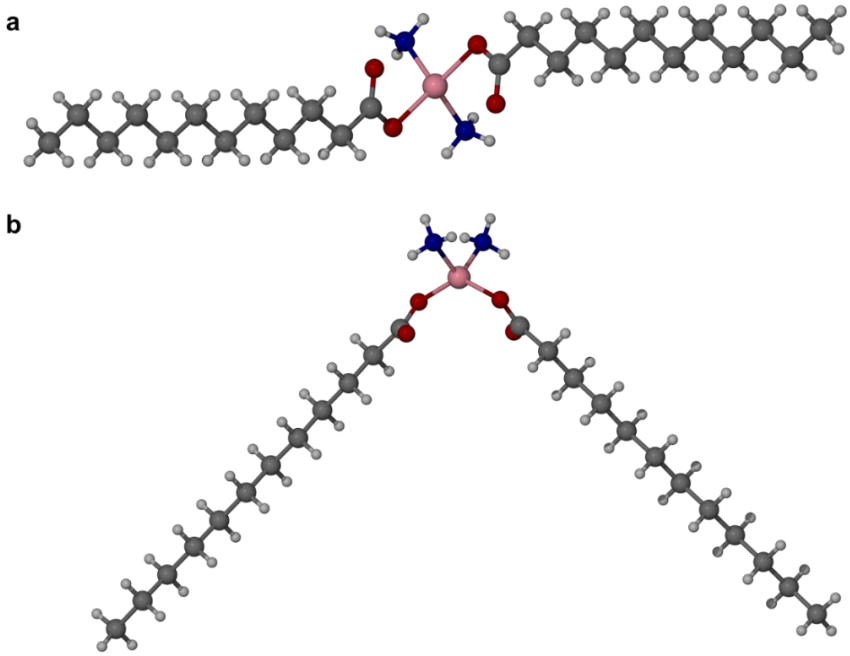

Figure 2.5. The X-ray structure of diammine-bis(dodecanoato-O)-cobalt(II), displayed in the crystallographic a) (010) and b) (001) axes.[29]

An additional diamine structure with two *n*-alkyl carboxylate ligands consists of a platinum(II) carboxylate complex with two monodentate pentadecanoate ligands and a homopiperazine ligand in a boat conformation, forming a chelate ring with platinum(II).[30] The metal centre is in a slightly distorted square planar geometry, with Pt-N distances of 2.00 and 2.01 Å, and Pt-O distances of 2.00 and 2.04 Å (Figure 2.6). The long aliphatic carboxylate ligands display variations in conformation. For instance, chain 1 is in an all-*trans* conformation until C11 where the chain shows a 74.6 ° *gauche* twist and continues to C15 in a *trans* conformation, whereas chain 2 displays a 44.1 ° twist in the chain at C2, indicative of a *gauche* conformation, with the remainder of the alkyl chain in an all-*trans* conformation. Intramolecular hydrogen bonds occur from the amine hydrogen atoms of the homopiperazine to the carbonyl oxygen atoms of the pentadecanoate ligands, at N···O distances of 2.80 and 2.83 Å.

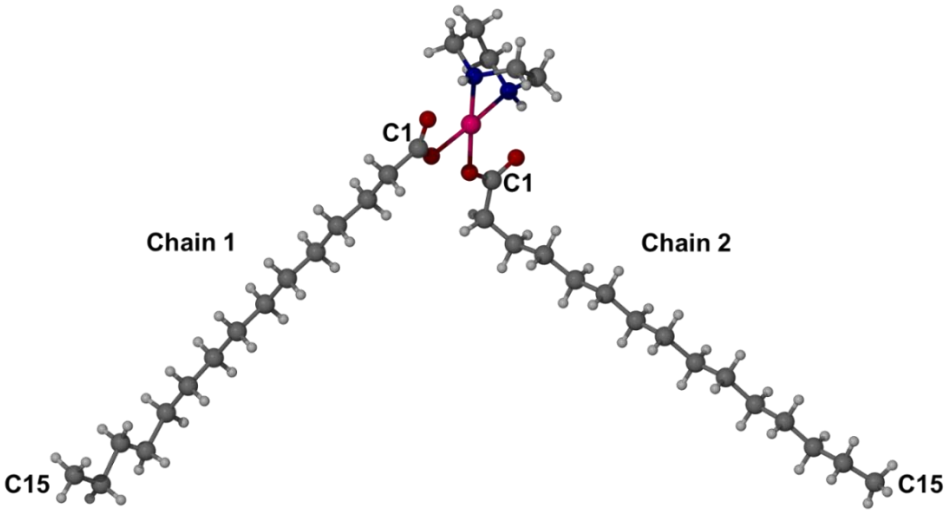

Figure 2.6. The X-ray structure of (homopiperazine)-bis(pentadecanoato)-platinum(II), with both pentadecanoate chains displaying both *trans* and *gauche* conformations.[30]

The structure in the CSD with the longest *n*-alkyl carbon chains in this set of results is a structure of a copper(II) centre bound to hexadecanoate and 2,2'-bipyridyl ligands with methanol solvent molecules. The copper(II) ion is in a square pyramidal geometry and is bridged by two monodentate centrosymmetric hexadecanoate ligands.[31] These carboxylate ligands are arranged in an all-*trans* conformation. The Cu(II) centre is also bound to two nitrogen atoms from a 2,2'-bipyridyl ligand, which take part in π-π stacking interactions in the structure, with a centroid-centroid separation distance of the bipyridyl rings at 3.77 Å.[31] Hydrogen bonds occur from the methanol O-H to the carbonyl oxygen atom of the hexadecanoate ligands, at an O···O distances of 2.73 Å. Weak CH···O interactions also occur from the aromatic rings of 2,2'-bipyridyl ligands to nearby oxygen atoms of the carboxylate ligands, at C···O distances ranging between 3.09 and 3.26 Å.[31]

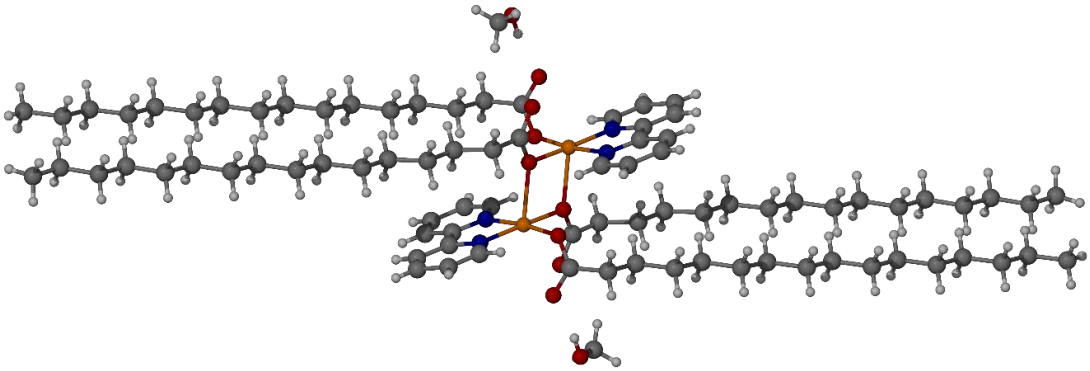

Figure 2.7. The X-ray structure of bis(μ-hexadecanoato-κ^2O:O)bis[(2,2'-bipyridine-κ^2*N*,*N*')(hexadecanoato-κO)-copper(II)] methanol disolvate.[31]

In contrast to coordinate bonding of one metal to two carboxylate ligands, metal *n*-alkyl carboxylates also involve coordinate bonding from at least two metal centres to one carboxylate ligand and are more abundant in the literature by comparison. The search criteria outlined in Figure 2.8 resulted in 10,943 hits, with the number of hits decreasing as the *n*-alkyl chain increases from zero to twenty-two carbon atoms in length. An important structure to illustrate this coordination mode of to the metal ion is the structure of lithium pentanoate (Figure 2.9).[32] The pentanoate ligands display both chelating and bridging bidentate coordination to the lithium(I) ion, with the metal centre in a tetrahedral coordination environment. The distances from the carboxyl oxygen atom to the lithium ion vary between 1.90 and 2.0 Å. The structure forms a bilayer and packs in a tail-to-tail arrangement, with the pentanoate ligands in an all-*trans* conformation. Temperature-dependant polymorphism also occurs in this structure and in the related lithium propanoate.[32]

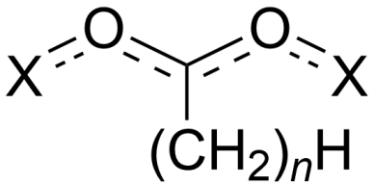

Figure 2.8. The search criteria to search the CSD of one carboxylate ligand coordinated to two metal ions. The dashed double bond denotes 'any bond type', while the 'X' indicates 'any metal atom'.

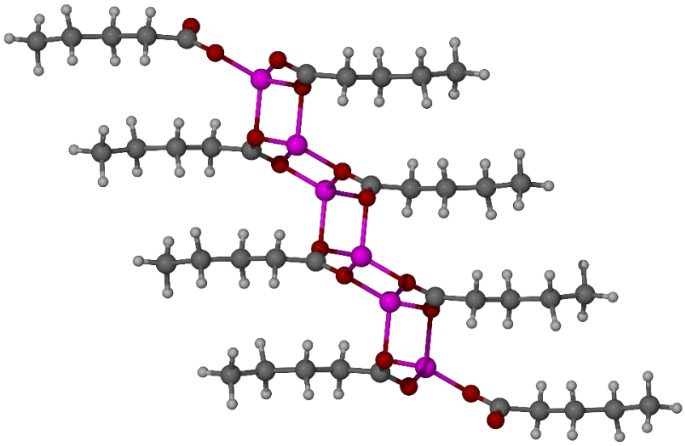

Figure 2.9. The X-ray structure of catena-[(μ$_4$-pentanoato)-lithium(I)] viewed in the crystallographic (010) axis.[32]

A silver(I) complex with ligands consisting of twenty-two carbon atoms has been described in the literature (Figure 2.10).[33] The structure crystallises in the $P\bar{1}$ space group, with a long *c*-axis of 58.34 Å. The carboxylate head groups form an eight-membered dimer with Ag-O bond distances of 2.06 and 2.29 Å. Opposite silver atoms are at an Ag-Ag distance of 2.81 Å. Additional carboxylate ligands join to the silver atom in the dimer, at an Ag-O distance of 2.41 Å forming a four-membered ring and a polymeric network, with opposite Ag^+ ions at a distance of 3.29 Å.[33] The structure packs in a tail-to-tail arrangement.

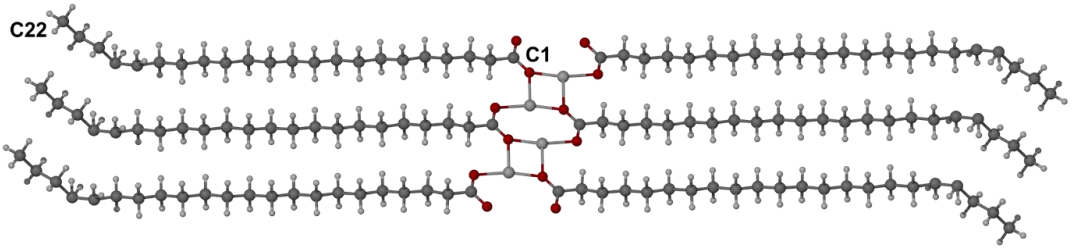

Figure 2.10. The X-ray structure of catena-[(μ-docosanoato)-silver(I)] viewed in the crystallographic (010) axis. Alkyl chains are in an all-*trans* conformation (note there are incorrectly placed hydrogen atoms of the C18 and C19 CH_2 groups).[33]

The CSD results display varied long *n*-alkyl chain carboxylate structures bound to different metal ions, either by two oxygen atoms of different carboxylate ligands or by one carboxylate ligand bound to two metal ions by the oxygen atoms of the ligand. These structures provide important insights into the possible coordination of the

carboxylate groups of PCDA to lithium(I) metal centres, with lithium pentanoate (Figure 2.9) of particular relevance.

2.2. Results and Discussion

2.2.1. PCDA

PCDA Structure

The commercially important diacetylene PCDA is used to provide a colourimetric change in practical chemosensors,[34-37] biosensors,[38-41] and dosimeters.[42-45] However, the preparation of single crystals of such surfactant-like compounds is generally regarded as difficult. Preliminary PXRD analysis indicated that PCDA supplied by Ashland is crystalline with a lamellar structure, evident by the progression of low-angle peaks from 1.9-17.1 °, all correlating to reflections of (00*l*) type (Figure 2.11).[46, 47] Additionally, the PXRD pattern of PCDA from Ashland is comparable to the PCDA obtained from Sigma Aldrich with the two samples exhibiting almost identical diffraction patterns (Figure 2.11). Slow evaporation of an acetone solution of PCDA (obtained from Ashland) gave a high-quality sample suitable for analysis at the I19 beamline at the Diamond Light Source, Oxfordshire. Some decay of photosensitive PCDA in the high-intensity synchrotron X-ray beam was noted, however, a structure determination was successfully carried out. The X-ray structure of PCDA revealed a centrosymmetric structure ($P\bar{1}$ space group) based on the well-known OH···O $R_2^2(8)$ ring hydrogen-bonded carboxylic acid dimer synthon (Figure 2.12).[48, 49] The O···O distance of the dimer is 2.6581(9) Å which is typical length when compared to other long-chain *n*-alkyl acids in the literature.[14-16] The structure is based on a head-to-head bilayer arrangement of molecules and the aliphatic substituents at either end of the dialkyne unit adopt an *anti*-conformation. The crystallographic *c*-axis of 46.647(3) Å is long which is also reflected by the lamellar progression of low-angle peaks in the PXRD pattern. The structure conforms to the topochemical postulate for dialkyne photoreactivity with a translational repeat distance of ≤4.9 Å, at 4.574(1) Å, along with a tilt angle of 44.7 ° that is very close to the optimal value of 45 °. The inter-alkyne C1-C4’ distance between adjacent molecules of PCDA is 3.712(1) Å, which is close to the upper limit of the topochemical postulate for alkyne reactivity (a maximum distance of 3.8 Å).[50]

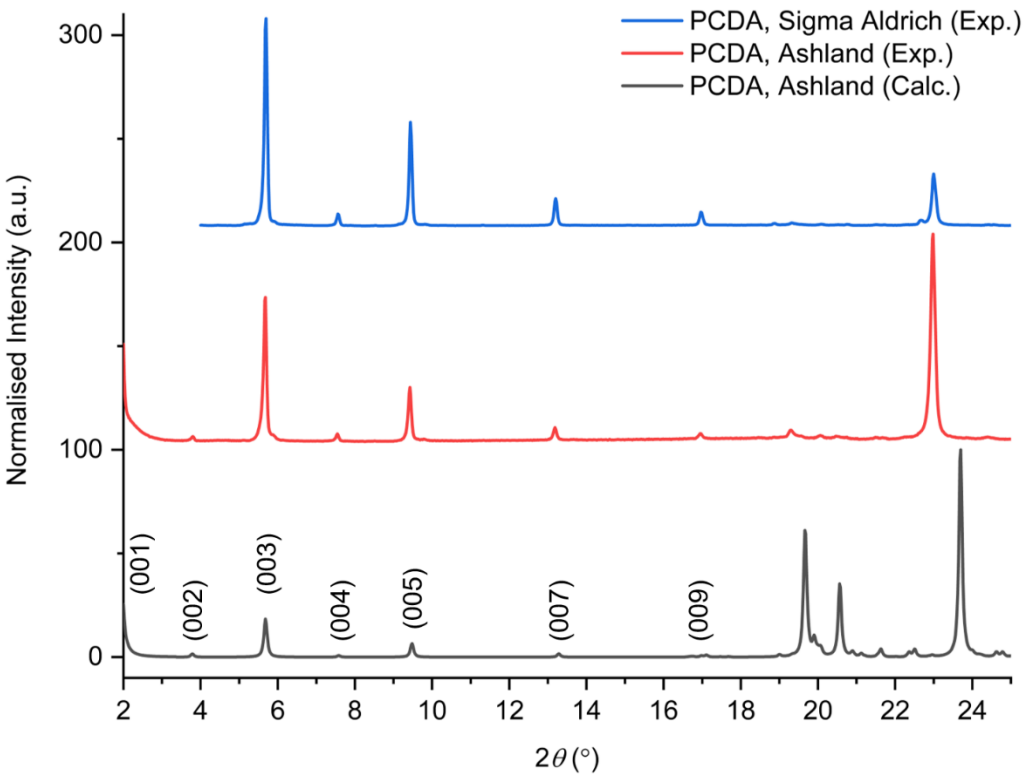

Figure 2.11. The experimental and calculated PXRD patterns of PCDA obtained from Ashland and Sigma Aldrich, highlighting the initial (00*l*) reflections. The experimental data was collected at room temperature (approx. 293 K), while the single crystal data underlying the calculated pattern was collected at 100 K. The calculated pattern highlights the preferred orientation present in the experimental patterns (due to the needle morphology of the PCDA crystals) and is noted in the relative high intensity of the low angle peaks.

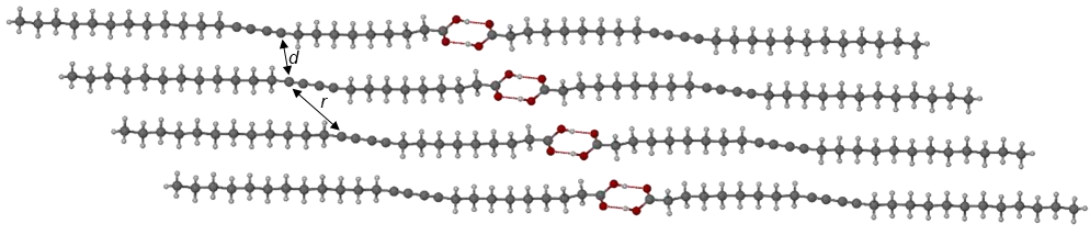

Figure 2.12. The X-ray structure of PCDA showing the carboxylic acid dimer (O···O distance of 2.6581(9) Å) and the *anti*-conformation of the diacetylene substituents. The C1-C4' distance and intermolecular repeat distance are denoted by *d* and *r*, respectively.

The solid state Fourier-transform Infrared (FTIR) spectrum of PCDA supplied by Ashland displays bands in the range of 3000-2800 cm^{-1} which represent the $\nu(CH_3)_{asym}$

and $\nu(CH_2)_{asym}$ and $\nu(CH_2)_{symm}$ stretches (Figure 2.13). The band at 1692 cm^{-1} is indicative of a $\nu(C=O)$ stretch of the free acid. An intense band at 1467 cm^{-1} corresponds to a CH_2 bending mode, along with multiple CH_2 wagging bands between 1350 cm^{-1} and 1194 cm^{-1}. Additionally, the sharp band at 722 cm^{-1} is attributable to the CH_2 rocking mode of PCDA. As observed in the PXRD patterns, the PCDA supplied by Sigma Aldrich displays an almost identical spectrum to the PCDA supplied by Ashland, which are consistent with FTIR spectra of PCDA in the literature.[47, 51-54]

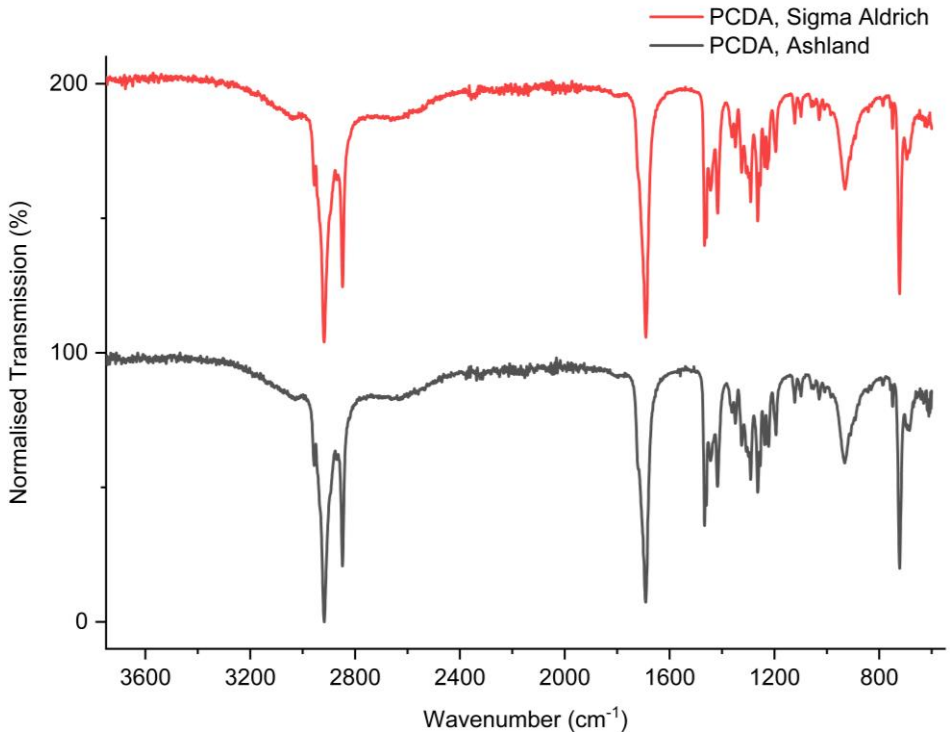

Figure 2.13. The FTIR spectra of PCDA supplied by Ashland and Sigma Aldrich.

The CP-MAS ^{13}C solid-state NMR (ssNMR) spectrum of PCDA supplied by Ashland displays a peak in the carboxylate region of the spectrum at 182.4 ppm with an additional peak at 181.9 ppm, while PCDA supplied by Sigma Aldrich displays an intense single peak at 182.5 ppm (Figure 2.14). The additional carboxylate peak in the Ashland sample may correlate with defects or an additional polymorph, though as there is minimal evidence in the PXRD pattern and FTIR spectra for an additional polymorph, the former is more likely. Distinct peaks in the alkyne region of the spectrum for the PCDA supplied by Ashland and Sigma Aldrich are present at the same chemical shifts at 77.5 ppm (with a small shoulder at 79.2 ppm) and 65.3 ppm (with a less-intense shoulder at 66.1 ppm), representative of two different alkyne

environments. Also for PCDA from different suppliers, the intense peak (with multiple shoulders) at 34.2 ppm is the result of an accumulation of CH_2 peaks with slightly different chemical environments, which are followed by two distinct CH_2 peaks at 26.1 ppm and 21.7 ppm. The peaks assignable to the CH_3 group in both samples are at 16.1 ppm with a small shoulder at 15.1 ppm. Therefore, as the main difference between PCDA from Ashland and Sigma Aldrich is in the carboxylate region due to defects, it can be hypothesised at this stage that PCDA is not polymorphic.

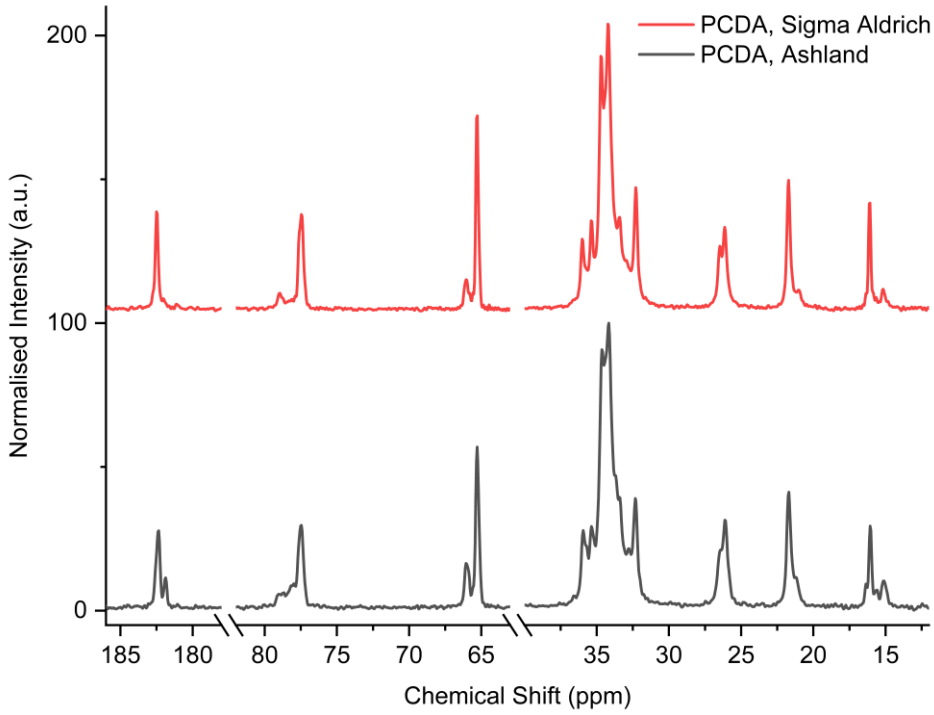

Figure 2.14. The ssNMR spectra of PCDA supplied by Ashland and Sigma Aldrich. The carboxylate region is 180-190 ppm, while alkyne peaks are shown in the 60-80 ppm region, and the alkane peaks are between 10-40 ppm. Breaks are added in the *x*-axis to increase the intensity of the peaks for comparative purposes.

Additionally, DSC was employed to characterise PCDA supplied by Ashland in a heat-cool-heat cycle, heated from room temperature to 200 °C and cooled to room temperature and then heated to 200 °C for the second heating cycle (Figure 2.15). The thermogram revealed a single peak with a melting onset endotherm at 62.3 °C, consistent with literature reports.[47, 51, 52, 55-58] On the cooling to room temperature cycle, a crystallisation exotherm is displayed in the thermogram with an onset temperature of 60.0 °C, and on the final heat cycle, an endotherm at an onset temperature of 61.4 °C. Small impurity peaks of an unknown nature are present at

80.4 °C in the first heat cycle, 70.8 °C on the cooling cycle, and 82.7 °C on the second heat cycle. No additional peaks were present after 100 °C after heating to 200 °C, and so only the temperature range of 25 – 100 °C are shown in the thermogram.

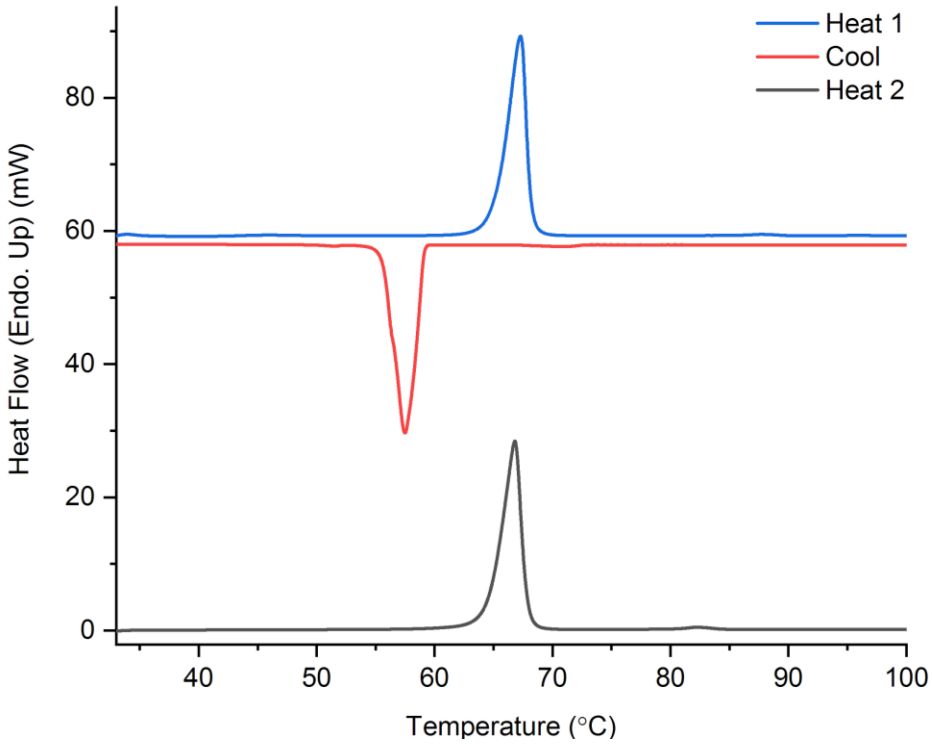

Figure 2.15. The DSC thermogram of PCDA supplied by Ashland in a heat-cool-heat cycle. The thermogram only displays the temperature range of 30 – 100 °C, as the thermogram remained unchanged from 100 – 200 °C.

PCDA Photoreactivity and Thermochromism

The structural parameters for PCDA are within the range of values for photopolymerisation according to the topochemical postulate. This photosensitivity is reflected by the change in colour from light blue to dark blue upon exposure to UV radiation at 254 nm (Figure 2.16). However, as the topochemical parameters for PCDA are at the upper limit of the postulate, limited solid state photoreactivity is observed in the PXRD pattern (Figure 2.17) and FTIR spectra (Figure 2.18) of PCDA before and after irradiation; the diffraction pattern and FTIR spectrum remain essentially unchanged. The lack of change with irradiation is also established in the ssNMR spectra of PCDA, evident by the absence of peaks that can be assigned to the alkene functionalities expected in the photoproduct (in the 100-135 ppm region of the spectrum) (Figure 2.19). The lack of alkene peaks in the ssNMR spectra of irradiated

PCDA implies that there is less than 1 % conversion even upon prolonged exposure which is surprising given the profound colour change. Therefore, the dramatic colour change suggests a surface effect.

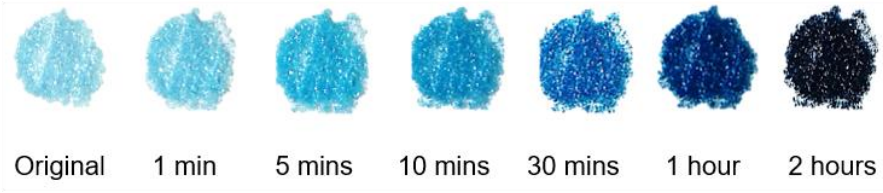

Figure 2.16. Photographs of PCDA before and after exposure to 254 nm of UV radiation for different durations. The blue surface colouration of the powder before irradiation is not representative of the bulk material as there is no spectroscopic evidence of polymerisation.

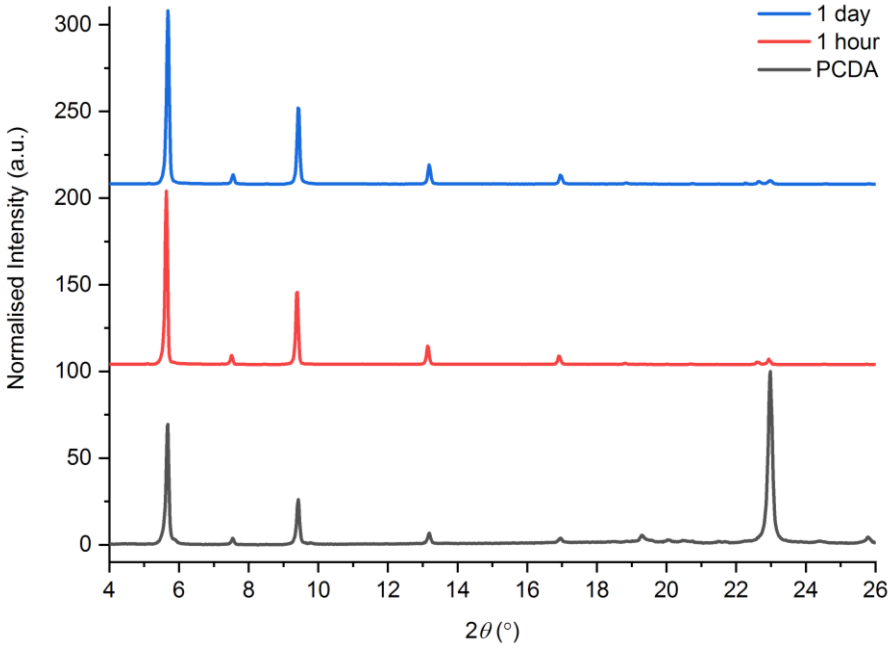

Figure 2.17. The experimental PXRD patterns of PCDA irradiated with 254 nm of UV radiation for one hour and one day. Preferred orientation occurs in the original PCDA pattern and in the irradiated patterns and is apparent when compared to the calculated pattern of PCDA in Figure 2.11.

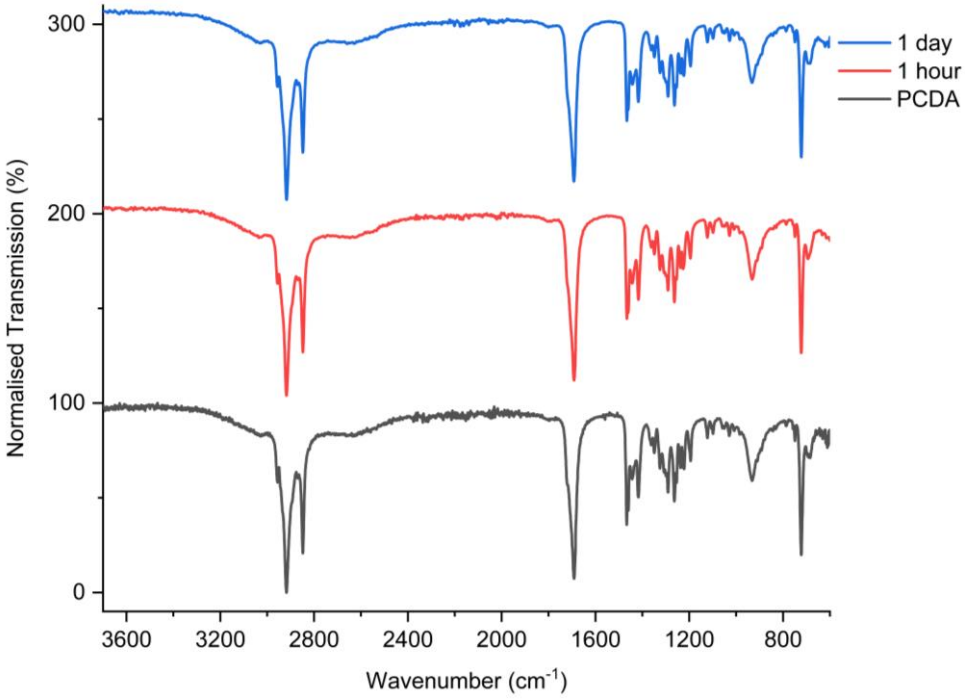

Figure 2.18. The FTIR spectra of PCDA exposed to UV radiation (254 nm) for one hour and one day.

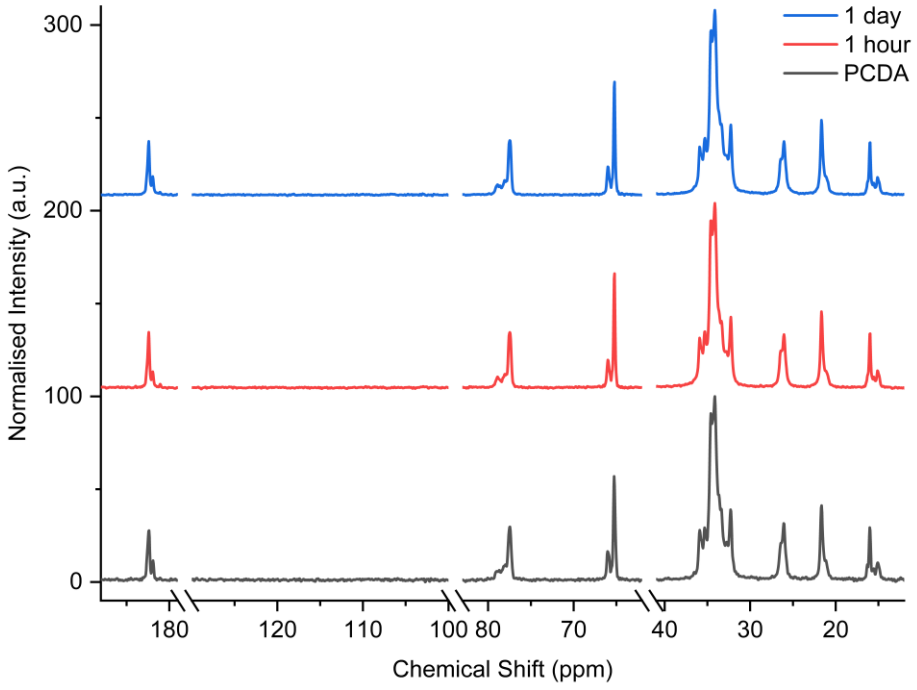

Figure 2.19. The ssNMR spectra of PCDA exposed to UV radiation (254 nm) for different durations. The carboxylate region is 180-190 ppm, while the presence of any polymer alkene peaks should occur in the 100-130 ppm region. Alkyne peaks are

shown in the 60-80 ppm region, and the alkane peaks are between 10-40 ppm. Breaks in the *x*-axis are added to compact the spectra.

In addition to UV irradiation, PCDA was also exposed to 100 Gy of X-rays. X-ray irradiated PCDA was analysed by Raman spectroscopy in collaboration with Dr. Larry Senak at Ashland. Unirradiated PCDA exhibits a monomeric alkyne band at 2256 cm^{-1}, and surprisingly, a photopolymer (ene-yne) alkyne band at 2100 cm^{-1}, along with an alkene band at 1444 cm^{-1}, revealing the presence of photopolymer even before any X-ray irradiation (Figure 2.20). When PCDA is irradiated with 100 Gy of X-ray radiation, the C-H stretching bands (3000-2800 cm^{-1}) and the monomeric alkyne band (2256 cm^{-1}) in the spectrum appear reduced relative to the intensity of the photopolymer alkyne and alkene bands at 2100 cm^{-1} and 1444 cm^{-1}. This observation can be explained by a marked enhancement of the intensity of the alkyne and alkene photopolymer chromophore bands by a pre-resonance Raman effect. This arises because the excitation wavelength of the laser (754 nm) slightly overlaps with the absorption band of the photopolymer. The presence of the photopolymer bands in the Raman spectrum of the unirradiated sample, the lack of alkene bands in the solid state NMR spectrum, accompanied by the faint blue colouration of the PCDA powder before irradiation indicates a low degree of surface polymerisation of the material that does not represent the bulk of the sample.

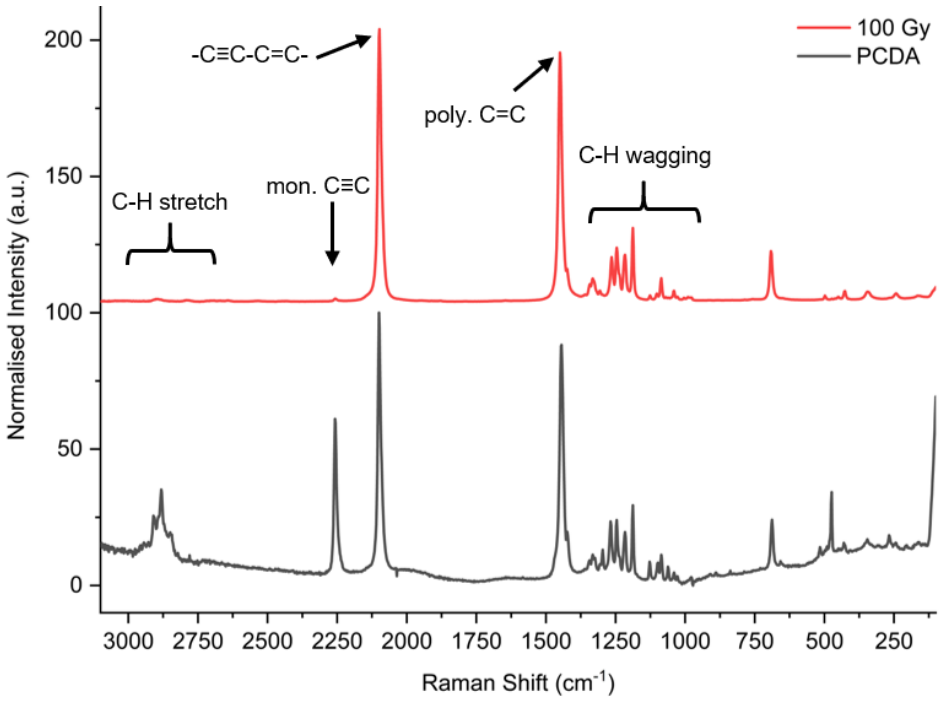

Figure 2.20. The Raman spectra of PCDA and PCDA irradiated with 100 Gy of X-ray radiation. Even before irradiation, the PCDA sample displays bands for both monomeric (2256 cm^{-1}) and polymeric (2100 cm^{-1} and 1444 cm^{-1}) PCDA because of traces of photopolymer, while the irradiated sample is dominated by the photopolymer bands which experience considerable intensity enhancement as a result of pre-resonance Raman effects.

PCDA undergoes irreversible thermochromism above 65 °C due to increased thermal motion of the alkyl chains and the consequent weakening of the hydrogen-bonded dimers as temperature increases.[59] Reversible thermochromism can be achieved by increasing the capabilities for hydrogen bonding in the structure, such as introducing a peptide sequence at the PCDA headgroup.[60] To further understand the irreversible thermochromic nature of PCDA, and whether PCDA responds to heat in the same way as UV or X-ray irradiation, PCDA was exposed to elevated temperature in solvents that it is soluble in and without solvent, for varying durations, outlined in Table 2.1.

	PCDA (mg)	Temperature (°C)	Duration	Solvent (mL)
Reflux (R)	500	58	1 day	Acetone, 100
	500	72	7 days	*n*-Butanol, methanol (1:1), 100
Oven (O)	100	65	1 hour	n/a
	100	85	5 minutes	n/a
	100	100	5 minutes	n/a

Table 2.1. The conditions PCDA supplied by Ashland was exposed to for the different heating experiments. The solvents were chosen due to their differences in polarity. PCDA readily dissolved in acetone and *n*-butanol and methanol (1:1).

The samples produced under the conditions listed in Table 2.1 reveal that refluxing monomeric PCDA at 58 °C in acetone for one day and removing the solvent by exposure to vacuum does not change the structure, evidenced by the unchanged nature of the PXRD diffractogram, with characteristic peaks at 5.7, 7.6, 9.4, and 13.2 °. This is likely because 58 °C is below the melting temperature of 62.3 °C for PCDA. However, refluxing PCDA at 72 °C for seven days in a mixture of *n*-butanol and methanol results in the same pattern with additional peaks of low intensity at 5.9, 9.9, and 13.8 ° (Figure 2.21), indicating the partial transformation to a new material. Although, when the oven was used to heat solid PCDA at a constant temperature at 65 °C for one hour, 85 °C and 100 °C for five minutes, peaks of an increased intensity compared to the patterns of refluxed PCDA are observed at 5.7, 5.9, 7.6, 7.9, 9.5, 9.9, 13.2, and 13.8 °. The new peaks that arise are likely due to the presence of a new polymorph and are not due to the polymerisation of PCDA, which is clear from the absence of resonances attributable to alkene functionality in the range of 100-135 ppm in the ssNMR spectra of each product (Figure 2.22). The ssNMR spectra of the different products also display differences in the carboxylate region (180-185 ppm). PCDA supplied by Ashland displays peaks in the carboxylate region of the ssNMR spectra at 182.4 ppm and 181.9 ppm, consistent with the reflux experiment at 58 °C, suggesting that PCDA remains unchanged unless it is heated at or above its melting temperature of 62.3 °C. This is also evident from the PCDA heating experiments when PCDA is refluxed at 72 °C, and when heated as a solid in the oven at 65 °C, 85 °C, and 100 °C, as an additional carboxylate peak at 181.1 ppm is observed in the ssNMR spectra. Additionally, when PCDA is heated to 100 °C, a small peak also is present at

181.4 ppm. Therefore, when PCDA is exposed to temperatures ≥65 °C regardless of duration, distinct changes occur in the PXRD pattern and ssNMR spectra that are consistent with the presence of a second polymorph. A second potentially metastable polymorph of PCDA would not necessarily be observed in the DSC thermogram if the phase transition occurred due to the cooling of the melt, as only the recrystallisation endotherm would be observed. However, additional thermal and PXRD analyses are required to fully understand the changes in PCDA with heat.

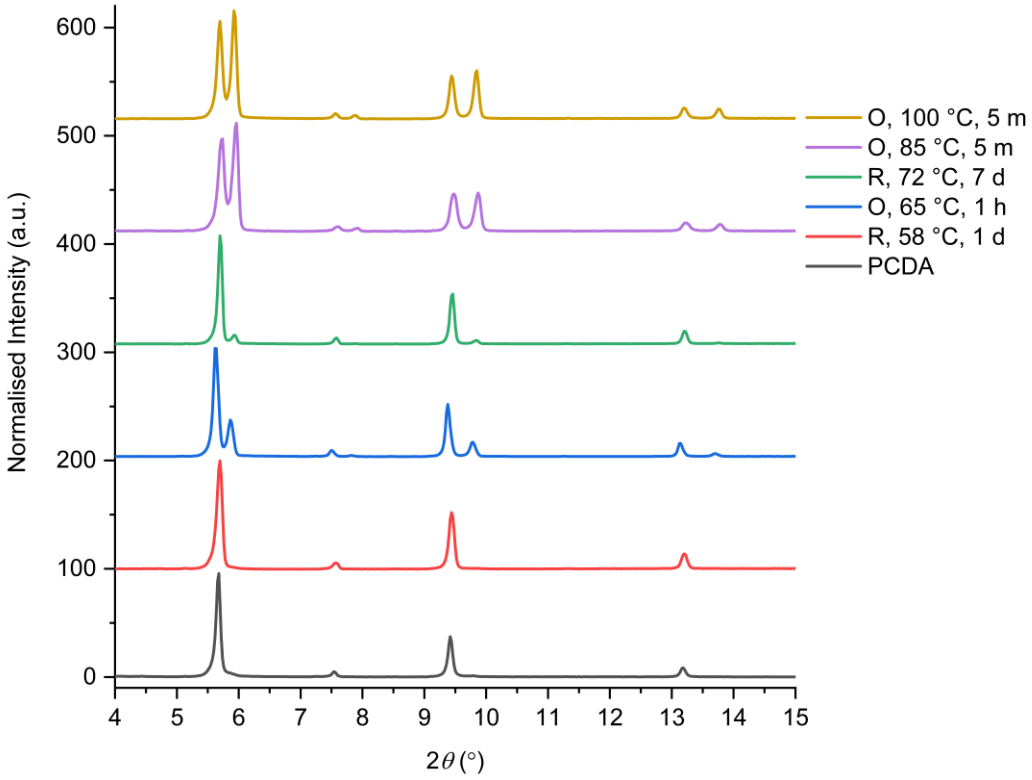

Figure 2.21. The PXRD patterns of PCDA supplied by Ashland heated to different temperatures for different durations, with or without solvent. 'R' and 'O' in the figure legend suggests whether the experiment was heated by refluxing PCDA in solution (R) or by heating PCDA as a solid in the oven (O).

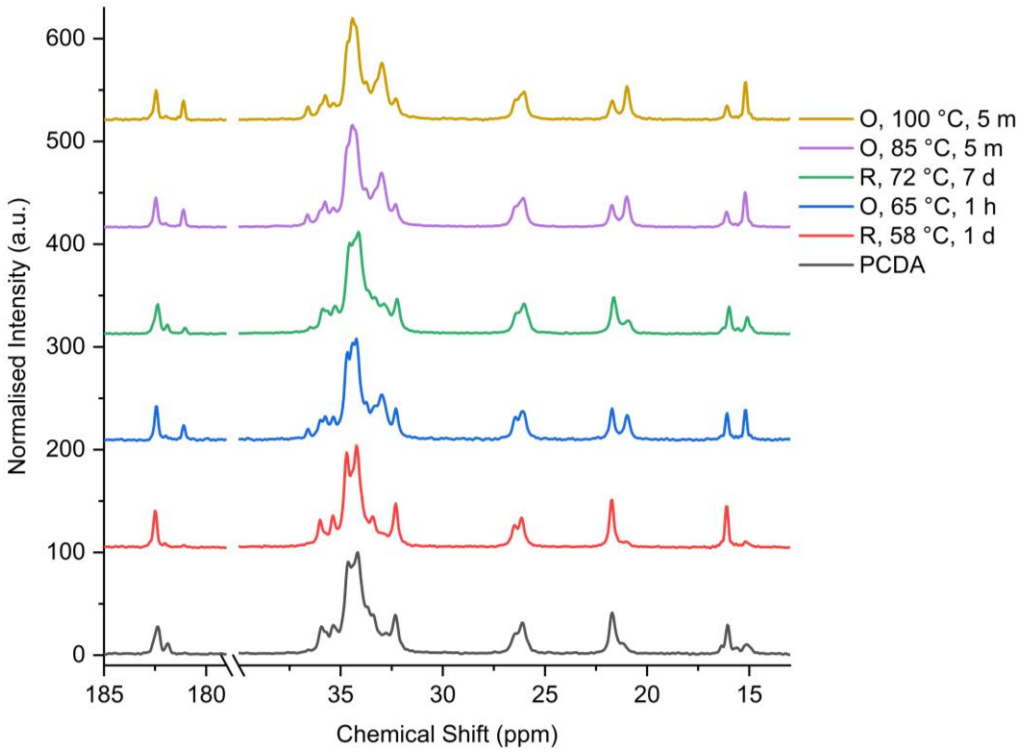

Figure 2.22. The ssNMR spectra of PCDA heated to different temperatures for different durations. 'R' and 'O' in the figure legend suggests whether the experiment was heated by refluxing PCDA in solution (R) or by heating PCDA as a solid in the oven (O). A break in the *x*-axis was included to compact the spectra.

2.2.2. The Lithium Salt of PCDA

Li-PCDA Model Compounds

Neither the lithium salt of PCDA nor any long-chain lithium carboxylate salts have been structurally characterised and so model compounds of Li-PCDA were synthesised to try to gain insight into the lithium environment of the salt. Short-chain *n*-carboxylic acids butanoic acid, pentanoic acid, and hexanoic acid were combined with lithium hydroxide monohydrate ($LiOH{\cdot}H_2O$) in 1:1 ratios in acetone and ethanol (1:1) and stirred for 24 hours with the product isolated under vacuum. This resulted in the preparation of lithium butanoate (Li-but), lithium pentanoate (Li-pent, which is already known in the literature),[32] and lithium hexanoate (Li-hex). The PXRD pattern of each salt displays intense low angle peaks at 7.3, 6.2, and 5.3 °, for Li-but, Li-pent and Li-hex, respectively, with smaller 2θ values corresponding to larger unit cells (Figure 2.23). The calculated PXRD patterns of Li-propanoate (Li-prop) and Li-pent from the literature are also shown for comparison and display intense low angle peaks at 9.2 and 6.3 °, respectively.[32]

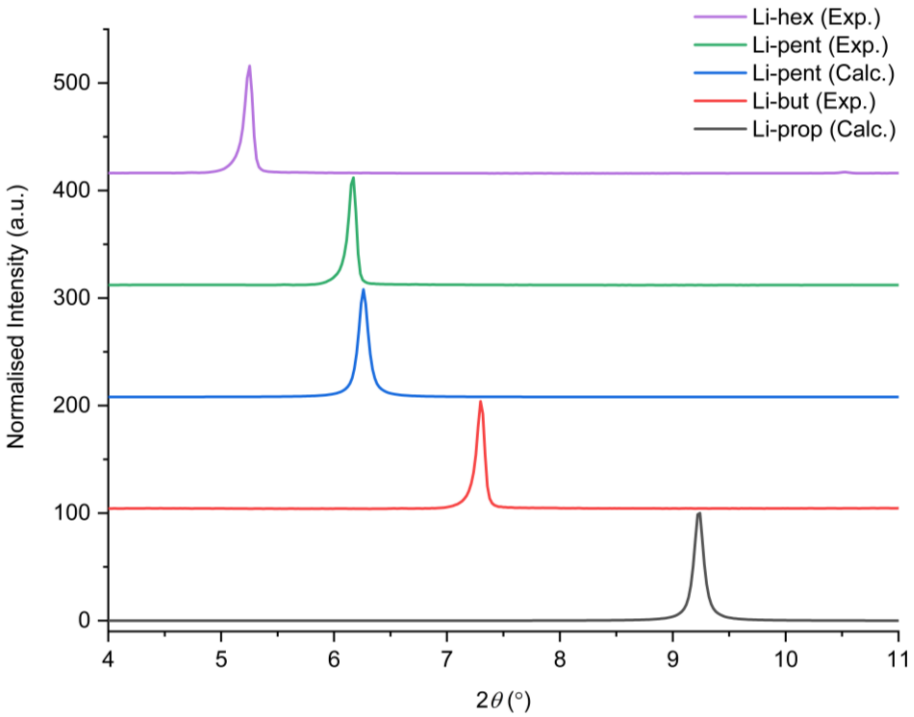

Figure 2.23. The experimental PXRD patterns of Li-but, Li-pent, and Li-hex, and the calculated patterns of Li-prop and Li-pent.[32]

The crystal structures of Li-prop and Li-pent (Figure 2.9) display a chelating bridging bidentate coordination of the carboxylate to the lithium ion. This coordination mode is, therefore, also expected for the structures of Li-but, Li-pent, and Li-hex, and is consistent with the FTIR data of the short *n*-alkyl chain lithium salts (Figure 2.24). A summary of the peak assignments for each salt are displayed in Table 2.2 which also state the presence unreacted residual acid present in the salts, as the FTIR spectrum of Li-pent in the literature shows no evidence of a free carboxylic acid C=O peak.[32] Although, the elemental analyses of the salts suggest the materials are pure. The asymmetric and symmetric stretch bands of the COO^- group of the salts are split, which suggests reduced carboxyl symmetry due to the coordination with the lithium ion.[32, 61] The FTIR spectra are sensitive to coordination mode of each salt, evident by the difference in wavenumber of the asymmetric and symmetric stretching bands, $\Delta\nu = \nu(COO)_{asym} - \nu(COO)_{symm}$.[62, 63] If $\Delta\nu > 200$ cm^{-1}, monodentate binding is likely to occur.[62, 64] However, if $\Delta\nu$ is between 170 and 150 cm^{-1}, then bridging coordination is likely, compared to a $\Delta\nu$ of approximately 100 cm^{-1} for chelating coordination.[62, 65 68] The experimental $\Delta\nu$ for Li-but (1579 – 1434 cm^{-1}) is 145 cm^{-1} while the $\Delta\nu$ for Li-pent (1577 – 1440 cm^{-1}) and Li-hex (1578 – 1441 cm^{-1}) is 137 cm^{-}

[1]. As all Δν values are greater than for chelating bonding and lower than the range for bridging coordination, a combination of chelating bridging bidentate coordination of the carboxylate to the lithium ion is likely given the structure of Li-pent. Additionally, the CH_2 bending modes groups between 750 cm^{-1} and 650 cm^{-1} are split for each salt, suggesting a monoclinic or orthorhombic space group,[68] which is in agreement with the $P2_1/c$ space group of Li-pent.[32] The ssNMR spectra of the short-chain lithium salts all display a single carboxyl carbon peak at 187.4 ppm (Figure 2.25), compared to the carboxylate peaks of PCDA at 182.4 and 181.1 ppm. The remainder of the ssNMR spectra of the salts reveals distinct peaks corresponding to the carbon atoms of the methylene groups ranging from 41.7-19.8 ppm. The peaks assigned to the terminal methyl group carbon atoms occur at 15.2 ppm in each case.

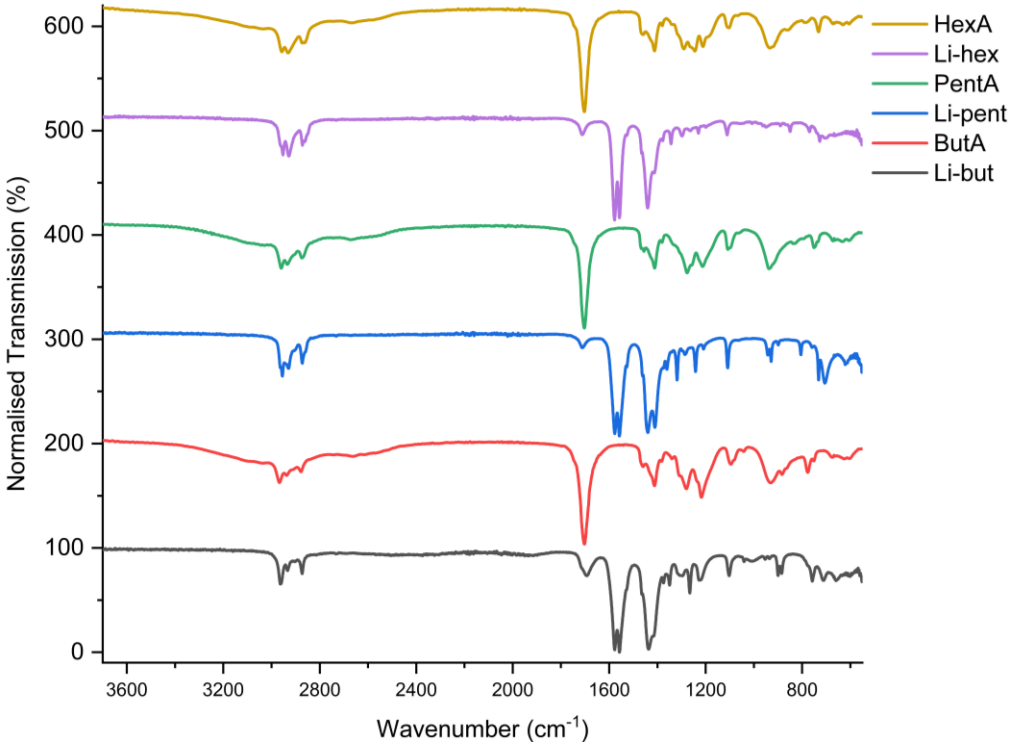

Figure 2.24. The FTIR spectra of Li-but, Li-pent, and Li-hex.

Vibrational assignment	Frequency (cm^{-1})		
	Li-but	Li-pent	Li-hex
$\nu(CH_3)_{asym}$	2964	2955	2953
$\nu(CH_2)_{asym}$	2934	2930	2929
$\nu(CH_2)_{symm}$	2873	2873	2872
ν(C=O) (residual acid)	1697	1712	1711
$\nu(COO)_{asym}$	1579, 1557	1577, 1557	1578, 1558
$\delta(CH_2)$	1461	1463	1461
$\nu(COO)_{symm}$	1434, 1415	1440, 1409	1441, 1413
$\omega(CH_2)$	1353-1219	1360-1208	1343-1230
ν(C-C)	1105	1108	1110
νC-C(COO)	901	928	850
$\rho(CH_2)$	756, 710	732, 704	768, 726

Table 2.2. The assigned wavenumbers for each peak present in the FTIR spectra of Li-but, Li-pent, and Li-hex. Vibrational modes: ν = stretching; δ = bending; ω = wagging; ρ = rocking.

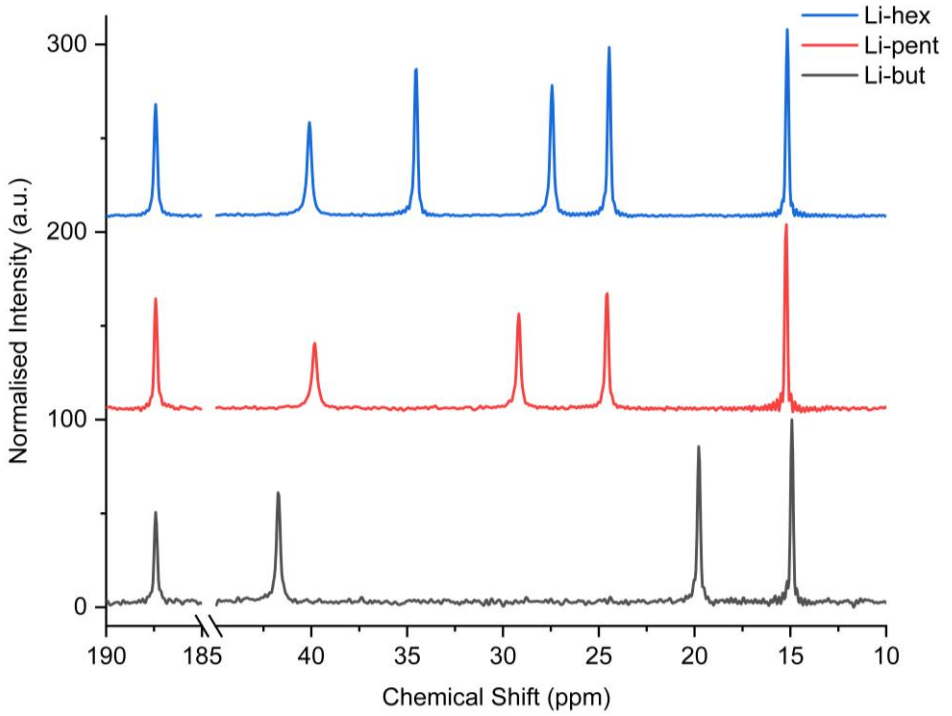

Figure 2.25. The ssNMR spectra of Li-but, Li-pent, and Li-hex. The carboxylate region is 180-190 ppm while alkane peaks appear between 10-45 ppm. A break is present in the *x*-axis to compact the spectra.

Li-PCDA Structure

The active ingredient in GAFchromic EBT3 dosimetric films is the lithium salt of PCDA.[44, 69] The preparation of Li-PCDA is described in a European patent application.[70] The formulation is synthesised by dissolving PCDA in a basic solution (e.g. aqueous tetraethylammonium hydroxide) at elevated temperatures. When PCDA is dissolved, 30 wt. % aqueous solution of lithium hydroxide is added to form nuclei that are then ripened by Ostwald ripening. Scanning electron microscopy (SEM) micrographs show a platelet morphology of the particles before ripening (Figure 2.26a). After ripening, the resulting hair-like filaments are typically greater than 100 μm in length and because of this, the filaments entangle and agglomerate and therefore, cannot form uniform coatings for films (Figure 2.26b). This material is known as the "long hair" morphology. As a result, the "long hairs" are sonicated to produce a smooth, uniform coating, consisting of particles less than 50 μm in length known as "short hairs" (Figure 2.26c). The "short hairs" are then ripened at temperatures at 62 °C for 18 hours to ensure all of the material has converted to the "short hair" morphology (Figure 2.26d). Gafchromic EBT3 films currently use the "short hairs" due to their smoother coating properties, although the "long hair" morphology seems to be more radiation-sensitive.

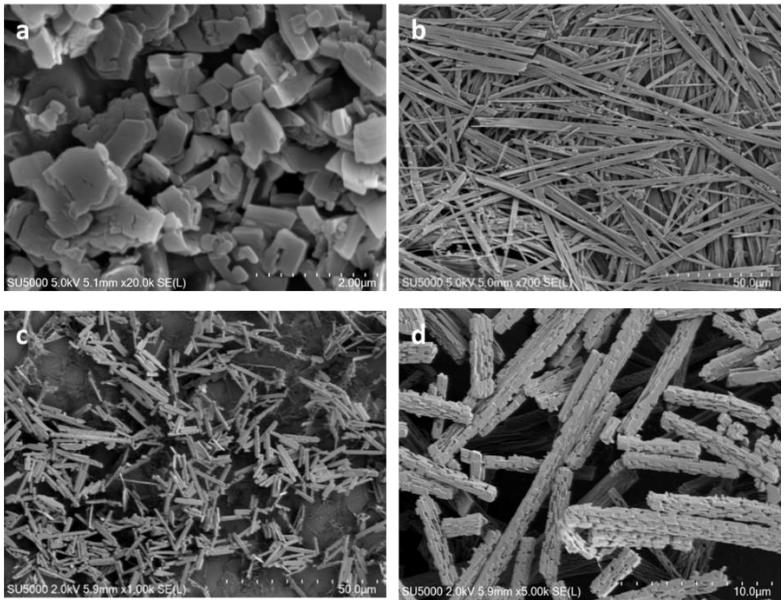

Figure 2.26. SEM micrographs of Li-PCDA a) as a platelet morphology before ripening in the oven b) the "long hairs" after ripening c) the "long hairs" after sonication to give "short hairs" and d) the ripened "short hairs" the oven for 18 hours at 63 °C. Micrographs courtesy of Ashland LLC.

The PXRD pattern of the initial platelet morphology shows that it is, in fact, unreacted PCDA, though with additional small peaks at 5.9, 7.9, and 9.9 ° (Figure 2.27) that correspond to peaks in the PXRD pattern of heated PCDA (page 80). The FTIR spectra of PCDA and the material with platelet morphology are almost identical (Figure 2.28). It is particularly noteworthy that this plate-like material exhibits a free carboxylic acid carbonyl band at 1691 cm^{-1} confirming that this initial material is unreacted PCDA. The material with platelet morphology is also very similar to PCDA by ssNMR, though with a low intensity additional peak in the carboxylate region, with a chemical shift of 181.0 ppm (Figure 2.29).

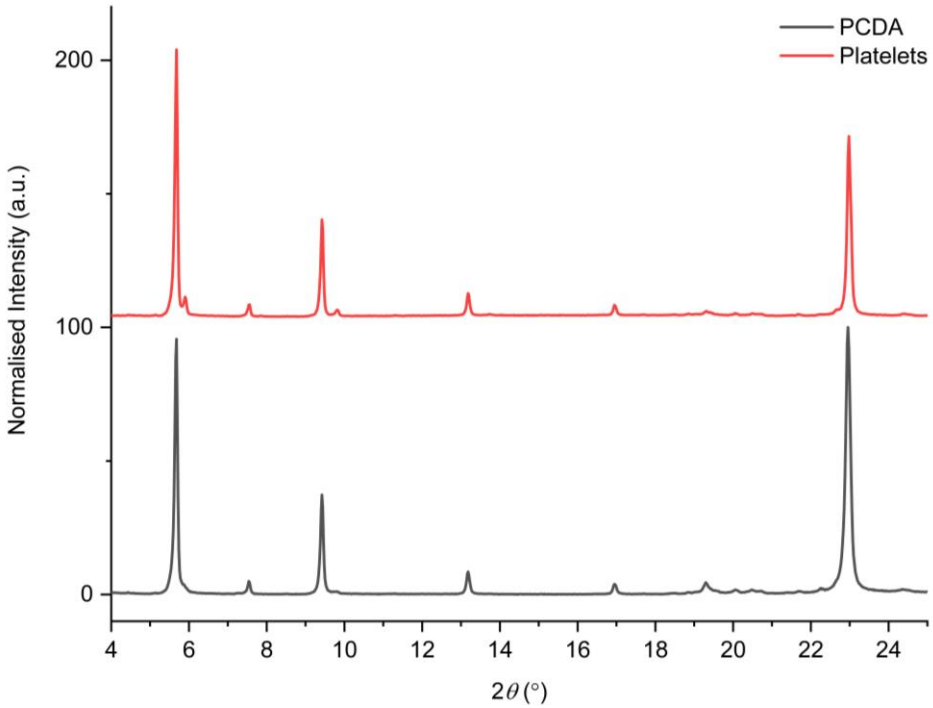

Figure 2.27. The PXRD patterns of the platelet morphology of Li-PCDA and PCDA, highlighting that the platelet morphology is unreacted PCDA.

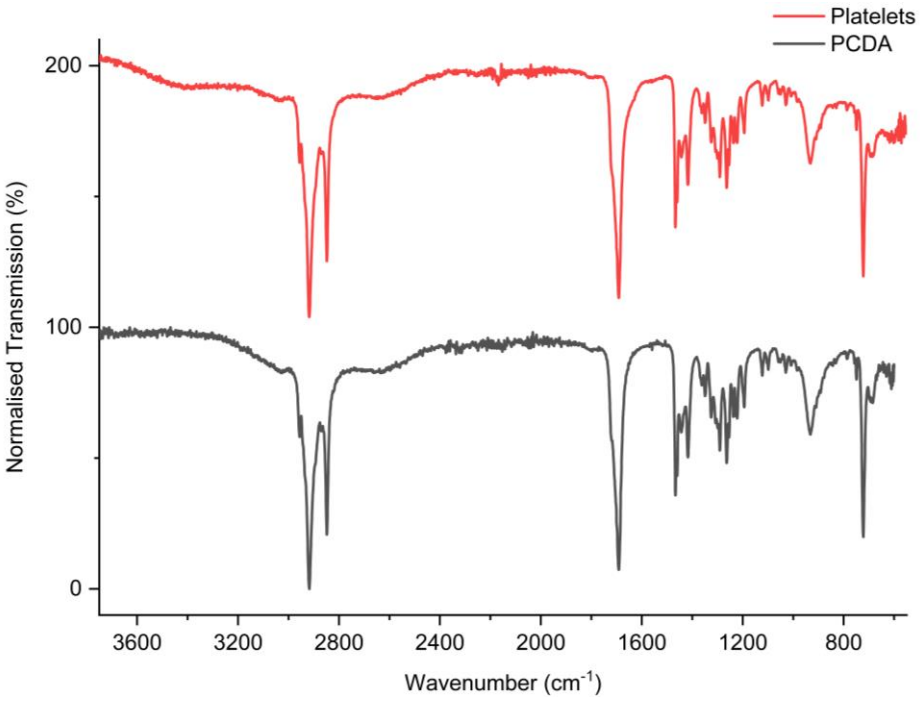

Figure 2.28. The FTIR spectra of PCDA and the initial platelet material formed during the synthesis of Li-PCDA.

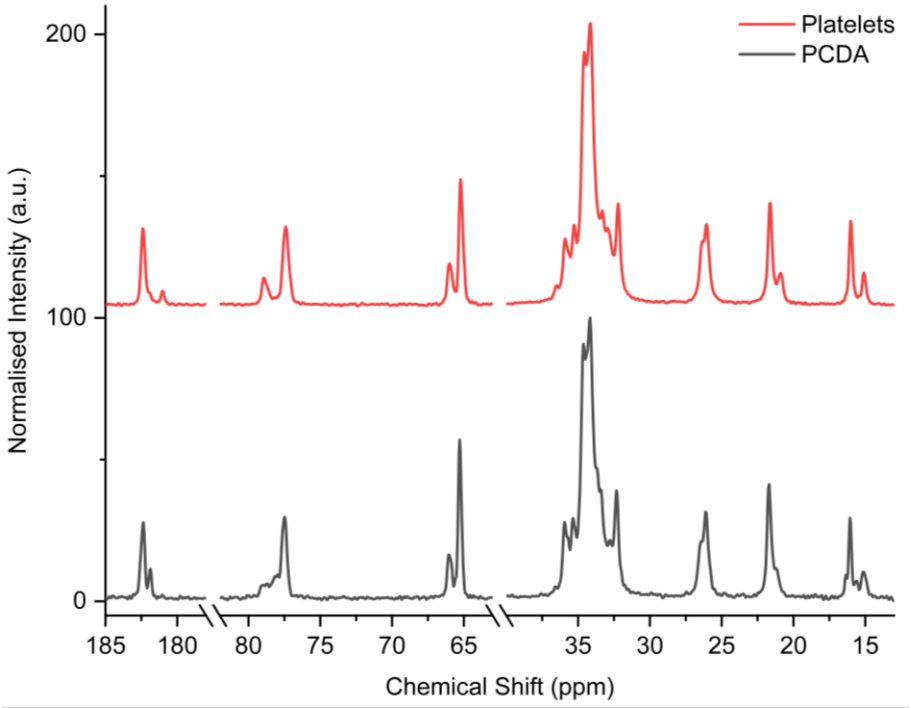

Figure 2.29. The ssNMR spectra of PCDA and the initial platelet morphology product formed in the synthesis of Li-PCDA. The carboxylate region is 180-190 ppm while alkyne peaks are shown in the 60-80 ppm region, and the alkane peaks are between 10-40 ppm. Added breaks are included in the *x*-axis to compact the spectra.

The PXRD patterns of the "short hair" and "long hair" morphologies show that Li-PCDA exists as two different polymorphic or solvate forms (Figure 2.30). The "short hairs" comprise a metastable form termed Form A. The "long hairs" are a mixture of Form A, and a second form termed Form B. Form B was isolated by heating the "long hairs" to either 80 °C for one hour, or 60 °C for one day implying that Form B may be the most thermodynamically stable form under ambient conditions. The different heating experiments are outlined in Table 2.3. Form A is quite similar in structure in terms of lamellar spacing to PCDA itself with the first three peaks in the PXRD pattern at essentially the same 2θ values. This implies that Form A of Li-PCDA may exhibit similar photoreactivity to PCDA. The positions of the low angle PXRD peaks for PCDA, the initial platelet morphology material formed on the preparation of Li-PCDA, Form A/"short hairs", the "long hairs" mixed material, and Form B are summarised in Table 2.4. The thermodynamic Form B appears to have a slightly larger unit cell compared to metastable Form A and PCDA itself, exemplified by the lowest angle PXRD peak at 5.0 ° compared to 5.7 °. As with PCDA, the two Li-PCDA forms also show a progression of (00*l*) peaks, indicating a lamellar structure. In a similar way to the Li-PCDA forms, a silver(I) complex with docosanoate ligands (Ag-doco, $P\bar{1}$ space group, Figure 2.10) has a chelating bidentate coordinate bonding and displays a (00*l*) lamellar progression, with the initial peaks at 4.5 ° (003), 6.1 ° (004), 7.6 ° (005), and 9.1 ° (006), implying a similar unit cell length to the Li-PCDA forms along the *c*-axis (Figure 2.31).[33] The *c*-axis of Ag-doco (22 carbon atoms) is 58.34 Å compared to the *c*-axis of PCDA (25 carbon atoms) at 46.647(3) Å, this implies that PCDA has a more bent or inclined arrangement due to the smaller unit cell size.

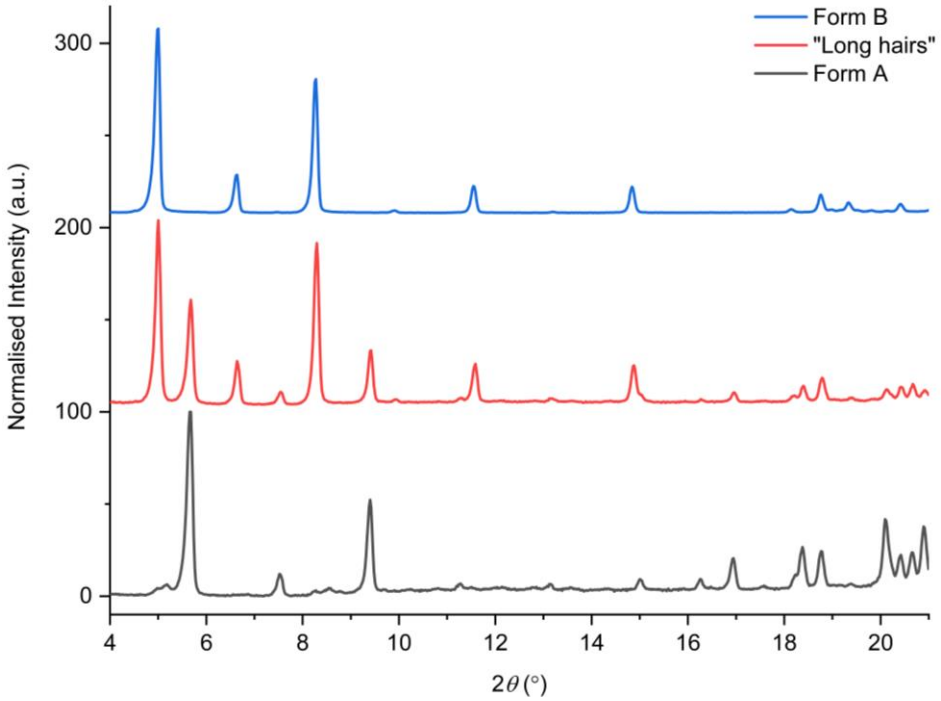

Figure 2.30. The PXRD patterns of Form A/“short hairs”, the "long hairs" of Li-PCDA, and Form B.

Sample	**“Short hairs”/ Form A**		**“Long hairs”/ Form A and B**	
Temperature (°C)	**1 hour**	**1 day**	**1 hour**	**1 day**
50	A	A	A and B	A and B
60	A	A and B	A and B	B
70	A	A and B	A and B	B
80	A and B	B	B	B
90	A and B	B	B	B
100	B	B	B	B
150	B	Amorphous	B	Amorphous

Table 2.3. Effect of heating the commercial “short hairs” (Form A) and “long hairs” (Form A and B) Li-PCDA samples, and the temperature and heating duration required to isolate Form B. Changes in the powders are confirmed by PXRD, FTIR, and ssNMR analyses.

	2θ values				
PCDA	5.7	7.5	9.4	13.2	17.0
	(003)	(004)	(005)	(007)	(009)
Platelets	5.7	5.9	7.5	7.9	9.4
"Short hairs"/Form A	5.7	7.5	9.4	11.3	13.2
"Long hairs"	5.0	5.7	6.6	7.5	8.3
Form B	5.0	6.6	8.3	9.9	11.6

Table 2.4. The 2θ values from the initial peaks of PCDA along with the respective (00l) reflections, the platelet morphology, the two forms of Li-PCDA, and the "long hairs" of Li-PCDA clearly showing a mixture of Form A and B. Each value is assigned a colour to easily observe which 2θ values are present each form of Li-PCDA. The values that do not correlate to the platelets, PCDA or any Li-PCDA form remain white.

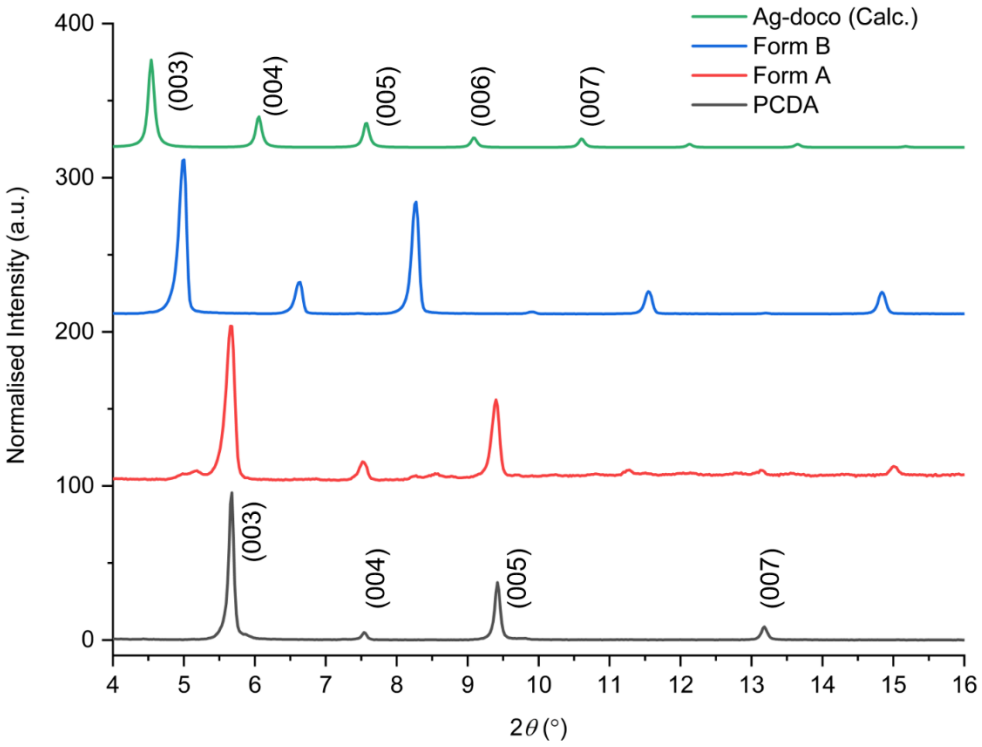

Figure 2.31. The calculated PXRD pattern of PCDA, the experimental patterns of Form A and Form B of Li-PCDA, compared to the calculated pattern of Ag-docosanoate (Ag-doco).[32, 33] As the peaks at 4.5 ° and 5.7 ° for Ag-doco and

PCDA, respectively, correspond to the (003) reflections it can be calculated that the peaks of 5.7 ° for Form A and 5.0 ° for Form B are also the (003) reflections.

The FTIR spectra of Form A and Form B of Li-PCDA reveal distinct features (Figure 2.32). For instance, the split asymmetric ($\nu(COO)_{asym,}$ 1581-1558 cm^{-1}) and symmetric ($\nu(COO)_{symm,}$ 1443-1412 cm^{-1}) carboxylate stretching bands. The bands are split due to the reduced carboxyl symmetry due to the coordination with the lithium ion.[32, 61] The carboxylate stretching bands reveal the type of coordination of the metal centre, evident by the difference in wavenumber of the asymmetric and symmetric stretching bands: $\Delta\nu = \nu(COO)_{asym} - \nu(COO)_{symm}$.[62, 63] For the Li-PCDA A and B forms, $\Delta\nu$ is 149 cm^{-1} (1581–1432 cm^{-1}) for Form A, and 134 cm^{-1} (1577–1443 cm^{-1}) for Form B and is calculated from the first asymmetric carboxylate stretching band minus the first symmetric carboxylate stretching band. As with the short-chain model lithium salts (page 82), the Δν values are greater than for chelating bonding and lower than the range for bridging coordination, and a combination of chelating bridging bidentate coordination of the carboxylate to the lithium ion is anticipated.[62, 67] X-ray structure determinations of lithium salts in the literature with short *n*-alkyl carboxylate chains display almost identical FTIR spectra to Li-PCDA, with $\Delta\nu$ values averaging 142 cm^{-1}.[61, 71-73] The lithium centres of long-chain carboxylates are also hypothesised to show asymmetric chelating bidentate bonding, which gives a tetrahedral environment of the lithium ion.[61, 71, 72] This lithium environment is also expected for the two Li-PCDA forms. Interestingly in the FTIR spectrum of Form B, a progression of evenly spaced methylene wagging bands are observed in the region of 1380-1100 cm^{-1}, indicating that all methylene groups crystallise in an all-*trans* conformation, similar to lithium pentanoate (Figure 2.33).[32, 61] However, Form A displays additional wagging bands of a reduced intensity when compared to Form B (for example the bands at 1277 cm^{-1} and 1269 cm^{-1}), suggesting *gauche* conformational features are present in the structure of Form A.[74] The CH_2 band with the greatest intensity is at 722 cm^{-1} and 723 cm^{-1} for Form A and Form B, respectively, and is representative of a methylene bending vibrational mode.[33, 61] This methylene band is related to the hydrocarbon chain packing and as a result, can determine the crystal system. For instance, a sharp peak without splitting (observed in Form B) is indicative of triclinic or hexagonal packing,[68] with triclinic being the most likely crystal system,[75, 76] which is in agreement with the $P\bar{1}$ space group of Ag-docosanoate

and long-chain lithium alkanoates.[33, 71] However, if the methylene band is split, as observed in Form A, that suggests a monoclinic or orthorhombic crystal system, such as the $P2_1/c$ space group of short-chain lithium alkanoates.[68, 71]

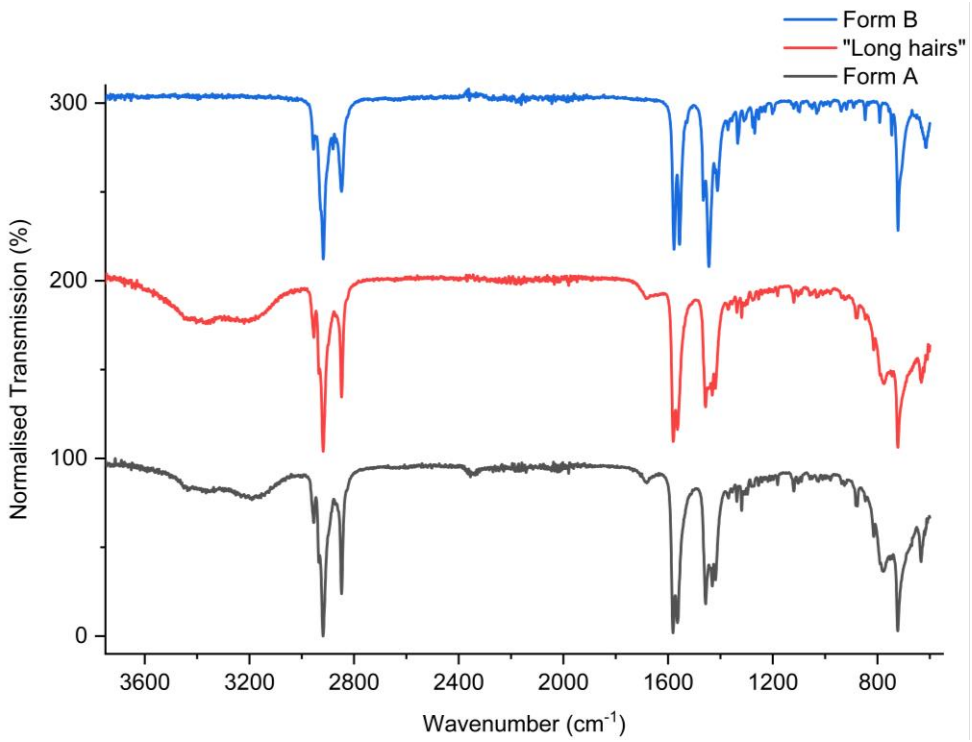

Figure 2.32. The FTIR spectra of PCDA and Form A, the “long hair” mixture, and Form B of Li-PCDA.

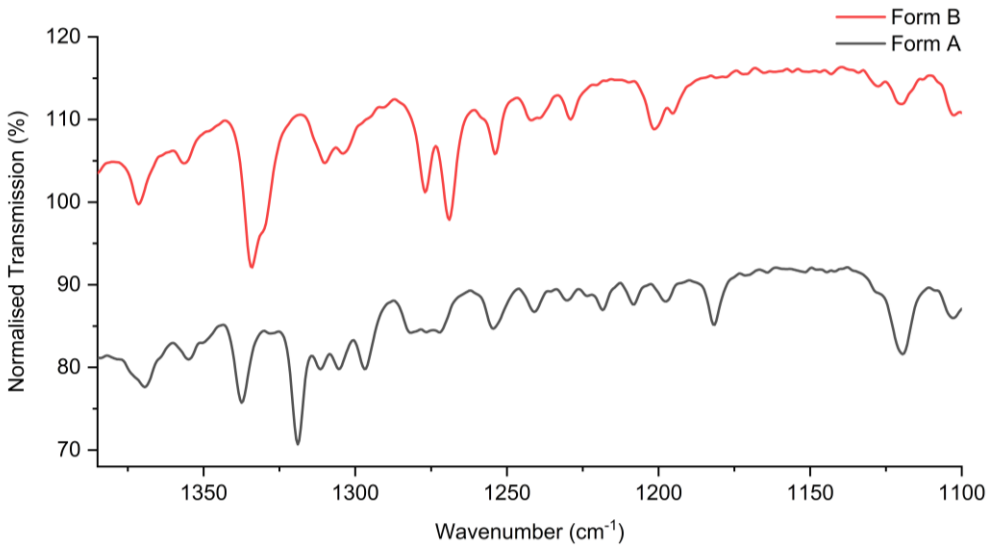

Figure 2.33. The FTIR spectra of Form A and Form B of Li-PCDA, displaying the methylene wagging bands in the region of 1380-1100 cm^{-1}.

The ssNMR spectra for Form A, “long hairs”, and Form B are shown in Figure 2.34. The main differences in the spectra of the forms is in the carboxylate region, implying some differences in the carboxylate coordination with the lithium ions (Figure 2.35). Form A has two carboxylate peaks at 183.7 ppm and 184.7 ppm, suggesting less symmetrical packing, while Form B has a single carboxylate peak at 187.3 ppm (almost identical to the model Li-PCDA compounds, page 84). These values are distinct from the two carboxylate carbon peaks of PCDA at 182.4 ppm and 181.9 ppm. Lithium alkanoates of 8-19 carbon atoms in length all have a single carboxylate peak at an average value of 183 ppm, suggesting that the lithium alkanoates have a similar coordination environment to Form B of Li-PCDA.[71] Also, the intense peaks in the ssNMR spectra of Form A and Form B at 33.8 ppm and 33.9 ppm, respectively, correspond to methylene group carbon atoms in similar environments. This is the same chemical shift of approximately 30 ppm observed for the long-chain lithium alkanoates.[71] Also, the terminal methyl carbon atoms of Forms A and B have a chemical shift of 15.3 ppm and 15.5 ppm, respectively, while the same carbon atoms for the lithium alkanoates resonate at 11.1 ppm.[71] Though the lithium alkanoates in the literature are helpful in the characterisation of the ssNMR spectra of the Li-PCDA forms, it is difficult to suggest differences between the structures of Form A and Form B by ssNMR spectroscopy alone.

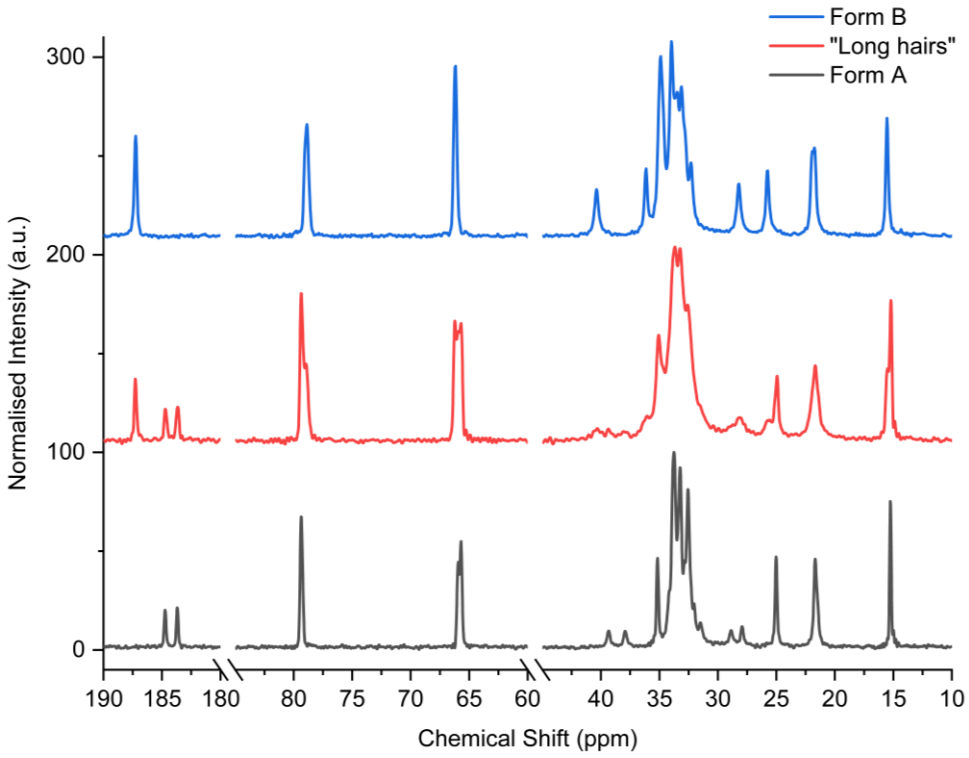

Figure 2.34. The ssNMR spectra of the different Li-PCDA forms. The carboxylate region is 180-190 ppm while alkyne and alkane peaks are shown in the 60-80 ppm and 10-40 ppm region, respectively. Added breaks in the *x*-axis are included to compact the spectra.

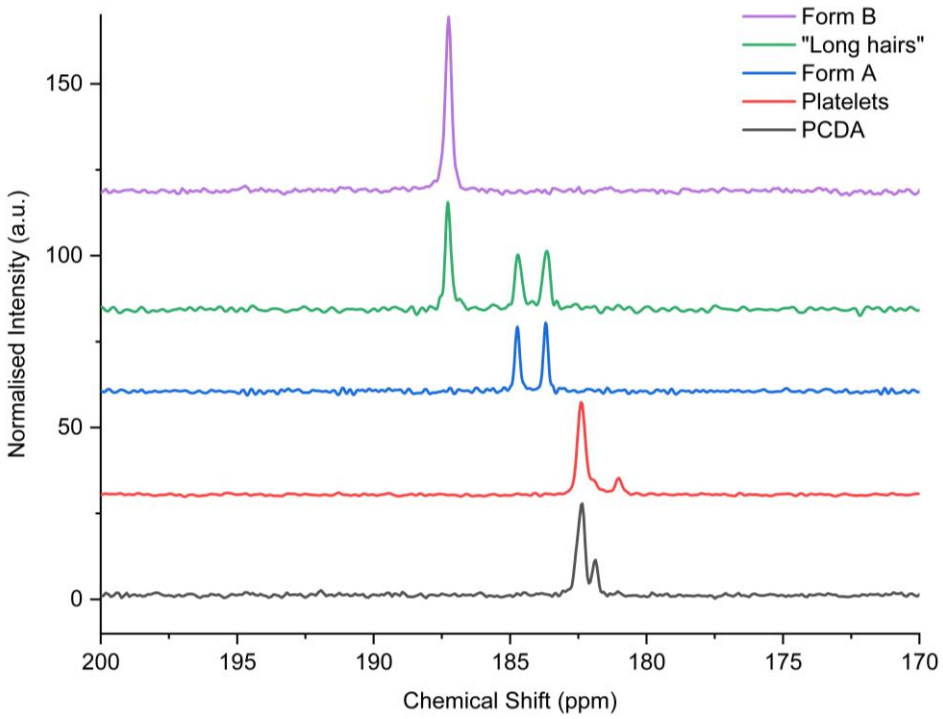

Figure 2.35. The ssNMR spectra of PCDA and the forms of Li-PCDA, focussing on the changes in the carboxylate region of the spectra (180-190 ppm).

The ssNMR data shows that the "short hairs" (Form A) and "long hairs" (Form A and B mixture) are exclusively monomeric, however, the Raman spectra (analysed by Dr Larry Senak at Ashland LLC) of the different Li-PCDA forms reveals bands assignable to polymeric material (Figure 2.36). Therefore, it is hypothesised that exposure to ambient light gives rise to very small amounts of photopolymer (ene-yne) bands that are greatly enhanced due to the pre-resonance Raman effect in the same way as PCDA itself, and is consistent with the faint blue colouration of the monomeric "short hairs" and "long hairs". The "short hairs" have a photopolymer band at 2062 cm^{-1}, while the "long hairs" have two photopolymer bands at 2062 cm^{-1} and 2096 cm^{-1}. Polymeric alkene bands are also present in the spectra for both samples at 1444 cm^{-1}. The enhanced intensity of the photopolymer bands results in the relative intensity decrease of other bands, such as the monomeric alkyne bands at 2260 cm^{-1}, the C-H stretching bands between 3000 and 2800 cm^{-1} and the and C-C bands between

515 and 355 cm^{-1}. The decreased intensity of these bands is particularly noticeable in the "long hair" sample, suggesting that the "long hair" sample has a greater polymer content. Therefore, the presence of only very small amounts of photopolymer gives rise to pre-resonance Raman enhanced bands which are consistent with the ssNMR findings.

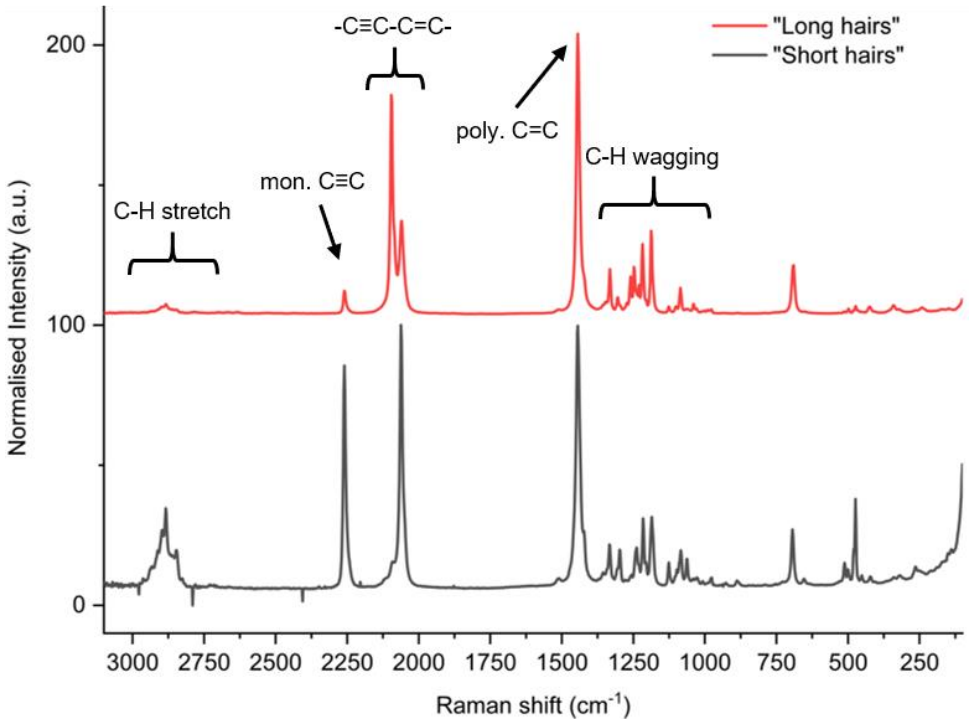

Figure 2.36. The Raman spectra of the "short hair" and the "long hair" samples of Li-PCDA.

The DSC thermograms of Form A and Form B were recorded by heating from room temperature to 200 °C, cooling back to room temperature, and heating again to 200 °C. Form A shows multiple broad endotherms in the first heating cycle (Figure 2.37). The first broad peak has an onset of 55.4 °C with two additional shoulders and is likely to be a dehydration endotherm. The second broad endothermic peak has an onset temperature of 99.7 °C, while the third broad endotherm has an onset temperature of 138.8 °C. Upon cooling to room temperature, multiple exothermic peaks are observed, with onset temperatures of 196.0 °C, 142.5 °C, 99.3 °C, and 58.2 °C. On the second heating cycle, three endothermic peaks are observed, with onset temperatures of 53.5 °C and 86.2 °C, with the broad peak from the first heat cycle with an onset temperature of 138.8 °C, splitting into two peaks with onset melt temperatures of 135.2 °C, and 152.5 °C. However, it is difficult to understand the endo- and exotherms

present in the thermogram, and therefore, additional work is required to investigate the thermal behaviour of Form A.

The DSC thermogram of Form B displays a single, sharp melt endotherm at 57.2 °C contrasting to the initial endotherm of Form A (Figure 2.38). A further two endotherms are present in the first heating cycle of Form B, with a broad endotherm at onset temperature of 93.5 °C, and a endotherm at 142.9 °C. The cooling cycle of Form B displays fewer exothermic peaks when compared to Form A, consisting of a broad peak with an onset temperature of 145.7 °C, and a peak at 102.6 °C. On the second heating cycle, Form B displays a very broad endotherm with an onset temperature of 79.6 °C, and two broad peaks with onset temperatures of 128.6 °C and 153.8 °C, similar to Form A. Therefore, the main difference between the two thermograms of the two forms is the presence of one or multiple peaks in the initial melt endotherm at temperatures between 55.4 and 57.2 °C. It is unclear whether the peaks observed in the DSC thermograms of both forms are phase transitions or arise from impurities. There is no evidence of liquid crystal behaviour in either of the forms, evident by heating the powdered samples on the hot stage microscope to temperatures up to 300 °C. The similarities and differences between the onset temperatures of each endothermic and exothermic peak in the DSC thermogram of Form A and Form B are summarised in Table 2.5. The DSC thermograms of long-chain lithium alkanoates display different phase sequences depending on the length of the chain. For instance, shorter alkyl chains of lithium alkanoates display solid-to-solid phase transitions, followed by a solid-to-liquid (melt) phase transition, and then decomposition, whereas lithium alkanoates with longer chains display the same sequence as the shorter chains, but with an additional solid-to-solid phase transition after the initial transition.[61, 71, 73, 77] For instance, lithium dodecanoate displays a metastable solid-solid transitions at onset temperature of 41.3 °C and 78.9 °C, and a melt at 227.4 °C,[73] with similar solid-solid transition temperatures observed in Form A and Form B. In addition, all lithium alkanoates have melting temperatures of greater than 224 °C,[71, 73] and when the “short hairs”, “long hairs”, and Form B were heated to heated to 350 °C, the resulting thermograms suggest a similar melting temperature, though the DSC experiments need to be repeated.

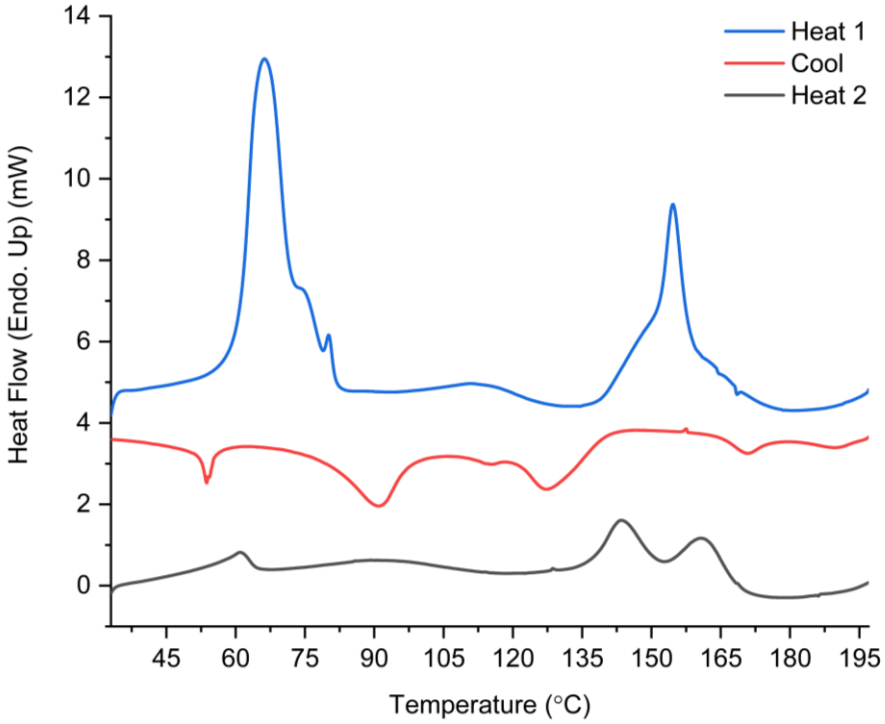

Figure 2.37. The DSC thermogram of a heat-cool-heat cycle of Form A from room temperature to 200 °C.

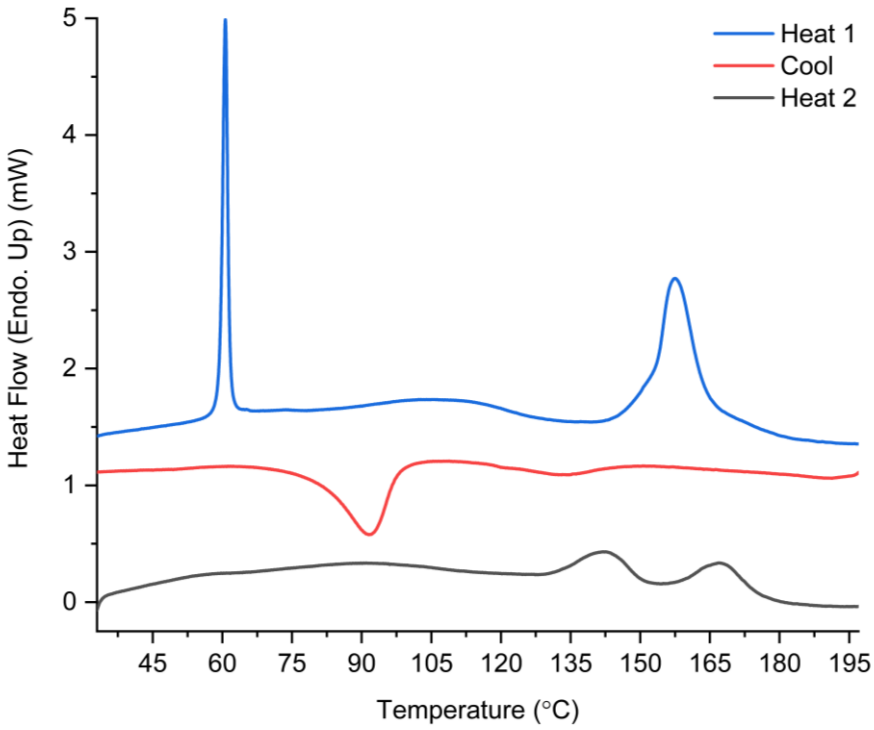

Figure 2.38. The DSC thermogram of a heat-cool-heat cycle of Form B from room temperature to 200 °C.

	Form A (°C)	Form B (°C)
Heat 1	55.4, 99.7, 138.8	57.2, 93.5, 142.9
Cool	**196.0**, 142.5, 99.3, **85.2**	145.7, 102.6
Heat 2	**53.5**, 86.2, 135.2, 152.5	79.6, 128.6, 153.8

Table 2.5. The onset temperatures for the endothermic and exothermic peaks of the DSC thermograms of Form A and Form B. The peaks that are present in Form A but not in Form B are highlighted in **red**.

Exposure of Li-PCDA to Vacuum

As the "short hairs" contain residual water, the powdered sample was placed under vacuum for different durations to remove the surface water. Exposing the "short hairs" to vacuum under ambient conditions for one hour did not change the form, however, exposure to vacuum for two hours gave a mixture of Form A and B, while vacuum for one day changed Form A to Form B. The change is evident by the differences in the low angle peaks in the PXRD patterns (Figure 2.39) that can be correlated to the different peaks for each form found in Table 2.4. Additionally, when the "long hairs" sample was exposed to vacuum for one hour and one day, the sample remained unchanged, though the relative intensity of the Form B peaks in the mixture compared to the Form A peaks was enhanced in the one day sample compared to the one hour sample (Figure 2.40). In addition to the PXRD analyses of the different Li-PCDA forms under vacuum, the FTIR analyses of the "short hairs" and "long hairs" exposed to vacuum for one day indicates the complete conversion to Form B for the "short hairs", and a partial conversion to Form B for the "long hairs". The partial conversion to Form B is evident by the band of low intensity at 1688 cm^{-1}, attributable to a water H-O-H bending mode and is present even after the removal of surface water shown by the flat baseline of in the FTIR spectra between 3000-3600 cm^{-1}. The remaining H-O-H bend may indicate that Form B contains crystalline water. Also, the ssNMR spectra further confirm the transformation of Form A into Form B after one day of vacuum exposure for the "short hairs" and the partial conversion for the "long hairs" (Figure 2.42). The full and partial conversion to Form B is easily observed in the carboxylate region of the ssNMR spectra. The presence of a single carboxylate peak for the "short hairs" exposed to vacuum for one day indicates the presence of Form B only, while the three carboxylate peaks of a mixture of Form A and B, with the Form A peaks of low intensity in relation to the Form B peak for the "long hairs" exposed

to vacuum for one day. As a result, it can be assumed that the “long hairs” require a longer duration under vacuum to change to the thermodynamic Form B. Thus, Form A is stabilised by the presence of residual moisture and dehydration of Form A results in a change to Form B, suggesting that Form A is, in fact, a hydrate.

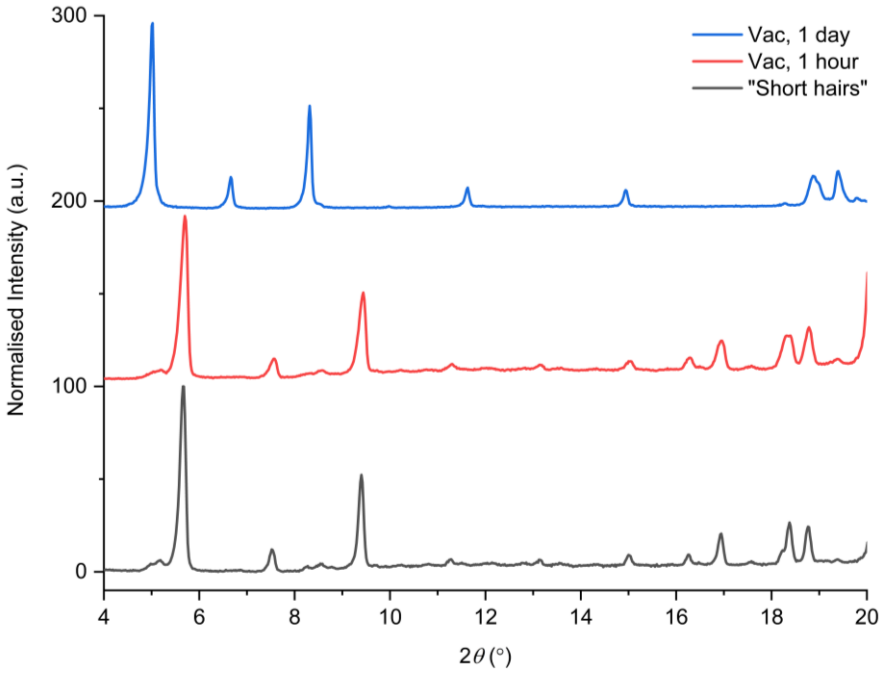

Figure 2.39. The PXRD patterns of the “short hairs” exposed to vacuum at room temperature. After one hour of vacuum exposure, no change is observed, however, Form A converts to Form B occurs after one day of exposure to vacuum.

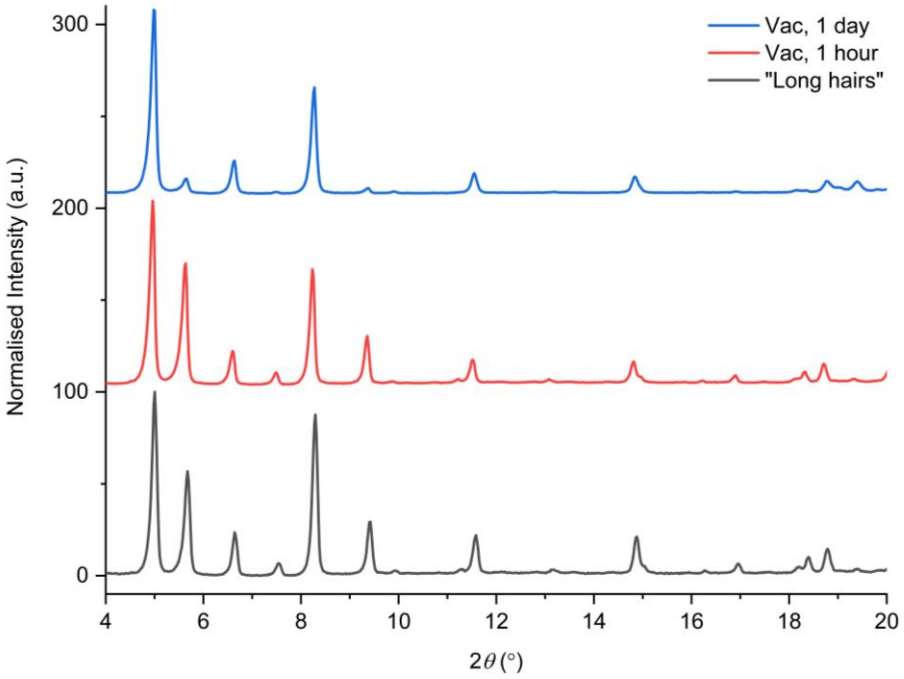

Figure 2.40. The PXRD patterns of the "long hairs" exposed to vacuum. After one hour of vacuum exposure, the sample remains unchanged as a mixture of Form A and B. Exposure to vacuum after one day resulted in a mixture of Form A and B though with the intensity of the Form A peaks reduced.

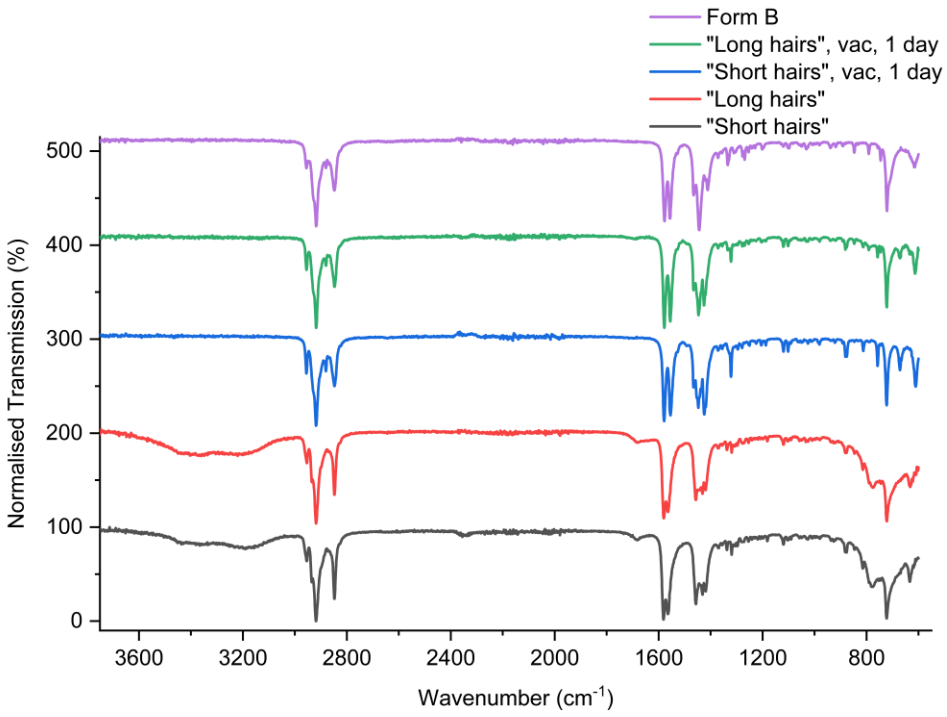

Figure 2.41. The FTIR spectra of the "short hairs" completely converting to Form B, while the "long hairs" partially convert to Form B after one day after exposure to vacuum at room temperature.

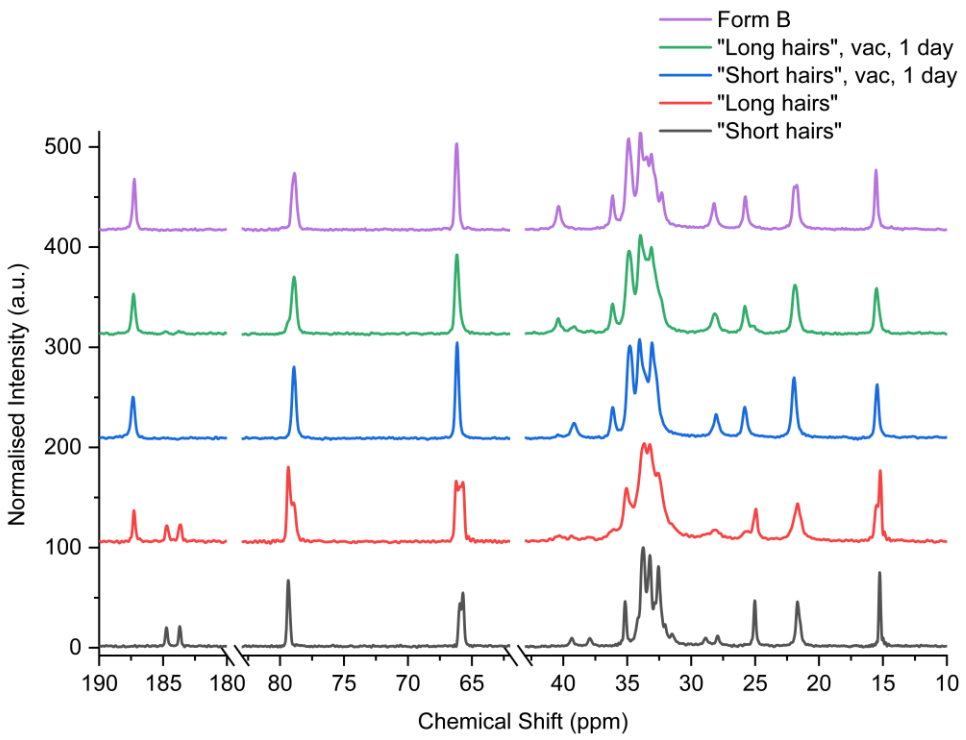

Figure 2.42. The ssNMR spectra of the "short hairs" completely converting to Form B, while the "long hairs" partially convert to Form B after one day after exposure to vacuum at room temperature. The carboxylate region is 180-190 ppm while alkyne and alkane peaks are shown in the 60-80 ppm and 10-40 ppm region, respectively. The *x*-axis has added breaks to compact the spectra.

To further investigate hydrated Form A, the "short hair" sample was analysed by Thermogravimetric Analysis (TGA). The thermogram reveals the removal of surface water between temperatures of 25 °C and 55 °C (Figure 2.43), with a further distinct weight loss step between 56 °C and 66 °C, until the weight loss plateaus up to the decomposition temperature of Form A at an onset temperature of 311.5 °C. The TGA thermogram was repeated with the "short hairs" pressed on a filter paper in an attempt to remove excess surface water from the powder, and the small, distinct weight loss step persisted, now occurring between 75 °C and 84 °C. A monohydrate of Li-PCDA equates to 4.5 % water content (18 g/mol ÷ ($C_{25}H_{41}O_2Li \cdot H_2O$) 398.51 g/mol). For the "short hairs" with excess water, the thermogram reveals surface water is 73.4 % to leave 26.6 % of material, and the small bump in the thermogram tentatively assigned to crystalline hydrate dehydration in the region of 56 °C to 66 °C equates to 1.5 %. 1.5 % ÷ 26.6 % = 5.6 % of crystalline water. Once the "short hairs" were pressed on filter paper, a significant amount of surface water was removed, and the same

calculation as above (initial weight loss of 27.0 % to leave 73.0 % of remaining material with the small weight loss in the thermogram around 74 °C equating to 3.7 %. 3.7 % ÷ 73.0 % = 5.1 % reveals 5.1 % of crystalline water, which is consistent with the water sample and close to the value of 4.5 % of water in Li-PCDA for a monohydrate. Therefore, the reproducible results suggest that Form A is monohydrated. Further experimental work to attempt to get a dry sample of Form A involved washing the "short hairs" in methanol for five minutes under vacuum filtration and leaving the powder to air dry. Exposure of the "short hairs" to vacuum for five minutes was not long enough to convert the forms, as observed by the vacuum studies mentioned previously. The resulting PXRD (Figure 2.44) and TGA of the sample washed in methanol (Figure 2.43) shows the majority of Form A converts to Form B, suggesting that the dehydration of Form A results in the change. The hydrate hypothesis is also supported by the ssNMR of the two forms, as the two peaks are observed in the carboxylate region of the spectra, with only one carboxylate peak for Form B, suggesting a less symmetrical carboxylate environment in Form A possibly correlating to water coordination to the metal ion. The single carboxylate peak observed in Form B is consistent with the anhydrous lithium carboxylates in the literature.[32, 71] Therefore, this suggests that Form A is hydrated, and dehydration of Form A by exposure to vacuum for over two hours or by heating to temperatures above 80 °C for one hour, results in anhydrous Form B. This finding is also supported by the dehydration endotherm observed in the DSC thermogram of the "short hairs".

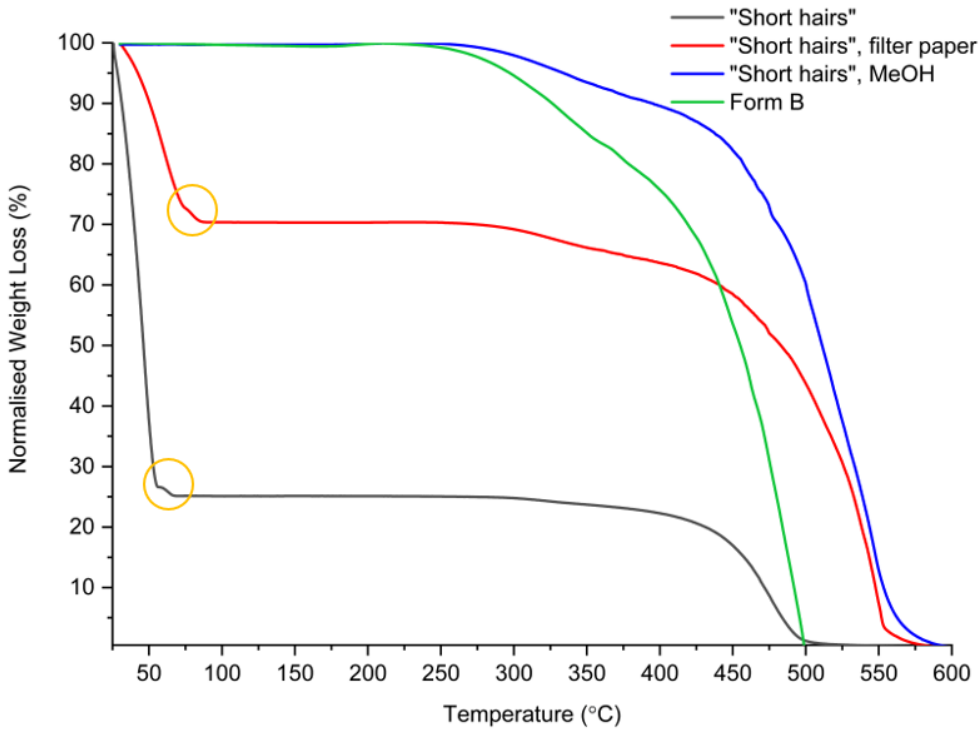

Figure 2.43. The TGA of the "short hairs" as received from Ashland, pressed on filter paper, and washed in methanol (MeOH), and Form B of Li-PCDA. The yellow circles highlight the crystal dehydration features of the "short hairs".

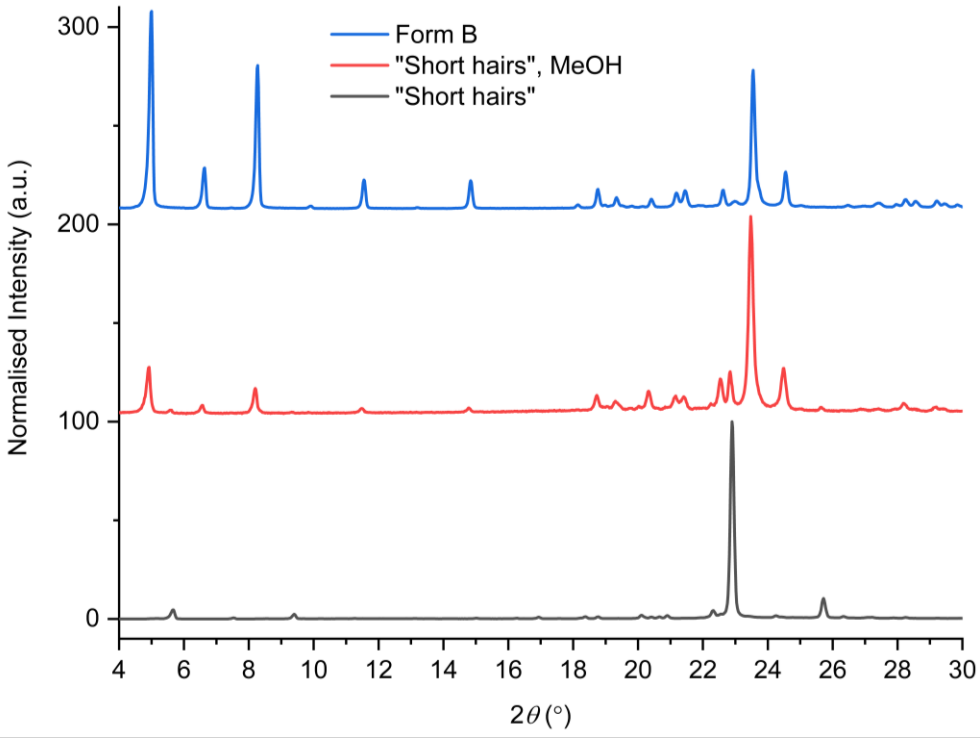

Figure 2.44. The PXRD of the "short hairs" washed in methanol (MeOH) compared to the "short hairs" and Form B.

Li-PCDA Synthesis

As the different morphologies ("short hairs"/Form A and "long hairs"/Form A and B) of Li-PCDA were supplied by Ashland LLC, the synthesis of Li-PCDA was repeated in-house to investigate whether a route to Forms A and B was possible, without the use of the "long hairs" mixture and whether Form B could be modified into a more easily processable short needle-like or block morphology. The synthesis of the salt was also undertaken to investigate whether the different Li-PCDA forms could be recreated by following the preparation outlined by Ashland. Ashland's method to synthesise the salt can be separated into stages:

> Stage 1 – Combine PCDA, lithium hydroxide monohydrate, sodium hydroxide, tetraethylammonium hydroxide, and water into a vial.
>
> Stage 2 – Stir the formulation and sonicate in a water bath at 60 °C until the colour of the suspension changes from blue to pink (approximately 30 minutes).
>
> Stage 3 – Add a seed of Form A to the suspension and place the formulation in the oven for four hours at 65 °C to Ostwald ripen, ultimately producing an entangled hair-like particle morphology. Ashland term this material "long hairs".
>
> Stage 4 – Sonicate the fibres in a cold-water bath (for approximately five minutes) to give a particle morphology that is significantly shorter in length (Ashland's "short hairs"). Further ripen the sample in the oven for four hours at 65 °C to ensure that platelet morphology has converted to "short hairs".

To monitor the nature of the product at each stage when synthesising the Li-PCDA forms, PXRD and FTIR analyses of each stage were performed. Stage 1 involves the combination of reagents before any heat or sonication and displays a pattern indicative of unreacted PCDA although an additional small peak at 4.9 ° suggests the presence of some Form B (Figure 2.45). At Stage 2 where the mixture is sonicated and heated to 60 °C, the peaks present in the initial platelet morphology pattern are replaced with Form A, along with additional peaks that correspond to Form B (4.9, 5.7, 5.9, 6.6, 7.5, 8.3, 9.4 °). The products of Stages 3 and 4 display almost identical PXRD patterns with peaks corresponding only to Form B (5.0, 6.6, 8.3, 9.9 °). The lack of Form A further reinforces that it is a metastable form that is readily dehydrated, while Form B

is the thermodynamically stable form in the absence of moisture. Therefore, PXRD analysis reveals that recreating Ashland's procedure gives rise to a clean route to Form B. As a result, Form A may only be obtained using a more powerful sonicator; Ashland use a Sonics (VC505) 500 Watt ultrasonic processor with a 13 mm probe, whereas the sonicator used to obtain the Li-PCDA forms in this instance is a VWR ultrasound cleaning bath (USC500TH) with a maximum power output of only 100 Watts without the presence of an ultrasonic probe. This suggests that the ultrasound bath is not powerful enough to give Form A.

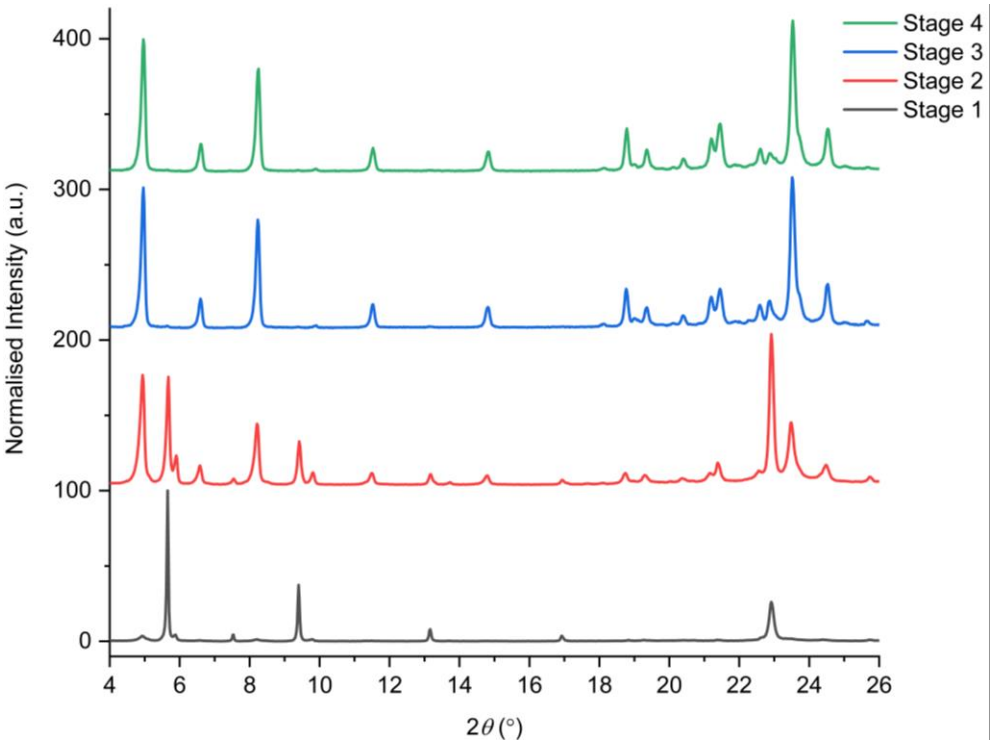

Figure 2.45. The PXRD patterns of the product at different stages of the preparation of Li-PCDA, following the procedure outlined by Ashland.

The FTIR spectra of the Li-PCDA synthesis stages also reflect the results of the PXRD analysis. For instance, the spectrum of Stage 1 mostly resembles that of PCDA with a C=O stretch at 1691 cm^{-1}, however, the presence of some low intensity COO^- asymmetric and symmetric bands ranging between 1577-1412 cm^{-1} indicates that some lithium salt is beginning to form before any mixing or sonication of the formulation (Figure 2.46). The FTIR data for the Stage 2 product shows that much of the free acid has reacted and the material appears to be a mixture of free PCDA and Forms A and B of Li-PCDA, evident by the increased intensity of the COO^-

asymmetric and symmetric stretches ranging between 1577-1412 cm^{-1}. The spectra for the Stage 3 and Stage 4 products are consistent solely with Form B Li-PCDA.

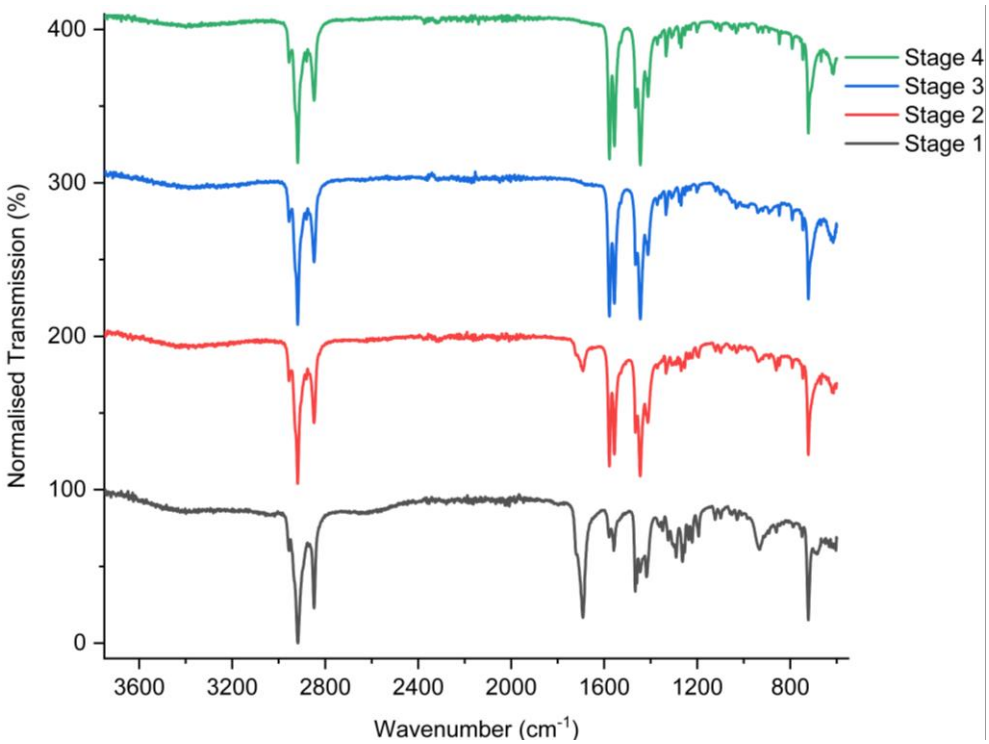

Figure 2.46. The FTIR spectra of the different stages of the Li-PCDA forms, following the procedure outlined by Ashland.

In addition to the synthesis of Li-PCDA by Ashland's procedure, Li-PCDA was synthesised using only $LiOH{\cdot}H_2O$ and PCDA. The reagents were combined in a 1:1 ratio with acetone and sonicated for 15 minutes. Excess solvent was left to slowly evaporate under ambient conditions. Initial PXRD analysis demonstrated that the synthesised Li-PCDA was a mixture of Form A and B (Figure 2.47). This observation is also supported by FITR analysis, though with the presence of residual PCDA indicated by the by the free acid carbonyl band at 1691 cm^{-1} (Figure 2.48). Heating the powdered sample for one hour and 30 minutes at 100 °C converted the mixture of forms to Form B only, confirmed by PXRD analysis. This procedure resulted in crystals potentially suitable for single-crystal X-ray structure determination, however, after data collection attempts using MoKα radiation (D8 Venture) and at the high-intensity synchrotron beam at Diamond (I19 instrument), no structure determination was possible due to the poor quality of the crystals.

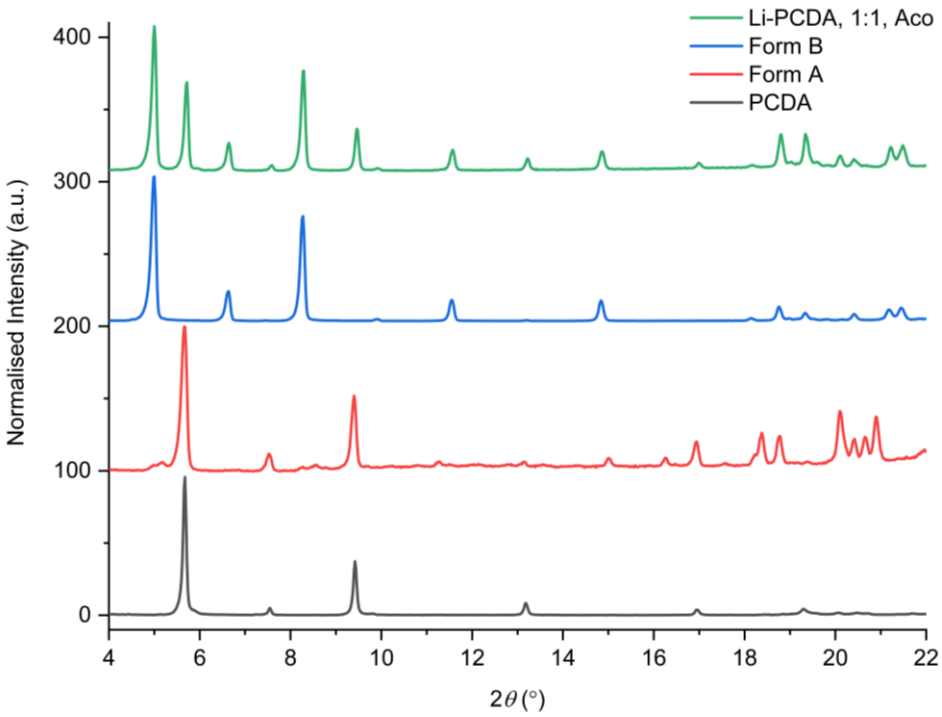

Figure 2.47. The PXRD pattern of Li-PCDA prepared in acetone (Aco) using $LiOH \cdot H_2O$ (1:1 ratio with PCDA) compared to the patterns of PCDA, Form A and Form B of Li-PCDA.

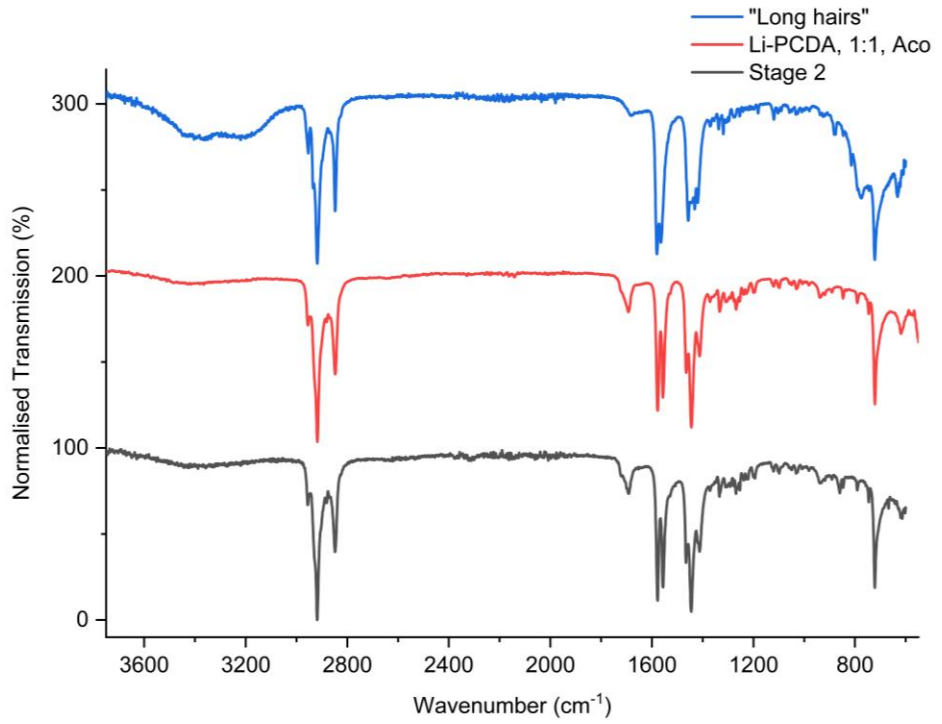

Figure 2.48. The FTIR spectrum of Stage 2 of Li-PCDA following Ashland's procedure and synthesised Li-PCDA in a 1:1 ratio of lithium hydroxide monohydrate and PCDA, compared to the spectrum of the "long hairs" supplied by Ashland.

The synthesis of Li-PCDA was also attempted by mechanochemical methods. $LiOH{\cdot}H_2O$ was combined with PCDA in 1:1, 1:2, and 1:3 ratios, respectively, and placed in a ball mill for 45 minutes at a frequency of 20 s^{-1}. However, the PXRD (Figure 2.49) and FTIR (Figure 2.50) analysis of the ball-milled product reveal that the reaction had not occurred. However, Li-PCDA 1:1 displays asymmetric COO^- bands of low intensity at 1581 cm^{-1} and 1559 cm^{-1}, while ratios 1:2 and 1:3 do not. The emergence of COO^- bands indicates the presence of a small amount of Li-PCDA formation in the equimolar ratio sample of PCDA and LiOH. Therefore, the mechanochemical synthesis experiments are less effective than solution-based methods at synthesising Li-PCDA.

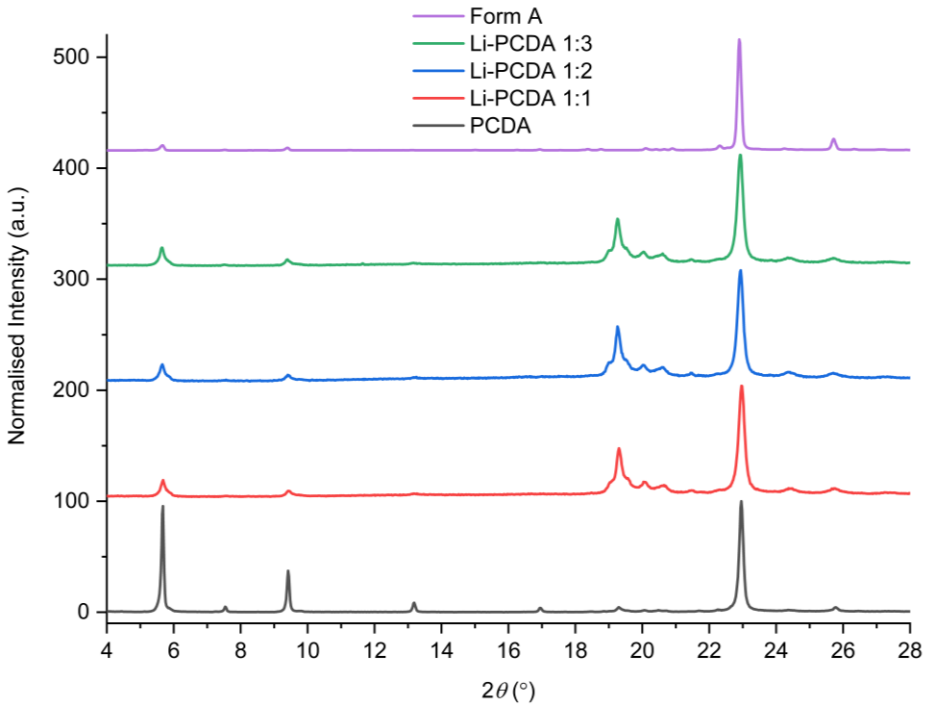

Figure 2.49. The PXRD patterns of $LiOH{\cdot}H_2O$ and PCDA mixed in a ball mill for 45 minutes in varying ratios. The patterns of PCDA and Form A of Li-PCDA are displayed for comparative purposes, however, the difference between the patterns are difficult to distinguish at low angles.

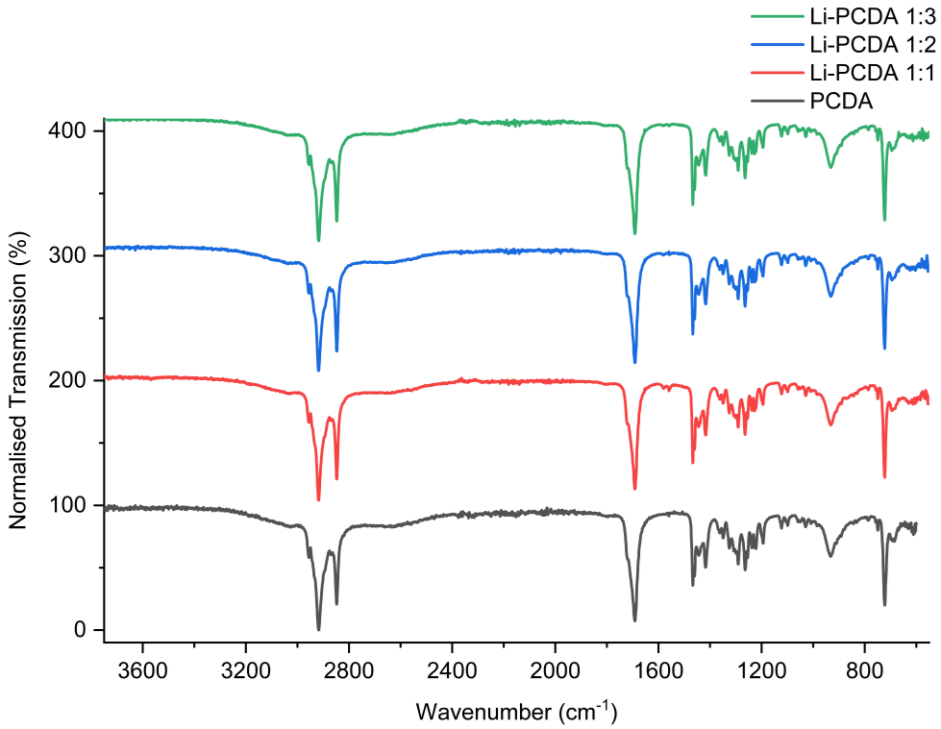

Figure 2.50. The FTIR spectra of $LiOH{\cdot}H_2O$ and PCDA combined in a ball mill in varying ratios for 45 minutes. The resulting spectra reveal that the ball-milled material are identical to PCDA, apart from Li-PCDA 1:1 which displays asymmetric stretches of low intensity.

Li-PCDA Photoreactivity

Powders

While the X-ray structures of both solid forms of Li-PCDA are unknown, its use in commercial radiochromic films suggests that the salt must conform to the topochemical postulate. While both forms are indeed photoactive, it is the "short hair" material that is composed of solely Form A of Li-PCDA that is currently used in Gafchromic EBT3 films, due to its improved coatability compared to the "long hair" morphology of Li-PCDA. The "long hairs" are a mixture of Form A and Form B but experience at Ashland suggests that this material is more photosensitive than the short hair alternative. As a result, there is likely to be a difference in radiation sensitivity between the two forms. Both the "short hair" and "long hair" morphologies were irradiated with X-ray radiation, ranging between 1 Gy and 100 Gy. The radiation sensitivity between the two forms is not easily observed by PXRD analysis. Only subtle changes are observed when the "short hairs" (Figure 2.51) and "long hairs" (Figure 2.52) are irradiated with varying doses of X-ray radiation. However, it appears

this batch of “short hairs” is contaminated with Form B by the presence of the peaks at 5.0, 6.6, and 8.3 °. Additionally, no distinct photopolymer peaks are observed which suggests the lack of polymer formation, or that the polymer is amorphous. The subsequent broadening of the monomer peaks suggests the crystallinity of the monomer is reduced, possibly by the formation of small amounts of polymer in the monomer lattice.

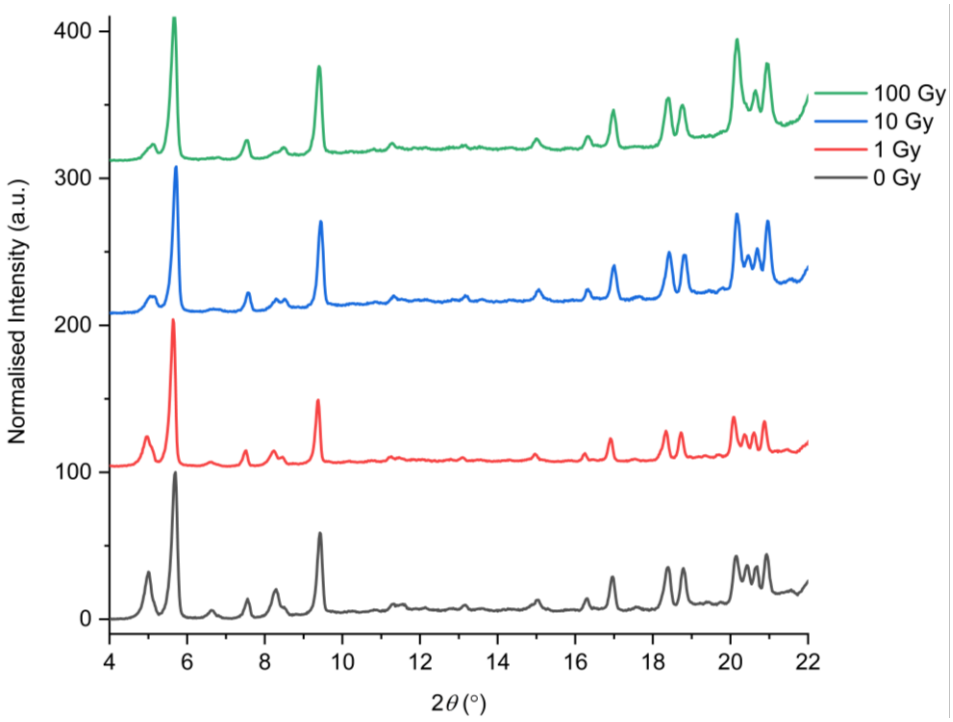

Figure 2.51. The PXRD patterns of Form A (contaminated with Form B) exposed to increasing doses of X-ray radiation.

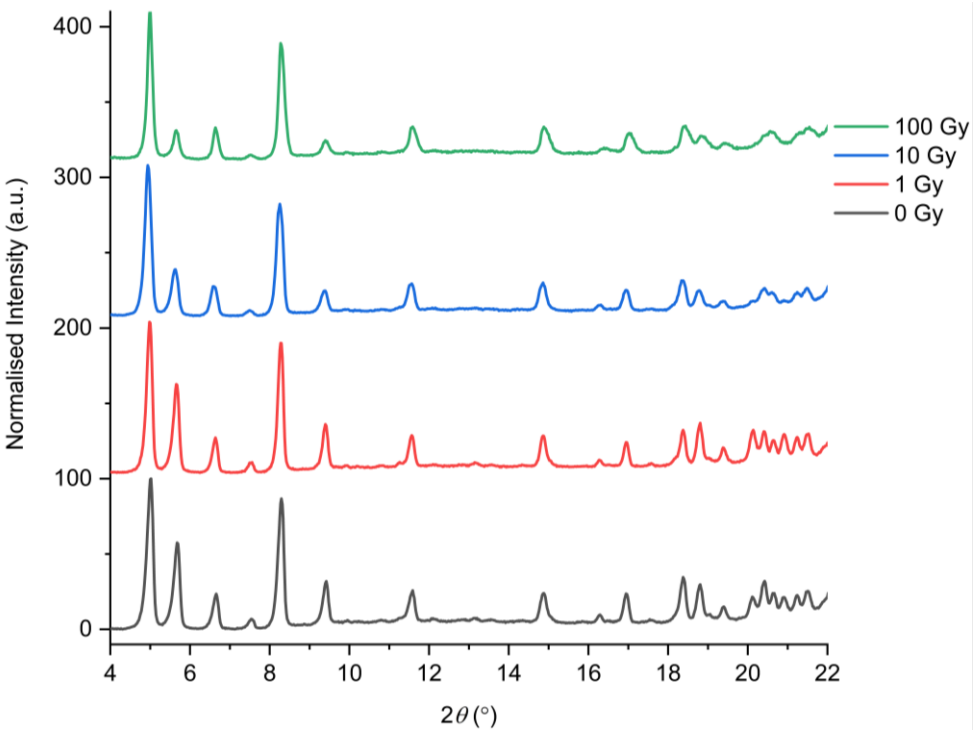

Figure 2.52. The PXRD patterns of the "long hair" morphology exposed to increasing doses of X-ray radiation.

The FTIR analyses of the two types of material exposed to increasing doses of X-ray radiation show no changes in for the "short hair" (Figure 2.55) or the "long hair" (Figure 2.56) samples. Therefore, FTIR is not a sensitive technique for the identification of polymerised material. However, ssNMR analyses are more useful for detecting the presence of photopolymer. For instance, specific alkene peaks are expected in the region of 100-135 ppm, as a result of the formation of an alternating ene-yne backbone in response to radiation. Alkene peaks of low intensity were observed in the spectra of both the "short hair" and "long hair" samples prepared by Ashland after 100 Gy of X-ray radiation, at 107.3 ppm and 130.5 ppm. However, ≤15 % of monomer to polymer conversion was observed for the "short hairs" by the integration of the relative alkyne and alkene peaks, while the "long hairs" gave a total conversion of ≤20 %, suggesting the "long hairs" are more sensitive to radiation. It is also important to note that the samples were not mixed while being irradiated, therefore, polymer builds up on the outside of the sample with the majority of the bulk remaining as unreacted monomer. Thus, the amount of photoconversion can be increased if the sample is equally exposed to X-rays.

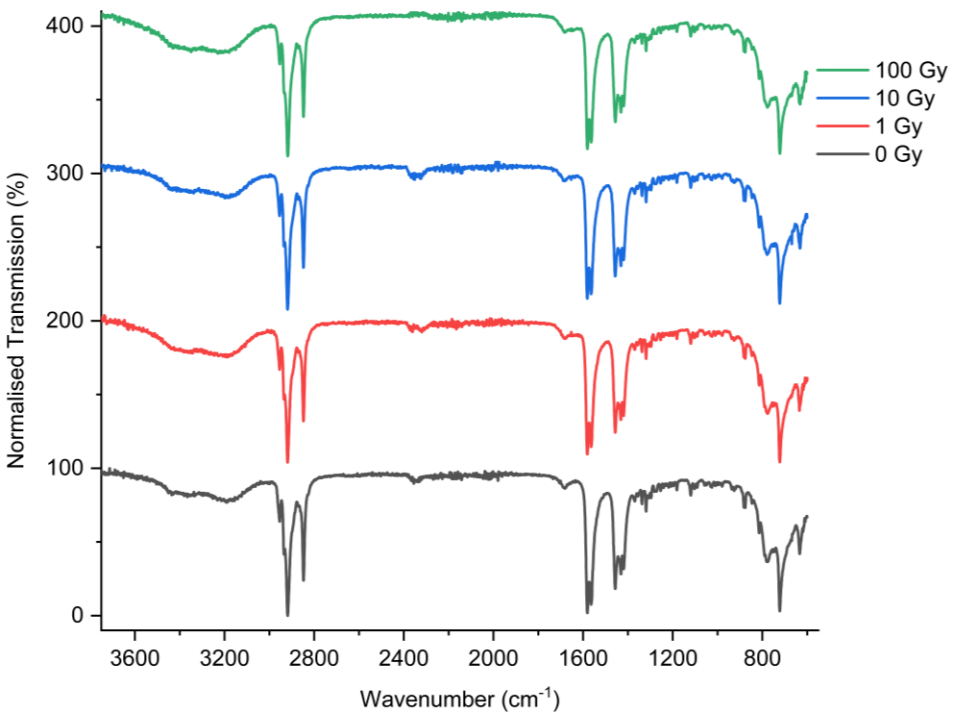

Figure 2.53. The FTIR spectra of the "short hairs" exposed to increasing doses of X-ray radiation.

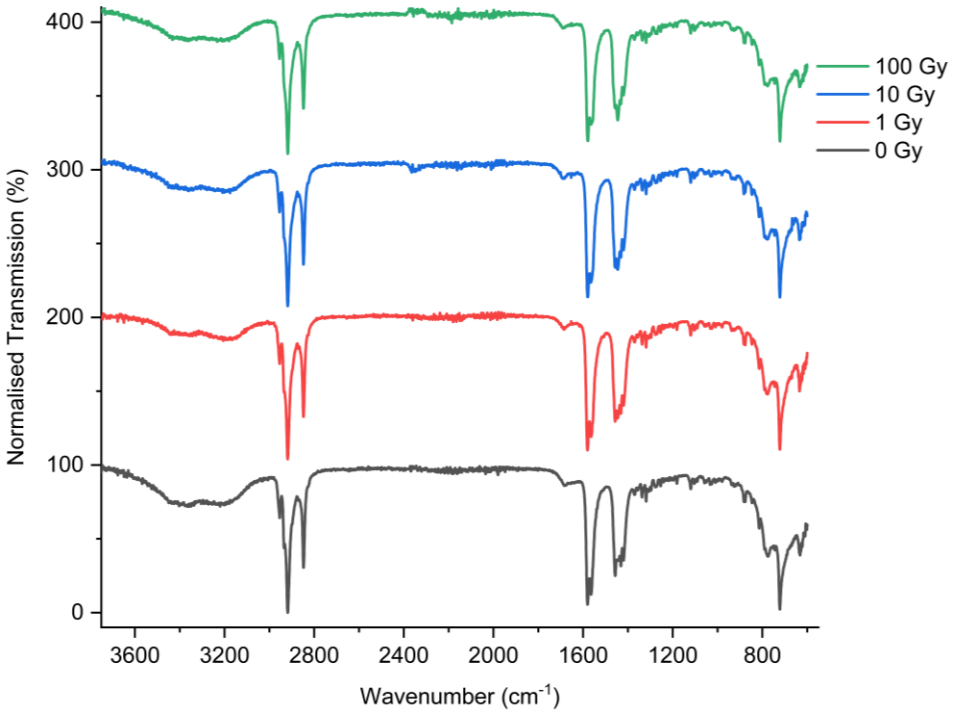

Figure 2.54. The FTIR spectra of the "long hairs" exposed to increasing doses of X-ray radiation.

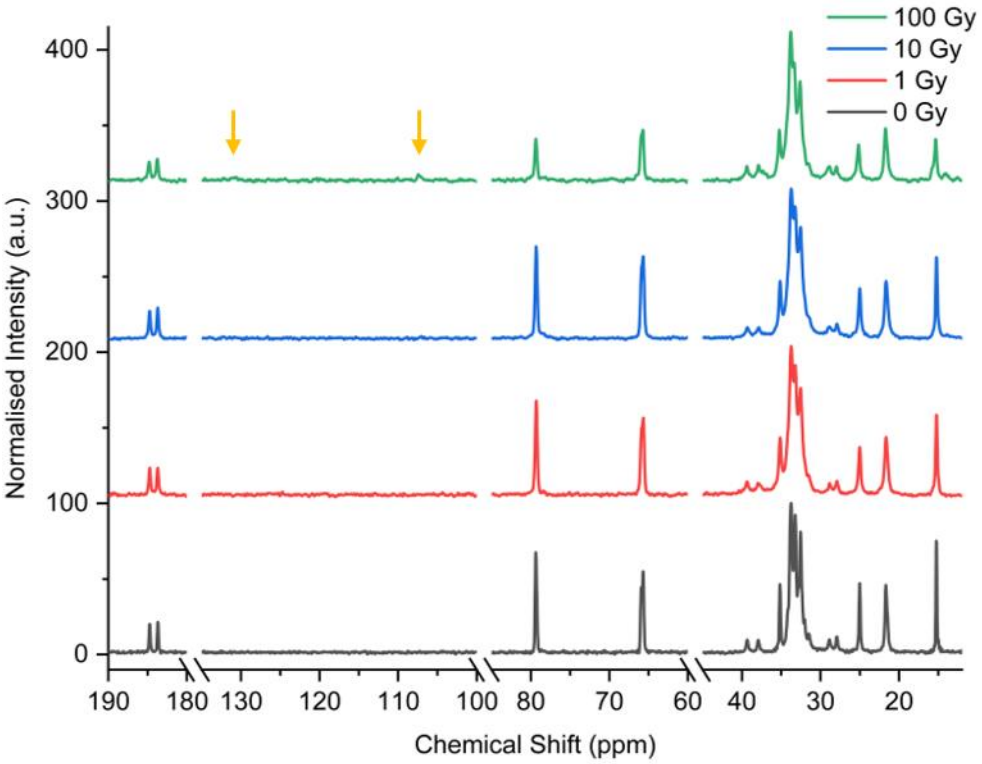

Figure 2.55. The ssNMR spectra of the "short hair" sample (Form A Li-PCDA) exposed to increasing doses of X-ray radiation. The carboxylate region is 180-190 ppm while any alkene peaks will occur in the 100-130 ppm region (highlighted by the yellow arrows in the 100 Gy spectrum). Alkyne and alkane peaks are shown in the 60-80 ppm and 10-40 ppm region, respectively. The *x*-axis has added breaks to make the spectra compact.

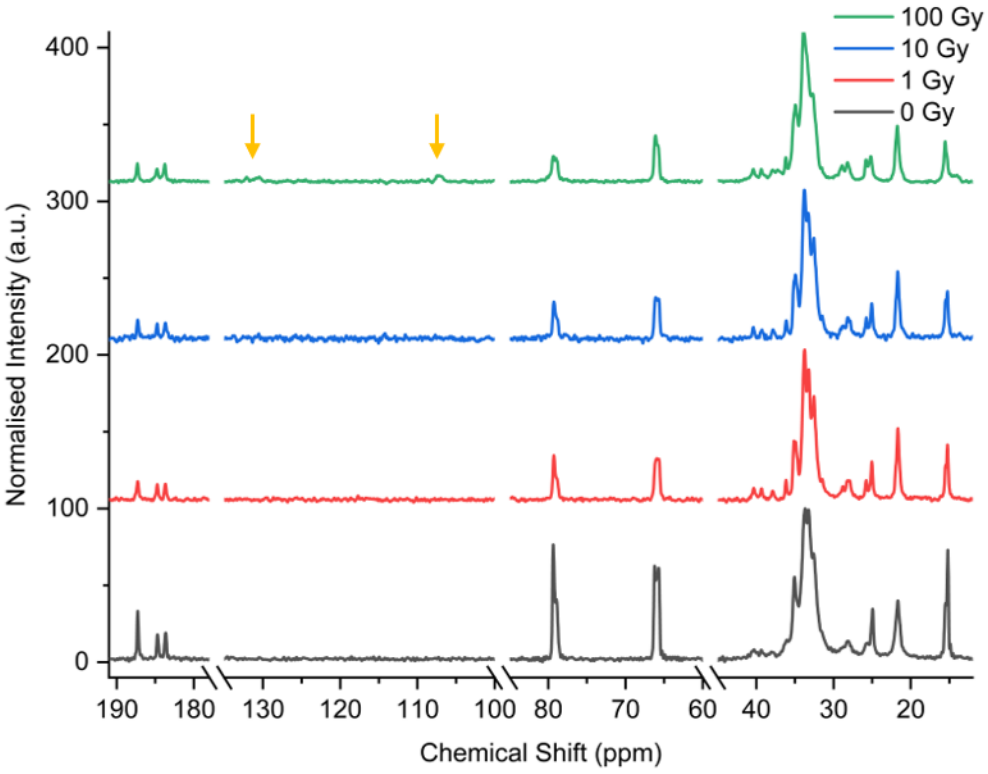

Figure 2.56. The ssNMR spectra of the "long hair" sample (a mixture of Form A and B Li-PCDA) exposed to increasing doses of X-ray radiation. The carboxylate region is 180-190 ppm while any alkene peaks will be displayed in the 100-130 ppm region (highlighted by the yellow arrows in the 100 Gy spectrum). Alkyne and alkane peaks are shown in the 60-80 ppm and 10-40 ppm region, respectively. The *x*-axis has added breaks to make the spectra compact.

The Raman spectra of the Li-PCDA "short hair" and "long hair" samples were measured by Dr Larry Senak at Ashland LLC. As mentioned on page 93, samples of Li-PCDA before radiation exposure display photopolymer bands in the Raman spectra. These bands arise due to the presence of trace quantities of photopolymer with chromophore bands markedly enhanced in intensity as a result of a pre-resonance Raman effect. Unfortunately, the "short hairs" were not exposed to 100 Gy of X-ray radiation, however, the "long hairs" before irradiation display two photopolymer bands at 2066 cm^{-1} and 2094 cm^{-1}, with the latter band present in the spectrum of the unirradiated "short hairs" (Figure 2.57). After the "long hairs" are exposed to X-ray radiation, the photopolymer band becomes a single band with a Raman band at 2066 cm^{-1} and is therefore red-shifted. As expected, the monomeric alkyne band at

2260 cm^{-1} is also no longer present in the spectrum upon irradiation, while the alkene band at 1444 cm^{-1} remains in the spectrum of the irradiated “long hairs”.

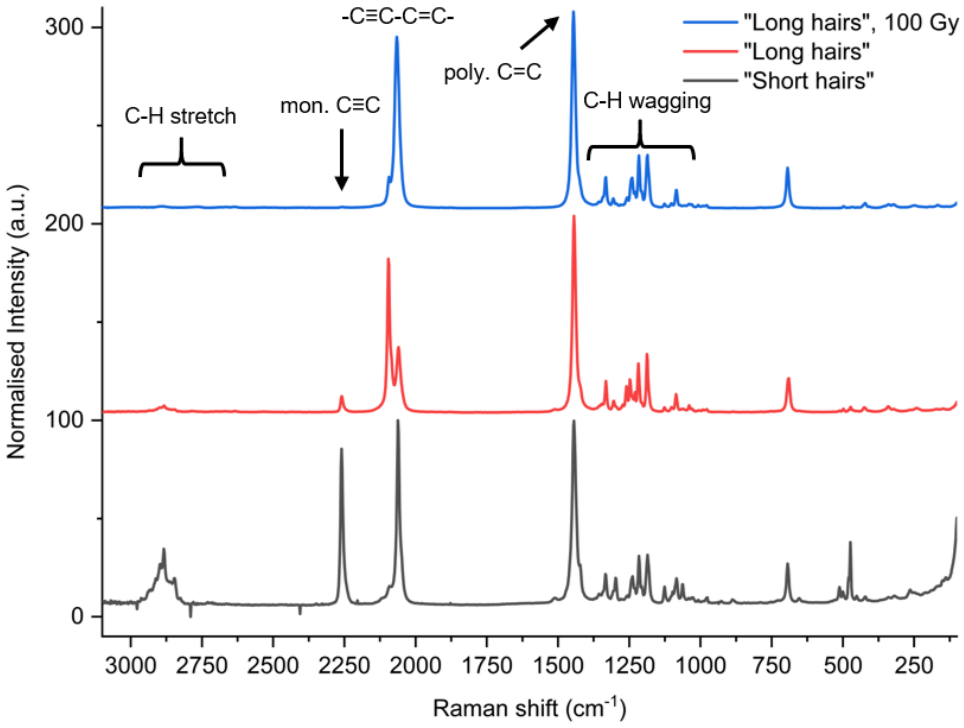

Figure 2.57. The Raman spectra of the “short hairs” (Form A) before X-ray irradiation, and the “long hairs” (a mixture of Form A and B) before and after 100 Gy of X-ray radiation.

In addition to X-ray radiation, the powdered samples were also exposed to UV radiation. Powdered samples of the “short hair” and the “long hair” samples were placed on a watch glass and exposed to 254 nm of UV radiation for one day investigate their photoreactivity (Figure 2.58). The ssNMR spectra of the “short hair” and “long hair” samples irradiated with UV for one day (Figure 2.59) reveal peaks in the alkene region (at chemical shifts of 107.0 ppm and 130.8 ppm). Surprisingly, the alkene peaks of the “short hairs” are of a greater intensity when compared to the “long hairs”, revealing a monomer to polymer conversion of ≤27 % and ≤11 %, respectively. This unexpected result can be attributed to the number of times the samples were mixed. The “short hairs” were mixed frequently with one day of irradiation, while the “long hairs” were only mixed once. Therefore, UV radiation was not exposed to the bulk of the sample which resulted in the amount of photopolymer that is not representative of the “long hairs” sample. The irradiation of the “long hairs” is planned to be repeated in the future.

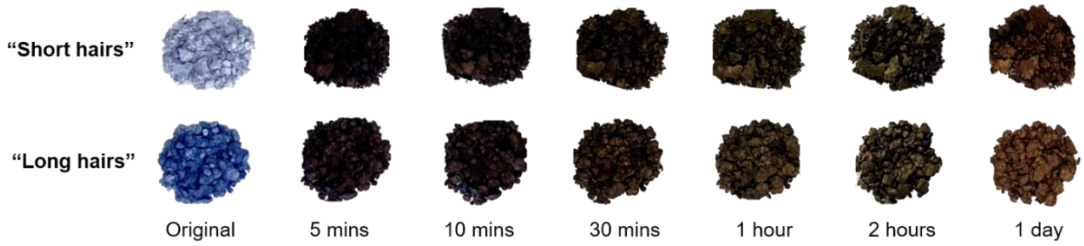

Figure 2.58. Photographs of irradiated "short hairs" and "long hairs" at different durations of UV radiation (254 nm) and reveal a darkening of the sample, proportional to the duration of irradiation.

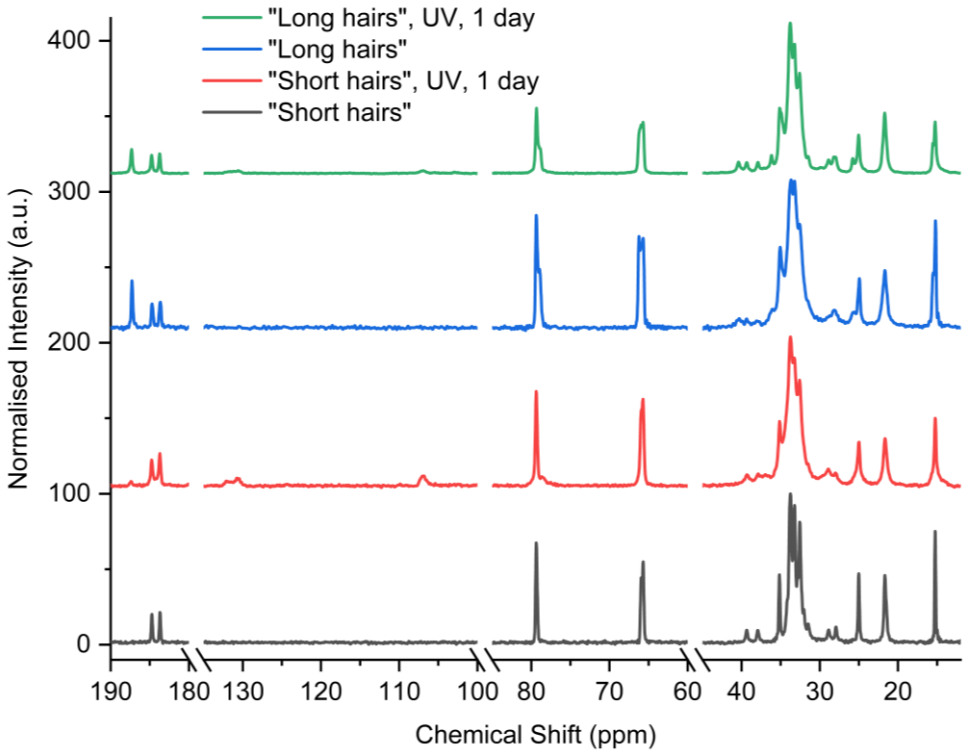

Figure 2.59. The ssNMR of the "short hairs" and "long hairs" irradiated with UV for one day. The carboxylate region is 180-190 ppm while any alkene peaks will be displayed in the 100-130 ppm region. Alkyne and alkane peaks are shown in the 60-80 ppm and 10-40 ppm region, respectively. The *x*-axis has added breaks to make the spectra compact.

Radiochromic films

In addition to the irradiation Li-PCDA, the Gafchromic EBT3 films that contain the "short hairs" (Form A) were also exposed to radiation and heat. The films change colour depending on how much radiation they are exposed to. The films are initially yellow and change to almost black after 100 Gy of X-ray radiation (Figure 2.60). The

PXRD pattern of the films both before and after irradiation show low-angle peaks at 5.7 ° and 9.4 ° that are indicative of the presence of monohydrated Form A Li-PCDA. However, when the films are heated to 80 °C for one day, the dehydration of the film shows the transformation of Form B with peaks at 5.0 ° and 8.3 ° (Figure 2.61). Therefore, the formulated Li-PCDA within the films behaves in the same way as the isolated powder.

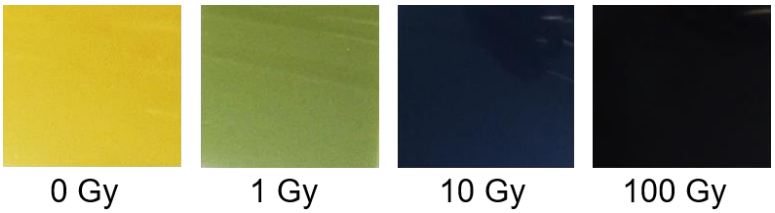

Figure 2.60. Photographs of Gafchromic EBT3 films that have been irradiated with increasing doses of X-rays, ranging from 1 Gy to 100 Gy.

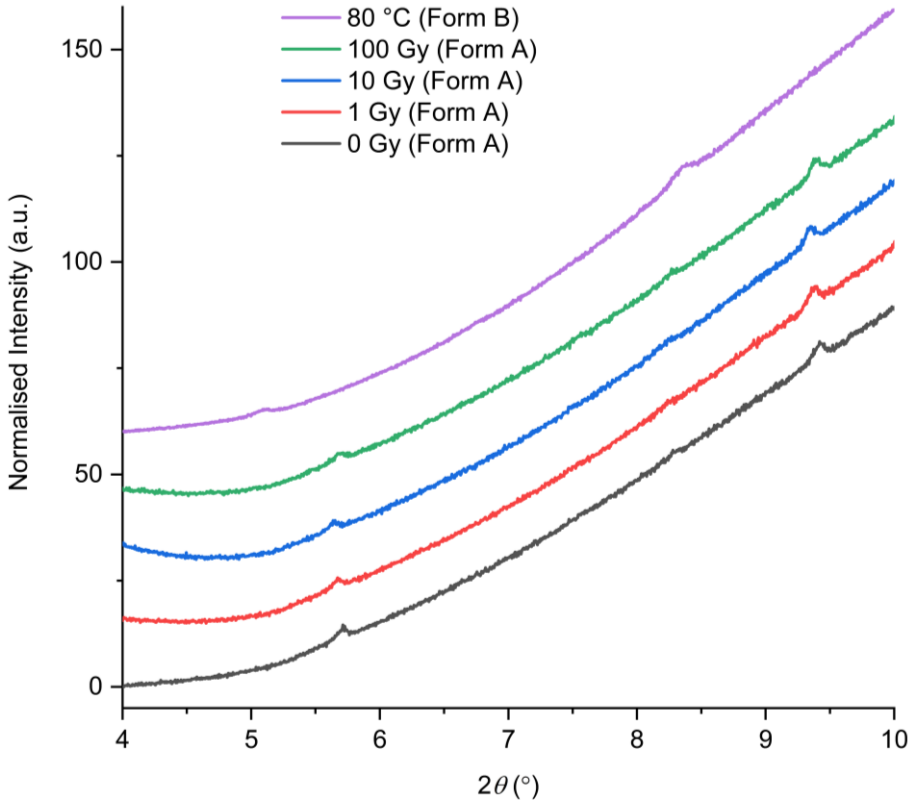

Figure 2.61. The PXRD patterns of the Gafchromic EBT3 films containing Form A before and after X-ray irradiation, and Form B after heating at 80 °C for one day.

The Raman analysis of the Gafchromic EBT3 films before and after exposure to 10 Gy of X-ray radiation and 60 °C display differences in the relative intensities of the

photopolymer bands, depending on whether the films were exposed to radiation or heat. Before irradiation, the photopolymer band has a Raman shift of 2060 cm^{-1} and remains at the same shift when the film is exposed to 10 Gy of X-ray radiation (Figure 2.62). However, when the film is heated to 60 °C, the photopolymer band is blue-shifted to 2092 cm^{-1}, in a similar way to heating Form A in powder form to the same temperature. A magnified section of the spectra to show the shift in the alkyne polymer band is displayed in Figure 2.63. Additionally, the monomeric alkyne band at 2260 cm^{-1} decreases in intensity from the untreated film when compared to the films exposed to radiation and heat due to the polymerisation of Li-PCDA. Also, the alkene band of the photopolymer at in the film before and after heating to 60 °C is split (1416 cm^{-1} and 1444 cm^{-1}) with differing intensities, while the irradiated film has a single band at 1444 cm^{-1}, suggesting multiple conformations in the material before and after heating. It is important to note that heating the film to 60 °C overnight was not great enough to convert Form A into Form B alone.

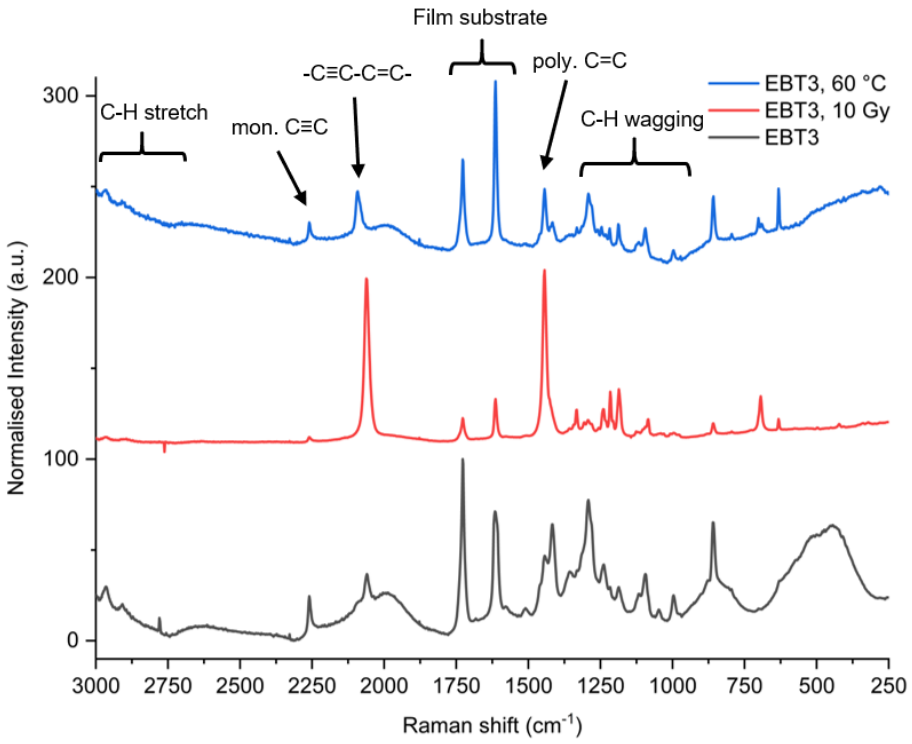

Figure 2.62. The Raman spectra of Gafchromic EBT3 films exposed to X-ray radiation and 60 °C heat.

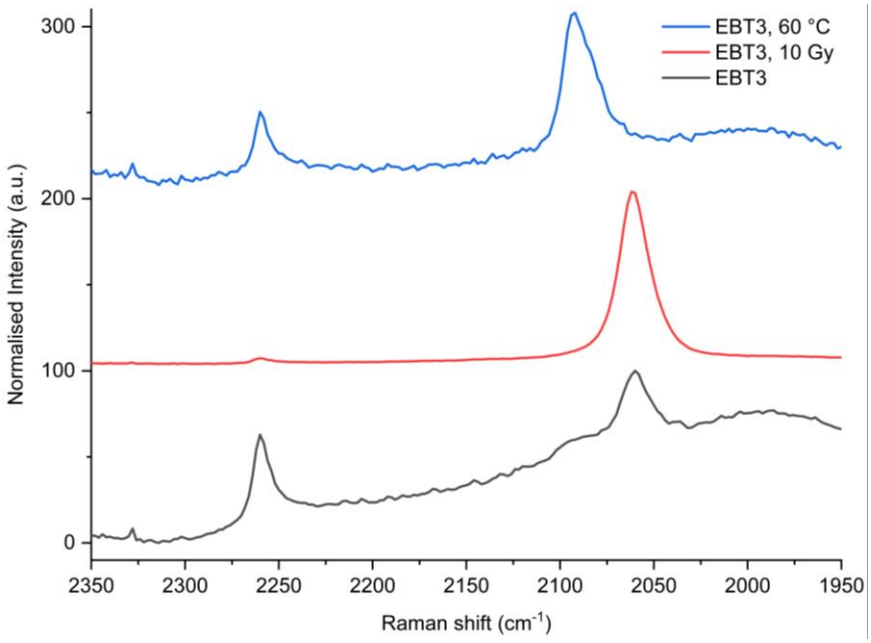

Figure 2.63. The Raman spectra of Gafchromic EBT3 films exposed to X-ray radiation and 60 °C heat, magnified to display the shift in the alkyne photopolymer bands between 2030 cm^{-1} and 2110 cm^{-1}.

2.2.3. The Lithium Salt of a PCDA Analogue

Li-HDDA Structure

To investigate an alternative radiation-sensitive diacetylene to PCDA and to potentially improve the performance of radiation dosimetry materials, the structure and photoreactivity of 5,7-hexadecadiynoic acid (HDDA, Figure 2.64) and its lithium salt (Li-HDDA) were explored. Li-HDDA was synthesised by stirring HDDA and $LiOH{\cdot}H_2O$ in a 1:1 ratio in acetone for 24 hours. The product was isolated under vacuum and gave a pink powder that gradually darkened in colour under ambient light, suggesting possible photoreactivity. The PXRD pattern of HDDA only has peaks at 2.7, 5.3, 8.0 and 13.0 °, compared to the PXRD pattern of the lithium salt product at 2.5, 5.0, 6.5, 7.4, 9.9, and 12.5 °, suggesting the formation of a new material (Figure 2.65).

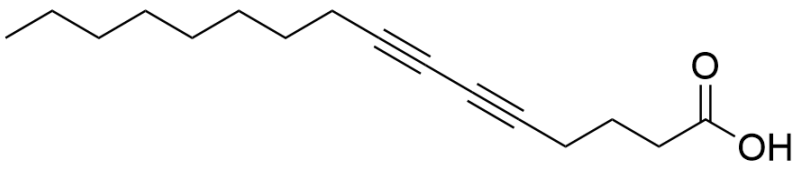

Figure 2.64. The structure of HDDA.

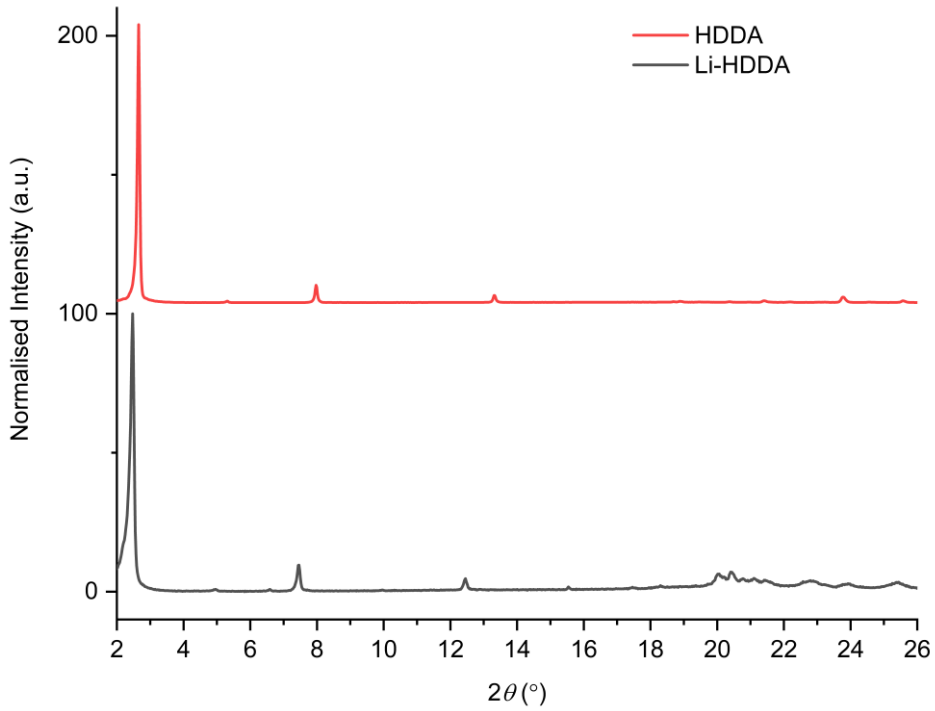

Figure 2.65. The PXRD patterns of HDDA and Li-HDDA.

The FTIR spectra of Li-HDDA compared to the pure acid displays no differences in the peaks in the 3000-2800 cm^{-1} region assigned to $(CH_3)_{asym}$ and $(CH_2)_{asym}$ and $(CH_2)_{symm}$ stretches (Figure 2.66). The free acid C=O band at 1687 cm^{-1} for HDDA is replaced by asymmetric COO^- stretching bands in the salt at 1573 cm^{-1} and 1556 cm^{-1}, along with symmetric COO^- modes at 1435 cm^{-1} and 1410 cm^{-1}. The $\Delta\nu$ (1573-1435 cm^{-1}) for Li-HDDA is 138 cm^{-1}, which suggests a mixed bridging and chelating bidentate coordination of the carboxylate to the lithium ion, in the same way as the bonding of the short-chain lithium carboxylates, and the two Li-PCDA solid forms. Also, the CH_2 bending mode in Li-HDDA at 721 cm^{-1} is split, which suggests a monoclinic or orthorhombic space group,[68] similar to the FTIR of Form A of Li-PCDA, and therefore does not display an all-*trans* conformation of the alkyl chain.

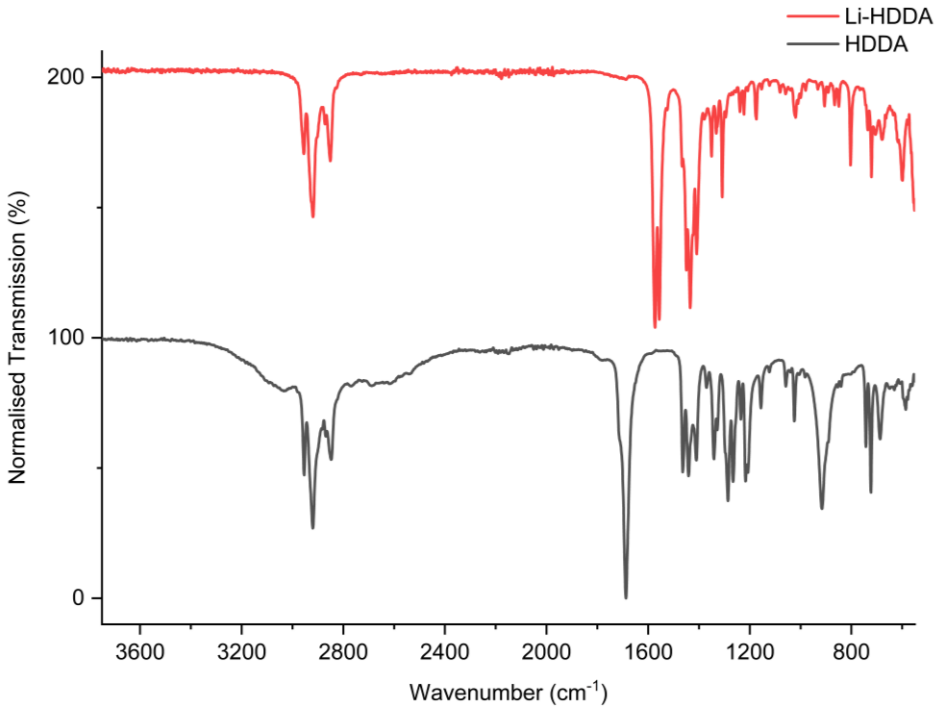

Figure 2.66. The FTIR spectra of Li-HDDA compared with HDDA.

The ssNMR spectra of HDDA and Li-HDDA display a significant difference in the carboxylate region of the spectra, as HDDA has a peak at 181.2 ppm, while Li-HDDA has a peak at 187.3 ppm. The differences in the carboxylate region suggest the coordination of the lithium ion to HDDA is the same as observed in Form B of Li-PCDA (Figure 2.67). Additionally, the alkyne peaks for HDDA are split at chemical shifts of 79.0, 78.7, 66.1, and 65.8 ppm, suggesting four different alkyne environments. However, Li-HDDA has two split alkyne peaks that suggest two (80.1 and 78.6 ppm) and three (67.4, 66.2, and 65.3 ppm) different alkyne environments, which are not observed in HDDA or either of the Li-PCDA forms. Li-HDDA also displays additional peaks in the alkane region of the spectra (10-40 ppm) compared to HDDA alone, suggesting asymmetric environments of the CH_2 groups of the structure.

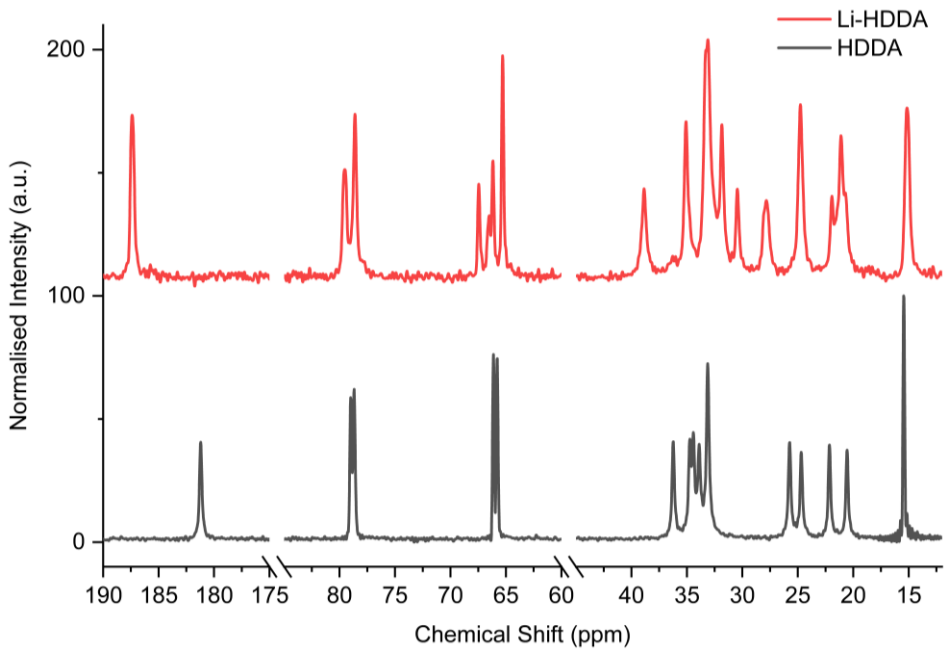

Figure 2.67. The ssNMR spectra of HDDA and Li-HDDA. The carboxylate region is 180-190 ppm while alkyne and alkane peaks are shown in the 60-80 ppm and 10-40 ppm region, respectively. Breaks in the *x*-axis have been added to make the spectra compact.

Li-HDDA Photoreactivity

Upon exposure to UV (254 nm) radiation, it is evident that HDDA and Li-HDDA are photoresponsive by the colour changes of the powder from blue to black for HDDA and light pink to red for Li-HDDA after only five minutes of irradiation. The dramatic colour changes indicate that the structures adhere to the topochemical postulate of photoreactivity (Figure 2.68). For HDDA, the FTIR spectrum shows negligible changes after one hour and one day of irradiation (Figure 2.69), however, the ssNMR spectra displays alkene peaks correlating with the duration of UV exposure (Figure 2.70). The amount of photoconversion of HDDA after one hour of irradiation is estimated to be ≤6 % and ≤15 % after one day, which is greater than the monomer to polymer conversion for PCDA after one day of UV radiation exposure.

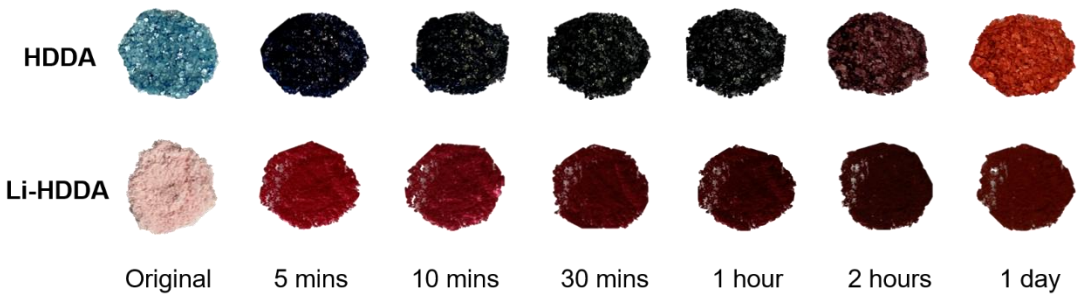

Figure 2.68. Photographs of HDDA and Li-HDDA irradiated with 254 nm of UV radiation for different durations. The lighter colouration of the powders after one day of irradiation suggest a rearrangement from an ordered 'blue' state to a disordered 'red' state.

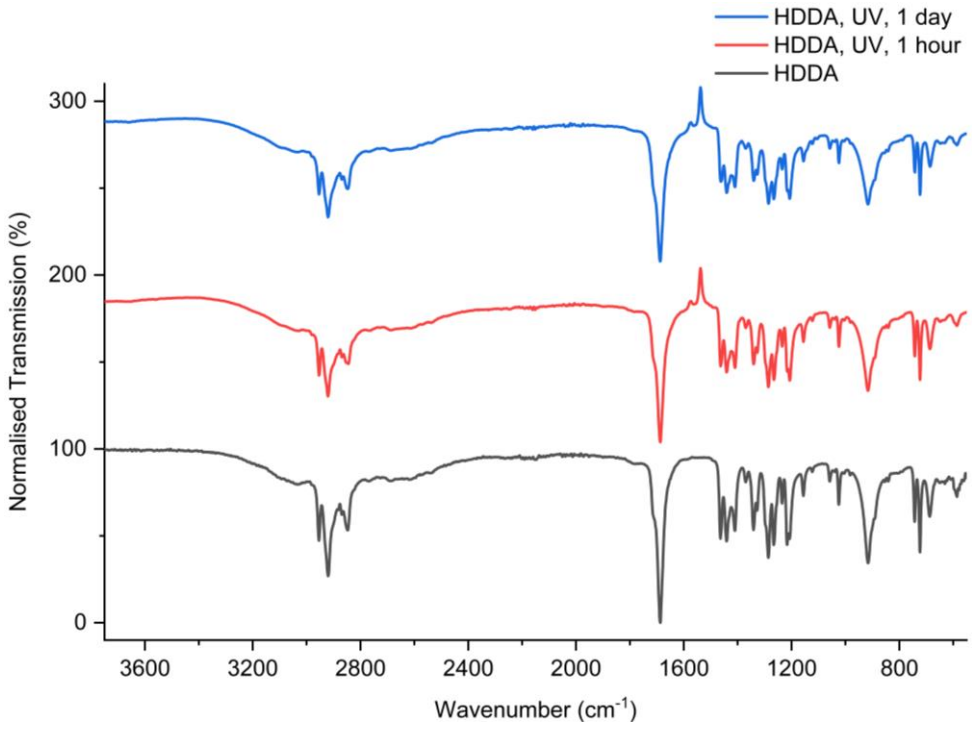

Figure 2.69. The FTIR spectra of HDDA exposed to UV radiation for one hour and one day (baseline artifacts are present at 1575 cm^{-1} and 1538 cm^{-1}).

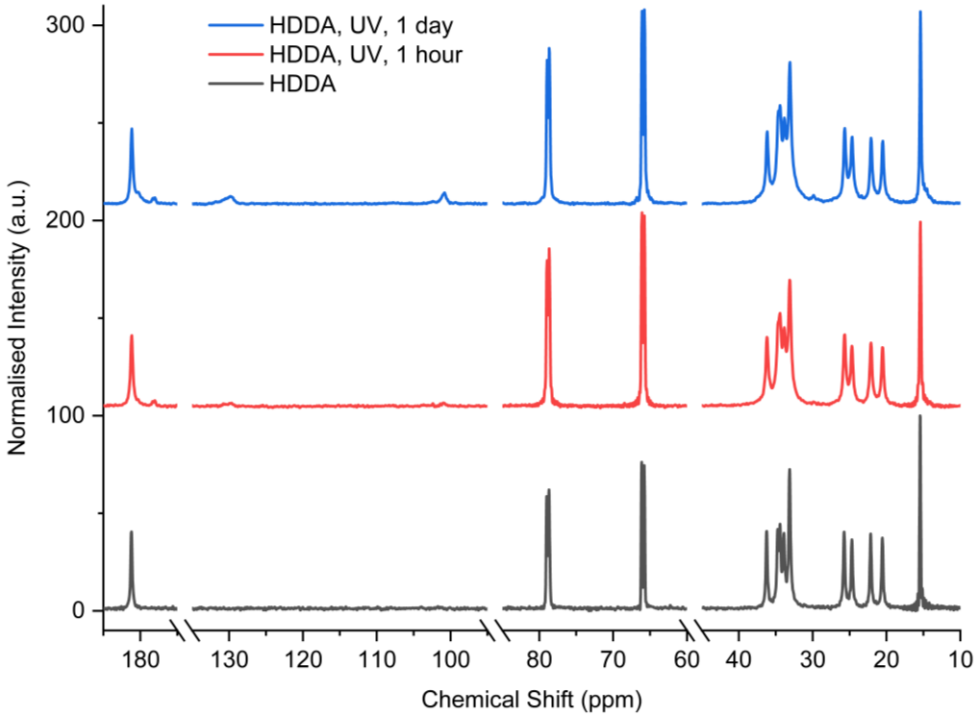

Figure 2.70. The ssNMR spectra of HDDA before and after exposure to UV radiation for one hour and one day. The carboxylate region is 180-190 ppm while any alkene peaks will be displayed in the 100-130 ppm region. Alkyne and alkane peaks are shown in the 60-80 ppm and 10-40 ppm region, respectively. The *x*-axis has added breaks to make the spectra compact.

In comparison to HDDA, Li-HDDA upon irradiation displays subtle changes in the FTIR spectra, especially with the increased intensity of the band at 1691 cm^{-1} and the reduced intensities of the symmetric COO^- bands at 1430 cm^{-1} and 1410 cm^{-1} as the duration of UV exposure increases (Figure 2.71). Changes with irradiation are also displayed in the methylene wagging band region (1380-1100 cm^{-1}) suggesting the introduction of a *gauche* conformation of the HDDA chain as the polymerisation of Li-HDDA occurs. The ssNMR spectra of Li-HDDA exposed to UV radiation is consistent with what is observed in the FTIR spectra. The carboxylate peak at 187.3 ppm broadens with UV exposure duration, however, the most noticeable change with irradiation is the growth of peaks assigned to the alkene functionality in the photopolymer product peaks at 131.4 ppm and 103.0 ppm (Figure 2.72). Integrating the alkyne peaks to the alkyne peaks reveals a ≤10 % and ≤33 % conversion of monomer to polymer after one hour and one day of irradiation, respectively. The photoconversion of Li-HDDA after one day of UV radiation is greater than observed

in either of the Li-PCDA forms, suggesting a highly photosensitive material. Also, in the ssNMR spectra, the intensities of the alkyne and alkane peaks are reduced along with increased peak broadening with irradiation, suggesting decreased crystallinity with increasing photoconversion of monomer to polymer. The reduced peak intensity and peak broadening is not observed in the spectra of HDDA exposed to UV for one day, suggesting that salt formation with the lithium ion greatly enhances the photoreactivity of HDDA in a similar way to Li-PCDA.

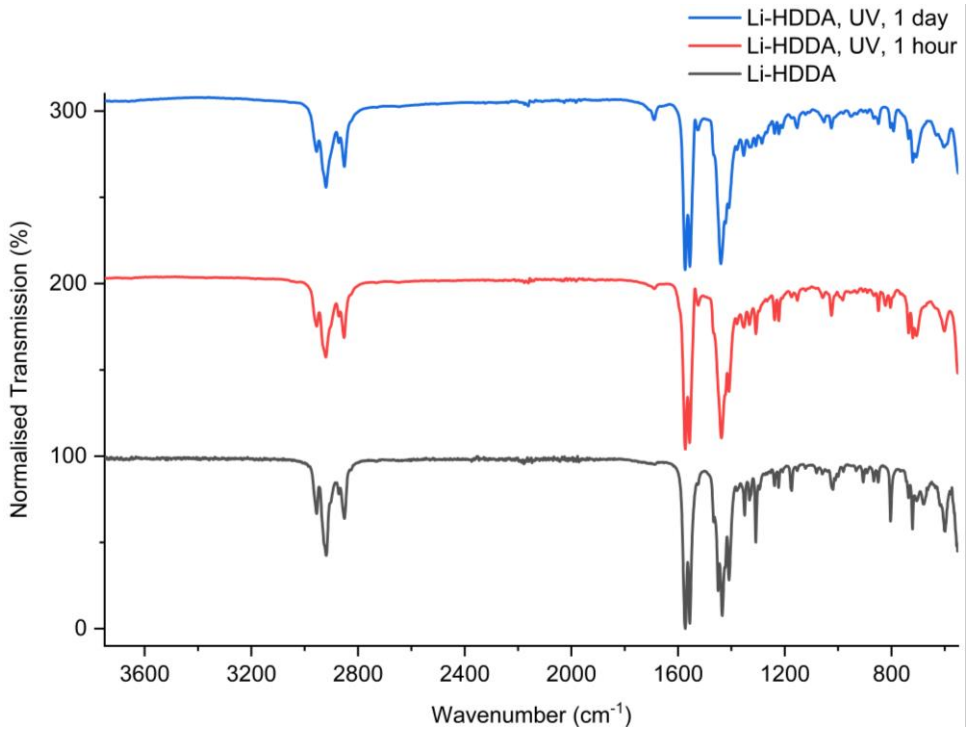

Figure 2.71. The FTIR spectra of Li-HDDA exposed to UV radiation for one hour and one day.

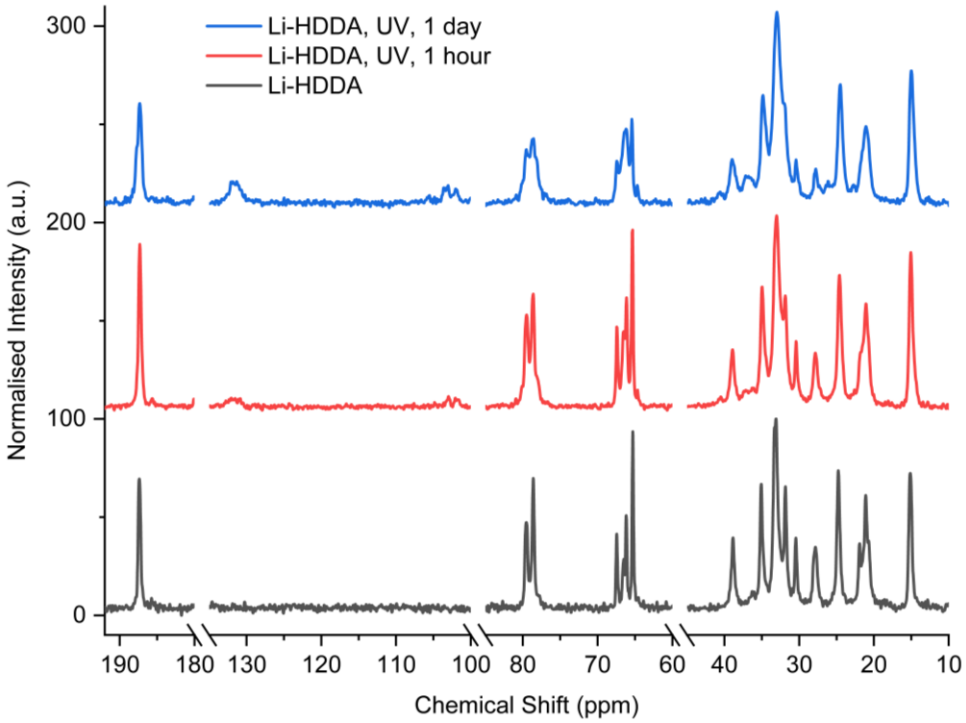

Figure 2.72. The ssNMR spectra of Li-HDDA exposed to UV radiation for one hour and one day. The carboxylate region is 180-190 ppm with alkene peaks displayed in the 100-130 ppm region. Alkyne and alkane peaks are shown in the 60-80 ppm and 10-40 ppm region, respectively. The *x*-axis has added breaks to make the spectra compact.

2.2.4. The Sodium Salt of PCDA

Na-PCDA Structure

To investigate group one alternatives to lithium that may adhere to the topochemical postulate of photoreactivity, the sodium salt of PCDA (Na-PCDA) was synthesised. Sodium hydroxide and PCDA were combined in 1:1 and a 1:3 ratio, respectively, in a ball mill for 45 minutes at a frequency of 20 s^{-1}. The resulting 1:1 product was a pale blue powder, while the 1:3 product was a peach colour. Serendipitous crystals of Na-PCDA grew from the mixture of PCDA and 3-aminopyridine in a 3:1 ratio, respectively from the slow evaporation of under ambient conditions which yielded colourless plate crystals and were analysed by the I19 beamline at the Diamond Light Source. It is assumed that the sodium present was from a contamination in the glass crystallisation vial. The X-ray structure of Na-PCDA reveals a PCDA sodium salt, free acid cocrystal that crystallises in the space group of $P\bar{1}$, with the sodium cation bound to one PCDA salt ($PCDA^-$) ligand and three PCDA acid ligands with a formula

of $Na^{+}PCDA^{-}\cdot 3PCDA$ (Figure 2.73a). In addition, the PCDA salt ligand has a disordered carboxylic acid proton which allows it to either act as an anion or a neutral molecule, as the proton has a site occupancy factor of 50 %. The sodium cation displays a distorted octahedral geometry (evident by the average O-Na-O bond angle of 85.7 °), with the sodium ion bound to carbonyl oxygen atoms at distances of 2.3580(13) Å and 2.3723(11) Å, and a Na-O distance from the sodium ion to the carboxyl O-H of the PCDA ligands at a distance of 2.6176(11) Å (Figure 2.73b). Two PCDA ligands coordinate to an adjacent sodium ion by bridging bidentate (*syn-anti*) oxygen atoms from the carboxyl ligands to form a continuous chain,[62] while the remaining ligands have monodentate bonding, which greatly differs from the hypothesised coordination sphere of Li-PCDA. Hydrogen bonds are also present within the structure, occurring from the hydrogen atom of the carboxyl group to neighbouring carbonyl oxygen atom, at an O···O distance of 2.6290(16) Å. The long PCDA aliphatic chains are in an all-*trans* conformation and pack in a bilayer arrangement and tail-to-tail, which is reflected by the long *c*-axis of the unit cell at 54.510(6) Å. The previously reported structure of sodium hydrogen dihexadecanoate is similar to Na-PCDA in that there are two aliphatic chains in the asymmetric unit, though the sodium ion coordination sphere involves a total of five oxygen atoms.[78] Two of the ligands consist of hexadecenoic acid chains, while the remaining three ligands are of hexadecanoate chains. Similar to Na-PCDA, two oxygen atoms from adjacent hexadecanoate ligands bridge a neighbouring sodium ion, to give a mono- and bidentate coordination to the sodium ion. The aliphatic chains are also in an all-*trans* conformation and stack to give an overall tail-to-tail bilayer structure.[78]

It is apparent by the PXRD analyses of the ball milled products that the 1:1 product is a mixture of PCDA and Na-PCDA 1:3 (Figure 2.74). The PXRD pattern of Na-PCDA 1:3 displays a lamellar progression of the initial peaks 3.3-11.4 ° that correspond to crystallographic planes of (002) to (007), reflecting the bilayer arrangement of layers observed in the crystal structure which is also observed in *n*-alkyl sodium carboxylates.[61, 78, 79]

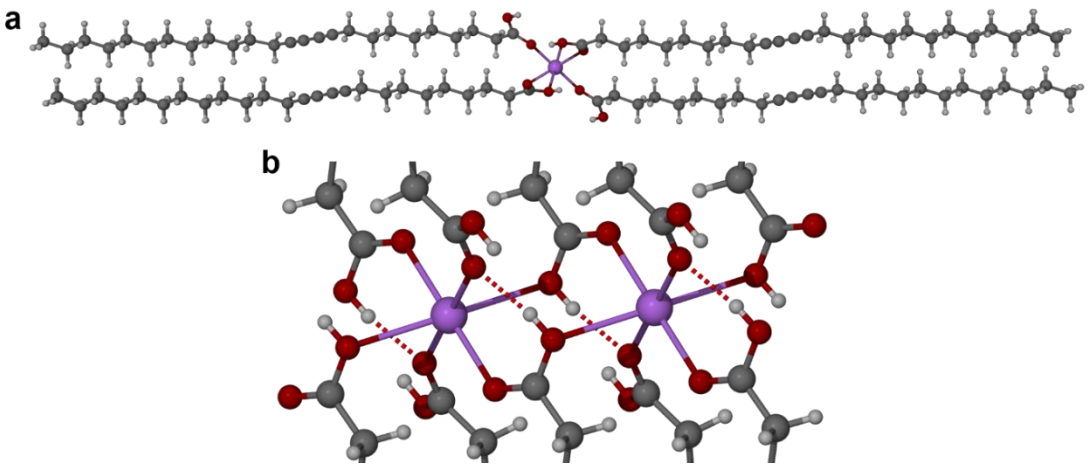

Figure 2.73. a) The X-ray structure of Na-PCDA in the crystallographic (100) direction. b) An enlarged section of Na-PCDA head groups to show the hydrogen bonds between PCDA acid ligands and the salt ligands (with a disordered proton).

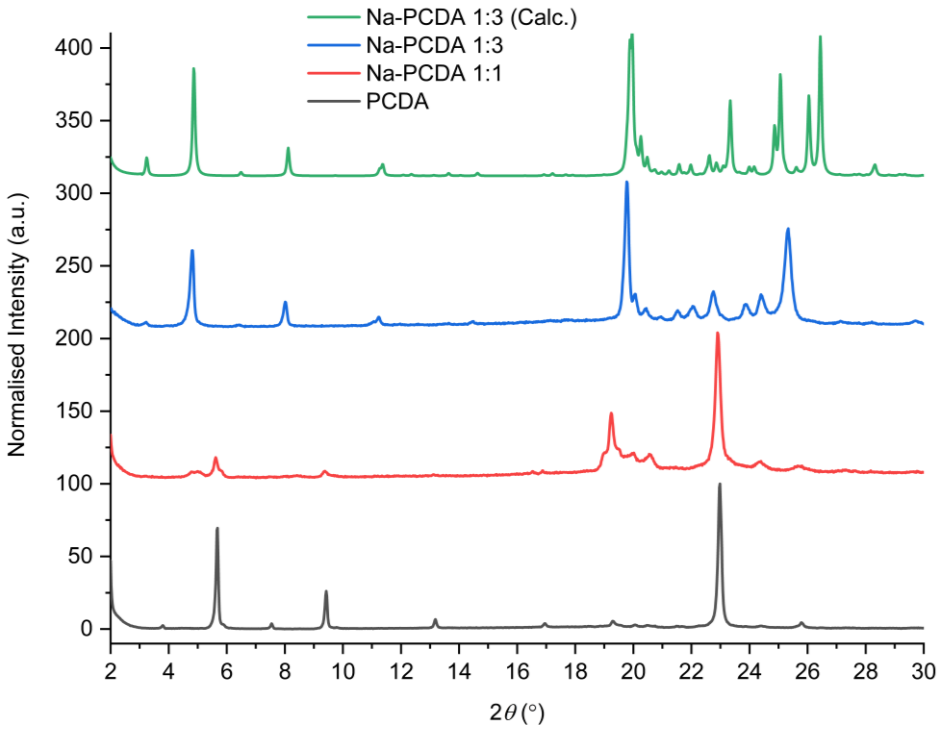

Figure 2.74. The experimental PXRD patterns of Na-PCDA synthesised by ball milling in 1:1 and 1:3 ratios. The experimental PXRD pattern of PCDA and the calculated pattern of Na-PCDA 1:3 is included for comparative purposes.

The FTIR spectra of Na-PCDA 1:1 and 1:3 reveals the same $\nu(CH_3)_{asym}$ and $\nu(CH_2)_{asym}$ and $\nu(CH_2)_{symm}$ bands between 3000 cm^{-1} and 2850 cm^{-1}, corresponding with the PCDA chain. Also, the FTIR spectrum of Na-PCDA 1:1 shows similarities to the

spectra of PCDA, though with an asymmetric stretch at 1559 cm^{-1} which is in neither the spectra of PCDA or Na-PCDA in a 1:3 ratio (Figure 2.75). The difference between the $\nu(COO^-)_{asym}$ band and the first $\nu(COO^-)_{symm}$ reveals a $\Delta\nu$ of 99 cm^{-1} (1559-1460 cm^{-1}) which is indicative of chelating bonding.[62] Thereby suggesting that Na-PCDA 1:1 contains complexed carboxylates, alongside free PCDA in the bulk of the material (with the carbon $\nu(C=O)$ at the same position of PCDA at 1692 cm^{-1}). While the crystal structure of Na-PCDA 1:3 displays monodentate and bidentate coordination. Additionally, Na-PCDA (1:3) has an intense $\delta(CH_2)$ band present at 1472 cm^{-1} which is not present in either PCDA or Na-PCDA 1:1. The methylene wagging bands in Na-PCDA 1:3 (from 1323 cm^{-1} to 1192 cm^{-1}) are also at different wavenumbers and different intensities to Na-PCDA 1:1 and PCDA, suggesting a different packing structure of the aliphatic chains. A structure of sodium hydrogen dihexadecanoate in the literature displays a $\nu(C=O)$ band of 1725 cm^{-1},[78] and suggest a different type of coordination to the metal ion when compared to the forms of Li-PCDA.

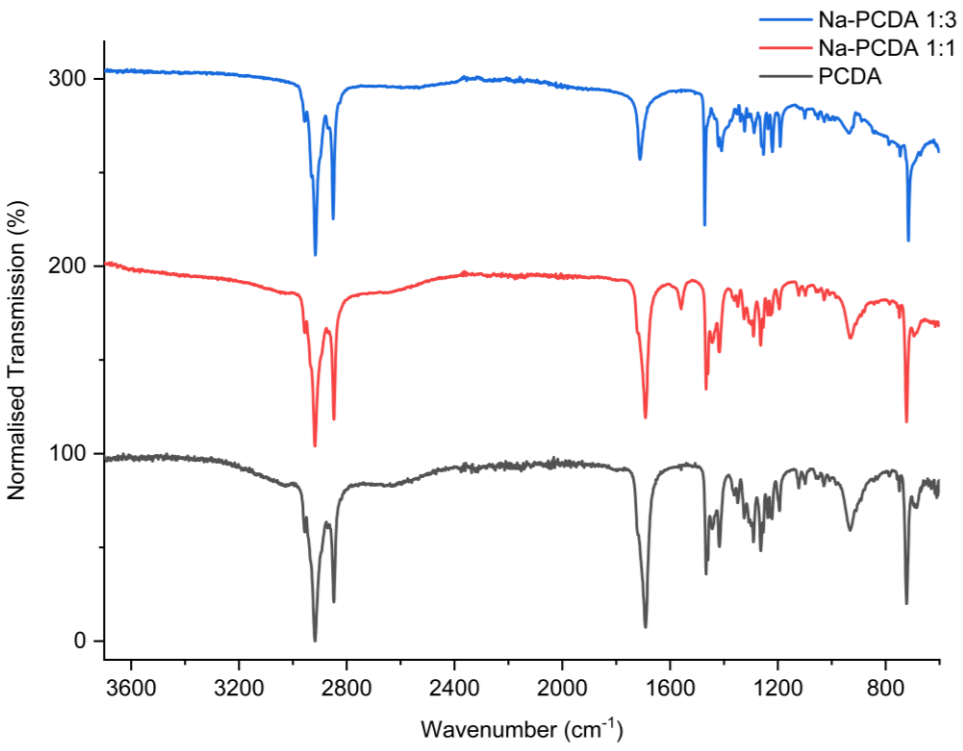

Figure 2.75. The FTIR spectra of ball-milled Na-PCDA in 1:1 and 3:1 ratio, respectively. The spectra of PCDA is added to compared to Na-PCDA 1:1.

The ssNMR spectra of Na-PCDA 1:1 and 1:3 reveals differences in the carboxyl region of the spectra, with Na-PCDA 1:1 displaying a single peak at 182.3 ppm (similar to the carboxylate peak in PCDA at 182.4 ppm), implying that Na-PCDA 1:1 is mostly unreacted PCDA. However, Na-PCDA 1:3 displays two distinct peaks at 182.0 ppm and 179.1 ppm, demonstrating the carboxylic acid region of the PCDA acid ligands, and the carboxylate structure of the salt ligand, respectively. The ssNMR spectra of sodium structures with long aliphatic chains in the literature display a single carboxylate peak at 184 ppm which is the same for the long-chain lithium carboxylates. This indicates that no protonated acid ligands are present in the literature, only carboxylate ligands which differ to the structure of Na-PCDA.[61] Subtle differences occur in the alkyne region of the spectra, as PCDA and Na-PCDA 1:1 display peaks at 77.5 ppm with shoulders at 78.8 ppm, and an additional alkyne peaks at 66.1 ppm and 65.3 ppm, while Na-PCDA 1:3 shows peaks at the aforementioned chemical shifts, though with less broad peaks. The region of the spectra corresponding to CH_2 carbon atoms (40-20 ppm) is the same for PCDA, Na-PCDA 1:1 and 1:3, however, an additional peak is present for Na-PCDA 1:3 at 28.6 ppm, suggesting a different environment in the CH_2 wagging of the PCDA chain. These differences are also observed for the single CH_3 peak at 14.8 ppm in Na-PCDA 1:3, while PCDA and Na-PCDA 1:1 have peaks at 16.0 ppm and 15.2 ppm, again showing their similarity.

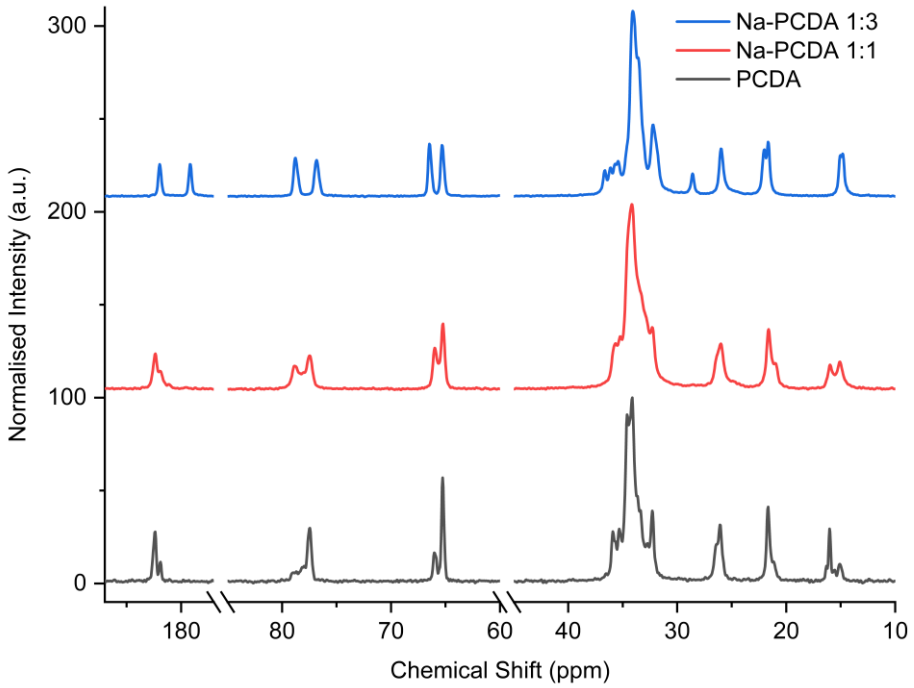

Figure 2.76. The ssNMR spectra of Na-PCDA ball-milled in ratios of 1:1 and 1:3, respectively. The spectra of PCDA is added to show similarity to the spectra of Na-PCDA 1:1. The carboxylate region is 180-190 ppm while alkyne and alkane peaks are shown in the 60-80 ppm and 10-40 ppm region, respectively. Breaks are added in the *x*-axis to compact the spectra.

Na-PCDA 1:3 was heated to approximately 200 °C and the DSC thermogram only displays a single endotherm at an onset temperature of 70.3 °C (Figure 2.77). Upon cooling, a single exothermic peak with an onset temperature of 60.6 °C was observed. On the second heating cycle from room temperature, the thermogram displays an endothermic peak with an onset temperature of 63.3 °C, indicative of PCDA, an exothermic recrystallisation of the melt at 69.0 °C, and a peak with an onset temperature of 70.5 °C, suggestive of Na-PCDA 1:3 from the initial heating cycle. Therefore, upon crystallisation and reheating, the majority of the Na-PCDA 1:3 is retained while some of the salt reverts to free PCDA. Sodium complexes with long-chain aliphatic carboxylate ligands typically display polymorphic phase transitions around 250 °C,[61] however, these polymorphic characteristics are not observed in the DSC thermogram when Na-PCDA 1:3 is heated to 350 °C, though further work such as analysing Na-PCDA 1:3 by hot stage microscopy is required to understand if any phase changes occur in the material.

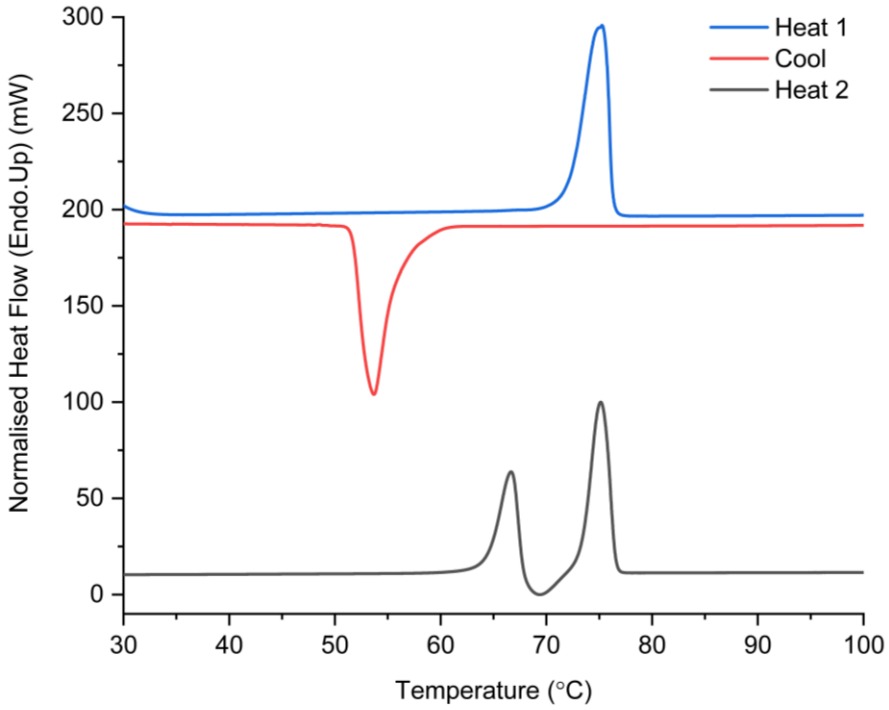

Figure 2.77. The DSC thermogram of a heat-cool-heat cycle of Na-PCDA 1:3. The thermogram only displays the temperature range of 30 – 100 °C, as the thermogram remained unchanged from 100 – 200 °C.

The topochemical parameters of the Na-PCDA 1:3 salt free acid cocrystal structure show that values change depending on the measurements from the different symmetry independent PCDA ligands of the different or the same Na-PCDA molecule. For instance, measuring the topochemical parameters between PCDA ligands coordinated to the same sodium atom or from neighbouring sodium atoms. The topochemical parameters are summarised in Table 2.6. As all three of the topochemical criteria are not adhered to in the Na-PCDA salt free acid structure, it is expected to be unreactive when exposed to radiation.

	C1-C4' distance (Å)	C1-C1' distance (Å)	Tilt angle (°)
Topochemical postulate	≤ 3.8	≤ 4.9 Å	45
Between PCDA ligands coordinated to the same Na atom	4.382(3)	4.685(3)	32.6
Between PCDA ligands of neighbouring Na atoms	3.572(3)	5.3007(6)	33.2

Table 2.6. The topochemical parameters of the Na-PCDA salt, free acid cocrystal depending on which PCDA ligands of the sodium atom were used to measure the distances and tilt angles.

Na-PCDA Photoreactivity

As Na-PCDA 1:1 is likely a mixture of Na-PCDA 1:3 and free PCDA, Na-PCDA 1:1 and 1:3 were irradiated to investigate their photoreactivity. The powders were placed on a filter paper and exposed to different durations of UV (254 nm) radiation. The powders were moved around the paper and pressed with a spatula at approximately hourly intervals to ensure the bulk of the powder was exposed to radiation. Na-PCDA 1:1 shows a gradual colour change from pale blue to bright blue after one day of irradiation (consistent with PCDA, though with a less intense colour change), while Na-PCDA 1:3 shows very little colour change until one day of UV irradiation (Figure 2.78). As the X-ray structure of Na-PCDA 1:3 shows, the distances between PCDA ligands are too great for photopolymerisation, the colour change to orange may be due to the sample being heated from prolonged irradiation or due to a rearrangement from an ordered to a more disordered state. To confirm the lack of polymerisation, Na-PCDA 1:3 was analysed by PXRD (Figure 2.79), FTIR (Figure 2.80), and ssNMR (Figure 2.81) to investigate any changes in the structure upon prolonged irradiation for seven days. However, there was no evidence of any photopolymerisation. The technique most likely to show the presence of any structural changes is ssNMR, and no alkene peaks were observed in the region of 100-130 ppm of the spectra.

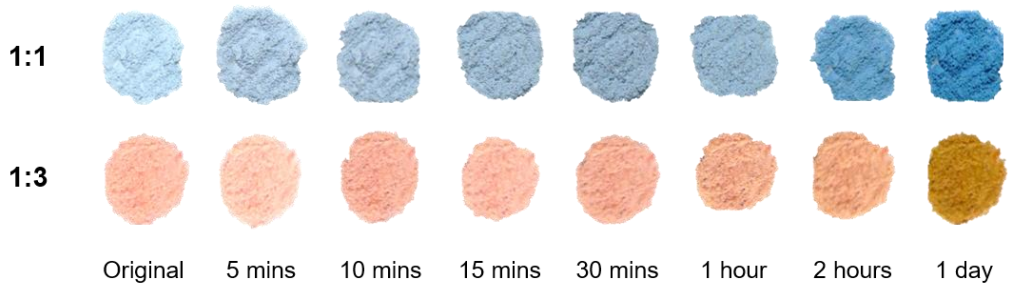

Figure 2.78. Photographs of Na-PCDA 1:1 and 1:3 irradiated for increasing durations of UV (254 nm) radiation. The powders were placed on a glass slide and exposed to radiation without any rotation of the powder, and so only the surface of the powder was exposed.

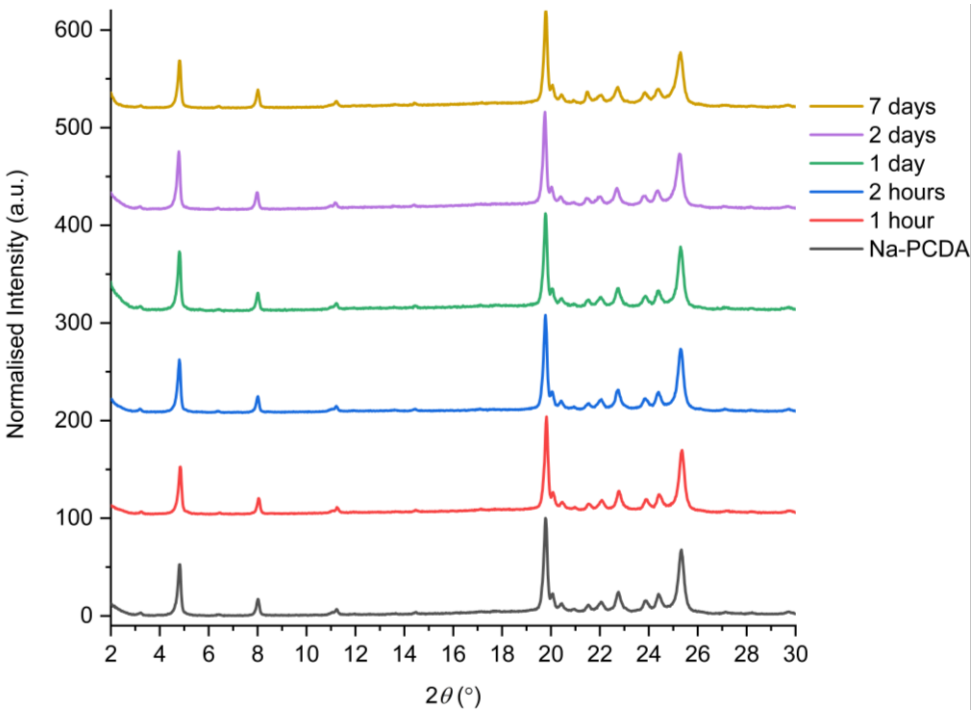

Figure 2.79. The PXRD patterns of Na-PCDA 1:3 irradiated with UV radiation (254 nm) for different durations.

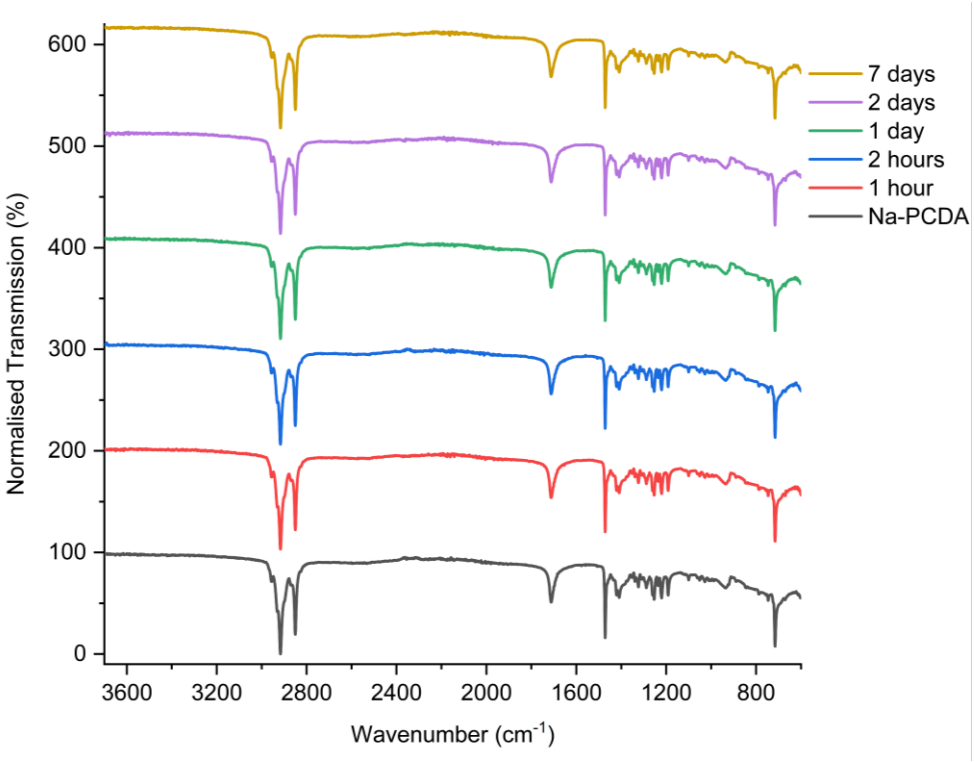

Figure 2.80. The FTIR spectra of Na-PCDA 1:3 irradiated with UV radiation (254 nm) for durations from one hour to seven days.

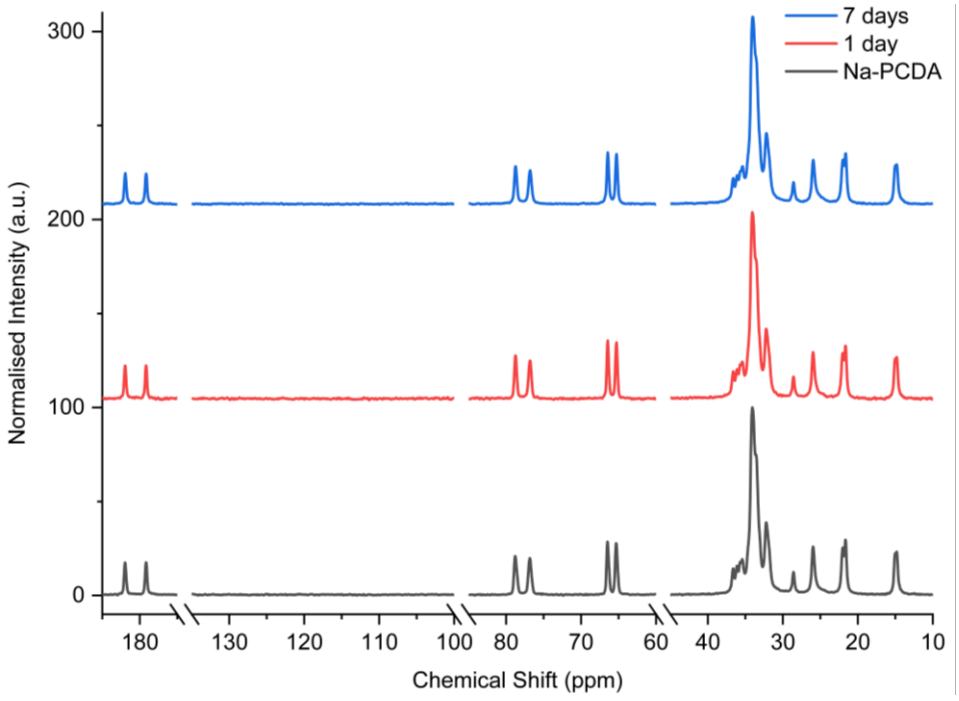

Figure 2.81. The ssNMR spectra of Na-PCDA 1:3 exposed to UV radiation (254 nm) for one day and seven days remains unchanged. The carboxylate region is 180-190 ppm while any alkene peaks will be displayed in the 100-130 ppm region. Alkyne and

alkane peaks are shown in the 60-80 ppm and 10-40 ppm region, respectively. Breaks are added in the *x*-axis to compact the spectra.

2.3. Conclusion

The X-ray structure of PCDA is the first reported structure of its kind and adheres to the topochemical postulate for photoreactivity.[1] The structure of PCDA gives insight into the structures of the Li-PCDA forms, supported by the short-chain lithium model salts. It is hypothesised that the Form A hydrate crystallises in a monoclinic space group with a similar lamellar spacing to PCDA itself, while Form B crystallises in a triclinic space group. Both carboxylate head groups of each form have the same chelating bidentate coordination to the lithium ion, even though Form A has a coordinated water molecule. Therefore, the difference in the structures is due to the packing of the aliphatic chains. The difference in chain behaviour would explain the reduced photosensitivity in Form A (which is most similar to PCDA) and the enhanced photoreactivity in Form B, due to the relative positioning of the reactive moieties. Additionally, due to the photoreactive nature of both forms of Li-PCDA, they must also adhere to the topochemical postulate. The lithium salt of HDDA proves to be more photosensitive than either of the forms of Li-PCDA, evident by the ≤33 % monomer to polymer conversion after one day of UV exposure and therefore must be within the topochemical parameters for polymerisation. In contrast, the X-ray structure of Na-PCDA (1:3) has a different bonding environment to Li-PCDA due to monodentate and bridging ligands and is not sensitive to radiation. The lack of photoreactivity in Na-PCDA 1:3 reinforces the importance of the topochemical postulate to predict the photoreactivity of a system which can only be confirmed by the X-ray structure.

2.4. Experimental

Additional information relating to the materials and instrumentation used in this work can be found in Chapter 6.

PCDA

10,12-Pentacosadiynoic acid was obtained from Ashland LLC. Analysis calc. for $C_{25}H_{42}O_2$: C 80.16, H 11.30 %, found: C 80.05, H 11.18 %; FTIR (cm^{-1}): 2956 $\nu(CH_3)_{asym}$, 2918 $\nu(CH_2)_{asym}$, 2848 $\nu(CH_3)_{symm}$, 1691 ν(C=O), 1467 $\delta(CH_2)$, 1443, 1417, 1350 $\omega(CH_2)$, 1326 $\omega(CH_2)$, 1291 $\omega(CH_2)$, 1264 $\omega(CH_2)$, 1222 $\omega(CH_2)$, 1194 $\omega(CH_2)$, 1124 ν(C-C), 1098 ν(C-C), 1029, 933 νC-C(COO), 722 $\rho(CH_2)$, 685. Colourless needle crystals of high quality were grown from the slow evaporation of acetone at room temperature for one week from a failed cocrystallisation experiment with pyrazine. Crystal data: M = 374.58 g/mol, 0.12 × 0.04 × 0.01 mm^3, triclinic, space group $P\bar{1}$ (no. 2), a = 4.5738(3) Å, b = 5.3909(3) Å, c = 46.647(3) Å, α = 88.6499(15) °, β = 88.5073(14) °, γ = 81.4017(14) °, V = 1136.64(12) $Å^3$, Z = 2, D_c = 1.094 g/cm^3, F000 = 416.0, synchrotron radiation, λ = 0.6889 Å, T = 100 K, $2\theta_{max}$ = 58.994 °, 21023 reflections collected, 6893 unique (R_{int} = 0.0574). Final GooF = 1.035, R_1 = 0.0640, wR_2 = 0.1772, R indices based on 6893 reflections with $I >= 2\sigma(I)$ (refinement on F^2), 249 parameters, 0 restraints, μ = 0.063 mm^{-1}. Full crystallographic information for PCDA can be found in Table 8.1 in Chapter 8.

Ashland Li-PCDA

Lithium 10,12-pentacosadiynoate was received in the form of moist “short hairs” and “long hairs” and was found to be hydrated Form A and a mixture of Form A and B, respectively.

<u>Form A</u>

The “short hair” sample contained excess water, and so was placed under vacuum at room temperature for one day before analysis (which changes Form A to Form B). Analysis calc. for $C_{25}H_{41}O_2Li$: C78.91, H 10.86 %, found: C 78.76, H 10.76 %; FTIR (cm^{-1}): 3570-3040 ν(OH), 2956 $\nu(CH_3)_{asym}$, 2934 $\nu(CH_2)_{asym}$, 2918 $\nu(CH_3)_{symm}$, 2847 $\nu(CH_2)_{symm}$, 1688 δ(HOH), 1581 $\nu(COO)_{asym}$, 1564 $\nu(COO)_{asym}$, 1457 $\delta(CH_2)$, 1432 $\nu(COO)_{symm}$, 1418 $\nu(COO)_{symm}$, 1370 $\omega(CH_2)$, 1355 $\omega(CH_2)$, 1338 $\omega(CH_2)$, 1318 $\omega(CH_2)$, 1311 $\omega(CH_2)$, 1306 $\omega(CH_2)$, 1297 $\omega(CH_2)$, 1277 $\omega(CH_2)$, 1254 $\omega(CH_2)$, 1241 $\omega(CH_2)$, 1231 $\omega(CH_2)$, 1219 $\omega(CH_2)$, 1208 $\omega(CH_2)$, 1197 $\omega(CH_2)$, 1182 $\omega(CH_2)$, 1119 $\omega(CH_2)$, 1103 $\omega(CH_2)$, 1090 ν(C-C), 1058 ν(C-C), 1050 ν(C-C), 1030 ν(C-C), 1026 ν(C-C), 1009 ν(C-C), 999 ν(C-C), 990 ν(C-C), 979 ν(C-C), 877 ν(C-C)COO, 780 $\rho(CH_2)$, 722 $\rho(CH_2)$, 634.

Form B

Form B was prepared by heating Form A in oven at 100 °C for one hour, or by heating the "long hairs" in the oven at 80 °C for one hour. Analysis calc. for $C_{25}H_{41}O_2Li$: C78.91, H 10.86 %, found: C 79.02, H 10.78 %; FTIR (cm^{-1}): 2956 $\nu(CH_3)_{asym}$, 2918 $\nu(CH_2)_{asym}$, 2880 $\nu(CH_3)_{symm}$, 2847 $\nu(CH_2)_{symm}$, 1577 $\nu(COO)_{asym}$, 1558 $\nu(COO)_{asym}$, 1467 $\delta(CH_2)$, 1443 $\nu(COO)_{symm}$, 1412 $\nu(COO)_{symm}$, 1371 $\omega(CH_2)$, 1356 $\omega(CH_2)$, 1333 $\omega(CH_2)$, 1310 $\omega(CH_2)$, 1304 $\omega(CH_2)$, 1277 $\omega(CH_2)$, 1269 $\omega(CH_2)$, 1254 $\omega(CH_2)$, 1229 $\omega(CH_2)$, 1202 $\omega(CH_2)$, 1195 $\omega(CH_2)$, 1120 $\omega(CH_2)$, 1103 $\omega(CH_2)$, 1097 ν(C-C), 1050 ν(C-C), 1032 ν(C-C), 1026 ν(C-C), 1007 ν(C-C), 995 ν(C-C), 981 ν(C-C), 847 ν(C-C)COO, 792 $\rho(CH_2)$, 747 $\rho(CH_2)$, 723 $\rho(CH_2)$, 617.

Durham Li-PCDA

Following Ashland's procedure

Following the procedure outlined by Ashland:[80] 10,12-pentacosadiynoic acid (0.07 g, 0.19 mmol) was combined with lithium hydroxide monohydrate (0.074 g, 1.76 mmol), tetraethylammonium hydroxide (0.011 g, 0.075 mmol), and sodium hydroxide (0.015 g, 0.38 mmol) in deionised water (0.83 mL) for the formulation to total 1 g. The formulation was stirred then sonicated in a water bath at 60 °C for 30 minutes which facilitates a blue to pink colour change. A seed of Form A (0.004 g, 0.01 mmol) was added to the formulation, stirred, and placed in an oven at 65 °C for four hours to Ostwald ripen. After this time, the formulation was sonicated in a cold-water bath for five minutes. The formulation mixture was placed in the oven at 65 °C for a further four hours. Only Form B of Li-PCDA was present in both the sonicated half and the further heated sample half after completing the procedure (total yield = 0.12 g, 0.21 mmol, 73 %).

Equimolar Li-PCDA in solution

Li-PCDA was synthesised by combining 10,12-pentacosadiynoic acid (0.10 g, 0.27 mmol) and lithium hydroxide monohydrate (0.011 g, 0.27 mmol) in 20 mL of acetone and sonicated for 10 minutes. Solvent was left to evaporate from large vials under ambient conditions and excess remaining solvent was removed by pressing the powder on filter paper (yield = 0.094 g, 0.23 mmol, 85 %). The synthesised Li-PCDA was a mixture of Form A and B by PXRD. Analysis calc. for $C_{25}H_{41}O_2Li$: C 78.91, H 10.86 %, found: C 79.00, H 10.73 %; FTIR (cm^{-1}): 2955 $\nu(CH_3)_{asym}$, 2918 $\nu(CH_2)_{asym}$, 2848 $\nu(CH_2)_{symm}$, 1691 ν(C=O) (residual PCDA), 1578 $\nu(COO)_{asym}$, 1556 $\nu(COO)_{asym}$,

1464 δ(CH_2), 1445 ν($COO)_{symm}$, 1370 ω(CH_2), 1334 ω(CH_2), 1308 ω(CH_2), 1269 ω(CH_2), 1194 ω(CH_2), 1121 ω(CH_2), 1098 ν(C-C), 937, 847 ν(C-C)COO, 790 ρ(CH_2), 722 ρ(CH_2), 618.

Li-ButA Salt

Lithium butanoate was prepared by combining butanoic acid (0.09 mL, 0.95 mmol) and lithium hydroxide monohydrate (0.040 g, 0.95 mmol) with 20 mL of acetone and ethanol (1:1) and left to stir at room temperature for 24 hours. The product was isolated by vacuum to yield a cream powder (yield = 0.047 g, 0.50 mmol, 38 %). Analysis calc. for $C_4H_7O_2Li$: C 51.09, H 7.50 %, found: C 51.07, H 7.58 %; FTIR (cm^{-1}): 2964 ν($CH_3)_{asym}$, 2934 ν($CH_2)_{asym}$, 2873 ν($CH_2)_{symm}$, 1697 ν(C=O) (residual ButA), 1579 ν($COO)_{asym}$, 1557 ν($COO)_{asym}$, 1461 δ(CH_2), 1434 ν($COO)_{symm}$, 1415 ν($COO)_{symm}$, 1353 ω(CH_2), 1299 ω(CH_2), 1266 ω(CH_2), 1219 ω(CH_2), 1105 ν(C-C), 901 ν(C-C)COO, 887, 756 ρ(CH_2), 710 ρ(CH_2), 660.

Li-PentA Salt

Lithium pentanoate was prepared by combining pentanoic acid (0.11 mL, 0.95 mmol) and lithium hydroxide monohydrate (0.040 g, 0.95 mmol) with 20 mL of acetone and ethanol (1:1) and left to stir at room temperature for 24 hours. The product was isolated by vacuum to yield a white powder (yield = 0.067 g, 0.62 mmol, 49 %). Analysis calc. for $C_5H_9O_2Li$: C 55.57, H 8.39 %, found: C 55.76, H 8.64 %; FTIR (cm^{-1}): 2955 ν($CH_3)_{asym}$, 2934 ν($CH_2)_{asym}$, 2873 ν($CH_2)_{symm}$, 1712 ν(C=O) (residual PentA), 1577 ν($COO)_{asym}$, 1557 ν($COO)_{asym}$, 1463 δ(CH_2), 1440 ν($COO)_{symm}$, 1409 ν($COO)_{symm}$, 1360 ω(CH_2), 1321 ω(CH_2), 1287 ω(CH_2), 1244 ω(CH_2), 1208 ω(CH_2), 1108 ν(C-C), 946, 928 νC-C(COO), 895, 803, 732 ρ(CH_2), 704 ρ(CH_2), 624.

Li-HexA Salt

Lithium hexanoate was prepared by combining hexanoic acid (0.12 mL, 0.95 mmol) and lithium hydroxide monohydrate (0.040 g, 0.95 mmol) with 20 mL of acetone and ethanol (1:1) and were stirred at room temperature for 24 hours. The product was isolated by vacuum to yield a white powder (yield = 0.095 g, 0.78 mmol, 63 %). Analysis calc. for $C_6H_{11}O_2Li$: C 59.02, H 9.08 %, found: C 58.28, H 8.97 %; FTIR (cm^{-1}): 2953 ν($CH_3)_{asym}$, 2929 ν($CH_2)_{asym}$, 2872 ν($CH_2)_{symm}$, 1711 ν(C=O) (residual HexA), 1578 ν($COO)_{asym}$, 1558 ν($COO)_{asym}$, 1461 δ(CH_2), 1441 ν($COO)_{symm}$, 1413

$\nu(COO)_{symm}$, 1343 $\omega(CH_2)$, 1298 $\omega(CH_2)$, 1263 $\omega(CH_2)$, 1230 $\omega(CH_2)$, 1110 ν(C-C), 845 νC-C(COO), 768 $\rho(CH_2)$, 726 $\rho(CH_2)$.

Li-HDDA Salt

Lithium hexadecadiynoate was prepared by combining 5,7-hexadecadiynoic acid (0.20 g, 0.81 mmol) and lithium hydroxide monohydrate (0.034 g, 0.81 mmol) with 20 mL of acetone and left to stir at room temperature for 24 hours. The product was isolated under vacuum to yield a pink powder (yield = 0.10 g, 0.40 mmol, 43 %). Analysis calc. for $C_{16}H_{23}O_2Li$: C 75.57, H 9.12 %, found: C 75.12, H 8.94 %; FTIR (cm^{-1}): 2956 $\nu(CH_3)_{asym}$, 2919 $\nu(CH_2)_{asym}$, 2851 $\nu(CH_2)_{symm}$, 1573 $\nu(COO)_{asym}$, 1556 $\nu(COO)_{asym}$, 1450 $\delta(CH_2)$, 1435 $\nu(COO)_{symm}$, 1410 $\nu(COO)_{symm}$, 1349 $\omega(CH_2)$, 1331 $\omega(CH_2)$, 1306 $\omega(CH_2)$, 1237 $\omega(CH_2)$, 1223 $\omega(CH_2)$, 1174 ν(C-C), 1020, 905 νC-C(COO), 865, 847, 802, 735, 721 $\rho(CH_2)$, 680 $\rho(CH_2)$, 600.

Na-PCDA Salt Cocrystal

1:1 stoichiometry –10,12-Pentacosadiynoic acid (0.20 g, 0.53 mmol) and sodium hydroxide (0.021 g,0.53 mmol) were ground in a Retsch MM 200 mixer mill for 45 minutes at a frequency of 20 s^{-1} to yield a pale blue powder, however, PXRD analysis revealed a mixture of free acid and sodium salt. FTIR (cm^{-1}): 2956 $\nu(CH_3)_{asym}$, 2918 $\nu(CH_2)_{asym}$, 2848 $\nu(CH_2)_{symm}$, 1691 ν(C=O) (residual PCDA), 1559 $\nu(COO)_{asym}$, 1467 $\delta(CH_2)$, 1445 $\nu(COO)_{symm}$, 1418 $\nu(COO)_{symm}$, 1349 $\omega(CH_2)$, 1326 $\omega(CH_2)$, 1291 $\omega(CH_2)$, 1265 $\omega(CH_2)$, 1227 $\omega(CH_2)$, 1195 $\omega(CH_2)$, 1123, 1098, 1028, 930 νC-C(COO), 722 $\rho(CH_2)$ 695.

1:3 stoichiometry – Sodium 10,12-pentacosadiynoate / 10,12-pentacosadiynoic acid cocrystal was prepared by grinding 10,12-pentacosadiynoic acid (0.60 g, 1.59 mmol) and sodium hydroxide (0.021 g,0.53 mmol) in a Retsch MM 200 mixer mill for 45 minutes at a frequency of 20 s^{-1} to yield a peach coloured powder (yield = 0.57 g, 1.15 mmol, 91 %). Analysis calc. for $C_{100}H_{167}O_8Na$: C 78.76, H 10.84 %, found: C 78.40, H 10.81 %; FTIR (cm^{-1}): 2957 $\nu(CH_3)_{asym}$, 2916 $\nu(CH_2)_{asym}$, 2851 $\nu(CH_2)_{symm}$, 1712 ν(C=O), 1472 $\delta(CH_2)$, 1421, 1408, 1323 $\omega(CH_2)$, 1287 $\omega(CH_2)$, 1254 $\omega(CH_2)$, 1222 $\omega(CH_2)$, 1192 $\omega(CH_2)$, 1100 ν(C-C), 936 νC-C(COO), 715 $\rho(CH_2)$. The X-ray structure of Na-PCDA came from a failed crystallisation of PCDA and 3-aminopyridine in a 3:1 ratio, respectively, from the slow evaporation of acetone at room temperature, which yielded colourless plate crystals. It is assumed that the

presence of sodium was from a contamination in the glass vial. Crystal data: M = 1520.32 g/mol, 0.203 × 0.029 × 0.008 mm^3, triclinic, space group $P\bar{1}$ (no. 2), a = 5.3007(6) Å, b = 7.9037(9) Å, c = 54.510(6) Å, α = 91.674(3) °, β = 92.680(3) °, γ = 92.463(4) °, V = 2278.0(4) Å^3, Z = 1, D_c = 1.108 g/cm^3, F_{000} = 842.0, synchrotron radiation, λ = 0.6889 Å, T = 100 K, $2\theta_{max}$ = 49.998 °, 27970 reflections collected, 8701 unique (R_{int} = 0.1030). Final GooF = 1.005, R_1 = 0.0998, wR_2 = 0.2260, R indices based on 8701 reflections with $I >= 2\sigma(I)$ (refinement on F^2), 497 parameters, 0 restraints, μ = 0.068 mm^{-1}. Full crystallographic information for Na-PCDA 1:3 can be found in Table 8.2 in Chapter 8.

2.5. References

1. V. Enkelmann, *Adv. Polym. Sci.*, 1984, **63**, 91-136.
2. E. Moreno, R. Cordobilla, T. Calvet, M. A. Cuevas-Diarte, G. Gbabode, P. Negrier, D. Mondieig and H. A. J. Oonk, *New J. Chem.*, 2007, **31**, 947-957.
3. E. Moreno-Calvo, T. Calvet, M. A. Cuevas-Diarte and D. Aquilano, *Cryst. Growth Des.*, 2010, **10**, 4262-4271.
4. G. Gbabode, P. Negrier, D. Mondieig, E. Moreno, T. Calvet and M. A. Cuevas-Diarte, *J. Alloys Compd.*, 2009, **469**, 539-551.
5. G. Gbabode, P. Negrier, D. Mondieig, E. Moreno, T. Calvet and M. A. Cuevas-Diarte, *Chem. Phys. Lipids*, 2008, **154**, 68-77.
6. I. Nahringbauer, *Acta Crystallogr., Sect. B: Struct. Sci.*, 1978, **34**, 315-318.
7. I. Nahringbauer, *Acta Chem. Scand.*, 1970, **24**, 453-462.
8. F. J. Strieter, D. H. Templeton, R. F. Scheuerman and R. L. Sass, *Acta Crystallogr.*, 1962, **15**, 1233-1239.
9. F. J. Strieter and D. H. Templeton, *Acta Crystallogr.*, 1962, **15**, 1240-1244.
10. R. Scheuerman and R. L. Sass, *Acta Crystallogr.*, 1962, **15**, 1244-1247.
11. A. D. Bond, *New J. Chem.*, 2004, **28**, 104-114.
12. E. Moreno, R. Cordobilla, T. Calvet, F. J. Lahoz and A. I. Balana, *Acta Crystallogr., Sect. C: Struct. Chem.*, 2006, **62**, 129-131.
13. M. Goto and E. Asada, *Bull. Chem. Soc. Jpn.*, 1984, **57**, 1145-1146.
14. M. Goto and E. Asada, *Bull. Chem. Soc. Jpn.*, 1978, **51**, 2456-2459.
15. G. Gbabode, P. Negrier, D. Mondieig, E. M. Calvo, T. Calvet and M. A. Cuevas-Diarte, *Chem. - Eur. J.*, 2007, **13**, 3150-3159.
16. E. Moreno-Calvo, G. Gbabode, R. Cordobilla, T. Calvet, M. A. Cuevas-Diarte, P. Negrier and D. Mondieig, *Chem. - Eur. J.*, 2009, **15**, 13141-13149.
17. C. R. Groom, I. J. Bruno, M. P. Lightfoot and S. C. Ward, *Acta Crystallogr., Sect. B: Struct. Sci., Cryst. Eng. Mater.*, 2016, **72**, 171-179.
18. S. Abrahamsson and E. Vonsydow, *Acta Crystallogr.*, 1954, **7**, 591-592.
19. D. M. Crowfoot, *J. Chem. Soc.*, 1936, 716-718.
20. J. Bernstein, R. E. Davis, L. Shimoni and N. L. Chang, *Angew. Chem., Int. Ed.*, 1995, **34**, 1555-1573.
21. X. He and B. M. Craven, *Acta Crystallogr., Sect. C: Cryst. Struct. Commun.*, 1984, **40**, 1157-1159.

22. D. A. Jaeger, P. A. Goodson, N. Arulsamy and J. Wettstein, *Chem. Phys. Lipids*, 1998, **92**, 99-104.
23. F. Lacouture, M. Francois, C. Didierjean, J. P. Rivera, E. Rocca and J. Steinmetz, *Acta Crystallogr., Sect. C: Cryst. Struct. Commun.*, 2001, **57**, 530-531.
24. F. Lacouture, J. Peultier, M. Francois and J. Steinmetz, *Acta Crystallogr., Sect. C: Cryst. Struct. Commun.*, 2000, **56**, 556-557.
25. A. Mesbah, C. Juers, M. Francois, E. Rocca and J. Steinmetz, *Z. Kristallogr.*, 2007, 593-598.
26. C. Sivasankar, N. Sadhukhan, J. K. Bera and A. G. Samuelson, *New J. Chem.*, 2007, **31**, 385-393.
27. B. Gustafsson, M. Hakansson and S. Jagner, *New J. Chem.*, 2003, **27**, 459-461.
28. M. Petric, I. Leban and P. Segedin, *Polyhedron*, 1996, **15**, 4277-4282.
29. N. Liakakos, B. Cormary, X. J. Li, P. Lecante, M. Respaud, L. Maron, A. Falqui, A. Genovese, L. Vendier, S. Koinis, B. Chaudret and K. Soulantica, *J. Am. Chem. Soc.*, 2012, **134**, 17922-17931.
30. M. S. Ali, C. A. Powers, K. H. Whitmire, I. Guzman-Jimenez and A. R. Khokhar, *J. Coord. Chem.*, 2001, **52**, 273-287.
31. A. N. C. Mat, N. Abdullah, H. Khaledi and J. T. Tee, *Acta Crystallogr., Sect. E: Struct. Rep. Online*, 2011, **67**, 599-600.
32. F. J. M. Casado, M. R. Riesco, M. V. G. Perez, M. I. Redondo, S. Lopez-Andres and J. A. R. Cheda, *J. Phys. Chem. B*, 2009, **113**, 12896-12902.
33. T. N. Blanton, M. Rajeswaran, P. W. Stephens, D. R. Whitcomb, S. T. Misture and J. A. Kaduk, *Powder Diffr.*, 2011, **26**, 313-320.
34. R. Kassis, M. Bassil and A. Al Choueiry, *Mater. Res. Express*, 2019, **6**, 1-7.
35. Y. J. Gwon, C. Kim and T. S. Lee, *Sens. Actuator, B*, 2019, **281**, 343-349.
36. D. E. Wang, X. H. Gao, G. B. Li, T. Xue, H. Yang and H. Y. Xu, *Sens. Actuators, B*, 2019, **289**, 85-92.
37. T. Kim, D. Moon, J. H. Park, H. Yang, S. Cho, T. H. Park and D. J. Ahn, *Nanoscale*, 2019, **11**, 7582-7587.
38. J. L. Deng, Z. H. Sheng, K. Zhou, M. X. Duan, C. Y. Yu and L. Jiang, *Bioconjugate Chem.*, 2009, **20**, 533-537.
39. J. P. Jeong, E. Cho, D. Yun, T. Kim, I. S. Lee and S. Jung, *Polymers*, 2017, **9**, 1-9.
40. J. Luo, K. Y. Fu, H. Y. Dong and D. Y. Chen, *Chin. J. Chem. Phys.*, 2016, **29**, 749-753.
41. A. Kamphan, C. J. Gong, K. Maiti, S. Sur, R. Traiphol and D. P. Arya, *RSC Adv.*, 2017, **7**, 41435-41443.
42. P. Sun, Y. C. Fu, J. Hu, N. Hao, W. Huang and B. Jiang, *Radiat. Meas.*, 2016, **85**, 116-125.
43. S. Devic, N. Tomic and D. Lewis, *Eur. J. Med. Phys.*, 2016, **32**, 541-556.
44. A. Rink, D. F. Lewis, S. Varma, I. A. Vitkin and D. A. Jaffray, *J. Med. Phys.*, 2008, **35**, 4545-4555.
45. Y. S. Soliman, A. A. Abdel-Fattah, A. A. Hamed and A. M. M. Bayomi, *Radiat. Phys. Chem.*, 2018, **144**, 56-62.
46. M. Okaniwa, Y. Oaki, S. Kaneko, K. Ishida, H. Maki and H. Imai, *Chem. Mat.*, 2015, **27**, 2627-2632.
47. K. Y. Fu and D. Y. Chen, *Chin. J. Chem. Phys.*, 2014, **27**, 465-470.
48. M. C. Etter, *Acc. Chem. Res.*, 1990, **23**, 120-126.

49. F. H. Allen, W. D. S. Motherwell, P. R. Raithby, G. P. Shields and R. Taylor, *New J. Chem.*, 1999, **23**, 25-34.
50. G. M. J. Schmidt, *Pure Appl. Chem.*, 1971, **27**, 647-678.
51. A. Patlolla, J. Zunino, A. I. Frenkel and Z. Iqbal, *J. Mater. Chem.*, 2012, **22**, 7028-7035.
52. J. M. Kim, J. S. Lee, S. Y. Woo and D. J. Ahn, *Macromol. Chem. Phys.*, 2005, **206**, 2299-2306.
53. N. Mino, H. Tamura and K. Ogawa, *Langmuir*, 1991, **7**, 2336-2341.
54. J. M. Kim, J. S. Lee, H. Choi, D. Sohn and D. J. Ahn, *Macromolecules*, 2005, **38**, 9366-9376.
55. O. Mapazi, P. K. Matabola, R. M. Moutloali and C. J. Ngila, *Sens. Actuators, B*, 2017, **252**, 671-679.
56. T. Pattanatornchai, J. Rueangsuwan, N. Phonchai, N. Traiphol and R. Traiphol, *Colloids Surf., A*, 2020, **594**, 1-10.
57. N. Charoenthai, T. Pattanatornchai, S. Wacharasindhu, M. Sukwattanasinitt and R. Traiphol, *J. Colloid Interf. Sci.*, 2011, **360**, 565-573.
58. Q. Wang, G. Wang, X. Y. Huang and D. Y. Chen, *Chin. J. Chem. Phys.*, 2020, **33**, 357-364.
59. S. H. Park, J. Roh and D. J. Ahn, *Macromol. Res.*, 2017, **25**, 960-962.
60. X. Lu, Z. D. Zhang, X. M. Sun, P. N. Chen, J. Zhang, H. Guo, Z. Z. Shao and H. S. Peng, *Chem. Sci.*, 2016, **7**, 5113-5117.
61. P. N. Nelson, H. A. Ellis and N. A. S. White, *Spectrochim. Acta, Part A*, 2015, **145**, 440-453.
62. G. B. Deacon and R. J. Phillips, *Coord. Chem. Rev.*, 1980, **33**, 227-250.
63. K. Nakamoto, J. Fujita, S. Tanaka and M. Kobayashi, *J. Am. Chem. Soc.*, 1957, **79**, 4904-4908.
64. Y. Furutani, T. Murata and H. Kandori, *J. Am. Chem. Soc.*, 2011, **133**, 2860-2863.
65. D. A. Edwards and R. N. Hayward, *Can. J. Chem.*, 1968, **46**, 3443-3446.
66. N. Nordin, B. H. Yahaya and M. R. Yusop, *New J. Chem.*, 2018, **42**, 15127-15135.
67. R. F. P. Pereira, A. J. M. Valente, M. Fernandes and H. D. Burrows, *Phys. Chem. Chem. Phys.*, 2012, **14**, 7517-7527.
68. E. F. Marques, H. D. Burrows and M. D. Miguel, *J. Chem. Soc., Faraday Trans.*, 1998, **94**, 1729-1736.
69. J. D. Cho, J. Son, J. W. Sung, C. H. Choi, J. S. Kim, H. G. Wu, J. M. Park and J. I. Kim, *Med. Phys.*, 2020, **47**, 3204-3213.
70. J. Anyumba, D. F. Lewis, H.-Y. Shih, X. Yu, *Europe Pat.*, EP1614002A4, 2004.
71. N. A. S. White, H. A. Ellis, P. N. Nelson and P. T. Maragh, *J. Chem. Thermodyn.*, 2011, **43**, 584-590.
72. N. A. S. White and H. A. Ellis, *J. Mol. Struct.*, 2008, **888**, 386-393.
73. H. L. Bui and A. de Klerk, *J. Chem. Eng. Data*, 2013, **58**, 1039-1049.
74. L. Senak, Ashland LLC, internal work, 2018, 1-11.
75. R. G. Snyder, *J. Mol. Spectrosc.*, 1961, **7**, 116-144.
76. J. R. Nielsen and C. E. Hathaway, *J. Mol. Spectrosc.*, 1963, **10**, 366-377.
77. P. Ferloni and E. F. Westrum, *Pure Appl. Chem.*, 1992, **64**, 73-78.
78. M. L. Lynch, F. Wireko, M. Tarek and M. Klein, *J. Phys. Chem. B*, 2001, **105**, 552-561.

79. J. B. Pang, L. Yang, B. F. McCaughey, H. S. Peng, H. S. Ashbaugh, C. J. Brinker and Y. F. Lu, *J. Phys. Chem. B*, 2006, **110**, 7221-7225.
80. M. Menchon, Ashland LLC, internal report, 2017, 1.

3. Model Cocrystals of *n*-Alkyl Carboxylic Acids with Pyridyl Coformers

3.1. Introduction

It is well known that compounds with long, flexible chains are more difficult to crystallise than their short-chain counterparts, with polymers as a common example.[1, 2] For this reason, in this chapter, short-chain carboxylic acids have been employed as a substitute for PCDA in cocrystallisation experiments, which are more likely to give single crystal structures and provide an insight into the established carboxylic acid···pyridine heterosynthon.[3] In the CSD,[4] organic structures that exhibit the established $OH\cdots N_{pyridine}$ heterosynthon are common, however, the number of structures of *n*-alkyl monocarboxylic acids with pyridyl coformers is limited. As a result, a CSD search was conducted to examine any organic, aliphatic monocarboxylic acid cocrystals with pyridyl coformers already present in the literature. The search criteria involved manually identifying *n*-alkyl carboxylic acids with an intermolecular non-bonded contact from the carboxylic acid proton to a pyridyl nitrogen atom at a distance within the sum of the van der Waals radii. The pyridyl group was generalised to include 'any non-metal' atoms on the remaining five positions on the ring. The search criteria are illustrated in Figure 3.1. The CSD search results revealed 75 cocrystal structures consisting of only *n*-alkyl carboxylic acids ranging from one to eighteen carbon atoms in length, cocrystallised with various pyridyl-containing coformers. The search with the greatest number of results involved 37 (49 % of the total hits) structures of ethanoic acid cocrystallised with pyridyl structures. Additionally, over half of the total structures (44 structures, 59 %) crystallised in the triclinic $P\bar{1}$ space group, with eight (18 %) of the $P\bar{1}$ structures containing pyrazine as a coformer.

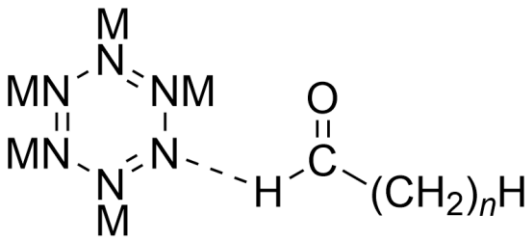

Figure 3.1. The CSD search criteria, with the carbon chain length of the carboxylic acid increasing in each search as the *n* of CH_2 groups ranged from zero to twenty

carbon atoms in length. 'NM' denotes 'any non-metal' atom, and the dashed line from N to H indicates a hydrogen bond.

Important studies by Bond demonstrate the cocrystallisation of pyrazine with *n*-alkyl carboxylic acids ranging from one to 13 carbon atoms in length, grown in glass capillaries for ambient temperature SC-XRD analysis.[5, 6] Each structure shows a 2:1 ratio of acid to pyrazine linked by a $R_2^2(7)$ hydrogen bonded motif. This smaller ring size contrasts to the $R_2^2(8)$ dimer for each of the individual carboxylic acids.[7, 8] In the cocrystal structures, the supramolecular hydrogen bond heterosynthon, OH···N, occurs from the carboxylic hydrogen atom to the nitrogen atom of pyrazine, with O···N distances in the cocrystals ranging from 2.701 – 2.760 Å. Additionally, coplanar CH···O interactions occur between the aromatic ring and neighbouring carbonyl oxygen atom of the acid. Interestingly, the mean planes through the pyrazine ring in adjacent molecules are either parallel or perpendicular, depending on the length of the carboxylic acid used. Examples are shown in Figure 3.2 and Figure 3.3.[6] Bond recognised that the cocrystallisation of the *n*-alkyl carboxylic acids with pyrazine changed the melting point properties. For instance, the melting points of the pure carboxylic acids (ranging from six to fifteen carbon atoms in length) alternate depending on whether the number of carbon atoms is odd or even. This is because the odd structures pack less efficiently due to their terminal methyl group orientations and as a result, have a reduced crystal density.[8] However, when the same acids are cocrystallised with pyrazine, the melting point alternation is inverted as the melting points of the cocrystals with an odd number of carbon atoms are greater than the even cocrystals. This is caused by the reduction in crystal density due to the unfavourable arrangements of the methyl group in each even cocrystal.[6]

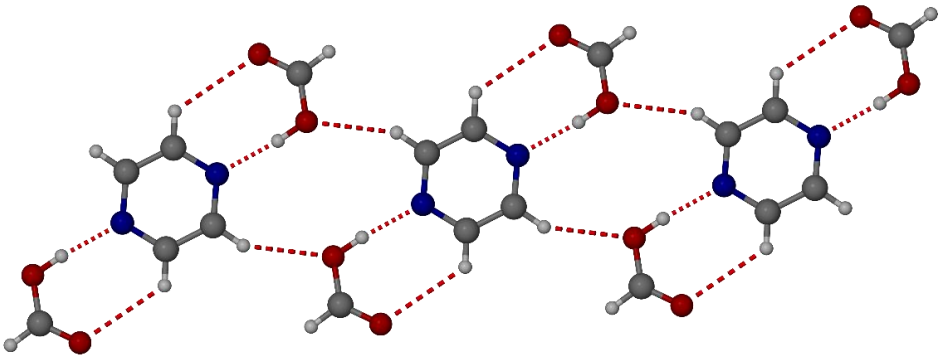

Figure 3.2. The X-ray structure of the methanoic acid and pyrazine cocrystal in a 2:1 stoichiometry, respectively.[5]

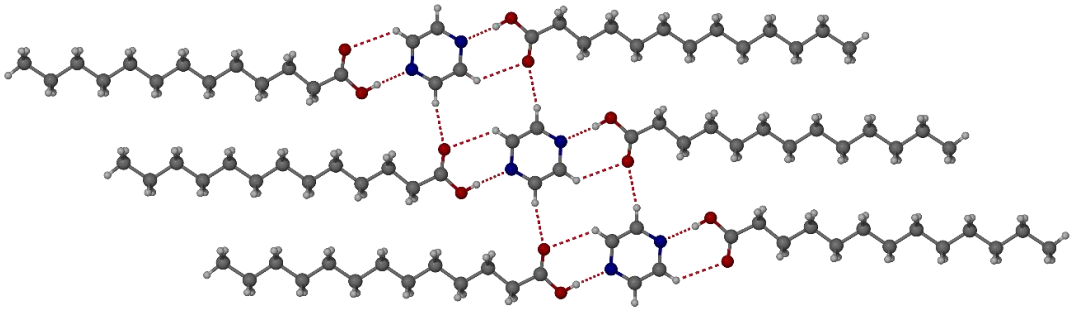

Figure 3.3. The X-ray structure of a undecanoic acid and pyrazine cocrystal, in a 2:1 stoichiometry, respectively.[6]

Out of the 75 cocrystal structures from the CSD search, there are six monocarboxylic acids cocrystallised with pyridinecarboxamide isomers, making pyridinecarboxamide the most commonly occurring pyridyl coformer in this set of results. One example is propanoic acid cocrystallised with 4-pyridinecarboxamide in a 2:1 ratio, respectively. The cocrystal is produced by dissolving solid 4-pyridinecarboxamide in excess propanoic acid and slowly cooling the solution to yield single crystals. The X-ray structure reveals that the components are joined by OH···N hydrogen bonds from the hydrogen atom of the carboxylic acid to the pyridyl nitrogen atom, at a O···N distance of 2.66 Å. Weaker CH···O hydrogen bonds are also present, with C···O distances between 3.33 Å and 3.35 Å for the two structures in the asymmetric unit, forming a $R_2^2(7)$ hydrogen bonded motif.[9] The propanoic acid molecule also forms an intermolecular hydrogen bond between the carbonyl oxygen atom of the carboxylic acid to the amine hydrogen atom of neighbouring 4-pyridinecarboxamide (O···N distances of 2.90 Å). The intermolecular hydrogen bond allows the structure to form

hydrogen-bonded chains that run parallel to the [100] direction.[9] Additionally, the carboxylic acid forms a $R_2^2(8)$ motif with the amide of 4-pyridinecarboxamide,[7] resulting in a OH···O (O···O distance of 2.64 Å) and a NH···O (N···O distances of 2.87 and 2.88 Å) heterosynthon. This N-H of 4-pyridinecarboxamide also acts as a hydrogen bond donor to a neighbouring carbonyl oxygen atom of propanoic acid (N···O distance of 2.90 Å), further linking the cocrystal chains. The chains are linked together by CH···O hydrogen bonds from the carbonyl oxygen atom of propanoic acid to a C-H on the aromatic ring (with C···O distances of 3.32 Å and 3.33 Å) along with π-stacking interactions that give layers perpendicular to (010).[9] The X-ray structure of the propanoic acid and 4-pyridinecarboxamide cocrystal is shown in Figure 3.4.

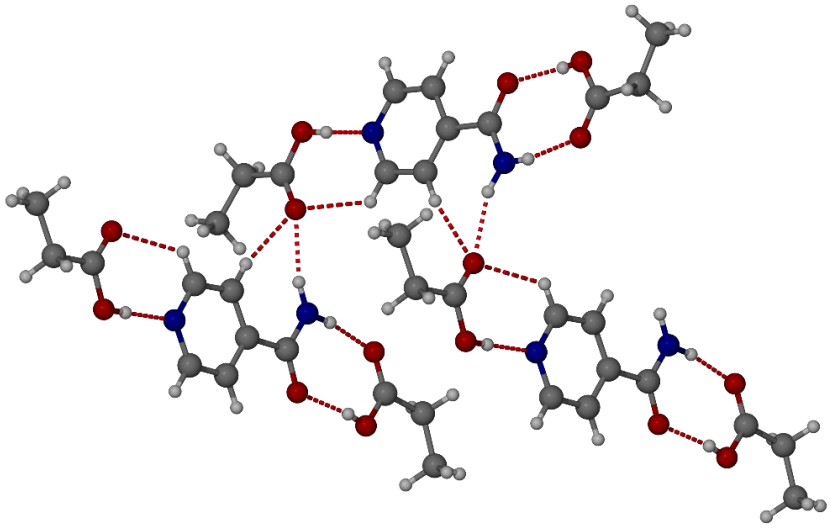

Figure 3.4. The X-ray structure of a propanoic acid and 4-pyridinecarboxamide cocrystal in a 2:1 ratio, respectively, displaying the OH···N, CH···O, NH···O, and OH···O hydrogen bonds.[9]

In addition to decanoic acid with pyrazine described by Bond,[6] a cocrystal of decanoic acid and *trans*-1,2-bis(4-pyridyl)ethylene in a 2:1 ratio, respectively, has been crystallised by the slow evaporation of acetone and ethanol (1:1). The X-ray structure shows the two coformers are joined by an OH···N hydrogen bond from the carboxyl group of the acid, to the pyridyl nitrogen atom of the base, with an O···N distance of 2.63 Å, forming a $R_2^2(7)$ hydrogen bonded motif (Figure 3.5).[10] A weak CH···O hydrogen bond is also present from the pyridyl ring to the carbonyl oxygen atom of decanoic acid, with a C···O distance of 3.44 Å. The structure also displays an overall 'Z-like' or herringbone pattern. The decanoic acid substituent of the cocrystal has a

117.7 ° bend at the α-carbon, with a C1-C4 torsion angle of 66.2 °. After the twist in the chain at C2, the remaining alkyl chain obtains an all-*trans* conformation with torsion angles clustered close to either −180 ° or +180 °.[10] The alkyl chains in the same layer are separated by a C10-C10' distance of 5.14 Å, with the closest distance between adjacent alkyl chains (C1-C3') is 3.96 Å.

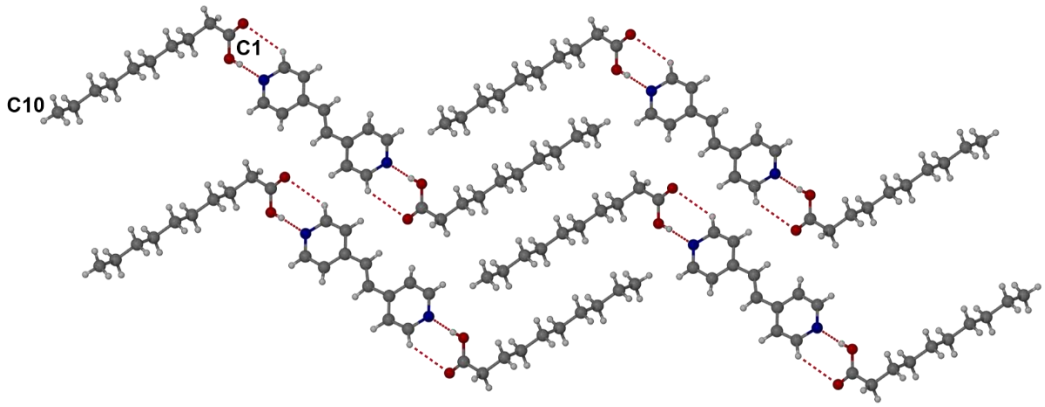

Figure 3.5. The X-ray structure of decanoic acid and *trans*-1,2-bis(4-pyridyl)ethylene cocrystal in a 2:1 ratio, respectively, showing the CH···N and weak CH···O hydrogen bonds. The crystal packing structure is displayed in the crystallographic (100) axis.[10]

The cocrystal structure with the longest *n*-alkyl chain hydrogen bonded to a pyridyl coformer in the CSD is the 1:1 structure of octadecanoic acid and 3-pyridinecarboxamide formed from the slow evaporation of acetone at room temperature. The X-ray structure reveals a lamellar structure with four different types of hydrogen bonding interactions (Figure 3.6).[11] A hydrogen bond forms between the carboxyl hydrogen atom of the acid to the pyridyl nitrogen atom (OH···N) at an O···N distance of 2.69 Å, with weak CH···O interactions, at a C···O distance of 3.35 Å to form a $R_2^2(7)$ hydrogen bonded motif. In addition, a hydrogen bond dimer with an $R_2^2(8)$ motif forms between the amide group of 3-pyridinecarboxamide to an additional 3-pyridinecarboxamide molecule consisting of NH···O hydrogen bonds at a N···O distance of 2.94 Å. This amide group is involved with further hydrogen bonding, as each of the amide nitrogen atoms act as hydrogen bond donors to carbonyl oxygen atoms on neighbouring 3-pyridinecarboxamide molecules (N···O distance of 2.90 Å) to create a hydrogen-bonded network. The alkyl chain of each octadecanoic acid molecule are in an all-*trans* conformation with torsion angles clustered close to either −180 ° or +180 °, and pack in a tail-to-tail bilayer. The aliphatic chains are

separated by a (C18-C18') distance of 5.04 Å between neighbouring cocrystals, with the closest distance between aliphatic chains occurring from C1-C3' atoms at 4.06 Å.

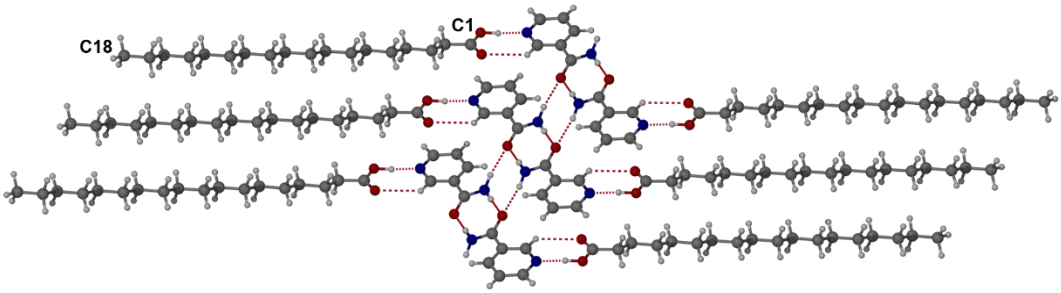

Figure 3.6. The X-ray structure of a 3-pyridinecarboxamide and octadecanoic acid cocrystal, showing the OH···N, NH···O, and CH···O hydrogen bonding environments displayed in the crystallographic (100) axis.[11]

As the long aliphatic chains of PCDA are difficult to crystallise and characterise by X-ray crystallography without radiation decay of the crystals, the use of non-radiation sensitive surfactants will be employed, focussing on the OH···N supramolecular heterosynthon in the presence of aliphatic carboxylic acids. In this chapter we report the cocrystallisation of varying length *n*-alkyl carboxylic acids with pyridyl-containing coformers, through solution crystallisation and mechanochemical synthesis methods. The resulting cocrystals are designed to model the interactions and molecular packing of photosensitive PCDA cocrystals, intended to further shed light on the topochemistry of PCDA when incorporated into different multicomponent solid forms.

3.2. Results and Discussion

3.2.1. Solution Crystallisations

A series of crystallisation attempts were carried out according to Table 3.1, whereby different length *n*-carboxylic acids, butanoic acid (butA), pentanoic acid (pentA), hexanoic acid (hexA), and eicosanoic acid (eicoA) were chosen for cocrystallisation with bifunctional pyridyl or related coformers 2,2'-bipyridyl (2bipy), 4,4'-bipyridyl (4bipy), 4,4'-azopyridine (azp), *trans*-1,2-bis(4-pyridyl)ethylene (bpe), pyrazine (pyz), and pyrazine carboxamide (pca) (Figure 3.7). The specific compounds were chosen as they are readily accessible and likely to form cocrystals as opposed to salts.

Cocrystals are expected because the carboxylic acids are weak acids (with pK_a values of approximately 4.5-5.0)[12] and therefore unlikely to protonate the pyridyl base (pK_a values of the conjugate acids range from approximate values of 0.5-5.5 depending on the base).[13, 14] When cocrystallised, it is expected that each bifunctional heterocyclic base will be joined to two acid molecules by the OH···$N_{pyridyl}$ heterosynthon from the carboxyl hydrogen atom to the pyridyl nitrogen atom, acting as a hydrogen bond acceptor. In each case, 50 mg of monocarboxylic acid was combined with a pyridyl coformer in a 2:1 molar ratio respectively, with 1-5 mL of solvent. The mixtures were briefly sonicated and allowed to stand to bring about slow evaporation of the solvent under ambient conditions. The details of each experiment are given in the experimental section. These experiments resulted in three novel cocrystal structures consisting of 2butA·bpe, 2pentA·bpe, and 2eicoA·azp, all in 2:1 ratios, respectively.

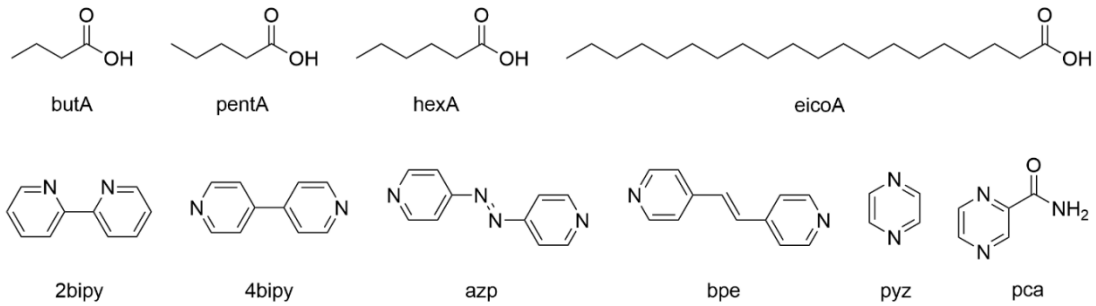

Figure 3.7. The compound key for the *n*-alkyl carboxylic acids and bifunctional pyridyl related coformers.

Coformers	**ButA** Water/Acetone /Ethanol	**PentA** Water/Acetone /Ethanol	**HexA** Acetone/Ethanol	**EicoA** Acetone/Ethanol
2Bipy	N/N/N	N/N/N	N/N	Y/Y
4Bipy	Y/Y/Y	N/N/N	**Y**/Y	N/Y
Azp	Y/**Y**/N	N/Y/Y	**Y**/Y	N/**Y**
Bpe	**Y**/**Y**/Y	**Y**/Y/Y	Y/N	N/Y
Pyz	N/N/N	N/N/N	N/N	N/Y
Pca	**Y**/Y/Y	N/**Y**/Y	Y/Y	N/Y

Table 3.1 The combinations of carboxylic acids and pyridyl compounds used in different solution crystallisation experiments. Yes (Y) or no (N) indicates whether crystals formed regardless of the quality. The experiments in **red** gave novel cocrystals characterised by single crystal X-ray diffraction. The experiments in **blue** resulted in crystals of the respective pyridyl coformer which are already reported in the CSD,

while the experiment in **green** yielded a new chloro-substituted coformer not before reported.

Saturated short-chain carboxylic acids, butA and pentA, formed diffraction quality cocrystals with bpe in ratios of 2:1, respectively. The X-ray structures of both cocrystals show very similar hydrogen bonding interactions, namely strong OH···N bonds from the carboxylic hydrogen atom to the pyridyl nitrogen atom, and weak CH···O interactions from the C-H groups of the pyridyl ring to the carbonyl oxygen atom of the carboxylic acid. These two interactions form a hydrogen-bonded dimer $R_2^2(7)$ motif.[7] For 2butA·bpe (Figure 3.8a), O···N and C···O distances are 2.658(1) Å and 3.254(2) Å, respectively. While 2pentA·bpe (Figure 3.9a) has hydrogen bond distances that are marginally longer, with O···N and C···O distances of 2.6725(2) Å and 3.2772(2) Å, respectively. Both cocrystal structures crystallise in the $P\bar{1}$ space group with the inversion centre present on the ethylene bond of the pyridyl coformer. Additionally, both cocrystals contain face-to-face π-π stacking interactions as the mean planes of the molecules are coplanar. For the 2butA·bpe cocrystal, the pyridyl-pyridyl centroid distances are 3.5335(8) Å with an offset of only 0.9404(16) Å, while the 2pentA·bpe cocrystal displays a pyridyl-pyridyl centroid distance of 3.5323(3) Å and an offset of 1.0448(4) Å. Interestingly, the alkyl chain of butA in the 2butA·bpe cocrystal adopts an all-*trans* conformation with a C1-C4 torsion angle of 173.9 °, while the alkyl chain of pentA in 2pentA·bpe contains both *trans* and *gauche*-conformations with a C1-C4 torsion angle of 174.4 ° and a C2-C5 torsion angle of 71.7 °. Combinations of *anti* and *gauche* conformations are commonly observed in the short alkyl chains of organic structures, however, a combination of conformations have been recognised in structures containing up to 18 carbon atoms in length.[15-20] A long-chain structure with a similar end-*gauche* conformation of the alkyl chain has been reported in a dodecyl trimethylammonium salt with a C12-C15 torsion angle of 70.4 °.[21] In the 2butA·bpe cocrystal, the closest distance between adjacent alkyl chains occurs at a C1-C4' distance of 4.6266(17) Å, while in the 2pentA·bpe cocrystal, the same atoms of the chain give a shorter distance of 4.5963(4) Å, and in both cases, the cocrystals stack in a tail-to-tail arrangement (Figure 3.8b and Figure 3.9b). The alkyl chains are separated by a translational repeat distance (C4-C4') of 4.142(3) Å in 2butA·bpe and by a C5-C5' distance of 3.9938(3) Å in 2pentA·bpe. Additionally, the tilt angles of each carboxylic acid respective to the translational axis

is 43.3 ° for 2butA·bpe and 18.9 ° in 2pentA·bpe. The 2butA·bpe cocrystal was left undisturbed for two years in the original crystallisation vial which resulted in the formation of large single crystals of the same material (identified by X-ray structure determination), demonstrating the stability of the cocrystal (Figure 3.10).

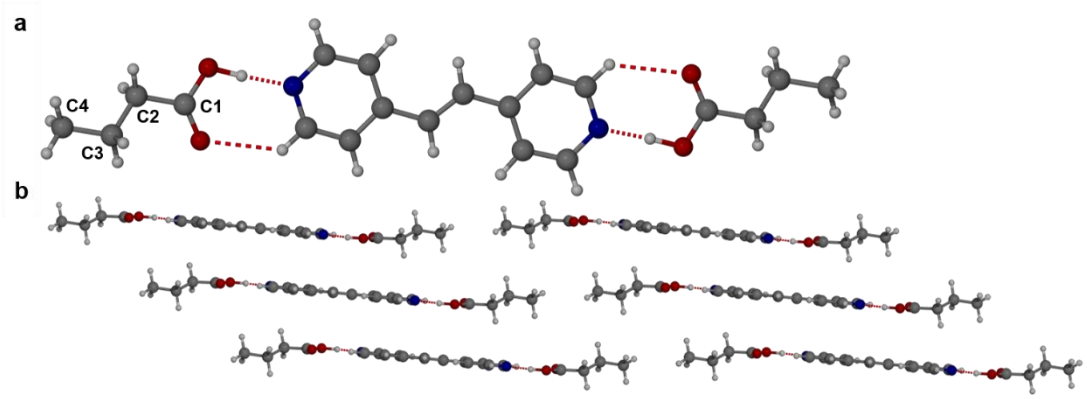

Figure 3.8. a) The X-ray structure of a 2:1 butanoic acid and *trans*-1,2-bis(4-pyridyl)ethylene (2butA·bpe) cocrystal in the crystallographic (001) axis displaying CH···N and weak CH···O hydrogen bonds. b) The cocrystal packing diagram showing a tail-to-tail packing arrangement.

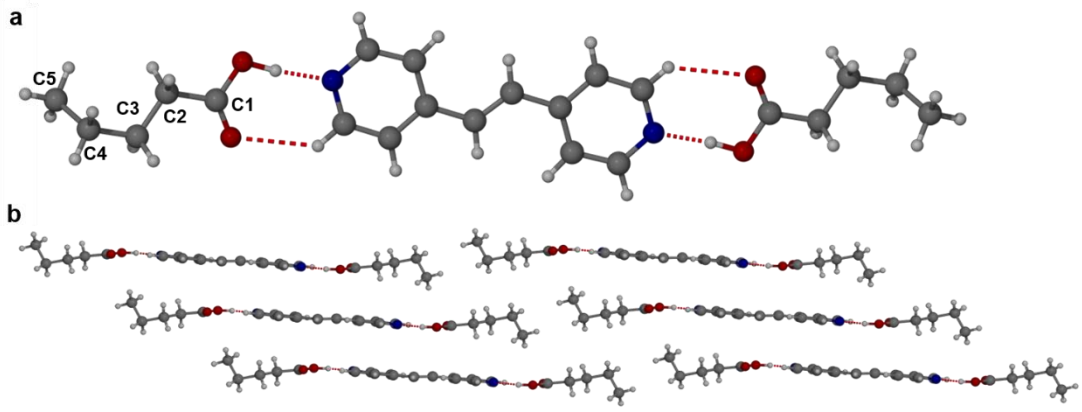

Figure 3.9. a) The X-ray structure of a 2:1 cocrystal containing pentanoic acid and *trans*-1,2-bis(4-pyridyl)ethylene (2pentA·bpe) in the crystallographic (001) axis, displaying CH···N and weak CH···O hydrogen bonds, and b) the cocrystal packing diagram showing a tail-to-tail arrangement.

Figure 3.10. A photograph of the large crystals formed from the slow evaporation of solvent after two years.

The X-ray structure of 2eicoA·azp acid shows a 2:1 stoichiometry, respectively, with OH···N hydrogen bonds occurring from the carboxylic hydrogen atom of eicoA to the pyridyl nitrogen atom of azp, at an O···N distance of 2.6785(10) Å (Figure 3.11a). A weak CH···O interaction also occurs from the C-H of the pyridyl ring to the carbonyl oxygen atom of eicoA, at a C···O distance of 3.2891(12) Å to complete the hydrogen-bonded dimer $R_2^2(7)$ motif.[7] Additional weak CH···O hydrogen bonds also occur between layers from the C-H of the pyridyl rings to the carbonyl oxygen atom on an adjacent eicoA molecule, at a C···O distance of 3.1915(11) Å. Though the mean planes of the molecules are coplanar, the pyridyl-pyridyl centroid distance is 4.233(3) Å with an offset of 2.445(7) Å, and therefore, no π-π interactions occur between planes. Additionally, the long aliphatic chains of eicoA display an all-*trans* conformation with the eicoA chains in a tail-to-tail arrangement in the packing diagram (Figure 3.11b). As eicoA contains 20 carbon atoms, this carboxylic acid coformer has the most similar carbon chain length to PCDA, and therefore, is the cocrystal to best predict how the PCDA chains will pack when cocrystallised with azp. For instance, the calculated PXRD pattern of 2eicoA·azp demonstrates a lamellar progression of (001) peaks from 2.7 – 13.3 °, the same progression that is observed for PCDA (page 69), indicating a bilayer arrangement of the cocrystal molecules. Additionally, pure eicoA (with the crystal structure determined from PXRD analysis) has a C10-C13' distance between adjacent alkyl chains of 5.0875 Å,[22] while PCDA itself has an inter-dialkyne C1-C4' distance (spanning carbon atoms C10-C13) of 3.7120(13) Å. However, when eicoA is cocrystallised with azp, the closest distance between the alkyl chains occurs between C10 and C13' at 4.044(6) Å, thereby showing the influence of cocrystallisation on crystal packing compared to the pure acids. Also,

the translational repeat distance (C20-C20') and tilt angles of pure eicoA and cocrystallised eicoA with azp is 4.965 Å[22] and 40.6 °, and 5.460(3) Å and 43.4 °, respectively. Therefore, as cocrystallisation changes the stacking of the carboxylic acid molecules, it can be assumed that the cocrystallisation of PCDA with azp and related bipyridyl coformers will similarly alter the molecular packing properties and hence the topochemistry of the system.

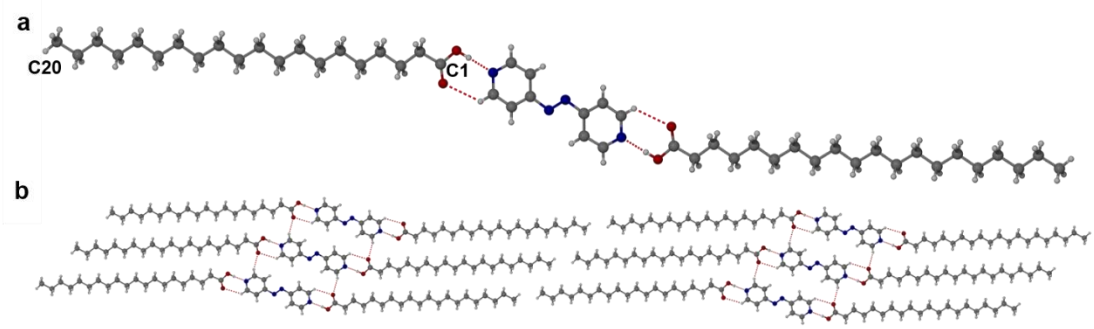

Figure 3.11. a) The X-ray structure of an eicosanoic acid and 4,4'-azopyridine (2eicoA·azp) cocrystal in the crystallographic (001) axis displaying the OH···N and weak CH···O hydrogen bonds. b) The packing diagram of 2eicoA·azp shown in the crystallographic (100) axis displaying weak CH···O interactions between layers.

The cocrystallisation of butA with azp in a 2:1 stoichiometry was attempted. Small crystals were observed after two weeks of slow evaporation of solvent at room temperature but were not suitable for X-ray structure determination. The sample was sealed and left undisturbed for two years. After this time, large crystals were observed, occurring in two types of crystal habit, either elongated prisms or platelets. SC-XRD analysis revealed that the prisms consist of an azp monohydrate that has already been reported in the CSD (refcode KUGKAZ).[23] The platelets proved to be crystals of mono-chloro azopyridine (azp-Cl). The structure was determined by SC-XRD although precision is limited due to twinning and disorder. It can be assumed that the chlorine-containing impurity originated from the azp sample bottle. The disordered chlorine atoms are present on the C2 and C4 atoms in the pyridyl ring with occupancies of 0.44:0.06. Two azp-Cl molecules are present in the unit cell, with an inversion centre present on the azo bond at the centre of the molecule, the disorder also occurs on the symmetry-related ring, resulting in a molecular formula of $C_{10}H_7N_4Cl$. The chlorine atoms of the minor component are omitted from the structure diagram in Figure 3.12. Intermolecular CH···Cl hydrogen bonds occur in both layers of the

molecules in the unit cell, at C···Cl distances of 3.76 Å, though aryl halide substituents are notably very weak hydrogen bond acceptors.[24-26] Additionally, intermolecular CH···N hydrogen bond interactions occur from the hydrogen atom of the pyridyl ring to a neighbouring pyridyl nitrogen atom, at C···N distances of 3.50 Å and 3.51 Å. The pyridyl rings in both layers are coplanar, with the pyridyl rings in one layer displaying face-to-face π-π stacking interactions at pyridyl ring centroids distances of 3.7694(4) Å and an offset of 1.5954(3) Å.

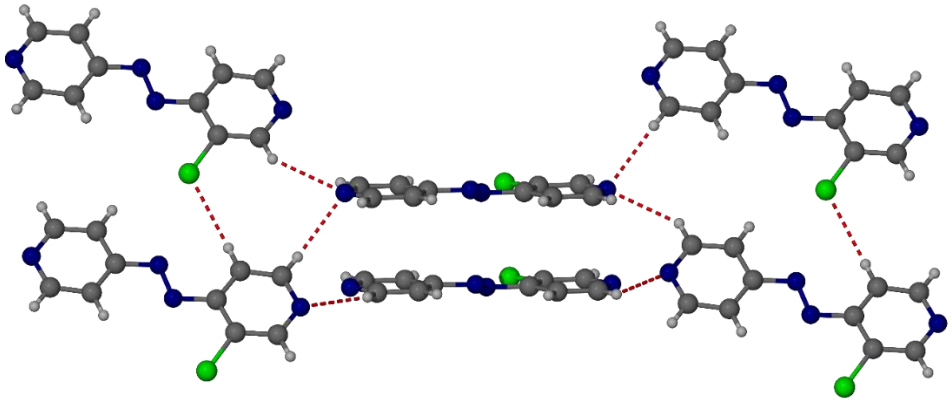

Figure 3.12. The X-ray structure of a disordered mono-chloro-substituted 4,4'-azopyridine with CH···N and CH···Cl interactions. Minor components are omitted.

In addition to monocarboxylic acid cocrystallisation with pyridyl coformers, aromatic dicarboxylic acids, namely 2,5-pyridinedicarboxylic acid (pdA) and 4,4'-biphenyldicarboxylic acid (bpdA), were also used to cocrystallise pyridyl coformers (Figure 3.13). Any structural results would allow the further investigation of the OH···N heterosynthon, especially with the cocrystal structures currently absent from the CSD. Only two experiments consisting of pdA-4bipy (1:1) and pdA·azp (1:1) in 3 mL of acetone yielded crystals after the slow evaporation of solvent at room temperature. However, in both cases, the crystal quality was insufficient for SC-XRD analysis. No crystals of bpdA with any pyridyl coformer formed in 3 mL of acetone under the same conditions outlined above.

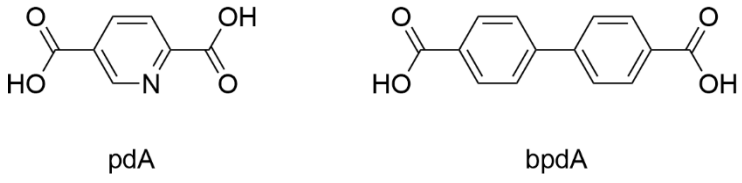

Figure 3.13. The structures of pdA and bpdA.

3.2.2. Mechanochemistry

The formation of cocrystals by grinding is well-established in the literature, and has an important role in the pharmaceutical industry.[27-31] The grinding of different cocrystal components can be achieved manually or mechanically and is an attractive method for cocrystal synthesis due to the simplicity and relatively solvent-free approach. The two main techniques of mechanochemistry involve the grinding of the neat components, or through the addition of a drop of solvent to further encourage cocrystallisation (LAG), whereby the reactant solubility does not affect the outcome of the synthesis.[32] In addition to the solution cocrystallisation experiments, cocrystal synthesis by mechanochemistry was also explored using the same compounds listed in Table 3.1 that formed crystalline material (regardless of quality). The monocarboxylic acids and pyridyl coformers were manually ground together with a pestle and mortar in 2:1 ratio at 30-minute intervals, either neat or with a drop of acetonitrile to facilitate LAG. The formation of a cocrystal was confirmed by PXRD and FTIR spectroscopy. The cocrystals that formed from the neat grinding of components consisted of 2butA·4bipy, 2pentA·bpe, 2pentA·azp, and 2hexA·4bipy, all in 2:1 stoichiometries, respectively.

The cocrystals that formed with 4bipy display PXRD patterns that are indicative of new materials, as they contain additional peaks that are not present in the PXRD patterns of the pure coformers alone. For instance, the experimental PXRD of 2butA-4bipy cocrystal shows new peaks at 6.2, 12.3, 15.6, 16.2, and 26.9 ° (Figure 3.14). Similarly, for cocrystal 2hexA-4bipy, the experimental PXRD reveals peaks that do not correlate with either of the starting materials are 5.3, 15.6, 17.5, 23.5, 24.7, and 27.4 ° (Figure 3.14). For both cocrystals, the FTIR spectra display a broad peak at 2458 cm^{-1} attributable to the O-H stretch of the hydrogen-bonded acid.[33-35] Additionally, a broad peak at 1906 cm^{-1} is present which is indicative of the N-H stretch of the OH···$N_{pyridyl}$ interaction (Figure 3.15).[36, 37] Also, the carbonyl stretches of the cocrystals are slightly red-shifted compared to their corresponding free acids. For example, the free acids of butA and hexA have carbonyl bands of 1702 cm^{-1} and 1701 cm^{-1}, respectively, while the 2butA·4bipy and 2hexA·4bipy have carbonyl bands of 1690 cm^{-1} and 1685 cm^{-1}, respectively. The small shift in carbonyl stretches of the acids before and after cocrystallisation is likely due to the weak intermolecular CH···O

hydrogen bond present in the cocrystals from the C-H of the pyridyl ring to the carbonyl oxygen atom of butA and hexA.

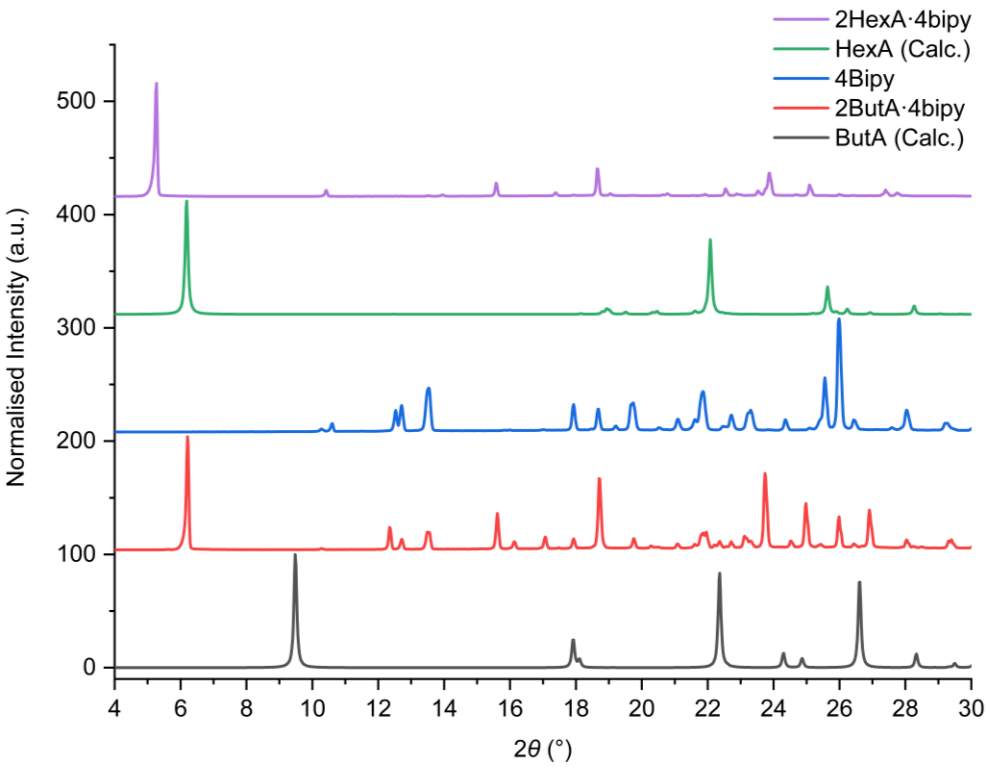

Figure 3.14. The PXRD patterns of 2butA·4bipy and 2hexA·4bipy cocrystals and their respective coformers.[8]

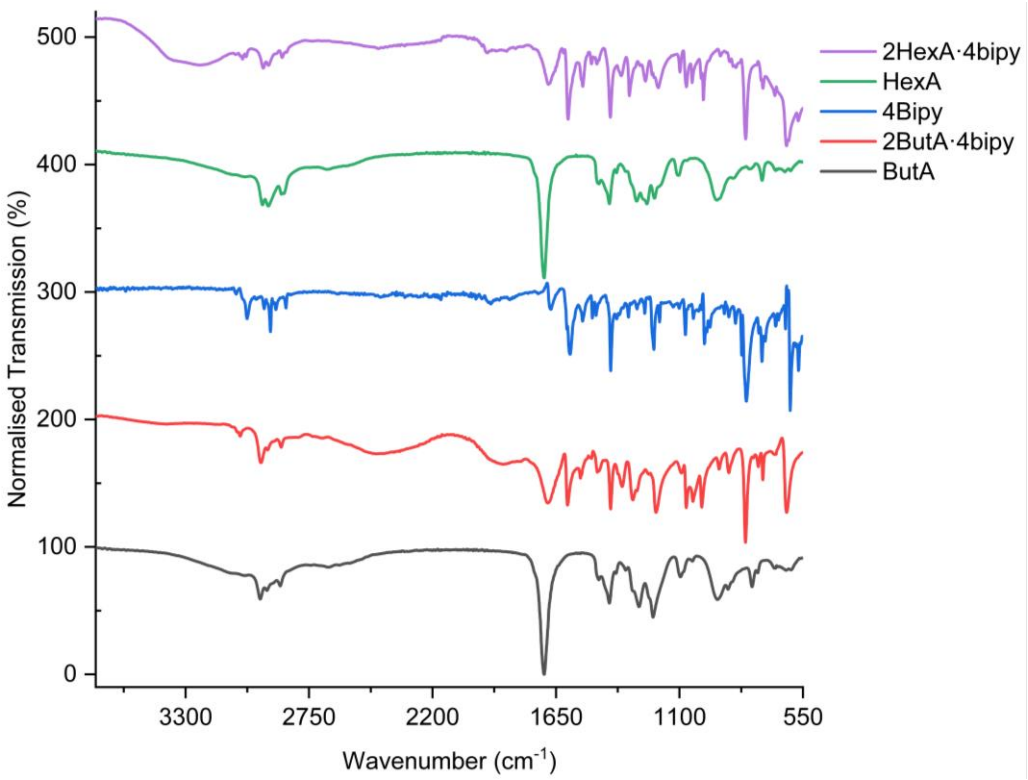

Figure 3.15. The FTIR spectra of the 2butA·4bipy and 2hexA·4bipy cocrystals and the respective coformers butA, hexA, and 4bipy.

Though the solution crystallisation experiments of butA, pentA, hexA, and eicoA with 4bipy did not yield suitable single crystals for X-ray diffraction, the cocrystal structures of methanoic acid (methA) and ethanoic acid (ethA) with 4bipy have been reported in the CSD (Refcodes GOKCEQ[38] and SITDIJ,[39] respectively). Both cocrystal structures consist of OH···N interactions with O···N distances ranging between 2.61 Å and 2.68 Å, and weak CH···O interactions at C···O distances between 3.24 Å and 3.43 Å. In both instances, the pyridyl rings have dihedral angle of 28.2 ° and 31.8 ° which correlate to *gauche* conformations, thereby causing two different hydrogen bond distances between the pyridyl hydrogen bond acceptors and the carboxylic acid hydrogen bond donors. Comparisons of the calculated PXRD patterns of 2methA·4bipy and 2ethA·4bipy with the experimental PXRD patterns of 2butA·4bipy and 2hexA·4bipy are shown in Figure 3.16. The progression of initial peaks from low to high 2θ values are inversely proportional to the carbon chain length of the carboxylic acid in the cocrystal, correlating with increasing unit cell size with increasing chain length. For example, the peaks 5.3, 6.2, 7.9, and 8.5 ° belong to 2hexA·4bipy, 2butA·4bipy, 2ethA·4bipy, and 2methA·4bipy, respectively.

Additionally, smaller initial 2θ values are correlated to a larger unit cell indicating a larger structure, suggesting that the 2hexA·4bipy structure has the largest unit cell when compared to the other 4bipy cocrystals.

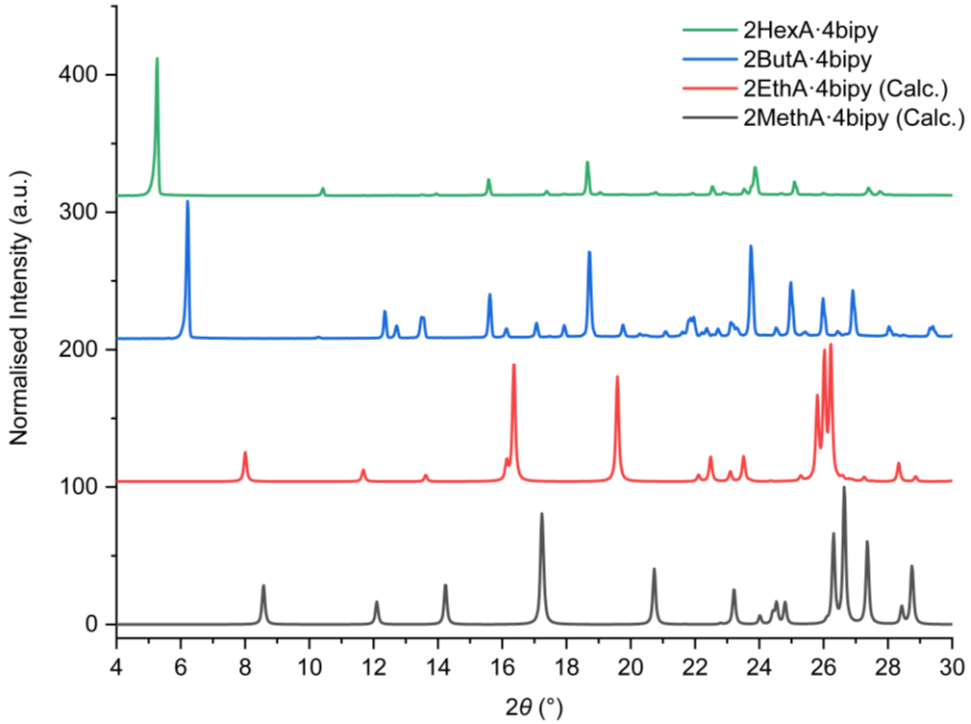

Figure 3.16. The calculated PXRD patterns of cocrystals 2methA·4bipy and 2ethA·4bipy, and the experimental patterns of 2butA·4bipy and 2hexA·4bipy.[38, 39]

The pentA cocrystals with azp and bpe that formed by the neat grinding of reagents display new peaks when compared to the PXRD patterns of the starting materials, evident by the emergence of peaks in the 2pentA·azp cocrystal at 6.2, 17.1, and 20.7 °, and in the 2pentA·bpe cocrystal at 7.3, 14.5, 14.9, 16.2, 19.6, 23.6 and 23.9 ° (Figure 3.17). Without the X-ray structure of 2pentA·azp it is difficult to directly compare the two pentA cocrystals on a molecular level, however, it can be assumed that the 2pentA·azp cocrystal has a larger unit cell than the 2pentA·bpe cocrystal, due to the smaller initial peak at 6.2 ° compared to 7.3 ° in 2pentA·bpe. The shift of the initial first peak in each pattern reflects the slight difference in packing in the cocrystals, as azp and bpe are of an almost identical size and molecular weight. In addition to PXRD analysis, FTIR analysis for both cocrystals show broad bands at 2481 cm^{-1} and 1905 cm^{-1} and can be attributed to the stretching modes of the O-H and N-H involved in the OH···$N_{pyridyl}$ interaction, respectively (Figure 3.18).[34, 37, 40] Additionally, the carbonyl stretches are slightly red-shifted in each cocrystal when compared to the pure

acids, which is indicative of hydrogen-bonded systems.[41] For instance, the free acid of pentA has a carbonyl stretch of 1704 cm^{-1} and shifts to 1701 cm^{-1} in 2pentA·azp and 1699 cm^{-1} in 2pentA·bpe. The shifts in carbonyl stretches are due to the weak intermolecular CH···O hydrogen bonds present in the structures, occurring from a pyridyl hydrogen atom adjacent to the carbonyl oxygen atom of pentA.

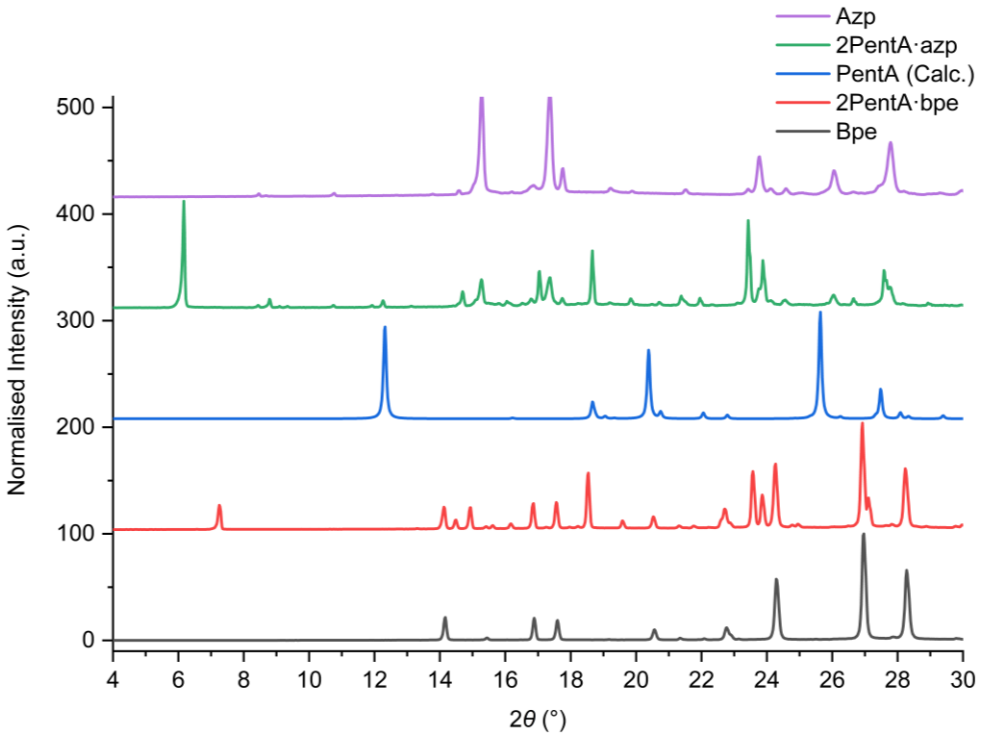

Figure 3.17. The PXRD patterns of cocrystals 2pentA·azp and 2pentA·bpe with the respective coformers.

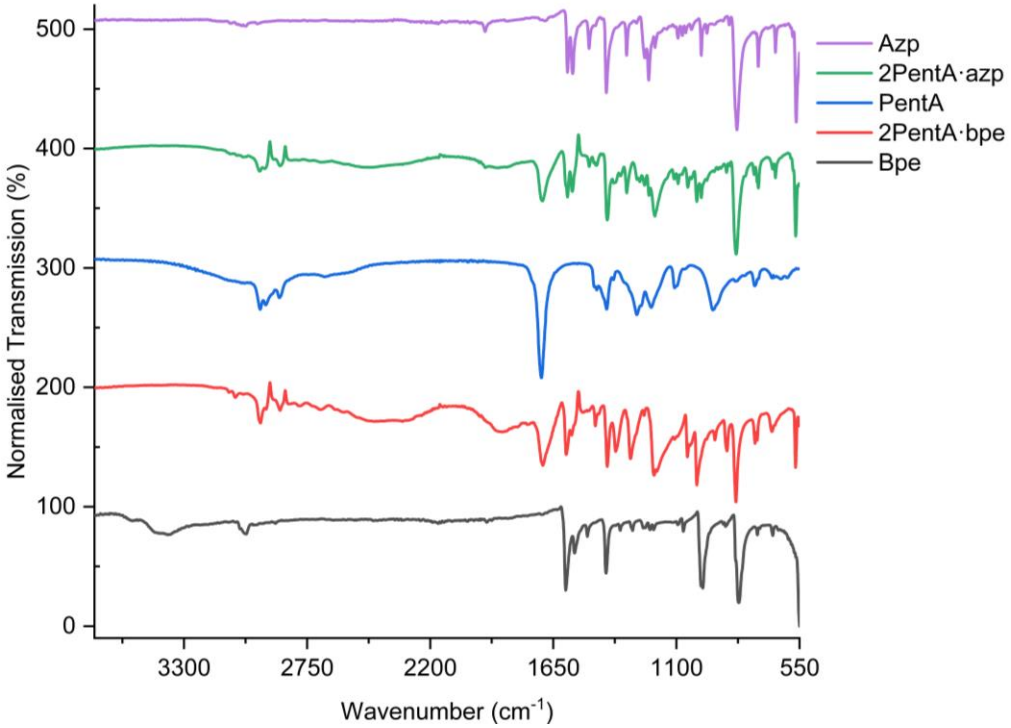

Figure 3.18. The FTIR spectra of the 2pentA·azp cocrystal and the coformers pentA and azp. Baseline artefacts are present in the spectra of 2pentA·azp and 2pentA·bpe.

The process of grinding reagents to form cocrystals will not necessarily yield the same cocrystal as solution-based crystallisation experiments,[42, 43] however, we have demonstrated that mechanochemistry and solution crystallisations form the same stable cocrystal in each case, for 2pentA·bpe, 2butA·bpe, and 2eicoA·azp. The experimental PXRD pattern of 2pentA·bpe prepared from the manual grinding of the coformers, compared to the PXRD pattern calculated by the X-ray structure from the solution crystallisation of the coformers reveals an offset in peaks, along with additional peaks in the experimental pattern attributable to unreacted bpe (Figure 3.19). The offset is most noticeable for the initial peaks of 7.3 ° and 7.9 ° in the experimental and calculated patterns, respectively. A slight offset in peaks is expected, due to the difference in the temperature the experimental data (288 K) and data calculated from the single crystal structure (120 K) were obtained. There are also additional peaks present in the experimental pattern when compared to the calculated pattern, potentially due to a phase change, though this observation requires further investigation. Additional work would involve obtaining an experimental pattern from the crystals used in the single crystal experiment and analysing the crystals of 2pentA·bpe at higher temperatures.

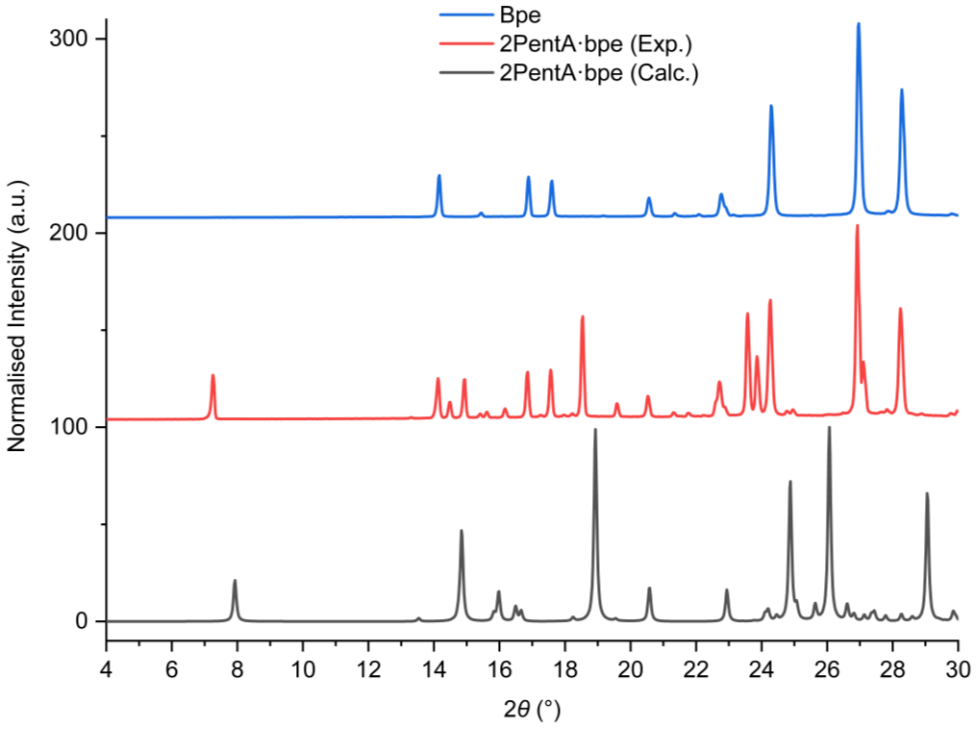

Figure 3.19. A comparison of the experimental and calculated PXRD patterns of the 2pentA·bpe cocrystal and the experimental pattern of bpe for comparison.

In addition to manual grinding, mechanical grinding of coformers was also explored using a mixer mill. The combination of butA and bpe in a mixer mill for 45 minutes at a frequency of 20 s^{-1} gives rise to a product with an experimental PXRD pattern comparable to the calculated PXRD pattern from the X-ray structure of 2butA·bpe. Though the calculated and experimental patterns have similarities, the peaks are offset because of the difference in unit cell size at the different temperatures the data were obtained at (Figure 3.20). The PXRD patterns of the reactants are also included in Figure 3.20 for comparison. The experimental pattern of 2butA·bpe confirms the formation of a cocrystal by the presence of peaks at 7.5, 15.0, and 19.0 °, for example. Coformers eicoA and azp were also ground by mechanical mixer mill in a 2:1 ratio and analysed by PXRD which suggests the formation of a cocrystal due to the presence of peaks at 19.4, 21.1, and 22.5 ° that do not correspond to either coformer. However, the comparison of the experimental and calculated PXRD pattern show significant differences, especially with the presence of a peak at 6.0 ° which is not observed in the calculated pattern and therefore, may be due to residual unreacted eicoA in the bulk sample (Figure 3.21). There may therefore be a phase change between ambient conditions and the temperature at which the X-ray structure was recorded, however,

due to the COVID-19 pandemic, the collection of this data at room temperature was not possible. The FTIR analysis of both 2butA·bpe and 2eicoA·azp reveal the same broad shifts of the O-H and N-H stretches of the OH···$N_{pyridyl}$ interaction, at 2408 cm^{-1} and 1881 cm^{-1} for 2butA·bpe, and 2499 cm^{-1} and 1904 cm^{-1} for 2eicoA·azp (Figure 3.22).[34, 37, 40] The cocrystals also display red-shifted carbonyl stretches compared to the pure acids. The carbonyl stretches of the free acids are at 1702 cm^{-1} and 1700 cm^{-1} for butA and eicoA, respectively, and shift to 1693 cm^{-1} and 1694 cm^{-1} in 2butA·bpe and 2eicoA·azp, respectively, implying stronger hydrogen bonding of the cocrystals compared to the pure acids.

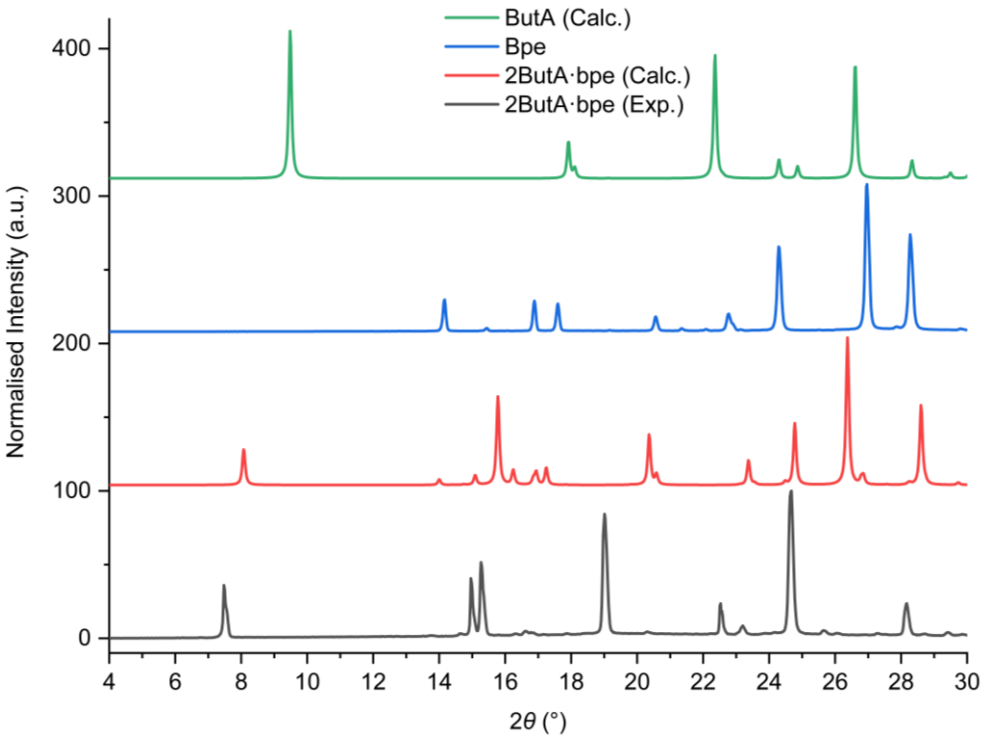

Figure 3.20. The experimental and calculated PXRD patterns of the 2butA·bpe cocrystal and its coformers.

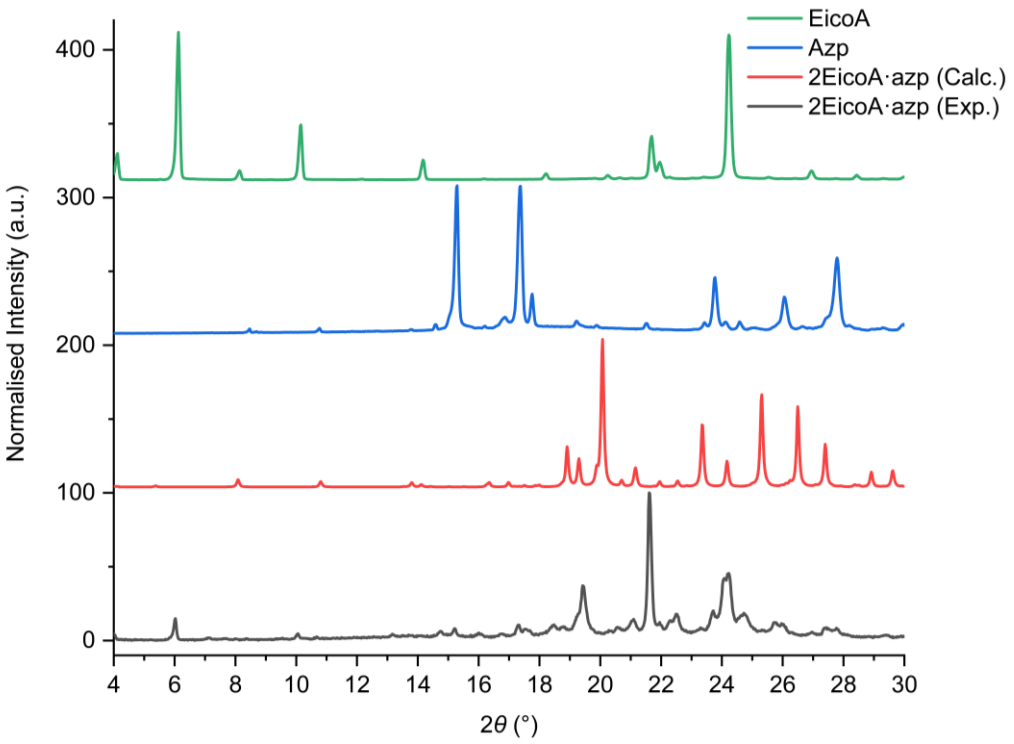

Figure 3.21. The experimental and calculated PXRD patterns of the 2eicoA·azp cocrystal and experimental PXRD patterns of the respective coformers.

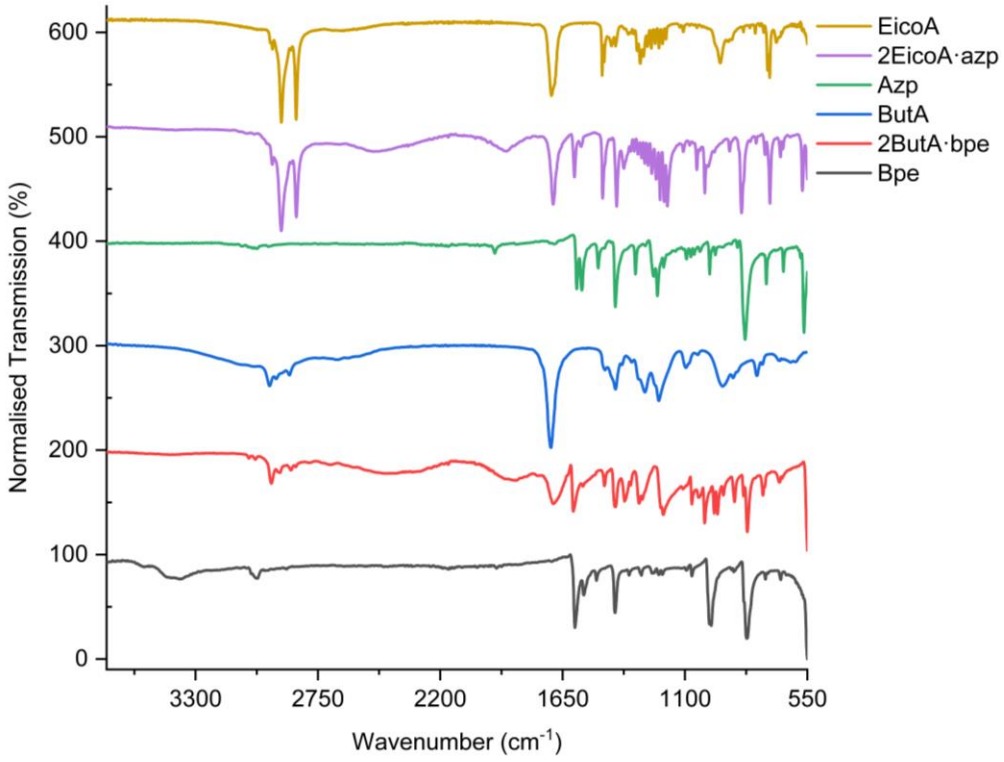

Figure 3.22. The FTIR spectra of the cocrystals 2butA·bpe and 2eicoA·azp and the respective coformers.

In contrast with the aliphatic monocarboxylic acid coformers used, aromatic dicarboxylic acids, pdA and bpdA both formed cocrystals with 4bipy in 1:1 stoichiometries through manual LAG with acetonitrile for thirty minutes. The PXRD patterns of these products pdA·4bipy and bpdA·4bipy cocrystals along with the PXRD patterns of the coformers are shown in in Figure 3.23. The peaks that are unique to pdA·4bipy and do not belong pdA or 4bipy are 16.6 ° and 17.4 °, however, pdA·4bipy contains unreacted 4bipy, evident by the almost identical patterns, and as a result, the experiment is required to be repeated. The PXRD pattern of bpdA·4bipy shows different peaks of the cocrystal compared to its coformers at 16.5 ° and 18.2 °. The FTIR spectra of the cocrystals pdA·4bipy and bpdA·4bipy reveal carbonyl stretches at 1709 cm^{-1} and 1689 cm^{-1}, respectively. The carbonyl peak of pdA·4bipy is red-shifted from the pure acid with a carbonyl peak at 1718 cm^{-1}. However, the carbonyl stretch of bpdA·4bipy is at a higher wavenumber than the pure acid (1674 cm^{-1}), which implies weaker hydrogen bonding within the cocrystal, compared to the stronger hydrogen bonding of pdA·4bipy. Salt formation of pdA·4bipy has been ruled out as the ΔpK_a of pdA and 4bipy is within the three base units, with the very similar pK_a values of 3.24[44] and 3.27,[13] respectively.

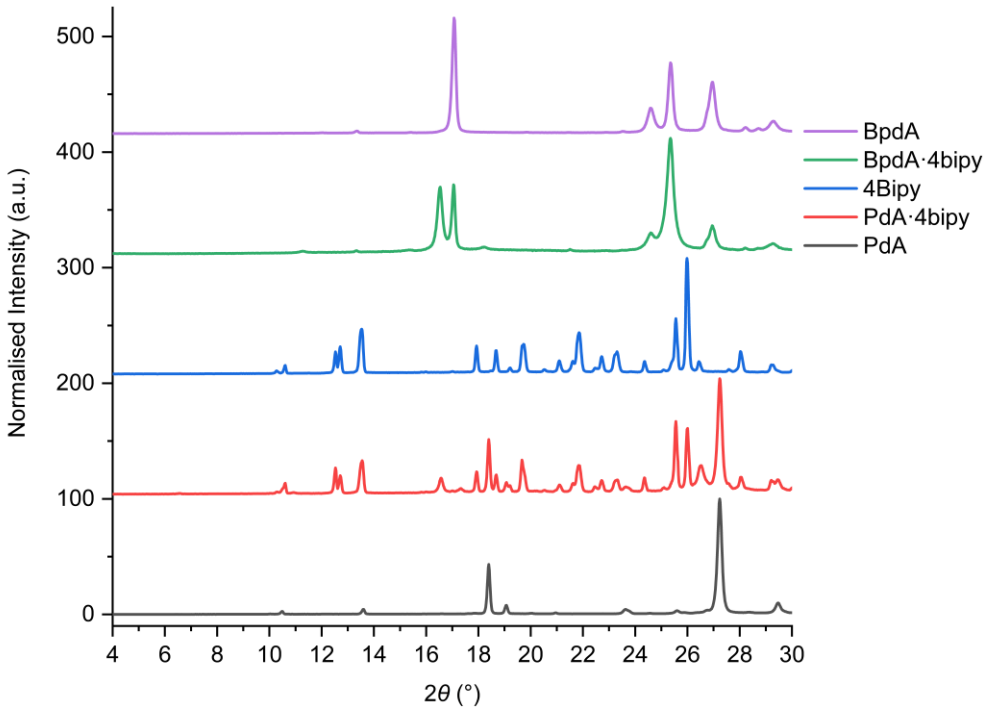

Figure 3.23. The PXRD patterns of pdA·4bipy and bpdA·4bipy cocrystals and their respective coformers.

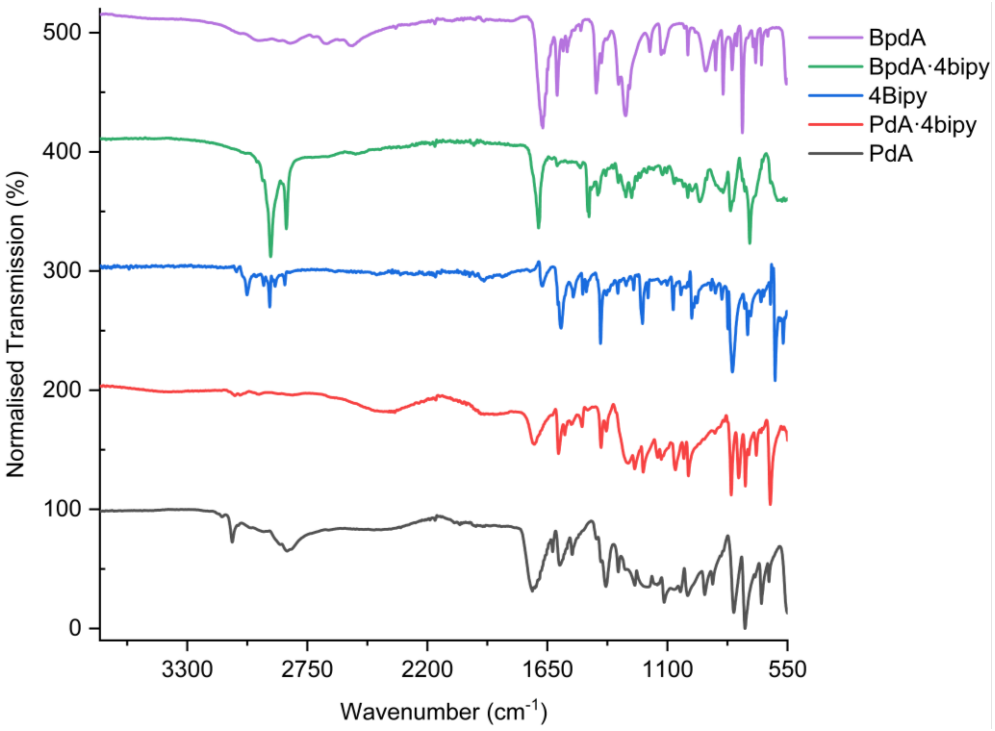

Figure 3.24. The FTIR spectra of pdA·4bipy and bpdA·4bipy cocrystals and their respective coformers.

3.3. Conclusion

Three new cocrystals involving the OH···$N_{pyridyl}$ supramolecular synthon have been prepared, consisting of 2butA·bpe, 2pentA·bpe, and 2eicoA·azp which all crystallise in the $P\bar{1}$ space group and pack in a tail-to-tail arrangement with an all-*trans* conformation of the alkyl chains, apart from 2pentA·tpe which displays a *gauche* twist at the end of the chain. Additionally, the X-ray structure of 2eicoA·azp is the first example of a single-crystal diffraction study of this acid, along with the first example of this carboxylic acid incorporated into a multicomponent structure. These three unique cocrystal structures model the interactions between pyridyl coformer and PCDA and give an insight into the potential molecular packing and topochemistry of PCDA cocrystals. Additionally, it has been generally demonstrated that the resulting cocrystal structures from solution-based crystallisation experiments can be reproduced by manual and mechanical grinding methods, illustrating the importance of mechanochemistry in the role of cocrystal formation. However, additional room-temperature SC-XRD data collection is required to investigate the ambiguous mismatched calculated and experimental PXRD patterns of the cocrystals to

understand whether the difference in patterns are anomalous due to thermal expansion or due to the structural phase changes of the cocrystals.

3.4. Experimental

Additional information relating to the materials and instrumentation used in this work can be found in Chapter 6.

2ButA·bpe Cocrystal

Butanoic acid (50 mg, 0.57 mmol) and *trans*-1,2-bis(4-pyridyl)ethylene (51 mg, 0.28 mmol) crystallised from the slow evaporation of a solution of the two reactants under ambient conditions open to the atmosphere in distilled water (1 mL). ButA-bpe can also be synthesised by the mechanical grinding of neat butanoic acid (200 mg, 2.27 mmol) and *trans*-1,2-bis(4-pyridyl)ethylene (207 mg, 1.14 mmol) for 45 minutes at a frequency of 20 s^{-1}. The formation of a cocrystal was confirmed by PXRD and FTIR analysis. Analysis calc. for $C_{20}H_{26}N_2O_4$: C 67.02, H 7.31, N 7.82 %, found: C 66.66, H 7.27, N 7.76 %; FTIR (cm^{-1}): 3061, 3033 $\nu(CH)_{asym,pyr}$, 2959 $\nu(CH_3)_{asym}$, 2921 $\nu(CH_2)_{asym}$, 2869 $\nu(CH_2)_{symm}$, 2408 ν(OH) of OH···N, 1881 ν(NH) of OH···N, 1693 ν(C=O), 1602, 1558, 1462 $\delta(CH_2)$, 1415, 1368 $\omega(CH_2)$, 1308 $\omega(CH_2)$, 1290 $\omega(CH_2)$, 1197, 1070, 1012, 988, 967, 952, 903, 877, 820, 750 $\rho(CH_2)$, 673, 547, 464. Crystal data: M = 358.43 g/mol, 0.43 × 0.24 × 0.11 mm^3, triclinic, space group $P\bar{1}$ (no. 2), a = 6.5688(4) Å, b = 6.9189(4) Å, c = 11.4828(7) Å, α = 78.001(3) °, β = 78.333(3) °, γ = 70.295(3) °, V = 475.61(5) $Å^3$, Z = 1, D_c = 1.251 g/cm^3, F_{000} = 192.0, MoKα radiation, λ = 0.71073 Å, T = 120 K, $2\theta_{max}$ = 58.992 °, 10103 reflections collected, 2644 unique (R_{int} = 0.0481). Final GooF = 1.039, R_1 = 0.0409, wR_2 = 0.1138, R indices based on 2644 reflections with $I >= 2\sigma(I)$ (refinement on F^2), 170 parameters, 0 restraints, μ = 0.087 mm^{-1}. Crystals from the same vial were analysed and re-collected two years later and show the cocrystals were unchanged. Full crystallographic information for 2butA·bpe can be found in Table 8.3 in Chapter 8.

2PentA·bpe Cocrystal

Pentanoic acid (50 mg, 0.49 mmol) and *trans*-1,2-bis(4-pyridyl)ethylene (45 mg, 0.25 mmol) crystallised from the slow evaporation of a solution of the two reactants under ambient conditions open to the atmosphere in distilled water (1 mL) after two years. PentA-bpe can also be synthesised by the manual grinding of neat pentanoic acid

(50 mg, 0.49 mmol) and *trans*-1,2-bis(4-pyridyl)ethylene (45 mg, 0.25 mmol) for 30 minutes. Formation of a cocrystal was confirmed by PXRD and FTIR analysis. Analysis calc. for $C_{22}H_{30}N_2O_4$: C 68.37, H 7.82, N 7.25 %, found: C 69.28, H 6.32, N 10.53 % consistent with excess bpe in the sample; FTIR (cm^{-1}): 3031 $\nu(CH)_{asym,pyr}$, 2963 $\nu(CH_3)_{asym}$, 2938 $\nu(CH_2)_{asym}$, 2867 $\nu(CH_2)_{symm}$, 2481 ν(OH) of OH···N, 1905 ν(NH) of OH···N, 1699 ν(C=O), 1602, 1559, 1507, 1460 $\delta(CH_2)$, 1422, 1370 $\omega(CH_2)$, 1318 $\omega(CH_2)$, 1260 $\omega(CH_2)$, 1196 $\omega(CH_2)$, 1113, 1069, 1011, 967, 951, 903, 877, 838, 828, 790, 754 $\rho(CH_2)$, 675, 568. Crystal data: M = 386.48 g/mol, 0.38 × 0.22 × 0.19 mm^3, triclinic, space group $P\bar{1}$ (no. 2), a = 6.8211(5) Å, b = 7.1875(6) Å, c = 11.8334(10) Å, α = 91.310(4) °, β = 105.957(3) °, γ = 111.187(3) °, V = 515.24(7) $Å^3$, Z = 1, D_c = 1.246 g/cm^3, F_{000} = 208.0, MoKα radiation, λ = 0.71073 Å, T = 120 K, $2\theta_{max}$ = 57.988 °, 10001 reflections collected, 2725 unique (R_{int} = 0.0282). Final GooF = 1.072, R_1 = 0.0414, wR_2 = 0.1151, R indices based on 2725 reflections with $I >= 2\sigma(I)$ (refinement on F^2), 187 parameters, 0 restraints, μ = 0.086 mm^{-1}. Full crystallographic information for 2pentA·bpe can be found in Table 8.4 in Chapter 8.

2EicoA·azp Cocrystal

Eicosanoic acid (50 mg, 0.16 mmol) and 4,4'-azopyridine (15 mg, 0.08 mmol) crystallised from the slow evaporation of a solution of the two reactants under ambient conditions open to the atmosphere ethanol (2 mL). 2EicoA-azp can also be synthesised by the mechanical grinding of neat eicosanoic acid (200 mg, 0.64 mmol) and 4,4'-azopyridine (59 mg, 0.32 mmol) for 45 minutes at a frequency of 20 s^{-1}. The formation of a cocrystal was confirmed by PXRD and FTIR analysis. Analysis calc. for $C_{50}H_{88}N_4O_4$: C 74.21, H 10.96, N 6.92 %, found: C 73.45, H 10.82, N 6.58 %; FTIR (cm^{-1}): 2956 $\nu(CH_{3asym})$, 2916 $\nu(CH_{2asym})$, 2849 $\nu(CH_{2symm})$, 2499 ν(OH) of OH···N, 1904 ν(NH) of OH···N, 1696 ν(C=O), 1594, 1540, 1471 $\delta(CH_2)$, 1408, 1375 $\omega(CH_2)$, 1328 $\omega(CH_2)$, 1312 $\omega(CH_2)$, 1296 $\omega(CH_2)$, 1282 $\omega(CH_2)$, 1267 $\omega(CH_2)$, 1251 $\omega(CH_2)$, 1232 $\omega(CH_2)$, 1213 $\omega(CH_2)$, 1196, 1181, 1108, 1048, 1012, 997, 900, 844, 780 $\rho(CH_2)$. Crystal data: M = 809.24 g/mol, 0.31 × 0.05 × 0.02 mm^3, triclinic, space group $P\bar{1}$ (no. 2), a = 5.460(3) Å, b = 6.853(3) Å, c = 33.412(18) Å, α = 85.955(14) °, β = 87.011(14) °, γ = 74.218(15) °, V = 1199.5(11) $Å^3$, Z = 1, D_c = 1.120 g/cm^3, F_{000} = 448.0, MoKα radiation, λ = 0.71073 Å, T = 120 K, $2\theta_{max}$ = 53.996 °, 19656 reflections collected, 5216 unique (R_{int} = 0.2025). Final GooF = 0.921, R_1 = 0.0873, wR_2 = 0.1403, R indices based on 5216 reflections with $I >= 2\sigma(I)$ (refinement on F^2),

267 parameters, 0 restraints, μ = 0.070 mm^{-1}. Full crystallographic information for 2eicoA·azp can be found in Table 8.5 in Chapter 8.

Azp-Cl

Butanoic acid (50 mg, 0.57 mmol) and 4,4'-azopyridine (52 mg, 0.28 mmol) crystallised from a solution of the two reactants under ambient conditions open to the atmosphere in acetone (1 mL), resulting in a mono-chloro-substituted 4,4'-azopyridine structure (with the chlorine present as an impurity). Analysis calc. for $C_{10}H_7N_4Cl$: C 54.93, H 3.23, N 25.62 %, found: C 59.12, H 6.33, N 17.71 % consistent with butanoic acid present in the sample; FTIR (cm^{-1}): Crystal data: M = 218.65 g/mol, 0.36 × 0.15 × 0.03 mm^3, monoclinic, space group $P2_1/c$ (no. 14), a = 3.7694(4) Å, b = 6.0715(6) Å, c = 21.0713(19) Å, α = 90 °, β = 93.130(4) °, γ = 90 °, V = 481.52(8) $Å^3$, Z = 2, D_c = 1.508 g/cm^3, F_{000} = 224.0, MoKα radiation, λ = 0.71073 Å, T = 296.15 K, $2\theta_{max}$ = 56.968 °, 6773 reflections collected, 1204 unique (R_{int} = 0.0555). Final GooF = 1.217, R_1 = 0.0678, wR_2 = 0.1464, R indices based on 1204 reflections with $I > = 2\sigma(I)$ (refinement on F^2), 78 parameters, 1 restraint, μ = 0.364 mm^{-1}. Full crystallographic information for azp-Cl can be found in Table 8.6 in Chapter 8.

2ButA·4bipy Cocrystal

Butanoic acid (50 mg, 0.57 mmol) and 4,4'-bipyridyl (44 mg, 0.28 mmol) was synthesised by the manual grinding of neat components for 30 minutes. Formation of a cocrystal was confirmed by PXRD and FTIR analysis. Analysis calc. for $C_{18}H_{24}N_2O_4$: C 65.04, H 7.28, N 8.43 %, found: C 61.21, H 6.69, N 8.67 %. The experiment needs to be repeated to improve the elemental analysis result; FTIR (cm^{-1}): 3055 $\nu(CH)_{asym,pyr}$, 2965 $\nu(CH_3)_{asym}$, 2874 $\nu(CH_2)_{symm}$, 2458 ν(OH) of OH···N, 1906 ν(NH) of OH···N, 1687 ν(C=O), 1602, 1545, 1469 $\delta(CH_2)$, 1411, 1364 $\omega(CH_2)$, 1312 $\omega(CH_2)$, 1207 $\omega(CH_2)$, 1074, 1045, 1003, 925, 885, 809, 749 $\rho(CH_2)$, 728, 621.

2HexA·4bipy Cocrystal

Hexanoic acid (50 mg, 0.43 mmol) and 4,4'-bipyridyl (34 mg, 0.22 mmol) was synthesised by the manual grinding of neat components for 30 minutes. Formation of a cocrystal was confirmed by PXRD and FTIR analysis. Analysis calc. for $C_{22}H_{32}N_2O_4$: C 68.01, H 8.30, N 7.21 %, found: C 65.21, H 7.23, N 9.13 %. The experiment needs to be repeated to improve the elemental analysis result; FTIR (cm^{-1}): 2956 $\nu(CH_3)_{asym}$, 2929 $\nu(CH_2)_{asym}$, 2871 $\nu(CH_2)_{symm}$, 2458 ν(OH) of OH···N, 1906

ν(NH) of OH···N, 1685 (C=O), 1600, 1541, 1469 δ(CH_2)), 1409, 1365 ω(CH_2), 1318 ω(CH_2), 1251 ω(CH_2), 1195 ω(CH_2), 1102, 1070, 1039, 1004, 921, 878, 852, 804, 728 ρ(CH_2), 623.

2PentA·azp Cocrystal

Pentanoic acid (50 mg, 0.49 mmol) and 4,4'-azopyridine (45 mg, 0.25 mmol) was synthesised by the manual grinding of neat components for 30 minutes. Formation of a cocrystal was confirmed by PXRD and FTIR analysis. Analysis calc. for $C_{20}H_{28}N_4O_4$: C 61.84, H 7.27, N 14.42 %, found: C 60.17, H 6.01, N 18.89 %. The experiment needs to be repeated to improve the elemental analysis result; FTIR (cm^{-1}): 3041 $\nu(CH)_{asym,pyr}$, 2962 $\nu(CH_3)_{asym}$, 2932 $\nu(CH_2)_{asym}$, 2871 $\nu(CH_2)_{symm}$, 2481 ν(OH) of OH···N, 1905 ν(NH) of OH···N, 1701 ν(C=O), 1598, 1568, 1460 δ(CH_2), 1411, 1373 ω(CH_2), 1325 ω(CH_2), 1265 ω(CH_2), 1203 ω(CH_2), 1112, 1096, 1052, 1012, 992, 879, 837, 756 ρ(CH_2), 658, 566.

PdA·4bipy Cocrystal

2,5-Pyridinedicarboxylic acid (50 mg, 0.30 mmol) and 4,4'-bipyridyl (47 mg, 0.30 mmol) was by the manual liquid-assisted grinding of components for 30 minutes with acetonitrile. Formation of a cocrystal was confirmed by PXRD analysis. Analysis calc. for $C_{24}H_{18}N_4O_8$: C 58.78, H 3.70, N 11.42 %, found: C 58.64, H 3.87, N 11.81 %; FTIR (cm^{-1}): 3082, 3058 $\nu(CH)_{asym,pyr}$, 2971 $\nu(CH_3)_{asym}$, 2815 $\nu(CH_2)_{symm}$, 2381 ν(OH) of OH···N, 1946 ν(NH) of OH···N, 1709 ν(C=O), 1599, 1570, 1491 δ(CH_2), 1404, 1379 ω(CH_2), 1281 ω(CH_2), 1250 ω(CH_2), 1211 ω(CH_2), 1145, 1129, 1064, 1025, 1003, 808, 773 ρ(CH_2), 743, 693, 629, 543.

BpdA·4bipy Cocrystal

4,4'-Biphenyldicarboxylic acid (50 mg, 0.21 mmol) and 4,4'-bipyridyl (32 mg, 0.21 mmol) was synthesised by the manual liquid-assisted grinding of components for 30 minutes with acetonitrile. Formation of a cocrystal was confirmed by PXRD analysis. Analysis calc. of $C_{38}H_{28}N_2O_8$: C 71.24, H 4.41, N 4.37 %, found: C 70.38, H 4.34, N 4.50 %; FTIR (cm^{-1}): 2953 $\nu(CH_3)_{asym}$, 2917 $\nu(CH_2)_{asym}$, 2845 $\nu(CH_2)_{symm}$, 1689 ν(C=O), 1605, 1458 δ(CH_2), 1413, 1325 ω(CH_2), 1290 ω(CH_2), 1262 ω(CH_2), 1122 ω(CH_2), 1107, 1066, 1005, 945, 847, 810, 723 ρ(CH_2), 589.

3.5. References

1. B. Wunderlich, *J. Therm. Anal. Calorim.*, 2012, **109**, 1117-1132.
2. J. Xu, S. J. Zhang and B. H. Guo, *Chin. Chem. Lett.*, 2017, **28**, 2092-2098.
3. G. R. Desiraju, *Angew. Chem., Int. Ed. Engl.*, 1995, **34**, 2311-2327.
4. C. R. Groom, I. J. Bruno, M. P. Lightfoot and S. C. Ward, *Acta Crystallogr., Sect. B: Struct. Sci., Cryst. Eng. Mater.*, 2016, **72**, 171-179.
5. A. D. Bond, *Chem. Commun.*, 2003, 250-251.
6. A. D. Bond, *CrystEngComm*, 2006, **8**, 333-337.
7. J. Bernstein, R. E. Davis, L. Shimoni and N. L. Chang, *Angew. Chem., Int. Ed.*, 1995, **34**, 1555-1573.
8. A. D. Bond, *New J. Chem.*, 2004, **28**, 104-114.
9. I. D. H. Oswald, W. D. S. Motherwell and S. Parsons, *Acta Crystallogr., Sect. E: Crystallogr. Commun.*, 2004, **60**, 2380-2383.
10. Y. Wu, J. Zhang, X. L. Hou, L. Ye, G. D. Yang and L. X. Wu, *Chem. Res. Chin. Univ.*, 2002, **18**, 471-473.
11. M. Amai, T. Endo, H. Nagase, H. Ueda and M. Nakagaki, *Acta Crystallogr., Sect. C: Cryst. Struct. Commun.*, 1998, **54**, 1367-1369.
12. K. Quast, *Adv. Powder Technol.*, 2016, **27**, 207-214.
13. P. K. Goswami, R. Thaimattam and A. Ramanan, *Cryst. Growth Des.*, 2016, **16**, 1268-1281.
14. J. G. Leipoldt, G. J. Lamprecht and E. C. Steynberg, *J. Organomet. Chem.*, 1991, **402**, 259-263.
15. Y. Abe, K. Harata, M. Fujiwara and K. Ohbu, *Carbohydr. Res.*, 1995, **269**, 43-51.
16. Y. Abe, M. Fujiwara, K. Ohbu and K. Harata, *Carbohydr. Res.*, 1995, **275**, 9-16.
17. Y. Abe, K. Harata, M. Fujiwara and K. Ohbu, *J. Chem. Soc., Perkin Trans. 2*, 1998, 177-186.
18. K. Ueji, S. Ichimura, Y. Tamaki and K. Miyamura, *CrystEngComm*, 2014, **16**, 10139-10147.
19. E. Lee, Y. Kim and D. Y. Jung, *Inorg. Chem.*, 2002, **41**, 501-506.
20. D. J. Abdallah, R. E. Bachman, J. Perlstein and R. G. Weiss, *J. Phys. Chem. B*, 1999, **103**, 9269-9278.
21. K. Dai, K. Nomoto, S. Ueno, K. Tomono and K. Miyamura, *Bull. Chem. Soc. Jpn.*, 2011, **84**, 312-319.
22. E. Moreno-Calvo, G. Gbabode, R. Cordobilla, T. Calvet, M. A. Cuevas-Diarte, P. Negrier and D. Mondieig, *Chem. - Eur. J.*, 2009, **15**, 13141-13149.
23. O. Theilmann, W. Saak, D. Haase and R. Beckhaus, *Organometallics*, 2009, **28**, 2799-2807.
24. L. Brammer, E. A. Bruton and P. Sherwood, *Cryst. Growth Des.*, 2001, **1**, 277-290.
25. J. A. K. Howard, V. J. Hoy, D. Ohagan and G. T. Smith, *Tetrahedron*, 1996, **52**, 12613-12622.
26. Y. Y. Zhu, H. P. Yi, C. Li, X. K. Jiang and Z. T. Li, *Cryst. Growth Des.*, 2008, **8**, 1294-1300.
27. D. Braga, L. Maini and F. Grepioni, *Chem. Soc. Rev.*, 2013, **42**, 7638-7648.
28. T. Friscic, *Chem. Soc. Rev.*, 2012, **41**, 3493-3510.
29. T. Friscic and W. Jones, *Cryst. Growth Des.*, 2009, **9**, 1621-1637.
30. S. L. James, C. J. Adams, C. Bolm, D. Braga, P. Collier, T. Friscic, F. Grepioni, K. D. M. Harris, G. Hyett, W. Jones, A. Krebs, J. Mack, L. Maini, A. G. Orpen,

I. P. Parkin, W. C. Shearouse, J. W. Steed and D. C. Waddell, *Chem. Soc. Rev.*, 2012, **41**, 413-447.
31. J. W. Steed, *Trends Pharmacol. Sci.*, 2013, **34**, 185-193.
32. T. Friscic, C. Mottillo and H. M. Titi, *Angew. Chem., Int. Ed.*, 2020, **59**, 1018-1029.
33. Z. Dega-Szafran, A. Komasa, M. Grundwald-Wyspianska, M. Szafran, G. Buczak and A. Katrusiak, *J. Mol. Struct.*, 1997, **404**, 13-23.
34. Z. Dega-Szafran, G. Dutkiewicz, Z. Kosturkiewicz and M. Szafran, *J. Mol. Struct.*, 2009, **923**, 72-77.
35. R. Langner and G. Zundel, *J. Chem. Soc., Faraday Trans.*, 1995, **91**, 3831-3838.
36. S. L. Johnson and K. A. Rumon, *J. Phys. Chem.*, 1965, **69**, 74-86.
37. K. Thanigaimani, N. C. Khalib, E. Temel, S. Arshad and I. A. Razak, *J. Mol. Struct.*, 2015, **1099**, 246-256.
38. A. Ilyukhin, *CSD Communication*, 2014.
39. L. Ye, *Acta Crystallogr., Sect. E: Crystallogr. Commun.*, 2008, **64**, 46.
40. S. L. Johnson and K. A. Rumon, *J. Phys. Chem.*, 1965, **69**, 74-&.
41. T. K. Adalder, R. Sankolli and P. Dastidar, *Cryst. Growth Des.*, 2012, **12**, 2533-2542.
42. D. R. Weyna, T. Shattock, P. Vishweshwar and M. J. Zaworotko, *Cryst. Growth Des.*, 2009, **9**, 1106-1123.
43. G. Ayoub, V. Strukil, L. Fabian, C. Mottillo, H. Z. Bao, Y. Murata, A. Moores, D. Margetic, M. Eckert-Maksic and T. Friscic, *CrystEngComm*, 2018, **20**, 7242-7247.
44. FooDB, Showing Compound 2,6-Pyridinedicarboxylic acid (FDB011167), https://foodb.ca/compounds/FDB011167, (accessed 12/07/2020).

4. The Crystal Engineering of 10,12-Pentacosadiynoic Acid Cocrystals and Salts

4.1. Introduction

The commercially important diacetylene PCDA is used to provide a colourimetric change in practical chemosensors,[1-6] biosensors,[7-10] and dosimeters.[11-14] Although PCDA is somewhat photoreactive, further tuning of its photoresponse is of considerable interest, especially for radiation dosimetry applications. Covalent modification offers a viable strategy to PCDA analogues with a tuned photoresponse.[15-17] However, since the solid state reactivity of dialkynes depends on the crystal packing arrangement, a simpler strategy to address dialkyne reactivity is through the modification of non-covalent interactions by cocrystal or salt formation.[18-21] Whether a cocrystal or salt will form depends on the difference in pK_a of the two components. For a cocrystal, the ΔpK_a must be < 2-3 log units, while salt formation is expected for a greater difference.[22, 23] Cocrystals of carboxylic acids can be prepared using the robust hydrogen-bonded COOH···$N_{pyridine}$ heterosynthon (discussed for the model compounds in Chapter 3), while salts can be based on ammonium complexes of more basic amines.[24-28] In this work we explore the relationship between structure and photochemistry for PCDA with three different pyridine-containing coformers azp, 4bipy, and bpe and compare the photoreactivity of the resulting cocrystals with aliphatic amine salts of 4,4'-bipiperidine (bipip), morpholine (morph), piperidine (piper), ethylenediamine (etdiam), diethylamine (dietam), and *n*-butylamine (butam).

4.2. Results and Discussion

4.2.1. PCDA Cocrystals

PCDA Cocrystal Structure

Based on the characterisation of the model compounds with azp, 4bipy, and bpe with short-chain aliphatic *n*-carboxylic aids, the synthesis of PCDA with bifunctional aromatic coformers were undertaken by the combination of PCDA and the coformer in a 2:1 ratio (which reflects the single hydrogen bond donor group of PCDA and the two hydrogen bond acceptor groups of the pyridyl coformers), respectively (Figure 4.1). Grinding PCDA and azp in a Retsch MM 200 mixer mill for one hour gave a

powder of cocrystal 2PCDA·azp, which was characterised by PXRD (Figure 4.2) and used for seeding the cocrystallisation of PCDA and azp in acetone. After the evaporation of solvent at room temperature for one week, plate-shaped crystals of 2PCDA·azp formed and were analysed by SC-XRD. The structure of 2PCDA·azp reveals the aliphatic chains of PCDA are in an *anti*-conformation, analogous to the structure of PCDA, with OH···N hydrogen bonds from the carboxylic acid proton of PCDA to the pyridyl nitrogen atom of azp at an O···N distance of 2.677(4) Å (Figure 4.3). An additional weak CH···O hydrogen bond between the pyridyl C-H group and the carbonyl oxygen atom of PCDA (at a C···O distance of 3.303(4) Å) which completes hydrogen-bonded dimer $R_2^2(7)$ motif. The structure of the 2eicoA·azp in Chapter 3 effectively models the structure and interactions of 2PCDA·azp. For instance, both cocrystals crystallise in the same space group of $P\bar{1}$ and have very similar hydrogen-bonding environments, as the O···N distances only differ by 0.001 Å, both with estimated standard deviations of ±0.004 Å. Interestingly, the topochemical parameters in 2PCDA·azp are also similar to the 2eicoA·azp cocrystal model. The translational repeat distance of 2PCDA·azp is 5.3541(1) Å while 2eicoA·azp is 5.460(3) Å, and the tilt angles are 48.4 ° and 43.4 °, respectively. In 2PCDA·azp, the inter-dialkyne distance is 3.633(1) Å from C10 to C13 on adjacent molecules while the same carbon atoms in 2eicoA·azp mimic the C1-C4’ distance of the dialkynes at 4.0447(15) Å. Overall, eicoA is an excellent saturated derivative of PCDA to imitate the hydrogen bonding and packing of PCDA cocrystallised with azp, though, the topochemical parameters are more difficult to predict. In addition to 2PCDA·azp, the cocrystal displays significant anisotropic thermal expansion along the *c*-axis which increases from 39.33 Å to 40.99 Å between 120 and 273 K. The differences in the unit cell made the calculated and experimental PXRD data difficult to compare, although it is clear that the crystal studied is representative of the bulk material (Figure 4.4).

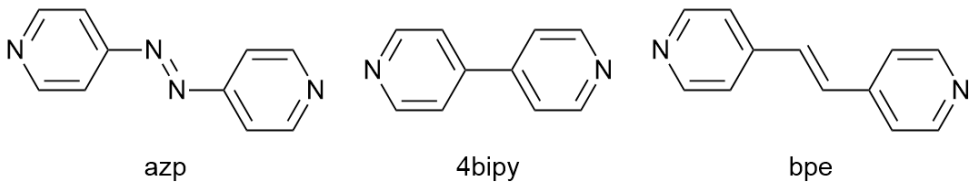

Figure 4.1. The aromatic coformers used for the cocrystallisation of PCDA.

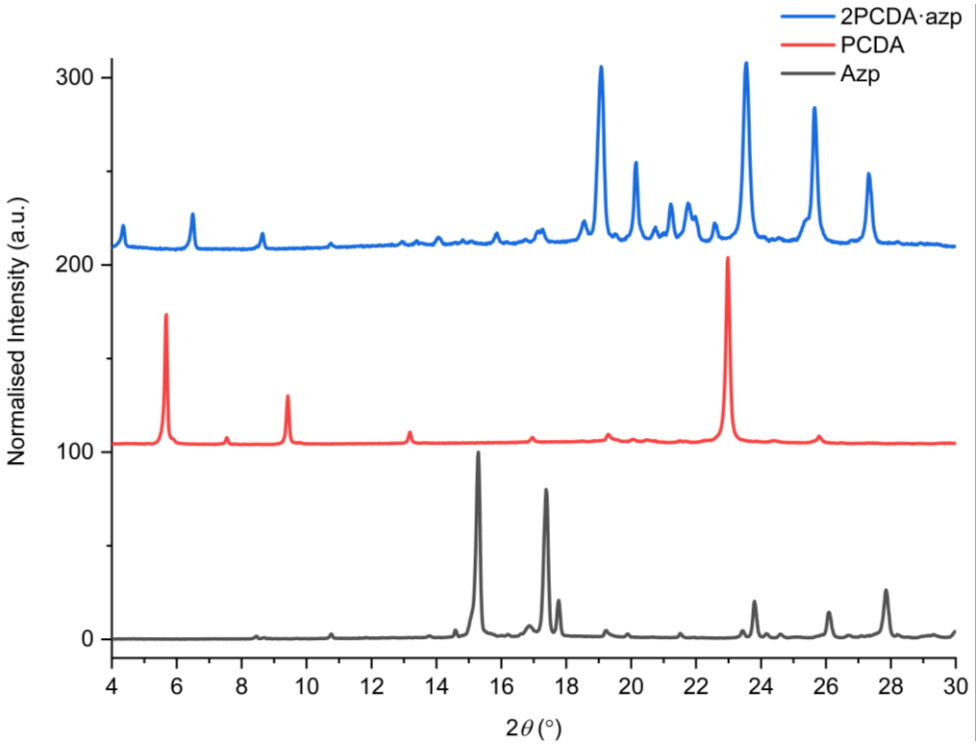

Figure 4.2. The experimental PXRD patterns of PCDA, azp, and the cocrystal 2PCDA·azp, synthesised after one hour of the mechanical grinding of the coformers in a 2:1 ratio, respectively.

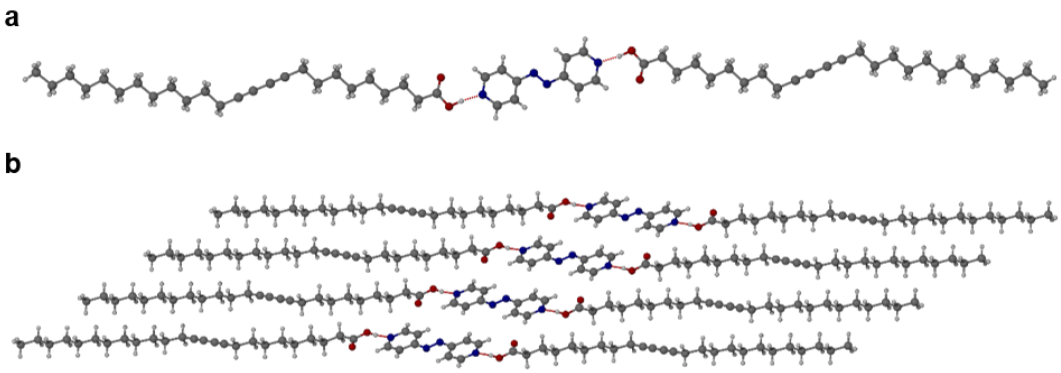

Figure 4.3. a) The X-ray structure of 2PCDA·azp showing the OH···N hydrogen bond (O···N distance of 2.677(4)) with the diacetylene substituents in an *anti*-conformation. b) The packing diagram of 2PCDA·azp in the (100) crystallographic plane.

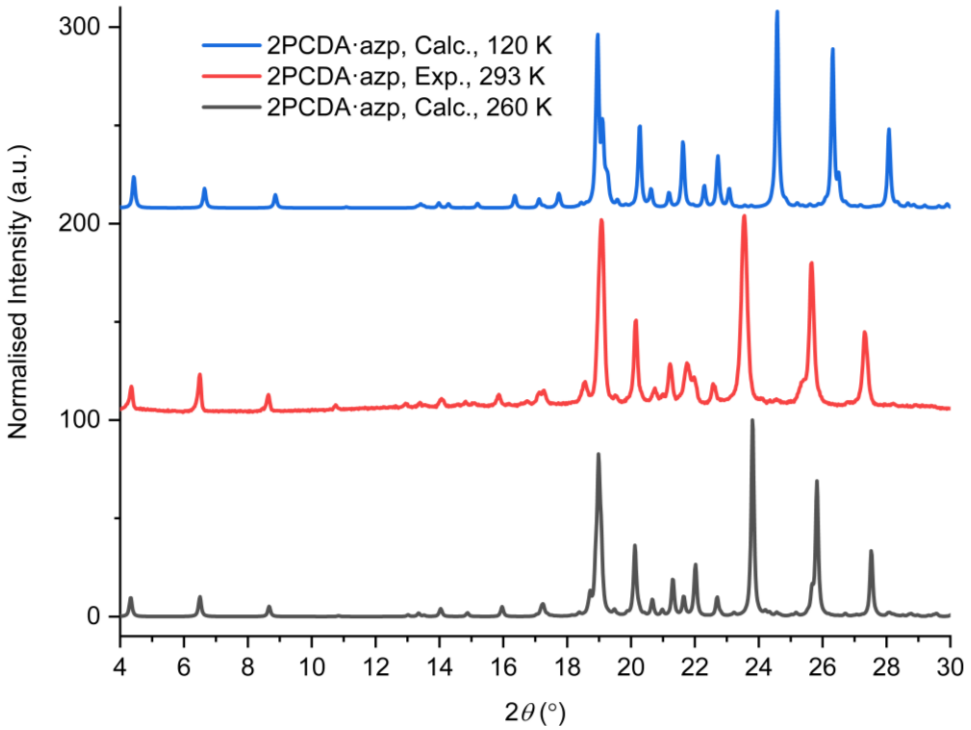

Figure 4.4. The calculated and experimental PXRD pattern of 2PCDA·azp collected at different temperatures.

Similar to the FTIR spectra of the model cocrystals in Chapter 3, the spectrum of 2PCDA·azp displays broad bands at 2522 cm^{-1} and 1908 cm^{-1} that can be attributed to the stretching modes of the O-H and N-H involved in the OH···$N_{pyridyl}$ interaction (Figure 4.5). Additionally, the spectrum shows a hydrogen-bonded carbonyl stretching band at 1695 cm^{-1} that is blue-shifted when compared to 1691 cm^{-1} in pure PCDA, which implies slightly weaker hydrogen bonding than the carboxylic acid dimer of PCDA itself. Also, the ssNMR of 2PCDA·azp displays a shift in the carboxylate peak at 177.0 ppm, compared to the same peak at 182.4 ppm in PCDA, suggesting a different environment in the cocrystal compared to the free acid (Figure 4.6). The cocrystal 2PCDA·azp was also characterised by DSC which revealed a melting onset temperature of 57 °C, which is lower than the melting temperatures of the individual components (62 °C for PCDA and 96 °C for 4,4'-azopyridine[29]) implying relatively weak interactions, consistent with the FTIR spectrum interpretation (Figure 4.7).

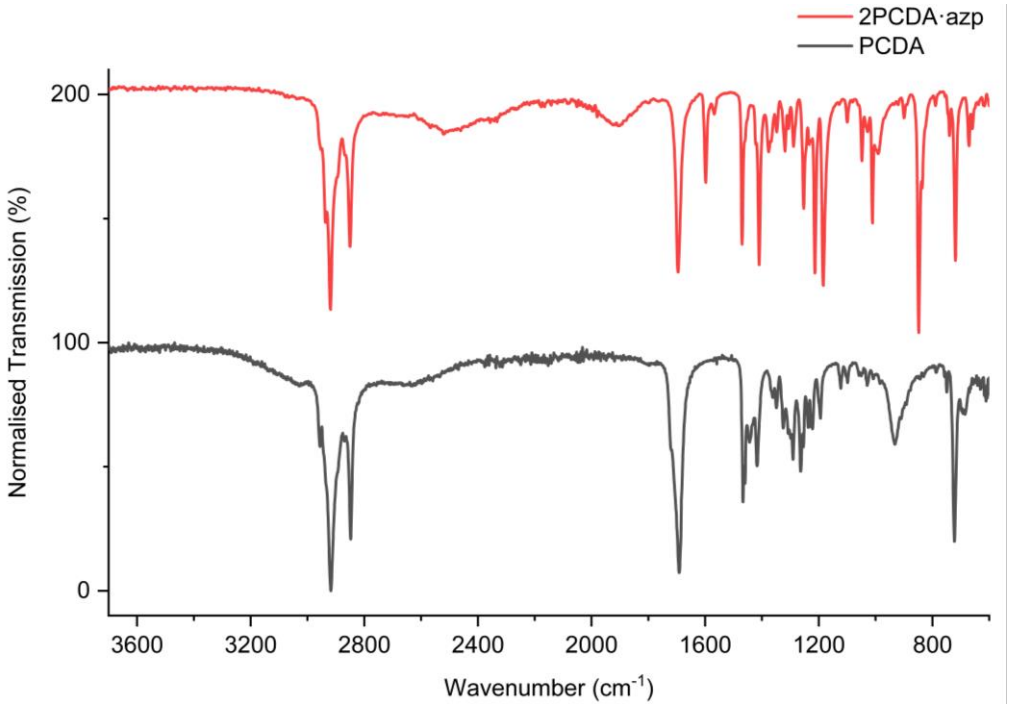

Figure 4.5. The FTIR spectra of PCDA and 2PCDA·azp.

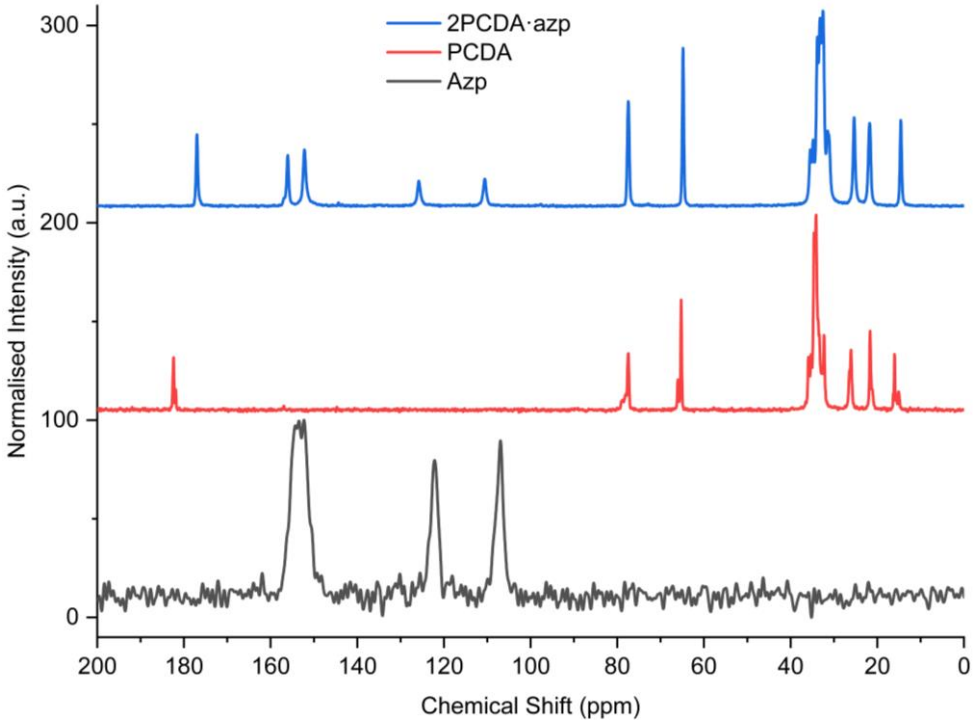

Figure 4.6. The ssNMR spectra of azp, PCDA, and 2PCDA·azp.

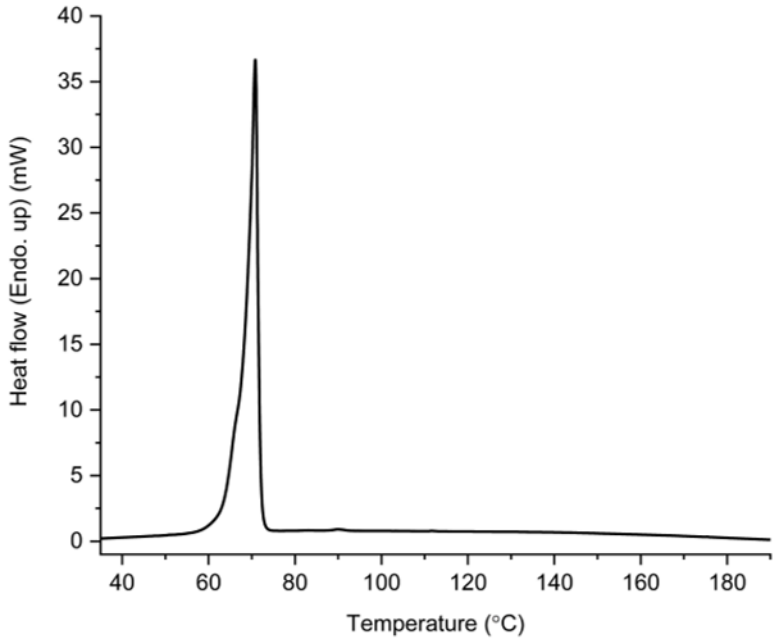

Figure 4.7. The DSC thermogram of 2PCDA·azp with a melt onset endotherm at 56.9 °C.

Two further cocrystals, 2PCDA·4bipy and 2PCDA·bpe, were synthesised by grinding the coformers 4bipy and bpe with PCDA, respectively, in a 2:1 ratio for 45 minutes in a mixer mill, to yield the cocrystal in powder form. Samples were characterised by PXRD (Figure 4.8 and Figure 4.9) and then used in seeded crystallisations in acetone and yielded plate and block crystals, respectively, as the solvent evaporated under ambient conditions. A single crystal of 2PCDA·4bipy was analysed at the I19 beamline at the Diamond Light Source at 100 K, while crystals of 2PCDA·bpe were analysed on a Bruker D8 Venture diffractometer at 120 K. The two materials are isostructural and crystallise in the monoclinic space group $P2_1/c$. The X-ray structures of cocrystals 2PCDA·4bipy and 2PCDA·bpe consist of hydrogen bonds between the carboxylic acid hydrogen atom of PCDA and the pyridyl nitrogen atom of the coformer at an O···N distance of 2.652(4) Å in 2PCDA·4bipy (Figure 4.10a) and 2.6579(17) Å in 2PCDA·bpe (Figure 4.10b). Interestingly the dialkyne moieties in both structures adopt a *syn*-conformation, in contrast to the *anti*-conformation in PCDA and 2PCDA·azp indicating that subtle modification of coformer can have a significant effect on crystal packing mode. The X-ray structures of 2PCDA·4bipy and 2PCDA·bpe and their packing diagrams are shown in Figure 4.10c and Figure 4.10d. The ethylene bond of 2PCDA·bpe is disordered over two positions.

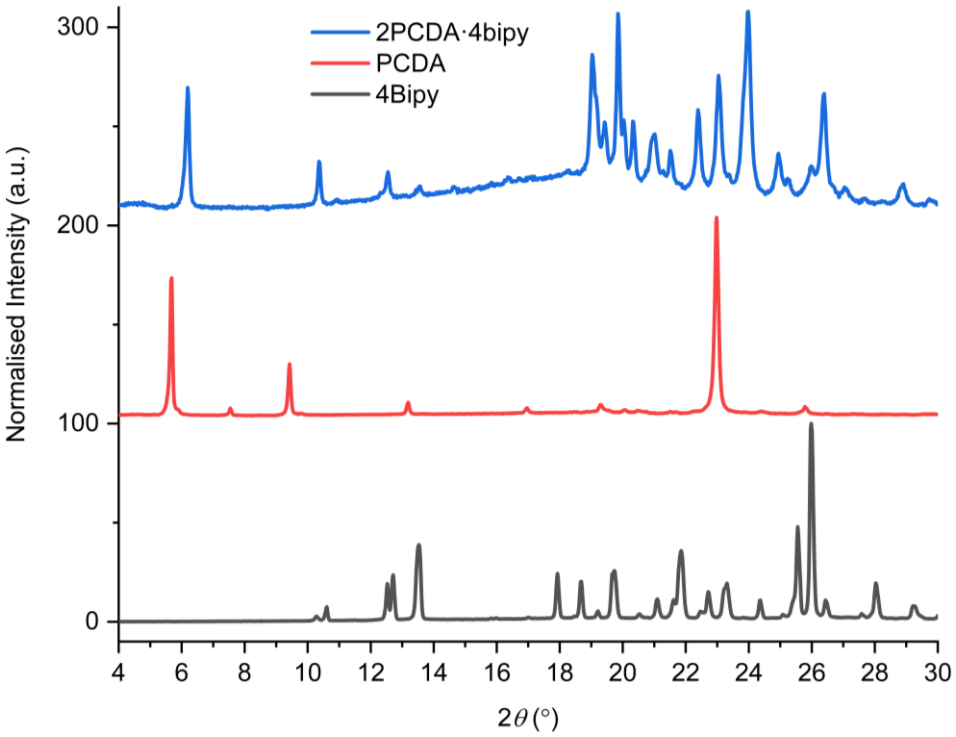

Figure 4.8. The experimental PXRD patterns of 4bipy, PCDA, and the cocrystal 2PCDA·4bipy.

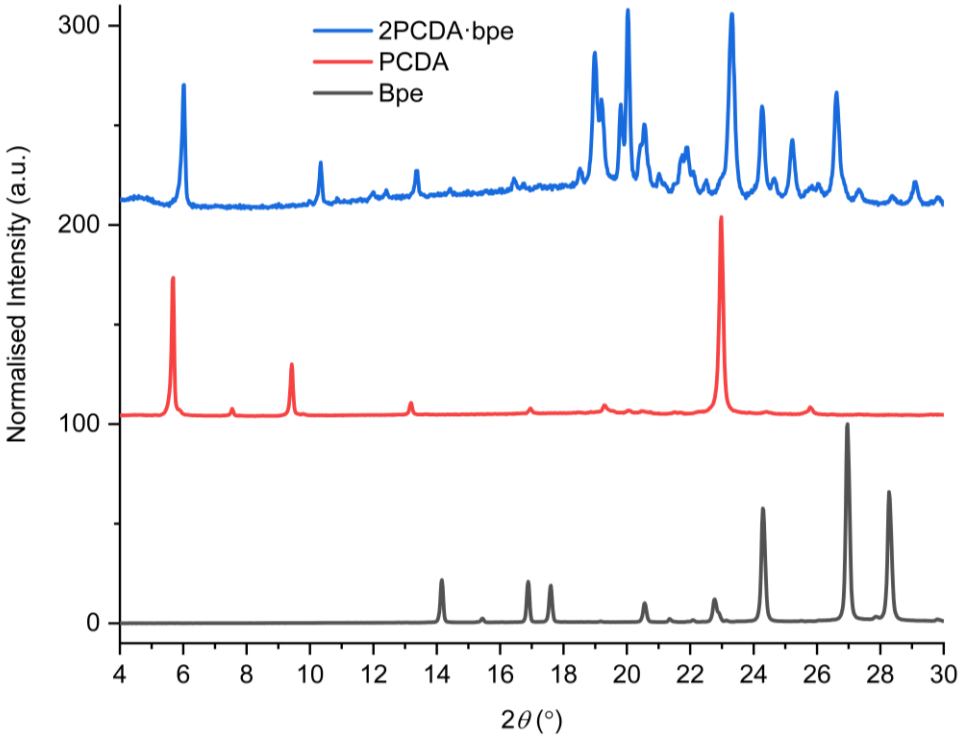

Figure 4.9. The experimental PXRD patterns of bpe, PCDA, and the cocrystal 2PCDA·bpe.

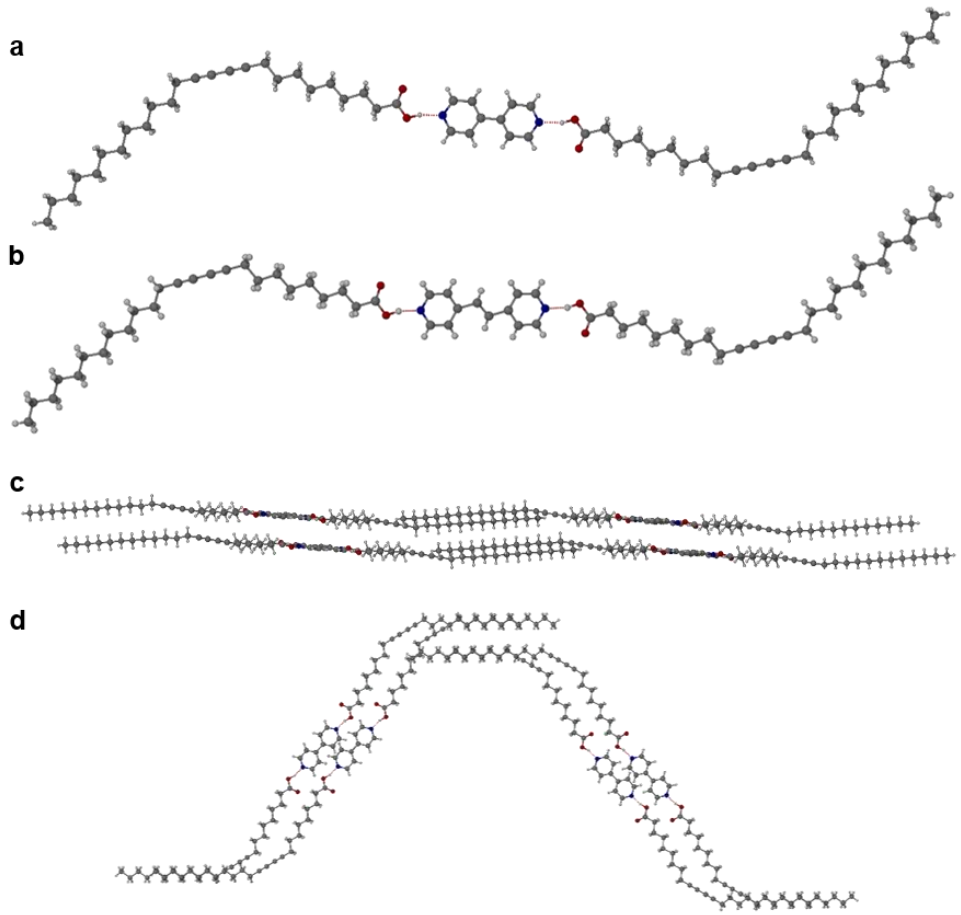

Figure 4.10. a) The X-ray structure of 2PCDA·4bipy with components joined by an OH···N hydrogen bond (O···N distance of 2.6448(9) Å) showing the *syn*-conformation of the dialkyne substituents. b) The X-ray structure of 2PCDA·bpe with OH···N hydrogen bonds (O···N distance of 2.6579(17) Å) and the diacetylene substituents in a *syn*-conformation (disorder omitted). Packing diagram of 2PCDA·4bipy in the c) (010) and d) (001) crystallographic planes.

The C1-C4' inter-alkyne distances between adjacent PCDA molecules in 2PCDA·4bipy is within the topochemical postulate at distances of 3.730(1) Å, although it is longer than those found in PCDA and 2PCDA·azp, because of the *syn* conformation of the dialkyne fragments. However, the tilt angle and the translational repeat distance for 2PCDA·4bipy is 47.4 ° and 5.442(1) Å, respectively. To directly compare the 2PCDA·bpe cocrystal, the model compound structures 2butA·bpe and 2pentA·bpe show very similar hydrogen bonding interactions, with the N···O hydrogen bond lengths of 2.6579(17) Å, 2.6583(12) Å, and 2.6723(13), respectively (Chapter 3). It appears that only the 2butA·bpe cocrystal has alkyl substituents in an all-*trans* conformation, compared to the *syn*-conformations observed in the

2PCDA·bpe and 2pentA·bpe cocrystals. Additionally, 2PCDA·bpe is the only cocrystal with disorder on the ethylene bond of bpe coformer, and the only cocrystal out of the three that crystallises in the space group of $P2_1/c$, as the two model cocrystals crystallise in the $P\bar{1}$ space group. When comparing the topochemical parameters of each cocrystal (though the model cocrystals do not have a photoreactive moiety), the translational repeat distance for 2PCDA·bpe is 5.449(2) Å, while the model cocrystals have values within the optimum value for this parameter (≤4.9 Å), as 2butA·bpe has a C4-C4' distance of 4.821(3) Å, and 2pentA·bpe has a C5-C5' distance of 3.9938(3) Å. Interestingly, the model cocrystals have tilt angles of 43.3 ° for 2butA·bpe and 18.9 ° for 2pentA·bpe, whereas the tilt angle for 2PCDA·bpe is greater than the optimum value (45 °) at 47.3 °. However, for the C1-C4' inter-alkyne distance, 2PCDA·bpe is within the ideal value (≤3.8 Å) at 3.726(2) Å, but the model cocrystals are outside the optimum value, at distances of 4.6266(17) Å and 4.5963(4) Å for 2butA·bpe and 2pentA·bpe, respectively. Therefore, the model cocrystals provide insights into similarities in hydrogen bonding of the carboxylic acid-pyridyl interaction, but however, do not replicate the same outlook in terms of the packing of the molecules and the topochemical postulate, likely due to their very short chains (4-5 carbon atoms) compared to PCDA (25 carbon atoms). A structure to contrast the 2PCDA·bpe cocrystal is the structure of decanoic acid cocrystallised with bpe (Figure 3.5) whereby the decanoic acid substituent of the cocrystal has a 117.7 ° bend at the α-carbon, allowing a herringbone packing of the cocrystal compared to the lamellar packing of PCDA and the *syn*-conformation of the PCDA chains in 2PCDA·bpe. The *syn* conformation of the dialkyne substituents of 2PCDA·4bipy and 2PCDA·bpe allows an interdigitated, bilayer packing arrangement which translates to the much longer crystallographic *c*-axes which encompass four folded molecules in the cocrystals of 4bipy and bpe as opposed to two extended molecules in 2PCDA·azp. In a similar way to 2PCDA·azp, cocrystals 2PCDA·4bipy and 2PCDA·bpe show considerable anisotropic thermal expansion on warming (Table 4.1). This makes the calculated PXRD patterns appear somewhat different to the room temperature experimental patterns (Figure 4.11 and Figure 4.12).

Cocrystal	Temp. (K)	*a* (Å)	*b* (Å)	*c* (Å)	*β* (°)	Volume (Å^3)
2PCDA·4bipy	100	5.4415(2)	8.9535(4)	55.673(3)	90.8823(10)	2712.1(2)
	260	5.4783(3)	8.9976(5)	56.951(4)	92.506(2)	2804.5(3)
	273	5.4761(3)	8.9950(5)	57.173(4)	92.710(2)	2813.0(5)
2PCDA·bpe	120	5.4494(3)	8.9235(5)	57.441(3)	92.643(2)	2790.2(3)
	260	5.4847(4)	8.9801(6)	58.562(4)	90.849(3)	2884.1(3)
	273	5.503(5)	9.023(7)	58.93(5)	90.24(3)	2927.0(7)

Table 4.1. The unit cell axes of 2PCDA·4bipy and 2PCDA·bpe collected at various temperatures.

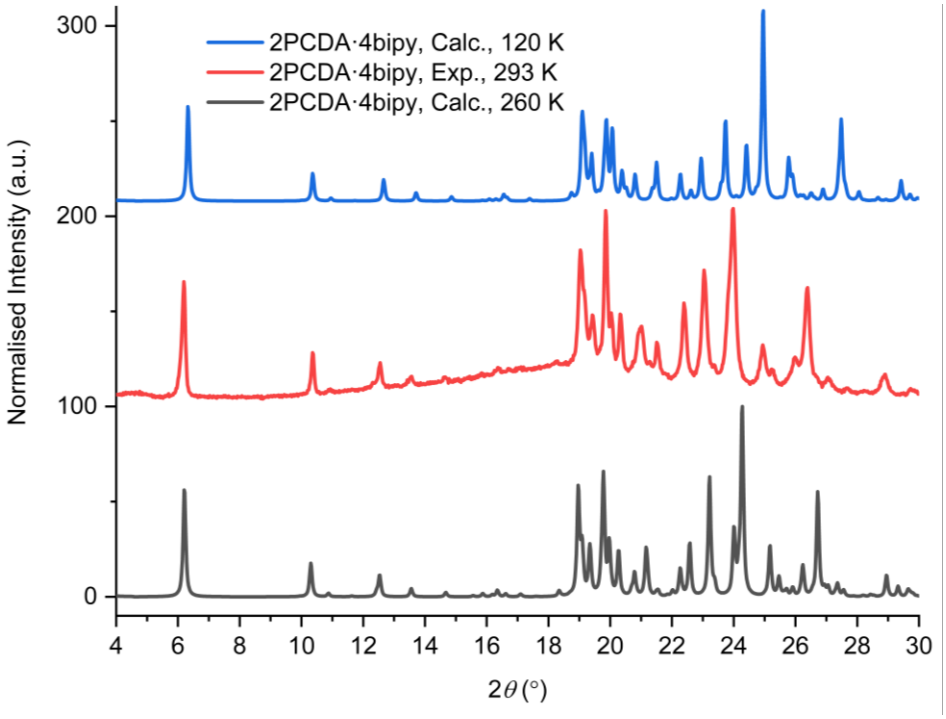

Figure 4.11. The calculated and experimental PXRD patterns of 2PCDA·4bipy at different temperatures.

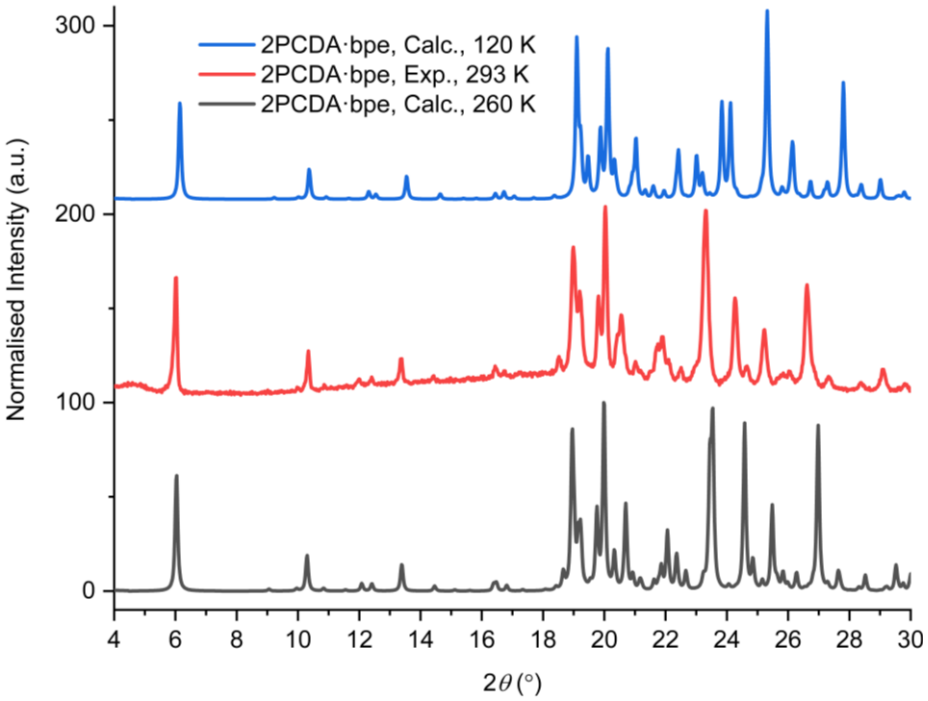

Figure 4.12. The calculated and experimental PXRD patterns of 2PCDA·bpe collected at different temperatures.

Similar to the FTIR spectra of the model cocrystals in Chapter 3 and 2PCDA·azp, the spectra for 2PCDA·4bipy and 2PCDA·bpe displays broad bands at 2467 cm^{-1} and 1920 cm^{-1}, and 2462 cm^{-1} and 1912 cm^{-1}, respectively, that can be attributed to the stretching modes of the O-H and N-H involved in the OH···$N_{pyridyl}$ interaction (Figure 4.13). Additionally, the spectrum of the cocrystals reveal a red-shifted hydrogen-bonded carbonyl stretch at 1683 cm^{-1} and 1688 cm^{-1} respectively, compared to 1692 cm^{-1} in pure PCDA, implying slightly stronger hydrogen bonding. In addition to the FTIR spectra, the ssNMR spectra of 2PCDA·4bipy and 2PCDA·bpe display carboxylate peaks at 177.4 ppm and 176.9 ppm, respectively, in comparison to the carboxylate peak of PCDA with a chemical shift of 182.4 ppm (Figure 4.14 and Figure 4.15), suggesting new carboxylate environments of the cocrystals. The DSC thermogram of 2PCDA·4bipy reveals a melt onset endotherm of 73 °C (Figure 4.16) (compared to the coformer melt temperatures for PCDA and 4bipy of 62 °C and 114 °C,[30] respectively), while 2PCDA·bpe exhibits a melting onset temperature of 72 °C (Figure 4.17), compared to 150 °C for bpe.[31] The similar melting temperatures for the two cocrystals are expected due to the isostructural nature of these materials.

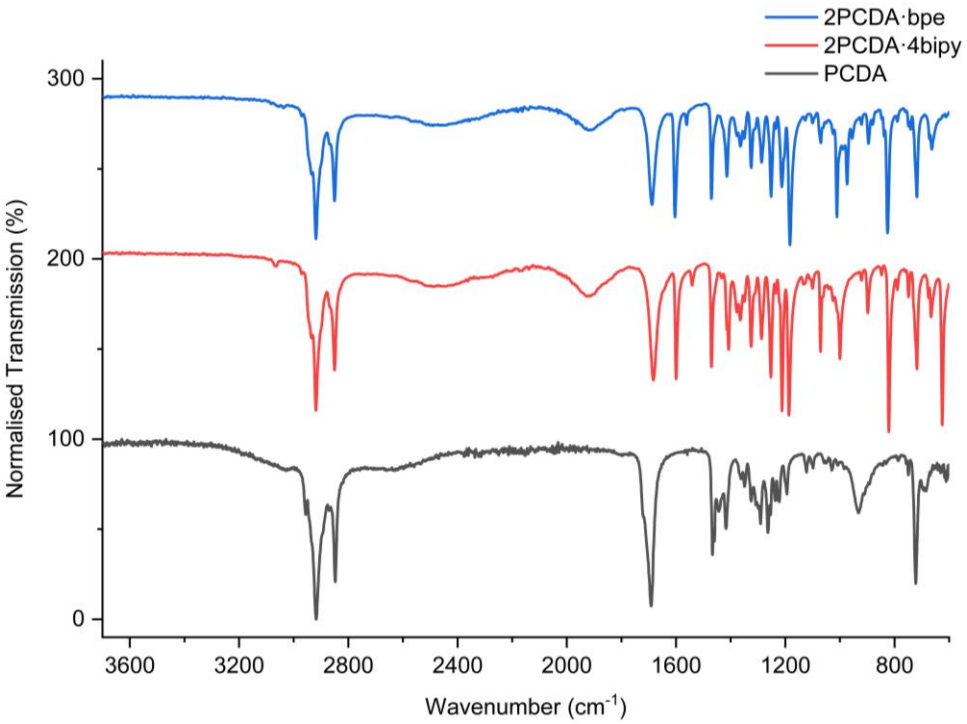

Figure 4.13. The FTIR spectra of cocrystals 2PCDA·4bipy and 2PCDA·bpe compared to PCDA.

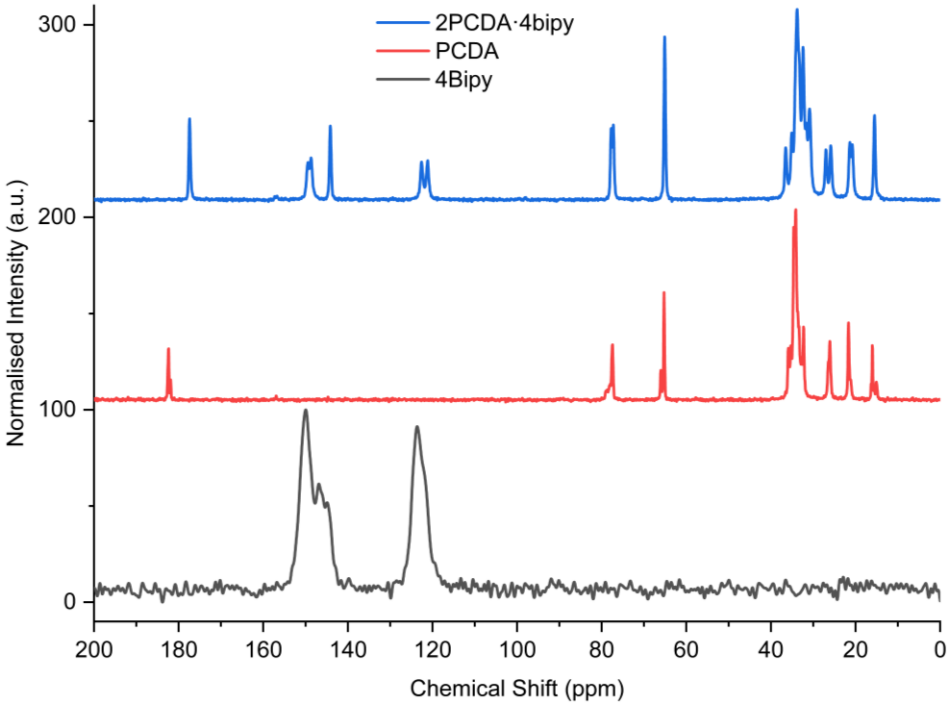

Figure 4.14. The ssNMR spectra of 4bipy, PCDA, and 2PCDA·4bipy.

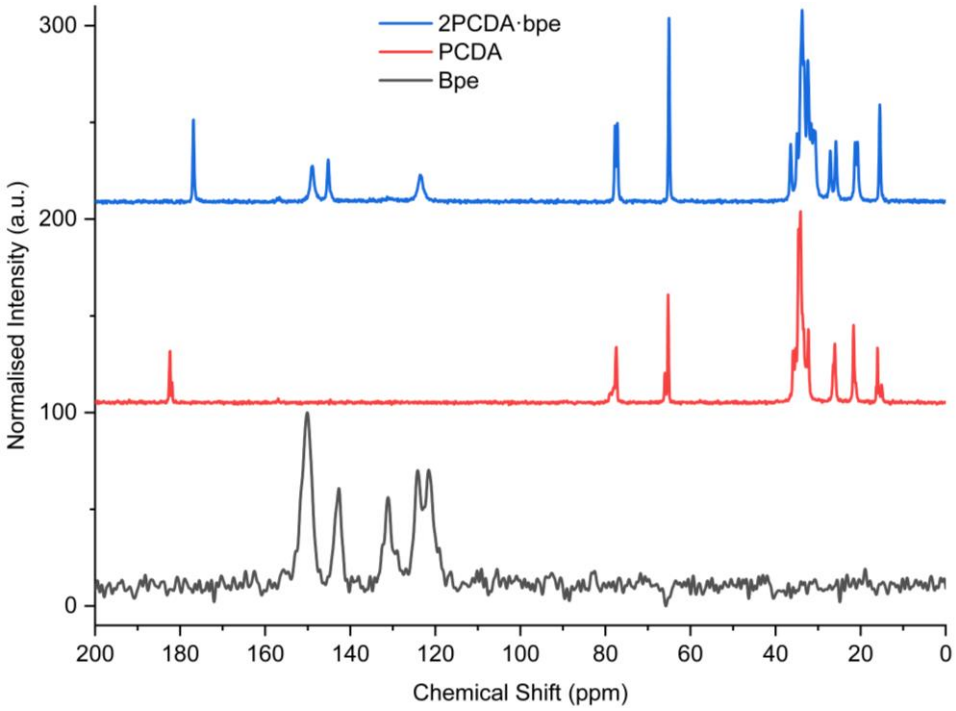

Figure 4.15. The ssNMR spectra of bpe, PCDA, and 2PCDA·bpe.

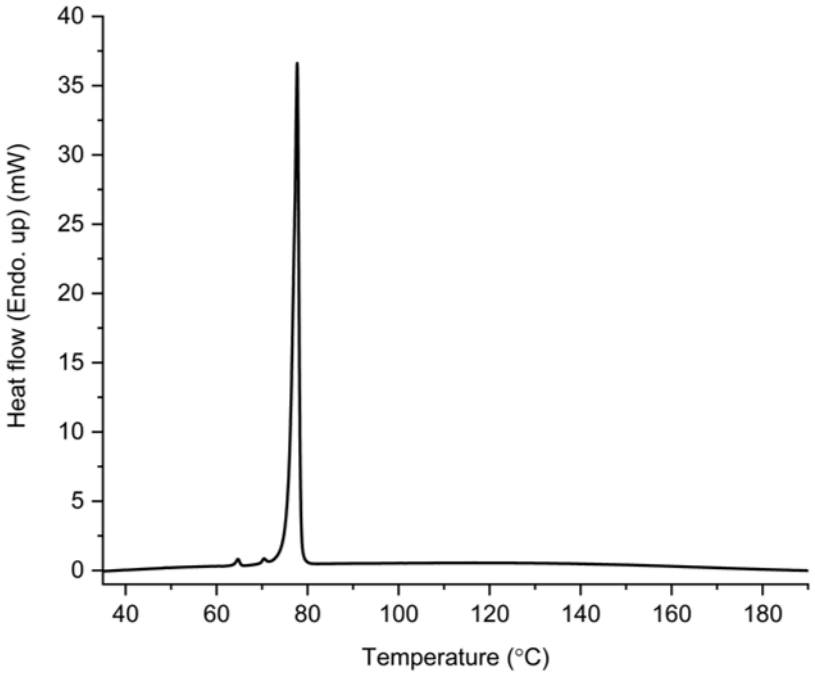

Figure 4.16. The DSC thermogram of 2PCDA·4bipy with a melt onset endotherm at 73.4 °C, with a residual peak of PCDA at 63.7 °C.

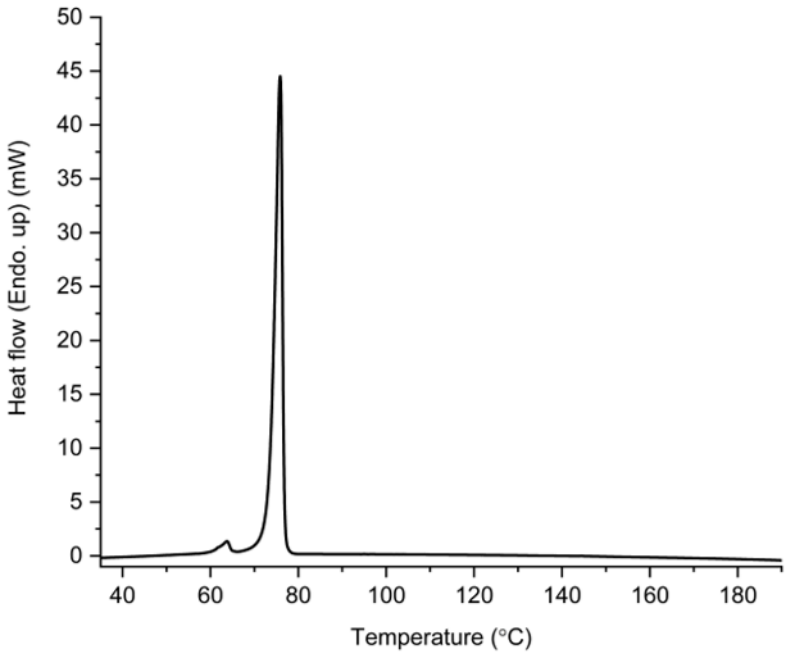

Figure 4.17. The DSC thermogram of 2PCDA·bpe displaying a melt onset endotherm at 72.2 °C, with residual unreacted PCDA at 62.6 °C.

PCDA Cocrystal Photoreactivity

The powder of each PCDA cocrystal was placed on filter paper in a dark box and exposed to a 6-Watt handheld UV radiation at 254 nm for varying durations (Figure 4.18). It is known that the azobenzene coformer azp itself undergoes photoisomerisation to the *cis* form when irradiated at 365 nm[32] and so 2PCDA·azp was also irradiated at this wavelength in order to probe the photoresponse of the coformer component within the cocrystal. While PCDA powder itself gradually darkens from a white to deep blue upon irradiation, all of the cocrystals with coformers azp, 4bipy, and bpe do not change colour despite the close C1-C4' proximity of the dialkyne functionalities, which are within the distance specified by the topochemical postulate. However, the tilt angles of PCDA in the cocrystals, and the translational repeat distances of the cocrystals are outside of the desired values.

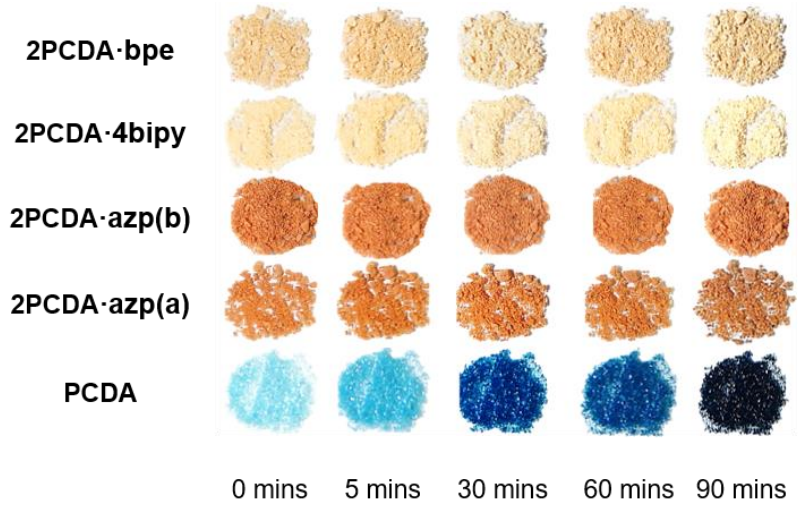

Figure 4.18. The coformer PCDA and cocrystals 2PCDA·azp, 2PCDA·4bipy and 2PCDA·bpe before and after UV irradiation at 254 nm for different durations. The 2PCDA·azp(a) sample was exposed to UV radiation at 365 nm while 254 nm radiation was used for the 2PCDA·azp(b) sample.

The irradiated cocrystals were analysed by PXRD (Figure 4.19, Figure 4.20, Figure 4.21, and Figure 4.22), FTIR spectroscopy (Figure 4.23, Figure 4.24, Figure 4.25, and Figure 4.26) and ssNMR spectroscopy (Figure 4.27, Figure 4.28, Figure 4.29, and Figure 4.30). This data confirmed that the cocrystal samples do not undergo photopolymerisation after irradiation. However, after one hour and one day, 2PCDA·azp and 2PCDA·bpe, display additional peaks in the PXRD patterns and solid-state NMR spectra that are attributable to PCDA. This suggests that irradiation decomposes the cocrystals to liberate free PCDA, particularly in the case of the azobenzene complex 2PCDA·azp. This behaviour is attributed to the photoisomerisation of coformer azp resulting in degradation of the cocrystal. The PXRD pattern and ssNMR spectra also imply a less-crystalline state at one hour in 2PCDA·azp and show the presence of crystalline PCDA after one day of irradiation.

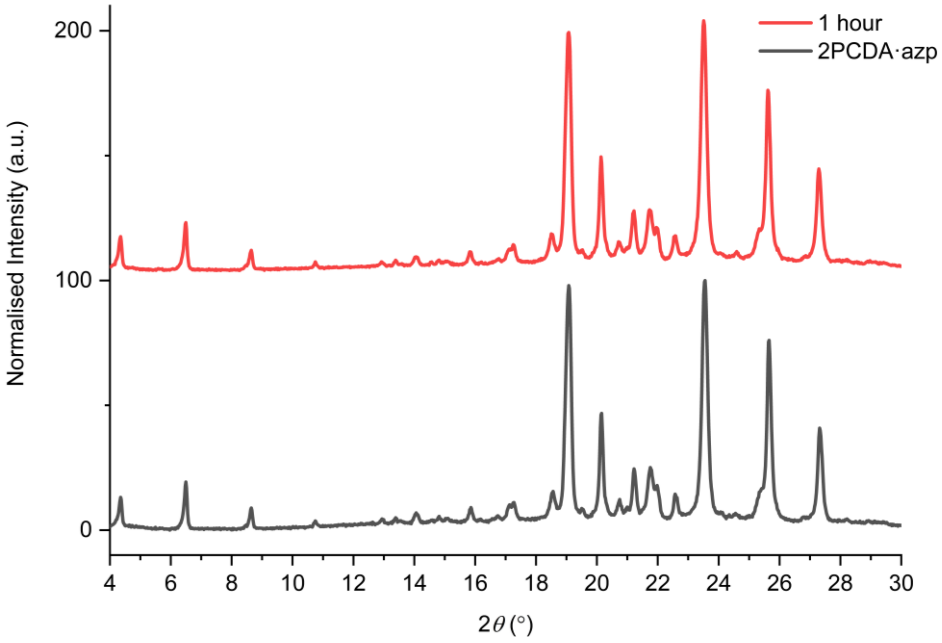

Figure 4.19. The experimental PXRD patterns of 2PCDA·azp that was exposed to UV radiation (254 nm) for one hour.

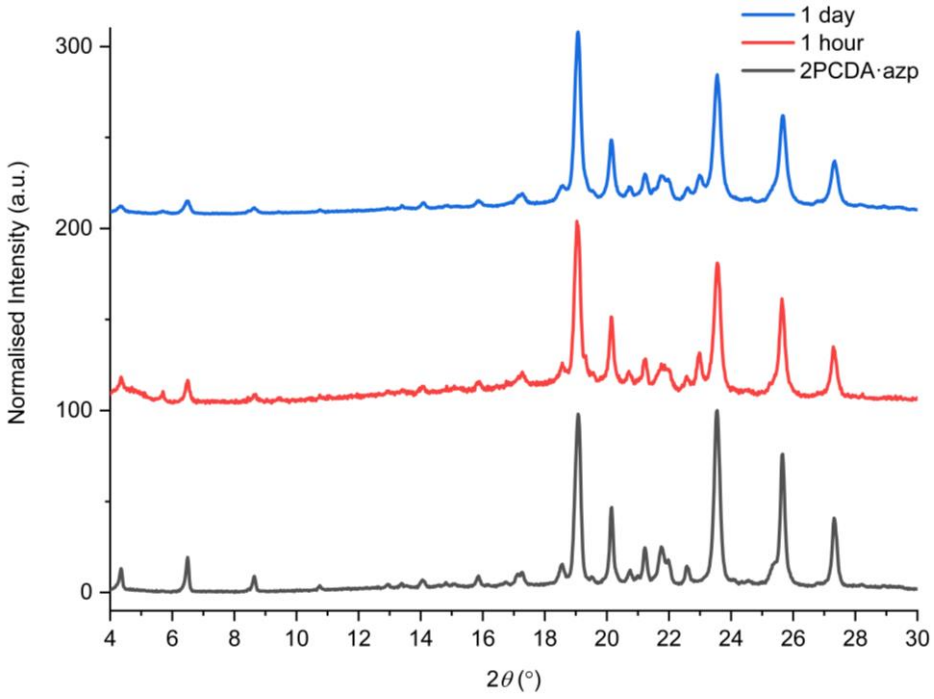

Figure 4.20. The experimental PXRD patterns of 2PCDA·azp that was exposed to UV radiation (365 nm) for one hour. The additional peak at 23.0 ° in the one hour and one day patterns correlates to PCDA.

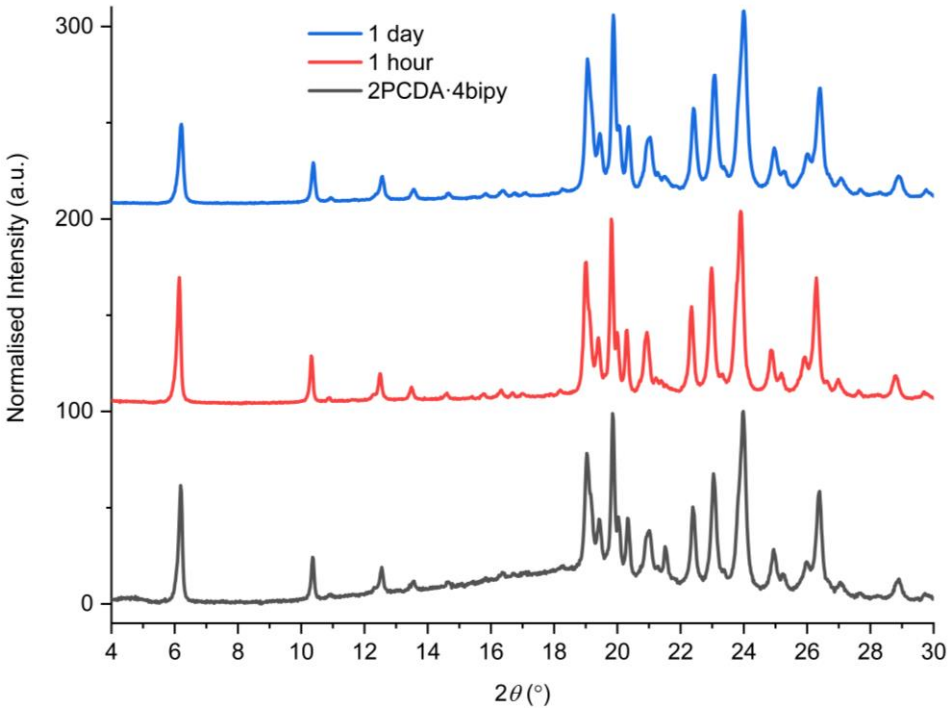

Figure 4.21. The experimental PXRD patterns of 2PCDA·4bipy that was exposed to UV radiation (254 nm) for one hour.

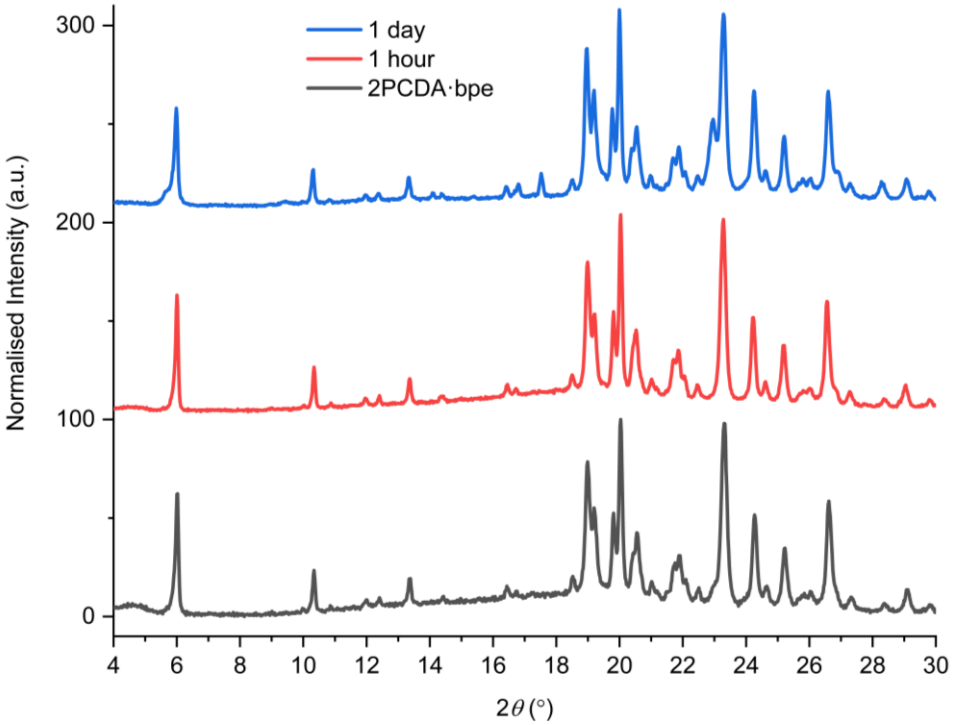

Figure 4.22. The experimental PXRD patterns of 2PCDA·bpe that was exposed to UV radiation (254 nm) for one hour. The peaks emerging in the one-day irradiated patterns at 5.7, 17.5, and 23.0 °, correlate to peaks of PCDA.

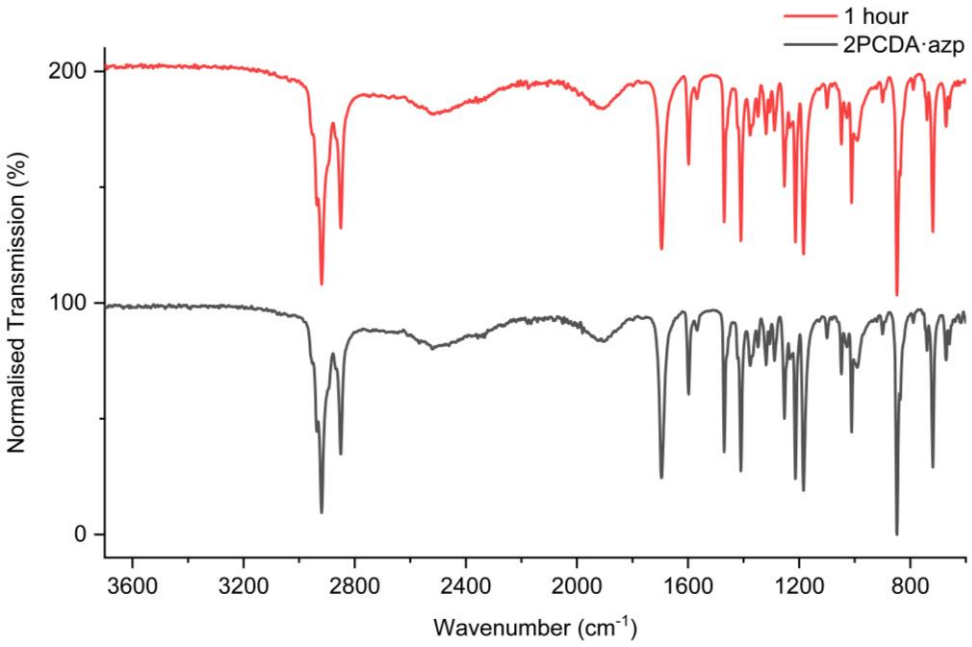

Figure 4.23. The FTIR spectra of 2PCDA·azp that was exposed to UV radiation (254 nm) for one hour.

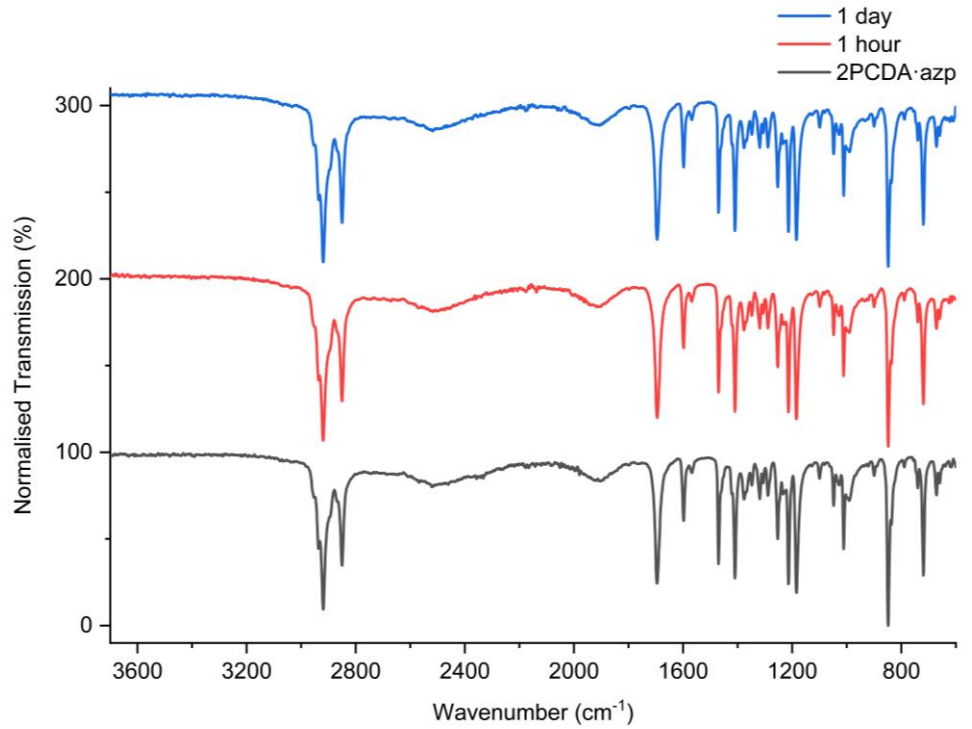

Figure 4.24. The FTIR spectra of 2PCDA·azp that was exposed to UV radiation (365 nm) for one hour and one day.

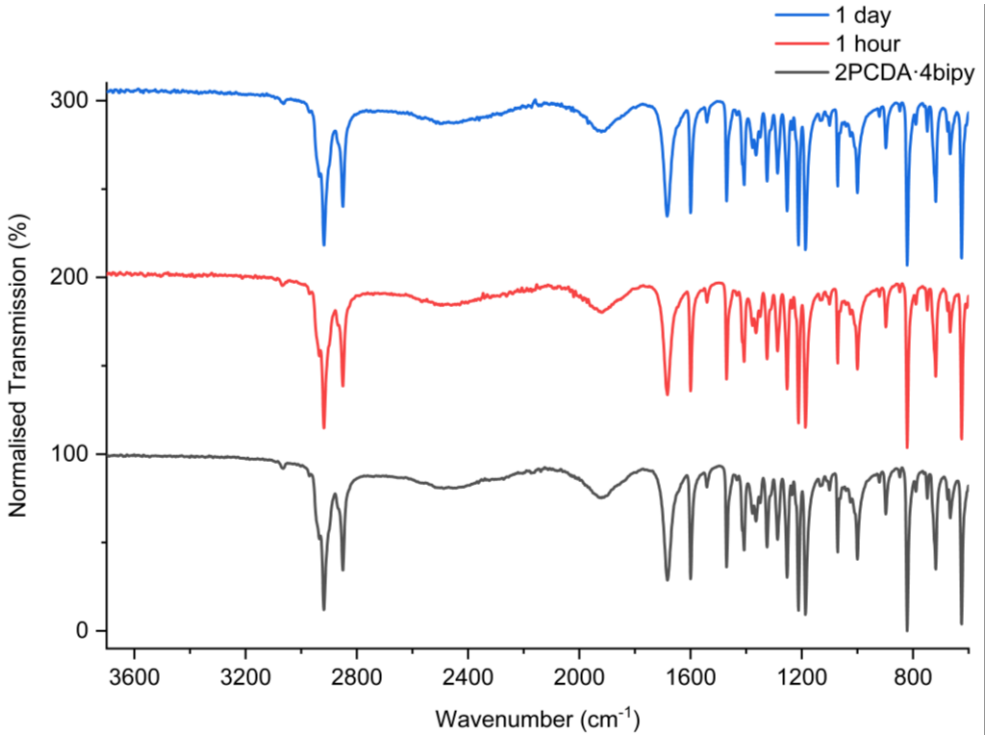

Figure 4.25. The FTIR spectra of 2PCDA·4bipy that was exposed to UV radiation (254 nm) for one hour and one day.

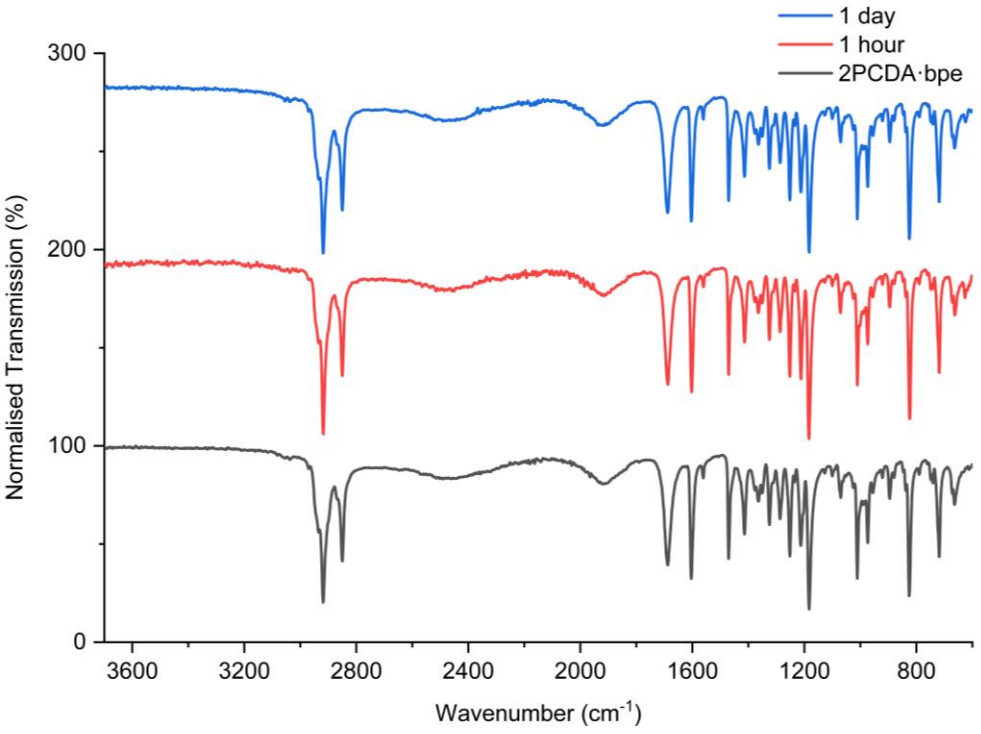

Figure 4.26. The FTIR spectra of 2PCDA·bpe that was exposed to UV radiation (254 nm) for one hour and one day.

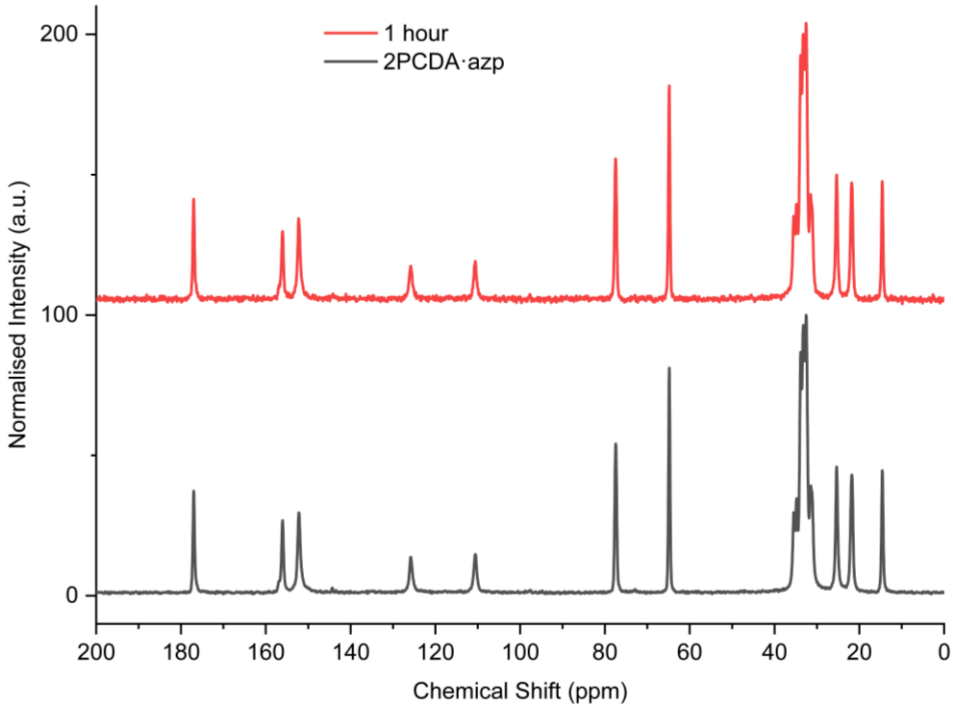

Figure 4.27. The ssNMR spectra of 2PCDA·azp that was exposed to UV radiation (254 nm) for one hour.

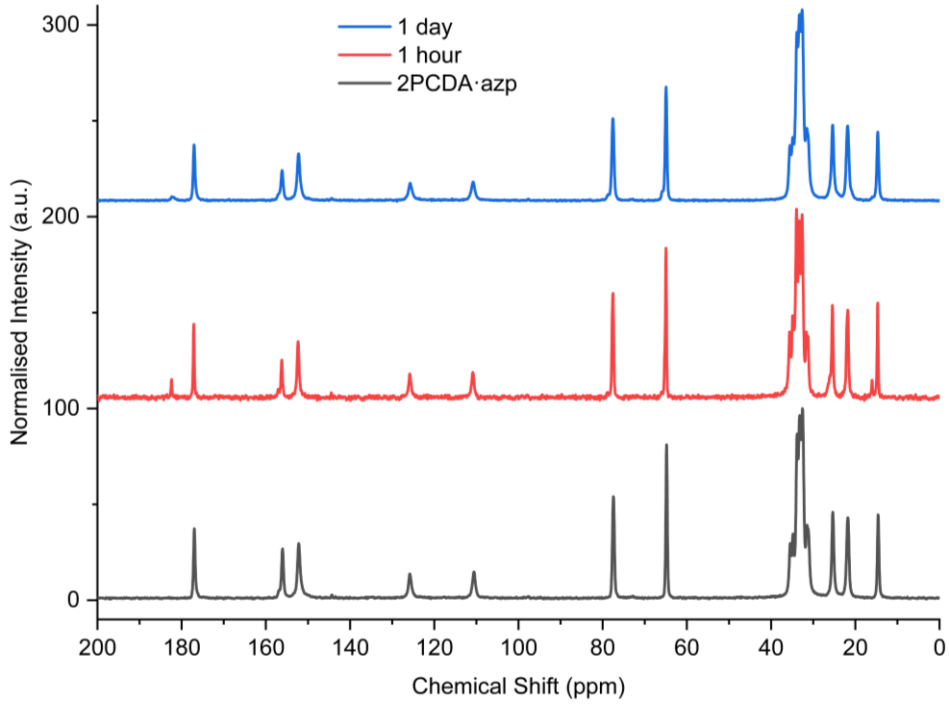

Figure 4.28. The ssNMR spectra of 2PCDA·azp that was exposed to UV radiation (365 nm) for one hour. The additional peak at 182.5 ppm which correlates to the carboxylate peak of PCDA.

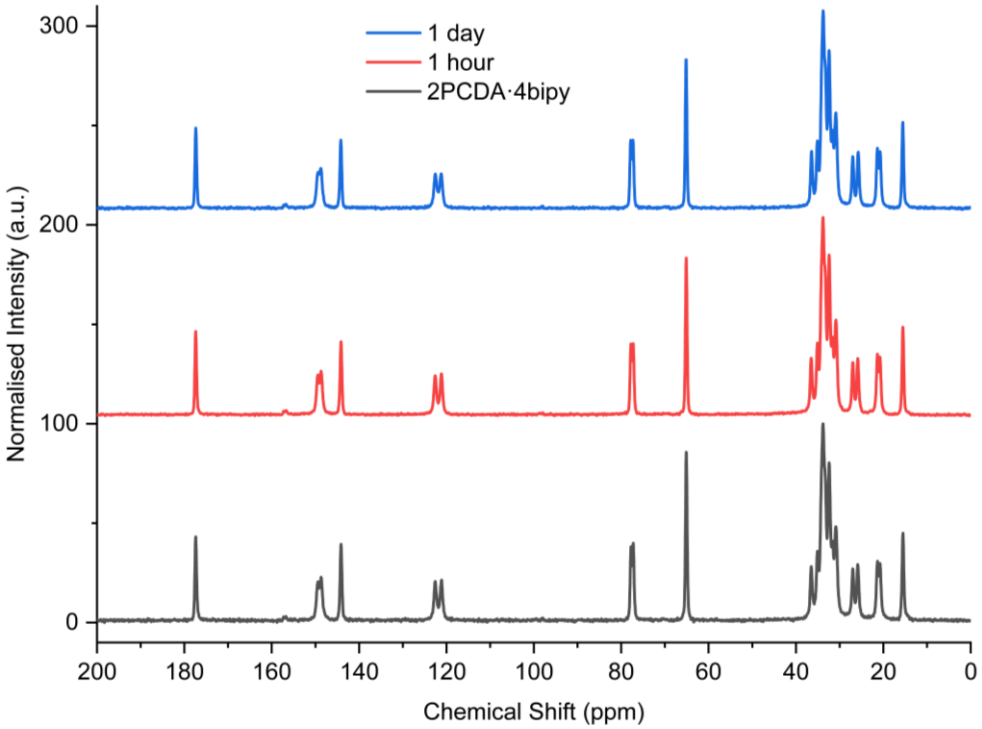

Figure 4.29. The ssNMR spectra of 2PCDA·4bipy that was exposed to UV radiation (254 nm) for one hour.

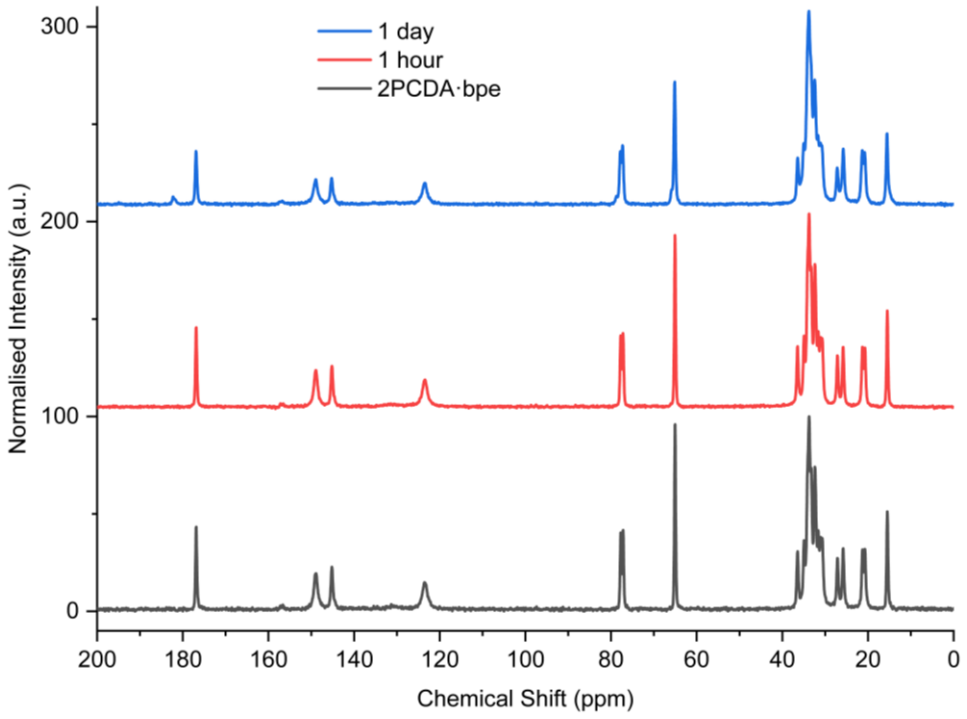

Figure 4.30. The ssNMR spectra of 2PCDA·bpe that was exposed to UV radiation (365 nm) for one hour. The additional peak at 180.3 ppm in the one-day irradiated spectra corresponds to the carboxylate peak of PCDA.

When all PCDA cocrystals were irradiated with 10 Gy of X-ray radiation and analysed by Raman spectroscopy, they showed very little photoreactivity as evidenced by the low intensity peaks in the conjugated ene-yne region (approx. 2100 cm^{-1})[33] that exists before and after irradiation (Figure 4.31). Due to the pre-resonance Raman effect mentioned previously, cocrystal 2PCDA·azp has a small ene-yne band present at 2100.4 cm^{-1} compared to the other two cocrystals likely arising from small amounts of PCDA photopolymer present as a contaminant in the starting PCDA sample.

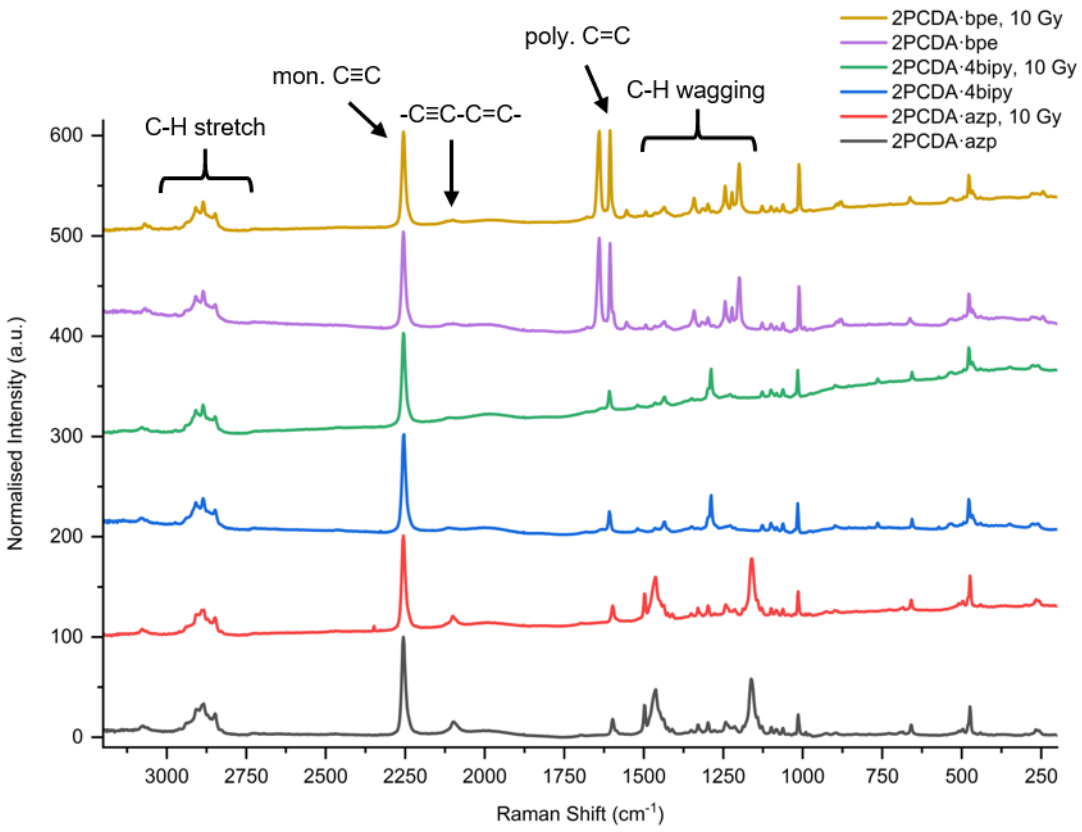

Figure 4.31. The Raman spectra of 2PCDA·azp, 2PCDA·4bipy, and 2PCDA·bpe before and after exposure to 10 Gy of X-ray radiation.

4.2.2. PCDA Salts

PCDA Salt Structure

Cocrystals of PCDA with bifunctional coformers azp, 4bipy, and bpe appear to give structures that are not photoreactive due to their topochemical metrics. To further investigate the topochemical postulate of different multicomponent materials, both mono- and bifunctional coformers with higher basicity were explored, intended to

deprotonate the PCDA acid functionality in order to alter the hydrogen bonding pattern and change the consequent stacking of the PCDA units. Salt formation was undertaken with bipip, morph, piper, etdiam, dietam, and butam (Figure 4.32).

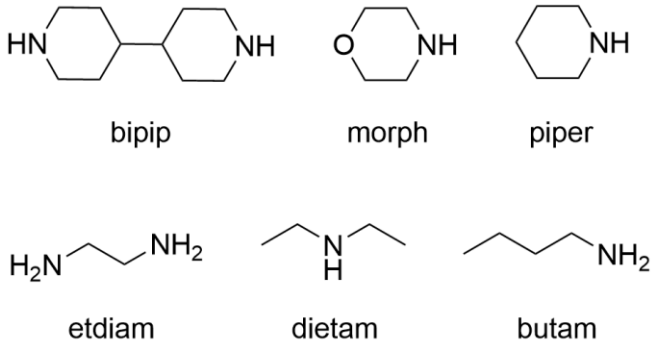

Figure 4.32. The aliphatic salt formers combined with PCDA to form salts.

The combination of PCDA and compounds bipip (2:1), morph (1:1), piper (1:1), etdiam (2:1), dietam (2:1), and butam (1:1) were mechanochemically ground in a mixer mill to give a range of new salt materials as indicated by PXRD, FTIR, and ssNMR analysis. The PXRD of each new salt reveals additional peaks that are not present in either of the patterns for the individual components, suggesting the formation of a new material. For instance, the salt 2PCDA·bipip displays a peak at 5.1 ° compared to the initial peak of PCDA and bipip at 5.7 ° and 6.2 °, respectively (Figure 4.33). The initial peak at 2.6 ° for PCDA·morph is different to that of PCDA and the calculated pattern of morph (15.9 °)[34] (Figure 4.34), while PCDA·piper and 2PCDA·etdiam have an initial PXRD peak at 5.4 ° which is different to that of PCDA and the calculated pattern of piper (10.2 °)[34] (Figure 4.35) or etdiam (19.5 °)[35] (Figure 4.36). The salt 2PCDA·dietam has an initial peak at 6.1 ° (though with a residual PCDA peak at 5.7 °) in contrast to PCDA and the calculated pattern of dietam (11.4 °)[36] (Figure 4.37), while the salt PCDA·butam has an initial peak of 6.2 °, compared to the peaks of PCDA and the calculated pattern of butam (6.6 °)[37] (Figure 4.38).

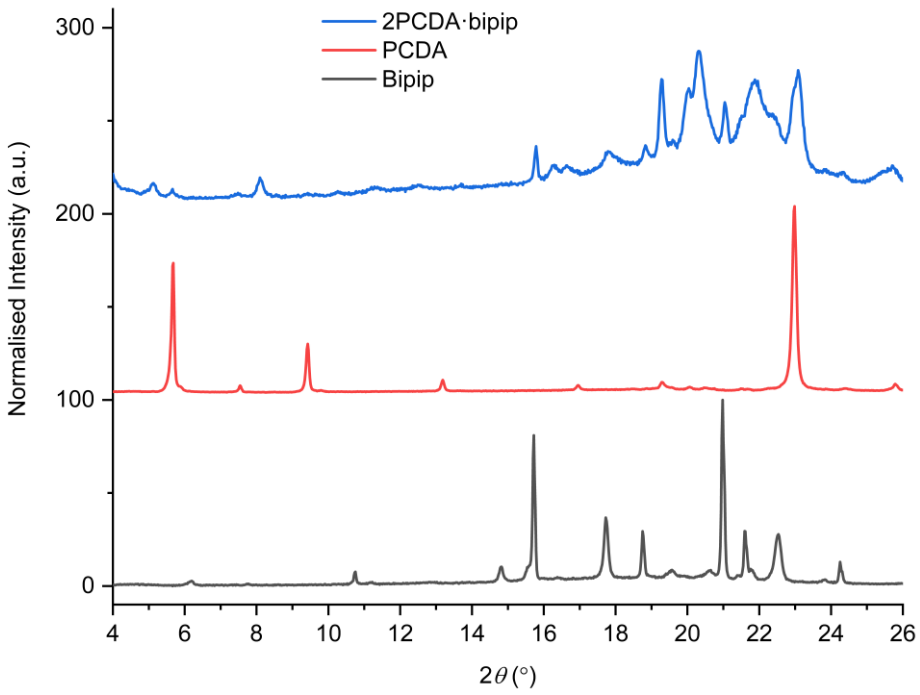

Figure 4.33. The experimental PXRD patterns of bipip, PCDA, and 2PCDA·bipip.

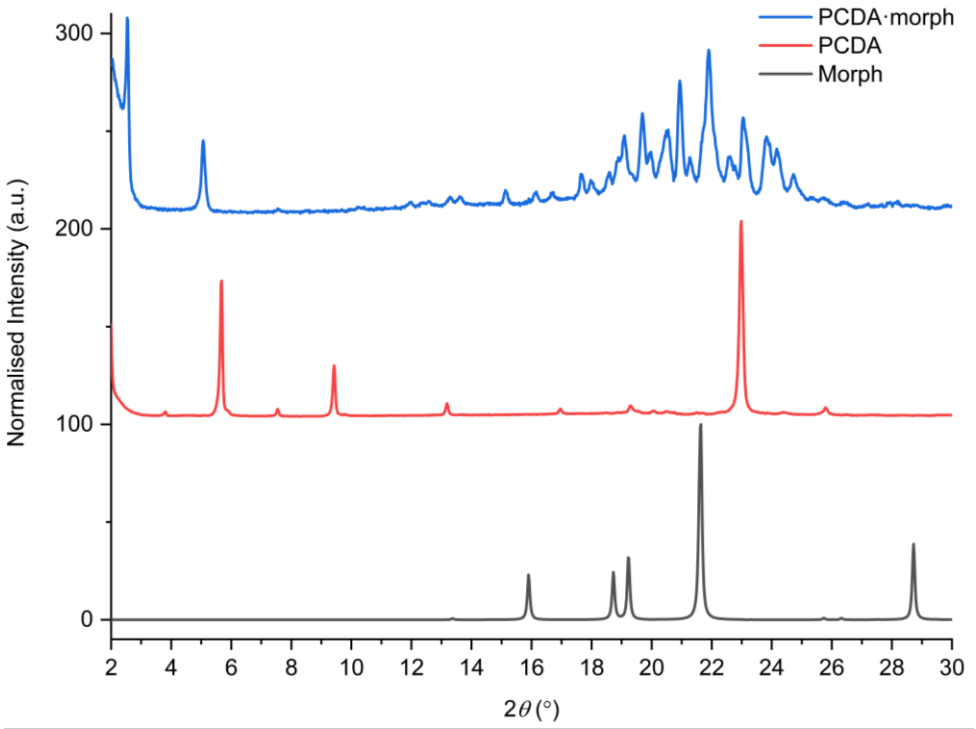

Figure 4.34. The experimental PXRD patterns of PCDA, PCDA·morph, and the calculated pattern of morph.[34]

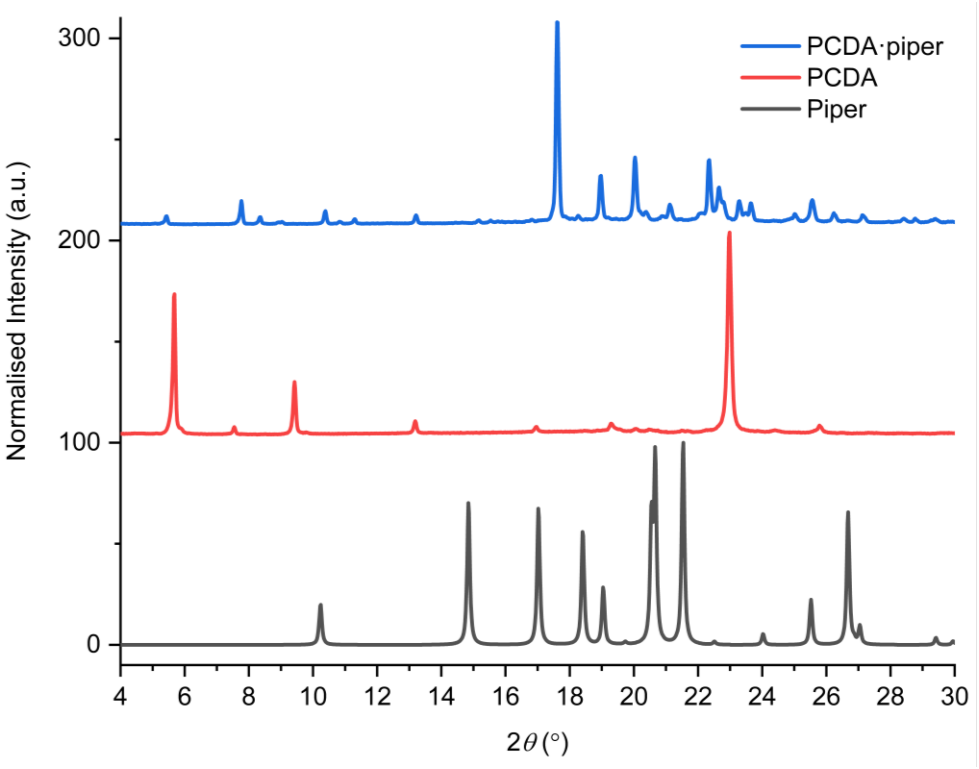

Figure 4.35. The experimental PXRD patterns of PCDA, PCDA·piper, and the calculated pattern of piper.[34]

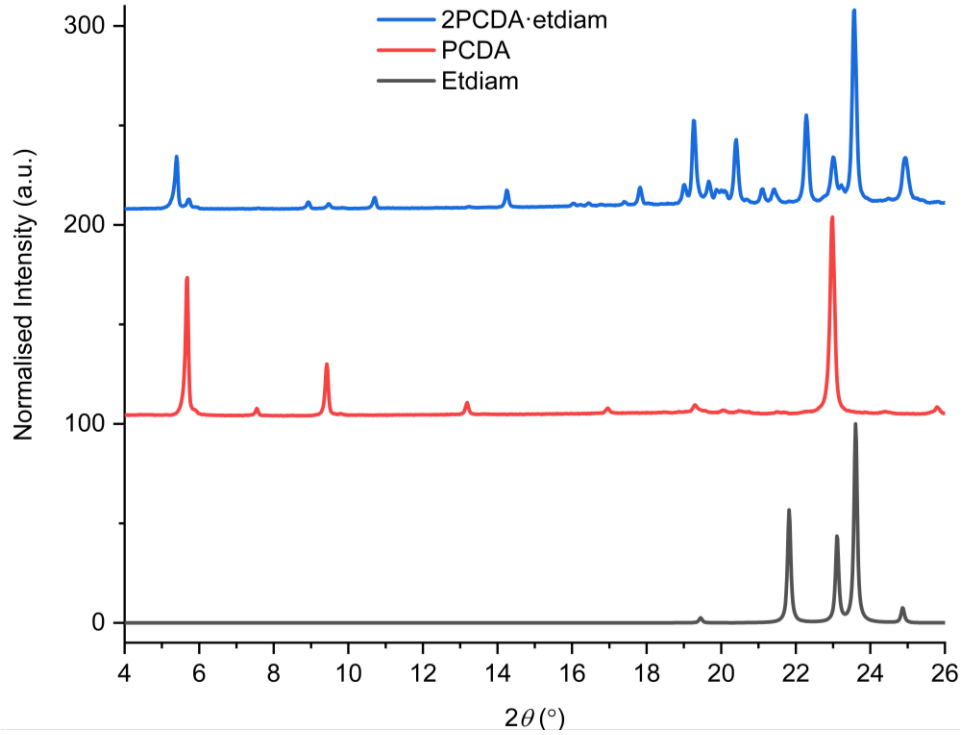

Figure 4.36. The experimental PXRD patterns of PCDA, PCDA·etdiam, and the calculated pattern of etdiam.[35]

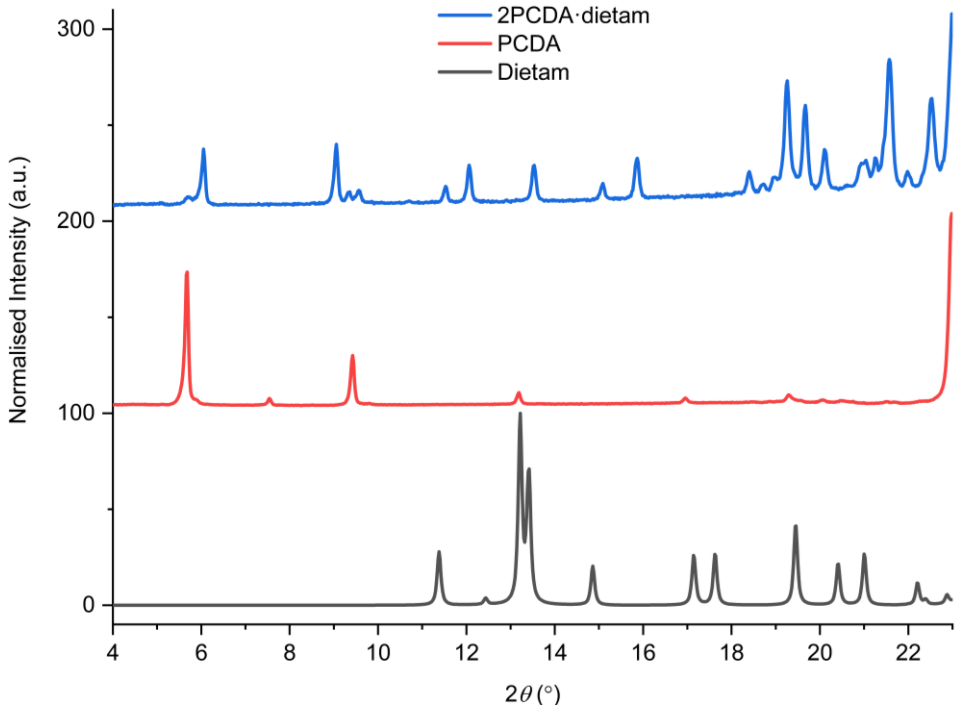

Figure 4.37. The experimental PXRD patterns of PCDA and 2PCDA·dietam, and the calculated pattern of dietam.[36]

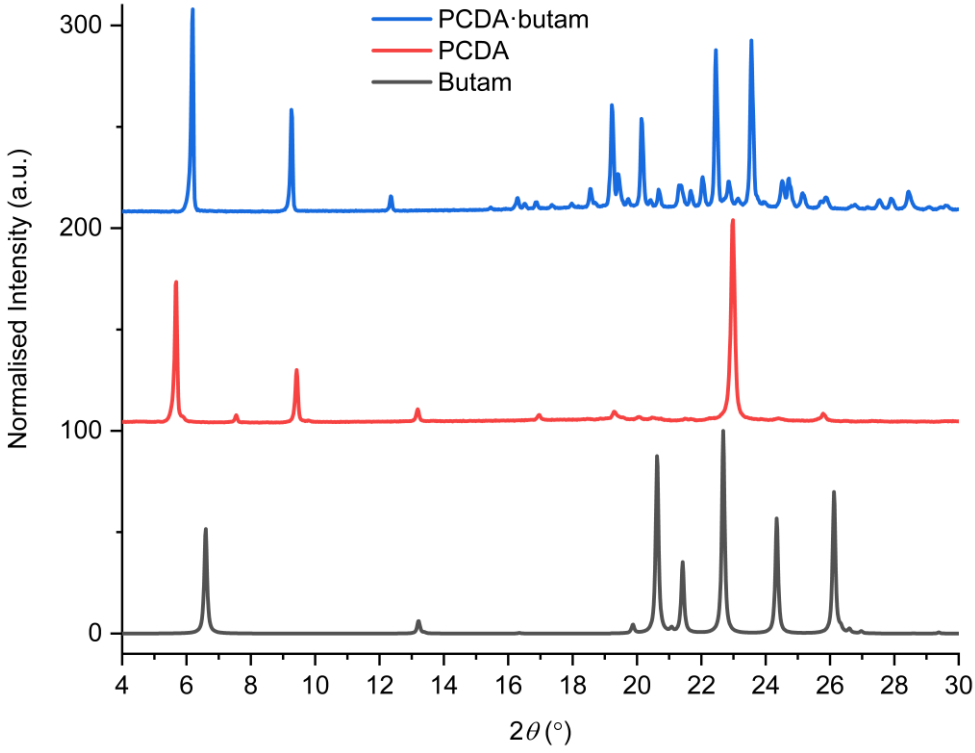

Figure 4.38. The experimental PXRD patterns of PCDA and PCDA·butam, and the calculated pattern of butam.[37]

Additionally, FTIR analysis reveals that the carbonyl stretching modes are at lower wavenumbers than in the free acid (PCDA, 1691 cm^{-1}) with a carbonyl stretch at 1653 cm^{-1} in 2PCDA·bipip, PCDA·morph, and PCDA·piper, 1659 cm^{-1} in 2PCDA·etdiam, 1627 cm^{-1} in 2PCDA·dietam, and 1649 cm^{-1} in PCDA·butam, suggesting stronger hydrogen bonding in the salts than the cocrystals and a delocalised carboxylate anion structure (Figure 4.39). In addition to FTIR spectroscopy, ssNMR spectroscopy is able to distinguish between different chemical environments. For instance, the carboxylate environment of PCDA is at a chemical shift of 182.4 ppm, though this environment changes depending on which salt former is combined with PCDA. The salt 2PCDA·bipip has a carboxylate peak at 182.6 ppm (Figure 4.40), while PCDA·morph and PCDA·piper have carboxylate peaks at 181.9 (Figure 4.41), and 181.6 ppm (Figure 4.42), respectively. The salt 2PCDA·etdiam has a small carboxylate peak at 183.7 ppm in (Figure 4.43), while 2PCDA·dietam (Figure 4.44) and PCDA·butam (Figure 4.45) have a carboxylate peaks at 181.4 ppm and 183.2 ppm, respectively.

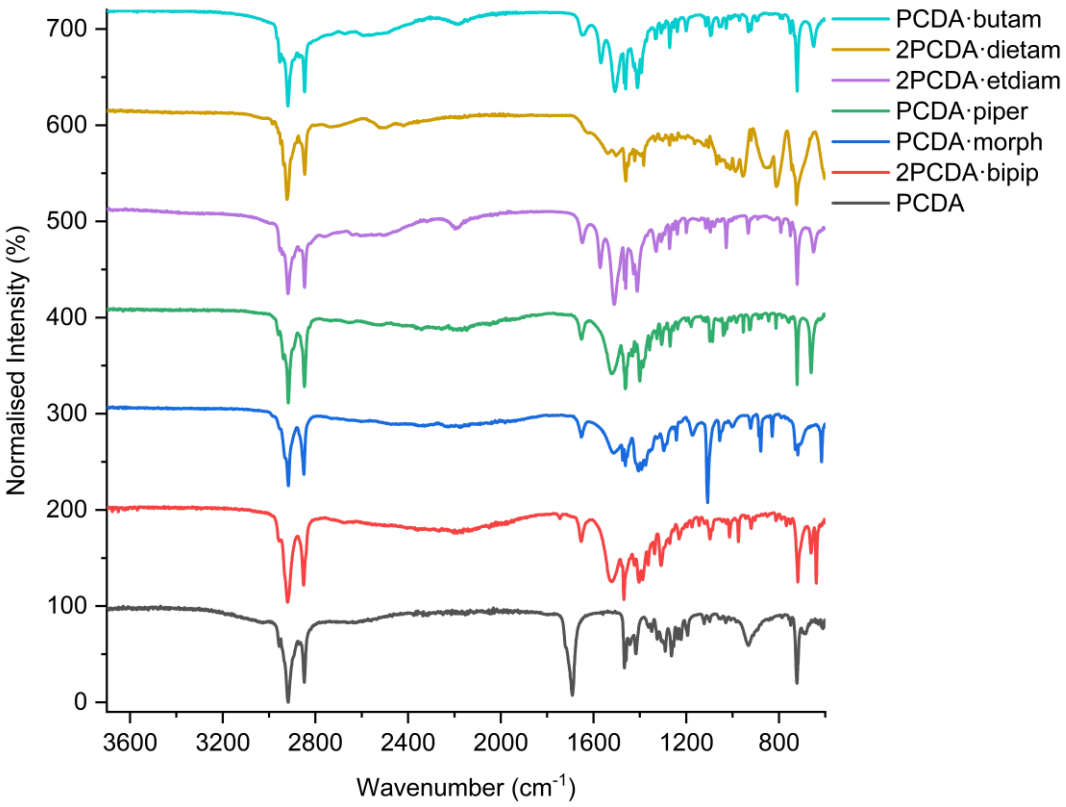

Figure 4.39. The FTIR spectra of salts 2PCDA·bipip, PCDA·morph, PCDA·piper, 2PCDA·etdiam, 2PCDA·dietam, and PCDA·butam compared to the free acid.

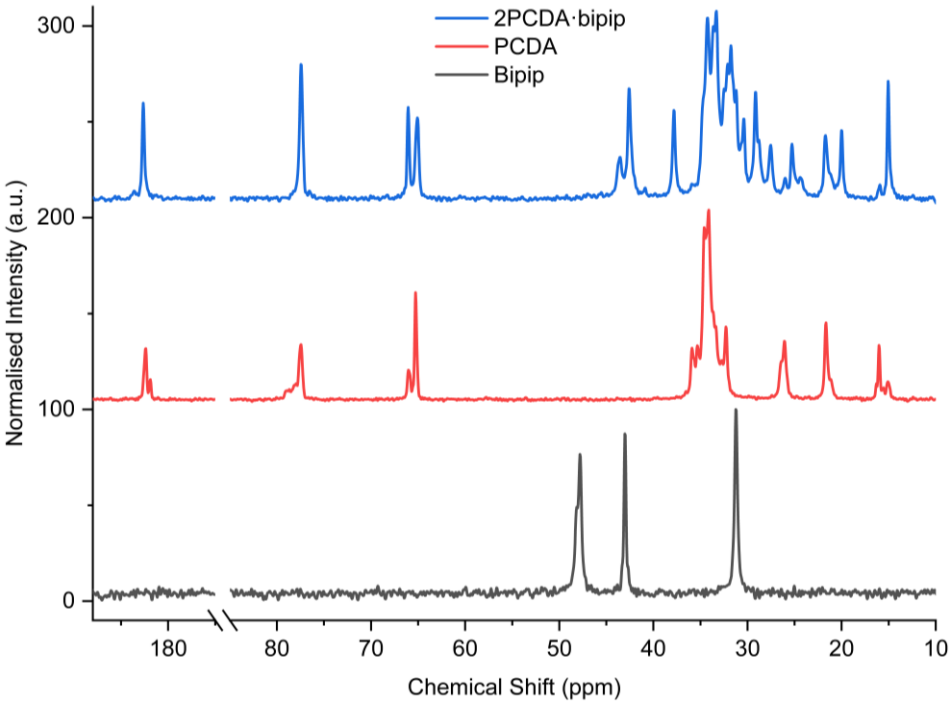

Figure 4.40. The ssNMR spectra of bipip, PCDA, and 2PCDA·bipip. An added break is included in the *x*-axis to compact the spectra.

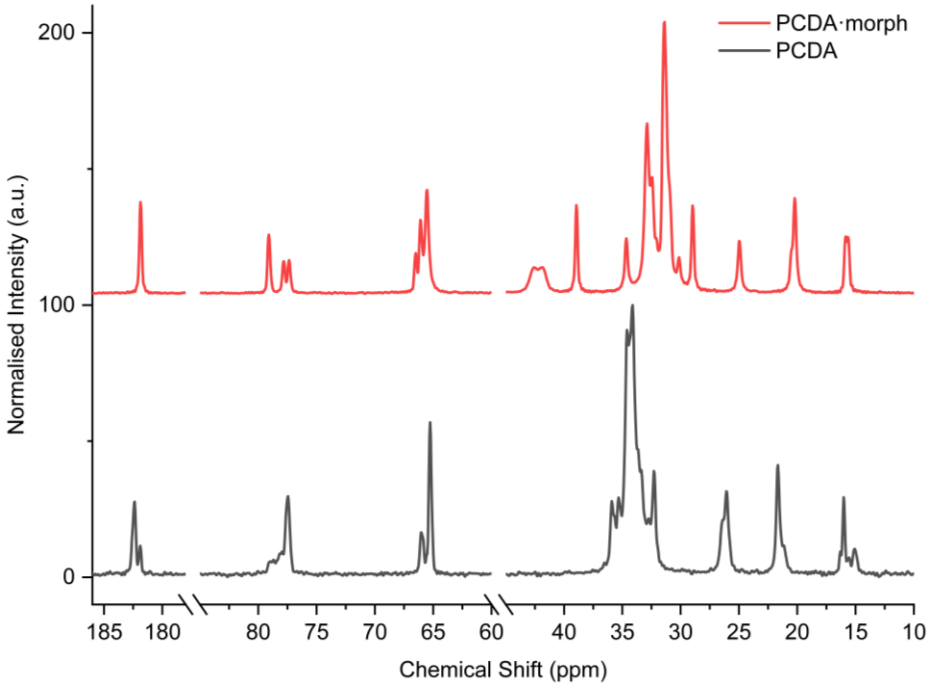

Figure 4.41. The ssNMR spectra of PCDA and PCDA·morph. Added breaks are included in the *x*-axis to compact the spectra.

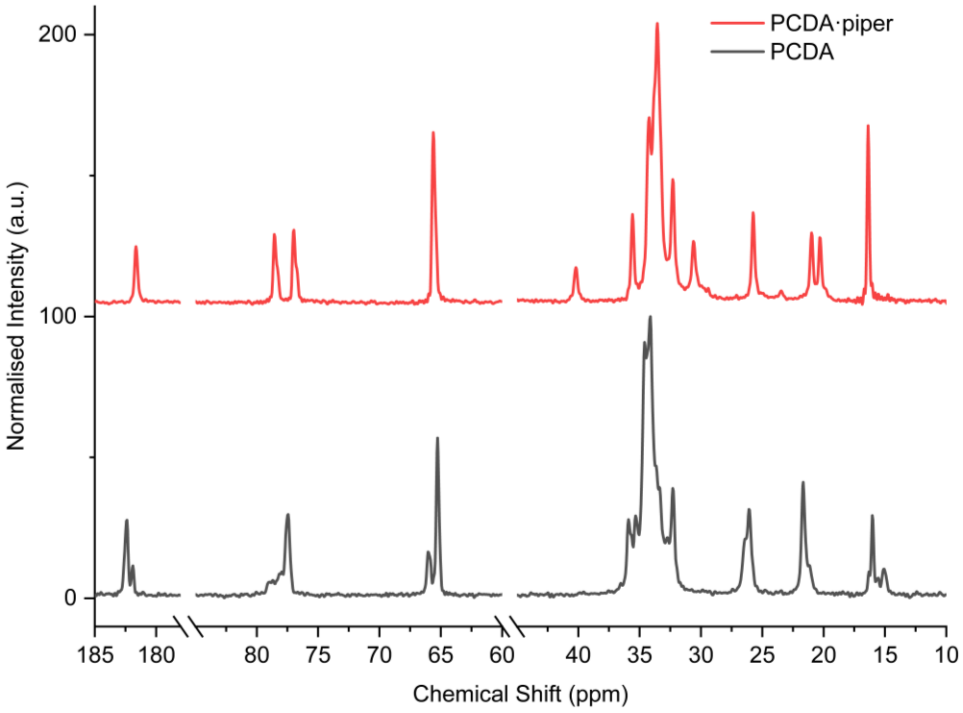

Figure 4.42. The ssNMR spectra of PCDA and PCDA·piper. Added breaks are included in the *x*-axis to compact the spectra.

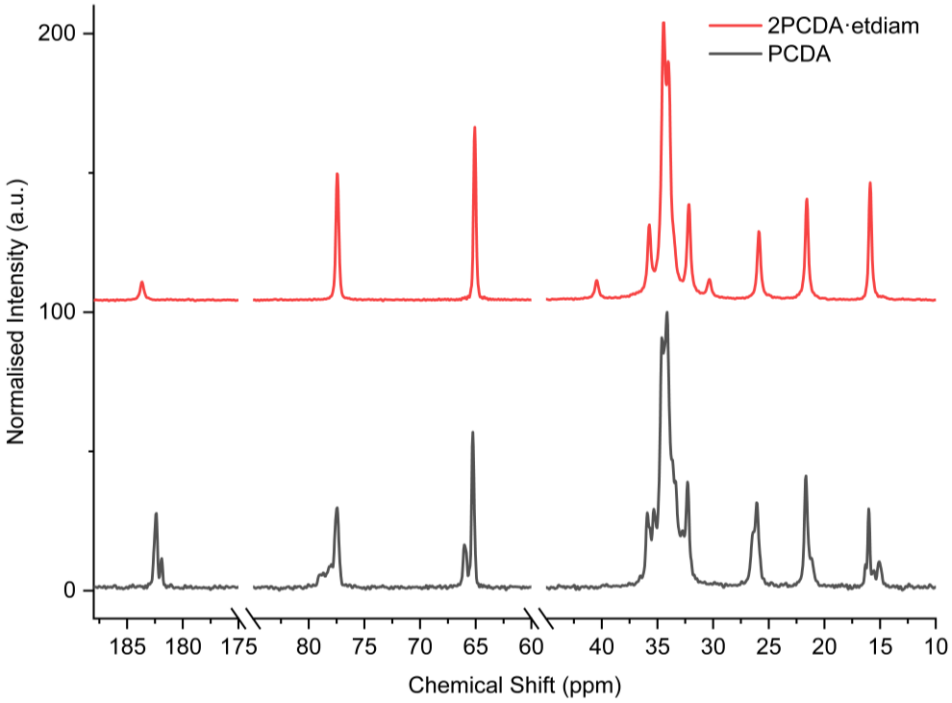

Figure 4.43. The ssNMR spectra of PCDA and PCDA·etdiam. Added breaks are included in the *x*-axis to compact the spectra.

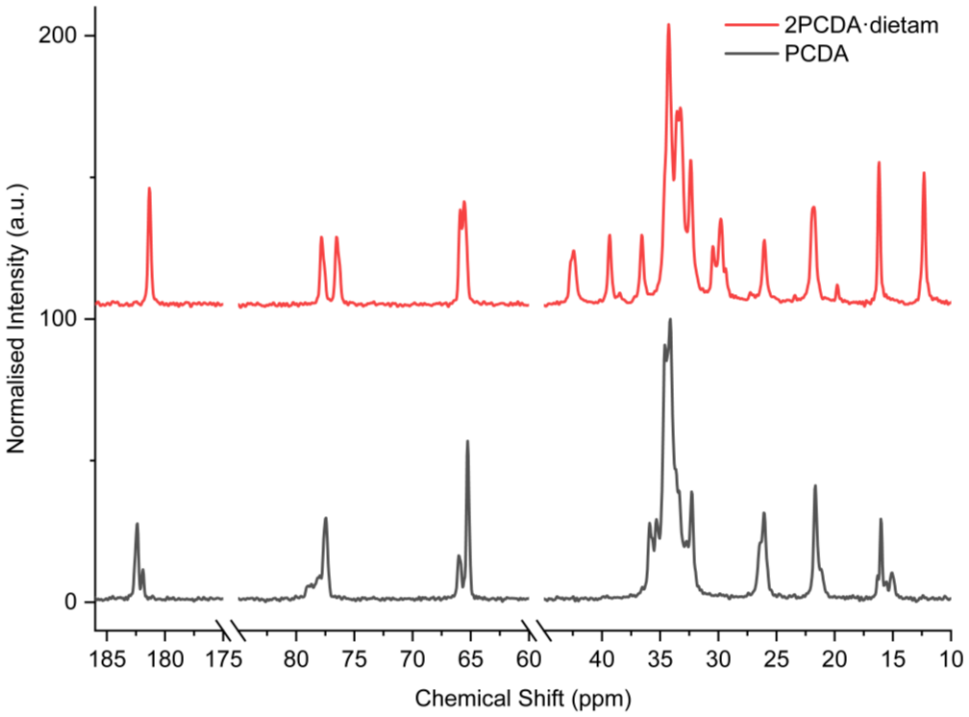

Figure 4.44. The ssNMR spectra of PCDA and 2PCDA·dietam. Added breaks are included in the *x*-axis to compact the spectra.

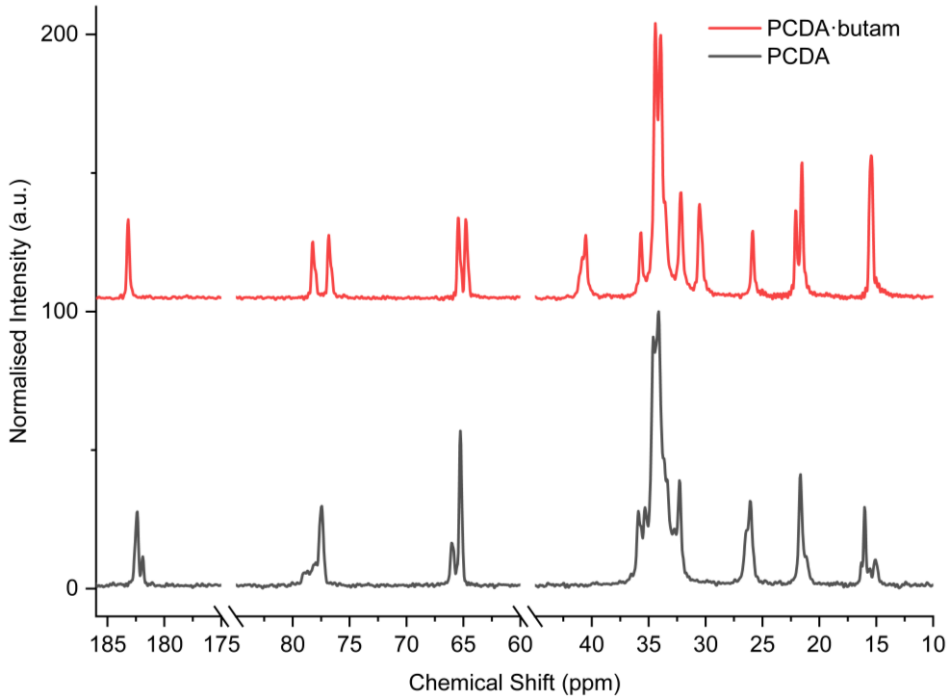

Figure 4.45. The ssNMR spectra of PCDA and PCDA·butam. Added breaks are included in the *x*-axis to compact the spectra.

The X-ray structure of 2PCDA·bipip reveals a salt with two anions of PCDA and a dication of double protonated bipip in a 2:1 stoichiometry, respectively. Also, NH···O hydrogen bonds occur from the amine hydrogen atom of bipip and the oxygen atom of PCDA, at an N···O distance of 2.717(1) Å (Figure 4.46). The salt 2PCDA·bipip crystallises with the same symmetry as PCDA and 2PCDA·azp in the space group $P\bar{1}$, with the crystallographic *c*-axis at the shortest observed so far at 23.0041(15) Å. The C1-C4' inter-alkyne distance between adjacent molecules of PCDA is 3.760(2) Å, which is within the topochemical postulate for the reactivity of diacetylenes (≤3.8 Å), however, the tilt angle of PCDA in the salt cocrystal is far below the desired value (45 °) at 24.1 °, and the translational repeat distance of 5.577(2) Å is outside the maximum distance for this parameter (≤4.9 Å), again suggesting limited photoreactivity.

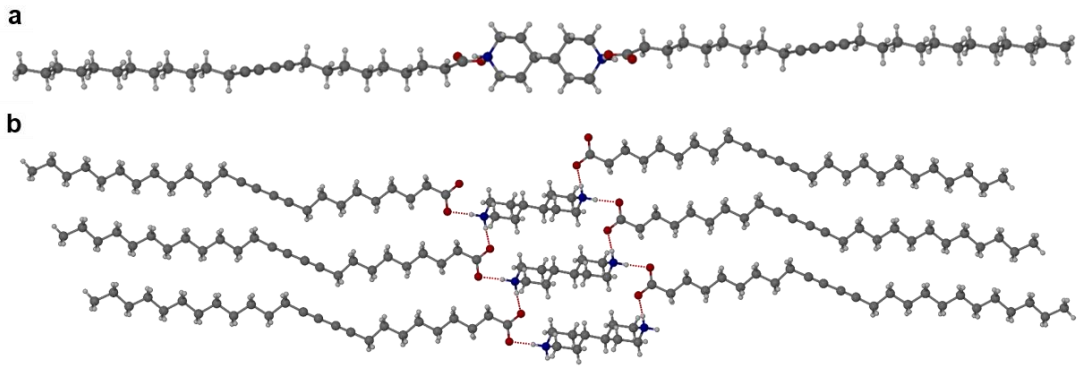

Figure 4.46. The X-ray structure of the salt cocrystal 2PCDA·bipip in the a) (100) and b) (001) crystallographic planes.

The PCDA·morph salt was crystallised by the slow evaporation of acetone at room temperature, however, due to poor crystal quality after repeated crystallisation attempts, no SC-XRD analysis of PCDA·morph could be undertaken. To model the interactions between the two components, the synthesis of a butA·morph salt was attempted. Large single crystals of butA·morph formed from equimolar amounts of reagents in a sealed flask allowed to stand overnight. The X-ray structure reveals a salt with a butanoate anion and protonated morpholinium cation (Figure 4.47). The structure involves two unique NH···O hydrogen bonding interactions with N···O distances of 2.673(1) Å and 2.732(1) Å. Based on the similar pK_a of PCDA and butA it is possible that PCDA·morph is also a salt with similar head-group structure, although the relevance of this model system to the PCDA analogue is otherwise

limited. Additionally, no crystal structures of PCDA·piper or 2PCDA·etdiam were possible after repeated crystallisation attempts.

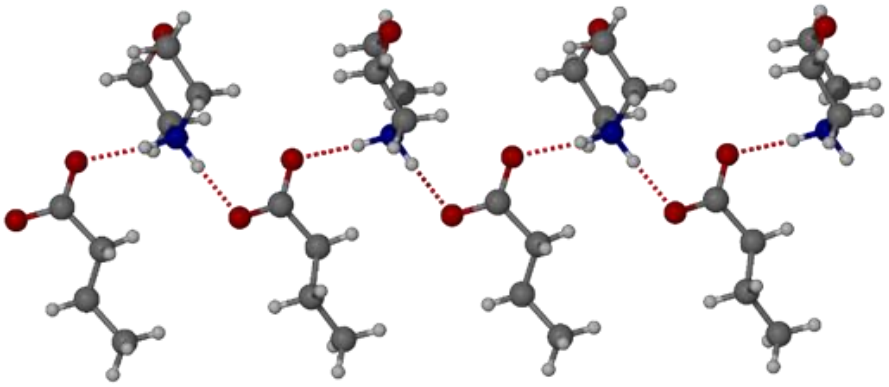

Figure 4.47. The X-ray structure of butA·morph showing two different hydrogen bonding interactions.

The salts 2PCDA·dietam and PCDA·butam crystallised by slow evaporation of acetone solutions at room temperature. Surprisingly, the crystals are highly coloured purple and blue, respectively, consistent with facile photopolymerisation (Figure 4.48). However, the X-ray structure determinations reveal salts of unpolymerised PCDA and hence the colouration is likely to be a surface effect. Indeed, cutting a single crystal in half revealed a colourless inner core. The structure of the diethylammonium salt proved to be a salt cocrystal that also includes a neutral molecule of PCDA (Figure 4.49). The butylammonium compound is a 1:1 salt and the structure adopts a stacked bilayer arrangement (Figure 4.50). In 2PCDA·dietam, hydrogen bonding occurs from the ammonium N-H hydrogen atoms to the carbonyl oxygen of PCDA, with an N···O distance of 2.737(1) Å. The carboxylic acid group of the neutral PCDA hydrogen bonds to the carboxylate functionality on the PCDA anion with a very short O···O distance of 2.444(1) Å (the additional hydrogen atom present between PCDA and the PCDA anion is disordered). In the 1:1 salt PCDA·butam, there are three different hydrogen bond interactions from the NH_3^+ cation to the carboxylate oxygen atoms of the PCDA anion, with NH···O distances of 2.671(1) Å, 2.725(1) Å, and 2.784(1) Å. The 2PCDA·dietam structure also has a large *c*-axis of 57.520(4) Å, which is the longest *c*-axis of all the structures studied reflecting the linear, parallel arrangement of the PCDA components. Salts 2PCDA·dietam and PCDA·butam have similar C1-C4' inter-alkyne distances of 3.776(2) Å and 3.779(1) Å, respectively, with tilt angles of 41.9 ° and 43.7 °, and translational repeat distances of 4.644(3) Å and 4.593(1) Å. For

these two salts, all three values are well within the optimum parameters of the topochemical postulate, and they are therefore are expected to show significant photoreactivity, consistent with the spontaneous surface colouration of the crystals.

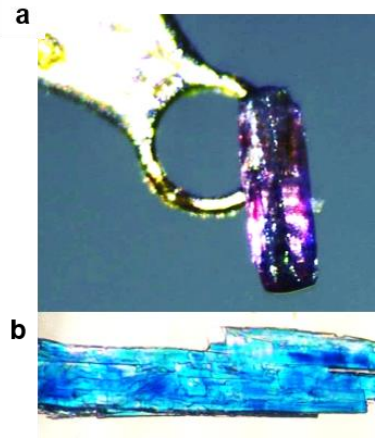

Figure 4.48. Photographs of a) the purple crystal of 2PCDA·dietam and b) the blue crystals of PCDA·butam, taken before X-ray irradiation.

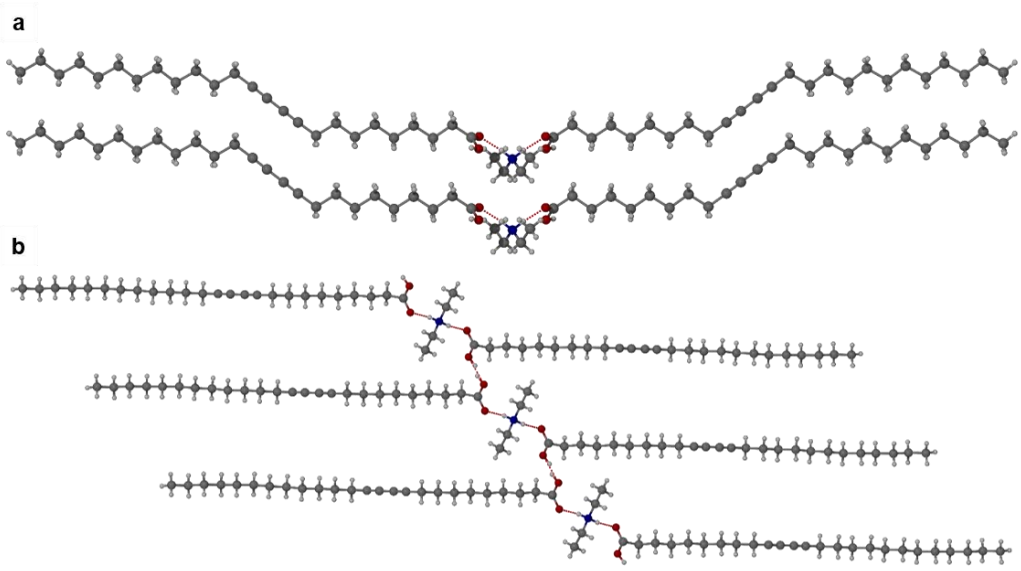

Figure 4.49. The X-ray structure of 2PCDA·dietam in the a) (100) and b) (010) crystallographic planes.

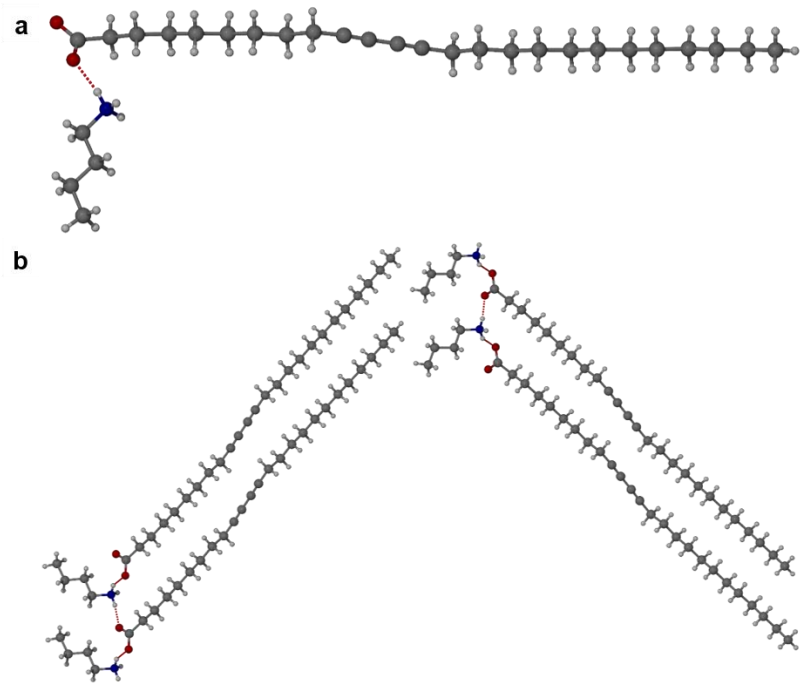

Figure 4.50. The X-ray structure of PCDA·butam b) in the (100) crystallographic plane.

The DSC analyses of the PCDA salts reveal melt onset endotherms of 107 °C for 2PCDA·bipip (Figure 4.51) (compared to 62 °C and 170 °C[38] for the parent components PCDA and bipip, respectively). This relatively high value likely reflects the fact that proton transfer has occurred as well as the higher melting point of the bipip coformer. The salt PCDA·morph has a low melting onset of 44 °C (Figure 4.52) consistent with the fact that morph is a liquid at room temperature (it freezes and boils at −5.8 °C and 128 °C, respectively).[39] The DSC thermogram of PCDA·piper displays a split onset of endotherm at 41.3 °C and 46.4 °C, which do not correspond to the melting point of PCDA or the boiling point of piper (106 °C)[40] (Figure 4.53). Unfortunately, a DSC thermogram of 2PCDA·etdiam could be obtained. However, the salt 2PCDA·dietam exhibits a melt onset endotherm of 46 °C (Figure 4.54), in comparison to the boiling temperature of 55 °C for dietam,[41] while PCDA·butam displays a melt onset endotherm at 57 °C (Figure 4.55), with the salt former butam boiling at 77 °C.[42]

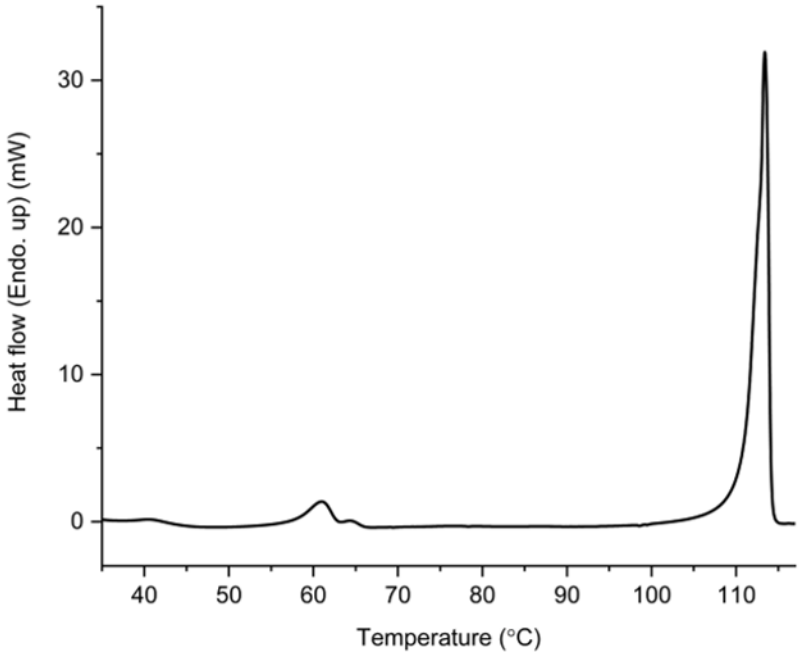

Figure 4.51. The DSC thermogram of 2PCDA·bipip displaying a melt onset endotherm at 107.4 °C with residual unreacted PCDA between 59.5-64.6 °C

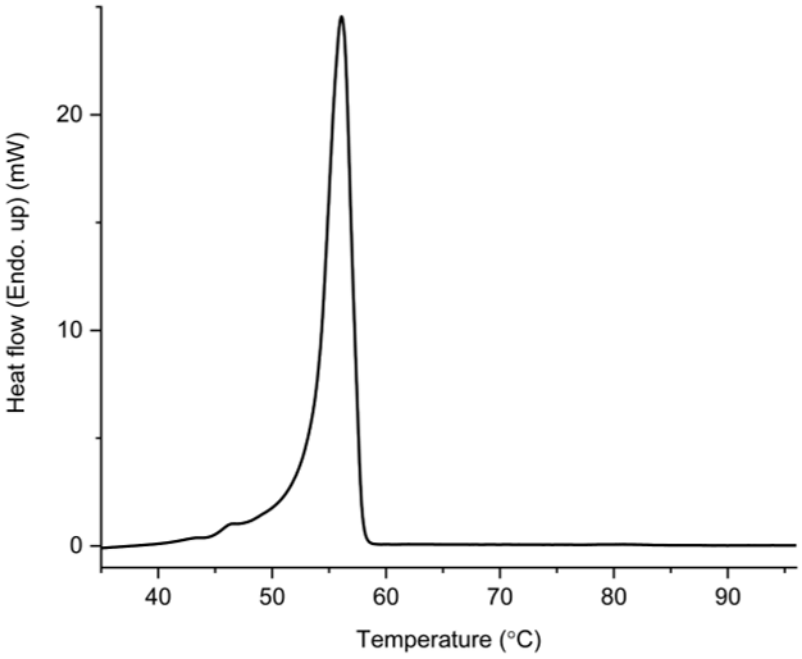

Figure 4.52. The DSC thermogram of PCDA·morph displaying a melt onset endotherm at 43.8 °C.

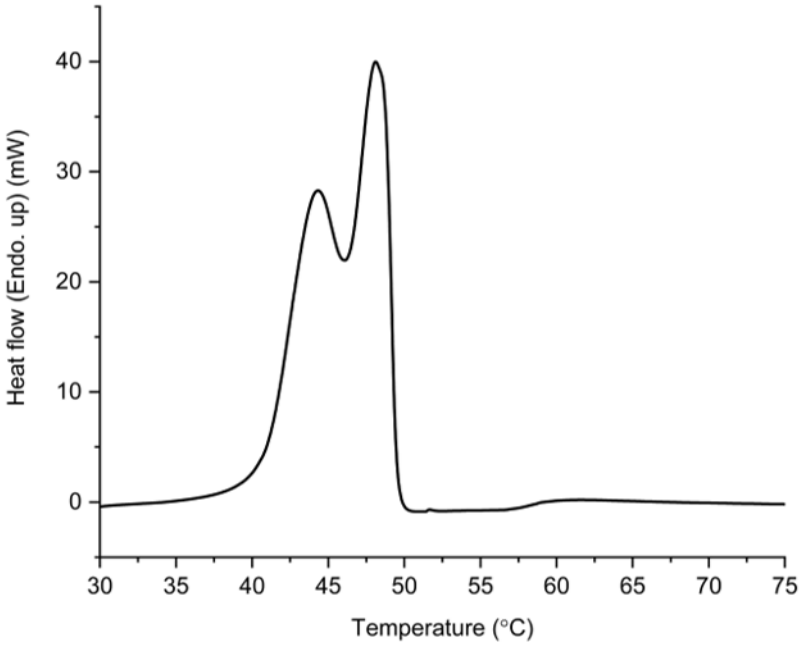

Figure 4.53. The DSC thermogram of PCDA·piper displaying a split melt onset endotherm at 41.3 °C and 46.4 °C, suggesting the presence of an impurity.

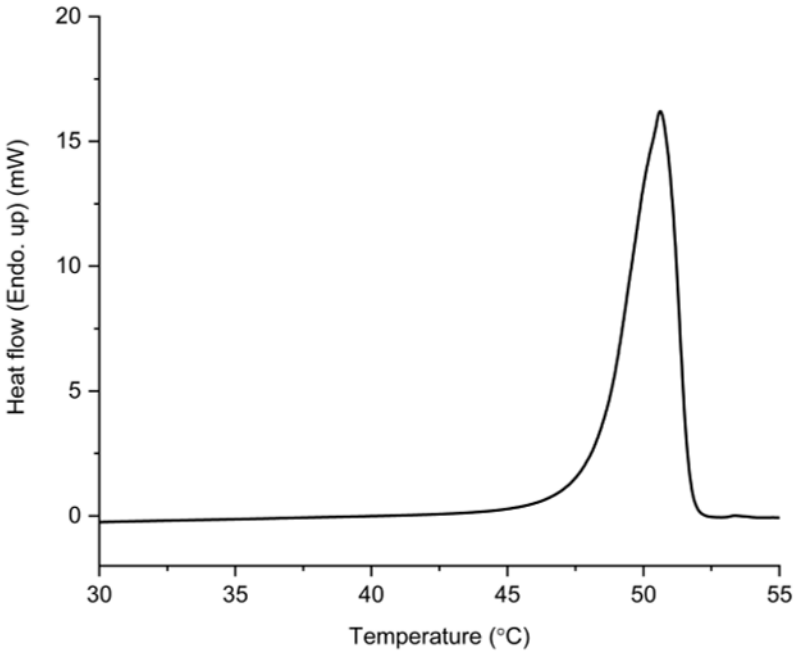

Figure 4.54. The DSC thermogram of 2PCDA·dietam displaying a melt onset endotherm at 45.8 °C

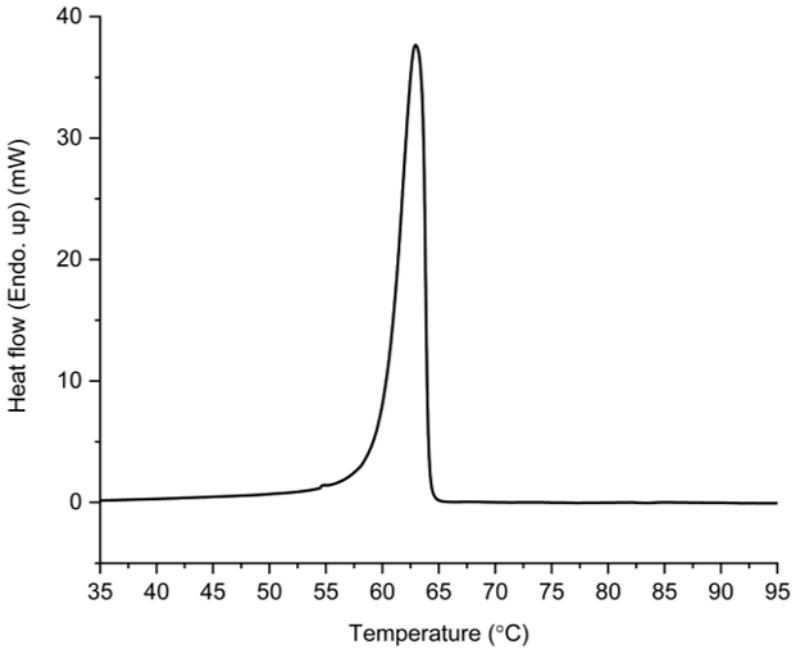

Figure 4.55. The DSC thermogram of PCDA·butam displaying a melt onset endotherm at 57.3 °C.

PCDA Salt Photoreactivity

The salts 2PCDA·bipip, PCDA·morph, PCDA·piper, 2PCDA·dietam, and PCDA·butam were exposed to UV radiation (254 nm) for different durations to investigate whether the new materials were photoresponsive. Initial photoreactivity studies indicate that all salts (apart from 2PCDA·bipip) are sensitive to radiation due to the significant darkening of the powders with prolonged irradiation (Figure 4.56).

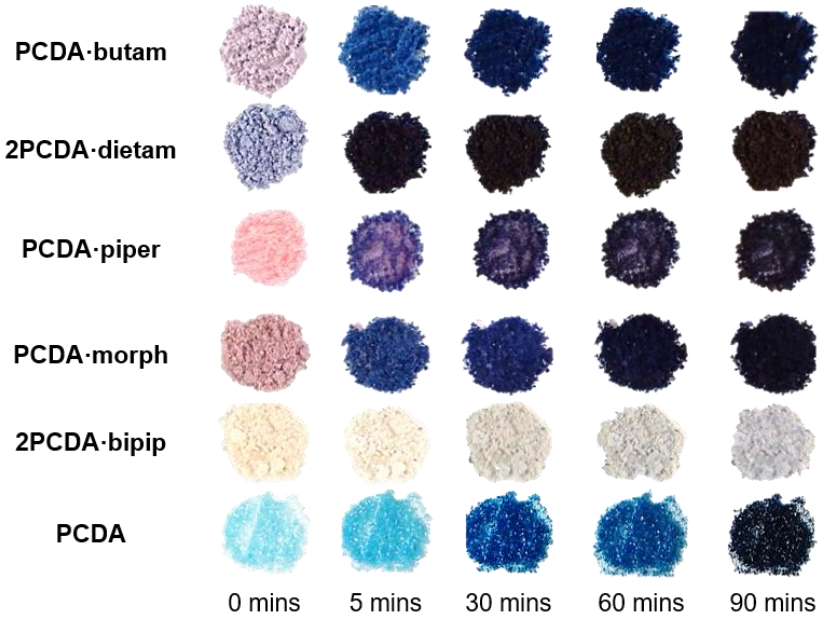

Figure 4.56. The salts 2PCDA·bipip, PCDA·morph, PCDA·piper, 2PCDA·dietam, and PCDA·butam exposed to UV radiation (254 nm) for different durations. Photographs of 2PCDA·etdiam before and after UV irradiation are not currently available.

The bipiperidinium salt 2PCDA·bipip is not photoresponsive, evident by the PXRD (Figure 4.57), FTIR (Figure 4.58), and ssNMR analyses (Figure 4.59), consistent with the unfavourable translational repeat distance observed in the X-ray structure. From these results, bifunctional salt/coformers in general seem to give rise to a slightly offset packing mode that consistently results in an unfavourable repeat distance and tilt angle and hence essentially no photosensitivity. In contrast, the salts of monofunctional ammonium cations are all highly photoactive. Significant visual colour change occurs after just five minutes of irradiation for the salts PCDA·morph, PCDA·piper, 2PCDA·dietam, and PCDA·butam (Figure 4.56). Signals assigned to photopolymerised material are clearly visible by solid-state NMR spectroscopy. The salt PCDA·morph displays a monomer to polymer conversion of ≤7 % after one day and ≤27 % after seven days of exposure to UV radiation (Figure 4.60). The amount of polymerised material is determined by integrating the alkyne peak of greatest intensity compared to the alkene peaks (100-140 ppm). However, the salt PCDA·piper displays a greater sensitivity to UV radiation with the photoconversion after one day of UV exposure to be ≤30 %, increasing to ≤98 % after seven days of exposure (Figure 4.61). Similarly, 2PCDA·dietam shows the greatest sensitivity towards UV radiation by

ssNMR spectroscopy with the most significant change occurring in the alkene region of the spectrum corresponding to the ene-yne photopolymer functionality. The photoconversion of 2PCDA·dietam is suggested to be ≤42 % after one day of UV irradiation, and increases to almost complete conversion of monomer to polymer (≤99 %) after seven days of irradiation (Figure 4.62). In contrast, PCDA·butam only shows ≤10 % of monomer to polymer conversion after one day of irradiation, increasing to ≤33 % of photoconversion after exposure to UV radiation for one week (Figure 4.63). However, even in these systems the conversion is slow, and the sharpness of the NMR resonances imply a relatively low degree of oligomerisation. This kind of slow reactivity reflects the solid-state nature of the process resulting in poor radiation penetration into the bulk of the sample. However, this gradual response is desirable in dosimetry applications making these materials of considerable commercial interest. The photoreactivity of 2PCDA·dietam and PCDA·butam is consistent with the crystal packing revealed by their structures, which both show parameters within the range specified by the topochemical postulate. While structural data is not available for the morpholinium or piperidinium salts, it seems likely that these too are within the topochemical postulate range. The topochemical parameters for each compound are summarised in Table 4.2.

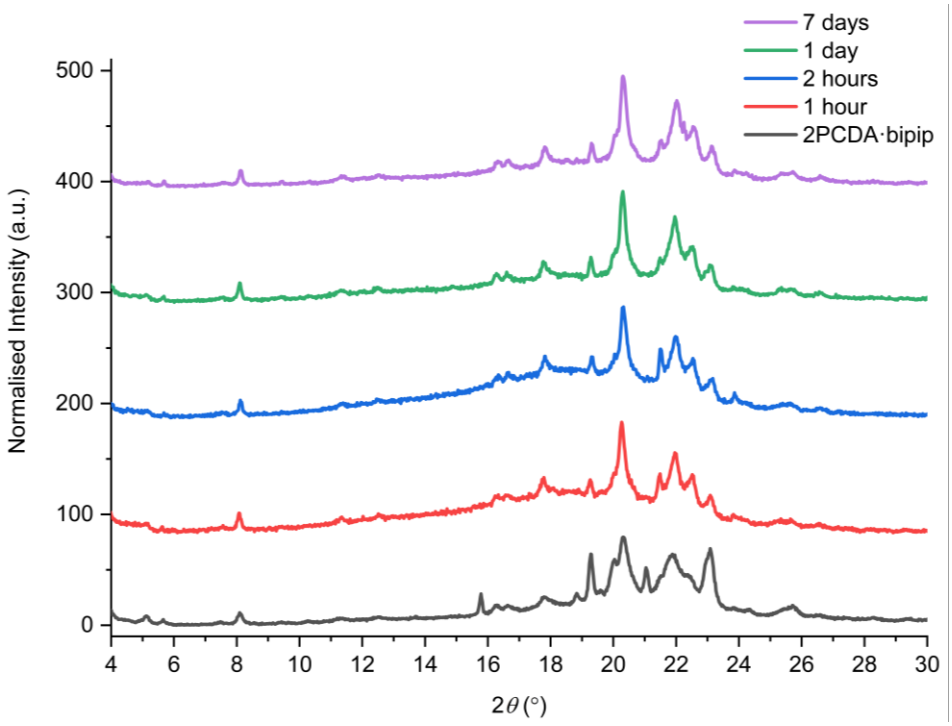

Figure 4.57. The experimental PXRD patterns of 2PCDA·bipip exposed to different durations of UV radiation (254 nm).

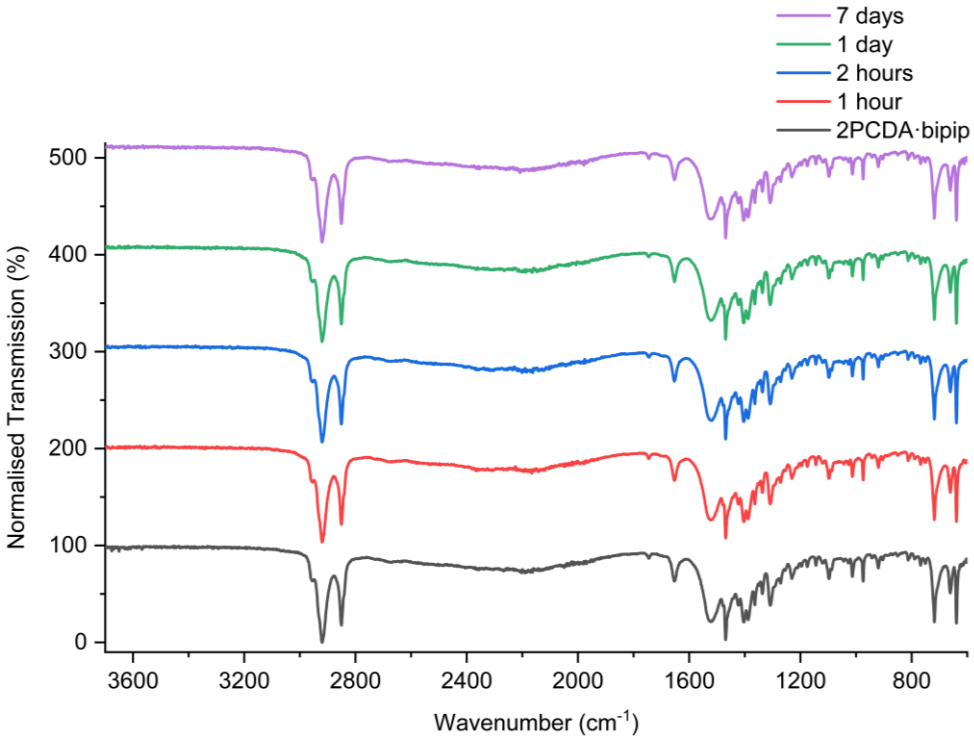

Figure 4.58. The FTIR spectra of 2PCDA·bipip exposed to UV radiation (254 nm) for different durations.

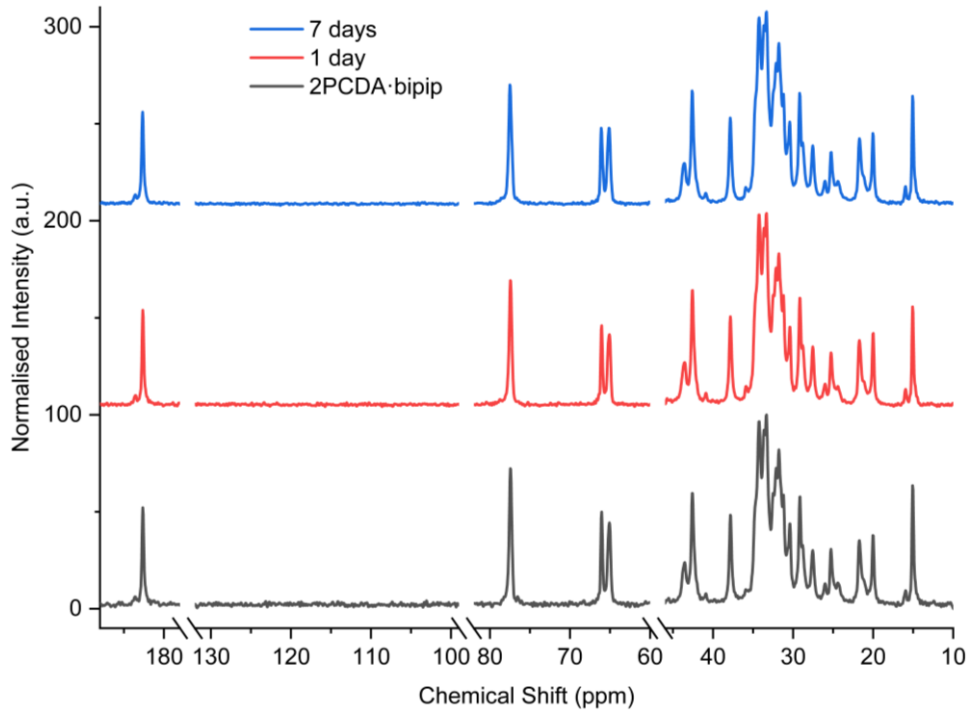

Figure 4.59. The ssNMR spectra of 2PCDA·bipip exposed to different durations of UV radiation (254 nm). Added breaks are included in the *x*-axis to compact the spectra.

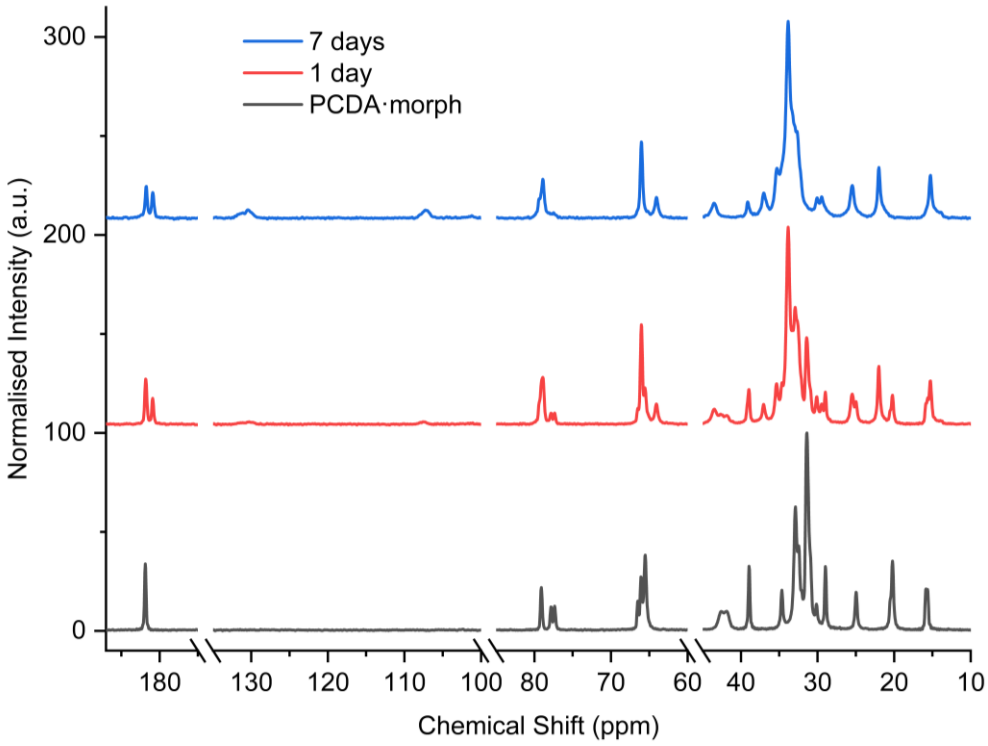

Figure 4.60. The ssNMR spectra of PCDA·morph exposed to different durations of UV radiation (254 nm). Added breaks are included in the *x*-axis to compact the spectra.

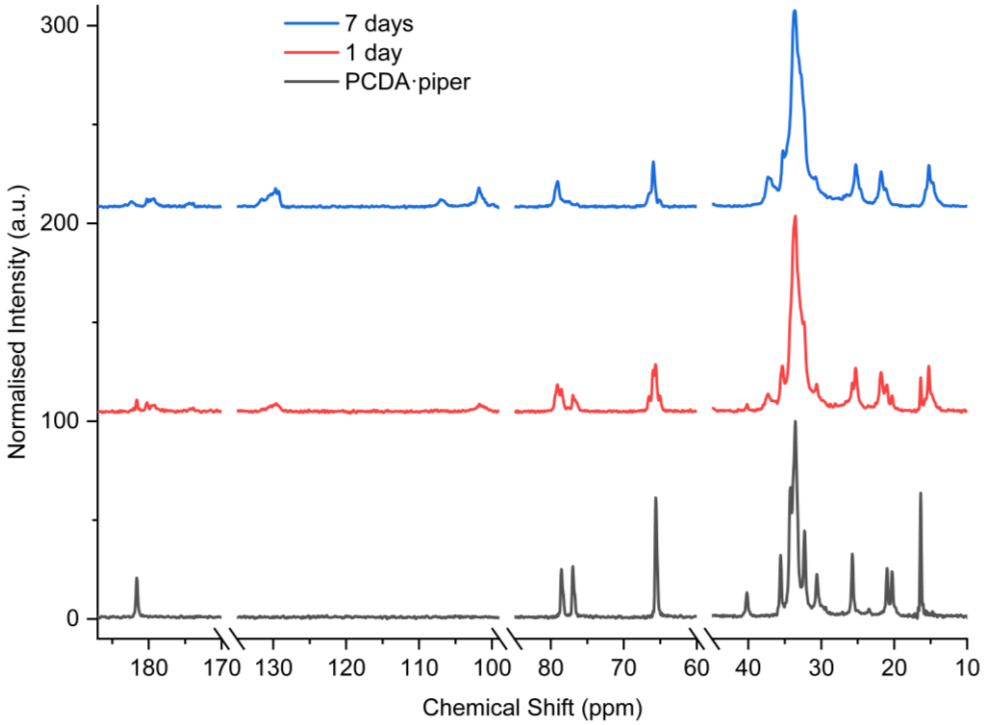

Figure 4.61. The ssNMR spectra of PCDA·piper exposed to different durations of UV radiation (254 nm). Added breaks are included in the *x*-axis to compact the spectra.

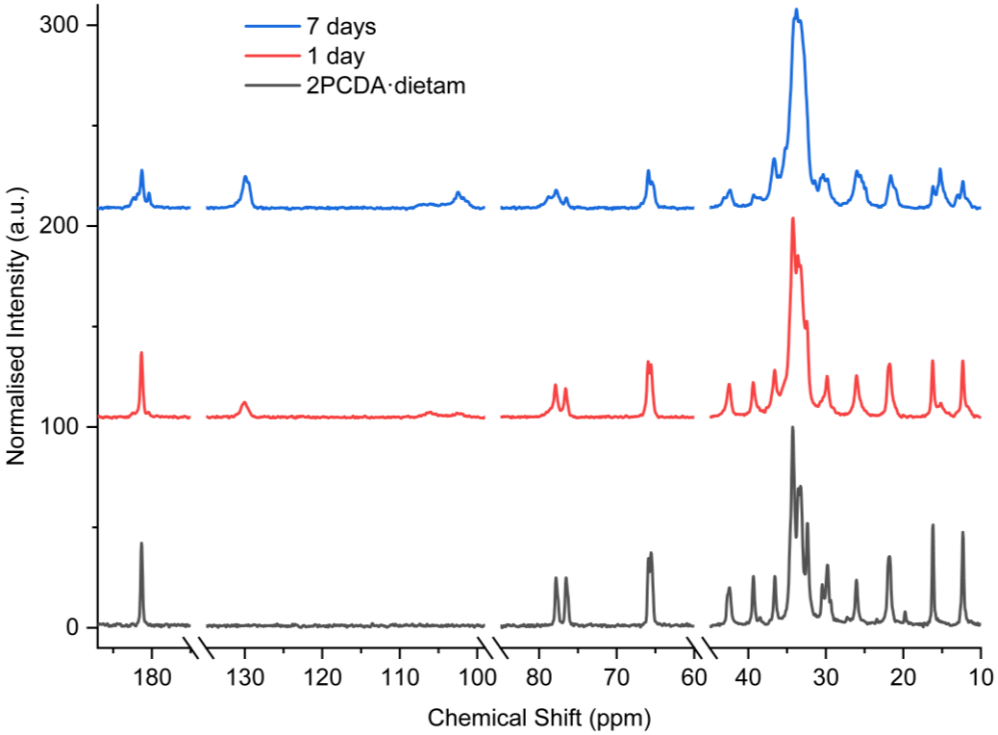

Figure 4.62. The ssNMR spectra of 2PCDA·dietam exposed to different durations of UV radiation (254 nm). Added breaks are included in the *x*-axis to compact the spectra.

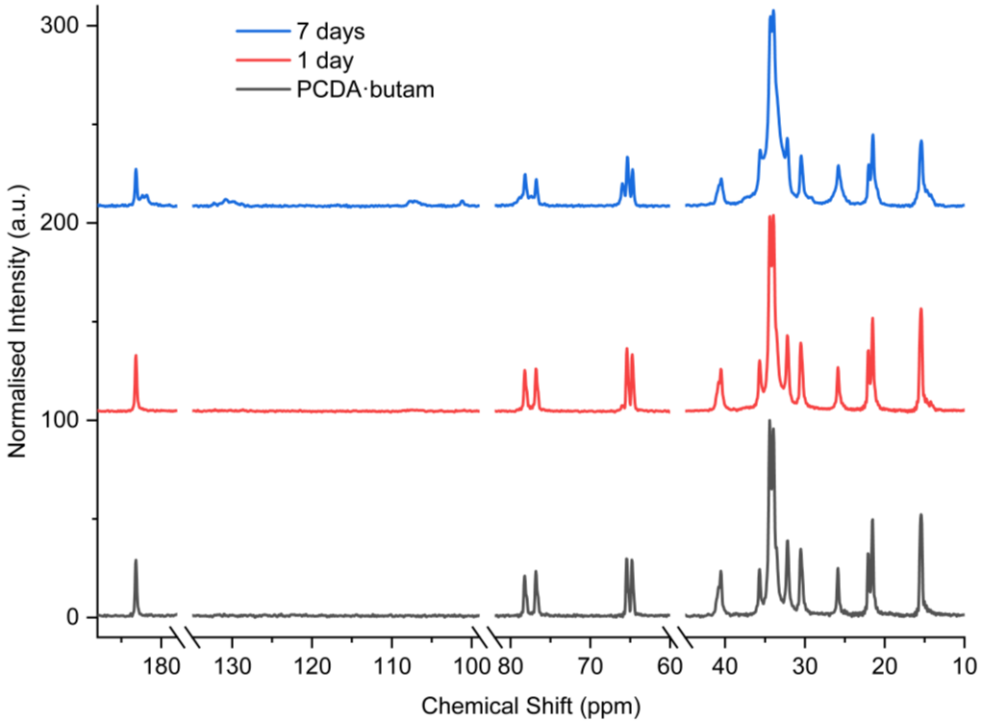

Figure 4.63. The ssNMR spectra of PCDA·butam exposed to different durations of UV radiation (254 nm). Added breaks are included in the *x*-axis to compact the spectra.

Topochemical postulate	***d* (Å)**	***r* (Å)**	***θ* (°)**
	≤3.8	≤4.9	45
PCDA	3.712(1)	4.574(1)	44.7
2PCDA·azp	3.633(1)	5.354(1)	48.4
2PCDA·4bipy	3.730(1)	5.442(1)	47.4
2PCDA·bpe	3.726(2)	5.449(2)	47.3
2PCDA·bipip	3.760(2)	5.577(2)	24.1
2PCDA·dietam	3.776(2)	4.644(3)	41.9
PCDA·butam	3.779(1)	4.593(1)	43.7

Table 4.2. Topochemical parameters for PCDA cocrystals and salts structurally characterised in this work. The parameter '*d*' is the C1-C4 distance, while '*r*' is the translational repeat distance. The tilt angle (*θ*) is calculated from the orientation of PCDA in the cocrystal and salt cocrystal samples.

The FTIR analysis of the salt cocrystals after irradiation shows that salts PCDA·morph (Figure 4.64), PCDA·piper (Figure 4. 65), 2PCDA·dietam (Figure 4.66), and PCDA·butam (Figure 4.67) begin to lose their volatile coformers after prolonged UV exposure and revert to free carboxylic acids. This is evidenced by the decrease in

intensity of the carboxylate asymmetric stretch band $\nu(CO_2)_{asym}$ of the salt (1653 cm^{-1} in PCDA·morph, 1627 cm^{-1} in 2PCDA·dietam, and 1649 cm^{-1} in PCDA·butam) and the emergence of a free acid peak at 1691 cm^{-1} as the sample is irradiated. The effect is highly pronounced for the morpholinium and piperdinium salts which reverts to free acid after just one hour while dietam and butam begin to separate from their respective salts after one day of irradiation, indicating potential weaker hydrogen bonding in PCDA·morph and PCDA·piper, though this cannot be confirmed due to a lack of structural evidence. Interestingly, given the very limited photoreactivity of PCDA itself, salt formation followed by removal of the amine in this way gives an interesting route to the free acid photopolymer and hence transient amine complexation effectively catalyses the photopolymerisation reaction of PCDA itself. The salts PCDA·morph, 2PCDA·dietam, and PCDA·butam were also exposed to ambient conditions for seven days to investigate whether the amine is lost from the salts without irradiation. The FTIR of salts PCDA·morph and PCDA·butam display changes consistent with UV irradiation for one day, while salt 2PCDA·dietam displays total loss of amine from the salt under ambient conditions after seven days (the FTIR spectrum of PCDA·piper exposed to ambient conditions for seven days is not currently available). The resulting carboxylic acid is a mixture of free PCDA and photopolymer. These findings are also supported by PXRD analysis of the irradiated salts (Figure 4.68, Figure 4.69, Figure 4.70, and Figure 4.71).

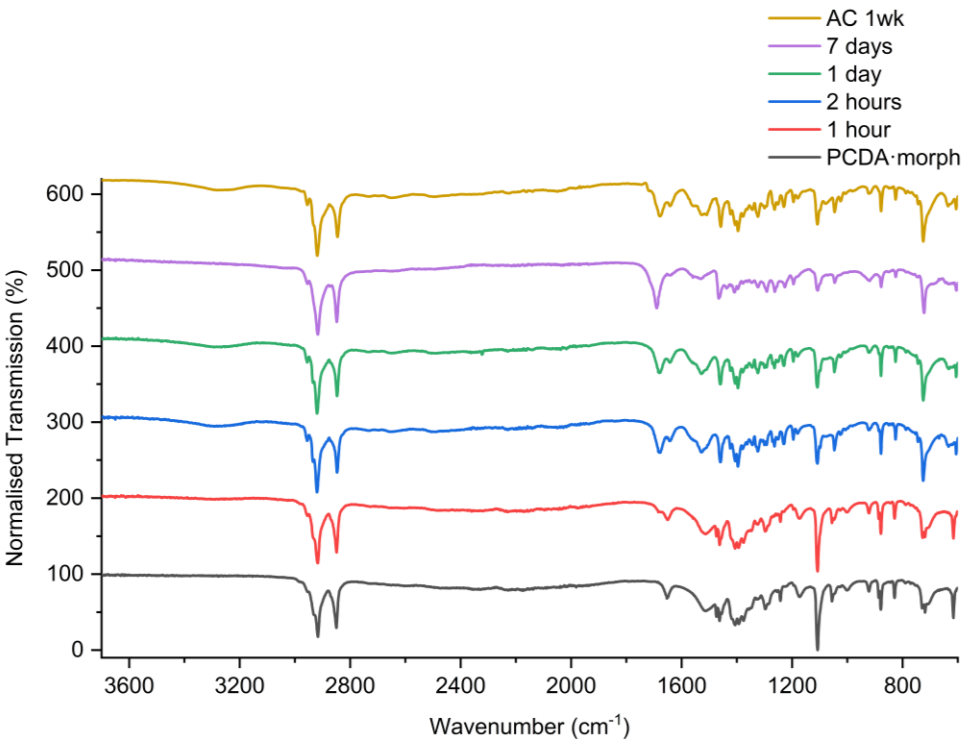

Figure 4.64. The FTIR spectra of PCDA·morph exposed to UV radiation (254 nm) for different durations, and the exposure to ambient conditions (AC) in the laboratory for one week.

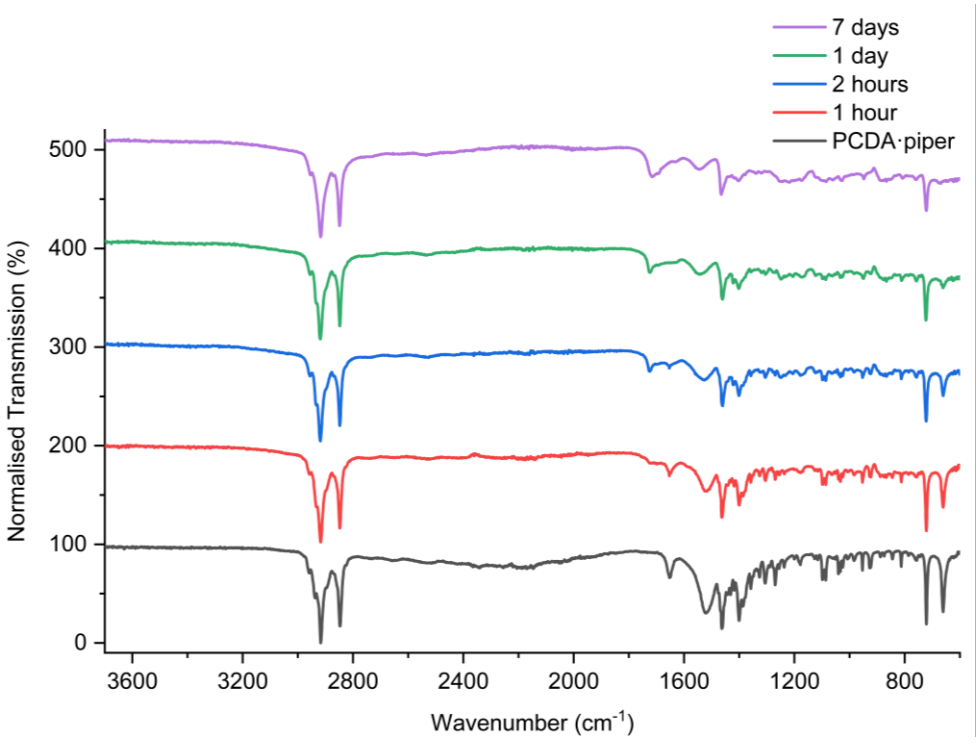

Figure 4. 65. The FTIR spectra of PCDA·piper exposed to UV radiation (254 nm) for different durations.

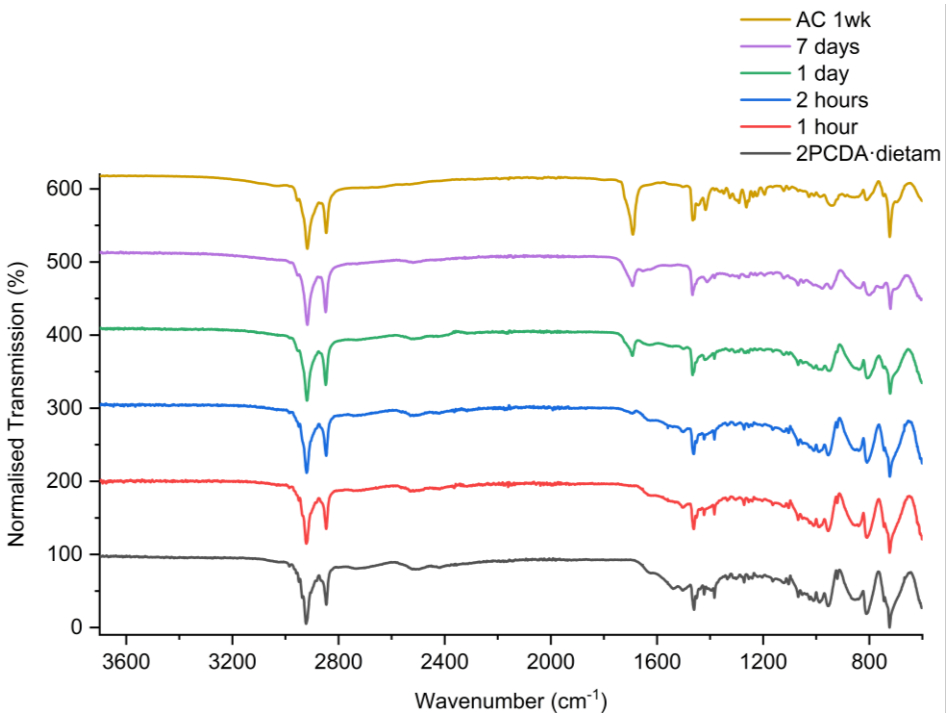

Figure 4.66. The FTIR spectra of 2PCDA·dietam exposed to UV radiation (254 nm) for different durations and the exposure to ambient conditions (AC) in the laboratory for one week.

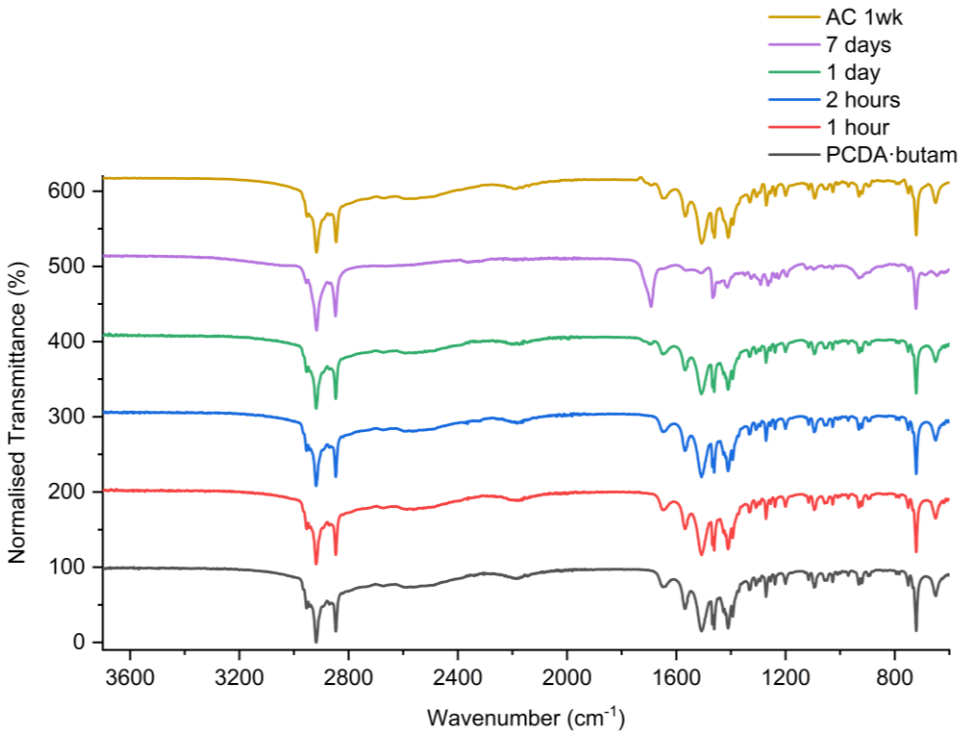

Figure 4.67. The FTIR spectra of PCDA·butam exposed to UV radiation (254 nm) for different durations and the exposure to ambient conditions (AC) in the laboratory for one week.

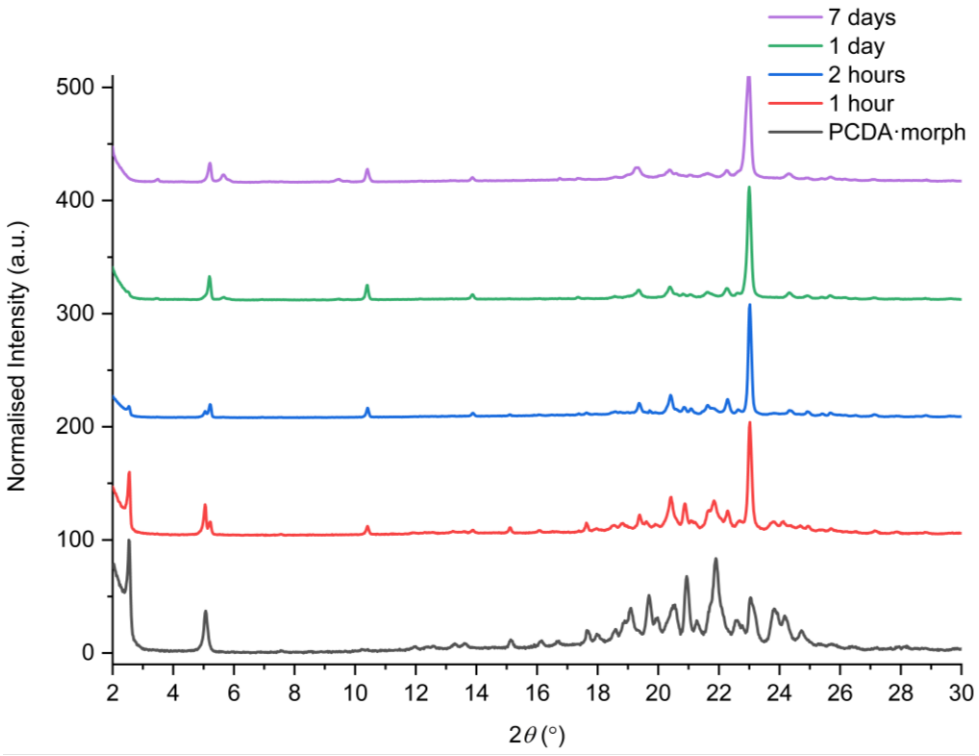

Figure 4.68. The experimental PXRD patterns of PCDA·morph exposed to different durations of UV radiation (254 nm).

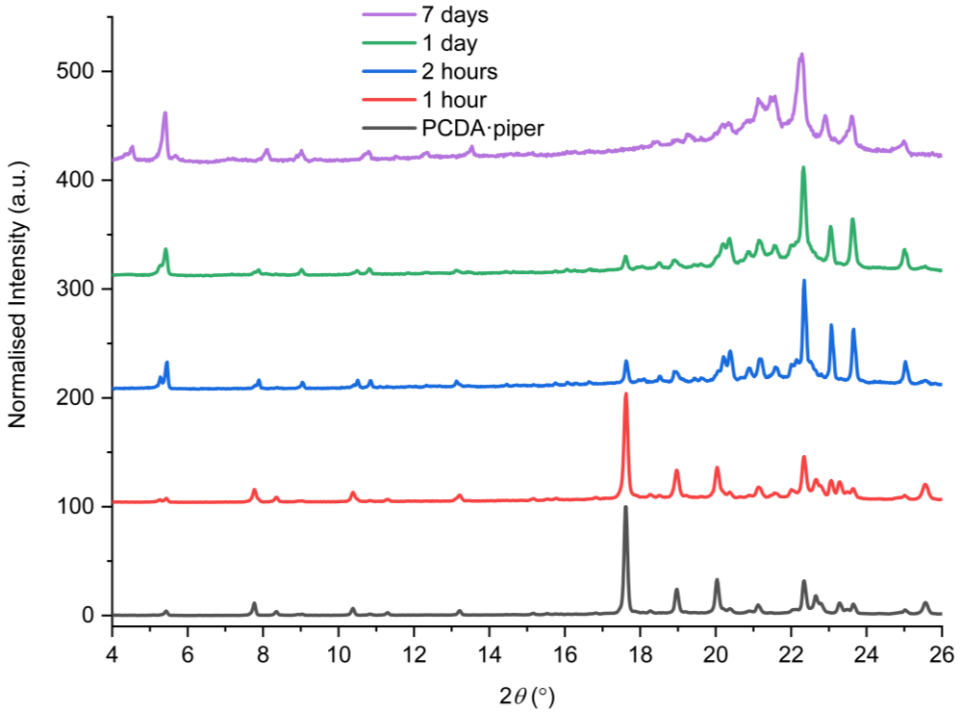

Figure 4.69. The experimental PXRD patterns of PCDA·piper exposed to different durations of UV radiation (254 nm).

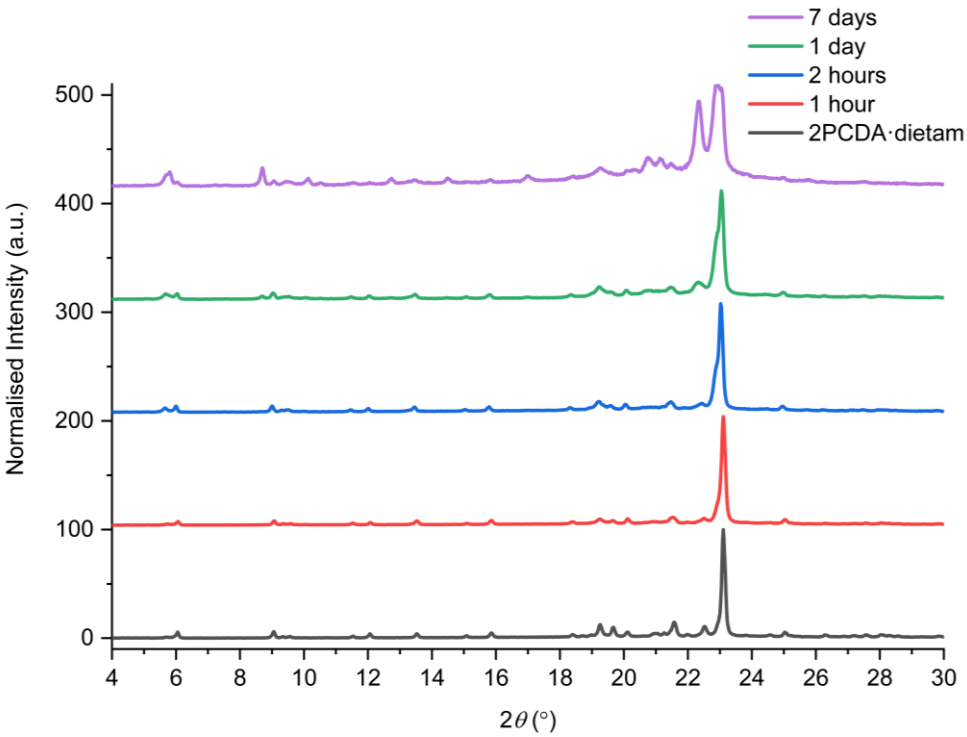

Figure 4.70. The experimental PXRD patterns of 2PCDA·dietam exposed to different durations of UV radiation (254 nm).

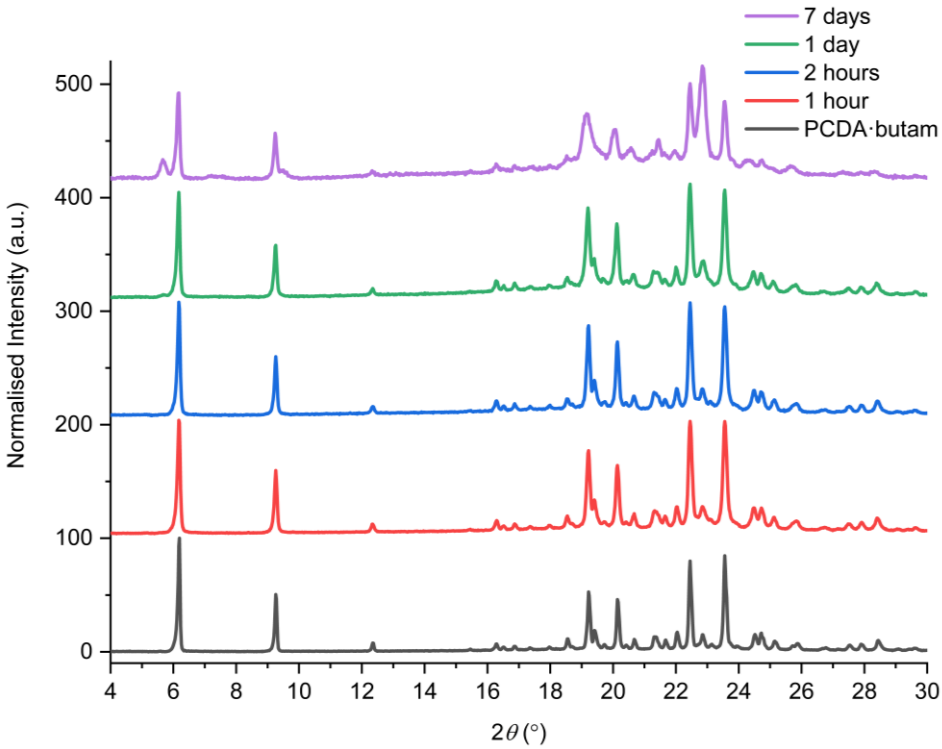

Figure 4.71. The experimental PXRD patterns of PCDA·butam exposed to different durations of UV radiation (254 nm).

Similar to the unreactive PCDA cocrystals, the Raman analysis of the salt 2PCDA·bipip reveals a band at 2258.4 cm^{-1} assigned to unreacted dialkyne even after 100 Gy of X-ray irradiation which further reinforces that the salt is photostable (Figure 4.72). The small ene-yne photopolymer band at 2100.3 cm^{-1} is likely to arise from small amounts of photopolymerised PCDA impurities. On the other hand, PCDA·morph shows impressive sensitivity X-ray radiation as indicated by the presence of the significant ene-yne band at 2088.1 cm^{-1} (Figure 4.73). This band is significantly red-shifted compared to photopolymerised PCDA, indicating a more planar, conjugated conformation of the chromophore. This is in contrast to PCDA alone which exhibits torsional strain on the π-bonds of the chromophore when irradiated.[68] Salt PCDA·morph also shows significantly more visual colour change upon irradiation compared to PCDA alone. It is likely that the increased hydrogen bonding in the salt brings the monomers of PCDA in a closer spatial arrangement and hence makes it more photosensitive. Unfortunately, the photoreactive salt PCDA·piper was unable to be analysed by Raman spectroscopy. After 100 Gy of X-ray irradiation, salt 2PCDA·dietam also displays a prominent photopolymer alkyne band at 2097.7 cm^{-1} with minimal residual dialkyne signal (Figure 4.74). The pre-resonance Raman effect is very evident in 2PCDA·dietam and can be seen in the exaggeration of the ene-yne band relative to the dialkyne band in the region of 2250 cm^{-1}. Interestingly in the Raman spectrum of 2PCDA·dietam, the breadth of the ene-yne band, and the presence of an additional alkene peak at 1500 cm^{-1} at slightly higher wavenumber than the typical major 1445 cm^{-1} alkene band indicates multiple conformations of the polymerised material, and implies some structural differences in the resulting chromophore suggesting that multiple conformations of the polymerised salt exist. For PCDA·butam, Raman analysis of the 100 Gy X-ray irradiated sample shows that the salt gradually photopolymerises and has a similar radiation sensitivity as PCDA alone, with an ene-yne band at 2098.1 cm^{-1} (Figure 4.75). Additionally, for the photosensitive salts, the C-H wagging progressions arising between 1300 cm^{-1} and 1150 cm^{-1} from the polymer side chains of PCDA in the salts change with irradiation to suggest a changed conformational structure. The change of the side chain conformation is due to difference in phase angles of coupled oscillations between methylene groups. These differences in C-H wagging progressions can be used as an additional conformational tool for detecting the presence of a PCDA polymer. Close examination of the differences in frequency within the wagging mode progressions

may also indicate stresses on the side chains due to their close approach to each other as the polymer is formed. Interestingly, the positions of the ene-yne alkyne bands in the irradiated diethylammonium and butylammonium salts of around 2100 cm^{-1} contrast sharply with the value of 2066.3 cm^{-1} obtained for Li-PCDA. This significantly red-shifted value implies a much more planar 'ordered' chromophore in the lithium salt and hence while the commercial material exists in an ordered 'blue state' the use of the organic salt-formers give a less ordered 'red state' photopolymer. The value of 2088 cm^{-1} for the morpholinium salt is somewhere in between and implies that the polymer ordering and hence, potentially, colour may be tunable.

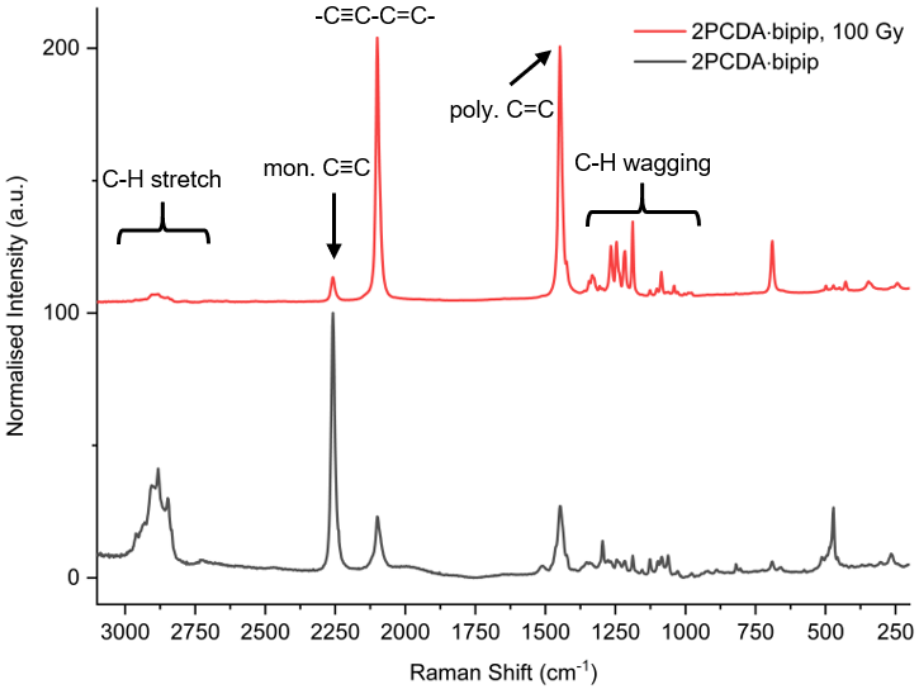

Figure 4.72. The Raman spectra of 2PCDA·bipip before and after exposure to 100 Gy of X-ray radiation.

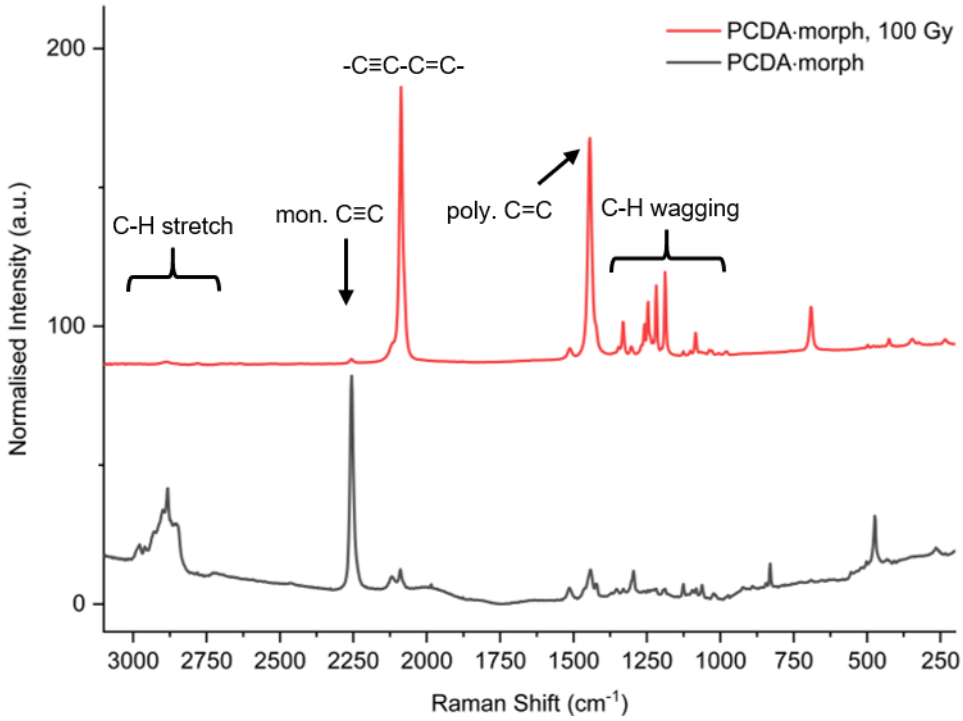

Figure 4.73. The Raman spectra of PCDA·morph before and after exposure to 100 Gy of X-ray radiation.

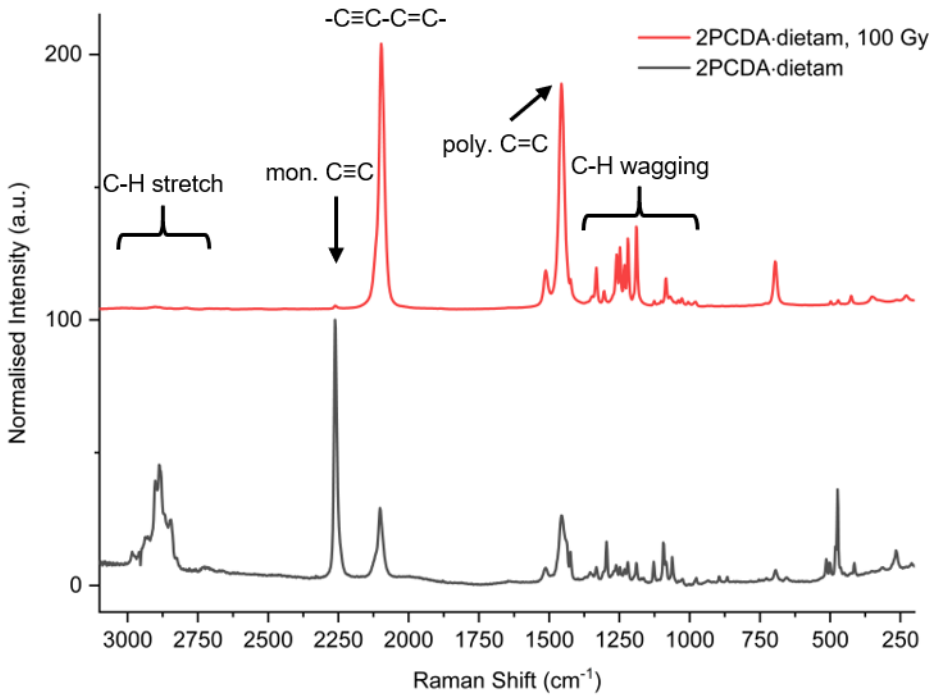

Figure 4.74. The Raman spectra of 2PCDA·dietam before and after exposure to 100 Gy of X-ray radiation.

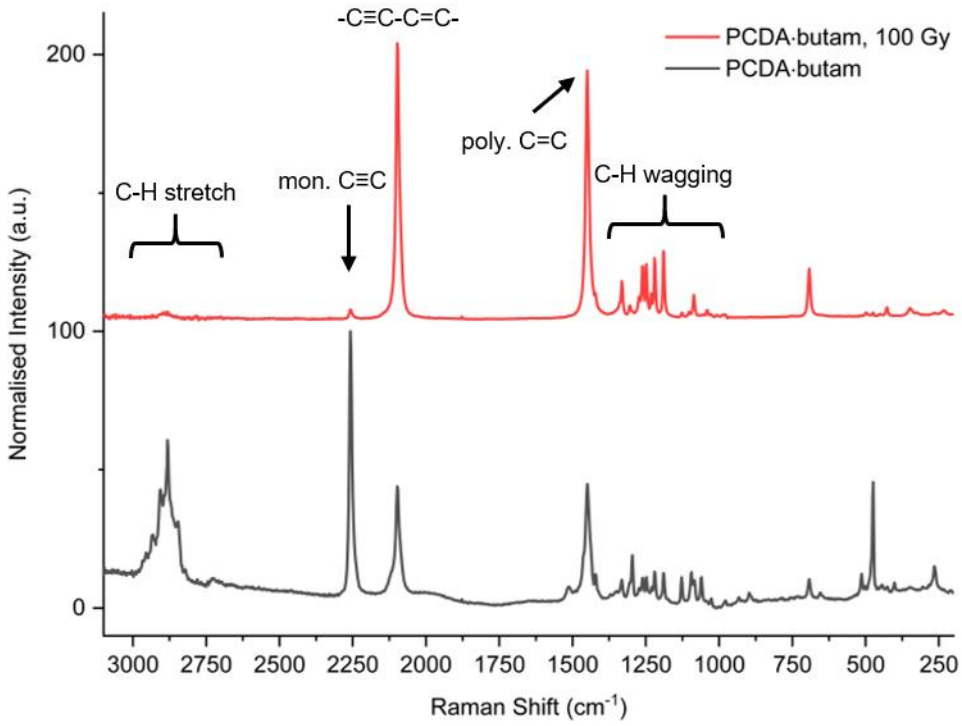

Figure 4.75. The Raman spectra of PCDA·butam before and after exposure to 100 Gy of X-ray radiation.

In an attempt to assess the degree of polymerisation the irradiated samples were analysed by two different mass spectrometry techniques, matrix-assisted laser desorption/ionisation (MALDI) and atmospheric solid analysis probe (ASAP). However, neither method was able to fully quantify the amount of polymer present in the samples nor the molecular weight distribution, as MALDI did not generate any signals assignable to photopolymerised material. In contrast, the ASAP technique did show peaks assigned to PCDA monomer, dimer, and trimer, however, the distribution of these signals was the same before and after UV irradiation for one day for PCDA itself and even for 2PCDA·dietam UV irradiated for 14 days. It is likely that higher molecular weight oligomers are present given the broadness of the ssNMR spectra, therefore, the PCDA salts are not volatile enough to be detected by mass spectrometry in this way. Similarly, the poor solubility of the polymerised materials made them unsuitable for gel permeation chromatography.

Preliminary Photoreactivity Results

In addition to the salt photoreactivity studies, preliminary studies were conducted to investigate how free radical photoinitiators affected the photoreactivity of the system

when combined with a photoreactive salt. To explore this, a 5 % molar ratio of benzophenone (BP) and 2-methyl-4′-(methylthio)-2-morpholinopropiophenone (MPP) (Figure 4.76) were combined with PCDA and morph (1:1) in a mixer mill for 45 minutes at a frequency of 20 s^{-1}. Upon exposure to UV radiation (254 nm), the PCDA morpholinium salt in the presence of the photoinitiators displayed a reduced reactivity compared to PCDA·morph alone, evident by the lack of colour change in the powdered samples until one hour of UV irradiation for PCDA·morph with MPP, and after two hours of irradiation for PCDA·morph with BP (Figure 4.77). These findings suggest that the photoinitiators are able to control the photoreactivity of the radiation-sensitive salt. No further characterisation of these systems was conducted.

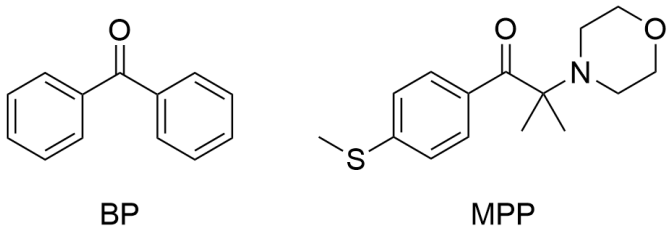

Figure 4.76. The photoinitiators used in this study, benzophenone (BP) and 2-methyl-4′-(methylthio)-2-morpholinopropiophenone (MPP).

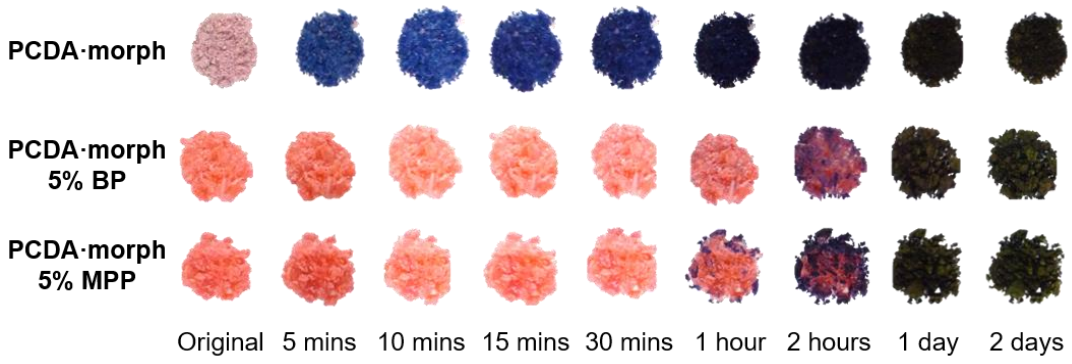

Figure 4.77. Photographs of PCDA·morph exposed to UV radiation (254 nm) for two days compared to the salt ball milled with a 5% molar ratio of BP and MPP.

4.3. Conclusion

Three PCDA cocrystals 2PCDA·azp, 2PCDA·4bipy, and 2PCDA·bpe have been prepared which were engineered to exhibit the common carboxylic acid···pyridine supramolecular synthon. The lamellar structures of these surfactant-like compounds

exhibit two very different packing modes with either a *syn* or *anti* conformation of the dialkyne substituents and display considerable thermal expansion in the *c*-axis direction upon warming. The cocrystal with the shortest dialkyne distance of 3.631(6) Å is 2PCDA·azp, which is shorter than in PCDA itself, and all cocrystals have inter-alkyne distances within the topochemical postulate. However, all PCDA cocrystals exhibit very little response to UV and X-ray radiation, because the translational repeat distances are greater than the maximum value. Hence, cocrystallisation appears to significantly stabilise PCDA in the solid state. This observation is somewhat surprising in the light of the photoreactivity of related pyridyl-containing cocrystals of di- and trialkynes.[19, 43] Due to the bulky nature of bipip, the salt 2PCDA·bipip also did not photopolymerise. In contrast, salts of monofunctional amines gave photoreactive materials. For example, the morpholinium salt, PCDA·morph, changes from pink-to-blue-to-black in under 10 minutes of UV irradiation. Also, the PCDA·piper and 2PCDA·dietam salts displayed significant photoreactivity and undergo an impressive pink-to-blue colour change for PCDA·piper and lilac-to-black colour change with under five minutes of UV irradiation for 2PCDA·dietam. The photoreactive salt PCDA·butam also displays impressive photoreactivity. The X-ray crystal structures of 2PCDA·dietam and PCDA·butam indicate that these salts adhere to the topochemical postulate. These radiation-sensitive salts are of considerable commercial interest for the development of radiochromic films and due to their different sensitivities to radiation, can be applied to different radiation dose ranges, and therapeutic areas. Preliminary indications suggest that they outperform the commercial lithium salt in terms of photosensitivity, while Raman spectroscopy shows that the photopolymers are relatively disordered with ene-yne bands in the range 2088 – 2100 cm^{-1}, potentially allowing access to a range of colours. The novel feature of amine evaporation over time means that transient ammonium salt formation with a volatile amine effectively catalyses the solid-state photopolymerisation of the relatively unreactive PCDA.

4.4. Experimental

Additional information relating to the materials and instrumentation used in this work can be found in Chapter 6.

PCDA 4,4'-Azopyridine Cocrystal

Cocrystal 2PCDA·azp was prepared by grinding PCDA (0.15 g, 0.40 mmol) and azp (0.037 g, 0.20 mmol) in a 2:1 ratio, respectively, in a Retsch MM 200 mixer mill for one hour at a frequency of 20 s^{-1} (yield 0.10 g, 0.22 mmol, 55 %). The resulting powder was used as a seed (*ca*. 0.005 g, 0.011 mmol) for the cocrystallisation of PCDA (0.025 g, 0.067 mmol) and azp (0.006 g, 0.033 mmol) in acetone (2 mL). After brief sonication, the solution was left to crystallise by slow evaporation at room temperature, which yielded large colourless plate crystals. Analysis calc. for $C_{30}H_{46}N_2O_2$: C 77.19, H 9.94, N 6.01 %, found: C 77.19, H 9.93, N 5.32 %; FTIR (cm^{-1}): 2936 $\nu(CH_3)_{asym}$, 2919 $\nu(CH_2)_{asym}$, 2850 $\nu(CH_2)_{symm}$, 2522 ν(OH) of OH···N, 1908 ν(NH) of OH···N, 1695 ν(C=O), 1598, 1567, 1470 $\delta(CH_2)$, 1410, 1376 $\omega(CH_2)$, 1348 $\omega(CH_2)$, 1318 $\omega(CH_2)$, 1289 $\omega(CH_2)$, 1253 $\omega(CH_2)$, 1214 $\omega(CH_2)$, 1184, 1101, 1048, 1011, 990, 900, 848, 739, 719 $\rho(CH_2)$, 671, 660. Crystal data: M = 466.69 g/mol, 0.32 × 0.09 × 0.02 mm^3, triclinic, space group $P\bar{1}$ (no. 2), a = 5.3544(3) Å, b = 6.8239(4)Å, c = 39.920(2) Å, α = 87.742(4) °, β = 88.869(4) °, γ = 75.291(4) °, V = 1409.64(14) $Å^3$, Z = 2, D_c = 1.100 g/cm^3, F_{000} = 512.0, CuKα radiation, λ = 1.54178 Å, T = 120 K, $2\theta_{max}$ = 137.98 °, 33397 reflections collected, 5160 unique (R_{int} = 0.1445). Final GooF = 1.090, R_1 = 0.0994, wR_2 = 0.1798, R indices based on 5160 reflections with $I >= 2\sigma(I)$ (refinement on F^2), 312 parameters, 0 restraints, μ = 0.522 mm^{-1}. Full crystallographic information for 2PCDA·azp can be found in Table 8.7 in Chapter 8.

PCDA 4,4'-Bipyridyl Cocrystal

Cocrystal 2PCDA·4bipy was prepared by grinding PCDA (0.15 g, 0.40 mmol) and 4bipy (0.032 g, 0.20 mmol) in a Retsch MM 200 mixer mill for 45 minutes at a frequency of 20 s^{-1} (yield = 0.091 g, 0.20 mmol, 50 %). The resulting powder was used as a seed (*ca*. 0.005 g, 0.011 mmol) for the cocrystallisation of PCDA (0.025 g, 0.067 mmol) and 4bipy (0.053 g, 0.034 mmol) in acetone (2 mL). After brief sonication, the solution was left to crystallise by slow evaporation at room temperature, which yielded small colourless plate crystals. Analysis calc. for $C_{30}H_{46}N_2O_2$: C 79.60, H 10.24, N 3.09 %, found: C 79.24, H 10.20, N 3.12 %; FTIR (cm^{-1}): 3062, 2935 $\nu(CH_3)_{asym}$, 2919 $\nu(CH_2)_{asym}$, 2850 $\nu(CH_2)_{symm}$, 2467 ν(OH) of OH···N, 1920 ν(NH) of OH···N, 1683 ν(C=O), 1600, 1541, 1471 $\delta(CH_2)$, 1408, 1365 $\omega(CH_2)$, 1325 $\omega(CH_2)$, 1287 $\omega(CH_2)$, 1253 $\omega(CH_2)$, 1212 $\omega(CH_2)$, 1187, 1128, 1102, 1071, 1000, 898, 821, 749,

718 ρ(CH_2), 666, 625. Crystal data: M = 452.68 g/mol, 0.12 × 0.04 × 0.03 mm^3, monoclinic, space group $P2_1/c$ (no. 14), a = 5.4415(2) Å, b = 8.9535(4) Å, c = 55.673(3) Å, β = 90.8823(10) °, V = 2712.1(2) $Å^3$, Z = 4, D_c = 1.109 g/cm^3, F_{000} = 996.0, synchrotron radiation, λ = 0.6889 Å, T = 100 K, $2\theta_{max}$ = 57.994 °, 47696 reflections collected, 7923 unique (R_{int} = 0.0663). Final GooF = 1.069, R_1 = 0.0529, wR_2 = 0.1510, R indices based on 7923 reflections with $I >= 2\sigma(I)$ (refinement on F^2), 303 parameters, 0 restraints, μ = 0.064 mm^{-1}. Full crystallographic information for 2PCDA·4bipy can be found in Table 8.8 in Chapter 8.

PCDA *trans*-1,2-Bis(4-pyridyl)ethylene Cocrystal

Cocrystal 2PCDA·bpe was prepared by grinding PCDA (0.15 g, 0.40 mmol) and bpe (0.039 g, 0.21 mmol) in a Retsch MM 200 mixer mill for 45 minutes at a frequency of 20 s^{-1} (yield = 0.12 g, 0.26 mmol, 65 %). The resulting powder was used as a seed (*ca.* 0.005 g, 0.011 mmol) for the cocrystallisation of PCDA (0.025 g, 0.067 mmol) and bpe (0.0061 g, 0.033 mmol) in acetone (2 mL). After brief sonication, the solution was left to crystallise by slow evaporation at room temperature and yielded small colourless block crystals. Analysis calc. for $C_{31}H_{47}NO_2$: C 79.95, H 10.17, N 3.01 %, found: C 79.84, H 10.14, N 2.86 %; FTIR (cm^{-1}): 3037, 2928 ν(CH_3)$_{asym}$, 2919 ν(CH_2)$_{asym}$, 2850 ν(CH_2)$_{symm}$, 2462 ν(OH) of OH···N, 1912 ν(NH) of OH···N, 1688 ν(C=O), 1604, 1560, 1471 δ(CH_2), 1414, 1365 ω(CH_2), 1325 ω(CH_2), 1287 ω(CH_2), 1252 ω(CH_2), 1235 ω(CH_2), 1213 ω(CH_2), 1183, 1127, 1100, 1070, 1011, 974, 921, 895, 826, 749, 718 ρ(CH_2), 664. Crystal data: M = 465.69 g/mol, 0.36 × 0.31 × 0.23 mm^3, monoclinic, space group $P2_1/c$ (no. 14), a = 5.4494(3) Å, b = 8.9235(5) Å, c = 57.441(3) Å, β = 92.643(2) °, V = 2790.2(3) $Å^3$, Z = 4, D_c = 1.109 g/cm^3, F_{000} = 1024.0, MoKα radiation, λ = 0.71073 Å, T = 120 K, $2\theta_{max}$ = 56.98 °, 34945 reflections collected, 6537 unique (R_{int} = 0.0635). Final GooF = 1.034, R_1 = 0.0560, wR_2 = 0.1073, R indices based on 6537 reflections with $I >= 2\sigma(I)$ (refinement on F^2), 321 parameters, 1 restraint, μ = 0.067 mm^{-1}. Full crystallographic information for 2PCDA·bpe can be found in Table 8.9 in Chapter 8.

PCDA 4,4'-Bipiperidine Salt

Salt 2PCDA·bipip was prepared by grinding PCDA (0.2 g, 0.53 mmol) and bipip (0.045 g, 0.27 mmol) in a 2:1 ratio in a Retsch MM 200 mixer mill for 90 minutes at a frequency of 20 s^{-1} (yield = 0.22 g, 0.40 mmol, 89 %). The resulting powder (0.030 g) was combined with ethanol (2 mL) and briefly sonicated and left to crystallise by slow

evaporation at room temperature. Colourless plate crystals formed after two weeks. Analysis calc. for $C_{60}H_{104}N_2O_4$: C 78.55, H 11.43, N 3.05 %, found: C 77.94, H 11.36, N 2.83 %; FTIR (cm^{-1}): 2958 $\nu(CH_3)_{asym}$, 2917 $\nu(CH_2)_{asym}$, 2849 $\nu(CH_2)_{symm}$, 2676, 1750, 1654 ν(C=O), 1523, 1467 $\delta(CH_2)$, 1421, 1405, 1388 $\omega(CH_2)$, 1364 $\omega(CH_2)$, 1336 $\omega(CH_2)$, 1307 $\omega(CH_2)$, 1273 $\omega(CH_2)$, 1231 $\omega(CH_2)$, 1197, 1175, 1145, 1121, 1099, 1011, 975, 920, 814, 769, 752, 719 $\rho(CH_2)$, 662, 640. Crystal data: M = 917.45 g/mol, 0.767 × 0.314 × 0.1 mm^3, triclinic, space group $P\bar{1}$ (no. 2), a = 5.5770(4) Å, b = 11.8339(8) Å, c = 23.0041(15) Å, α = 100.670(2) °, β = 96.096(2) °, γ = 103.007(2) °, V = 1436.25(17) $Å^3$, Z = 1, D_c = 1.061 g/cm^3, F_{000} = 510.0, MoKα radiation, λ = 0.71073 Å, T = 120 K, $2\theta_{max}$ = 65 °, 36532 reflections collected, 10400 unique (R_{int} = 0.0455). Final GooF = 1.019, R_1 = 0.0497, wR_2 = 0.1263, R indices based on 10400 reflections with $I >= 2\sigma(I)$ (refinement on F^2), 312 parameters, 0 restraints, μ = 0.064 mm^{-1}. Full crystallographic information for 2PCDA·bipip can be found in Table 8.10 in Chapter 8.

PCDA Morpholine Salt

Salt PCDA·morph was prepared by grinding PCDA (0.2 g, 0.53 mmol) and morph (0.046 mL, 0.53 mmol) in a Retsch MM 200 mixer mill for 45 minutes at a frequency of 20 s^{-1} (yield = 0.24 g, 0.52 mmol, 98 %). The resulting powder (0.030 g) was combined with acetone (3 mL) and briefly sonicated and left to crystallise by slow evaporation at room temperature. Colourless plate crystals formed after two weeks, however, crystallisations with and without seeding yielded poor-quality crystals that did not diffract sufficiently to allow single crystal structure determination. Analysis calc. for $C_{29}H_{51}NO_3$: C 75.45, H 11.14, N 3.03 %, found C 75.18, H 11.08, N 2.80 %; FTIR (cm^{-1}): 2945 $\nu(CH_3)_{asym}$, 2917 $\nu(CH_2)_{asym}$, 2850 $\nu(CH_2)_{symm}$, 1652 ν(C=O), 1515, 1474, 1463 $\delta(CH_2)$, 1406, 1394 $\omega(CH_2)$, 1375 $\omega(CH_2)$, 1296 $\omega(CH_2)$, 1243 $\omega(CH_2)$, 1173, 1108, 1056, 1002, 922, 887, 879, 830, 728, 719 $\rho(CH_2)$, 616.

Morpholinium Butanoate Salt

Salt butA·morph was prepared by combining butanoic acid (0.05 mL, 0.55 mmol) and morpholine (0.047 mL, 0.55 mmol) to give a yellow oil and was left to precipitate slowly overnight in a sealed round-bottom flask to yield large colourless plate crystals (yield = 0.088 g, 0.5 mmol, 91 %). Analysis calc. for $C_8H_{17}NO_3$: C 54.84, H 9.78, N 7.99 %, found: C 54.38, H 10.06, N 7.70 %; FTIR (cm^{-1}): 2961 $\nu(CH_3)_{asym}$, 2871 $\nu(CH_2)_{symm}$, 1711 ν(C=O), 1545, 1456 $\delta(CH_2)$, 1394 $\omega(CH_2)$, 1379 $\omega(CH_2)$, 1303

ω(CH_2), 1243 ω(CH_2), 1195, 1107, 1049, 997, 878, 829, 766 ρ(CH_2), 615. Crystal data: M = 175.22 g/mol, 0.44 × 0.25 × 0.21 mm^3, monoclinic, space group *C*2/*c* (no. 15), *a* = 20.0926(14) Å, *b* = 8.0678(6) Å, *c* = 11.6061(8) Å, *β* = 97.064(3) °, *V* = 1867.1(2) $Å^3$, *Z* = 8, D_c = 1.247 g/cm^3, F_{000} = 768.0, MoKα radiation, λ = 0.71073 Å, *T* = 120 K, $2\theta_{max}$ = 58.994 °, 13471 reflections collected, 2587 unique (R_{int} = 0.0313). Final GooF = 1.023, R_1 = 0.0356, wR_2 = 0.0931, *R* indices based on 2587 reflections with $I >= 2\sigma(I)$ (refinement on F^2), 177 parameters, 0 restraints, μ = 0.094 mm^{-1}. Full crystallographic information for butA·morph can be found in Table 8.11 in Chapter 8.

PCDA Piperidine Salt

Salt PCDA·piper was prepared by grinding PCDA (0.2 g, 0.53 mmol) and piper (0.053 mL, 0.53 mmol) in a Retsch MM 200 mixer mill for 45 minutes at a frequency of 20 s^{-1} (yield = 0.23 g, 0.50 mmol, 91 %). The resulting powder (0.030 g) was combined with acetone (2 mL) and briefly sonicated and left to crystallise by slow evaporation at room temperature. However, no crystals of suitable quality for SC-XRD were obtained. Analysis calc. for $C_{30}H_{53}NO_2$: C 78.37, H 11.62, N 3.05 %, found: C 75.81, H 11.03, N 2.63 %. The synthesis of the salt is required to be repeated and placed in a vacuum desiccator before analysis; FTIR (cm^{-1}): 2960 ν(CH_3)$_{asym}$, 2917 ν(CH_2)$_{asym}$, 2848 ν(CH_2)$_{symm}$, 2661, 2542, 1750, 1653 ν(C=O), 1522, 1463 δ(CH_2), 1430, 1400, 1385 ω(CH_2), 1359 ω(CH_2), 1327 ω(CH_2), 1306 ω(CH_2), 1269 ω(CH_2), 1239 ω(CH_2), 1179, 1099, 1087, 1040, 982, 954, 924, 845, 812, 721 ρ(CH_2), 661, 572.

PCDA Ethylenediamine Salt

Salt 2PCDA·etdiam was prepared by grinding PCDA (0.2 g, 0.53 mmol) and etdiam (0.018 mL, 0.27 mmol) in a Retsch MM 200 mixer mill for 45 minutes at a frequency of 20 s^{-1} (yield = 0.21 g, 0.47 mmol, 94 %). The resulting powder (0.030 g) was combined with acetone (2 mL) and briefly sonicated and left to crystallise by slow evaporation at room temperature. However, no crystals of suitable quality for SC-XRD were obtained. Analysis calc. for $C_{52}H_{92}N_2O_4$: C 77.17, H 11.46, N 3.46 %, found: C 74.30, H 10.90, N 3.27 %. The synthesis of the salt is required to be repeated and placed in a vacuum desiccator before analysis; FTIR (cm^{-1}): 2955 ν(CH_3)$_{asym}$, 2919 ν(CH_2)$_{asym}$, 2846 ν(CH_2)$_{symm}$, 2758, 2561, 2189, 1659 ν(C=O), 1571, 1509, 1461 δ(CH_2), 1411, 1329 ω(CH_2), 1271 ω(CH_2), 1239 ω(CH_2), 1200 ω(CH_2), 1117, 1096, 1028, 933, 792, 750, 721 ρ(CH_2), 651.

PCDA Diethylamine Salt Cocrystal

Salt cocrystal 2PCDA·dietam was prepared by grinding PCDA (0.2 g, 0.53 mmol) and dietam (0.055 mL, 0.53 mmol) in a Retsch MM 200 mixer mill for 45 minutes at a frequency of 20 s^{-1} (yield = 0.22 g, 0.5 mmol, 94 %). The resulting powder (0.030 g) was combined with acetone (3 mL) and briefly sonicated and left to crystallise by slow evaporation at room temperature. Purple plate crystals formed after two weeks to reveal a 2:1 (PCDA:dietam) stoichiometry with the formula $(C_{25}H_{42}O_2)\cdot(C_{25}H_{41}O_2)^-\cdot(C_4H_{12}N^+)$. Analysis calc. for $C_{54}H_{95}NO_4$: C 78.87, H 11.64, N 1.70 %, found: C 77.47, H 11.61, N 1.70 %; FTIR (cm^{-1}): 2950 $\nu(CH_3)_{asym}$, 2923 $\nu(CH_2)_{asym}$, 2846 $\nu(CH_2)_{symm}$, 2728, 2515, 1627 ν(C=O), 1538, 1504, 1461 $\delta(CH_2)$, 1452, 1423, 1384 $\omega(CH_2)$, 1334 $\omega(CH_2)$, 1302 $\omega(CH_2)$, 1272 $\omega(CH_2)$, 1256 $\omega(CH_2)$, 1241 $\omega(CH_2)$, 1203 $\omega(CH_2)$, 1163 $\omega(CH_2)$, 1123, 1103, 1068, 1054, 1027, 1010, 986, 955, 920, 854, 811, 745, 724 $\rho(CH_2)$, 592. Crystal data: M = 822.3 g/mol, 0.5 × 0.12 × 0.1 mm^3, monoclinic, space group *P*2/*n* (no. 13), *a* = 9.5968(6) Å, *b* = 4.6441(3) Å, *c* = 57.520(4) Å, β = 92.590(2) °,*V* = 2561.0(3) $Å^3$, *Z* = 2, D_c = 1.066 g/cm^3, F_{000} = 916.0, MoKα radiation, λ = 0.71073 Å, *T* = 120 K, $2\theta_{max}$ = 55.996 °, 30938 reflections collected, 6051 unique (R_{int} = 0.0502). Final GooF = 1.049, R_1 = 0.0561, wR_2 = 0.1217, *R* indices based on 6051 reflections with $I >= 2\sigma(I)$ (refinement on F^2), 274 parameters, 0 restraints, μ = 0.065 mm^{-1}. Full crystallographic information for 2PCDA·dietam can be found in Table 8.12 in Chapter 8.

PCDA *n*-Butylamine Salt

Salt PCDA·butam was prepared by grinding PCDA (0.2 g, 0.53 mmol) and butam (0.053 mL, 0.53 mmol) in a Retsch MM 200 mixer mill for 45 minutes at a frequency of 20 s^{-1} (yield = 0.23 g, 0.5 mmol, 96 %). The resulting powder (0.030 g) was combined with acetone (2 mL) and briefly sonicated. A powder seed (*ca.* 0.004 g, 0.0089 mmol) was added to the sample and left to crystallise by slow evaporation at room temperature. Blue block crystals formed after one month. Analysis calc. for $C_{29}H_{53}NO_2$: C 77.79, H 11.93, N 3.13 %, found: C 77.50, H 11.84, N 3.08 %; FTIR (cm^{-1}): 2954 $\nu(CH_3)_{asym}$, 2919 $\nu(CH_2)_{asym}$, 2870 $\nu(CH_2)_{symm}$, 2848, 2675, 2594, 2183, 1650 ν(C=O), 1567, 1508, 1468, 1461 $\delta(CH_2)$, 1428, 1411, 1334 $\omega(CH_2)$, 1309 $\omega(CH_2)$, 1272 $\omega(CH_2)$, 1254 $\omega(CH_2)$, 1239 $\omega(CH_2)$, 1201 $\omega(CH_2)$, 1115, 1095, 1056, 1028, 932, 921, 750, 722 $\rho(CH_2)$, 650. Crystal data: M = 447.72 g/mol, 0.36 × 0.08 × 0.05 mm^3, monoclinic, space group $P2_1$ (no. 4), *a* = 4.5934(6) Å,

b = 56.597(9) Å, c = 5.5096(6) Å, β = 99.130(10) °, V = 1414.2(3) Å^3, Z = 2, D_c = 1.051 g/cm^3, F_{000} = 500.0, MoKα radiation, λ = 0.71073 Å, T = 120 K, $2\theta_{max}$ = 53.97 °, 14179 reflections collected, 5663 unique (R_{int} = 0.1264). Final GooF = 1.026, R_1 = 0.1156, wR_2 = 0.2163, R indices based on 5663 reflections with $I > = 2\sigma(I)$ (refinement on F^2), 293 parameters, 22 restraints, μ = 0.064 mm^{-1}. Full crystallographic information for PCDA·butam can be found in Table 8.13 in Chapter 8.

4.5. References

1. R. Kassis, M. Bassil and A. Al Choueiry, *Mater. Res. Express*, 2019, **6**, 1-7.
2. Y. L. Su, *React. Funct. Polym.*, 2006, **66**, 967-973.
3. Y. J. Gwon, C. Kim and T. S. Lee, *Sens. Actuator, B*, 2019, **281**, 343-349.
4. D. E. Wang, X. H. Gao, G. B. Li, T. Xue, H. Yang and H. Y. Xu, *Sens. Actuators, B*, 2019, **289**, 85-92.
5. S. Ali, F. Ahmed and A. Khatri, *Mehran Univ. Res. J. Eng. Technol.*, 2016, **35**, 287-292.
6. M. Kim, Y. J. Shin, S. W. Hwang, M. J. Shin and J. S. Shin, *J. Appl. Polym. Sci.*, 2018, **135**, 1-5.
7. J. L. Deng, Z. H. Sheng, K. Zhou, M. X. Duan, C. Y. Yu and L. Jiang, *Bioconjugate Chem.*, 2009, **20**, 533-537.
8. J. P. Jeong, E. Cho, D. Yun, T. Kim, I. S. Lee and S. Jung, *Polymers*, 2017, **9**, 1-9.
9. J. Luo, K. Y. Fu, H. Y. Dong and D. Y. Chen, *Chin. J. Chem. Phys.*, 2016, **29**, 749-753.
10. A. Kamphan, C. J. Gong, K. Maiti, S. Sur, R. Traiphol and D. P. Arya, *RSC Adv.*, 2017, **7**, 41435-41443.
11. P. Sun, Y. C. Fu, J. Hu, N. Hao, W. Huang and B. Jiang, *Radiat. Meas.*, 2016, **85**, 116-125.
12. S. Devic, N. Tomic and D. Lewis, *Eur. J. Med. Phys.*, 2016, **32**, 541-556.
13. A. Rink, D. F. Lewis, S. Varma, I. A. Vitkin and D. A. Jaffray, *J. Med. Phys.*, 2008, **35**, 4545-4555.
14. Y. S. Soliman, A. A. Abdel-Fattah, A. A. Hamed and A. M. M. Bayomi, *Radiat. Phys. Chem.*, 2018, **144**, 56-62.
15. K. Fahsi, J. Deschamps, K. Chougrani, L. Viau, B. Boury, A. Vioux, A. van der Lee and S. G. Dutremez, *CrystEngComm*, 2013, **15**, 4261-4279.
16. H. Matsuzawa, S. Okada, A. Sarkar, H. Matsuda and H. Nakanishi, *Polym. J.*, 2001, **33**, 182-189.
17. B. C. Roy and S. Mallik, *Org. Lett.*, 2001, **3**, 1877-1879.
18. S. M. Curtis, N. Le, F. W. Fowler and J. W. Lauher, *Cryst. Growth Des.*, 2005, **5**, 2313-2321.
19. J. J. Kane, R. F. Liao, J. W. Lauher and F. W. Fowler, *J. Am. Chem. Soc.*, 1995, **117**, 12003-12004.
20. N. S. Goroff, S. M. Curtis, J. A. Webb, F. W. Fowler and J. W. Lauher, *Org. Lett.*, 2005, **7**, 1891-1893.

21. L. Luo, C. Wilhelm, A. W. Sun, C. P. Grey, J. W. Lauher and N. S. Goroff, *J. Am. Chem. Soc.*, 2008, **130**, 7702-7709.
22. W.-Q. Tong and G. Whitesell, *Pharm. Dev. Technol.*, 1998, **3**, 215-223.
23. D. J. Berry and J. W. Steed, *Adv. Drug Deliv. Rev.*, 2017, **117**, 3-24.
24. M. Khan, V. Enkelmann and G. Brunklaus, *Cryst. Growth Des.*, 2009, **9**, 2354-2362.
25. G. R. Desiraju, *Angew. Chem., Int. Ed. Engl.*, 1995, **34**, 2311-2327.
26. G. R. Desiraju, *J. Am. Chem. Soc.*, 2013, **135**, 9952-9967.
27. T. R. Shattock, K. K. Arora, P. Vishweshwar and M. J. Zaworotko, *Cryst. Growth Des.*, 2008, **8**, 4533-4545.
28. T. K. Adalder, R. Sankolli and P. Dastidar, *Cryst. Growth Des.*, 2012, **12**, 2533-2542.
29. C. B. Aakeroy, S. Panikkattu, B. DeHaven and J. Desper, *CrystEngComm*, 2013, **15**, 463-470.
30. A. O. Surov, A. A. Simagina, N. G. Manin, L. G. Kuzmina, A. V. Churakov and G. L. Perlovich, *Cryst. Growth Des.*, 2015, **15**, 228-238.
31. K. Tsaggeos, N. Masiera, A. Niwicka, V. Dokorou, M. G. Siskos, S. Skoulika and A. Michaelides, *Cryst. Growth Des.*, 2012, **12**, 2187-2194.
32. M. Zhu and L. Yu, *J. Therm. Anal. Calorim.*, 2018, **132**, 463-469.
33. Y. Y. Xu, S. Y. Fu, F. Y. Liu, H. Y. Yu and J. G. Gao, *Soft Matter*, 2018, **14**, 8044-8050.
34. A. Parkin, I. D. H. Oswald and S. Parsons, *Acta Crystallogr., Sect. B: Struct. Sci., Cryst. Eng. Mater.*, 2004, **60**, 219-227.
35. V. R. Thalladi, R. Boese and H. C. Weiss, *Angew. Chem., Int. Ed.*, 2000, **39**, 918-922.
36. F. Hanke, C. J. Pugh, E. F. Kay, J. B. Taylor, S. M. Todd, C. M. Robertson, B. J. Slater and A. Steiner, *Chem. Comm.*, 2018, **54**, 6012-6015.
37. A. G. P. Maloney, P. A. Wood and S. Parsons, *CrystEngComm*, 2014, **16**, 3867-3882.
38. Sigma-Aldrich, 4,4′-Bipiperidine, https://www.sigmaaldrich.com/catalog/product/aldrich/705845?lang=en&region=GB, (accessed 27/01/2020, 2020).
39. D. Vedal, O. H. Ellestad, P. Klaboe and G. Hagen, *Spectrochim. Acta, Part A*, 1976, **32**, 877-890.
40. A. Das, N. A. M. Gadalla, S. Kudchadker, K. N. Marsh, A. S. Rodgers and R. C. Wilhoit, *J. Phys. Chem. Ref. Data*, 1993, **22**, 659-782.
41. A. Aucejo, S. Loras, R. Munoz, J. Wisniak and H. Segura, *J. Chem. Eng. Data*, 1997, **42**, 1201-1207.
42. M. Dominguez, S. Martin, H. Artigas, M. C. Lopez and F. M. Royo, *J. Chem. Eng. Data*, 2002, **47**, 405-410.
43. J. Xiao, M. Yang, J. W. Lauher and F. W. Fowler, *Angew. Chem., Int. Ed.*, 2000, **39**, 2216-2219.

5. Bismuth Complexes of 10,12-Pentacosadiynoic Acid

5.1. Introduction

Bismuth was once considered as one of the most stable heavy element in the periodic table.[1-3] The most common oxidation state of bismuth is +3, though oxidation states of −3 to +5 also exist.[4] Bismuth is non-toxic and non-carcinogenic and its compounds are used in medicine to treat conditions such as leishmaniasis,[5-8] gastritis caused by *Helicobacter pyrlori*,[9-12] and cancer.[13-16] Because of the high atomic number of bismuth (Z = 83),[17] bismuth nanoparticles can be used as radiation sensitisers to amplify radiation dose.[18-20] This property of bismuth makes it attractive in dosimetry technologies and can be utilised by incorporating bismuth into dosimeter films to enhance their photosensitivity, which has been explored in a medical setting.[21-25] For this reason, it is of significant interest to synthesise bismuth complexes with radiation-sensitive ligands, with PCDA as an important example. To investigate if any bismuth complexes of aliphatic long-chain carboxylates are present in the literature, a CSD search for bismuth carboxylates was undertaken with three different sets of criteria, outlined in Figure 5.1. The search of a bismuth atom with a minimum of one coordinated carboxylate ligand (monodentate coordination, Type A) resulted in 290 hits, while two carboxylate ligands coordinated to one metal atom (Type B) resulted in 215 entries, while only one carboxylate ligand chelating to one bismuth atom (Type C) resulted in 305 hits. Lastly, a search for a bidentate coordination of one carboxylate ligand bound to two bismuth atoms (Type D) resulted in a total 230 hits. For all structure types, the resulting hits were largely dominated by carboxylate ligands with aromatic substituents. No *n*-alkyl carboxylate ligands were found in either of the four different searches. Specific examples of Type A, B, C, and D structures and structures of a mixture of types found in the CSD are discussed below.

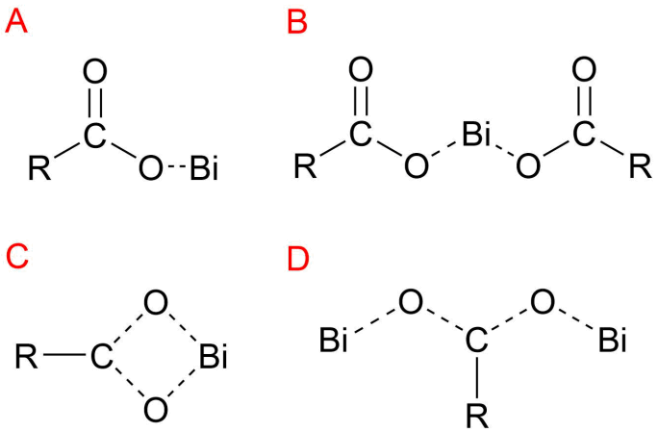

Figure 5.1. The search criteria for bismuth carboxylates in the CSD. Type A involves monodentate coordination from one carboxylate ligand to one bismuth atom. Type B includes bismuth bound to a minimum of two carboxylate ligands. Type C displays a chelating coordination to the bismuth atom with one carboxylate ligand. Type D displays a bidentate coordination of one carboxylate ligand to two bismuth atoms. The dashed line denotes 'any bond type', while 'R' denotes either a carbon or hydrogen atom.

An example of a Type A (monodentate) coordination is the structure of a bismuth(III) centre with an ethanoate ligand and a tetradentate ligand of N,N'-dimethyl-N,N'-bis(2-thiolatoethyl)ethane-1,2-diamine (Figure 5.2).[26] The Bi-O distance is 2.38 Å, while the Bi-S distances are 2.53 Å and 2.58 Å, and the Bi-N distances are 2.56 Å and 2.79 Å, respectively. The bismuth centre displays a distorted pentagonal pyramidal geometry due to the stereochemically active valence lone pair of electrons.[26]

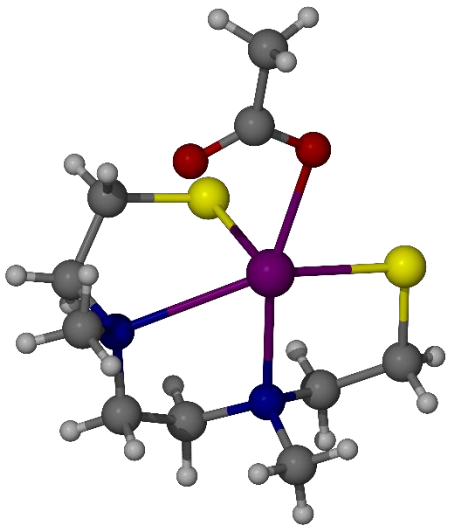

Figure 5.2. The X-ray structure of ethanoxy-(N,N'-dimethyl-N,N'-bis(2-thiolatoethyl)ethane-1,2-diamine)-bismuth(III).

An example of a Type B structure involves a bismuth(V) atom bound to three phenyl groups and two methanoate groups (Figure 5.3). Crystals of triphenylbismuth(V) dimethanoate grew from acetone under ambient conditions.[27] The X-ray structure reveals a distorted trigonal bipyramidal geometry. The distances between the bismuth centre and the bonded carbon atom of the phenyl groups are 2.19 Å and 2.23 Å, while the distances between the bismuth atom and the carboxyl oxygen atom of methanoate are 2.27 Å. The bond distances are comparable to those of triphenyl bismuth(V) bis(trifluoroacetate).[28]

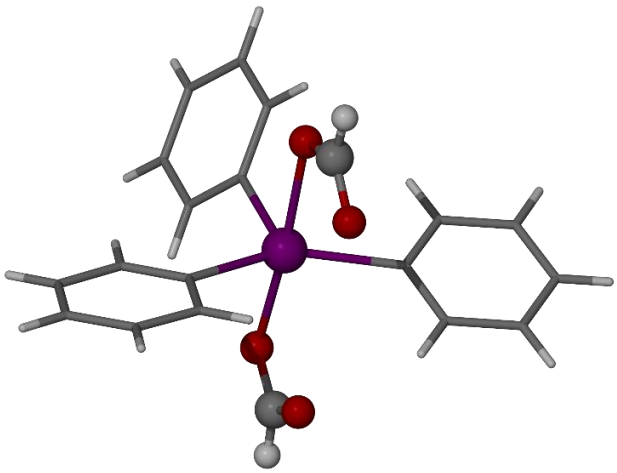

Figure 5.3. The X-ray structure of bis(methanoato)-triphenyl-bismuth(V).[27] The phenyl rings are rendered in a stick arrangement for clarity.

A Type C example involves a complex of bis(pyridine)bismuth(III) triethanoate which forms an eight-coordinated structure and has a distorted dodecahedron geometry (Figure 5.4) (which has been observed for other bismuth complexes).[29-31] Six of the eight coordination sites are filled by ethanoate ligands.[29] The distances from the bismuth atom to the oxygen atoms of the ethanoate ligands range between 2.25 Å and 2.80 Å while the distances from the metal centre to the nitrogen atoms of the pyridyl rings are at distances of 2.53 Å and 2.62 Å.

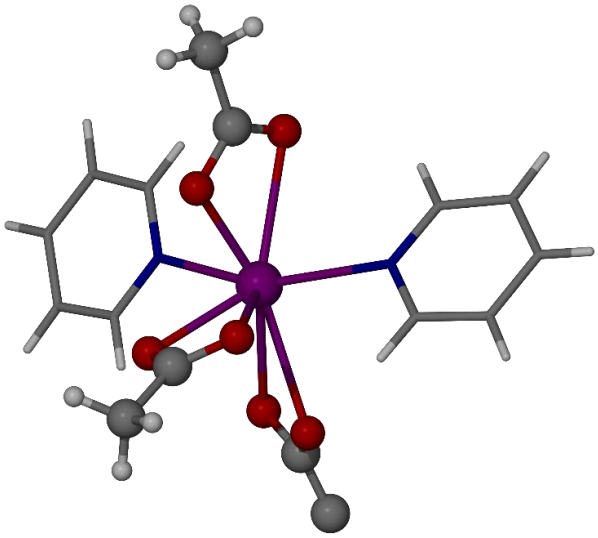

Figure 5.4. The X-ray structure of tris(ethanoato-O,O')-bis(pyridine-N)-bismuth(III).[29] The piridyl rings are rendered in a stick arrangement for clarity. The positions of the hydrogen atoms of one methyl group of ethanoate ligands were not determined.

A Type D structure involves bidentate coordination to the metal centre, with an example of bismuth(II) trifluoroacetate. Crystals of bismuth(II) trifluoroacetate are well-defined and rhombohedral in shape, though when exposed to air turn red and rapidly degrade to metallic bismuth over time, however, crystals can be preserved in solvents (mainly benzene, xylene, toluene) under an inert atmosphere at low temperatures for long periods of time.[32] The X-ray structure reveals two crystallographically independent dibismuth(II) tetrabridged units of trifluoroacetate, with each metal centres in distorted square pyramidal geometries with one bismuth atom and four oxygen atoms (Figure 5.5). One of the independent units resides on an inversion centre. The Bi-Bi distances are 2.94 Å and 2.96 Å, while the Bi-O distances

range from 2.34 Å to 2.43 Å and are typical distances when compared to similar bismuth(II) and bismuth(III) complexes that also exhibit a paddle wheel structure.[32-34]

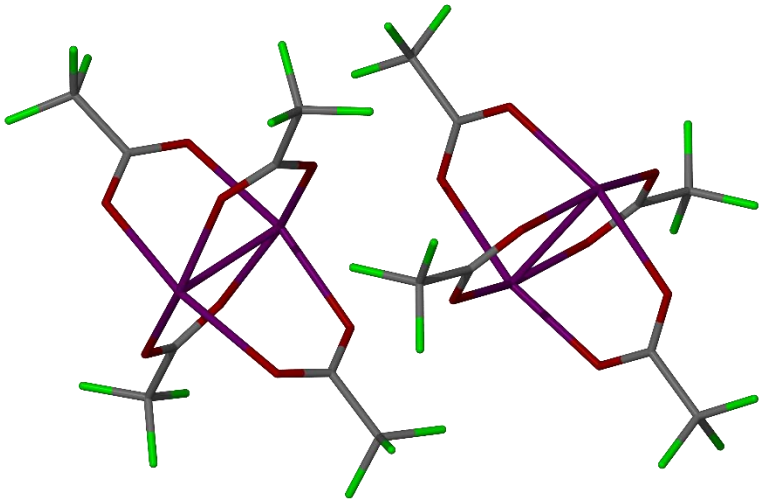

Figure 5.5. The X-ray structure of tetrakis(μ2-trifluoroethanoato-O,O')-di-bismuth(II) displaying both crystallographically independent structures in the unit cell rendered in a stick arrangement for clarity.[32]

Structures in the CSD also involve more than one carboxylate bonding type to the metal centre. For instance, the X-ray structure of bismuth(III) 2,5-pyridinedicarboxylate salt hydrate with a monoprotonated 2,5-pyridinedicarboxylic acid ligand. Crystals (stable to moisture unlike the bismuth(II) complexes discussed above) of a prism morphology formed from the cooling of a reaction mixture of bismuth(III) nitrate pentahydrate and 2,5-pyridinedicarboxylic acid in water.[35] The coordination sphere around the bismuth(III) atom involves five oxygen atoms and two nitrogen atoms to create a distorted polyhedral geometry.[35] The X-ray structure contains Type B and C coordination bonding to the bismuth(III) atom, along with a zigzag pattern of the packing structure, displayed in Figure 5.6. Type B bonding is involved with the monoprotonated and 2,5-pyridinedicarboxylate ligands at Bi-O distances of 2.25 Å and 2.21 Å, respectively. Type C (chelate) bonding occurs from the carboxylate group of the 2,5-pyridinedicarboxylate ligand, at Bi-O distances of 2.39 Å and a longer distance of 2.87 Å. The bismuth(III) centre also coordinates to two nitrogen atom of monoprotonated and 2,5-pyridinedicarboxylate ligands at distances Bi-N of 2.56 Å and 2.54 Å, respectively. Additionally, a water molecule is coordinated to the metal centre at a Bi-O distance of 2.49 Å. Hydrogen bonding also occurs from one of the

hydrogen of the water molecule to the carbonyl oxygen atom of an opposite molecule of a monoprotonated 2,5-pyridinedicarboxylate ligands, at an OH···O distance of 2.66 Å. The hydrogen bond between water and adjacent monoprotonated 2,5-pyridinedicarboxylate ligand results in an overall 3D framework.[35]

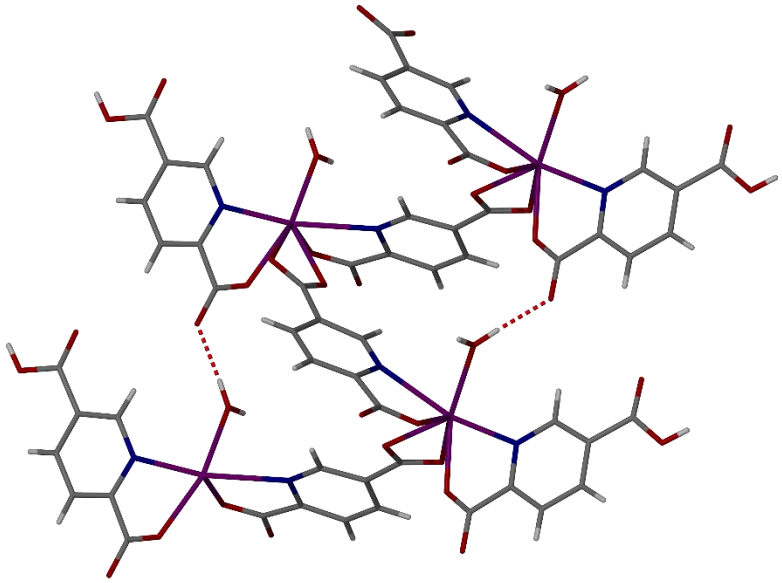

Figure 5.6. The X-ray structure of catena-[(μ_2-pyridine-2,5-dicarboxylato)-aqua-(5-carboxypyridine-2-carboxylato)-bismuth(III)].[35] The structures is rendered in a stick arrangement for clarity of the ligands.

A structure in the CSD that exhibits both Type C and D coordination to a bismuth(III) centre is that of bismuth(III) 2,2-dimethylpropanoate. Crystals of this compound were obtained by slow sublimation in a vacuum-sealed tube placed in a furnace at temperatures below its melting point (164 °C).[36] The X-ray structure reveals crystallographically independent tetrameric units of $Bi(O_2C_5H_9)_3$ (Figure 5.7). The Bi(III) atoms in each tetramer obtain a tetrahedron geometry and each tetramer includes chelating Type C and bidentate Type D coordination. The chelating Bi-O distances range between 2.13 Å and 2.77 Å, while the bidentate Bi-O distances range between of 2.19 Å and 2.52 Å.

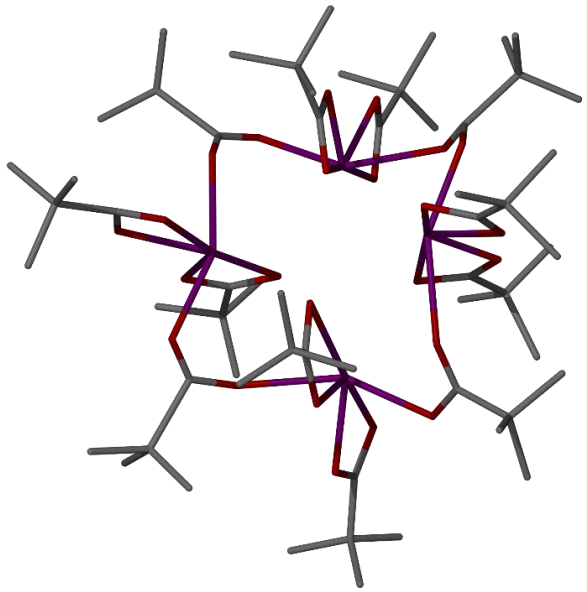

Figure 5.7. The X-ray structure of tetrakis((μ$_2$-2,2-dimethylpropanoato-O,O')-bis(2,2-dimethylpropanoato-O,O')-bismuth(III)), rendered in a stick arrangement for clarity of the ligands.[36] The positions of the hydrogen atoms of the propanoate ligands were not determined.

Lastly, Type B and D coordination is present in structures in the literature with 2,2'2"-nitrilotriacetate (NTA) bismuth(III) dihydrate as an example. Crystals formed from the recrystallisation of this complex from water to give crystals suitable for X-ray analysis. The X-ray structure revealed that the NTA ligand coordinates in a tetradentate arrangement involving the nitrogen atom (a Bi-N distance of 2.50 Å) and three carboxylate oxygen atoms (a Bi-O distances ranging between 2.25 Å and 2.50 Å) (Figure 5.8).[37] The bismuth(III) centre is eight-coordinate, and coordinates to two water molecules (at Bi-O distances of 2.40 Å and 2.77 Å) and to the oxygen atoms of an adjacent NTA bismuth(III) unit (at Bi-O distances of 2.54 Å and 2.67 Å). The bismuth(III) centre is in an intermediate geometry between square antiprism and a dodecahedron arrangement.[37] Hydrogen bonds are also present between one of the hydrogen atoms of a water molecule to the carboxylate oxygen atom of the NTA ligand at a long O···O distance of 2.88 Å, while another hydrogen bond also occurs from the hydrogen atom of the other water molecule to the carbonyl oxygen atom of the NTA ligand, at a shorter O···O distance of 2.64 Å.

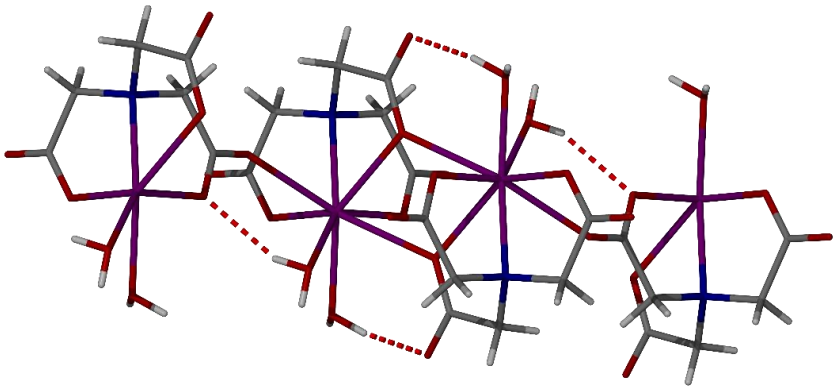

Figure 5.8. The X-ray structure of catena-((μ$_3$-nitilotriethanoato)-di-aqua-bismuth(III)).[37] The structure is rendered in a stick arrangement for the clarity of the ligands.

Based on the CSD results and the lack of bismuth complexes with long-chain aliphatic ligands, the synthesis of bismuth(III) carboxylates with PCDA was undertaken. Bismuth chloride ($BiCl_3$) and triphenylbismuth ($BiPh_3$) were combined with PCDA in solution. Also, bismuth oxide (Bi_2O_3) and aluminium oxide (Al_2O_3) were mechanically ground with the salt Li-PCDA (Form A), with and without LAG using water. It is important to note that this work was started in February 2020 and represents a preliminary study due to the COVID-19 pandemic.

5.2. Results and Discussion

5.2.1. Synthesis of Bismuth Complexes in Solution

A mixture of $BiCl_3$ and PCDA in methanol was stirred at room temperature for seven hours in 1:2 and 1:3 ratios, respectively. The product of the 1:2 reaction was isolated after the solvent was removed under vacuum to give a pale pink powder, while the product of the 1:3 ratio was isolated by filtration and placed on top of a drying oven overnight to remove excess solvent, which also resulted in a pale pink powder. Initial PXRD analyses of $BiCl_3$ and PCDA in both stoichiometries reveal that the 1:2 product is a mixture of PCDA and a new material, evident by the initial peaks at 5.2 ° (new material) and 5.6 ° (which belongs to PCDA), along with additional peaks that do not belong to either $BiCl_3$ or PCDA (Figure 5.9). However, the product of the 1:3 ratio only displays one additional peak that is not present in either of the starting materials, but is present in 1:2 ratio, at a 2θ value of 12.0 °. Therefore, $BiCl_3$ and PCDA in the

1:3 ratio is mostly unreacted PCDA. These findings are also supported by the FTIR analyses of the materials (Figure 5.10). The product in the 1:2 ratio displays similarities with PCDA (such as the CH_2 and CH_3 stretches in the range of 2950 and 2850 cm^{-1}), and reduced intensities of the carbonyl stretch (1691 cm^{-1}), the methylene wagging bands (in the range of 1350 – 1000 cm^{-1}), the C-C(COO) stretch (930 cm^{-1}), and the CH_2 rocking mode (723 cm^{-1}), which suggests the sample is mostly unreacted PCDA. The product also has similarities with $BiCl_3$ due to the broad band at 3471 cm^{-1} (indicative of the O-H stretch of the water impurity in $BiCl_3$) and the band at 1740 cm^{-1}. The FTIR spectra of the 1:3 product and pure PCDA are identical, confirming that it is unreacted PCDA.

The ssNMR spectra of $BiCl_3$ and PCDA in a 1:2 ratio shows multiple additional peaks in the alkane region (14-36 ppm) when compared to the spectrum of PCDA, suggesting multiple differences in the chemical environments of aliphatic chains in the two compounds (Figure 5.11). The positions of the alkyne and carboxylate peaks in the spectra of $BiCl_3$ and PCDA in a 1:2 ratio and PCDA are the same, apart from the intensities of the peaks are increased in the product mixture. Solution crystallisation experiments were also attempted using 10 mg and 20 mg of $BiCl_3$ and PCDA in a 1:2 ratio and (with and without seeds of the same material) dissolved in 2 mL of acetone after brief sonication. After the slow evaporation of solvent over two weeks, no crystals of suitable quality for SC-XRD were obtained, however.

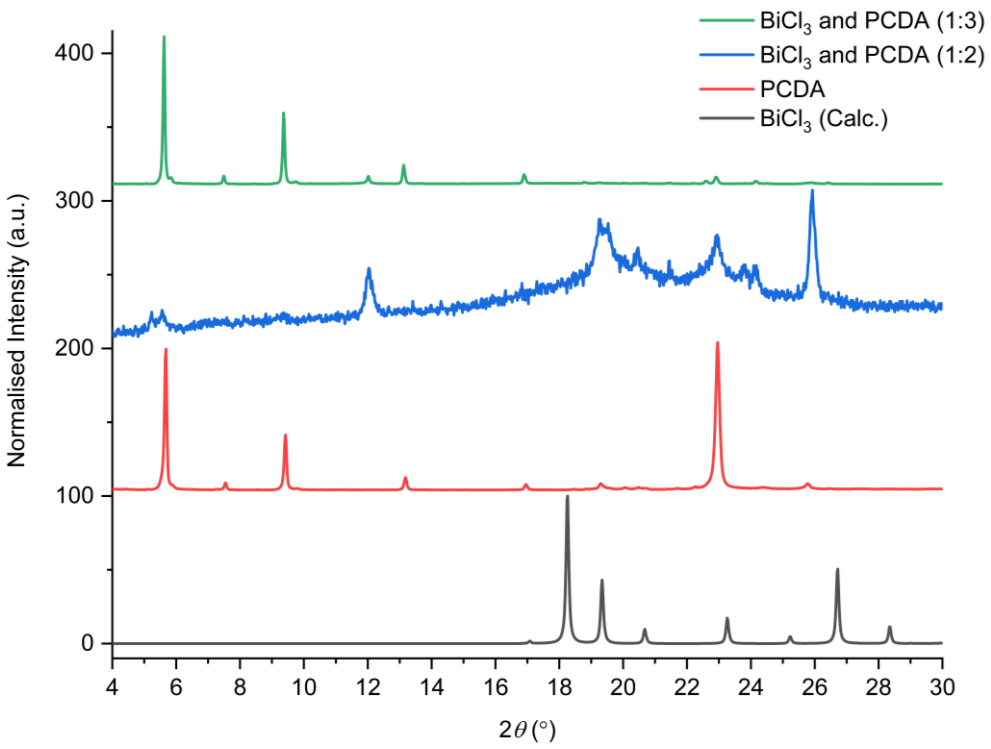

Figure 5.9. The experimental PXRD patterns of PCDA and the products in 1:2 and 1:3 stoichiometries, and the calculated pattern of $BiCl_3$.[38]

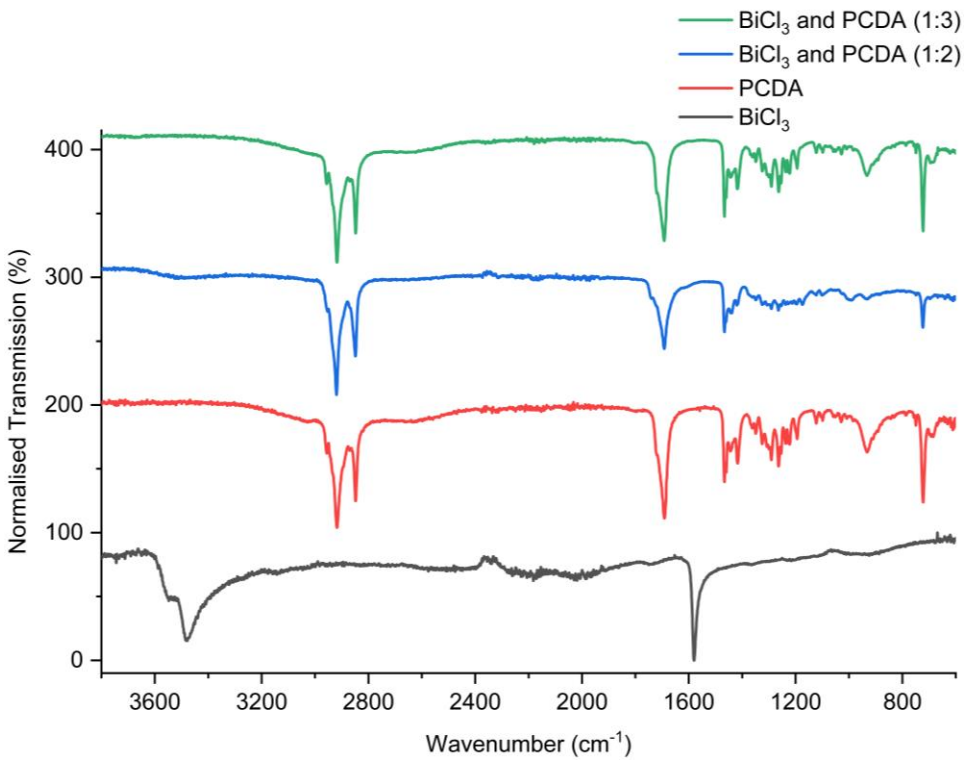

Figure 5.10. The FTIR spectra of $BiCl_3$, PCDA, and the products in 1:2 and 1:3 stoichiometries.

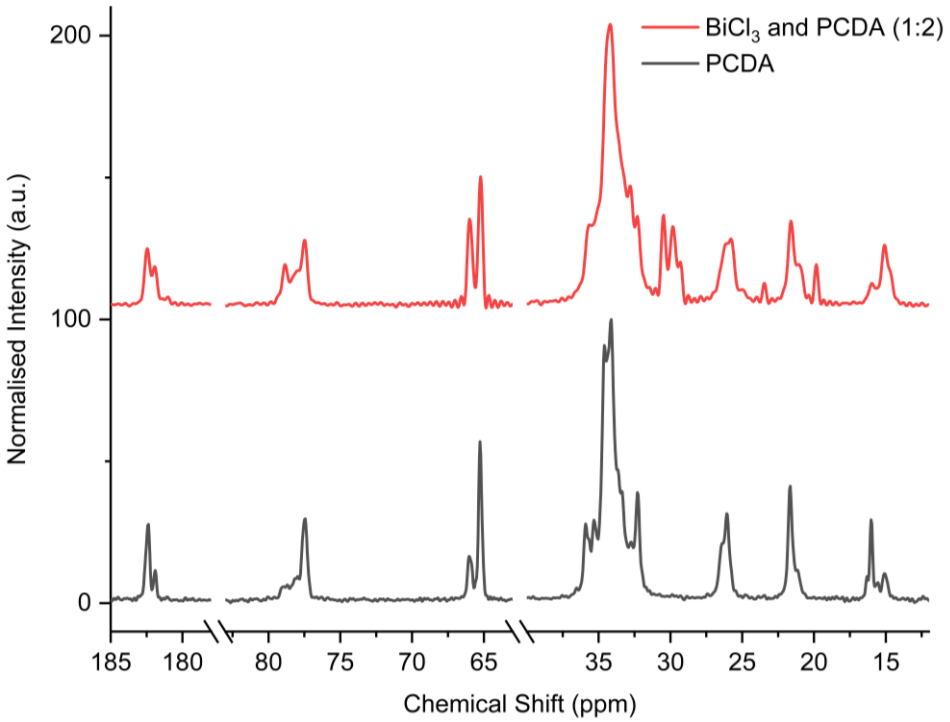

Figure 5.11. The ssNMR spectra of $BiCl_3$ and PCDA in a 1:2 ratio with added breaks in the *x*-axis for comparative purposes.

An important observation of $BiCl_3$ and PCDA in a 1:2 ratio is the colour change from pink to blue when exposed to ambient light for approximately six hours, which was not observed for PCDA alone (Figure 5.12). This finding suggests that the presence of bismuth greatly enhances the photosensitivity of PCDA. To further investigate this, the powder was exposed to UV radiation (254 nm) for varying durations and changed from pale pink to blue after one minute of irradiation, and from light blue to black after one hour (Figure 5.13), whereas PCDA alone turns black after two hours of irradiation. The enhanced photoreactivity of is reflected in the ssNMR spectra, particularly in the alkene region (100 – 130 ppm) (Figure 5.14). From integration of the intensities of the alkyne peaks to the intensities of the alkene peaks, it can be approximated that the monomer to polymer conversion for $BiCl_3$ and PCDA in a 1:2 ratio after one hour is ≤25 % and after one day is ≤45 %, which is greater than for PCDA itself for both durations of UV exposure.

Figure 5.12. Both sides of a glass vial containing $BiCl_3$ and PCDA in a 1:2 ratio and placed under a shelf in the lab for approximately six hours shows a colour change when exposed to ambient light.

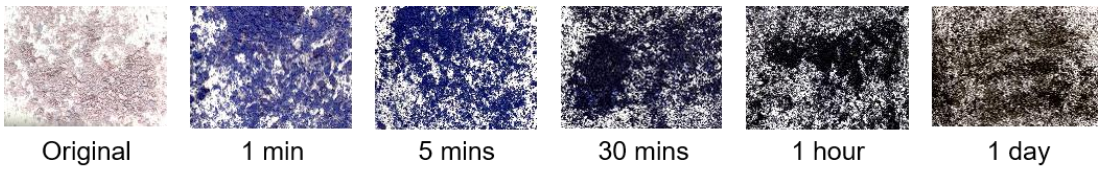

Figure 5.13. Photographs of $BiCl_3$ and PCDA in a 1:2 ratio exposed to UV radiation for one minute up to one day.

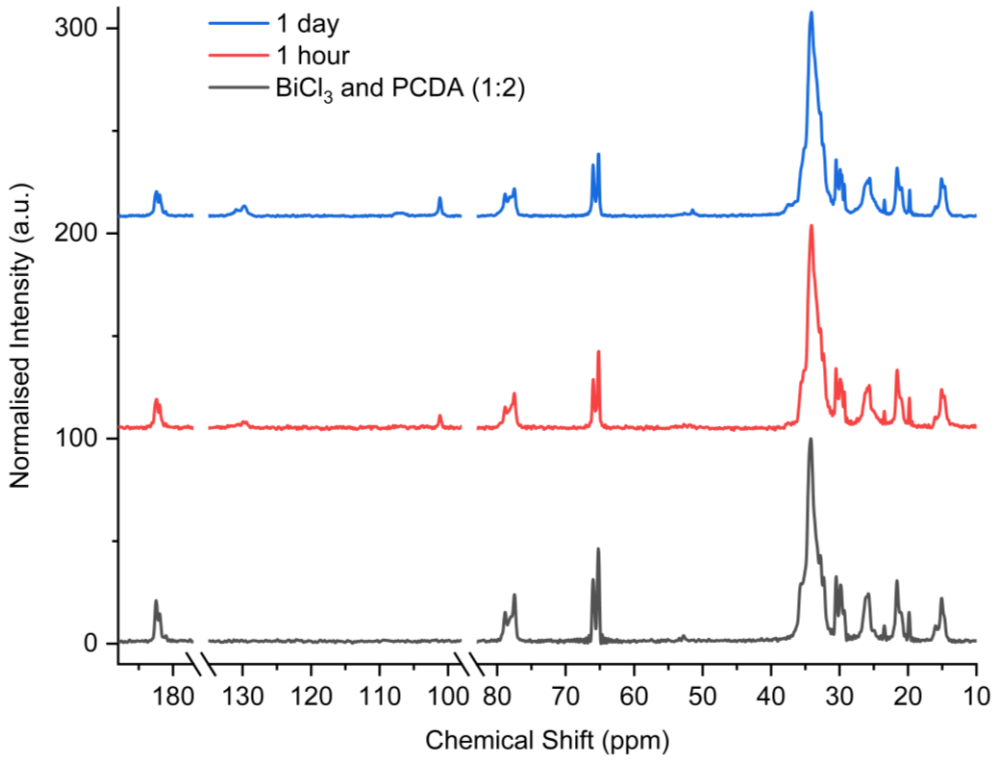

Figure 5.14. The ssNMR spectra of $BiCl_3$ and PCDA in a 1:2 ratio before and after exposure to UV radiation (254 nm) for one hour and one day.

As many of the resulting bismuth carboxylates in the CSD search contain triphenylbismuth, $BiPh_3$ was combined with PCDA in a 1:2 ratio, respectively, in

acetone and stirred at room temperature for seven hours. Excess solvent was removed under vacuum to yield a pale pink powder. The PXRD analysis of $BiPh_3$ combined with PCDA revealed many additional peaks that are not present in the patterns for PCDA or $BiPh_3$ alone (for example the peaks at 6.2, 10.0, 12.1 °), suggesting the formation of a new material (Figure 5.15). However, the FTIR spectrum of $BiPh_3$ combined with PCDA is almost identical to PCDA, apart from the bands that can be attributed to $BiPh_3$, such as the small band at 1569 cm^{-1} and the increased intensity of the band at 692 cm^{-1} (Figure 5.16). Therefore, the PXRD and FTIR analyses suggest that $BiPh_3$ combined with PCDA is a mixture of product and unreacted PCDA. Additionally, solution crystallisation experiments containing 10 mg and 20 mg of the product (with and without seeds of the same material) were dissolved in 2 mL of methanol after brief sonication. After the slow evaporation of solvent over two weeks, no crystals of suitable quality for SC-XRD were obtained. Therefore, further work is required to understand the synthesis and products of $BiPh_3$ and PCDA.

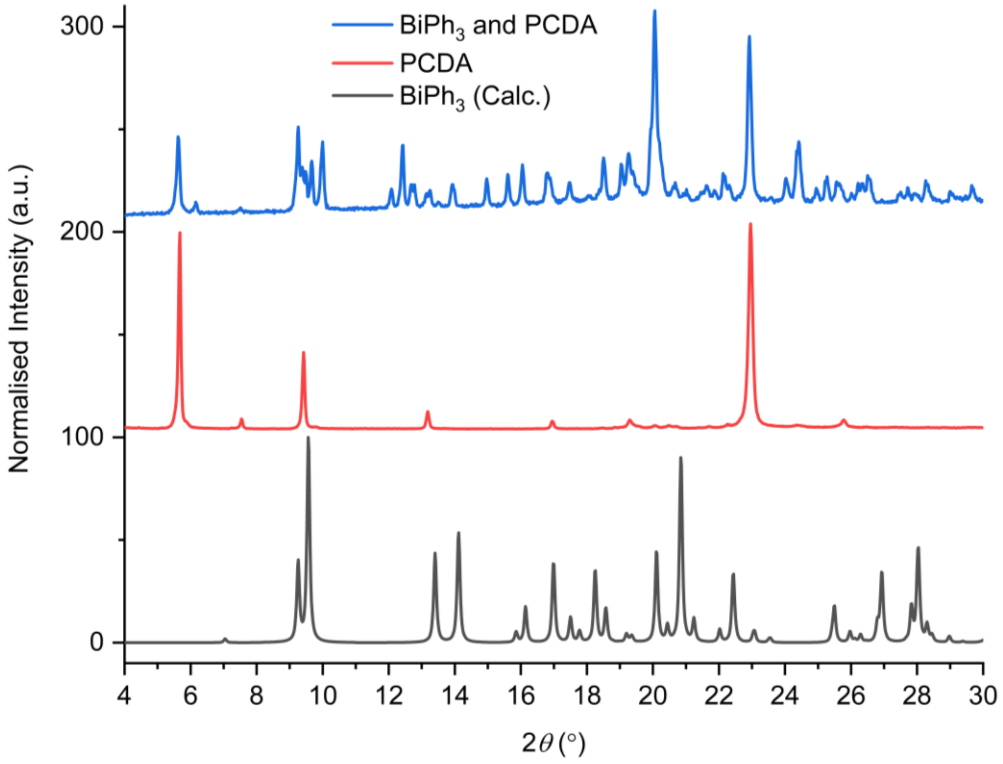

Figure 5.15. The experimental PXRD patterns of PCDA, $BiPh_3$ combined with PCDA, and the calculated pattern of $BiPh_3$.[39]

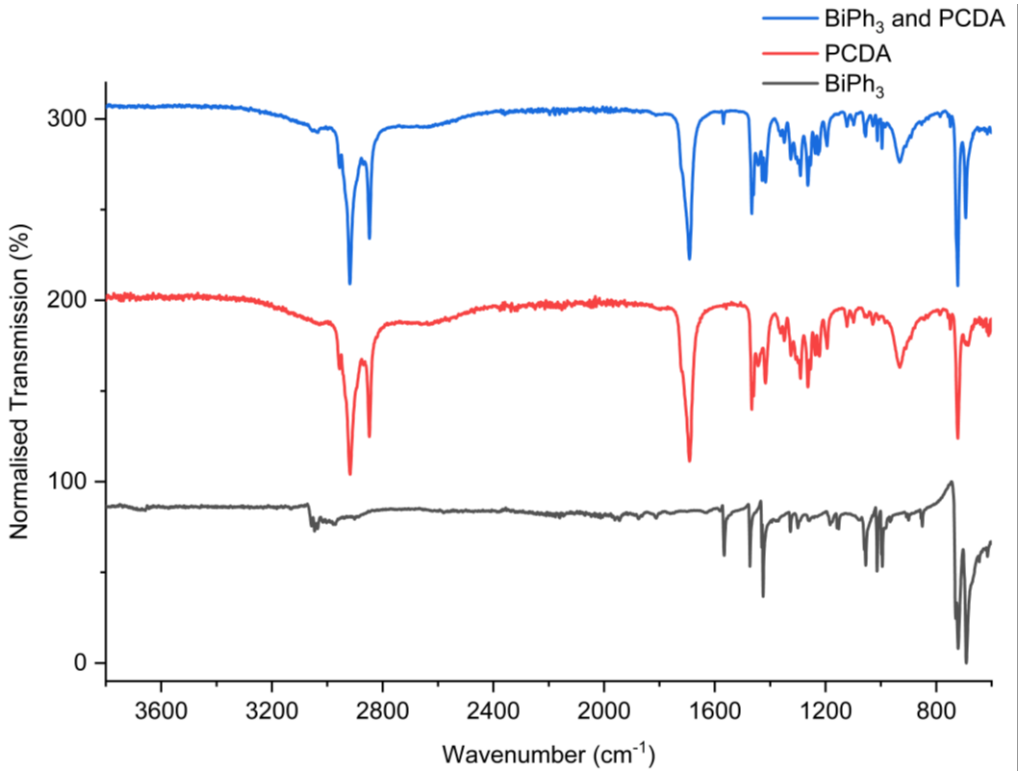

Figure 5.16. The FTIR spectra of $BiPh_3$, PCDA, and the product $BiPh_3 \cdot 2PCDA$.

5.2.2. Synthesis of Bismuth and Aluminium PCDA Complexes by Mechanochemical Grinding

Along with bismuth complexes, aluminium oxide is also radiation sensitive and is often incorporated into various types of dosimeters.[40-44] To contrast the stirring in solution experiments of bismuth chloride and triphenyl bismuth with PCDA, the mechanical grinding of bismuth and aluminium oxide (with and without the liquid assisted grinding of water) was undertaken with the lithium salt of PCDA (Li-PCDA, Form A) in 1:2 ratios, respectively. As Li-PCDA is already deprotonated, it was assumed to be a simple way to react with bismuth and aluminium oxide. The FITR spectra of Bi_2O_3 and Al_2O_3 combined with Li-PCDA with and without LAG display identical spectra to unreacted Li-PCDA (Figure 5.17). As Bi_2O_3 and Al_2O_3 and Li-PCDA with LAG remain unchanged, only the samples without LAG were submitted for PXRD analysis. The PXRD pattern of Bi_2O_3 and Li-PCDA is different to that of Li-PCDA alone (with the addition of the peak at 21.8 °), however, the noisy baseline of makes it difficult to conclude whether the sample is a mixture of a the reagents and a new material (Figure 5.18). The PXRD pattern of Al_2O_3 and Li-PCDA is identical to Li-PCDA. Therefore, grinding Bi_2O_3 and Al_2O_3 with Li-PCDA in a ball

mill did not yield new materials. Thus, the synthesis of Bi_2O_3 and Al_2O_3 with Li-PCDA by solution methods are more likely to result in bismuth carboxylates.

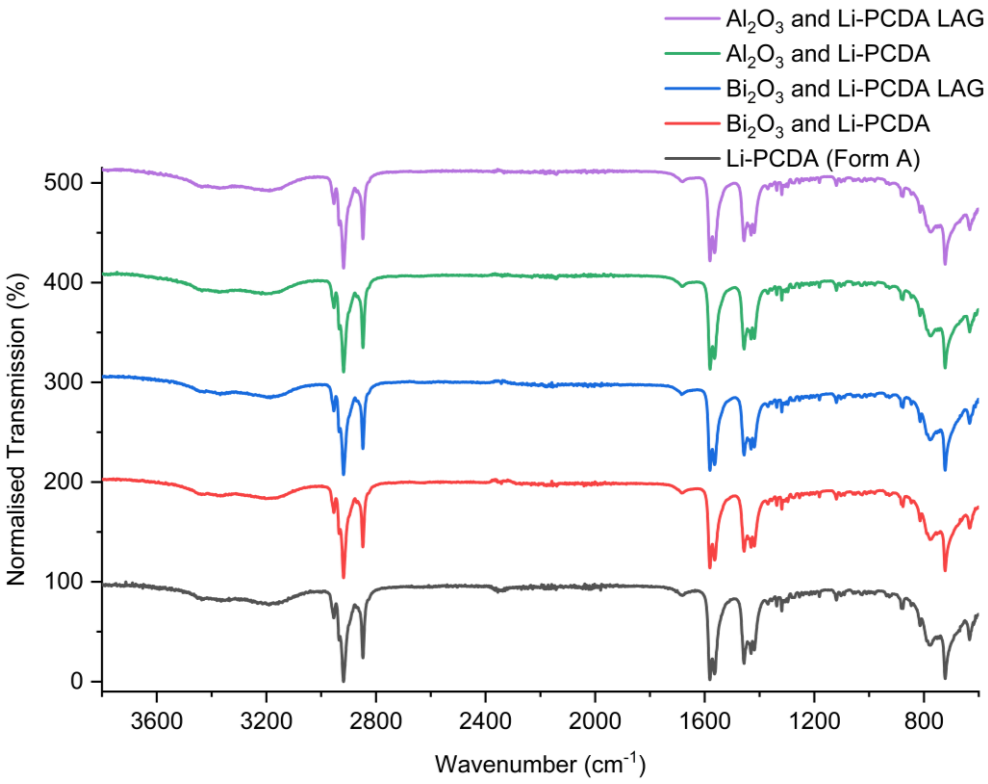

Figure 5.17. The FTIR spectra of Li-PCDA (Form A) combined with Bi_2O_3 and Al_2O_3, synthesised with and without water (LAG). All FTIR spectra are identical to Li-PCDA (Form A).

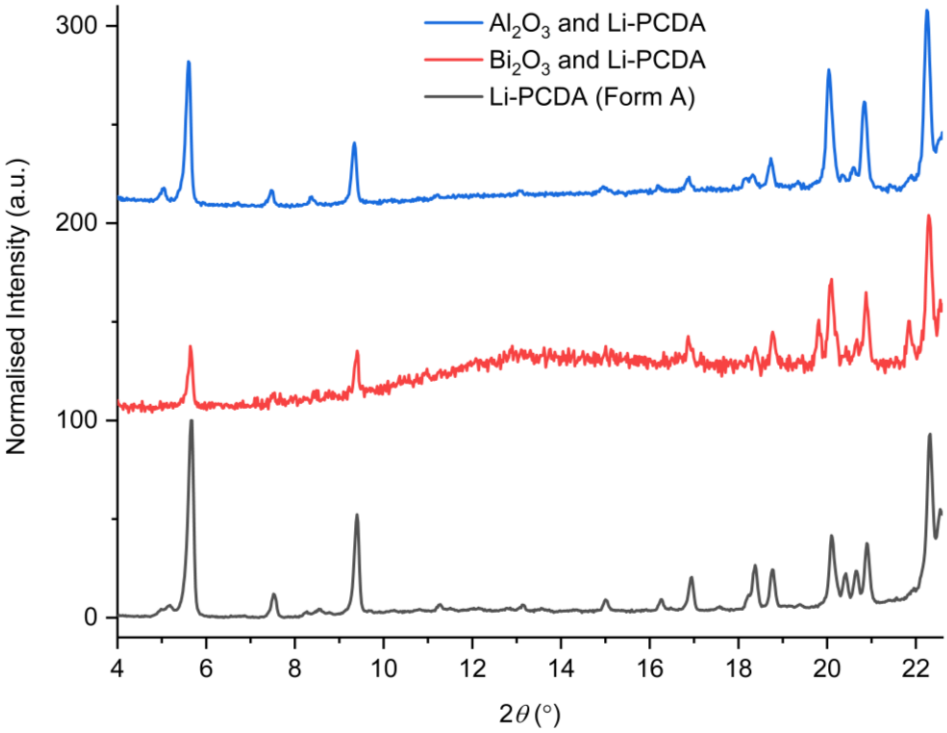

Figure 5.18. The PXRD patterns of Li-PCDA (Form A) combined with Bi_2O_3 and Al_2O_3.

5.3. Conclusion

No aliphatic long-chain bismuth carboxylates are currently reported in the literature. The preliminary results of reacting bismuth chloride with PCDA in a 1:2 ratio, respectively, suggests the formation of a highly photoreactive bismuth(III) PCDA complex, however, additional work is needed to fully characterise the new material. From the limited evidence available, it appears that $BiCl_3$ and PCDA (1:2) and $BiPh_3$ and PCDA (1:2) are mixtures of the starting reagents and did not form a bismuth carboxylate complex. Meanwhile, the reactions of Bi_2O_3 and Al_2O_3 with Li-PCDA in a ball mill with and without liquid assisted grinding, do not result in metal carboxylates and remain as unreacted Li-PCDA. These experiments should be repeated in solution with PCDA in an attempt to synthesise metal carboxylates of PCDA.

5.4. Experimental

Additional information relating to the materials and instrumentation used in this work can be found in Chapter 6.

$BiCl_3$ and PCDA (1:2)

$BiCl_3$ and PCDA was prepared by combining bismuth(III) chloride (0.20 g, 0.63 mmol) and PCDA (0.48 g, 1.27 mmol) in 80 mL of methanol and stirred for seven hours at room temperature with solvent removed under vacuum to give a pale pink powder. PXRD and FTIR analyses indicate a mixture of starting materials and product; FTIR (cm^{-1}): FTIR (cm^{-1}): 3471, 2956 $\nu(CH_3)_{asym}$, 2918 $\nu(CH_2)_{asym}$, 2848 $\nu(CH_3)_{symm}$, 1740, 1691 ν(C=O), 1466 $\delta(CH_2)$, 1439, 1415, 1350 $\omega(CH_2)$, 1326 $\omega(CH_2)$, 1291 $\omega(CH_2)$, 1264 $\omega(CH_2)$, 1222 $\omega(CH_2)$, 1194 $\omega(CH_2)$, 1173, 1124 ν(C-C), 1098 ν(C-C), 991, 933 νC-C(COO), 723 $\rho(CH_2)$.

$BiCl_3$ and PCDA (1:3)

$BiCl_3$ and PCDA was prepared by combining bismuth(III) chloride (0.20 g, 0.63 mmol) and PCDA (0.71 g, 1.90 mmol) in 100 mL of methanol and stirred for seven hours at room temperature. The pink powder was isolated by gravity filtration, however, the PXRD and FTIR analysis indicated that the reaction was unsuccessful; FTIR (cm^{-1}): 2956 $\nu(CH_3)_{asym}$, 2918 $\nu(CH_2)_{asym}$, 2848 $\nu(CH_3)_{symm}$, 1691 ν(C=O), 1467 $\delta(CH_2)$, 1443, 1417, 1350 $\omega(CH_2)$, 1326 $\omega(CH_2)$, 1291 $\omega(CH_2)$, 1264 $\omega(CH_2)$, 1222 $\omega(CH_2)$, 1194 $\omega(CH_2)$, 1124, 1098, 1029, 933 νC-C(COO), 722 $\rho(CH_2)$, 683.

$BiPh_3$ and PCDA

$BiPh_3$ and PCDA was prepared by combining triphenylbismuth(III) (0.15 g, 0.34 mmol) and PCDA (0.25 g, 0.68 mmol) in 60 mL of acetone and stirred for seven hours at room temperature. Excess solvent was removed under vacuum to give a pale pink powder, however, PXRD and FTIR analyses indicate a mixture of starting materials and product; FTIR (cm^{-1}): 3043, 2956 $\nu(CH_3)_{asym}$, 2918 $\nu(CH_2)_{asym}$, 2848 $\nu(CH_3)_{symm}$, 1691 ν(C=O), 1569, 1467 $\delta(CH_2)$, 1443, 1417, 1350 $\omega(CH_2)$, 1326 $\omega(CH_2)$, 1291 $\omega(CH_2)$, 1264 $\omega(CH_2)$, 1222 $\omega(CH_2)$, 1194 $\omega(CH_2)$, 1124, 1098, 1029, 933 νC-C(COO), 722 $\rho(CH_2)$, 692.

Bi_2O_3 and Li-PCDA

Bi_2O_3 and PCDA was prepared by grinding bismuth(III) oxide (0.20 g, 0.43 mmol) and Li-PCDA (Form A) (0.33 g, 0.86 mmol) in a ball mill in a Retsch MM 200 mixer mill for 45 minutes at a frequency of 20 s^{-1} to yield a grey coloured powder. PXRD and FTIR analyses indicate that the reaction was unsuccessful; FTIR (cm^{-1}): 2956 $\nu(CH_3)_{asym}$, 2918 $\nu(CH_2)_{asym}$, 2848 $\nu(CH_3)_{symm}$, 1691 ν(C=O), 1467 $\delta(CH_2)$, 1443,

1417, 1350 ω(CH_2), 1326 ω(CH_2), 1291 ω(CH_2), 1264 ω(CH_2), 1222 ω(CH_2), 1194 ω(CH_2), 1124, 1098, 1029, 933 *ν*C-C(COO), 722 ρ(CH_2), 685. Repeating the mechanochemical grinding of Bi_2O_3·2Li-PCDA with a drop of water to facilitate liquid assisted grinding resulted in the same FTIR analysis without LAG, therefore, no new material was synthesised.

Al_2O_3 and Li-PCDA

Al_2O_3 and PCDA was prepared by grinding aluminium(III) oxide (0.10 g, 0.98 mmol) and Li-PCDA (Form A) (0.75 g, 1.96 mmol) in a ball mill in a Retsch MM 200 mixer mill for 45 minutes at a frequency of 20 s^{-1} to yield a lilac coloured powder. PXRD and FTIR analyses indicate that the reaction was unsuccessful; FTIR (cm^{-1}): 2956 $\nu(CH_3)_{asym}$, 2918 $\nu(CH_2)_{asym}$, 2848 $\nu(CH_3)_{symm}$, 1691 ν(C=O), 1467 δ(CH_2), 1443, 1417, 1350 ω(CH_2), 1326 ω(CH_2), 1291 ω(CH_2), 1264 ω(CH_2), 1222 ω(CH_2), 1194 ω(CH_2), 1124, 1098, 1029, 933 *ν*C-C(COO), 722 ρ(CH_2), 685. Repeating the mechanochemical grinding of Al_2O_3·2Li-PCDA with a drop of water to facilitate liquid assisted grinding resulted in the same FTIR analysis without LAG, therefore, no new material was synthesised.

5.5. References

1. P. J. Sadler, H. Y. Li and H. Z. Sun, *Coord. Chem. Rev.*, 1999, **185-6**, 689-709.
2. J. S. Yadav, A. Antony and B. V. S. Reddy, in *Bismuth-Mediated Organic Reactions*, ed. T. Ollevier, Springer-Verlag Berlin, Berlin, 2012, vol. 311, pp. 229-269.
3. P. de Marcillac, N. Coron, G. Dambier, J. Leblanc and J. P. Moalic, *Nature*, 2003, **422**, 876-878.
4. B. D. Ellis and C. L. B. Macdonald, *Coord. Chem. Rev.*, 2007, **251**, 936-973.
5. P. C. Andrews, R. Frank, P. C. Junk, L. Kedzierski, I. Kumar and J. G. MacLellan, *J. Inorg. Biochem.*, 2011, **105**, 454-461.
6. A. Loh, Y. C. Ong, V. L. Blair, L. Kedzierski and P. C. Andrews, *J. Biol. Inorg. Chem.*, 2015, **20**, 1193-1203.
7. A. Islam, J. G. Da Silva, F. M. Berbet, S. M. da Silva, B. L. Rodrigues, H. Beraldo, M. N. Melo, F. Frezard and C. Demicheli, *Molecules*, 2014, **19**, 6009-6030.
8. M. L. Gomes, G. DeFreitas-Silva, P. G. dos Reis, M. N. Melo, F. Frezard, C. Demicheli and Y. M. Idemori, *J. Biol. Inorg. Chem.*, 2015, **20**, 771-779.
9. J. R. Lambert and P. Midolo, *Aliment. Pharmacol. Ther.*, 1997, **11**, 27-33.
10. D. Y. Graham, Y. C. Lee and M. S. Wu, *Clin. Gastroenterol. Hepatol.*, 2014, **12**, 177-186.

11. E. Roggero, E. Zucca, G. Pinotti, A. Pascarella, C. Capella, A. Savio, E. Pedrinis, A. Paterlini, A. Venco and F. Cavalli, *Ann. Intern. Med.*, 1995, **122**, 767-769.
12. J. C. Thijs, A. A. Vanzwet and H. B. Oey, *Scand. J. Gastroenterol.*, 1993, **28**, 934-938.
13. B. Desoize, *Anticancer Res.*, 2004, **24**, 1529-1544.
14. J. Li, F. Jiang, B. Yang, X. R. Song, Y. Liu, H. H. Yang, D. R. Cao, W. R. Shi and G. N. Chen, *Sci. Rep.*, 2013, **3**, 1-7.
15. M. Kowalik, J. Masternak and B. Barszcz, *Curr. Med. Chem.*, 2019, **26**, 729-759.
16. D. M. Keogan and D. M. Griffith, *Molecules*, 2014, **19**, 15258-15297.
17. K. L. Ai, Y. L. Liu, J. H. Liu, Q. H. Yuan, Y. Y. He and L. H. Lu, *Adv. Mater.*, 2011, **23**, 4886-4891.
18. S. M. Gafar, N. M. Abd El-Kader and T. M. Mohamed, *Radiat. Eff. Defects Solids*, 2020, **175**, 529-539.
19. S. Farahani, N. R. Alam, S. Haghgoo, A. Shirazi, G. Geraily, E. Gorji and N. Kavousi, *Radiat. Phys. Chem.*, 2020, **170**, 1-8.
20. M. Alqathami, A. Blencowe, U. J. Yeo, R. Franich, S. Doran, G. Qiao, M. Geso and Iop, in *7th International Conference on 3d Radiation Dosimetry*, 2013, vol. 444.
21. M. H. Faghfoori, H. Nosrati, H. Rezaeejam, J. Charmi, S. Kaboli, B. Johari and H. Danafar, *Int. J. Pharm.*, 2020, **582**, 1-9.
22. A. Rajaee, S. Wang, L. Y. Zhao, D. Wang, Y. Q. Liu, J. J. Wang and K. Ying, *Phys. Med. Biol.*, 2019, **64**, 1-11.
23. R. Y. Zhou, H. M. Wang, Y. F. Yang, C. Y. Zhang, X. H. Dong, J. F. Du, L. Yan, G. J. Zhang, Z. J. Gu and Y. L. Zhao, *Biomaterials*, 2019, **189**, 11-22.
24. F. Abhari, J. Charmi, H. Rezaeejam, Z. Karimimoghaddam, H. Nosrati, H. Danafar and A. Farajollahi, *ACS Sustainable Chem. Eng.*, 2020, **8**, 5260-5269.
25. H. Wang, X. Y. Mu, H. He and X. D. Zhang, *Trends Pharmacol. Sci.*, 2018, **39**, 24-48.
26. G. G. Briand, A. Decken, W. Shannon and E. E. Trevors, *Can. J. Chem.*, 2018, **96**, 561-569.
27. H. Suzuki, T. Ikegami, Y. Matano and N. Azuma, *J. Chem. Soc., Perkin Trans. 1*, 1993, 2411-2415.
28. G. Ferguson, B. Kaitner, C. Glidewell and S. Smith, *J. Organomet. Chem.*, 1991, **419**, 283-291.
29. T. J. Boyle, D. M. Pedrotty, B. Scott and J. W. Ziller, *Polyhedron*, 1998, **17**, 1959-1974.
30. M. X. Li, Y. L. Lu, M. Yang, Y. K. Li, L. Z. Zhang and S. Q. Xie, *Dalton Trans.*, 2012, **41**, 12882-12887.
31. O. Anjaneyulu, T. K. Prasad and K. C. K. Swamy, *Dalton Trans.*, 2010, **39**, 1935-1940.
32. E. V. Dikarev and B. Li, *Inorg. Chem.*, 2004, **43**, 3461-3466.
33. W. Frank, V. Reiland and G. J. Reiss, *Angew. Chem., Int. Ed.*, 1998, **37**, 2984-2985.
34. E. V. Dikarev, T. G. Gray and B. Li, *Angew. Chem., Int. Ed.*, 2005, **44**, 1721-1724.
35. A. C. Wibowo, M. D. Smith and H. C. zur Loye, *Cryst. Growth Des.*, 2011, **11**, 4449-4457.

36. S. I. Troyanov and A. P. Pisarevsky, *J. Chem. Soc., Chem. Commun.*, 1993, 335-336.
37. S. P. Summers, K. A. Abboud, S. R. Farrah and G. J. Palenik, *Inorg. Chem.*, 1994, **33**, 88-92.
38. S. C. Nyburg, G. A. Ozin and Szymansk.Jt, *Acta Crystallogr., Sect. B: Struct. Sci., Cryst. Eng. Mater.*, 1971, **B 27**, 2298-&.
39. P. G. Jones, A. Blaschette, D. Henschel and A. Weitze, *Z. Kristallogr.*, 1995, **210**, 377-378.
40. M. M. Mikhailov, T. A. Utebekov and V. V. Neshchimenko, *Radiat. Eff. Defects Solids*, 2013, **168**, 106-114.
41. G. Erfurt, M. R. Krbetschek, T. Trautmann and W. Stolz, *Radiat. Meas.*, 2000, **32**, 735-739.
42. A. R. Beierholm, C. E. Andersen, L. R. Lindvold, F. Kjaer-Kristoffersen and J. Medin, *Radiat. Meas.*, 2008, **43**, 898-903.
43. C. E. Andersen, C. J. Marckmann, M. C. Aznar, L. Botter-Jensen, F. Kjaer-Kristoffersen and J. Medin, *Radiat. Prot. Dosim.*, 2006, **120**, 7-13.
44. L. Bossin, I. K. Bailiff and I. Terry, *Radiat. Meas.*, 2018, **120**, 41-46.

6. Experimental

6.1. Materials

10,12-Pentacosadynoic acid and lithium 10,12-pentacosadiynoate (Li-PCDA) “short hairs” and “long hairs” morphology was supplied by Ashland LLC, with all other reagents and solvents purchased from standard commercial sources and used without further purification.

6.2. Instrumentation

Powder X-Ray Diffraction

Powder X-ray diffraction (PXRD) was performed using a Bruker D8 powder X-ray diffractometer. Samples were mounted on a silicon single-crystal wafer and analysed using CuKα radiation at a wavelength of 1.5406 Å. X-rays were produced using an operating voltage of 40 kV and current of 40 mA. Samples were scanned over an angle range of 2-40 ° 2θ, with a step size of 0.02 ° and a scan rate between 0.5-1.5 s/step.

Single Crystal X-ray Diffraction

Single Crystal X-ray Diffraction (SC-XRD) data were collected by either Dr Dmitry S. Yufit or Dr Andrei Batsanov using one of three methods:

1. At a temperature of 120.0(2) K, using either MoKα or CuKα radiation with wavelengths of 0.71073 Å and 1.54178 Å, respectively, on a Bruker D8 Venture diffractometer (Photon100 CMOS detector, IμS-microsource, focusing mirrors) equipped with a Cryostream 700+ (Oxford Cryosystems) open-flow nitrogen cryostat. Single crystals were coated in perfluoro polyether 225 oil, mounted on a MiTeGen sample holder and placed directly into the precooled cryostream.
2. At a temperature of 120.0(2) K on an XCalibur Agilent, Sapphire3 diffractometer equipped with Cryostream 700 Nitrogen cryostat and using MoKα radiation with a wavelength of 0.71073 Å.
3. At a temperature of 100.0(2) K at I19 beamline (Dectris Pilatus 2M pixel-array photon-counting detector, undulator, graphite monochromator, λ = 0.6889 Å) at the Diamond Light Source, Oxfordshire.

All structures were solved using direct methods and refined by full-matrix least squares on F^2 for all data using SHELXL[1] and OLEX2[2] software.[51] All non-hydrogen atoms were refined with anisotropic displacement parameters. C-H hydrogen atoms were placed in calculated positions, assigned an isotropic displacement factor that is a multiple of the parent carbon atom and allowed to ride. H atoms attached to oxygen atoms were located on the difference map when possible or placed in calculated positions. X-ray powder diffraction patterns were performed on glass slides, using a Bruker AXS D8 Advance diffractometer, with a Lynxeye Soller PSD Detector, using CuKα radiation at a wavelength of 1.5406 Å. CCDC deposition numbers 2000830-2000837.

Fourier Transform Infrared Spectroscopy

Fourier transform infrared spectroscopy (FTIR) was carried out using a Perkin Elmer Spectrum 100 spectrometer, fitted with a diamond universal Attenuated Total Reflectance (ATR) accessory. Eight scans were collected for each sample at a resolution of 2 cm^{-1} over a wavenumber region of 4000 cm^{-1} to 500 cm^{-1}.

Thermogravimetric Analysis

Thermogravimetric analysis (TGA) was carried out by Mr Douglas W. Carswell using a TA Instruments Q 500 TGA analyser. Between 1 and 5 mg of sample was weighed into platinum pans and dry nitrogen was used as the purge gas (flow rate: 60 mL min^{-1}).

Differential Scanning Calorimetry

Differential scanning calorimetry (DSC) was performed by Mr Douglas W. Carswell using a Perkin Elmer 8500 calorimeter, calibrated using an indium standard (melting point onset = 156.6 °C, heat of fusion = 28.57 J g^{-1}). Between 1 and 3 mg of sample was weighed accurately (±0.01 mg) into sealed aluminium pans and dry nitrogen was used as the purge gas (flow rate: 50 mL min^{-1}).

Solid-State Nuclear Magnetic Resonance Spectroscopy

^{13}C Solid-state NMR spectra were recorded at 100.63 MHz using a Bruker Avance III HD spectrometer and a 4 mm magic-angle spinning probe. Spectra were obtained using cross-polarisation with a 20 s recycle delay with 7 ms contact time at ambient probe temperature (approx. 25 °C) at a sample spin rate of 10 kHz with 400 repetitions. Spectral referencing was with respect to an external sample of neat tetramethylsilane.

Elemental Analysis

Elemental analysis was performed by Dr Emily R. Unsworth using an Exeter CE-440 Elemental Analyser.

Mass Spectrometry

Mass spectra data was collected by Dr David Parker. The ASAP technique were recorded using an LCT Premier XE mass spectrometer (Waters Ltd) heating approximately 1 mg of powder isothermally at 350 °C.

Raman Spectroscopy

Raman spectra were collected by Dr Larry Senak of Ashland LLC on a Perkin Elmer Ramanstation 400F with 5-10 accumulations of 10-60 second scans, using an excitation laser with a wavelength of 785 nm.

Ultraviolet Irradiation

The powdered cocrystal and salt samples were placed on filter paper in a dark box and exposed to a 6-Watt handheld UV light at 254 nm or 365 nm. The powdered samples were mixed at regular intervals to ensure an even exposure of the bulk to irradiation.

6.3. References

1. G. M. Sheldrick, *Acta Crystallogr., Sect. C: Struct. Chem.*, 2015, **71**, 3-8.
2. O. V. Dolomanov, L. J. Bourhis, R. J. Gildea, J. A. K. Howard and H. Puschmann, *J. Appl. Crystallogr.*, 2009, **42**, 339-341.

7. Closing Remarks

7.1. Conclusion

The X-ray structure of PCDA is the first reported structure of its kind and along with the short-chain lithium model salts, gives an insight into the structures of the Li-PCDA forms. It is hypothesised that Form A is hydrated and crystallises in a monoclinic space group with a similar lamellar spacing to PCDA itself, while Form B crystallises in a triclinic space group. The coordinated water molecule to the lithium centre changes how the carboxylate chains pack in Form A compared to Form B which subsequently affects the photoreactivity of the Li-PCDA forms. Form A displays a reduced photosensitivity in (which is most like PCDA) and Form B displays an enhanced photoreactivity compared to PCDA and Form A due to the relative positioning of the reactive moieties. An alternative to Li-PCDA is the lithium salt of HDDA as it proves to be more photosensitive than either of the forms of Li-PCDA, evident by the ≤33 % monomer to polymer conversion after one day of UV exposure. The Li-PCDA and Li-HDDA structures must adhere to the topochemical postulate, though no SC-XRD structures were obtained. In contrast, the X-ray structure of Na-PCDA (1:3) has a different bonding environment to Li-PCDA involving monodentate and bridging ligands, though is not sensitive to radiation, thus proving that a structure must comply to all of the topochemical postulate criteria for polymerisation to occur.

Model compounds of short-chain *n*-alkyl carboxylic acids cocrystallised with dipyridyl derivatives (4,4'-azopyridine, 4,4'-bipyridyl, *trans*-1,2-bis(4-pyridyl)ethylene) nicely model the interactions of PCDA with the same bifunctional aromatic compounds, though due to the bulky nature of the coformers, the cocrystals are outside of the optimum criteria for polymerisation. Interestingly, when PCDA is combined with bifunctional aliphatic 4,4'-bipiperidine, a salt is formed that also does not adhere to the topochemical postulate and is consequently photostable. However, PCDA forms salts with aliphatic amines (morpholine, piperidine, ethylenediamine, diethylamine, *n*-butylamine) and all change colour in response to UV radiation (though the photoreactivity of 2PCDA·ethylenediamine was not studied), with 2PCDA·piperidine and 2PCDA·diethylamine displaying the greatest photoconversion from monomer to polymer out of all the PCDA salts. Therefore, these materials are of commercial importance, especially for dosimetric applications. Additionally, the

photoreactivity of PCDA is further enhanced when complexed with bismuth, though additional work is required to fully understand the new material.

7.2. Future work

7.2.1. PCDA Cocrystals and Salts

Results from Chapter 4 show that all dipyridyl compounds (4,4'-azopyridine, 4,4'-bipyridyl, *trans*-1,2-bis(4-pyridyl)ethylene) with PCDA form cocrystals that do not photopolymerise as the topochemical criteria adhered to, and therefore, there is currently no example of a photoreactive PCDA cocrystal. As a result, additional cocrystallisation and salt formation experiments with PCDA were undertaken, with co- and salt formers chosen due to their pK_a values. For cocrystallisation to occur, the ΔpK_a must be less than 2 or 3 log units, while salt formation is expected for a greater difference.[1, 2] The pK_a of PCDA is 4.78.[3] The co- and salt formers shown in Table 7.1 were combined in varying ratios and placed in a ball mill for 45 minutes at a frequency of 20 s^{-1} and the formation of a new material (or not) was confirmed by PXRD, FTIR, and ssNMR analyses. However, the experiments in ratios that did not yield a new material (PCDA with phenazine, mebendazole, piroxicam, cytosine) should be repeated at a different stoichiometry. Additionally, none of the confirmed cocrystals or salts were exposed to UV radiation due to time constraints caused by the COVID-19 pandemic. It is of importance that these stoichiometry and irradiation studies are undertaken to investigate the photoreactivity of each new material, as they may be of commercial interest as the radiochromic ingredient in dosimeters.

Coformer	**ΔpK_a = pK_a (base) – pK_a (acid)**	**Expected new material**	**Ratio (base:acid)**		
			1:1	**1:2**	**1:3**
2-Aminopyridine	6.86[4] – 4.78 = 2.08	Cocrystal			
3-Aminopyridine	5.98[4] – 4.78 = 1.20	Cocrystal			
4-Aminopyridine	8.95[4] – 4.78 = 4.17	Salt			
Pyrazine	0.65[4] – 4.78 = −4.13	Salt			
2-Aminopyrazine	3.07[5] – 4.78 = −1.71	Cocrystal			
Piperazine	9.70[6] – 4.78 = 4.92	Salt			
Phenazine	1.60[4] – 4.78 = −3.18	Cocrystal			
2-Aminopyrimidine	3.68[4] – 4.78 = −1.10	Cocrystal			
Isoniazid	3.50[4] – 4.78 = −1.28	Cocrystal			
Iproniazid	13.66[7] – 4.78 = 8.88	Salt			

Imidazole	6.95[8] – 4.78 = 2.17	Cocrystal			
Mebendazole	5.01[9] – 4.78 = 0.23	Cocrystal			
Piroxicam	5.46[10] – 4.78 = 0.68	Cocrystal			
Cytosine	4.40[4] – 4.78 = −0.38	Cocrystal			

Table 7.1. The co- and salt formers mechanically ground with PCDA for 45 minutes at a frequency of 20 s^{-1}. A green box indicates the formation of a new material at a specific ratio, while a red box suggests that no new material was formed at that ratio. A white box indicates that ratio was not attempted.

Additional future work would also include choosing a coformer or a salt former not already attempted that is likely to contain the OH···N supramolecular synthon. Examples of compounds crystallised with PCDA to form a cocrystal are included in Table 7.2, along with potential salt formers that could further modify the photoreactivity of PCDA. The possibility of a salt cocrystal is not ruled out.

Compound	**ΔpK_a = pK_a (base) – pK_a (acid)**	**Ratio (base:acid)**
Cocrystals		
4-Cyanopyridine	1.90[4] – 4.78 = −2.88	1:1
2-Amino-5-chloropyridine	4.81[11] – 4.78 = 0.03	1:1
Pyridine	5.23[12] – 4.78 = 0.45	1:1
1,3-Di(4-pyridyl)propane	5.42[6] – 4.78 = 0.64	1:2
Salts		
1-Adamantylamine	10.71[13] - 4.78 = 5.93	1:1
Pyrrolidine	11.27[14] - 4.78 = 6.49	1:1
1-(4-Pyridyl)piperazine	10.73[15] – 4.78 = 5.95	1:2
Guanidine	13.60[16] - 4.78 = 8.82	1:3

Table 7.2. Examples of coformers and salt formers that can be combined with PCDA to form cocrystals and salts to further investigate the topochemical postulate of reactivity.

7.2.2. Photosensitive Metal Salts

Following on from Chapter 5, PCDA could be combined with other radiation-absorbing heavy metal elements such as lead, tin, antimony, and thallium, with the aim of synthesising PCDA-heavy metal carboxylates that enhance the photosensitivity of PCDA. The ability to enhance radiation sensitivity is of significant

commercial interest, especially to obtain a wide range of dose and therapy ranges for dosimetric applications.[17, 18]

7.2.3. Supramolecular Photoreactive Gels

Recent work highlights the use of PCDA with L- and D-glutamine to form supramolecular organogels.[19] It was found that enantiomeric and racemic assemblies of the amino acid adjust the packing of the PCDA monomer (and display nanotube, left and right handed twisted ribbons, and nanosheet structures observed by scanning electron microscopy) to result in significant colour differences when exposed to UV radiation. Using a similar methodology outlined in this paper, it may be possible to combine the PCDA cocrystals and (organic and metal) salts with amino acids and gelators to investigate their subsequent photoreactivity in gel media compared to powder form.

7.3. References

1. W.-Q. Tong and G. Whitesell, *Pharm. Dev. Technol.*, 1998, **3**, 215-223.
2. D. J. Berry and J. W. Steed, *Adv. Drug Deliv. Rev.*, 2017, **117**, 3-24.
3. Chemical Book, 10,12-Pentacosadiynoic acid, https://www.chemicalbook.com/ChemicalProductProperty_EN_CB2759393.htm, (accessed 10/08/2020).
4. P. K. Goswami, R. Thaimattam and A. Ramanan, *Cryst. Growth Des.*, 2016, **16**, 1268-1281.
5. AAT Bioquest, pKa and pKb Reference Table, https://www.aatbio.com/data-sets/pka-and-pkb-reference-table, (accessed 11/08/2020).
6. P. K. Goswami, V. Kumar and A. Ramanan, *J. Mol. Struct.*, 2020, **1210**.
7. ChemAxon, Iproniazid, https://www.drugbank.ca/drugs/DB04818, (accessed 11/08/2020).
8. D. D. Perrin, *J. Chem. Soc.*, 1965, 5590-5596.
9. J. M. Chen and T. B. Lu, *Chin. J. Chem.*, 2013, **31**, 635-640.
10. J. Jinno, D. M. Oh, J. R. Crison and G. L. Amidon, *J. Pharm. Sci.*, 2000, **89**, 268-274.
11. K. Thanigaimani, N. C. Khalib, E. Temel, S. Arshad and I. A. Razak, *J. Mol. Struct.*, 2015, **1099**, 246-256.
12. S. L. Johnson and K. A. Rumon, *J. Phys. Chem.*, 1965, **69**, 74-86.
13. R. Roy, J. Deb, S. S. Jana and P. Dastidar, *Chem. - Eur. J.*, 2014, **20**, 15320-15324.
14. C. Castellari, F. Comelli and S. Ottani, *Acta Crystallogr., Sect. C: Cryst. Struct. Commun.*, 2001, **57**, 1182-1183.
15. Chemical Book, 1-(4-Pyridyl)piperazine, https://www.chemicalbook.com/ChemicalProductProperty_EN_CB8417978.htm, (accessed 10/08/2020).

16. C. A. Fitch, G. Platzer, M. Okon, B. Garcia-Moreno and L. P. McIntosh, *Protein Sci.*, 2015, **24**, 752-761.
17. M. Alqathami, A. Blencowe, U. J. Yeo, R. Franich, S. Doran, G. Qiao, M. Geso and Iop, in *7th International Conference on 3d Radiation Dosimetry*, 2013, vol. 444.
18. S. M. Gafar, N. M. Abd El-Kader and T. M. Mohamed, *Radiat. Eff. Defects Solids*, 2020, **175**, 529-539.
19. H. H. Fan, H. J. Jiang, X. F. Zhu, M. S. Zhu, L. Zhang and M. H. Liu, *Eur. Polym. J.*, 2019, **118**, 146-152.

8. Appendices

8.1. Full Crystallographic Information for Structures in Chapter 2

PCDA

Crystal information	
Empirical formula	$C_{25}H_{42}O_2$
Formula weight (g/mol)	374.58
Temperature (K)	100.0
Crystal system	triclinic
Space group	*P*-1
a (Å)	4.5738(3)
b (Å)	5.3909(3)
c (Å)	46.647(3)
α (°)	88.6499(15)
β (°)	88.5073(14)
γ (°)	81.4017(14)
Volume (Å^3)	1136.64(12)
Z	2
ρ_{calc} (g/cm^3)	1.094
μ (mm^{-1})	0.063
F(000)	416.0
Crystal size (mm^3)	0.12 × 0.04 × 0.01
Radiation	Synchrotron (λ = 0.6889)
2Θ range for data collection (°)	1.694 to 58.994
Index ranges	-6 ≤ h ≤ 6, -7 ≤ k ≤ 7, -66 ≤ l ≤ 65
Reflections collected	21023
Independent reflections	6893 [R_{int} = 0.0574, R_{sigma} = 0.0775]
Data/restraints/parameters	6893/0/249
Goodness-of-fit on F^2	1.035
Final R indexes [I>=2σ (I)]	R_1 = 0.0640, wR_2 = 0.1772
Final R indexes [all data]	R_1 = 0.0802, wR_2 = 0.1886
Largest diff. peak/hole (Å^{-3})	0.53/-0.27

Table 8.1. The crystallographic information of PCDA.

Refinement Model Description

Number of restraints - 0, number of constraints - unknown.

Details:

1. Fixed Uiso

At 1.2 times of: All C(H,H) groups

At 1.5 times of: All C(H,H,H) groups

2.a Secondary CH2 refined with riding coordinates:

C2(H2A,H2B), C3(H3A,H3B), C4(H4A,H4B), C5(H5A,H5B), C6(H6A,H6B), C7(H7A,H7B), C8(H8A,H8B), C9(H9A,H9B), C14(H14A,H14B), C15(H15A,H15B), C16(H16A,H16B), C17(H17A,H17B), C18(H18A,H18B), C19(H19A,H19B), C20(H20A,H20B), C21(H21A,H21B), C22(H22A,H22B), C23(H23A,H23B), C24(H24A,H24B)

2.b Idealised Me refined as rotating group:

C25(H25A,H25B,H25C)

Na-PCDA

Crystal information	
Empirical formula	$C_{100}H_{167}NaO_8$
Formula weight (g/mol)	1520.32
Temperature (K)	100.0
Crystal system	triclinic
Space group	*P*-1
a (Å)	5.3007(6)
b (Å)	7.9037(9)
c (Å)	54.510(6)
α (°)	91.674(3)
β (°)	92.680(3)

γ (°)	92.463(4)
Volume (Å^3)	2278.0(4)
Z	1
ρ_{calc} (g/cm^3)	1.108
μ (mm^{-1})	0.068
F(000)	842.0
Crystal size (mm^3)	0.203 × 0.029 × 0.008
Radiation	Synchrotron (λ = 0.6889)
2Θ range for data collection (°)	2.176 to 49.998
Index ranges	-6 ≤ h ≤ 6, -9 ≤ k ≤ 9, -66 ≤ l ≤ 66
Reflections collected	27970
Independent reflections	8701 [R_{int} = 0.1030, R_{sigma} = 0.2141]
Data/restraints/parameters	8701/0/497
Goodness-of-fit on F^2	1.005
Final R indexes [I>=2σ (I)]	R_1 = 0.0998, wR_2 = 0.2260
Final R indexes [all data]	R_1 = 0.1257, wR_2 = 0.2559
Largest diff. peak/hole (Å^{-3})	0.56/-0.38

Table 8.2. The crystallographic information of Na-PCDA.

Refinement Model Description

Number of restraints - 0, number of constraints - unknown.

Details:

1. Fixed Uiso

At 1.2 times of: All C(H,H) groups

At 1.5 times of: All C(H,H,H) groups, All O(H) groups

2. Others

Fixed Sof: H2(0.5)

3.a Secondary CH2 refined with riding coordinates:

C2(H2A,H2B), C3(H3A,H3B), C4(H4A,H4B), C5(H5A,H5B), C6(H6A,H6B), C7(H7A,H7B), C8(H8A,H8B), C9(H9A,H9B), C14(H14A,H14B), C15(H15A,H15B), C16(H16A,H16B), C17(H17A,H17B), C18(H18A,H18B), C19(H19A,H19B), C20(H20A,H20B), C21(H21A,H21B), C22(H22A,H22B), C23(H23A,H23B), C24(H24A,H24B), C2A(H2AA,H2AB), C3A(H3AA, H3AB), C4A(H4AA,H4AB), C5A(H5AA,H5AB), C6A(H6AA,H6AB), C7A(H7AA,H7AB), C8A(H8AA,H8AB), C9A(H9AA,H9AB), C14A(H14C,H14D), C15A(H15C,H15D), C16A(H16C,

H16D), C17A(H17C,H17D), C18A(H18C,H18D), C19A(H19C,H19D), C20A(H20C,H20D),

C21A(H21C,H21D), C22A(H22C,H22D), C23A(H23C,H23D), C24A(H24C,H24D)

3.b Idealised Me refined as rotating group:

C25(H25A,H25B,H25C), C25A(H25D,H25E,H25F)

3.c Idealised tetrahedral OH refined as rotating group:

O2(H2), O3(H3)

8.2. Full Crystallographic Information for Structures in Chapter 3

2ButA·bpe

Crystal information	
Empirical formula	$2(C_4H_8O_2)$ x $C_{12}H_{10}N_2$
Formula weight (g/mol)	358.43
Temperature (K)	120.0
Crystal system	triclinic
Space group	*P*-1
a (Å)	6.5688(4)
b (Å)	6.9189(4)
c (Å)	11.4828(7)
α (°)	78.001(3)
β (°)	78.333(3)
γ (°)	70.295(3)

Volume ($Å^3$)	475.61(5)
Z	1
ρ_{calc} (g/cm^3)	1.251
μ (mm^{-1})	0.087
F(000)	192.0
Crystal size (mm^3)	0.43 × 0.24 × 0.11
Radiation	MoKα (λ = 0.71073)
2Θ range for data collection (°)	6.328 to 58.992
Index ranges	$-9 \leq h \leq 9$, $-9 \leq k \leq 9$, $-15 \leq l \leq 15$
Reflections collected	10103
Independent reflections	2644 [R_{int} = 0.0481, R_{sigma} = 0.0440]
Data/restraints/parameters	2644/0/170
Goodness-of-fit on F^2	1.039
Final R indexes [I>=2σ (I)]	R_1 = 0.0409, wR_2 = 0.1138
Final R indexes [all data]	R_1 = 0.0530, wR_2 = 0.1217
Largest diff. peak/hole ($Å^{-3}$)	0.42/-0.21

Table 8.3. The crystallographic information of 2butA·bpe.

2PentA·bpe

Crystal information	
Empirical formula	$C_{22}H_{30}N_2O_4$
Formula weight (g/mol)	386.48
Temperature (K)	120.0
Crystal system	triclinic
Space group	*P*-1
a (Å)	6.8211(5)
b (Å)	7.1875(6)
c (Å)	11.8334(10)
α (°)	91.310(4)
β (°)	105.957(3)
γ (°)	111.187(3)
Volume ($Å^3$)	515.24(7)

Z	1
ρ_{calc} (g/cm^3)	1.246
μ (mm^{-1})	0.086
F(000)	208.0
Crystal size (mm^3)	0.38 × 0.22 × 0.19
Radiation	MoKα (λ = 0.71073)
2Θ range for data collection (°)	6.136 to 57.988
Index ranges	-9 ≤ h ≤ 8, -9 ≤ k ≤ 9, -16 ≤ l ≤ 16
Reflections collected	10001
Independent reflections	2725 [R_{int} = 0.0282, R_{sigma} = 0.0291]
Data/restraints/parameters	2725/0/187
Goodness-of-fit on F^2	1.072
Final R indexes [I>=2σ (I)]	R_1 = 0.0414, wR_2 = 0.1151
Final R indexes [all data]	R_1 = 0.0534, wR_2 = 0.1211
Largest diff. peak/hole (Å^{-3})	0.41/-0.19

Table 8.4. The crystallographic information of 2pentA·bpe.

2EicoA·azp

Crystal information	
Empirical formula	2($C_{20}H_{40}O_2$) x $C_{10}H_8N_4$
Formula weight (g/mol)	809.24
Temperature (K)	120.0
Crystal system	triclinic
Space group	*P*-1
a (Å)	5.460(3)
b (Å)	6.853(3)
c (Å)	33.412(18)
α (°)	85.955(14)
β (°)	87.011(14)
γ (°)	74.218(15)
Volume (Å^3)	1199.5(11)
Z	1

ρ_{calc} (g/cm^3)	1.120
μ (mm^{-1})	0.070
F(000)	448.0
Crystal size (mm^3)	0.31 × 0.05 × 0.02
Radiation	MoKα (λ = 0.71073)
2Θ range for data collection (°)	4.892 to 53.996
Index ranges	-6 ≤ h ≤ 6, -8 ≤ k ≤ 8, -42 ≤ l ≤ 42
Reflections collected	19656
Independent reflections	5216 [R_{int} = 0.2025, R_{sigma} = 0.2931]
Data/restraints/parameters	5216/0/267
Goodness-of-fit on F^2	0.921
Final R indexes [I>=2σ (I)]	R_1 = 0.0873, wR_2 = 0.1403
Final R indexes [all data]	R_1 = 0.3014, wR_2 = 0.2036
Largest diff. peak/hole (Å^{-3})	0.23/-0.27

Table 8.5. The crystallographic information of 2eicoA·azp.

Refinement Model Description

Number of restraints - 0, number of constraints - unknown.

Details:

1. Fixed Uiso

At 1.2 times of: All C(H) groups, All C(H,H) groups

At 1.5 times of: All C(H,H,H) groups

2.a Secondary CH2 refined with riding coordinates:

C2(H2A,H2B), C3(H3A,H3B), C4(H4A,H4B), C5(H5A,H5B), C6(H6A,H6B), C7(H7A,H7B), C8(H8A,H8B), C9(H9A,H9B), C10(H10A,H10B), C11(H11A,H11B), C12(H12A,H12B), C13(H13A,H13B), C14(H14A,H14B), C15(H15A,H15B), C16(H16A,H16B), C17(H17A,H17B), C18(H18A,H18B), C19(H19A,H19B)

2.b Aromatic/amide H refined with riding coordinates:

C22(H22), C23(H23), C24(H24), C25(H25)

2.c Idealised Me refined as rotating group:

C20(H20A,H20B,H20C)

Azp-Cl

Crystal information	
Empirical formula	$C_{10}H_7ClN_4$
Formula weight (g/mol)	218.65
Temperature (K)	296.15
Crystal system	monoclinic
Space group	$P2_1/c$
a (Å)	3.7694(4)
b (Å)	6.0715(6)
c (Å)	21.0713(19)
α (°)	90
β (°)	93.130(4)
γ (°)	90
Volume (Å^3)	481.52(8)
Z	2
ρ_{calc} (g/cm^3)	1.508
μ (mm^{-1})	0.364
F(000)	224.0
Crystal size (mm^3)	0.36 × 0.15 × 0.03
Radiation	MoKα (λ = 0.71073)
2Θ range for data collection (°)	5.808 to 56.968
Index ranges	-5 ≤ h ≤ 5, -8 ≤ k ≤ 8, -28 ≤ l ≤ 28
Reflections collected	6773
Independent reflections	1204 [R_{int} = 0.0555, R_{sigma} = 0.0405]
Data/restraints/parameters	1204/1/78
Goodness-of-fit on F^2	1.217
Final R indexes [I>=2σ (I)]	R_1 = 0.0678, wR_2 = 0.1464

Final R indexes [all data]	R_1 = 0.0737, wR_2 = 0.1491
Largest diff. peak/hole ($Å^{-3}$)	0.57/-0.53

Table 8.6. The crystallographic information of azp-Cl.

Refinement Model Description

Number of restraints - 1, number of constraints - unknown.

Details:

1. Twinned data refinement

Scales: 0.9848(15) 0.0152(15)

2. Fixed Uiso

At 1.2 times of: All C(H) groups

3. Shared sites

{C2, C2A}{C4A, C4}

4. Restrained distances

Cl1A-C4A 1.73 with sigma of 0.005

5. Uiso/Uaniso restraints and constraints

Uanis(C4A) = Uanis(C4)Uanis(C2) = Uanis(C2A)

6. Others

Fixed Sof: Cl1(0.44) Cl1A(0.06) C2(0.5) C2A(0.5) H2A(0.5) C4(0.5) C4A(0.5)

7.a Riding coordinates:

C1(H1), C5(H5)

7.b Aromatic/amide H refined with riding coordinates:

C2A(H2A), C4(H4)

8.3. Full Crystallographic Information for Structures in Chapter 4

2PCDA·azp

Crystal information		
Temperature (K)	120	260
Empirical formula	$C_{30}H_{46}N_2O_2$	$C_{30}H_{46}N_2O_2$
Formula weight (g/mol)	466.69	466.69
Crystal system	triclinic	triclinic
Space group	*P*-1	*P*-1
a (Å)	5.3544(3)	5.3649(4)
b (Å)	6.8239(4)	6.8410(6)
c (Å)	39.920(2)	40.791(3)
α (°)	87.742(4)	89.513(3)
β (°)	88.869(4)	88.843(3)
γ (°)	75.291(4)	75.671(3)
Volume ($Å^3$)	1409.64(14)	1450.2(2)
Z	2	2
ρ_{calc} (g/cm^3)	1.100	1.069
μ (mm^{-1})	0.522	0.066
F(000)	512.0	512.0
Crystal size (mm^3)	0.32 × 0.09 × 0.02	0.31 × 0.08 × 0.01
Radiation	CuKα (λ = 1.54178)	MoKα (λ = 0.71073)
2Θ range for data collection (°)	4.43 to 137.98	3.994 to 51.992
Index ranges	-6 ≤ h ≤ 6, -7 ≤ k ≤ 8, -48 ≤ l ≤ 48	-6 ≤ h ≤ 6, -8 ≤ k ≤ 8, -50 ≤ l ≤ 50
Reflections collected	33397	19879
Independent reflections	5160 [R_{int} = 0.1445, R_{sigma} = 0.0888]	5727 [R_{int} = 0.0775, R_{sigma} = 0.0985]
Data/restraints/parameters	5160/0/312	5727/0/312
Goodness-of-fit on F^2	1.090	0.964
Final R indexes [I>=2σ (I)]	R_1 = 0.0994, wR_2 = 0.1798	R_1 = 0.0630, wR_2 = 0.1293

Final R indexes [all data]	R_1 = 0.1569, wR_2 = 0.2017	R_1 = 0.1894, wR_2 = 0.1707
Largest diff. peak/hole ($Å^{-3}$)	0.20/-0.20	0.22/-0.17

Table 8.7. The crystallographic information of 2PCDA·azp.

Refinement Model Description for the 120 K Structure

Number of restraints - 0, number of constraints - unknown.

Details:

1. Fixed Uiso

At 1.2 times of: All C(H) groups, All C(H,H) groups

At 1.5 times of: All C(H,H,H,H) groups

2.a Secondary CH2 refined with riding coordinates:

C2(H2A,H2B), C3(H3A,H3B), C4(H4A,H4B), C5(H5A,H5B), C6(H6A,H6B), C7(H7A,H7B), C8(H8A,H8B), C9(H9A,H9B), C14(H14A,H14B), C15(H15A,H15B), C16(H16A,H16B), C17(H17A,H17B), C18(H18A,H18B), C19(H19A,H19B), C20(H20A,H20B), C21(H21A,H21B), C22(H22A,H22B), C23(H23A,H23B), C24(H24A,H24B)

2.b Aromatic/amide H refined with riding coordinates:

C1S(H1S), C2S(H2S), C4S(H4S), C5S(H5S)

2.c Idealised Me refined as rotating group:

C25(H25A,H25B,H25C)

Refinement Model Description for the 260 K Structure

Number of restraints - 0, number of constraints - unknown.

Details:

1. Fixed Uiso

At 1.2 times of: All C(H) groups, All C(H,H) groups

At 1.5 times of: All C(H,H,H) groups

2.a Secondary CH2 refined with riding coordinates:

C2(H2A,H2B), C3(H3A,H3B), C4(H4A,H4B), C5(H5A,H5B), C6(H6A,H6B), C7(H7A,H7B), C8(H8A,H8B), C9(H9A,H9B), C14(H14A,H14B), C15(H15A,H15B), C16(H16A,H16B), C17(H17A,H17B), C18(H18A,H18B), C19(H19A,H19B), C20(H20A,H20B), C21(H21A,H21B), C22(H22A,H22B), C23(H23A,H23B), C24(H24A,H24B)

2.b Aromatic/amide H refined with riding coordinates:

C1S(H1S), C2S(H2S), C4S(H4S), C5S(H5S)

2.c Idealised Me refined as rotating group:

C25(H25A,H25B,H25C)

2PCDA·4bipy

Crystal information		
Temperature (K)	100	260
Empirical formula	$C_{60}H_{92}N_2O_4$	$C_{60}H_{92}N_2O_4$
Formula weight (g/mol)	905.35	905.35
Crystal system	monoclinic	monoclinic
Space group	$P2_1/c$	$P2_1/c$
a (Å)	5.4415(2)	5.4783(3)
b (Å)	8.9535(4)	8.9976(5)
c (Å)	55.673(3)	56.951(4)
α (°)	90	90
β (°)	90.8823(10)	92.506(2)
γ (°)	90	90
Volume (Å^3)	2712.1(2)	2804.5(3)
Z	2	2

ρ_{calc} (g/cm^3)	1.109	1.072
μ (mm^{-1})	0.064	0.065
F(000)	996.0	996.0
Crystal size (mm^3)	0.12 × 0.04 × 0.03	0.42 × 0.15 × 0.08
Radiation	Synchrotron (λ = 0.6889)	MoKα (λ = 0.71073)
2Θ range for data collection (°)	1.418 to 57.994	4.584 to 53.998
Index ranges	-7 ≤ h ≤ 7, -12 ≤ k ≤ 12, -78 ≤ l ≤ 78	-6 ≤ h ≤ 6, -11 ≤ k ≤ 11, -72 ≤ l ≤ 72
Reflections collected	47696	33629
Independent reflections	7923 [R_{int} = 0.0663, R_{sigma} = 0.0476]	6085 [R_{int} = 0.0445, R_{sigma} = 0.0442]
Data/restraints/parameters	7923/0/303	6085/0/303
Goodness-of-fit on F^2	1.069	1.092
Final R indexes [I>=2σ (I)]	R_1 = 0.0529, wR_2 = 0.1510	R_1 = 0.0631, wR_2 = 0.1373
Final R indexes [all data]	R_1 = 0.0562, wR_2 = 0.1553	R_1 = 0.1039, wR_2 = 0.1511
Largest diff. peak/hole (Å^{-3})	0.65/-0.34	0.19/-0.16

Table 8.8. The crystallographic information of 2PCDA·4bipy.

Refinement Model Description for the 100 K Structure

Number of restraints - 0, number of constraints - unknown.

Details:

1. Fixed Uiso

At 1.2 times of: All C(H) groups, All C(H,H) groups

At 1.5 times of: All C(H,H,H) groups

2.a Secondary CH2 refined with riding coordinates:

C2(H2A,H2B), C3(H3A,H3B), C4(H4A,H4B), C5(H5A,H5B), C6(H6A,H6B), C7(H7A,H7B), C8(H8A,H8B), C9(H9A,H9B), C14(H14A,H14B), C15(H15A,H15B), C16(H16A,H16B), C17(H17A,H17B), C18(H18A,H18B), C19(H19A,H19B), C20(H20A,H20B), C21(H21A,H21B), C22(H22A,H22B), C23(H23A,H23B), C24(H24A,H24B)

2.b Aromatic/amide H refined with riding coordinates:

C1S(H1S), C2S(H2S), C4S(H4S), C5S(H5S)

2.c Idealised Me refined as rotating group:

C25(H25A,H25B,H25C)

Refinement Model Description for the 260 K Structure

Number of restraints - 0, number of constraints - unknown.

Details:

1. Fixed Uiso

At 1.2 times of: All C(H) groups, All C(H,H) groups

At 1.5 times of: All C(H,H,H) groups

2.a Secondary CH2 refined with riding coordinates:

C2(H2A,H2B), C3(H3A,H3B), C4(H4A,H4B), C5(H5A,H5B), C6(H6A,H6B), C7(H7A,H7B), C8(H8A,H8B), C9(H9A,H9B), C14(H14A,H14B), C15(H15A,H15B), C16(H16A,H16B), C17(H17A,H17B), C18(H18A,H18B), C19(H19A,H19B), C20(H20A,H20B), C21(H21A,H21B), C22(H22A,H22B), C23(H23A,H23B), C24(H24A,H24B)

2.b Aromatic/amide H refined with riding coordinates:

C26(H26), C27(H27), C29(H29), C30(H30)

2.c Idealised Me refined as rotating group:

C25(H25A,H25B,H25C)

2PCDA·bpe

Crystal information		
Temperature (K)	120	260
Empirical formula	$C_{31}H_{47}NO_2$	$C_{31}H_{47}NO_2$
Formula weight (g/mol)	465.69	465.69
Crystal system	monoclinic	monoclinic
Space group	$P2_1/c$	$P2_1/c$
a (Å)	5.4494(3)	5.4847(4)
b (Å)	8.9235(5)	8.9801(6)
c (Å)	57.441(3)	58.562(4)
α (°)	90	90
β (°)	92.643(2)	90.849(3)
γ (°)	90	90
Volume (Å^3)	2790.2(3)	2884.1(3)
Z	4	4
ρ_{calc} (g/cm^3)	1.109	1.073
μ (mm^{-1})	0.067	0.065
F(000)	1024.0	1024.0
Crystal size (mm^3)	0.36 × 0.31 × 0.23	0.38 × 0.11 × 0.05
Radiation	MoKα (λ = 0.71073)	MoKα (λ = 0.71073)
2Θ range for data collection (°)	4.26 to 56.98	4.174 to 51.992
Index ranges	$-7 \le h \le 7$, $-11 \le k \le 11$, $-74 \le l \le 77$	$-6 \le h \le 6$, $-11 \le k \le 11$, $-71 \le l \le 72$
Reflections collected	34945	35479
Independent reflections	6537 [R_{int} = 0.0635, R_{sigma} = 0.0794]	5644 [R_{int} = 0.1111, R_{sigma} = 0.0964]
Data/restraints/parameters	6537/1/321	5644/0/311
Goodness-of-fit on F^2	1.034	1.030
Final R indexes [I>=2σ (I)]	R_1 = 0.0560, wR_2 = 0.1073	R_1 = 0.0797, wR_2 = 0.1370
Final R indexes [all data]	R_1 = 0.1242, wR_2 = 0.1255	R_1 = 0.1870, wR_2 = 0.1681

Largest diff. peak/hole ($Å^{-3}$)	0.20/-0.28	0.14/-0.18

Table 8.9. The crystallographic information of 2PCDA·bpe.

Refinement Model Description for the 120 K Structure

Number of restraints - 0, number of constraints - unknown.

Details:

1. Twinned data refinement

Scales: 0.707(3) 0.293(3)

2. Fixed Uiso

At 1.2 times of: All C(H) groups, All C(H,H) groups

At 1.5 times of: All C(H,H,H) groups, All O(H) groups

3. Others

Fixed Sof: C6S(0.6) H6S(0.6) C6SA(0.4) H6SA(0.4)

4.a Riding coordinates:

O1(H1)

4.b Secondary CH2 refined with riding coordinates:

C2(H2A,H2B), C3(H3A,H3B), C4(H4A,H4B), C5(H5A,H5B), C6(H6A,H6B), C7(H7A,H7B), C8(H8A,H8B), C9(H9A,H9B), C14(H14A,H14B), C15(H15A,H15B), C16(H16A,H16B), C17(H17A,H17B), C18(H18A,H18B), C19(H19A,H19B), C20(H20A,H20B), C21(H21A,H21B), C22(H22A,H22B), C23(H23A,H23B), C24(H24A,H24B)

4.c Aromatic/amide H refined with riding coordinates:

C1S(H1S), C2S(H2S), C4S(H4S), C5S(H5S), C6S(H6S), C6SA(H6SA)

4.d Idealised Me refined as rotating group:

C25(H25A,H25B,H25C)

Refinement Model Description for the 260 K Structure

Number of restraints - 0, number of constraints - unknown.

Details:

1. Fixed Uiso

At 1.2 times of: All C(H) groups, All C(H,H) groups

At 1.5 times of: All C(H,H,H) groups

2. Others

Fixed Sof: C6S(0.6) H6S(0.6) C7S(0.4) H7S(0.4)

3.a Secondary CH2 refined with riding coordinates:

C2(H2A,H2B), C3(H3A,H3B), C4(H4A,H4B), C5(H5A,H5B), C6(H6A,H6B), C7(H7A,H7B), C8(H8A,H8B), C9(H9A,H9B), C14(H14A,H14B), C15(H15A,H15B), C16(H16A,H16B), C17(H17A,H17B), C18(H18A,H18B), C19(H19A,H19B), C20(H20A,H20B), C21(H21A,H21B), C22(H22A,H22B), C23(H23A,H23B), C24(H24A,H24B)

3.b Aromatic/amide H refined with riding coordinates:

C1S(H1S), C2S(H2S), C4S(H4S), C5S(H5S), C6S(H6S), C7S(H7S)

3.c Idealised Me refined as rotating group:

C25(H25A,H25B,H25C)

2PCDA·bipip

Crystal information	
Empirical formula	$C_{60}H_{104}N_2O_4$
Formula weight (g/mol)	917.45
Temperature (K)	120
Crystal system	triclinic
Space group	*P*-1
a (Å)	5.5770(4)

b (Å)	11.8339(8)
c (Å)	23.0041(15)
α (°)	100.670(2)
β (°)	96.096(2)
γ (°)	103.007(2)
Volume (Å^3)	1436.25(17)
Z	1
ρ_{calc} (g/cm^3)	1.061
μ (mm^{-1})	0.064
F(000)	510.0
Crystal size (mm^3)	0.767 × 0.314 × 0.1
Radiation	MoKα (λ = 0.71073)
2Θ range for data collection (°)	4.388 to 65
Index ranges	-8 ≤ h ≤ 8, -17 ≤ k ≤ 16, -34 ≤ l ≤ 34
Reflections collected	36532
Independent reflections	10400 [R_{int} = 0.0455, R_{sigma} = 0.0478]
Data/restraints/parameters	10400/0/312
Goodness-of-fit on F^2	1.019
Final R indexes [I>=2σ (I)]	R_1 = 0.0497, wR_2 = 0.1263
Final R indexes [all data]	R_1 = 0.0754, wR_2 = 0.1398
Largest diff. peak/hole (Å^{-3})	0.51/-0.26

Table 8.10. The crystallographic information of 2PCDA·bipip.

ButA·morph

Crystal information	
Empirical formula	$C_8H_{17}NO_3$
Formula weight (g/mol)	175.22
Temperature (K)	120.0
Crystal system	monoclinic
Space group	*C*2/*c*
a (Å)	20.0926(14)
b (Å)	8.0678(6)

c (Å)	11.6061(8)
α (°)	90
β (°)	97.064(3)
γ (°)	90
Volume (Å^3)	1867.1(2)
Z	8
ρ_{calc} (g/cm^3)	1.247
μ (mm^{-1})	0.094
F(000)	768.0
Crystal size (mm^3)	0.44 × 0.25 × 0.21
Radiation	MoKα (λ = 0.71073)
2Θ range for data collection (°)	5.446 to 58.994
Index ranges	-27 ≤ h ≤ 27, -11 ≤ k ≤ 11, -16 ≤ l ≤ 16
Reflections collected	13471
Independent reflections	2587 [R_{int} = 0.0313, R_{sigma} = 0.0265]
Data/restraints/parameters	2587/0/177
Goodness-of-fit on F^2	1.023
Final R indexes [I>=2σ (I)]	R_1 = 0.0356, wR_2 = 0.0931
Final R indexes [all data]	R_1 = 0.0505, wR_2 = 0.1011
Largest diff. peak/hole (Å^{-3})	0.36/-0.20

Table 8.11. The crystallographic information of butA·morph

2PCDA·dietam

Crystal information	
Empirical formula	$(C_{25}H_{42}O_2)$ x $(C_{25}H_{41}O_2)^-$ x $C_4H_{12}N^+$
Formula weight (g/mol)	822.30
Temperature (K)	120.0
Crystal system	monoclinic
Space group	*P*2/*n*
a (Å)	9.5968(6)
b (Å)	4.6441(3)
c (Å)	57.520(4)

α (°)	90
β (°)	92.590(2)
γ (°)	90
Volume (Å^3)	2561.0(3)
Z	2
ρ_{calc} (g/cm^3)	1.066
μ (mm^{-1})	0.065
F(000)	916.0
Crystal size (mm^3)	0.5 × 0.12 × 0.1
Radiation	MoKα (λ = 0.71073)
2Θ range for data collection (°)	4.276 to 55.996
Index ranges	-12 ≤ h ≤ 12, -6 ≤ k ≤ 5, -72 ≤ l ≤ 75
Reflections collected	30938
Independent reflections	6051 [R_{int} = 0.0502, R_{sigma} = 0.0501]
Data/restraints/parameters	6051/0/274
Goodness-of-fit on F^2	1.049
Final R indexes [I>=2σ (I)]	R_1 = 0.0561, wR_2 = 0.1217
Final R indexes [all data]	R_1 = 0.0945, wR_2 = 0.1361
Largest diff. peak/hole (Å^{-3})	0.21/-0.18

Table 8.12. The crystallographic information of 2PCDA·dietam.

Refinement Model Description

Number of restraints - 0, number of constraints - unknown.

Details:

1. Fixed Uiso

At 1.2 times of: All C(H,H) groups

At 1.5 times of: All C(H,H,H) groups, All O(H) groups

2. Others

Fixed Sof: H2(0.5)

3.a Secondary CH2 refined with riding coordinates:

C2(H2A,H2B), C3(H3A,H3B), C4(H4A,H4B), C5(H5A,H5B), C6(H6A,H6B), C7(H7A,H7B), C8(H8A,H8B), C9(H9A,H9B), C14(H14A,H14B), C15(H15A,H15B), C16(H16A,H16B), C17(H17A,H17B), C18(H18A,H18B), C19(H19A,H19B), C20(H20A,H20B), C21(H21A,H21B), C22(H22A,H22B), C23(H23A,H23B), C24(H24A,H24B), C26(H26A,H26B)

3.b Idealised Me refined as rotating group:

C25(H25A,H25B,H25C), C27(H27A,H27B,H27C)

3.c Idealised tetrahedral OH refined as rotating group:

O2(H2)

PCDA·butam

Crystal information	
Empirical formula	$C_{29}H_{53}NO_2$
Formula weight (g/mol)	447.72
Temperature (K)	120.0
Crystal system	monoclinic
Space group	$P2_1$
a (Å)	4.5934(6)
b (Å)	56.597(9)
c (Å)	5.5096(6)
α (°)	90
β (°)	99.130(10)
γ (°)	90
Volume (Å^3)	1414.2(3)
Z	2
ρ_{calc} (g/cm^3)	1.051
μ (mm^{-1})	0.064
F(000)	500.0
Crystal size (mm^3)	0.36 × 0.08 × 0.05

Radiation	MoKα (λ = 0.71073)
2Θ range for data collection (°)	7.2 to 53.97
Index ranges	-5 ≤ h ≤ 5, -66 ≤ k ≤ 72, -6 ≤ l ≤ 7
Reflections collected	14179
Independent reflections	5663 [R_{int} = 0.1264, R_{sigma} = 0.2319]
Data/restraints/parameters	5663/22/293
Goodness-of-fit on F^2	1.026
Final R indexes [I>=2σ (I)]	R_1 = 0.1156, wR_2 = 0.2163
Final R indexes [all data]	R_1 = 0.2387, wR_2 = 0.2784
Largest diff. peak/hole ($Å^{-3}$)	0.32/-0.24

Table 8.13. The crystallographic information of PCDA·butam.

Refinement Model Description

Number of restraints - 22, number of constraints - unknown.

Details:

1. Fixed Uiso

At 1.2 times of: All C(H,H) groups, All N(H,H,H) groups

At 1.5 times of: All C(H,H,H) groups

2. Rigid body (RIGU) restrains

C15, C16, C17, C18, C19

with sigma for 1-2 distances of 0.001 and sigma for 1-3 distances of 0.001

3.a Secondary CH2 refined with riding coordinates:

C2(H2A,H2B), C3(H3A,H3B), C4(H4A,H4B), C5(H5A,H5B), C6(H6A,H6B), C7(H7A,H7B), C8(H8A,H8B), C9(H9A,H9B), C14(H14A,H14B), C15(H15A,H15B), C16(H16A,H16B), C17(H17A,H17B), C18(H18A,H18B), C19(H19A,H19B), C20(H20A,H20B), C21(H21A,H21B), C22(H22A,H22B), C23(H23A,H23B), C24(H24A,H24B), C26(H26A,H26B), C27(H27A, H27B), C28(H28A,H28B)

3.b Idealised Me refined as rotating group:

C25(H25A,H25B,H25C), N1(H1A,H1B,H1C), C29(H29A,H29B,H29C)